UNIVERSIDADE DE BRASÍLIA
INSTITUTO DE GEOCIÊNCIAS
PROGRAMA DE PÓS-GRADUAÇÃO EM GEOLOGIA
GEOLOGIA ECONÔMICA E PROSPECÇÃO

Nd–Sr ISOTOPES AND TRACE ELEMENT GEOCHEMISTRY ON HYPOGENE IOCG-ORES: A COMPARATIVE STUDY

"ISÓTOPOS DE ND–SR E GEOQUÍMICA DE ELEMENTOS TRAÇO EM MINERAIS MINÉRIO DE DEPÓSITOS DA CLASSE IOCG: UM ESTUDO COMPARATIVO"

Master Dissertation N°468

Dissertação de Mestrado N°468

Eduardo Esteban Fritis Pérez

This study was financed in part by the Coordenação de Aperfeiçoamento de Pessoal de Nível Superior – Brasil (CAPES) – Finance Code 001

O presente trabalho foi realizado com apoio da Coordenação de Aperfeiçoamento de Pessoal de Nível Superior – Brasil (CAPES) – Código de Financiamento 001

Brasília, DF, Brazil
2021

UNIVERSIDADE DE BRASÍLIA

INSTITUTO DE GEOCIÊNCIAS

PROGRAMA DE PÓS-GRADUAÇÃO EM GEOLOGIA

GEOLOGIA ECONÔMICA E PROSPECÇÃO

Nd–Sr ISOTOPES AND TRACE ELEMENT GEOCHEMISTRY ON HYPOGENE IOCG-ORES: A COMPARATIVE STUDY

"ISÓTOPOS DE ND–SR E GEOQUÍMICA DE ELEMENTOS TRAÇO EM MINERAIS MINÉRIO DE DEPÓSITOS DA CLASSE IOCG: UM ESTUDO COMPARATIVO"

Master Dissertation N°468

Eduardo Esteban Fritis Pérez

A Dissertation submitted in partial fulfillment of the requirements for the degree of Master of Science in Economic Geology and Prospecting at the Instituto de Geociências of the University of Brasilia

Advisor: Dr. Maria Emília Schutesky

Co-advisor: Dr. Jérèmie Garnier

Examination Board: Dr. Fernando Tornos – Spanish National Research Council

Dr. Elton Dantas – UnB

Dr. Claudinei G. de Oliveira – UnB (Substitute)

Brasília, DF, Brazil

January, 2021

Ficha catalográfica elaborada automaticamente,
com os dados fornecidos pelo(a) autor(a)

FF919n

Fritis Pérez, Eduardo Esteban
Nd-Sr ISOTOPES AND TRACE ELEMENT GEOCHEMISTRY ON HYPOGENE IOCG-ORES: A COMPARATIVE STUDY - "ISÓTOPOS DE ND-SR E GEOQUÍMICA DE ELEMENTOS TRAÇO EM MINERAIS MINÉRIO DE DEPÓSITOS DA CLASSE IOCG: UM ESTUDO COMPARATIVO" / Eduardo Esteban Fritis Pérez; orientador Maria Emilia Schutesky; co-orientador Jérèmie Garnier. -- Brasília, 2021.
259 p.

Dissertação (Mestrado - Mestrado em Geologia) -- Universidade de Brasília, 2021.

1. IOCG. 2. Carajás. 3. Candelaria-Punta del Cobre. 4. Sr-Nd isotopes. 5. Ore geochemistry. I. Schutesky, Maria Emilia, orient. II. Garnier, Jérèmie, co-orient. III. Título.

AGRADECIMIENTOS

A *Jehová*, rey de reyes, por guiarme, ser el aliento y sustento más importante en mi vida.

A mis padres *Juan Carlos Fritis* y *Lidia Pérez*, por ser cobijo, incentivo, maestros y amigos en cada etapa de mi vida.

A mis hermanas *Claudia Fritis* y *Fernanda Fritis* por su inmensurable cariño y lealtad.

A *Cristian Kienteca*, por ser esa persona tan difícil pero sumamente especial y única que he conocido.

A mis amadas abuelas *Sonia Matamala* y *Mirna Meléndez*, por siempre amarme.

A mis perros *Pedro*, *Vicente* y *Pablo*, por ser lo mejor de este mundo.

A *Paulo Dornelles* por siempre guiarme, escucharme y hacerme sentir cómodo fuera de mi país natal.

A mi orientadora *Dra. Maria Emilia Schutesky*, por su amistad, por las risas y por la oportunidad de cursar un magister en el extranjero.

A mi co-orientador *Dr. Jérèmie Garnier*, por los análisis ICP-MS.

Al Profesor *Dr. Thiago Jalowitzki*, Profesora *Dra. Natalia Hauser*, y al Profesor *Dr. Fernando Tornos* por su tiempo, y por brindarme una mano ante preguntas bobas que les realice.

A mis amados amigos *Carolina Riquelme*, *Carolina Valdivia*, *Sara Cortés*, *Marcelo Denzer*, *Tatiana Izquierdo*, *Yaritza Robles y Deusavan Costa Filho* porque a pesar de estar a miles de kilómetros de distancia, siempre han estado a mi lado, brindándome apoyo y cariño en los momentos que más lo he necesitado.

A *Aciolene*, *Lucivaldo*, *Ester*, *Silvana*, *Jessica*, *Elisangela*, *Bruna*, *Gabriel*, *Mari* y en general a todos los miembros de la iglesia MIES por orar por mí y mi familia, así como también por hacerme sentir parte de este hermoso país que es Brasil.

O presente trabalho foi realizado com apoio da Coordenação de Aperfeiçoamento de Pessoal de Nível Superior – Brasil (CAPES) – Código de Financiamento 001

A *Compañía Contractual Minera Candelaria* (subsidiaria de *Lundin Mining Corporation*) por brindarme muestras de sondajes de todo el distrito Candelaria-Punta del Cobre, por confiar en mí y por todo el soporte técnico de campo.

A *Minera Mantoverde* (subsidiaria de *Mantos Copper S. A.*) por brindarme muestras de sondajes de todo el distrito Mantoverde, apoyarme y por todo el soporte técnico de campo.

A *Compañía Minera VALE S. A.* por las muestras de sondajes de los depósitos de la Provincia Mineral de Carajás.

A *Minera Pucobre* (*Sociedad Punta del Cobre S. A.*) por las muestras de sondajes de la mina Punta del Cobre.

Al equipo de investigación *Metalogênese do Pré-Cambriano* por su colaboración con muestras de Ernest Henry y Olympic Dam, así como también por su apoyo en la realización de análisis de laboratorio.

A *Lila Ávila* y *Carla Sepulveda* por su incondicional amistad y fundamental apoyo en el muestreo y logística realizado en Minera Candelaria.

Esfuérzate y sé valiente. No temas ni desmayes, que yo soy el Señor tu Dios, y estaré contigo por dondequiera que vayas – Josué 1:6–9.

TABLE OF CONTENTS

LIST OF TABLES

LIST OF FIGURES

RESUMO EXPANDIDO

1. Introdução e justificativa

Os sistemas de óxido de ferro cobre-ouro (IOCG) são uma importante fonte mundial de Fe, Cu e Au, além de que podem conter quantidades significativas de outros elementos (F, P, As, Zn, Ni, Co, Ag, Mo, Ba , U e REE) (p.e., Hitzman et al., 1992; Sillitoe, 2003; Barton, 2014; Jaireth et al., 2014). Caracteristicamente, os sistemas IOCG ocorrem com fases abundantes de óxidos de Fe como magnetita (–mushketovita) e / ou hematita (–especular) em extensas assembléias de alteração Na-Ca (p.e., Haynes, 2000; Sillitoe, 2003; Williams et al., 2005; Skirrow, 2010; Barton, 2014; Chen, 2013; Hu et al., 2020), enquanto que a deposição de minério ocorre durante períodos de deformação estruturalmente controlados (extensional, transtensional ou transpressional) (p.e., Sillitoe, 2003 ; del Real et al., 2018) no Manto Litosférico Subcontinental (SCLM) além de estar espacialmente relaçõados com a produção de magmas alcalinos enriquecidos em voláteis (Groves et al., 2010). No entanto, apesar de suas principais contribuições econômicas fornecerem <5% de Cu e <1% de Au do mundo (Rusk, 2010), os sistemas IOCG são complexos, relativamente raros, e sua distribuição espacial no tempo é um remanescente que ainda não é totalmente decifrada.

No Brasil, a Província Mineral de Carajás no Cráton Amazônico, hospeda a mineralização do tipo IOCG mais antiga no mundo (100–900 Mt @ 0,77–1,4% Cu e 0,28–0,86 g / t Au; Xavier et al., 2017) além de uma grande diversidade de sistemas minerais, como por exemplo, Cu-Au, Au, PGE, Fe, Ni, Cr, Mn e depósitos de Sn-W (por exemplo, Trunfull et al., 2020), que derivam de um geologia Pré-cambriana fortemente debatida. Em relação aos sistemas IOCG, estes são complexos e mostram forte controle estrutural com as zonas de cisalhamento regionais e sistemas de falha perto do contato entre o embasamento e unidades supracrustais que variam em idades Meso a Neoarquiana (p.e., Tavares et al., 2018; Trunfull et al., 2020).

Até a data, a maioria das tentativas apontam para o riftamento intraplaca da crosta continental mais antiga como o ambiente tectônico mais confiável para a formação do sistema IOCG Neoarquiano (p.e., Gibbs et al., 1986; Wirth et al., 1986; DOCEGEO, 1988 ; Olszewski et al., 1989; Lindenmayer, 1990; Macambira, 2003; Groves et al., 2010; Tavares, 2015; Teixeira et al., 2015b; Martins et al., 2017; Tavares et al., 2018; Ganade et al., 2020; Trunfull et al., 2020) enquanto vários autores argumentam sua gênese com tectonismo transtensional relacionado a configurações de subducção (p.e., Meirelles & Dardenne, 1991; Teixeira, 1994; Teixeira & Eggler, 1994; Dardenne et al., 1998; Lindenmayer et al., 2005; Lobato et al., 2005; Zuchetti, 2007; Justo, 2018; Figuereido e Silva et al., 2020; Souza et al., 2020). No entanto, aquelas tentativas parecem não satisfazer na totalidade sua gênese e várias questões permanecem sem resposta.

Junto com este problema, também não há consenso sobre a fonte dos metais. Embora alguns autores apontem para uma origem magmático-hidrotérmica (p.e., de Melo et al., 2019a; Valadão, 2019; Campo, 2020; Pestilho et al., 2020; Schutesky & Oliveira, 2020), fontes endogênicas especializadas (p.e., Tallarico et al., 2005; Pollard, 2006; Grainger et al., 2008) e a combinação de sistemas híbridos envolvendo components de fontes externas também são sugeridos (p.e., Xavier et al., 2008; 2012; Torresi et al. , 2012; Moreto et al., 2015a; b; de Melo et al., 2019a).

A partir disso, este estudo tem como objetivo caracterizar os isótopos Sr–Nd a fim de desvendar os efeitos das distintas configurações tectônicas, tempos geológicos e contaminação crustal na gênese dos depósitos de IOCG, por meio do uso de elementos traços e geoquímica isotópica aplicada em magnetita e calcopirita de diferentes províncias de classe mundial IOCG na Sudamerica. Este tipo de estudo, além de caracterizar a assinatura geoquímica de um determinado depósito, também fornecerá pistas para discussões mais amplas em depósitos brasileiros e chilenos.

2. Métodos

Para caracterizar a assinatura isotópica, foram coletadas amostras de magnetita e calcopirita. Posteriormente, estes foram esmagados em cavacos de 0,5 cm pelo martelo geológico. Separados puros de magnetita e calcopirita foram colhidos manualmente sob um microscópio binocular para selecionar grãos semelhantes em aparência a lascas de tamanho de malha de 60-80 e, em seguida, foram moídos para tamanho de malha de 200 mesh em um almofariz de ágata. As análises isotópicas de Sr-Nd foram realizadas no Laboratório de Geocronologia da Universidade de Brasília, de acordo com o procedimento padrão descrito em Goia & Pimentel (2000). Os pós de sulfetos e magnetita foram diluídos e passados por colunas de troca catiônica para a separação dos elementos de interesse (Sr-Nd), enquanto as alíquotas foram analisadas em espectrômetro de massa de ionização térmica (TIMS) no Laboratório de Geocronologia de la Universidade de Brasília para Sr-Nd. Enquanto as concentrações de metal e REE foram determinadas após diluição adequada usando espectrometria de massa de plasma acoplado indutivamente (ICP-MS), Série X II (Thermo Fisher Scientific) equipado com uma câmera CCT (Collision Cell Technology) no Laboratório HSM (HydroSciences Montpellier, Universités Montpellier, França).

3. Resultados e discussoes

As razões de isótopos iniciais Sr e Nd nos concentrados de calcopirita e magnetita foram expressas em relação ao UR e CHUR e variam de ~ –3,30 a +2,19 e 0,7159 a 0,71973 nos depositos IOCG Neoarquiano e de –11,68 a –9,22 e 0,701802 a 0,75171 nos sistemas de Cu-Au de idade Orosiriana, respectivamente. Esses valores para os depositos IOCG Neoarquiano sugere que os metais derivaram de crosta antiga retrabalhada por meio da lixiviação de Meoarquianos, mas também envolvendo a assimilação e/ou contribuição de componentes derivados do manto juvenil Neoarquiano. Por outro lado, nos sistemas Orosirian Cu-Au as REE e, consequentemente, metais foram derivaram predominantemente de processos de remobilização de fontes crustais Meso a Neoarquianas de longa duração continuamente retrabalhadas por meio de eventos restritos de granitogênese.

As razões de isótopos iniciais Sr e Nd nos concentrados de calcopirita e magnetita foram expressas em relação ao UR e CHUR e variam de ~ + 3,21 a +4,32, e 0,70341 a 0,70465 no distrito IOCG Candelaria-Punta del Cobre. Esses valores sugerem que os metais foram derivados de fontes primitivas de composição semelhante às rochas do arco-vulcânico, provavelmente geradas por heterogeneidades na fonte do manto, ao invés de uma única fonte especializada.

Tudo acima é consistente com que os períodos de incubação prolongados são um fator chave para a dotação de minério, semelhante ao afirmado por Storey & Smith (2017). Assim, independentemente do ambiente tectônico, os deslocamentos tectônicos atuam como um gatilho principal para a deposição de minério, enquanto a partir de dados de elementos traços é sugerido mais composições máficas nos depósitos IOCG e Cu-Au de Carajás do que nos depósitos IOCG andinos.

4. Conclusões

Este estudo forneceu novas pistas sobre a fonte de metais de sistemas IOCG através da combinação de isótopos Sr-Nd e oligoelementos aplicados em minerais Cu-Au e Fe, juntamente com uma extensa compilação de dados da literatura. Com base nessa visão, podemos concluir que:

- A heterogeneidade na origem dos metais da Província Mineral de Carajás pode ser interpretada a partir do gráfico $^{87}Sr/^{86}Sr_i$ contra εNd (t).
- Tempos de residência crustal prolongados em concentrados de magnetita e calcopirita ($T_{DM-IOCG}$ = 3,35-2,74 Ga) e os dados εNd (t) (εNd_{IOCG} = –3,30 a +2,19) sugerem que fluidos e metais mineralizantes iniciais para IOCG Neoarquiano (Salobo, Sequeirinho) , e Alemão), foram provavelmente derivados de crosta antiga retrabalhada através da lixiviação de rochas do embasamento mesoarquiano, embora a assimilação e/ou contribuição de componentes mantélicos juvenis neoarquianos também estivessem envolvidos em sua gênese.
- A geração de magmas especializados em toda a província poderia ter exercido a principal fonte de calor para a circulação regional de fluidos mineralizantes previamente formados, ao invés da fonte de metais.
- A fonte de metal para magnetita e calcopirita nos sistemas Orosirian Cu-Au (TDM Cu-Au = 3,22–2,71 Ga; εNd Cu-Au = –11,68 a –9,22) envolve a derivação de fontes da crosta ígnea arqueana.
- Depósitos do distrito IOCG Candelaria-Punta del Cobre derivaram os metais de fontes primitivas de composição semelhante às rochas vulcânicas de arco, provavelmente por heterogeneidades na fonte do manto, ao invés de uma única fonte especializada.
- Dados de elementos traço e REE sugerem mais composições máficas nos depósitos IOCG e Cu-Au de Carajás do que nos depósitos IOCG andinos.
- Longos períodos de incubação de metais é um requisito para a precipitação de Cu-Au durante as mudanças tectônicas.

.

CHAPTER 1 – INTRODUCTION

1. 1. Introduction & Justification

Iron oxide copper-gold (IOCG) systems are an important world-source of Fe, Cu, and Au and may contain significant amounts of other elements – e.g., F, P, As, Zn, Ni, Co, Ag, Mo, Ba, U and REE (e.g., *Hitzman et al., 1992*; *Sillitoe, 2003*; *Barton, 2014*; *Jaireth et al., 2014*). Characteristically, IOCG systems are associated with abundant Fe-oxides phases as magnetite (–mushketovite) and/or hematite (–specular) in extensive Na-Ca pre-sulfide assemblages (e.g., *Haynes, 2000*; *Sillitoe, 2003*; *Williams et al., 2005*; *Skirrow, 2010*; *Barton, 2014*; *Chen, 2013*; *Hu et al., 2020*), and traditionally, ore deposition took place during structurally-controlled deformation periods – e.g., extensional, transtensional, or transpressional (e.g., *Sillitoe, 2003*; *del Real et al., 2018*) in the partial melting sub-continental lithosphere mantle (SCLM) and are spatially-related with the production of extensive alkaline enriched volatile magmas (*Groves et al., 2010*). However, notwithstanding their major economic contributions supply the <5% and <1% of the world's Cu and Au, respectively (*Rusk, 2010*), IOCG systems are complex, relatively rare, and their spatially-time distribution is a remnant that has not yet been fully deciphered.

In Brazil, the Carajás Mineral Province, Amazon Craton, hosts the oldest IOCG-type mineralization world-wide (100–900 Mt @ 0.77–1.4% Cu and 0.28–0.86 g/t Au; *Xavier et al., 2017*) and a wide diversity of ore systems – i.e., Cu-Au, Au, PGE, Fe, Ni, Cr, Mn, and Sn-W deposits (e.g., *Trunfull et al., 2020*), derived from a hotly debated Precambrian geology. Towards IOCG systems, these are intrinsically complex and show strong structural control throughout regional shear zones and fault systems near the contact between the basement and supracrustal units, which range in ages from Meso-to Neoarchean (e.g., *Tavares et al., 2018*; *Trunfull et al., 2020*).

Thus, most outstanding IOCG systems are located within two tectonothermal domains, from (1) the Northern Copper Belt which encompass Salobo (1,112 Mt @ 0.69 wt% Cu, 0.43 g/t Au, 55 g/t Ag; *de Melo et al., 2019a*), Igarapé Bahia/Alemão (219 Mt @ 1.4 wt% Cu, 0.86 g/t Au; *Tallarico et al., 2005*), Furnas (500 Mt @ 0.7% Cu) and Paulo Afonso (200 Mt @ 1.0 wt% Cu; *de Melo et al., 2019c*). Some other smaller Cu-Au targets are represented by GT-46, Grota Funda (15–40 Mt @ 0.8–1.2%

Cu; *Hunger et al., 2018*) and Bloco Cururu (QT-02 and AN-34 deposits; *de Melo et al., 2019c*), and (2) The Southern Copper Belt, which includes Sossego (Sequeirinho-Pista-Baiano orebody; 245 Mt @ 1.1% Cu, 0.28 g/t Au; *Lancaster-Oliveira et al., 2000*), Cristalino (500 Mt @ 1,0 wt% Cu; 0,3 g/t Au; *Huhn et al., 1999a*), Furnas (500 Mt @ 0.7% Cu; *Jesus, 2016*). Smaller deposits and Cu-Au prospects are represented by, Castanha, Bacaba, Bacuri, Jatobá (355 Mt @ 1.5% Cu, 0.28 g/t Au; *Lancaster-Oliveira et al., 2000*), Visconde, Borrachudos (35 Mt @ 1.0% Cu, 0.28 g/t Au; *da Costa Silva et al., 2015*), Pedra Branca (22.4 Mt @ 0.94% Cu, 0.27 g/t Au; *Mizuno, 2009*) and Pantera (*AVANCOCOPPER, 2018*).

Until the date, most of the attempts point towards the intraplate rifting of older continental crust as the most reliable tectonic environment for the formation of Neoarchean IOCG system (e.g., *Gibbs et al., 1986*; *Wirth et al., 1986*; *DOCEGEO, 1988*; *Olszewski et al., 1989*; *Lindenmayer, 1990*; *Macambira, 2003*; *Groves et al., 2010*; *Tavares, 2015*; *Teixeira et al., 2015b*; *Martins et al., 2017*; *Tavares et al., 2018*; *Ganade et al., 2020*; *Trunfull et al., 2020*) whereas several authors argues their genesis with transtensional tectonism related to subduction settings (e.g. *Meirelles & Dardenne, 1991*; *Teixeira, 1994*; *Teixeira & Eggler, 1994*; *Dardenne et al., 1998*; *Lindenmayer et al., 2005*; *Lobato et al., 2005*; *Zuchetti, 2007*; *Justo, 2018*; *Figuereido e Silva et al., 2020*; *Souza et al., 2020*). However, these do not fully satisfy the economic genesis of the mineral and several questions remain unanswered. Thus, modern hypotheses lean towards a shift from dome and keel tectonics in the Mesoarchean to modern style linear belts in the Neoarchean (e.g., *Oliveira, 2018*; *Costa et al., 2020*; *Ganade et al., 2020*; *Lacasse et al., 2020*).

Austin et al. (2019) summarizes that are three main factors that determine the location and architecture of an IOCG: (1) the fluid pathways, (2) trap/host, and (3) plumbing systems (i.e., mechanisms for depressuring the systems), which are loosely referred to as structural controls, but which exercise very different functions within the system. From that, is relevant to note that no single genetic model explains the formation of the whole spectrum of IOCG deposits. While several studies have proposed that the smaller and rarer Phanerozoic IOCG deposits were formed in tectonic settings where conditions similar to those in the Precambrian were replicated (*Groves et al., 2010*; *Richards & Mumin, 2013a*; *b*; *Groves & Santosh, 2020*) there is no consensus if these latest were formed pre, syn or post supercontinent cycle (Figure 1).

In addition to this plethora, there is also a controversy around the source of metals. Whilst some authors point towards a magmatic-hydrothermal origin for such fluids (e.g., *de Melo et al., 2019a*; *Valadão, 2019*; *Campo, 2020*; *Pestilho et al., 2020*; *Schutesky & Oliveira, 2020*), specialized endogenic sources (e.g., *Tallarico et al., 2005*; *Pollard, 2006*; *Grainger et al., 2008*), and a hybrid hydrothermal system involving externally-derived component are also suggested (e.g., *Xavier et al., 2008*; *2012*; *Torresi et al., 2012*; *Moreto et al., 2015a*; *b*; *de Melo et al., 2019a*).

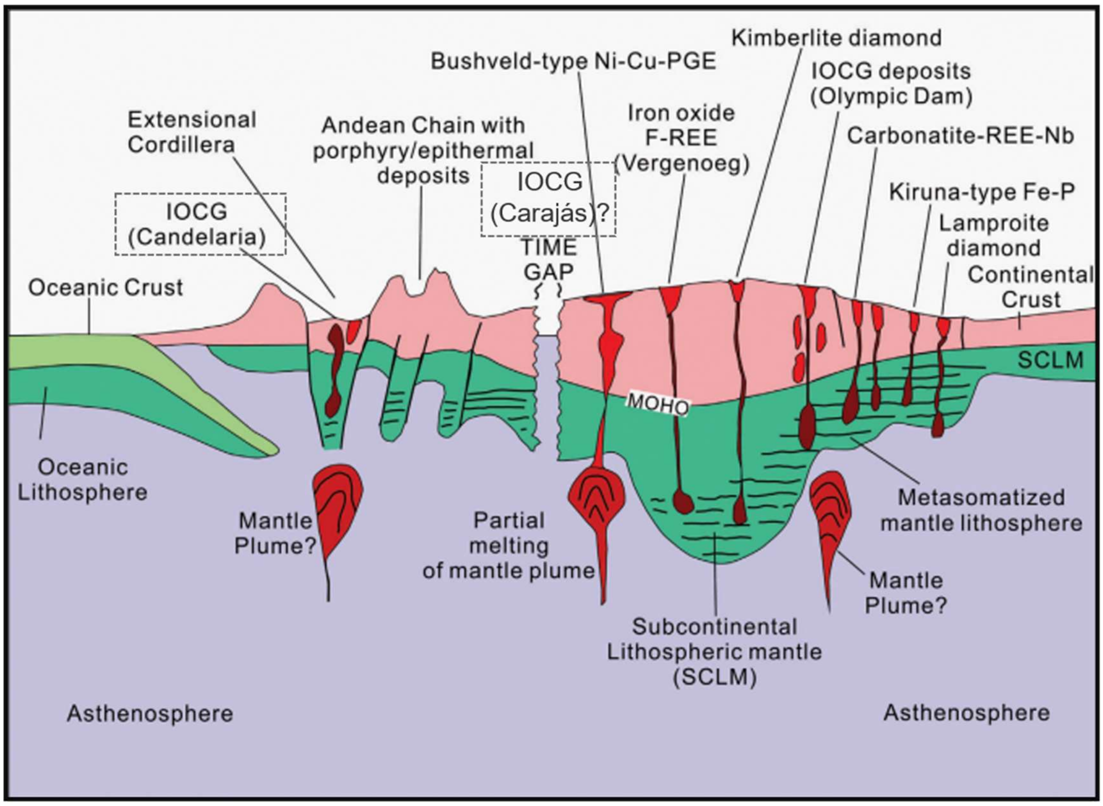

Figure 1. Schematic figure showing the position of various alkaline-magmatism-associated magmatic and magmatic-hydrothermal deposits on craton margins. The left-hand side of the figure represents Phanerozoic examples and the right-hand side represents Precambrian examples (*Groves & Santosh, 2020*).

From that, this study aims to characterize the Sr–Nd isotopes in order to unravel the effects of distinct tectonic settings, geological timing, and crustal contamination in the genesis of IOCG deposits, through the use of trace and isotopic geochemistry applied in magnetite and chalcopyrite from different spatially-time IOCG world-class provinces. These include dominant hematite (Olympic Dam) to magnetite systems (Salobo, Sossego, Sequeirinho, and Alemão) from cratonic environments, as well as magnetite (Candelaria–Punta del Cobre, Ernest Henry) to hematite (Mantoverde) IOCG systems in terrane areas. This sort of study, besides characterizing the geochemical signature of a particular deposit, will also provide clues for broader discussions in both Brazilian and Chilean deposits.

1. 2. Dissertation Objectives

The goal of this research is to determine the potential metal sources of Cu-Au and Fe-ores from IOCG-type mineralization in the Carajás Mineral Province, Brazil, and the Central Andes IOCG Province, Chile, through the comparison of trace element (including REE) and Sr-Nd isotope systematics.

To reach this purpose, three specific objectives were required, enumerated as:

1) Detailed qualitative and quantitative data compilation of the Carajás Mineral Province and the Central Andes IOCG Province.
2) Characterize the Sr-Nd isotope systematics, trace elements and REE geochemistry on hypogene iron oxides and copper sulfides from each province.
3) Discuss and compare the potential metal sources for the IOCG-type mineralization from the Carajás Mineral Province and Central Andes IOCG Province throughout the geological time.

1. 3. Dissertation Approach

The objectives proposed for this research were approached in two chapters and a final concluding chapter, which are summarized as:

Chapter 2 – provides an extensive review of the existing theoretical information. The regional context of each IOCG deposit included in this study, and a brief mineralogical and geochemical summary from hypogene ores were included, with the aim to accumulate information for their later application in the interpretation of the geological-isotopic context of the Carajás and Chilean IOCG deposits.

Chapter 3 – encompasses a journal manuscript titled "Nd–Sr isotopes and trace geochemistry on hypogene IOCG-ores: Implications on the genesis of South American IOCG systems" were the methodology and results of the study are displayed and discussed.

Chapter 4 – summarizes the main conclusions of this research based on the data presented and interpreted in this dissertation. Implications for mineral explorations, recommendations for future work are proposed for both Brazilian and Chilean IOCG provinces.

CHAPTER 2 – REVIEW OF LITERATURE

2. 1. Regional Geology

2. 2. 1. The Carajás Mineral Province

The Carajás Metallogenic Province or CMP is a diverse tectonostratigraphic cratonic area which comprises the oldest nucleus of the Southern Amazon Craton, Pará State, Northern Brazil, a large continental mass generated by the fission of the supercontinent Rodinia (de Oliveira et al., 2018) and its two highly diverse lithological, mineralized and tectonic domains (Santos, 2003): the Mesoarchean Rio Maria granitoid-greenstone terrane (or Rio Maria Domain; RMD) in the southern province, and the Paleo/Meso-to Neoarchean Carajás Domain (CD) to the north, also previously known by *Araújo et al. (1988)* as Itacaiúnas Shear Belt (**Figure 2**). Despite their differences, the exact limit between both remains unknown, with major orogenic processes exposed within the CD basement which is also linked as a deep tectonic discontinuity zone, favorable to later reactivation (*Tavares et al., 2018*). Interestingly, the CD contains the major part of IOCG-type mineralization and subdivided the Neoarchean Carajás basin into two tectonic subdomains bounded by two major high-strain zones, from north to south: Canaã dos Carajás (CCS) that represents the basement of the basin, and the Sapucaia (SS) which was strongly deformed by Neoarchean events, also considered an extension of the RMD (*Silva et al., 2018*, and references therein).

Thus, main episodes related to the genesis of IOCG and Cu-Au systems in the Carajás Mineral Province are frequently subdivided into three main rock associations:

(1) *Mesoarchean basement units*: composed by infracrustal mafic orthogranulites of the Xicrim-Cateté Complex (c.a. 3.00–2.86 Ga; *Pidgeon et al., 2000*), migmatitic orthogneisses (c.a. 3.07–2.83 Ga, e.g., Bom Jesus Orthogneiss; *Feio, 2011*; *Feio et al., 2013*), gneissified granitoids (ca. 3.00–2.68 Ga, Bacaba, Canaã dos Carajás, Campina Verde, Cruzadão and Serra Dourada plutons; Sardinha et al., 2004; *Moreto, 2010*; *Moreto et al., 2011*; *Feio, 2011*, *Feio et al., 2012*; *2013*), and lenticular greenstone fragments (e.g., Rio Novo, Sequeirinho and Sapucaia groups) that are attributed and correlates within the Xingu Complex (c.a. 3.0–2.85 Ga; *Machado et al., 1991*; *Pidgeon et al., 2000*; *Delinardo da Silva, 2014*; *Moreto et al., 2015b*; *de Melo et al., 2017*; *de Melo et al., 2019b*). According to *Tavares et al. (2018)*, the emplacement of CD basement has been related with

Mesoarchean collisional processes that subsequently led to the development of the Neoarchean Carajás Basin.

(2) *Neoarchean Carajás Basin:* composed of a meta-volcanosedimentary sequence, including thick Superior-type BIFs coeval grouped within the Itacaíunas Supergroup (ca. 2.77–2.72 Ga, although have been reported ages of 2.66 Ga; *Gibbs et al., 1986*; *Wirth et al., 1986*; *Machado et al., 1988; 1991; Macambira & Tassinari, 1998*; *Trendall et al., 1998*; *Galarza et al., 2001*; *2003*; *Krymsky et al., 2002*; *Santos, 2002*; *Pimentel et al., 2003*; *Tallarico et al., 2005*; *Cabral et al., 2013*; *Martins et al., 2017*; *Toledo et al., 2019*) that overlain the Mesoarchean basement rocks, and coevally formed bimodal magmatism that intrudes the supracrustal rocks. Bimodal magmatism occurs as (1) two distinct episodes of A-type granitogeneiss between 2.77–2.72 Ga and ~2.56 Ga are recorded in the province, although have been reported ages of 2.48 for it last (*Montalvão et al., 1984*; *Machado et al., 1991*; *Barros et al., 1992*; *Souza et al., 1996*; *Avelar et al., 1999*; *Huhn et al., 1999a*; *b*; *Barbosa et al., 2001*; *Galarza & Macambira, 2002*; *Tallarico, 2003*; *Barbosa, 2004*; *Sardinha et al., 2004*; *2006*; *Silva et al., 2005*; *2020*; *Santos et al., 2010*; *Souza et al., 2010*; *Feio, 2011*; *Feio et al., 2012*; *da Costa Silva et al., 2015*; *Moreto et al., 2015a*; *b*; *Dall'Agnol et al., 2017*; *de Melo et al., 2017*; *Marangoanha et al., 2019*; *2020*; *Toledo et al., 2019), and* (2) a layered mafic-ultramafic complexes(ca. 2.78–2.72 Ga, although have been reported ages of 2.44 Ga*; Machado et al., 1991*; *Dias et al., 1996*; *Mougeot et al., 1996*; *Lafon et al., 2000*; *Galarza & Macambira, 2002*; *Pimentel et al., 2003*; *Santos et al., 2013*; *Moreto et al., 2015b*; *Silva, 2015; Teixeira et al., 2015a*; *Souza et al., 2020*). Until the date, there is no consensus regarding the tectonic environment in which these rocks were formed, although as mentioned in Chapter 1, modern hypothesis (*Costa et al., 2020*; *Ganade et al., 2020*; *Lacasse et al., 2020*) point towards the shift from drip-to modern-tectonics as the responsible for this chaotic geologic scenario.

(3) *Paleoproterozoic magmatism:* characterized by widespread A-type magmatism at 1.88 Ga, although have been reported ages between 2.0 to 1.83 Ga; *Cordani, 1981*; *Wirth et al., 1986*; *Machado et al., 1991*; *Tallarico et al., 2004*; *Lindenmayer et al., 2005*; *Volp et al., 2006*; *Moreto et al., 2015b*; *Teixeira et al., 2017*; *2018*; *Borba et al., 2019*). According to *Dall'Agnol et al. (2005)*, the ~1.88

A-type granites occur as reflect of the breakup supercontinent related to a mantle super swell beneath it, whereas *Tavares et al. (2018)* suggest as the result of the Orosirian orogenic event that provokes oblique tectonism and regional counterclockwise rotation.

Overall, these rocks were strongly deformed by long-lived NW-trending transcurrent fault systems (e.g., Cinzento and Carajás strike-slip systems and the Carajás Fault) reactivated as transtensional/transpressional systems in the Late Archean, and transpressional/extensional systems in the Proterozoic (e.g., *Pollard et al., 2019; Ganade et al., 2020*; *Trunfull et al., 2020*), while the E–W shear zones (e.g., Canaã Shear Zone) might have been the responsible for the sigmoidal “S-shape” of the basin (*Pinheiro et al., 2013*).

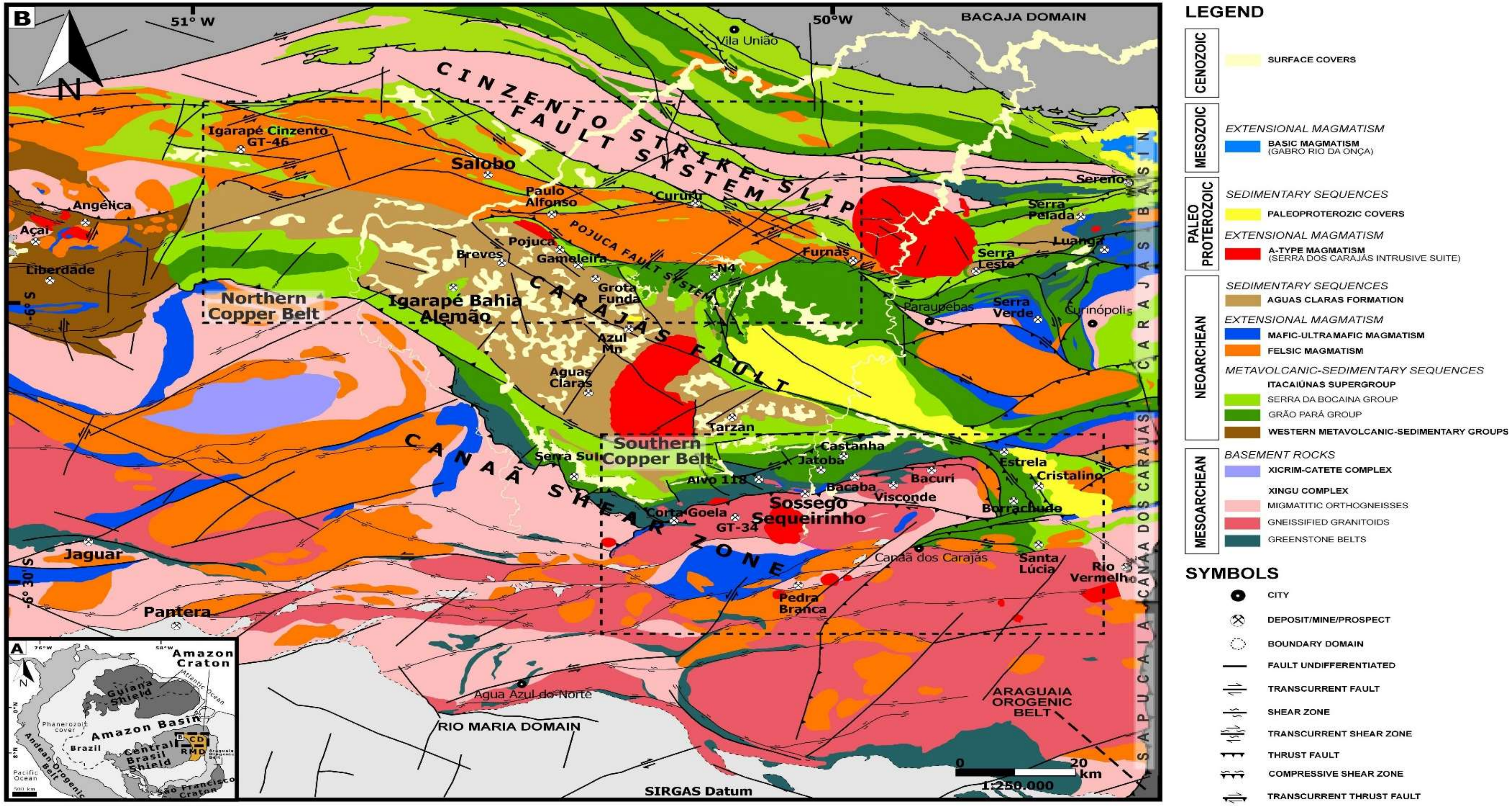

Figure 2. (A) Amazonian Craton tectonic subdivision, Pará Stage (*Vasquez & Rosa-Costa, 2008*). (B) Simplified geological map of the Carajás Domain and surroundings, Amazonian Craton, Northern Brazil. Modified from *Vasquez et al. (2008)*.

2. 2. 2. The Olympic Dam Cu-Au Province

The Olympic Dam Cu-Au Province is a worldwide Mesoproterozoic IOCG province, hosted by metamorphic and igneous basement rocks along the eastern margin of the Archean Gawler Craton, South Australia (*Skirrow et al., 2007*) (Figure 3). The Gawler Craton is separated from another cratonic block to the east, the Curnamona province, by Proterozoic continental supracrustal rocks preserved in the early Paleozoic Adelaide Fold Belt (*Müller & Groves, 2019*).

The emplacement of the Gawler Craton basement has been related with a long and complex Mesoarchean evolution and a subsequent early Mesoproterozoic cratonisation (*Skirrow et al., 2018*, and references therein) and primarily comprises:

(1) The Mesoarchean rocks from the Cooyerdoo Granite (~3.15 Ga; *Fraser et al., 2010*), an I-type granite derived from melting granitic crust with TTG affinities (*McAvaney, 2012*).

(2) The Neoarchean belt portions of supracrustal to intrusive rocks from the Sleaford and Mulgathing complexes (~2555-2480 Ma) with possible continental arc affinities (*Swain et al., 2005*; *Reid et al., 2009*), as well as mafic, ultramafic volcanic and a komatiite succession (~2.520 Ma; *Hoatson et al., 2005*). These were subsequent deformed/metamorphosed to amphibolite-granulite facies during the Sleafordian and Kimban Orogeny (~2480 Ma and ~1730 Ma subsequently; *Chapman et al., 2019*).

(3) Paleoproterozoic volcano-sedimentary sequences propitiated by an initial and localized felsic magmatism (~2000 Ma; *Skirrow et al., 2018*) that marks the onset of extensional conditions and the development of a series of rift basins and its subsequent deposition (between 2000-1740 Ma; *Szpunar et al., 2011*) mainly represented by the Hutchison Group (*Hand et al., 2007*).

(4) Paleoproterozoic magmatism of the Donington Granitoid Suite and associated deformation conditioned by the Cornian Orogeny (~1850 Ma) interrupt the rifting of the above basin sequences, although its deposition finished during the Kimban Orogeny (1735-1690 Ma) (*Hand et al., 2007*; *Reid et al., 2008*). It last involved the development of crustal-scale shear zones, granitic magmatism and widespread metamorphism (*Morrissey et al., 2019*).

(5) Post-Donington and previous Kimban Orogeny (~1770-1740 Ma) the extensional conditions return and localized basin formation occurred (Hand et al., 2007), mainly represented by the Paleoproterozoic Wallaroo Group basin successions (~1760-1740 Ma), and which constitutes one of the main host units for IOCG mineralization in the Olympic Dam Province (*Skirrow et al., 2018*).

(6) The Paleoproterozoic to Mesoproterozoic transition (1730-1700 Ma) was a time of significant I-to S type magmatism (e.g., Middlecamp Granite and Moody Suite, respectively; *Fanninng et al., 2007*), with the juvenile, arc-related intrusions of the St. Peter Suite (~1635-1604 Ma) (Reid, 2019, and references therein), as well as the continental magmatic I-type Tunkillia Suite (*Ferris et al., 2002*), and the widespread bimodal volcanic and intrusive activity during the Gawler SLIP (Gawler Silicic Large Igneous Province), which comprises: the Hiltaba Intrusive Suite (HS) (~1.58 Ga) and its co-magmatic extrusive equivalent, the Gawler Range Volcanics (GRV) (~1.59 Ga) (*Reeve et al., 1990*; *Daly et al., 1998*; *Skirrow et al., 2007*).

Particularly, the Gawler SLIP emplacement is related with the Hiltaba tectonothermal event, which was coeval with a series of tectonothermal events that occurred throughout Laurentia and Baltica in the Mesoproterozoic (*Ferguson et al., 2019*, and references therein), whereas the Hiltaba Suite was associated with regionally partitioned deformation and metamorphism that is generally referred to as the Kararan Orogeny (*Reid, 2019*, and references therein). This magmatism has been widely considered to have developed in an anorogenic or extensional setting, whereas an overall compressional regime coincides with its timing and the Olarian Orogeny in the Curnamona Province. Furthermore, evidence of a switch from compressional orogenesis (~1600-1595 Ma) to extension (~1595-1587 Ma) coincides with the major IOCG-ore-forming systems developed (*Skirrow et al., 2018*, and references therein).

Subsequent, the Gawler Craton basement was reworking along major shear zones with deformation, metamorphism (*Reid, 2019*, and references therein and restricted magmatism associated (~1500-1450) (e.g., Spilsby Suite; Fanninng et al., 2007), whereas continental sediments of Pandurra Formation (~1450 Ma; *Flint et al.,1993*) were deposited in half grabens in fluvial and lacustrine paleo-environments as part of a continental rift system (Morrissey et al., 2019). Later, bimodal dikes intrude (830 Ma; *Wingate et al., 1998*) the above formation, as well as the Hiltaba Suite (*Q. Huang et al., 2015*), while Mesozoic and Neogene sequences cover the region (*Reid et al., 2017*).

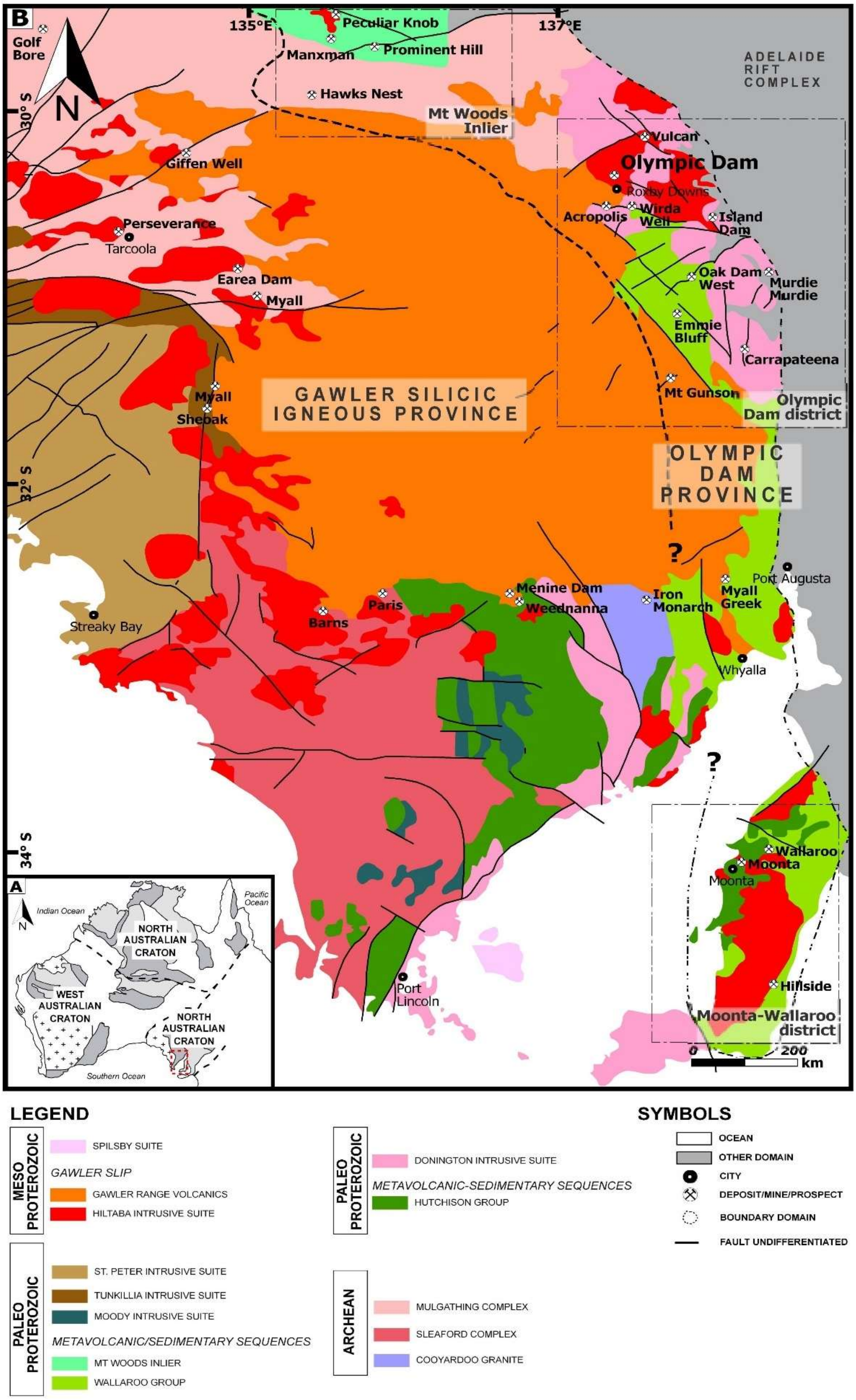

Figure 3. (A) Gawler Craton in the context of Proterozoic Australia (*Morrisey et al., 2019*). (B) Simplified geological map of the Gawler Craton and its metallogenetic provinces. Modified from *Chapman et al. (2019)*.

2. 2. 3. The Cloncurry district

The Cloncurry district is sited in the Eastern Fold Belt terrane of the Mount Isa Inlier, which is one of the world's most strongly metallogenic provinces for base metal and host to major IOCG deposit (*Jiang et al., 2019*, and references therein) (Figure 4). The Cloncurry district consists of a suite of metasedimentary and metavolcanics rocks deposits during three discrete episodes of deformation, metamorphism, and voluminous plutonism attributed to the basin formation during the Isan Orogeny at 1.8 and 1.6 Ga (*Lu et al., 2016*, and references therein). Deformed and metamorphosed rocks of the Plum Mountain Gneiss are the oldest rocks in the district, which are also deformed and metamorphosed in the Barramundi Orogeny (ca. 1.9–1.87 Ga) (*Etheridge et al., 1987*).

Continental rifting periods in the crystalline basement of the Mount Isa Inlier, develops the formation of three vertically stacked sedimentary basins: (1) Leichardt (1.79–1.74 Ga); (2) Calvert (1.73–1.64 Ga) and (3) Isa (1.635–1.575 Ga) (Jiang et al., 2019, and references therein). However, only the latest two are attributed to the sedimentary and volcanic sequences deposited in the district at ~1.72–1.67 and ~1.67–1.59 Ga (*Lu et al., 2016*, and references therein). Furthermore, these both are intruded by Mesoproteroic magmatic suites, where the Wonga Suite intruded in the Eastern Fold Belt during an extensional event (1.75–1.725 Ga; *Pearson et al., 1992*; *Withnall & Hutton, 2013*), whereas Naraku and Williams batholiths intruded the super basins in three different episodes (*Withnall & Hutton, 2013*).

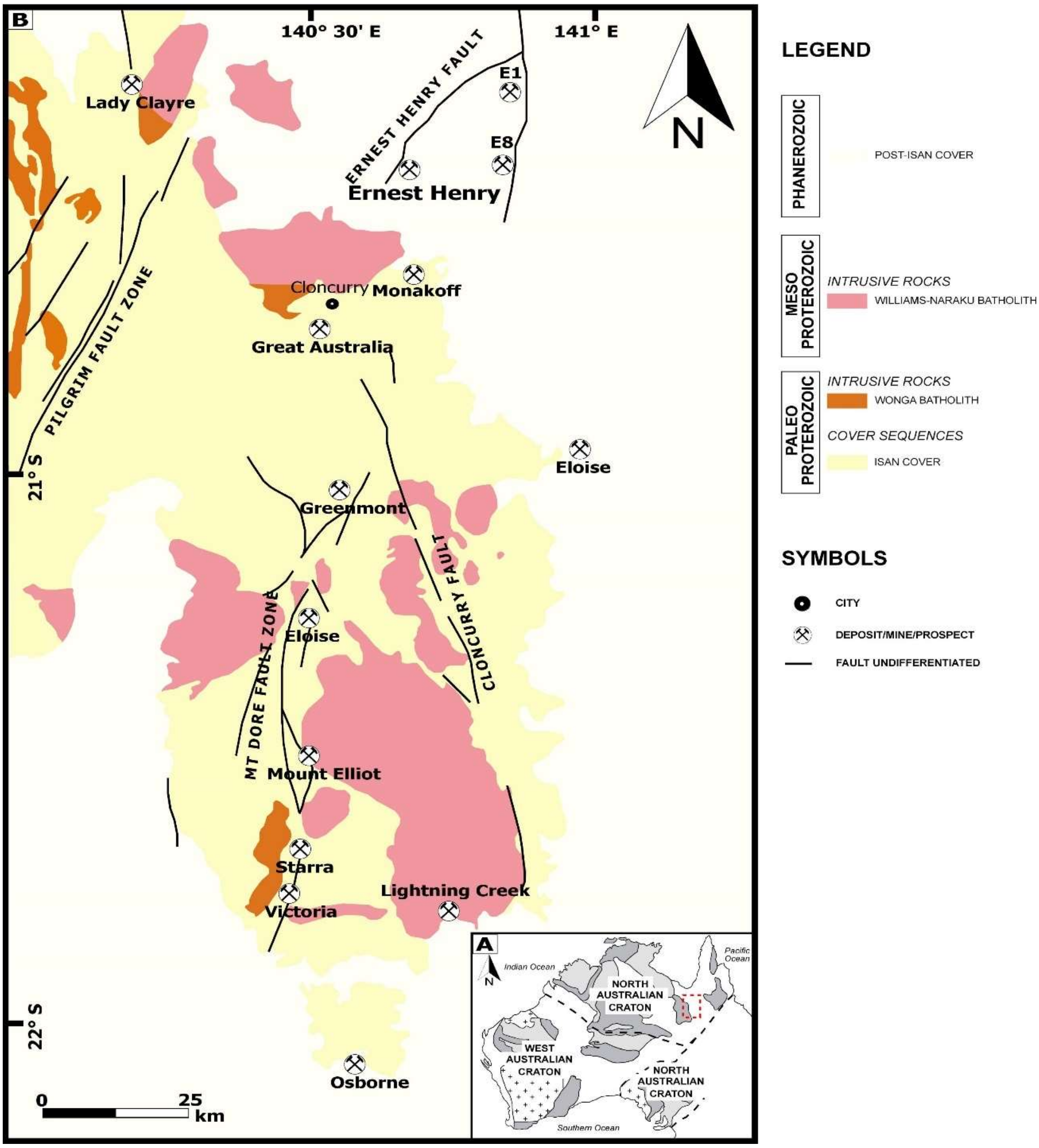

Figure 4. (A) Mount Isa Inlier in the context of Proterozoic Australia (*Morrissey et al., 2019*). (B) Simplified geological map of the Mount Isa Inlier and its metallogenetic deposits. Modified from *Fisher et al. (2008)*.

2. 2. 4. Central Andes IOCG Province

The Mantoverde district located in the Andean Coastal Range of northern Chile represents a Jurassic-Early Cretaceous continental magmatic arc back-arc environment related to the subduction of the Aluk plate under the South American continent (*Mpodozis & Ramos, 1990*; *Scheuber & Andriessen, 1990*) (Figure 5). It shows a strong structural control, divided into the east and west by two N-S trending branches (eastern and central branches) of the subduction-related, arc-parallel, strike-slip Atacama Fault System (Scheuber & Andriessen, 1990). These tectonic wedges are connected by an N to W-trending brittle Mantoverde fault (*Rieger et al., 2010*). The Mantoverde Fault is considered to be the main ore fluid conduit and hosts the majority of IOCG-ore mineralization (e.g., *Childress et al., 2020*).

Rocks of the district are composed by arc-derived volcanic and volcaniclastic rocks of La Negra Formation (~167.1 ± 1.8 Ma, U-Pb on zircon; *Rossel et al., 2013*) developed on a late Paleozoic to Triassic basement (*Mpodozis & Ramos, 1990*) and controlled by extensional to sinistral transtensional environment (*Charrier et al., 2007*, and references therein). These were subsequently intruded by Cretaceous granitoids of the Chilean Coastal Batholith (e.g., Las Tazas, Sierra Dieciocho, Sierra Merceditas-Remolino, Cerro Morado complexes), all of which range in age from 90 to 130 Ma (*Rieger et al., 2010*), and with share I-type patterns (*Chappell & White, 1974*). Both, the arc and basement are widely covered by Neogene to Quaternary alluvial and colluvial deposits, whereas intrusive stocks and swarm dikes crop out in many places of the La Negra Formation in the district (*Gelcich et al., 2003*; *Benavides et al., 2007*).

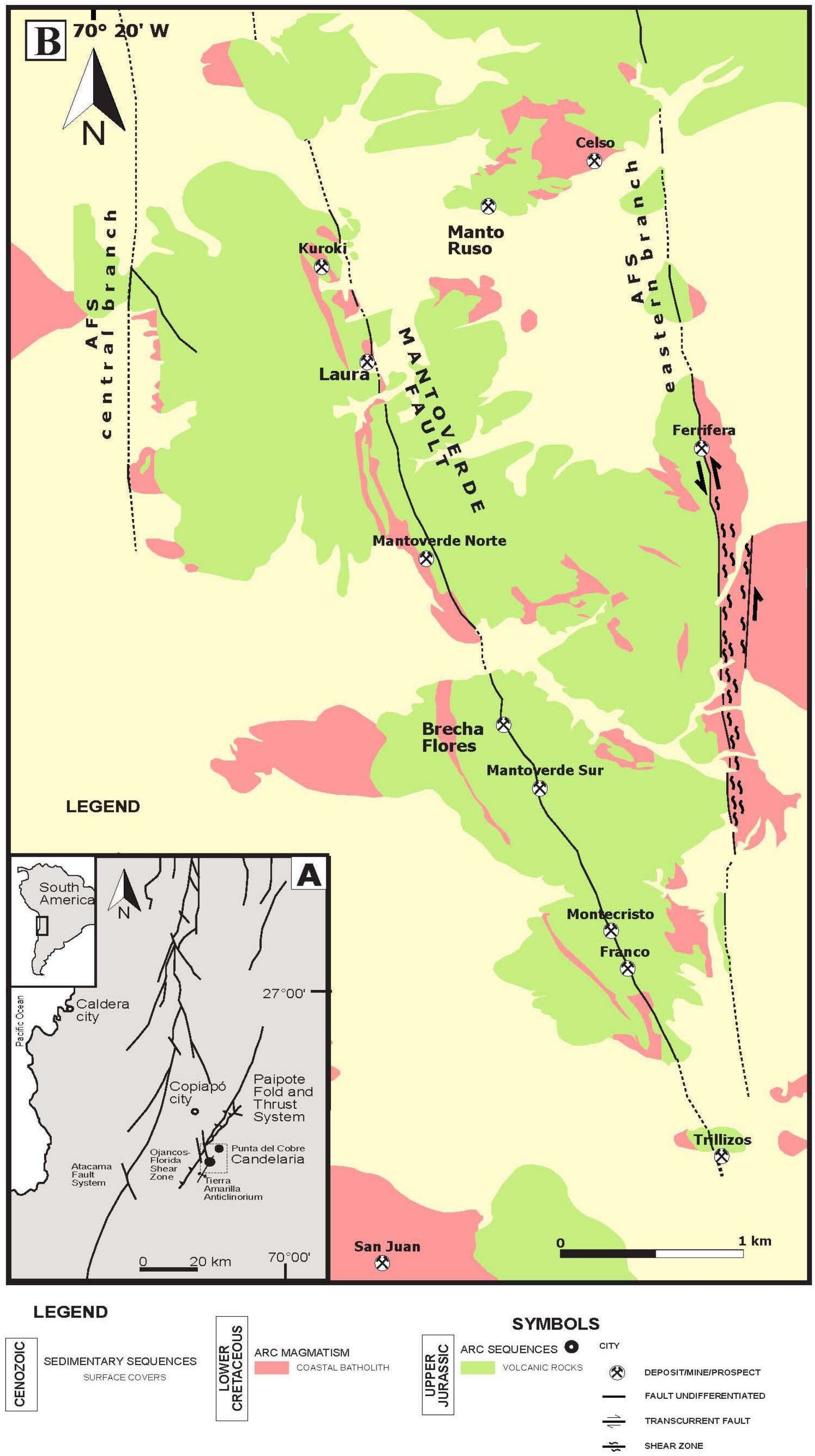

Figure 5. (A) Main structural patterns at the Coastal Cordillera and/or Copiapó Precordillera boundary. Modified from Arévalo et al., (2006). (B) Simplified geological map of the Mantoverde district and its metallogenetic deposit. Modified from *Rieger et al. (2012)*.

The Candelaria-Punta del Cobre district lies in the boundary between the Coastal Cordillera and Copiapó Precordillera, to the east of Atacama Fault System (AFS) along the Ojancos-Florida Shear Zone and in the core of Paipote Fold and Thrust System, Atacama region, northern Chile (*Arévalo et al., 2006*) (Figure 6). It is composed by volcanic-volcaniclastic deposits of Punta del Cobre Formation (135.3 ± 1.0 Ma to 132.4 ± 2.9 Ma, U-Pb on zircon; *del Real et al., 2018*), which probably corresponds to the deposits of the intermediate region between the arc and the back-arc Chañarcillo Basin (*Charrier et al., 2007*) derived from the Early Jurassic-Early Cretaceous magmatic arc (*Taylor et al., 2007*), and the overlying back-arc marine facies of Chañarcillo Group (~ 132 and 130 Ma, based on fossil data; *Jurgan, 1977*; *Corvalán, 1973*; *Mourgues, 2004*; *Mourgues et al., 2015*). All the Lower Cretaceous rocks in the district are later intruded by the Copiapó Batholith (~ 118 and 110 Ma, U-Pb on zircon; Marschik & Söllner, 2006) to the west of the district (*Marschik et al., 2003a*; *b*), and its subsequent development of a contact aureole with decreasing intensity to the east, which represents the most important intrusive system in the district.

The Punta del Cobre Formation corresponds to the oldest syn-rift series in the Chañarcillo Basin that comprises basaltic and basaltic-andesitic lava flows, volcaniclastic rocks and breccias (*Marschik & Fontboté, 2001a*; *b*). Originally defined by *Segerstrom & Ruiz (1962)*, and redefined by *Marschick & Fontboté (2001b)* for the Candelaria-Punta del Cobre area, it was subdivided among four main members which are conformably overlies each other, from older to younger: (1) Lower Andesites (135.3 ± 1.0 Ma, U-Pb on zircon; *del Real et al., 2018*); (2) Dacite (132.0 ± 1.3 Ma, U-Pb on zircon; *del Real et al., 2018*); (3) Volcanic-sedimentary, and (4) Upper Andesites (132.4 ± 2.9 Ma, U-Pb on zircon; *del Real et al., 2018*). The Lower Andesites hosts the mainly iron-oxide-rich IOCG deposits of the district (*Marschick & Fontboté, 2001b*; *Arévalo et al., 2006*).

Early pre-mineralization intrusions are related to small sub-volcanic granodiorite bodies (135.2 ± 1.3 Ma, U-Pb on zircon; *del Real et al., 2018*) which cuts locally parts of the Lower Andesite member. Similarly, a series of dacite (124.9 ± 0.4 and 121.9 ± 2.4 Ma, U-Pb on zircon; *Pop et al., 2000*) and dioritic dikes intrudes different parts of the Lower Andesite, Dacite, and Volcanic-sedimentary members.

Back-arc syn-rift succession represented by siliciclastic and calcareous deposits of the Chañarcillo Group overlies unconformably the Punta del Cobre Formation (*Sergerstrom & Parker, 1959*; *Segerstrom, 1960*; *Segerstrom & Ruiz, 1962*). Modified by *Segerstrom & Ruiz (1962)*, this group is divided into four concordant formations from bottom to the top as (1) Abundancia; (2) Nantoco; (3) Totoralillo, and (4) Pabellón.

Particularly, the Abundancia Formation as representing the lower part of the interfering zone of arc-derived volcanic debris of the Bandurrias Group, with the carbonatitic sedimentation of a shallow marine back-arc basin represented by Nantoco Formation (*Marschick & Fontboté, 2001b*). Towards the north and northwest of the district, the Chañarcillo Group interfingers with marine and continental volcanic rocks and conglomerates of the Bandurrias Formation (*Segerstrom, 1960*; *Segerstrom & Ruiz, 1962*), that correspond to the transition zone between the arc to the west and the back-arc basin to the east (Charrier et al., 2007), reflecting a contemporaneously deposition during the basin extension (*Marschick & Fontboté, 2001b*; *del Real et al., 2018).*

Continental alluvial red clastic sedimentary and volcanic rocks of Cerrillos Formation (110.7±1.7 and 99.7±1.6 Ma, U-Pb on zircon; Maksaev et al., 2009) rest unconformably on the eroded rocks on the rocks of the Chañarcillo Group and the Bandurrias Formation (*Sergerstrom & Parker, 1959*; *Zentilli, 1974*; *Charrier et al., 2007*; *del Real et al., 2018*) reflecting an abrupt change to non-marine conditions (*Arévalo, 1999*; *Mourgues, 2004*), which were deposited in a strongly subsiding extensional basin (*Charrier et al., 2007*). The Cerrillos Formation interpreted as syn-orogenic deposits, its accumulation was associated with eastward-displaced magmatic arc (at ~85 Ma; *Mpodozis & Ramos, 1990*; *Cornejo et al., 1993*). Nevertheless, some authors suggest volcano-sedimentary accumulations during the tectonic inversion of the basin (*Martínez et al., 2013*; *2016*).

The emplacement of the Copiapó Batholith, which is classified as subalkaline to alkaline, metaluminous magnetite-series, volcanic arc I-type granitoids (Marschik et al., 2003a; b), is characterized by three main intrusive phases: (1) La Brea diorite (118 ± 1 Ma, U-Pb on zircon; *Marschik & Söllner, 2006*), the largest dominant phase in the batholith; (2) San Gregorio monzodiorite (115.5 ± 0.4 Ma, U-Pb on zircon; *Marschik & Söllner, 2006*), represented by a deformation zone in the southern contact of Punta del Cobre Formation and Chañarcillo Group which defines the Ojancos Shear Zone (*Arévalo et al., 2006*), and (3) Los Lirios granodiorite to tonalite (110.7 ± 0.4 Ma, U-Pb on zircon; *Marschik & Söllner, 2006*), characterized by an vertical intrusive contact with La Brea diorite to the west and stratified contact between the Punta del Cobre Formation and Chañarcillo Group to the east (*Arévalo et al., 2006*). This latter cuts the upper limit between Upper Andesites of the Punta del Cobre Formation and the Abundancia Formation of the Chañarcillo Group and is related to local zones of porphyry-style alteration (*Barton et al., 2005*). Two smaller intrusive bodies have also present in the batholith, the Adamelite porphyry (116.3 ± 0.4 Ma, U-Pb on zircon; Marschik & Söllner, 2006), and a series of dacite dikes (115.2 ± 1.8 and 112.8 ± 1.3 Ma, U-Pb on zircon; *del Real et al., 2018*).

Late intrusions post-mineralization are related to suite of lamprophyric dikes (63.2 ± 2.5 Ma, K-Ar on whole-rock; *Pop et al., 2000*) which cuts the Upper part of the Lower Andesites member, brecciated zones around the dacitic domes of the Dacite member, and contact zones between Lower Andesite member and Volcano-sedimentary member of the Punta del Cobre Formation. Similarly, in the southern part of the district, a series of porphyritic dacitic dikes (47.3 3.9 Ma, U-Pb on zircon) cuts the Punta del Cobre Formation and the Chañarcillo Group (*del Real et al., 2018*).

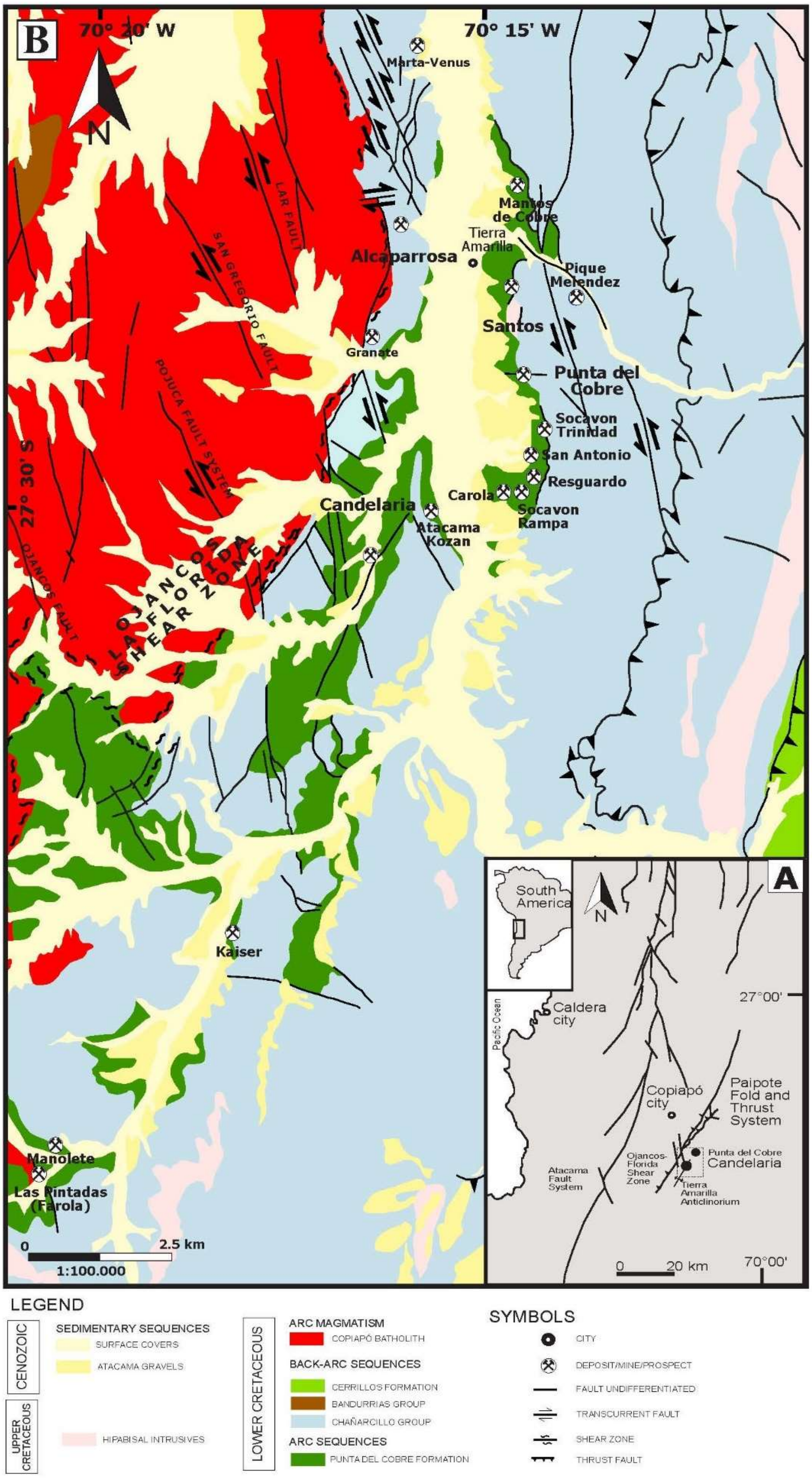

Figure 5. (A) Main structural patterns at the Coastal Cordillera and/or Copiapó Precordillera boundary. Modified from Arévalo et al. (2006). (B) Simplified geológical map of the Candelaria-Punta del Cobre district. Modified from *Arévalo (2005a*; *b)*.

2.3. Deposit Characteristics

2. 3. 1. Sosego

The Sossego deposit is composed by Sequeirinho-Pista-Baiano and Sossego-Curral orebodies (85 % and 15% of 355 Mt @ 1.1% Cu, 0.28 g/t Au, respectively; Lancaster-Oliveira et al., 2000) which are sited along the regional E–W to WNW–ESE-trending Canaã Shear Zone (*Pinheiro et al., 2013*). Until the date, is the biggest IOCG deposit in the Southern Copper Belt of the Carajás Metallogenetic Province.

Interestingly, the occurrence of distinct tectonic-hydrothermal systems within the deposit as in its surroundings is characterized by the older Neoarchean IOCG-forming system (ca. 2.71-2.68 Ga), which was the responsible for the genesis of the Sequeirinho-Pista and possibly Baiano orebodies, and a later Paleoproterozoic remobilization event (ca. 1.90-1.88 Ga) enabled the development, which marks strong differences in the mineralogy/alteration assemblages, as well as in the host rocks patterns in the Sossego-Curral orebodies (*Moreto et al., 2015a*). According to *Tavares et al. (2018)*, it latter can be possibly related to the oblique tectonism and regional counterclockwise rotation at the second Paleoproterozoic event that affected the CMP during the Orosirian, while until the date, the original IOCG-tectonic environment remains unclear.

In economic terms, chalcopyrite is the only and main hypogene Cu-ore in the entire deposit and is spatially associated with magnetite and pyrite with minor sulfides as molybdenite, siegenite, millerite, hessite, gold, Pd melonite and cassiterite. Pyrrhotite and traces of sphalerite and galena are only founded in the Sequeirinho-Pista-Baiano ore bodies (*Monteiro et al., 2008a*).

For Sequeirinho and its W-to E extensions, sulfides are synchronous with actinolite–chlorite–epidote–allanite–apatite–(monazite) alteration zones (*Hunh et al., 1999b; Monteiro et al., 2008a*; *b*). Thus, these ore bodies were mostly concentrated within an "S" shaped tabular sub-vertical orebody along an anastomosing ductile-brittle NE-SW sinistral strike-slip faults (Domingos, 2009; Moreto et al., 2015b), that cut their main hosts lithotypes as (1) fragments of magnetite- and actinolite-rich bodies cemented by chalcopyrite-pyrite in Mesoarchean rocks of the Xingu Complex and Sequeirinho Granite for the homonym orebody, (2) dissemination of chalcopyrite–(pyrrhotite–pyrite–molybdenite) along mylonitic fabric as well as within steeply dipping veins related actinolite–magnetite–epidote–apatite–calcite and stockwork breccias in the Mesoarchean greenstone belts units at felsic metavolcanics rocks for the Pista, and (3) chalcopyrite veins related calcite–chlorite–epidote–(albite) in the Neoarchean gabbronorite rocks of Baiano orebody (*Monteiro et al., 2008a*; *Moreto et al., 2015a*).

Differently, to the northeast of Sequeirinho, and separate from it by a vertical displacement of major E-W trending high-angle faults, the Sossego, and its SW ore extension were comprised into a subcircular, vertical pipe-like ore bodies with a central breccia surrounded by a stockwork array of sulfide veins, faults and shear zones within the homonymous granites (*Monteiro et al., 2008b*; *Carvalho, 2009*; *Domingos, 2009*; *Moreto et al., 2015a*), where calcite–quartz–chlorite–epidote–Ce allanite alteration assemblages were coeval with the chalcopyrite-pyrite occurrence (*Monteiro et al., 2008a*; *Monteiro et al., 2008b*; *Torresi et al., 2012*).

2. 3. 2. Salobo

The giant Salobo deposit (1112 Mt @ 0.69% Cu, 0.43 g/t Au; *de Melo et al., 2019c*) is located near to the limit between the Carajás and Bacajá domains and represents the biggest IOCG deposit in the Northern Copper Belt, as well as the whole Carajás Metallogenetic Province of Brazil. This steeply dipping, magnetite-dominant IOCG deposit is hosted by highly deformed rocks related to the Meso- to Neoarchean gneisses of the Xingu Complex and Neoarchean syn-tectonic granitoids of the Igarapé Gelado Suite and structurally controlled within the WNW-striking Cinzento Transcurrent Shear Zone (*de Melo et al., 2017*).

The complex hydrothermal alteration at the Salobo deposit has been previously defined by *Réquia et al. (2003)* and *de Melo et al. (2017)* where included multiple stages linked within one mineralization event. However, more recent studies as *Valadão (2019)* indicates that both previous paragenetic hydrothermal alteration schemes show some inconsistencies in their assemblages as well as in their formation temperature, and proposes that IOCG mineralization (chalcopyrite ± pyrite ± pyrrhotite ± siegenite) is characterized by a main Neoarchean magmatic-hydrothermal source event of Na and Ca-Fe alteration (hornblende–Fe-actinolite–grunerite–fayalite), while recrystallization and metamorphism in the host rocks were promoted within latter Neoarchean transitional Siderian deformational reactivation events within the Cinzento Shear Zone mainly related with K-alteration (biotite–almandine ± quartz), whereas later interaction events between the ore source and enriched F+CO2 low-temperature fluids represented by hydrolytic–propilitic alteration (calcite–sericite–greenalite) were the responsible for the ore remobilization event (bornite–chalcocite–magnetite ± molybdenite).

2.3.3. Alemão

The Alemão deposit (106 Mt @ 1.45% Cu, 1.01 g/t Au; *VALE, 2012*) is one of the four separates orebodies and the main segment of the Igarapé-Bahia deposit (total of 219 Mt @ 1.4% Cu, 0.86 g/t Au; *Tallarico et al., 2005*). It is sited at the Northern Copper Belt of the Carajás Metallogenic Province of Brazil and is hosted by metavolcanosedimentary sequences of the Igarapé Bahia Group and the overlying Águas Claras Formation (Melo et al. 2019a), which are brittle to ductile dissected by NE-SW, E-W, and NW-SE trending fault systems (*Ronzê et al., 2000*). Likewise, according to *de Melo et al. (2019b)*, the whole deposit could be representing the earliest manifestations of hydrothermal copper mineralization in the Carajás Domain synchronous with the deposition of the Neoarchean Itacaiúnas Supergroup.

The Alemão consists of a concordant, almost vertically dipping, mineralized fragmental rock body (Santos, 2002) which is confined to mylonitic zones and hydrothermal breccias where ore occurs main as chalcopyrite-magnetite lenses and with the abovementioned breccias (Melo et al., 2019a). The hydrothermal alteration includes (1) Fe metasomatism (grunerite+fayalite±magnetite±hematite); (2) Mg-Fe chloritization and biotitization; (3) ore-occurrence of chalcopyrite and bornite; (4) intense carbonate alteration (siderite-calcite-ankerite); and (6) local silicification and tourmalinization from early to late (*Barreira et al. 1999*; *Ronzê et al., 2000*).

2.3.4. Olympic Dam

The Olympic Dam deposit is by far the largest IOCG deposit in the world (10.100 Mt @ 0.78% Cu, 1 g/t Au; *Cherry et al., 2018*). The deposit is hosted within tectono-magmatic hydrothermal breccias, namely the Olympic Dam Breccia Complex (OBDC) itself enclosed by the Mesoproterozoic Roxby Downs Granite (*Oreskes & Einaudi, 1990*; *Reeve et al., 1990*; *McPhie et al., 2016*; *Cherry et al., 2018*), and is unconformably overlain by Neoproterozoic to Cambrian sediments of the Stuart Shelf (*Reeve et al., 1990*). Contemporaneous with the RDG, and also hosted within the ODBC, are a swarm of felsic to ultramafic dikes, including strongly altered olivine-phyric dolerites dikes (*Q. Huang et al., 2015*).

Hypogene mineralization comprises an inwards-upwards vertical zonation, characterized by magnetite+hematite+pyrite+chalcopyrite, also known as outer shell (*Verdugo-Ihl et al., 2019*), at the outermost and deepest ore zone, hematite+chalcopyrite+bornite and hematite+bornite+chalcocite at the inner-and uppermost ore zone (*Ehrig et al. 2012*; *Verdugo-lhl et al., 2017*), and which represents exsolutions along cooling paths from ≤ 400 °C solid solutions within the system Cu-Fe-S (*Ciobanu et al., 2017*). Furthermore, breccias are dominated by hematite and sericite, with lesser chlorite, siderite, and quartz (*Reynolds et al., 2000*), where only hematite-rich assemblages are closely associated with ore occurrences, whereas intense sericitic zones are usually barren (*Tappert et al., 2011*).

2.3.5. Ernest Henry

The Ernest Henry deposit (89.8 Mt @ 1.17% Cu, 0.6 g/t Au; *Valenta, 2018*) is the largest known IOCG deposit in the Eastern Succession of the Mount Isa Inlier, Cloncurry district, that comprises two main orebodies: the Ernest Henry, a single south-plunging shoot pipe-like breccia (*Mark et al., 2006*) bounded by the Hanging Wall Shear Zone (HWSZ) and the Footwall Shear Zone (FWSZ) (*Twyerould et al., 1997*) and the Ernie Junior, which have a similar plunge and is sited between the major orebody and the bounding FWSZ (*Sullivan, 2016*). Interestingly, a weakly mineralized and brecciated shear zone within the orebody, also known as “Inter-lens” separates the main orebody into two distinct lenses (*O’Brien, 2016*), which according to the pre-mineralization timing of the deposits, makes that the “explosive eruption” model be re-examined, whereas until the date, has been suggested that was formed as a result of competency contrast between the host rocks and structural controls are shear zones (*Cave et al., 2018*).

Cu-mineralization occurs as chalcopyrite, and Au occurs as native gold with minor electrum (*Foster et al., 2007*), and are characterized by a matrix dominated breccia with a co-precipitated breccia matrix of magnetite, with minor specular hematite, and chalcopyrite (*O’Brien, 2016*), hosted in metaandesite rocks attributed as coeval equivalent of the Mount Fort Constantine metavolcanics (*Page & Sun, 1985*). Metasomatism and hydrothermal alteration is strongly structurally controlled and is mainly represented by (1) an initial regional Na and Na-Ca alteration (albitization); (2) pre-mineralization stage with a first K-(Mn-Ba)-rich biotite-magnetite alteration, and

(3) a subsequent hematite dusted K-feldspar, which is also strongly related with the ore-occurrence (*Mark et al., 2006*; *O'Brien, 2016*).

Modern studies as *Austin et al. (2019)* indicates that Ernest Henry is characterized by an initial ductile-brittle metasomatic magnetite-albite trap is main associated with NE-trending shear zones, while a subsequently brittle stage that brecciated the deposit is characterized by a weakly oxidized alteration related with magnetite-hematite-pyrite-chalcopyrite occurrence, whereas an oxidized zone of quartz-calcite-chlorite-hematite-chalcopyrite overprints the breccia at the intersection of the NE-trending shear zones with the N-S strike-slip fault. Also, suggest that sodic, potassic and calcic alteration can be related to redox zonation within one event, or represent overprinting of metasomatic episodes.

2. 3. 6. Mantoverde

The Mantoverde deposit (440 Mt @ 0.56% Cu, 0.12 g/t Au; *Rieger et al., 2010*) is the major IOCG occurrence at Mantoverde district and is the second most economically IOCG occurrence in the Atacama Region, northern Chile. The Mantoverde is subdivided into two major open pits and continuous ore zones, from northern to southern also known as Mantoverde Norte and Mantoverde Sur deposits (101.6 Mt, and 18.521 Mt respectively). Currently, the Mantoverde Mine and its Development Project (extraction and processing of copper sulfides) has been recognized that the project contains resources by 1.146 Mton, where 231 Mton @ 0.60 % TCu and 0.11 g/t declared as exclusives reserves, further published Mantoverde Exploration Potential is 2.5 Bton @0.5% TCu (*Mantoverde Ltda, 2019*).

The Mantoverde deposit as well its peripherals smaller orebodies (e.g., Paloma, Kuroki, and Laura, to the northern and Franke to the south) are hosted and strongly controlled into the Mantoverde Fault (MF) a characteristic structural NNW-SSE striking, east-side-down, normal transfer fault and the major ore fluid conduit in the deposit that connects the central and eastern branches of the AFS (*Sanhueza & Robles, 1999*; *Grocott & Taylor, 2002*; *Marschik et al., 2015*; *Childress, 2019*) and which was also interpreted as a scissor fault, which caused the tilting and downthrow of the northeastern wedge to the northeast (*Zamora & Castillo, 2001*; *Rieger et al., 2010*).

Previous studies for the paragenetic hydrothermal sequences in the deposit as *Benavides et al. (2007)* distinguished four hydrothermal stages, where magnetite and hematite were formed almost entirely at different paragenetic stages, while hematites postdate magnetites were assumed, however, *Rieger et al., (2010)* suggest that magnetite at depth formed coevally with the bulk of the hematite at shallow levels. Nevertheless, recent studies as *Johansson et al. (2018)* redefined the hydrothermal alteration at Mantoverde into four main mineralization events as (1) Stage I, characterized by strong Fe-K metasomatism of magnetite-K-feldspar-biotite, and scarce pyrite and chalcopyrite; (2) Stage II, composed by chlorite-sericite-quartz-K-feldspar veins with pyrite + chalcopyrite ± pyrrhotite; (3) Stage III, characterized by an abundant specular hydrothermal breccia with the most important hypogene mineralization (chalcopyrite + pyrite ± digenite-djurleite-chalcocite); and (4) Stage IV, characterized by supergene Cu oxides.

Consequently, Mantoverde has been interpreted as a zoned system where the mineralization is primarily the result of magmatic-hydrothermal fluids (*Childress, 2019*) at relatively shallow crustal levels under brittle conditions (*Rieger et al., 2010*). Thus, magnetite-dominant zones occur at depth levels and proximal to the hydrothermal system (e.g., Altavista and Montecristo mines at Mantoverde Sur), whereas specular hematite-zones are present at shallow or distal portions of MF (e.g., Mantoverde Norte or Manto Ruso deposits) (*Rieger et al., 2010*; *Childress, 2019*).

2. 3. 7. Manto Ruso

The Manto Ruso deposit (15.1 Mt @ 0.56% Cu, 0.12 g/t Au; *Benavides et al., 2007*; *Rieger et al., 2010*) is a middle IOCG deposit sited in the northern part of the Mantoverde district. Unrelated to the MF, and to the east of it, the deposit is controlled by a dense NW fault system which represents the major IOCG ore fluid conduit, the hypogene mineralization is developed within a sub-vertical to vertical tabular specularite-cemented breccia pipe through volcanic-volcaniclastic rocks of La Negra Formation and diorites from Sierra Dieciocho complex, that represent the more distal outflow environment in the district (*Castillo & Zamora, 2003*; *Benavides et al., 2007*; *Rieger et al., 2010*). Hypogene sulfides as chalcopyrite, pyrite, and traces of bornite and digenite are commonly associated within specularite-dominated zones (e.g., cemented breccias, stockworks or within the matrix), whereas sulfides in magnetite-dominated zones also occur as disseminations and veinlets within a wide magnetite geometries pattern (e.g., veins, veinlets, replacement, fragment, massive or within the matrix) commonly cut by specularite–calcite veinlets (Rieger et al., 2010). Thus, accordingly to the structural configuration of the district, the upper portions of the system are commonly preserved in Manto Ruso deposit, where hematite is the predominant near-surface iron oxide phase, while magnetite is only exposure into deeper portions of the system, as occurs in the Mantoverde Sur deposit (*Rieger et al., 2010*; *Childress, 2019*).

2. 3. 8. Candelaria

The Candelaria deposit is the major IOCG deposit in the Candelaria-Punta del Cobre district which consists of two major mines: Candelaria Pit and Candelaria Norte (482.639 Mt @ 0.47% Cu, 0.11 g/t Au, and 226.211 Mt @ 1.01% Cu, 0.23 g/t Au respectively; *Couture et al., 2018*), where both are sited along the NE Candelaria Anticline within an NW fault block limited by extensional NW vertical faults (Perez-Flores & Sanchez, 2018a). Particularly, Candelaria Norte corresponds as the northeast continuation of stratigraphic mineralized “manto” horizon towards the north of the pit (*Lazcano & Corvalán, 2006*; *del Real et al., 2018*), while district drill-core explorations indicate the deeper continuity of the mineralization towards the south sector of the original deposit, known as Candelaria Sur prospect.

The emplacement of Candelaria deposit has been genetically associated with a syn-kinematic, syn-plutonic NNE-ductile shear fault zone, also known as Candelaria Shear Zone (CSZ) and intrusive emplacement during an early extensional regime (*Arévalo et al., 2006*). Nevertheless, several studies as Amilibia (2009), *del Real et al. (2018)*, and *del Real & Thompson (2019)* suggested that the main mineralizing event at ~115 Ma occurred syn-intrusion emplacement during transpression-inversion of the Chañarcillo sedimentary basin, which also indicates that Andean IOCG deposits are not exclusively extensional/transtensional settings where changes to transpressional deformation would have triggered the fractionation more primitive magma and ascend of hydrothermal fluids.

Stronger metasomatism, metamorphism, and deformation in the host rocks of the deposits (*Lazcano & Corvalán, 2006*) result in different alterations/ore styles related to different lithological/structural controls. Thus, hypogene ore mineralogy consists mainly of chalcopyrite and is spatially associated with magnetite, pyrite, pyrrhotite, specularite and minor molybdenite, arsenopyrite, sphalerite, gold (*Marschik and Fontboté, 2001a*; *Mathur et al., 2002*).

del Real et al. (2018) details the different types of Cu-ore occurrences as (1) the so-called "manto" or strata-bound orebody, commonly related with magnetite–actinolite–biotite–potassic feldspar–quartz zones linked to disseminated chalcopyrite–pyrrhotite ± pyrite within the Volcanic-sedimentary member, and subsequently overprinted by veins and disseminations of magnetite–biotite–chalcopyrite–pyrrhotite ± pyrite ± sphalerite ± mushketovite (e.g. Candelaria Norte mine), (2) fractured-controlled occurrences of chalcopyrite ± pyrite intimately associated with magnetite–actinolite–biotite–potassic feldspar ± mushketovite zones within the Lower Andesite member (e.g. Candelaria Pit mine), that also extends through the Volcanic-sedimentary member (e.g. Candelaria Norte mine) and locally into the base of the Upper Andesite member, and (3) chalcopyrite-rich structural breccias associated with pervasive magnetite–actinolite–biotite–potassic feldspar ± quartz ± pyrite within the Lower Andesite member, which is also a probable feeder of deepest chalcopyrite–pyrite ductile veins recorded in the Candelaria Norte mine (*Pérez-Flores & Sánchez, 2018a*).

2. 3. 9. Punta del Cobre

The Punta del Cobre deposit (180Mt at 0.9%Cu; *del Real et al., 2018*) is a magnetite IOCG system (*Chen, 2013*) in the eastern flank of the Tierra Amarilla Anticlinorium along in the east side of the Copiapó valley. The Punta del Cobre host two main orebodies. The deposit is structurally controlled by several of sub-vertical N-NW fault structures with limited strike extent, distal to the Cretaceous batholith, and within several breccias in the upper and lowermost parts of the dacitic cryptodome of the Punta del Cobre Formation (*del Real et al., 2018*). Main stage ore-assemblages include chalcopyrite–pyrite in association with magnetite–mushketovite–actinolite–biotite–potassic feldspar–quartz, and disseminated cut by veins with a similar composition which occurs as patches, disseminations and breccia filling within the base and top of the dacitic dome and associated cross-cutting sulfide veins (*del Real et al., 2018*).

2. 3. 10. Alcaparrosa

The Alcaparrosa deposit (10.215 Mt @ 0.77% Cu; *Couture et al., 2017*) is a middle IOCG deposit in the northern part of the Candelaria-Punta del Cobre district along the western flank of Tierra Amarilla Anticlinorium in the west side of the Copiapó valley. Their emplacement is genetically associated with an NNE-striking CSZ in the contact between La Brea-San Gregorio plutons, as well as a series of NNW to NW-striking faults and faults-veins (*Pérez-Flores & Sánchez, 2018b*). Similar to the Candelaria deposit, all the host rocks of the Punta del Cobre Formation were strongly affected by the batholith halo (*Lazcano & Corvalán, 2006*).

Chalcopyrite is the only hypogene Cu-ore and is spatially associated with magnetite and pyrite, with traces of pyrrhotite, molybdenite, and arsenopyrite (*Marschik and Fontboté, 2001a*; *Couture et al., 2018*). *del Real et al. (2018)* summarizes, the mineralized zones in Alcaparrosa deposit represent a northward continuation of the main "manto" ore body at Candelaria deposit. Thus, disseminated magnetite-sulfide patches and breccia filling geometries that concentrate the main ore are linked with magnetite–actinolite–biotite alteration zones within the basal part of the dacitic cryptodome of Dacite member, which is also interpreted as fractionation of the Lower Andesite member. Locally, minor superimposed sulfide veinlets cut the stratigraphically controlled mineralization.

2. 3. 11. Santos

The Santos deposit (13.295 Mt @ 0.94% Cu; *Couture et al., 2017*) is a middle IOCG deposit in the north-eastern part of the Candelaria-Punta del Cobre district along the eastern limb of the Tierra Amarilla anticline in the east side of the Copiapó valley.

Chalcopyrite is the only hypogene Cu-ore, and is spatially associated with magnetite and pyrite (*Marschik & Fontboté, 2001*). Mineralization is hosted as NNW to NW ductile-brittle veins and fault-veins dipping between 60° to 70° W, that cut volcanic and volcanic-clastic rocks of Punta del Cobre Formation similar than Candelaria Norte veins (*Perez-Flores & Sanchez, 2018c*), as disseminated and breccia filling magnetite-sulfide in the basal part of the dacitic dome, and an irregular pipe-like body that cuts through the center of the dacitic dome (*del Real et al., 2018*). The variable amount of Fe content in this deposit is characterized by magnetite dominant in the north and deeper areas, while to the south is dominated by specular hematite (*Couture et al., 2018*).

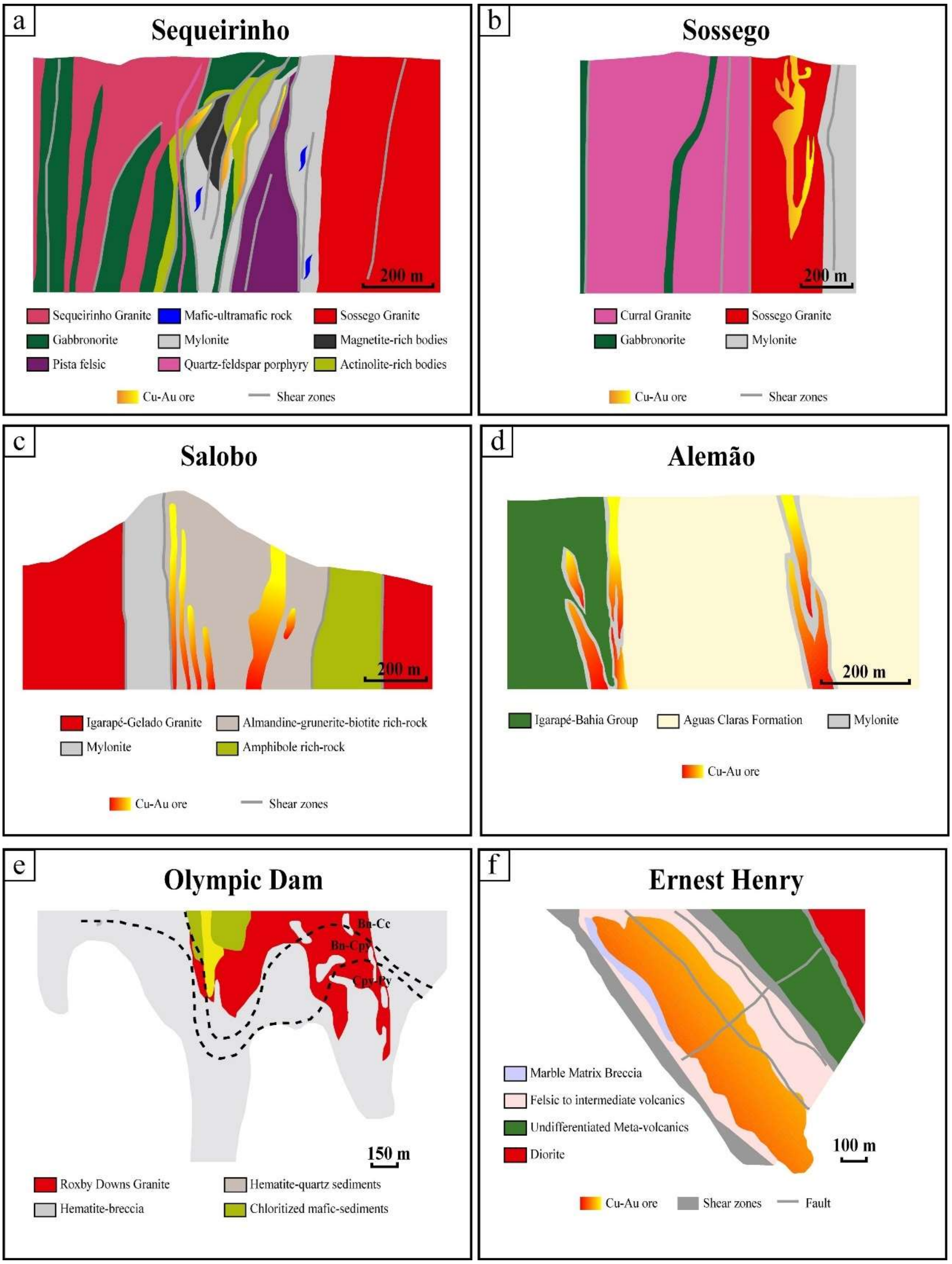

Figure 6. Cross-sections of selected deposits. (a, b) Sequeirinho and Sossego (Moreto et al., 2015a). (c) Salobo (*de Melo et al., 2019b*). (d) Alemão (*de Melo et al., 2019a*). (e) Olympic Dam (*Dmitrijeva et al., 2019*). (f) Ernest Henry (*Cave et al., 2018*).

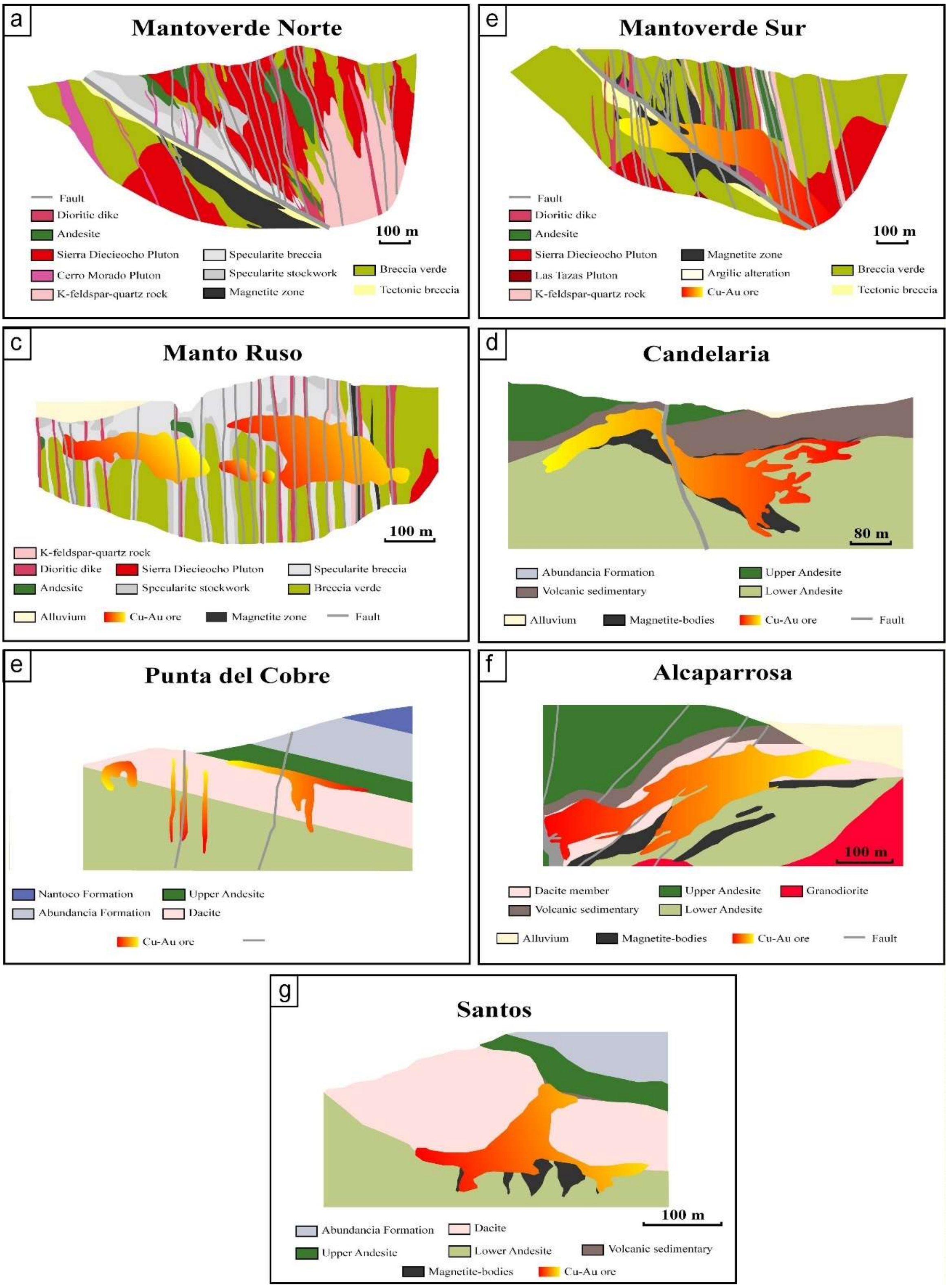

Figure 7. Cross-sections of selected deposits. (a–c) Mantoverde Norte, Mantoverde Sur, and Manto Ruso (*Rieger et al., 2010*). (d) Candelaria (*del Real et al., 2018*). (e) Punta del Cobre (*Marschik & Fontboté, 2001b*). (f, g) Alcaparrosa, and Santos (*del Real et al., 2018*).

Table 1. Selected geological features of IOCG deposits included in this study.

Deposit	Type	Reserves	Host rocks	Principal ore control	Ore morphology	Main hypogene	Associated minerals	Hydrothermal alteration	Deposit age (Ma)	Geochemical signature
Sequeirinho-Pista-Baiano orebody (Sossego)	IOCG sensu-stricto, magnetite-subclan	85% of 355 Mt @ 1.1% Cu, 0.28 g/t Au (1)	Sequeirinho Granite, gabbronorite, Pista felsic metavolcanic rock, gneiss (Xingu Complex) (2)	W-N-E-SW Canaã shear zone (3)	"S" tabular subvertical breccia, dissemination in mylonitic foliation, veins, stockwork (3)	Cpy, Mg, Py, Po (3)	Mo, Sph, Sg, Ml, Au, Pd, Pd-melon, Gn, Ct, Hs (3)	Na-(Ab-Hem), Na-Ca-(Act-rich) +Mg-(Ap), poorly K-Chl (3)	2710 ± 11 Ma (Re-Os on Mo) 2712 ± 4.7 Ma (U-Pb on Mnz) (2)	Cu-Fe-Au-Ni-Co-Pd-Se-V-P-LREE with low content of Ti-U (4)
Sossego-Curral orebody (Sossego)	Remobilization IOCG, magnetite-subclan	15% of 355 Mt @ 1.1% Cu, 0.28 g/t Au (1)	Sossego granophyric granite, Curral Granite (2)	NW-SE Shear zones (3)	Subvertical breccia pipes, veins (3)	Cpy, Mg, Py (3)	Sg, Ml, Hs, Pd-melon, Mo, Au, Ct (3)	Well developed K+Chl, late hydrolytic, poorly Na and Na-Ca (3)	1879 ± 4.1 Ma and 1904 ± 5.2 Ma (U-Pb on Mnz) (2)	Cu-Fe-Au-Ni-Co-Pd-Se-V-P-LREE-Y-Pb-Sn-Rb-Nb (4)
Salobo	IOCG sensu-stricto, magnetite-subclan	1112 Mt @ 0.69% Cu, 0.43 g/t Au (5)	Orthogneiss (Xingu Complex), Ig. Gelado Suite and crosscutted by Old Salobo granite (6)	WNW Cinzento shear zone (6)	Steeply dipping lenses with mylonitic foliation (6)	Cpy, Py, Mg, Po (7)	Uran, Sg, Sp, Gal, Pn (7)	IOCG ore related with Na, Ca-Fe alteration, Deformational post-IOCG (K-alteration) and hydrolytic-propilitc alteration (7)	2740 to 2730 Ma (7) 2705 ± 42 Ma (Pb-Pb leachates on Cc) (8)	Cu-Fe-Au-Co-Ni-As-Ag-Mo-F-REE-U (6)
Alemão	IOCG sensu-stricto, magnetite-subclan	106 Mt @ 1.45% Cu, 1.01 g/t Au (9)	Metavolcanosedimentary (Ig. Bahia Group) and the metasedimentary Águas Claras Formation (10)	Roof uplift and lateral shouldering along fault-related pluton (11)	Massive lenses, hydrothermal breccias (10)	Cpy, Mg, Py (10)	Bn, Cv, Uran, Gal, Cob, Mo, Au, Hes, Gerd (10)	Fe-rich replacement, Chl-Bt, and sulfidation. Post-ore Ca and Si (12)	2559 ± 34 Ma (U-Pb on Mnz) (10) and 2777 ± 22 Ma (Pb-Pb on Cpy) (13)	Cu-Fe-Au-U-Ag-Ba-F-P-LREE Mo-Zn-Pb (11)
Olympic Dam	IOCG sensu-stricto, hematite-subclan	10.1 Gt @ 0.78% Cu, 1 g/t Au (14)	Mafic-ultramafic volcanic, clastic facies of granitoids (Roxby Down Granite) (14)	Active fault-controlled sedimentary basin (15) N-S, NW, WNW, and NE fault systems (15)	Hydrothermal breccia (14)	Cpy, Hem, Py, Bn, Cc (15)	Gn, Mt, Sp, Fah, Dg, Cv, Dj, Id, Rx (15)	Redox Fe-oxide, Hem-Qz-Ba, destructive Hem-Ser, Advanced Argilic alteration (15)	1593.87 ± 0.21 Ma (U-Pb on Hem) (14)	Cu-Fe-Au-Ag-As-Ba-Bi-Cd-CO2-Cr-F-In-Mo-Nb-Ni-P-Pb-Sb-Se-Sn-Sr-Te-U-VW-Y-Zn-REE (15)
Ernest Henry	IOCG sensu-stricto, magnetite-subclan	89.8 Mt @ 1.17% Cu, 0.5 g/t Au (17)	Metandesites (Mt.Fort Const. Volc. eq.), metasediments intercalations (18)	NE shear zones (19)	Breccia pipe-like body, veins, lenses (20)	Cpy, Mg, Py (18)	Mo, Bn, Apy, Sf, Gn, electr. Rt, Mnz, Ba (18)	Albitization, Na-Ca, K+Ser metasomatism (18)	1514 ± 24 Ma and 1529 ± 11 Ma (U-Pb on Ttn) (18)	Cu-Fe-Au-K-S-Ba-Ca-As-Co-Mo-U-F REE-Bi-Ag-W-Sn-Mn-K (18)

References: (1) *Lancaster-Oliveira et al. (2000)*; (2) *Moreto et al. (2015a)*; (3) *Monteiro et al. (2008a)*; (4) *Carvalho (2009)*; (5) *de Melo et al. (2019c)*; (6) *Melo et al. (2017)*; (7) *Valadão (2019)*; (8) *Tassinari et al. (2003)*; (9) *VALE (2012); (10) de Melo et al. (2019a)*; (11) *Tallarico et al. (2017)*; (12) *Huang et al. (2019)*; (13) *Galarza et al. (2008); (14) Cherry et al., (2018)*; (15) *McPhie et al. (2016)*; (16) *Ehrig et al. (2012)*; (17) *Valenta (2018)*; (18) *Mark et al., (2006)*; (19) *Austin et al. (2019)*; (20) *Cave et al. (2018).*

Table 1. *(continued)*

Deposit	Type	Reserves	Host rocks	Principal ore control	Ore morphology	Main hypogene	Associated minerals	Hydrothermal alteration	Deposit age (Ma)	Geochemical signature
Candelaria	IOCG sensu-stricto, magnetite-subclan	484.76 Mt @ 0.67% Cu, 0.15 g/t Au (21)	Metandesites and metavolcanic-sedimentary rocks (Pta. del Cobre Fm.) (22)	NW-NNW faults, NS Candelaria shear zone (23)	"Mantos" stratabound stockwork, breccia, veins (22)	Cpy, Mg, Py, Po, Hem (24)	Sp, Msk, Mo, Apy, Nat. Au, Hg-Au-Ag Alloy (24)	Early Na to Na-Ca, Ca-Fe, K-Fe± Ca, Ca-Fe-Mg, late Ca-Fe-CO_2 (22)	115 ± 0.6 Ma (Re-Os on Mo) (25)	Cu-Fe-Au-Zn-Ag-Mo-REE (24)
Punta del Cobre	IOCG sensu-stricto, magnetite-subclan	180 Mt @ 0.9% Cu (22)	Upper part of metandesites and basal brecciated dacitic dome (Pta. del Cobre Fm.) (22)	NW-NNW faults	Patches, breccia filling, veins (22)	Cpy, Mg, Py, Hem (24)	Mo, Apy, Nat. Au, Hg-Au-Ag alloy (24)	Kfds/ab-chl(-act) (24)	115 ± 0.6 Ma (Re-Os on Mo) (25)	Cu-Fe-Au-Zn-Ag-Mo-REE (24)
Alcaparrosa	IOCG sensu-stricto, magnetite-subclan	14.47 Mt @ 0.79% Cu, 0.17 g/t Au (21)	Upper part of metandesites and basal brecciated dacitic dome (Pta. del Cobre Fm.) (22)	NW-NNE shear zone, NNW-NW fault-veins (26)	Disseminated patches, breccia filling, vein (22)	Cpy, Mg, Py, Hem (24)	Mo, Apy, Nat. Au, Hg-Au-Ag alloy (24)	Same as Candelaria with important Mg-Act-Bt, Ab-Ep-(Chl) (22)	115 ± 0.6 Ma (Re-Os on Mo) (25)	Cu-Fe-Au-Zn-Ag-Mo-REE (24)
Santos	IOCG sensu-stricto, magnetite-subclan	10.215 Mt @ 0.77% Cu (22)	Upper part of metandesites and brecciated zones around the dacitic dome (Pta. del Cobre Fm.) (22)	NW-NNW faults and NW fault dyke (27)	Veins, disseminated, breccia filling, irregular pipe-like body (22)	Cpy, Mg, Py, Hem (24)	Mo, Apy, Nat. Au, Hg-Au-Ag alloy (24)	Same as Candelaria with intense Mg-Act-Bt±Kfds (22)	115 ± 0.6 Ma (Re-Os on Mo) (25)	Cu-Fe-Au-Zn-Ag-Mo-REE (24)
Mantoverde	IOCG sensu-stricto, hematite-subclan	440 Mt @ 0.56% Cu, 0.12 g/t Au (27)	Volcanic (La Negra Fm.) intruded by Coastal Batholith (27)	Strong W-E and N-S brittle faults (28)	Tabular breccia, veins, cataclasite breccia (MV Norte sector) and elongate cemented breccia, discontinuous veinlets, dissemination (MV Sur sector) (27)	Cpy, Mg, Py (28)	Specular Hem (28)	Si± Chl, Kfds±Ser, ± Tour (28)	117 ± 3 Ma (K-Ar on Ser) (29) 128.9 ± 0.6 Ma (U-Pb on Zr) (30)	Cu-Fe-Au-Zn-Ag-HREE and slightly LREE (28)
Manto Ruso	IOCG sensu-stricto, hematite-subclan	15.1 Mt (supergene) @ 0.56% Cu, 0.12 g/t Au (28)	Contact between volcanic rocks and intrusives (28)	NW fault systems (28)	Subvertical breccia, dissemination, veinlets (28)	Cpy, specular Hem, Py (28)	Bn, Dg (28)	Strong Kfds, silicification ± Chl (28)	117 ± 3 Ma (K-Ar on Ser) (30)	Cu-Fe-Au-Zn-Ag-HREE and slightly LREE (28)

References: (21) *Couture et al. (2018)*; (22) *del Real et al. (2018)*; (23) *Sanchéz et al. (2018)*; (24) *Marschik et al. (2001a)*; (25) *Mathur et al. (2002)*; (26) *Pérez-Flores & Sanchéz (2018b)*; (27) *Pérez-Flores & Sanchéz (2018c)*; (28) *Rieger et al. (2010)*; (39) *Vila (1996)*; (30) *Gelcich et al., 2005.*

2. 4. Ore Characteristics

2. 4. 1. Chalcopyrite

Chalcopyrite ($CuFeS_2$) is the most important and major source of copper metal worldwide (*George et al., 2018*, among others). Frequently distributed within a wide spectrum of ore-deposits, that includes sedimentary exhalative (SEDEX), and epithermal deposits for moderate temperatures, and porphyry deposits, skarns, PGMs, and IOCG deposits for high-temperatures (*George et al., 2018*), whereas its occurrence can be related within an exsolution product in mafic igneous rocks, or within a sedimentary origin controlled by redox conditions (Anthony et al., 1990), however, chalcopyrite is essentially a hydrothermal mineral formed from Cu-rich saline hydrothermal fluids (*Zhao et al., 2014*) under different physicochemical conditions (e.g., the decrease in fO_2, temperature and in chloride ion concentration, as well an increase in pH; *Hezarkani et al., 1999*; *Landtwing et al., 2005*).

Chalcopyrite, as well the other major sulfides phases as pyrrhotite, and pentlandite plays a significant role in the mysterious behavior of Pb (*Hart & Gaetani, 2006*) during mantle melting, and also represent the most important petrogenetic agents in magmatic systems (*Kiseeva et al., 2017*). Nevertheless, it is generally a poor host for most trace elements and just incorporates these (e.g., Ag, As, Au, Bi, Cd, Co, Ga, Hg, In, Mn, Ni, Pb, Sb, Se, Sn, Te, Tl, Zn) in the absence of other co-crystallizing sulfides (e.g., sphalerite and galena), through its face-centered tetragonal lattice system with tetrahedrally-coordinated Cu, Fe, and S atoms (*Baba et al., 2012*; *Kimball, 2013*; *George et al., 2018*) where bonding in the mineral structure is covalent with an effective ionic state between $Cu^{+}Fe^{3+}S_2^{2-}$ and $Cu^{2+}Fe^{2+}S_2^{2-}$ (*Li et al., 2013*).

2. 4.2. Magnetite

Magnetite ($Fe^{2+}Fe_2^{3+}O_4$) is one of the '2-3 oxide spinels', $A^{2+}B_2^{3+}O_4$, where A is divalent and B is trivalent (*Biagioni et al., 2014*, and references therein). Thus, the tetrahedral coordination site and ferric (Fe^{3+}) and ferrous (Fe2+) occupy the octahedral sites in its crystalline structure (*Childress, 2019*). Magnetite is a common mineral in a wide range of geological environments, crystallizing from silicate and sulfide melts at high temperature, precipitating from hydrothermal fluids at variable temperatures or derived from sedimentary environments at low temperature. It can accommodate a variety of trace elements (Si, Al, Ti, Mn, Ca, P, Mg, V, Cr, Co, Ni, Cu, Zn, Ga, Zr, Ba, As, Ge, Sn, Sc, Sr, Y, Nb, Mo, W, Hf, Ta, and Bi) with its chemical composition varying in response to different mineralizing systems as IOCG, IOA, BIF's, porphyry Cu, and skarn deposits (Wu et al., 2019, and references therein). Magnetite formed from high-temperature hydrothermal fluids (~500–700 °C) associated with a magmatic-hydrothermal source (e.g., porphyry and IOCG deposits) is typically enriched in Ni, V, Co, Zn, Mn, and Sn almost to the same concentrations as magnetite from evolved intermediate magmas that crystallize apatite together with magnetite (e.g., andesite and Fe-Ti-P deposits). Although Cu and Pb are also common in these types of hydrothermal fluids, they are in less abundance due to the competition of magnetite with the precipitation of Cu sulfides and the incompatible nature of Pb into magnetite (*Dare et al., 2014*). Further, regional tectonic changes can destabilize magmatic bodies and cause the magnetite magnetite-fluid suspension to ascend through well-developed high-flux permeable channels (*Hersum et al., 2005*; *Hautmann et al., 2014*), which increase crystallinity of ductile magmas, and when subsequently reach buoyant levels propitiate the formation of structurally controlled magnetite orebodies (*Childress, 2019*).

2. 4. 3. Hematite

Hematite (α–Fe_2O_3) is the most thermodynamically stable Fe-oxide phase in the iron oxide family and occurs throughout the geologic record (Cornell & Schwertmann, 2003; Liu et al., 2016), also is the most abundant in IOCG and BIF's deposits. It forms under a wide variety of conditions, crystallizing as an accessory mineral in felsic magmas, also as part of late volcanic sublimates, as well as within high-temperature hydrothermal veins, or as the product of contact metamorphism, whereas is also abundant on weathered iron-bearing minerals and a common cement in sedimentary rocks (*Anthony, 1990*). Further, hematite crystals adopt the corundum structure, a rhombohedral crystal lattice system with space group $R\bar{3}c$ (*Piccinin, 2019*), whereas their composition depends by the composition of magma or subsequently the composition of hydrothermal fluids, as well as the physical-chemical conditions that influence the partition coefficients of elements (e.g., temperature, pressure, rate of cooling, fO_2, silica activity), and the co-crystallization minerals during which some specific elements may compete with hematite (*Huang et al., 2018*, and references therein).

Hematite is also a potential proxy for paleo-environmental conditions such as temperature, humidity, and soil pH during its formation, whereas in Precambrian rocks has been presented as evidence for oxygenated seawater and groundwater in Earth's early history (*Frierdich et al., 2018*, and references therein). Furthermore, it can incorporate a wide range of trace elements, including HFSE, REE, and REY, with patterns and variations among these that reflect evolving physiochemical conditions, whereas the incorporation of U and its decay products facilitates its use as a mineral geochronometer for hydrothermal ore-forming processes in IOCG deposits (*Verdugo-lhl et al., 2017*; *Courtney-Davies et al., 2019a*; *b*). Studies as *Simon et al. (2018)*, indicates that the presence of hematite in the shallow regions of IOCG deposits is consistent with oxidation of the ascending ore fluid, which helps the fluid maintain high concentrations of Cu and Au, while *Huang et al. (2018)* summarizes that hematite-group IOCG deposits have relatively high Si, Ca, Al, Sn, Cu, and Ti contents but low Mn, Mg, V, and Ni contents, possibly related with hematite crystal structure that incorporates larger hexavalent metal cations (Liu et al., 2012). Further, *Courtney-Davies et al. (2019a*; *b)* confirms that hematite can be used to compare the IOCG systems in terms of both the timing of ore formation and the geochemical signatures of mineralizing fluids, with potential application to all U-bearing Fe-oxide rich mineral systems. Thus, all the above suggests that hematite can be used as a petrogenetic tool (*Nadoll et al., 2014*; *Childress, 2019*).

2. 4. 4. Bornite

Bornite (Cu_5FeS_4) is the second major Cu-sulfide, and also the major Cu-carrier in many IOCG, high-sulfidation epithermal deposits, sedimentary-hosted copper deposits, volcanogenic massive sulfide (VMS)-type, and some porphyry-Cu deposits and associated Cu– and polymetallic skarns (*Cook et al., 2011*, and references therein). Bornite is essentially a hydrothermal mineral formed from Cu-rich saline hydrothermal fluids (*Zhao et al., 2014*). Particularly, its structure was the subject of several investigations and different polymorphs form at different temperatures (Martinelli et al., 2018). Thus, at high temperatures (> 235°C) crystallizes with an antifluorite-type structure that forms a face-centered cubic lattice with each occupied tetrahedral site comprising three-quarters of metal cations (*Morimoto, 1964*), whereas at medium temperatures (~170°C) crystallizes with an orthorhombic structure (*Kanazawa et al., 1978*), while at lower temperatures (~1.85°C) it crystallizes in the orthorhombic space group (*Martinelli et al., 2018*).

According Cook et al. (2011), bornite commonly hosts inclusions of mineral phases, notably Ag-, and more rarely, Bi-bearing chalcogenides, gold grains, and even platinum-group elements (PGE), although is a poor host for Au, whereas indicates significantly differences between trace element geochemical signatures from hypogene and supergene bornite.

2. 4. 5. Pyrrhotite

Pyrrhotite is a family of non-stoichiometric, metal-deficient iron sulfide minerals ($Fe_{(1-x)}\, S_{(0 \leq x \leq 0.125)}$) found in a variety of geologic environments within the Earth's crust and mantle, as well as in a range of meteorites (*Volk et al., 2018*). Pyrrhotite is common in magmatic ore deposits, contains fewer constituents than other sulfides (i.e., Fe and S only), and preliminary high-temperature experimental constraints exist for this sulfide alone (*Schuessler et al., 2007*). It has the NiAs structure but does not have the stoichiometric composition FeS because there is a shortage of iron in the unaffected sulfur lattice (*Becker et al., 2010*). The composition of the mineral is complex as the Fe/S ratio varies over a wide range. At one end is the complex Fe_7S_8 and at the other is FeS (troilite). Interestingly, the last phase is non-magnetic and is mostly found in extraterrestrial meteorites. Until the date, the origin of pyrrhotite non-stoichiometry (e.g., magmatic degassing, assimilation of S or post-igneous hydrothermal modification) is stilly debated (Lorand et al., 2018, and references therein). Likewise, the magnetic property is due to the iron vacancies in the crystal structures. In general, the vacancies disturb the crystal symmetry and hence affect the magnetic susceptibility (*Gupta & Yan, 2016*).

Particularly, the 4C polytype (Fe_7S_8) acts a recognizable ferrimagnetic phase which is also a common mineral in most sulfide ore deposits, especially in those that contain Ni, Cu, and PGE elements (Lilies & Villiers, 2012) including magmatic Fe-Ni-Cu-PGE and VMS deposits, metamorphic and low-temperature diagenetic environments (*Gordon & McDonald, 2015*; *Volk et al., 2018*). Furthermore, pyrrhotite contains fewer constituents than other sulfides (i.e., Fe and S only), and preliminary high-temperature experimental constraints exist for this sulfide alone (*Schuessler et al., 2007*).

Recent research as *Bilenker et al. (2018)* confirms that pyrrhotite plays a significant role in Fe isotope fractionation in magmatic systems and in the formation of magmatic sulfide deposits. Furthermore, it is known to be a reactive mineral that is highly prone to oxidation (*Rand, 1977*; *Belzile et al., 2004*). Thus, all the above makes pyrrhotite the ideal candidate to help begin to disentangle the Fe isotope signals of sulfides.

Table 2. Selected characteristics of mineral phases included in this study.

	Chalcopyrite	Magnetite	Hematite	Bornite	Pyrrhotite
Chemical formula	$CuFeS_2$	$Fe^{2+}Fe_2^{3+}O_4$	α–Fe2O3	Cu_5FeS_4	Fe(1−x) S(0 ≤ x ≤ 0.125)
Structural configuration	Face-centered tetragonal lattice	Tetrahedral-octahedral oxide inverse spinels	Corundum structure, rhombohedral lattice	Face-centered cubic lattice	Monoclinic (4C)
Common mineral association	Sph, Gal, Td, Py, many Cu sulfides	Cr, Ill, Ulvospinel, Rt, Ap, many silicates (igneous) Po, Py, Cpy, Pent, Sp, Hem, many silicates (hydrothermal, metamorphic) Hem, Qtz (sedimentary)	Ill, Rt, Mag (metamorphic and igneous) Goe, Sid, Lepidocrocite (sedimentary)	Cpy, Py, Gar, Cal, Woll, Qtz, other Cu and Fe sulfides	Py, Mar, Cpy, Pent, Mag, Cal, Dol, many other sulfides
Main trace elements interaction	Ag (most common) Se and Hg (common) Mn, Co, Zn, Ga, Se, Ag, Cd, In, Sn, Sb, Hg, Tl, Pb and Bi (common without Sph and Gal association) Sn and Ga (common with Sph and Gal association) (1)	Zr, Hf, Nb, Ta, and Sc (most common) Ni, V, Co, Zn, Mn, and Sn > Cu and Pb (common at high temperature) Ge and W (common at lower temperatures) Si and Ca (less common) (2) Ga, Mn, Zn, Ni, and Cr (common in magnetite-group IOCG's) Pb, Zr, and Hf (less common in magnetite group IOCG's) Mg, Co, and V (common in magnetite-group IOA deposits) (3)	Si, K, Ca, Al, Pb, Zr, Ge, W, Sn, Sc, Nb, Cu, and Mo (common in hematite-group IOCG's) Ga, Mn, Mg, Zn, Co, V, and Ni (less common in hematite-group IOCG's) Zr, W, Sn, Sc, and Ti (common in IOA's) Al and Mg (less common in IOA's) (3)	Ag and Bi (most common) Se and Te (common) Mo, Tl > Au, Co, Ni, Ga, Ge, In, As, Sb, Al, U, V, Cr, Mn, Nb, and W (less common) (4)	Ni (most common) (5) Mn, Mo, Al, V (common) Au, As, Bi (less common) (6)

References: (1) *George et al. (2018)*; (2) *Dare et al. (2014)*; (3) *Huang et al. (2019)*; (4) *Cook et al. (2011)*; (5) Becker et al. (2010); (6) *Hawley & Nichol (1961)*.

2. 5. Sr–Nd systematics

The Sr–Nd isotopic systematics is based in the joint application of Sm–Nd, Sr–Sr, and Pb–Pb methods. Sistematic compositions may serve as proxies for the mineralizing fluids and may be used to yield the source of mineralizing fluids and metals, due to: (1) Nd isotopes represent one of the best tools to investigate the processes involved in the evolution of the continental crust and mantle; mainly due to their similar geochemical behavior, where both LREE, which inhibits their fractionation during most varied geological process (*Goia & Pimentel, 2000*); (2) Radiogenic ^{87}Sr can be used as a tracer in petrogenetic processes, where the numerical value of initial $^{87}Sr/^{86}Sr$ ratio can be used to infer the source of the magma as well rock-water interaction processes (*Faure & Powell, 1972*)

Many researches have determined the source of mineralizing fluids or metals using the Sr–Nd systematics. Representative advances in the field are summarized in Table 3.

Table 3. Selected examples of Sr–Nd–Pb systematics studies of mineralizing fluids from different ore systems.

Reference	Isotopic system used	Sample type	Deposit (s) studied	Significant findings
Norman & Landis (1983)	Sr-Sr	Pyrite, wolframite, quartz, sphalerite, rhodochrosite, and fluorite	Pasto Bueno W deposit, Peru	Sulfide and base metal mineralization were from mixed derivation ore fluids
Kistler & McKee (1985)	Rb-Sr, Sm-Nd, U-Pb, and K-Ar	Pyrite, quartz, plagioclase, sericite, and host rocks	West Shasta Cu-Zn district, California, USA	The major component of mineralizing fluids was Devonian seawater
Simonetti & Bell (1985)	Rb-Sr, Sm-Nd, and U-Pb	Fluorite	Amba Dongar Carbonatite Complex, India	Mineralizing solutions involved interactions between a cooling F-rich fluid, derived from the carbonatite melt, and the continental crust
Yang & Zhou (2001)	Rb-Sr, Sm-Nd, and Pb compositions	Pyrite	Linglong gold mine, China	Hydrothermal fluids were probably derived from a mixed source that involves degassing of mafic magmas and meteoric water that had leached the country rocks
Peng et al. (2006)	Rb-Sr, Sm-Nd, and Pb compositions	Scheelite	Woxi W-Sb-Au deposit, W Hunan, China	Mineralization involved mixed fluids from diverse sources and evolved from the underlying mature continental crust
Ni et al. (2012)	Rb-Sr, Sm-Nd, and Pb compositions	Chalcopyrite, pyrite, galena, molybdenite, and host rocks	Dahu Au-Mo deposit, Qinling Orogen, Central China	The source of ore-forming fluids is from a depleted mantle or a depleted, subducted oceanic slab

Table 3. *(continued)*

Reference	Isotopic system used	Sample type	Deposit (s) studied	Significant findings
Li et al. (2014)	Rb-Sr, Sm-Nd, U-Pb, and Lu-Hf	Host rocks	Duolong porphyry Cu–Au deposit, Central Tibet	Volcanic rocks were predominantly derived from a mantle wedge, metasomatized by subducted slab fluid/melts
Zhang & Zuo (2014)	Rb-Sr, Sm-Nd, Pb compositions	Magnetite, and host rocks	Makeng Fe-Mo skarn deposit, S China	Initial mineralizing fluids may have been derived from granitic magmas but also involved materials originating from Hercynian diabases and/or the intruded strata
Deng et al. (2015)	S stable and Rb-Sr, Sm-Nd, Pb compositions	Fluorite	Tumen Mo-F deposit, Qinling Orogen, China	The initial ore-forming fluids were sourced from Neoproterozoic syenitic magmatism
Deng et al. (2016)	Re-Os, and Rb-Sr, Sm-Nd, Pb compositions	Pyrite, molybdenite, and galena	Zhifang Mo deposit, Qinling Orogen, China	Ore-forming fluids were sourced from the older basement
Xu et al. (2016)	Rb-Sr, Sm-Nd. Pb compositions, Lu-Hf and S stable	Feldspar, pyrrhotite, chalcopyrite, pyrite, arsenopyrite, sphalerite, galena, host rocks	Sn and Pb-Zn polymetallic ore deposits in the Pengshan district, S China	Hydrothermal fluids and metals were derived from mixing of the granitic magmas and the host metasedimentary rocks
G. Wu et al. (2017)	Re-Os, and Rb-Sr, Sm-Nd, Pb compositions	Host rocks	Caosiyao porphyry Mo deposit	The Mo deposit is sited within a post-orogenic setting after the Mongol-Okhostk ocean closure and coeval to the subduction of the Paleo-Pacific plate
Yen et al. (2017)	Lu-Hf, Sm-Nd, Rb-Sr, and Pb compositions	Pyrite, chalcopyrite, host rocks	Taoxihu Sn deposit, SE China	The crustal partial melting and Sn mineralization occurred during the mantle underplating in an extensional environment, probably associated with the subduction slab roll-back of the Paleo-Pacific Plate. The host rocks were generated by partial melting of the Mesoproterozoic crust with minor mantle input
Cao et al. (2018)	Sm-Nd, Rb-Sr, and Pb compositions	Wolframite	Xitian W-Sn polymetallic deposit, S China	The ore-forming metals are originated from a crust source

2. 5. 1. Sm–Nd method

The Sm-Nd method is based on the decay of ^{147}Sm to ^{143}Nd, with the emission of an α particle, where ^{144}Nd serve as reference. Both are LREE members and exhibit similar geochemical behavior for most geological processes, e.g., are accumulate in the later stages during the crystallization of a magma, and the Sm/Nd ratios do not greatly vary in common crustal rocks. Nd is a lighter lanthanide than Sm and therefore more incompatibly. This means that common igneous processes, such as partial melting and fractional crystallization, almost always result in not just higher LREE concentrations but also lower Sm/Nd ratios in the more siliceous end-members. Hence, greater amounts of radiogenic isotopes in the mantle are accumulated through the geological time and, consequently, in $^{143}Nd/^{144}Nd$ ratios higher than those observed in the crust. For example, rocks derived from mantle melting have higher Sm/Nd than generated by crustal melting material, while low Sm/Nd ratios indicate enrichment pattern in LREE in comparison with depletion patterns in HREE shows by high Sm/Nd ratios (*Champion, 2013*).

Throughout the Earth's evolutionary history, the continuous extraction of magmas by partial melting of the upper mantle allowed the incorporation of elements with large ionic radii (K, Rb, U, Th, Ba and LREE) in the crust. According to *DePaolo (1988)* model, the uniform evolution over time for the $^{143}Nd/^{144}Nd$ ratio is based on the depletion of the upper mantle in the abovementioned elements (DM – Depleted Mantle), in relation to a uniform primordial mantle, whose Sm/Nd ratio is equal to that of the chondritic meteorites (CHUR – Chondritic Uniform Reservoir) and represents the initial composition of the universe.

DePaolo & Wasserburg (1976) developed a notation whereby initial $^{143}Nd/^{144}Nd$ isotope ratios could be represented as parts per 10^4 deviations from the CHUR evolution line, termed εNd. The notation $\varepsilon Nd_{(0)}$ refers to the present time, and the calculation is performed with the $^{143}Nd/^{144}Nd$ analyzes obtained in the laboratory. $\varepsilon Nd_{(T)}$ represents the isotopic composition of the crust when it was formed and, as previously defined, is identical to the source signature. Thus, if the analyzed material has a higher Sm/Nd ratio than CHUR, with a positive εNd, it may have originated from the depleted mantle (depleted in incompatible elements during a previous partial melting event). In the case of negative εNd, an origin in the crust is inferred (derived or assimilated a great proportion of old crustal rocks). The crustal residence time will be greater the more negative εNd. Model ages (TDM) can be calculated based on the evolution model described above and interpreted as markers of the crustal residence time of the materials that compose it.

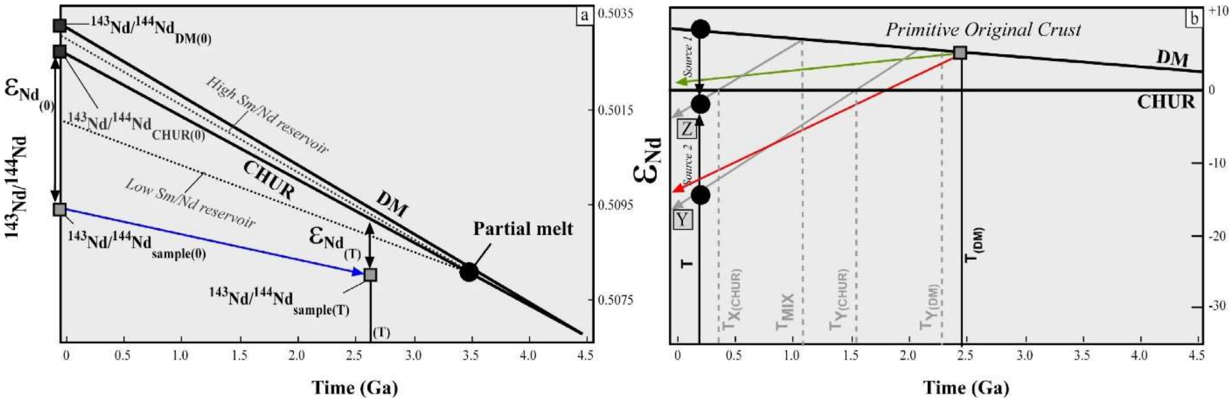

Figure 8. (A) Illustration of the parameters for the evolution of $^{143}Nd/^{144}Nd$ through time. The change in $^{143}Nd/^{144}Nd$ back through time is a function of the $^{147}Sm/^{144}Nd$ ratio. Variations of $^{143}Nd/^{144}Nd$ are small and so are typically reported as εNd values. If the reservoirs formed during partial fusion remain closed, the evolution of the $^{143}Nd/^{144}Nd$ ratio over time happens along the dashed curves proportional to the Sm/Nd ratio. Adapted from *White (2005)* and *Champion (2013)*. (B) Schematic principles of Nd model ages; only model ages calculated for rock Y correspond to time of separation from the mantle, model ages for rock Z (a mixture of two sources) do not represent separation from mantle reservoir, neither do they correspond to crystallization age T. Green line represents the mafic crust evolution, while the red line represents the crustal average composition. Adapted from *Kôsler (1998)* and *DePaolo (1988)*.

2. 5. 2. Sr–Sr method

The Sr-Sr method, based on the decay of ^{87}Rb to ^{87}Sr, with the emission of a negative β-particle, where ^{86}Sr is stable and serves as reference. Chemical differentiation of the Earth over its history due to partial melting has resulted in the mantle having relatively low Rb/Sr, and thus, over time, it has evolved to relatively unradiogenic $^{87}Sr/^{86}Sr$ (ca. 0.7035). In contrast, the continental crust has relatively high Rb/Sr and has thus evolved to have highly variable and typically radiogenic $^{87}Sr/^{86}Sr$ (e.g. >0.710). As Sr isotopic compositions are not modified by processes such as melting and crystallization, these signatures can be used to identify the source(s) of magma and to identify processes such as crustal contamination of mantle. The initial Sr isotopic composition of the system $^{87}Sr/^{86}Sr_i$ is a useful parameter to understand the geology history of the source rocks that melted to generate the magma (*Waight, 2013*).

DePaolo & Wasserburg (1976) plotted $^{143}Nd/^{144}Nd$ isotope ratios in the form of εNd against $^{87}Sr/^{86}Sr$, and found a negative correlation (between them in oceanic and some continental igneous rocks, and they suggested that the formation of basaltic magma source in the mantle involved the coupled fractionation of Sm/Nd and Rb/Sr, while some continental samples, which lay to the right of the main correlation line, could have been contaminated by radiogenic Sr in the crust. From the above, some authors defined at least five main mantle components based on the isotopic data of Nd, Sr, and Pb from oceanic basalts, which are the depleted residual mantle (DMM – Depleted MORB mantle), the mantle with high U/Pb ratio (HIMU), the primitive or prevalent mantle (PREMA) and two enriched mantle reservoirs (EM-I and EM-II).The position of these mantle components in the Nd–Sr isotopic correlation diagram is illustrated in Figure 10. Detailed reviews of isotopic characteristics, as the model proposed can be found in *Zindler & Hart (1986)*, *Hofmann et al. (1997)* and *Stracke (2012)*.

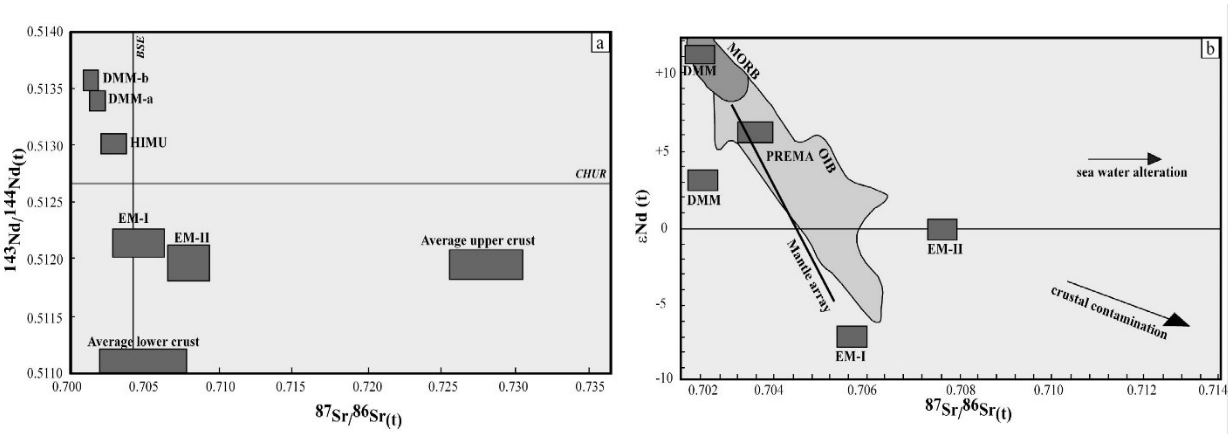

Figure 9. Illustration of Nd and Sr isotopic applications. (a) $^{143}Nd/^{144}Nd_{(t)}$ against $^{87}Sr/^{86}Sr_{(t)}$. (b) $\varepsilon Nd_{(t)}$ against $^{87}Sr/^{86}Sr_{(t)}$. The mantle components are taken from Zindler & Hart (1986). The boxes for average upper and lower crusts are taken from Taylor and McLennan (1985).

2. 6. Rare Earth Elements (REE)

Rare-earth elements (REE) are a group of seventeen chemical elements in the periodic table, in particular, the fifteen lanthanides (La, Ce, Pr, Nd, Pm, Sm, Eu, Gd, Tb, Dy, Ho, Er, Tm, Yb, and Lu) as well as Sc and Y as defined by the International Union of Pure and Applied Chemistry (IUPAC),, and can be further subdivided into light and heavy REE (LREE, HREE, respectively), on the basis of atomic weight. This subdivision is based on another characteristic of the REEs, namely lanthanide contraction, whereby successively heavier lanthanides (higher atomic number) have increasingly smaller atomic radii. This means that lighter REE are more incompatibly than heavier REE (*Champion, 2013*).

According to the *Balaram (2019)*, in nature, REE does not exist as individual native metals such as Au, Cu, and Ag because of their reactivity, instead, they occur together in numerous ore/accessory minerals as either minor or major constituents. Though REE are found in a wide range of minerals, including silicates, carbonates, oxides, and phosphates, they do not fit into most mineral structures and can only be found in a few geological environments. Further can be divided into (1) Primary deposits, whose are formed by magmatic, hydrothermal and/or metamorphic processes, commonly emplaced into extensional settings and related with alkaline igneous rocks (pegmatites and carbonatites) or as residual deposits (including IOCG deposits), and (2) Secondary deposits, whose are formed by erosion and weathering and may include heavy mineral placers, laterites, and bauxites, as well REE in coal and REE in the sediments of continental shelf and Ocean bottom. However, as REE deposits appear in a wide variety of geological environments, it is not very easy to classify them into different categories.

The inductively coupled plasma mass spectrometry (ICP-MS) and the inductively coupled plasma optical emission spectroscopy (ICP-OES) are the most favorable choices for the simultaneous determination of REEs in practical samples. However, ICP-MS can be hampered by isobaric interferences, such as those from barium oxides on Nd, Sm, and Eu measurements, and from lighter REE oxides (e.g., CeO and NdO) on heavier REEs (e.g., Gd, Tb, and Dy), while ICP-OES is used for the determination of REEs because of its inherent capability for rapid simultaneous multi-element detection over a wide range of concentrations (*Li et al., 2017*, and references therein).

Representative advances in the field of REE patterns in the studied ore phases are summarized in Table 4.

Table 4. *Selected examples of REEs studies on ore-phases studied in this research.*

Reference	Sample type	Deposit (s) studied	Significant REE observations
Gauthier et al. (2004)	Magnetite	The Kwyjibo Cu-REE-U-Au-Mo-F iron oxide deposit, NE Grenville province, Canada	Negative Eu anomaly, LREE>HREE, slightly positive Y anomaly (related with disseminated REE-minerals)
Yuwang et al. (2010)	Chalcopyrite, pyrrhotite (among other sulfides)	Kalatongke Cu-Ni deposit, Xinjiang, China	Multiple-bending pattern of REE of the sulfides suggests coexistence of multiple liquid phases (fluid and melt). Chalcopyrite and pyrrhotite have similar REE patterns (LREE>HREE), except that positive Eu and Y anomalies are only present in the first
Bonyadi et al. (2011)	Magnetite (among other minerals)	Se-Chahun IOA deposit, Bafq district, Iran	REE are present as abundant micro-inclusions. Negative Ce anomalies are not derived from apatite micro-inclusions
Elizarova & Bayanova (2012)	Chalcopyrite	Talnakh Cu-Ni PGE deposit, Kazakhstan	LREE<HREE, negative Eu anomaly
Goldsmith (2014)	Magnetite, hematite (two generations)	Samphire distal IOCG Project, Gawler Craton, Australia	Early hematite is characterized by strong enrichment in REE and Y, and strong negative Eu anomaly. Later hematite is characterized by negative Eu and Y anomalies related with the coexistence of hydrothermal REY-minerals. Magnetite carries high concentrations of REY

Table 4. *(continued)*

Reference	Sample type	Deposit (s) studied	Significant REE observations
Zhang & Zuo (2014)	Magnetite	Makeng Fe-Mo skarn deposit, S China	Weak enrichment of LREE compared to HREE and relatively flat pattern. REE patterns similar to those of the diabases and granitic rocks.
Beni & Panahpour (2015)	Magnetite	Choghart IOA deposit, Bafq district, Iran	High ratios of LREE/HREE reflect a progressive magmatic differentiation, and also indicates that the REE are placed within the magnetite crystalline network by post-magmatic solutions. Strong depletion of Eu and Ce, and enrichment of Gd and Pd. REE indicates a magmatic origin.
X. Huang et al. (2015)	Magnetite, hematite	Bayan Obo Fe-REE-Nb deposit, North China	Both shows a similar REE patterns and trace elements contents, indicating a similar origin. Magnetite from sedimentary origin are enriched in REEs, whereas from hydrothermal origin are relatively poor in REEs.
Sabet-Mobarhan-Talab (2015)	Magnetite	Chador-Malu IOA deposit, Bafq district, Iran	Negative Eu anomalie and LREE>HREE fractionation. Magnetites may have inherited their REE patterns from microinclusions of apatite and/or fluid-mineral interaction during the hydrothermally overprinting events
Li et al. (2015)	Magnetite	Lamandau IOCG deposit, SW Indonesia	Low REE concentrations. LREE enrichment relative to the HREEs. REE patterns are similar to those from rocks formed at the mid-ocean ridges indicating that the deposit formation was closely related to slab subduction
Zarei et al. (2016)	Magnetite	Khanlogh IOA deposit, Eastern Cenozoic Quchan-Sabzevar Magmatic Arc, NE Iran	Magnetite have a high concentration of REE and show weak to moderate LREE/HREE fractionation. They are comparable to the REE patterns in Kiruna-type iron ores
Mukherjee et al. (2017)	Magnetite	Carbonate-hosted Bhukia Gold Deposit, Rajasthan, W India	Magnetite and apatite suggest a magmatic hydrothermal origin and close association within Au (+Cu) province recommends their genesis in an IOCG-IOA setting
Dekov et al. (2018)	Chalcopyrite, hematite	Irina II vent site, Logatchev hydrothermal field, Mid-Atlantic Ridge	The primary hematite hydrothermal deposits at the seafloor may be a potential source of REE and trace elements more than chalcopyrite. Hematite layers exhibit a strong negative Eu anomaly, which is inferred to be a result of crystallographically-controlled REE fractionation during their precipitation
de Melo (2018); de Melo et al. (2019a)	Chalcopyrite	Igarapé-Bahia IOCG deposit, Brazil	Chalcopyrite from different ore-styles point to different origins, with positive Eu anomaly and slightly Ce anomaly in magnetite-rich zones and depletion of Eu and slightly Ho anomalies in nodules and layers ore styles
Sun et al. (2018)	Chalcopyrite	Shimensi W-Cu-Mo polymetallic deposit, S China	Chalcopyrite show LREE-enriched patterns, variable Eu negative anomalies, similar than granites and meta-sediments/volcanic rocks suggesting as the source for the ore-forming fluids

CHAPTER 3 – JOURNAL ARTICLE

To be submitted to Ore Geology Reviews

Nd–Sr isotopes and trace-element geochemistry on hypogene IOCG-ores: Implications on the genesis of South American IOCG systems

Eduardo Fritis*, Maria Emilia Schutesky, Jérémie Garnier

Instituto de Geociências, Universidade de Brasília, Brasília, DF 70910-900, Brazil

* Corresponding author.
E-mail address: eduardo.fritis.perez@gmail.com (E. Fritis).

Keywords: IOCG; Nd-Sr isotopes; trace elements; Carajás Mineral Province; Andean IOCG deposits; Candelaria-Punta del Cobre district

Abstract

Magnetite and chalcopyrite are the most economically essential ore minerals in the spectrum of IOCG systems and as the leading carriers of Cu, Fe, and Au, can also transport REEs through microinclusions. Initial Sr and Nd isotope ratios expressed relative to UR and CHUR range from ~ –3.30 to +2.19, and 0.71590 to 0.71973, respectively, in Neoarchean IOCG, and from –11.68 to –9.22, and 0.701802 to 0.75171, respectively, in Orosirian Cu-Au systems from the Carajás Mineral Province, and from ~ +1.81 to +4.03, and from 0.70155 to 0.70864 in the Cretaceous IOCG from the Candelaria-Punta del Cobre district. These values for the Precambrian Carajás Province are consistent with the derivation of the REE, Fe, Cu, and probably Au, from more than a single source. Neoarchean IOCG systems probably derived metals from reworked ancient crust through the leaching of Meoarchean basement rocks and involving the assimilation and contribution of Neoarchean juvenile mantle-derived components. Oppositely, metals in Orosirian Cu-Au systems derived predominantly from remobilization processes from long-lived Meso-to late-Neoarchean crustal sources continuously reworked through restricted granitogenesis events. Towards the Cretaceous Candelaria-Punta del Cobre IOCG district, metals were derived from primitive sources compositionally similar to the arc-volcanic rocks, probably by heterogeneities mantle source, rather than a single specialized source. Model ages indicate that prolongated incubation periods are a key factor for the ore endowment, similar as stated by Storey & Smith (2017). In contrast, tectonic shifts are the main trigger for mineralization, regardless of the tectonic environment. Alternatively, differences between South American IOCG systems respond to controls in the fluid-rock interaction and the composition of the mafic precursor in which each province evolves.

1. Introduction

Iron oxide copper-gold (IOCG) systems are an essential world-source of Fe, Cu, and Au and may contain significant amounts of other elements – e.g., F, P, As, Zn, Ni, Co, Ag, Mo, Ba, U and REE (***Sillitoe, 2003***; ***Barton, 2014***; ***Jaireth et al., 2014***). Overall, these structurally-controlled deposits are inherently associated with abundant Fe-oxides phases formed in association with extensive Na-Ca pre-sulfide hydrothermal alteration (e.g., ***Haynes, 2000***; ***Sillitoe, 2003***; ***Williams et al., 2005***; ***Skirrow, 2010***; ***Barton, 2014***; ***Chen, 2013***; ***Hu et al., 2020***). Notwithstanding the significant economic supplies of IOCG deposits, contributing with over 5% and 1% of the world's copper and gold, respectively (***Rusk, 2010***), questions on their geodynamic setting and fluid sources remain poorly understood.

IOCG systems are complex and particular differences between each architectural system involve the interaction of different structural mechanisms, physicochemical conditions, and rock-buffer relationships in which metals form and evolve (e.g., ***Austin et al., 2019***). To date, different hypotheses have been postulated to explain the controversy surrounding these mineral systems. Whilst magmatic-hydrothermal models (e.g., ***Pollard, 2000***; ***Sillitoe, 2003***; ***Groves et al., 2010***; ***Barton, 2014***; ***Richards & Mumin, 2013a***; ***b***) are suggested as the primary process for economic mineralization in many IOCG's worldwide – e.g., Carajás Province (***de Melo et al., 2019a***; ***Valadão, 2019***; ***Campo, 2020***; ***Schutesky & Oliveira, 2020; Pesilho et al., 2020***), Gawler Craton (***Oreskes & Einaudi, 1992***; ***Courtney-Davies et al., 2020b***), Mt. Isa Inlier (***Mark et al., 2004***; ***2006***), Great Bear Magmatic Zone (***Mumin, 2007***; ***Acosta-Góngora et al., 2018***), and the Central Andes IOCG Province (***Ullrich et al., 2001***; ***Sillitoe, 2003***; ***Rieger et al., 2010***; ***2012***; ***Tornos et al., 2010***; ***2012***; ***Marschik & Kendrick, 2015***; ***Richards et al., 2017***; ***del Real et al., 2020***; ***Childress et al., 2020***), several studies highlight the involvement of additional fluids, such as (1) specialized mantle-derived fluids (e.g., ***Marschik & Fontboté, 2001a***; ***Mathur et al., 2002***; ***Marschik et al., 2003a***; ***b***; ***Sillitoe, 2003***; ***Marschik & Söllner, 2006***; ***de Haller et al., 2006***; ***Baker et al., 2008***; ***Creixell et al., 2009***; ***Gleeson & Smith, 2009***; ***Rieger et al., 2010***; ***Williams et al., 2015***; ***Oyunjargal et al., 2020***), (2) non-magmatic-hydrothermal signatures (***Barton & Johnson, 1996***; ***2000***) – e.g., meteoric water (***Haynes et al., 1995***; ***Xavier et al., 2012***), sea-water (***Ripley & Ohmoto, 1977***; ***de Haller et al., 2002***; ***2009***; ***Monteiro et al., 2008a***; ***Chen et al., 2010***; ***2011***; ***Xavier et al., 2012***) or evaporitic sequences (***Davidson & Dixon, 1992***; ***Hitzman, 2000***; ***Hunt et al., 2005***; **de** ***Haller et al., 2002***; ***2009***; ***Benavides et al., 2007***; ***Dreher et al., 2008***; ***Monteiro et al., 2008a***; ***Gleeson & Smith, 2009***; ***Marschik & Kendrick, 2015***; ***Riehl & Cabral, 2018***; ***del Real et al., 2020***), (3) leach of crustal-derived magmas (e.g., ***Monteiro et al., 2008a***; ***Chen & Zhou, 2012***; ***Zhimin & Yali, 2013***; ***Storey & Smith, 2017***; ***Zhu et al., 2020***), (4) metamorphic-derived fluids (e.g., ***Requia, 1995***; ***Kendrick et al., 2007***; ***Fisher & Kendrick, 2008***), or (5) volcanic lake water-derived fluids (***Schlegel et al., 2020***). More recently, several others point towards the convergence of ore-forming processes as a single genetic continuum from IOA to IOCG via a combination of igneous and magmatic-hydrothermal fluids (***Hitzman, 2000***; ***Sillitoe, 2003***; ***Williams et al., 2015***; ***Knipping et al., 2015a***; ***b***; ***Corriveau et al., 2016***; ***Reich et al., 2016***; ***Barra et al., 2017***; ***Johansson et al., 2017***; ***Simon et al., 2018***; ***Huang & Beaudoin, 2019***; ***Childress et al., 2020***; ***Rodriguez-Mustafa et al., 2020***), or through the intrusion of magmatic-hydrothermal fluids similar to porphyry deposits (***Pollard, 2006***; ***Richards & Mumin, 2013a***; ***b***; ***Escolme et al., 2020***; ***Orlandea et al., 2020***; ***Verdugo-Ihl et al., 2020***).

Additionally, even though the "current formula" of IOCG systems are genetically linked with the super continental cycle, either during the intervening period between the breakup of largest landmasses (***Kerrich et al., 2005***; ***Porter, 2010***; ***Cawood & Hawkesworth, 2013***; ***Zhou et al., 2014***; ***Pirajno & Santosh, 2015***; ***Teixeira et al., 2015b***; ***Zhu et al., 2017***; ***Liu et al., 2019***; ***Zhu et al., 2020***) or the cyclic aggregation of plates (***Groves et al., 2005***; ***2010***; ***Chen et al., 2013***; ***Eilu & Lahtinen, 2013***; ***Kaur & Chaudhri, 2014***; ***Storey & Smith, 2017***; ***Skirrow et al., 2018***), the prolonged crustal residence times (***Storey & Smith, 2017***) are also highlighted as a genetic key factor previously to the ore crystallization. However, provincial-scale studies fail to reach a consensus regarding the dominant tectonism in which IOCG systems are formed and distributed (**Figure 1**; **ESM – Table 1**). Some global examples across time and space include (1) the Carajás Mineral Province, where there is no consensus about if Neoarchean IOCG ores were formed by intracontinental (e.g., ***Gibbs et al., 1986***; ***Wirth et al., 1986***; ***DOCEGEO, 1988***; ***Lindenmayer, 1990***; ***Olszewski et al., 1989***; ***Macambira, 2003***; ***Tavares, 2015***; ***Teixeira et al., 2015b***; ***Martins et al., 2017***; ***Ganade et al., 2020***; ***Lacasse et al., 2020***; ***Trunfull et al., 2020***), transtensional related convergence (e.g., ***Meirelles & Dardenne, 1991***; ***Teixeira, 1994; Teixeira & Eggler, 1994***; ***Dardenne et al., 1998***; ***Lindenmayer et al., 2005***; ***Lobato et al., 2005***; ***Zuchetti, 2007***; ***Justo, 2018***; ***Figuereido e Silva et al., 2020***; ***Souza et al., 2020***), or compressional to extensional (e.g., ***Martins et al., 2017***; ***Tavares et al., 2018***) tectonic environments, or if they were formed during the shift from Mesoarchean dome-and-keel and linear belts tectonics to Neoarchean, modern-style linear belts (e.g., ***Oliveira, 2018***; ***Costa et al., 2020***; ***Ganade et al., 2020***; ***Lacasse et al., 2020***); (2) Mesoproterozoic IOCG systems from the Olympic Dam Cu-Au Province and the Mt. Isa Inlier, southern and northern Australia, respectively; whilst for the first, several geodynamic environments have been suggested – i.e., mantle plume activity or mantle underplating (e.g., ***Giles, 1988***; ***Daly et al., 1998***; ***Wade et al., 2019***), intracontinental (***Page et al., 2005***), continental back-arc setting related to a nearby subduction system (***Wade et al., 2006***), switches from compression to extension driven by far-field subduction zones or subduction-related plume-modified orogenic setting (***Skirrow et al., 2018***), or subduction related plume-modified orogenic setting (***Betts et al., 2009***), the IOCG mineralization from Mt. Isa Inlier is associated with rift-related compression and magmatism of intracratonic basins (e.g. ***Mark & De Jong, 1996***; ***Pollard et al., 1998***; ***Davidson, 2002***; ***Blenkinsop et al., 2008***; ***Oliver et al., 2008***; ***Foster & Austin, 2008***; ***Porter, 2010***; ***Chen et al., 2013***; ***Williams et al., 2015***), though the emplacement of its host rocks remain unclear (***Mark et al., 2006***), and; (3) Cretaceous IOCG systems from the Andes, which are linked to transtensional (***Arévalo et al., 2006***; ***Groves et al., 2010***; ***Lopez et al., 2014***; ***Richards et al., 2017***) and transpressional (***Chen et al., 2013***; ***del Real et al., 2018***) structural settings in a continental arc environment (e.g., ***Marschik & Fontboté, 2001a***; ***b***; ***Sillitoe, 2003***; ***Chen et al., 2013***; ***del Real et al., 2018***; ***Heuser et al., 2020***).

Neodymium isotope geochemistry is a powerful tool to investigate the relative contribution of rare earth elements (REE) sources in mineralization, but also constraints the crustal processes and the relationship of the mineralization with the tectonic evolution of the province (e.g., ***Zachariah et al., 1997***; ***Skirrow et al., 2007***; ***Champion & Huston, 2016***; ***Storey & Smith, 2017***; ***Fernandes & Juliani, 2019***). Besides, the effectiveness of Sm-Nd isotopes as tracers in IOCG systems has been previously demonstrated in accessory minerals (***Gleason et al., 2000***; ***Reid et al., 2011***; ***Tornos et al., 2012***; ***Storey & Smith, 2017***; ***Li et al., 2018***; ***2019***; ***Smith et al., 2018***; ***Curtis & Thiel, 2019***; ***Maas et al., 2020***; ***Ngo et al., 2020***) and ore phases (***Johnson & McCullough, 1995***; ***Gleason et al., 2000***; ***Pimentel et al., 2003***; ***Neves, 2006***; ***Skirrow et al., 2007***). On the other hand, the combination of Sr and Nd isotopic combinations and trace element geochemistry is an excellent petrogenetic tool to unravel the source region of the mineral system (e.g., ***Zhang & Zuo, 2014***; ***Richards et al., 2017***; ***Tornos et al., 2020***). In this contribution, we compare new Nd–Sr isotopic and trace element geochemistry data of hypogene ore (concentrates of individual grains of ore mineral) of the two-spatial temporal opposing IOCG members worldwide – i.e., the Carajás Mineral Province, Brazil, and the Central Andes IOCG Province, Chile (**Figure 1**) with previously published data. Additionally, ore-bearing samples from two Australian IOCG deposits (Olympic Dam and Ernest Henry) and whole-rock samples from the Candelaria-Punta del Cobre district, Chile, were included for reference purposes only. We aim to constrain the metal source of Cu and Fe in each metallogenetic province and examine their relationships to the tectonic evolution of South America and the genesis of IOCG systems. Unraveling the key mechanisms that lead to metal enrichment in IOCG systems represents the first step towards more predictive exploration strategies.

FIGURE 1 SHOULD BE PLACED HERE OR NEAR HERE

2. Geological Background

2. 1. The Carajás Metallogenic Province

The Carajás Metallogenic Province (**Figure 2**), northwestern Brazil, is an Archean crustal segment that hosts one of the world's most striking Cu-Au systems. The deposits, contributing with more than 8 bt of Cu-Au ore at 0.9% Cu and 0.2 g/t Au (***Xavier et al., 2017***), are located in the tectonostratigraphic Carajás Domain (***Santos, 2003***) and are characterized by IOCG type (e.g., ***Réquia et al., 2003***; ***Tallarico et al., 2005***; ***Monteiro et al., 2008a***; ***b***; ***Grainger et al., 2008***; ***Moreto et al., 2015a***; ***b***; ***Jesus, 2016***; ***de Melo et al., 2017***; ***2019a***; ***b***; ***Hunger et al., 2018***; ***Craveiro et al., 2019***; ***2020***; ***Toledo et al., 2019***; ***Garcia et al., 2020***; ***Pestilho et al., 2020***; ***Previato et al., 2020***), intrusion-related (e.g., ***Lindenmayer et al., 2005***; ***Botelho et al., 2005***; ***Marschik et al., 2005***; ***Grainger et al., 2008***; ***Monteiro et al., 2008a***; ***b***; ***Torresi et al., 2012***; ***Moreto et al., 2015a***; ***b***; ***Pollard et al., 2019***), and polymetallic Cu-Au (e.g., ***Negrão, 2008***; ***Pinheiro, 2019***; ***Fernandes, 2020*****).** Neoarchean IOCG systems are magnetite-bearing, zoned, and display distal Na-Ca hydrothermal alteration at deeper zones and structurally controlled Ca-Fe and K-Fe alteration assemblages at proximal zones in Neoarchean IOCG systems (***Schutesky & Oliveira, 2020***). Shallower crustal K-Fe assemblages are typical in Paleoproterozoic granite-related Cu-Au systems (***Tallarico, 2003***; ***Torresi et al., 2012***; ***Xavier et al., 2017***; ***Pollard et al., 2019***). Overall, IOCG deposits are hosted within the Neoarchean Itacaíunas Supergroup, bimodal 2.76–2.73 Ga granitoids and gabbro, and Mesoarchean basement. In contrast, granite-related Cu-Au systems formed coevally with craton-wide, A-type, 1.88 Ga granite magmatism (e.g., ***Trunfull et al., 2020***). For a recent review on the Carajás IOCG System, the reader is referred to ***Pollard et al. (2019)***, ***Schutesky & Oliveira (2020)***, ***Trunfull et al. (2020)***, and ***Santiago et al. (2020)***. Summarizes characteristics are shown in **Table 1,** and specific characteristics of the studied deposits are displayed **ESM – Table 2**.

FIGURE 2. SHOULD BE PLACED HERE OR NEAR HERE

2. 2. The Central Andes IOCG Province

The Central Andes IOCG Province (**Figure 3**) of southern Peru and northern Chile is one of the world's youngest and best developed continental arc-related IOCG belts (***Sillitoe, 2003***). The province is intimately associated with trench-parallel intra-arc fault systems (>95% of Fe resources; ***Tornos et al., 2020***) that facilitate terrane translation throughout long-lived displacement stages (***Arévalo et al., 2006***; ***Cembrano et al., 2005***; ***2009***; ***Seymour et al., 2020***). IOCG deposits are emplaced near magnetite-apatite, manto-type Cu-(Ag), and porphyry Cu-Au deposits (e.g., ***Sillitoe, 2003***; ***Chen et al., 2013***; ***Barra et al., 2017***; ***del Real et al., 2018***; ***Tornos et al., 2020***). Cretaceous IOCG systems are zoned varying between magnetite-to hematite-bearing with depth (e.g., ***Marschik & Fontboté, 2001a***; ***Rieger et al., 2010***; ***Chen, 2013***; ***Barra et al., 2017***; ***del Real et al., 2018***; ***Childress et al., 2020***) and from structurally-to stratigraphically controlled geometries (***del Real et al., 2018***; ***Heuser et al., 2020***). Most of the deposits are commonly associated with K-Fe to Ca-K-Fe alteration assemblages, hosted within permeable volcanic-to volcaniclastic sequences (e.g., ***Marschik & Fontboté, 2001a***; ***Benavides et al., 2007***; ***de Haller et al., 2009***; ***Rieger et al., 2010***; ***del Real et al., 2018***; ***Li et al., 2018***; ***Heuser et al., 2020***). For a recent review on the central Andes IOCG Province and the major districts of northern Chile, here exemplified with the Candelaria-Punta del Cobre and Mantoverde, the reader is referred to ***Barra et al. (2017)***, ***del Real et al. (2018),*** and ***Childress et al. (2020)***, respectively. Summarizes characteristics are shown in **Table 1,** and specific characteristics of the studied deposits are displayed **ESM-Table 2**.

FIGURE 3. SHOULD BE PLACED HERE OR NEAR HERE

TABLE 1. SHOULD BE PLACED HERE OR NEAR HERE

3. Sampling and Analytical Methods

Samples of ore from the most representative IOCG provinces worldwide (Central Andes IOCG Belt, Mt. Isa Inlier, Olympic Dam Cu-Au Province, Carajás Mineral Province) (**ESM – Table 3**) were carefully collected from underground mines or deeper sections from the open-pit mines to avoid supergene modifications.

Ore-bearing samples from the Carajás Mineral Province (**Figure 4**) occurs within hydrothermal breccias akin to the main IOCG event, consistent with descriptions provided in the literature (Alemão – ***de Melo et al., 2019b***; Salobo – ***Valadão, 2019***; Sequeirinho/Sossego – ***Monteiro et al., 2008a***). Ore-bearing samples from the Central Andes IOCG Belt (**Figure 5**) occurs as veins, "manto" and hydrothermal breccias for

Candelaria-Punta del Cobre district, consistent with descriptions provided by ***del Real et al. (2018)*** and the IOCG event from the ***Marschik & Fontboté (2001a)***. On the other hand, ore-bearing samples from the Mantoverde district are consistent with the stage IV mineralization described by ***Benavides et al. (2007)*** and Late Stage mineralization ***by Rieger et al. (2010)***. Ore-bearing samples from Australian IOCG (Ernest Henry and Olympic Dam deposits) were included for comparison purposes only.

After petrographic study under polarized light microscopy, those free from external contamination were selected for analytical work. Notwithstanding, most samples display several small micron-sized inclusions, as is evidenced in some magnetite and chalcopyrite samples (**Figure 4j–l**).

FIGURE 4. SHOULD BE PLACED HERE OR NEAR HERE

FIGURE 5. SHOULD BE PLACED HERE OR NEAR HERE

3. 2. Sample preparation

The samples were crushed to 0.5 cm chips using a geological hammer and pulverized via micro-drill. Pure ore-bearing samples (chalcopyrite, magnetite, hematite, bornite, and pyrrhotite) separates were carefully hand-picked under a binocular microscope to select grains similar in appearance without inclusions and contaminations to chips of 60-80 mesh size. After, ore separate minerals were grounded to 200 mesh (ca. 2 g) size in an agate mortar. Sm and Nd contamination was below conventional detection limits for grinding times of 120 s producing 200 mesh powders (***Hickson & Juras, 1986***).

3. 3. ICP-MS

A total of 43 powders analyses by ICP-MS were obtained for 19 chalcopyrite, 16 magnetite, 4 hematite, 3 pyrrhotite, and 1 bornite mineral concentrates. Geochemical data (^{7}Li, ^{11}B, ^{23}Na, ^{24}Mg, ^{27}Al, ^{31}P, ^{39}K, ^{44}Ca, ^{47}Ti, ^{51}V, ^{52}Cr, ^{55}Mn, ^{59}Co, ^{60}Ni, ^{66}Zn, ^{75}As, ^{85}Rb, ^{88}Sr, ^{89}Y, ^{98}Mo, ^{107}Ag, ^{111}Cd, ^{118}Sn, ^{121}Sb, ^{133}Cs, ^{137}Ba, ^{139}La, ^{140}Ce, ^{141}Pr, ^{146}Nd, ^{147}Sm, ^{151}Eu, ^{160}Gd, ^{159}Tb, ^{163}Dy, ^{165}Ho, ^{166}Er, ^{169}Tm, ^{172}Yb, ^{175}Lu, ^{205}Tl, ^{208}Pb, ^{232}Th, and ^{238}U) were obtained after the total digestion procedure. Approximately 100 mg of dry material was digested in a Savillex® PFA reactor in 4 steps of 24 h at 130 °C and evaporated to dryness between each step: (1) a 5:2 mL HF (40 %, v/v)-HNO_3 (65 %, v/v) mixture; (2) a 3:1 mL HCl (6 M, v/v)-HNO_3 (65 %, v/v) mixture. After the solution was dried, the remaining material was redissolved in 10 mL of HNO_3 (0,1 M, v/v). All procedures, including the digestion, evaporation, and dilution steps, were carried out in a

1000 class cleanroom. Digestion was performed using double-distilled ultrapure acids (Merck®) at sub-boiling temperatures in Teflon stills. Dilution was performed using high-purity water (> 18.2 MΩ) produced by a Milli-Q (Nanop System®). Metals and REE concentrations were determined after an adequate dilution using an Inductively Coupled Plasma Mass Spectrometry (ICP-MS), X Series II (Thermo Fisher Scientific) equipped with a CCT (Collision Cell Technology) chamber at the HSM laboratory (HydroSciences Montpellier, Universités Montpellier, France). The quality of analytical methods was checked by analyzing international certified reference rock and waters ($CuFeS_2$ – Stock #42533, JA-3, SLRS-5, NIST1643e) and was generally better than 5% relative to the certified values. Analytical error (relative standard deviation) was better than 5% for concentrations ten times higher than the detection limits.

3. 4. Nd–Sr isotope analyses

The Nd–Sr isotope values were obtained following the ***Gioia and Pimentel (2000)*** method at the Laboratory of Geochronology of the University of Brasília, Brazil. Sample powders were prepared via microwave-assisted sample digestion in a multi-stage acid procedure, which involves a hot acid mixture of HNO_3 + HCl + HF and an alkali fusion. A spike solution, obtained through the isotope dilution method for each sub-sample solution, was used to determine the isotopic concentrations of Sm, Nd, and Sr while to measure the isotopic ratios, the other sub-samples solutions were dried first and then redissolved in HCl (Nd and Sr separation). Ion exchange chromatography was used to separate them from matrix digest as detailed ***Montañez et al. (2000)***. Isotope analysis was done on a Multi-Collector Thermal Ionization Mass Spectrometry (MC-TIMS) (Thermo Scientific TRITON™ Plus for $^{143}Nd/^{144}Nd$ and $^{87}Sr/^{86}Sr$ isotope measurements). The uncertainties on the $^{147}Sm/^{144}Nd$, $^{143}Nd/^{144}Nd$ and $^{87}Sr/^{86}Sr$ ratios are better than ± 0.1 (2σ) and ± 0.000006 (2σ), and ±0.00001 (2σ), respectively, according to repeated analyzes of the international BHVO-2 and BCR-1 rock standards for Sm-Nd measurement, and international NBS_9871 and NBS_9872 reference materials for Sr measurement. The $^{143}Nd/^{144}Nd$ ratios were normalized to $^{146}Nd/^{144}Nd$ of 0.7219 (***Jacobsen & Wasserburg, 1980***), and the $^{87}Sr/^{86}Sr$ ratios were normalized to $^{86}Sr/^{88}Sr$ of 0.1194 (***Nier, 1938***). $^{87}Rb/^{86}Sr$ ratios were recalculated from Rb and Sr ICP-MS data, following the procedures described by ***Janoušek et al. (2016)***. The decay constant (λ) used was 6.54×10^{-12}/years for Nd (***Lugmair & Marti, 1978***), and 1.42×10^{-11}/years for

Rb (***Steiger & Jäger, 1977***). The T_{DM} values were calculated using the model of ***DePaolo (1981)***.

Calculated εNd_i, I_{Nd} (initial $^{143}Nd/^{144}Nd$) and I_{Sr} (initial $^{87}Sr/^{86}Sr$) considered the ages of 2.74 Ga and 1.88 Ga (e.g., ***Moreto et al., 2015b***; ***Valadão, 2019***; ***Schutesky & Oliveira, 2020***; ***Trunfull et al., 2020***) for the Neoarchean IOCG and Orosirian granite-related Cu-Au deposits from the Carajás Mineral Province respectively, while the age of 0.12 Ga was used to for the Central Andes IOCG Belt, Chile (e.g., ***Vila et al., 1996***; ***Chen et al., 2013***; ***del Real et al., 2018***). For the Olympic Dam and Ernest Henry deposits, the U-Pb ages of ca. 1.59 Ga and 1.53 Ga represent the ore-forming ages, as has been reported by ***Cherry et al. (2018)*** and ***Mark et al. (2006)*,** respectively.

4. Results

4. 1. Ore geochemistry

Carajás Mineral Province: Boxplot diagrams for chalcopyrite and magnetite samples from Neoarchean and Orosirian Cu-Au systems (here exemplified as Sossego orebody) display enriched concentrations of almost all the granitophile element (U, Pb, and Sn) and high field-strength elements (HFSE) (LREE, HREE, Y, and Th), although these are typically higher in Neoarchean IOCG rather than Orosirian Cu-Au systems (**Figure 6**). The Ororisian Cu-Au system has higher amounts of V and Ti but lower Mo. Transition metals (Zr, Cr, and Ag) in the chalcopyrite are similar between both mineral systems. Neoarchean IOCGs have higher Mn and Co, while Cd is high in the Orosirian Cu-Au system. Siderophile elements as As, Sb, and Tl are poorly concentrated in both ore systems from the Carajás Mineral Province. Lithophile elements are similar in both ore systems, though they are slightly lower in the Neoarchean IOCG deposits.

Multielement diagrams for chalcopyrite and magnetite samples for both ore systems exhibit positive anomalies of U, Y, Th, Co, and As, and negative Ti, Ni, and Cr anomalies compared to the chondrite composition (***Palme & O'neill, 2007***) (**Figure 7a**, **c**). In both cases, anomalies are more pronounced in Neoarchean IOCG systems. In both ore systems, Ag and Cd exhibit an opposite anomaly, whereas negative Mg anomalies are exhibit in magnetite. A remarkable characteristic is that V, Ti, Ni, and Cd, in chalcopyrite and Ti, Na, Mg, Al, P, K, and Ca in magnetite, increase towards Paleoproterozoic granite-related Cu-Au systems whereas U, Sn, Mo, Y, Mn, and Sb, in chalcopyrite, and Mo, Co, and Sb in magnetite increase towards the Neoarchean IOCG systems. These can be interpreted as the most mobile elements from each ore system. Oppositely, Th and Cr are the most immobile elements in both ore systems.

The chondrite-normalized REE pattern (***Palme & O'neill, 2007***) (**Figure 7b**, **d**) exhibit that the overall slope geometry in both magnetite and chalcopyrite samples results from the relative enrichment of LREE to MREE ($162.37 \leq La_N/Sm_{N\ (IOCG)} \leq 205.71$, and $204.15 \leq La_N/Sm_{N\ (Cu\text{-}Au)} \leq 209.79$) and HREE ($20.92 \leq La_N/Yb_{N\ (IOCG)} \leq 46.63$, and $25.73 \leq La_N/Yb_{N\ (Cu\text{-}Au)} \leq 48.44$), and of MREE to HREE ($3.13 \leq Sm_N/Yb_{N\ (IOCG)} \leq 6.57$, and $5.35 \leq Sm_N/Yb_{N\ (Carajás\text{-}Cu\text{-}Au)} \leq 7.41$). Slightly impoverishment in LREE compared to HREE (LREE/HREE ~3.37) stands out in Neoarchean IOCG rather than in Orosirian Cu-Au systems (LREE/HREE = 7.86). Europium anomalies tend to be expressively negative in almost all the deposits ($\delta Eu_{\ (IOCG)} \sim 0.27$, and $\delta Eu_{\ (Cu\text{-}Au)} \sim 0.39$), except for one sample from Neoarchean IOCG display a flat pattern (δEu ~ 0.97). None of the analyzed samples display δCe anomalies.

Central Andes IOCG Province: Boxplot diagrams for sulfides from the Candelaria-Punta del Cobre district have higher amounts for most elements than those from the Mantoverde district, except for similar V and Sb in sulfides, and Mo, V, and Ca in iron-oxides. Tin is always higher in the Mantoverde district (**Figure 6**).

For both districts, multielement diagrams (**Figure 7a**, **c**) display positive anomalies of U, Th, Zn, Co, and As, but negative Ti, Mn, Ni, Cr, and Tl anomalies compared to the chondrite composition (***Palme & O'neill, 2007***). A remarkable characteristic for samples from Mantoverde is its positive Sn anomaly and negative Ti, Ni, Mg, and P anomalies. Towards the Candelaria-Punta del Cobre district, elements such as Zn, Ag, and As in sulfides plus P and K in iron oxides display marked positive anomalies, whereas Ti is preferentially depleted in all the cases.

The chondrite-normalized REE pattern (***Palme & O'neill, 2007***) (**Figure 7b**, **d**) of magnetite and chalcopyrite from the Candelaria-Punta del Cobre exhibit a smooth, flat to concave slope fractionation of LREE in relation to HREE ($16.43 \leq La_N/Yb_N \leq 26.76$) and negative Eu-anomaly (δEu ~0.67). Europium anomalies tend to be slightly negative in most of the cases. REE fractionation patterns from the chalcopyrite and hematite of the Mantoverde district exhibit a similar enrichment of LREE to HREE ($1.55 \leq La_N/Yb_N \leq 1.64$) and a slight impoverishment in MREE ($85.49 \leq La_N/Sm_N \leq 96.20$, and $0.71 \leq Sm_N/Yb_N \leq 0.73$), whereas one magnetite sample exhibit the typical negative slope pattern ($La_N/Yb_N = 12.75$). Europium anomalies vary between 0.76 for chalcopyrite and hematite and 0.85 for magnetite.

Australian IOCGs: Isolated results from Olympic Dam and Ernest Henry vary between a similar range with South American IOCG deposits. Small differences point towards enrichment in Mo for the Ernest Henry deposit and impoverishment in Mn for the Olympic Dam deposit. In terms of REE compositions, both Australian deposits display LREE enrichment ($54.50 \leq La_N/Yb_{N\ (EH)} \leq 73.40$, and $75.05 \leq La_N/Yb_{N\ (OD)} \leq 113.31$) with marked concave slopes and smooth, positive Eu anomalies (δEu (EH) ~ 1.24, and δEu (OD) ~ 1.07).

FIGURE 6 SHOULD BE PLACED HERE OR NEAR HERE

FIGURE 7 SHOULD BE PLACED HERE OR NEAR HERE

4. 2. Strontium isotopes

Carajás Mineral Province: Chalcopyrite and magnetite concentrates have variable Sr concentrations between Neoarchean IOCG (Sr_{cpy} = 7.25–18.40 ppm, average = 12.83 ppm; Sr_{mag} = 0.82–51.59 ppm; average = 13.62 ppm) and Orosirian Cu-Au systems (Sr_{cpy} = 6.31–19.31 ppm, average = 12.81 ppm; Sr_{mag} = 30.15–53.13 ppm, average = 41.64 ppm). On average, no apparent differences in Sr compositions were noted between magnetite and chalcopyrite from the same ore system. Rb/Sr is high in almost all the samples; 9 of 10 concentrates listed in ESM-Table 5 have Rb/Sr ≥0.02, ranging between 0.32 to 0.88 in chalcopyrite, and 0.14 to 0.89 in magnetite from Neoarchean IOCG, respectively, and ranging between 0.04 to 0.30 in chalcopyrite, and 0.15 to 0.82 in magnetite from Orosirian Cu-Au systems, respectively, whereas only 1 sample have low Rb/Sr ≤ 0.02. Eccentric values of Rb/Sr over 0.8 and an anomalous value of 3.30 were considered as outliers. Present-day $^{87}Sr/^{86}Sr$ ratios also display variations between Neoarchean IOCG ($^{87}Sr/^{86}Sr_{cpy}$ = 0.71355–0.75670, average = 0.72639; $^{87}Sr/^{86}Sr_{mag}$ = 0.71405–0.75807, average = 0.72661) and Cu-Au Orosirian systems ($^{87}Sr/^{86}Sr_{cpy}$ = 0.74121–0.75449, average = 0.74793; $^{87}Sr/^{86}Sr_{mag}$ = 0.73479–0.75416, average = 0.74448).

Initial $^{87}Sr/^{86}Sr$ ratios (I_{Sr}) are typically higher in Cu-Au Orosirian systems ($I_{Sr\text{-}cpy}$ = 0.71802–0.75171, average = 0.73486; $I_{Sr\text{-}mag}$ =0.72331), whereas low signals were obtained for Neoarchean IOCG systems ($I_{Sr\text{-}cpy}$ = 0.71973; $I_{Sr\text{-}mag}$ = 0.70159–0.71761, average = 0.70960). The anomalously low I_{Sr} ratios (<0.7) obtained are unreal values and meaningless to our discussion, given that they represent disturbances related to radiogenic

Sr input or Rb loss. The initial $^{87}Sr/^{86}Sr$ reference to terrestrial rocks is 0.7 (***Papanastassiou & Wasserburg, 1969***). The $^{87}Sr/^{86}Sr$ ratio for the primitive mantle is 0.70167 at 2.74 Ga, and 0.70279 at 1.88 Ga, calculated according to the present-day constraints $^{87}Sr/^{86}Sr = 0.7052$ and $^{87}Rb/^{86}Sr = 0.089$ for the bulk Earth (***Zindler & Hart, 1989***). Thus, the Sr isotope data points towards more enriched sources than the primitive mantle for both Neoarchean IOCG and Orosirian Cu-Au systems, although for it last are eventually more enriched. A summary of Sr-Sr results for Carajás Mineral Province is provided in **Table 2**. For full detailed Sr-Sr isotope ratios measured, please refer to **ESM – Table 5**. Additionally, our results are compared to published Sr-Nd isotopic data and are discussed in the next section. Compilation of published data can be found on **ESM – Table 8**.

Central Andes IOCG Province:

Sulfides and iron-oxides concentrates have variable Sr concentrations between IOCG deposits from the Candelaria-Punta del Cobre (Sr_{cpy} = 3.50–46.53 ppm, average = 21.81 ppm; Sr_{mag} = 6.71–36.39 ppm, average = 21.77 ppm; Sr_{po} =2.42–5.80 ppm; average = 3.93 ppm) and Mantoverde districts (Sr_{cpy} = 2.88–4.79 ppm, average = 3.84 ppm; Sr_{mag} = 13.18 ppm; Sr_{hem} = 15.77–21.89 ppm, average = 18.83 ppm). With some exceptions, Sr concentrations tend to be lowest in sulfides rather than in iron oxides, although on average are similar. Rb/Sr is high in almost all the concentrates listed in **ESM-Table 5** have Rb/Sr ≥0.02, although 7 of those display outliers values of Rb/Sr ≥0.8. From that, Rb/Sr ratios are lowest in ore samples from Mantoverde district (Rb/Sr_{cpy} = 0.07–0.16, average = 0.11; Rb/Sr_{hem} = 0.04–0.06, average = 0.05) rather than ore concentrates from Candelaria-Punta del Cobre district (Rb/Sr_{cpy} = 0.09–0.50, average = 0.30; Rb/Sr_{mag} = 0.38–0.59, average = 0.48; Rb/Sr_{po} = 0.22–0.71, average = 0.42). Present-day $^{87}Sr/^{86}Sr$ ratios also display variations between both districts, where higher amounts were detected for ore samples from Candelaria-Punta del Cobre district ($^{87}Sr/^{86}Sr_{cpy}$ = 0.70571–0.70901, average = 0.70703; $^{87}Sr/^{86}S_{mag}$ = 0.70632–0.70693, average =0.70658; $^{87}Sr/^{86}Sr_{po}$ = 0.70546–0.70665, average = 0.70592) rather than those of Mantoverde district ($^{87}Sr/^{86}Sr_{cpy}$ = 0.70396–0.7048, average = 0.70658; $^{87}Sr/^{86}Sr_{hem}$ = 0.70393–0.70727, average = 0.70560). For Candelaria-Punta del Cobre district, these isotopic ratios are higher than $^{87}Sr/^{86}Sr$ in quartz (0.70584– 0.70599) from Candelaria deposit (***Chiaradia et al., 2006***). Similarly, for Mantoverde district, these isotopic ratios are higher than $^{87}Sr/^{86}Sr$ in hydrothermal calcite (0.703700–0.703735) from Mantoverde Norte and Mantoverde Sur deposits (***Rieger et al., 2010***).

Initial $^{87}Sr/^{86}Sr$ ratios (I_{Sr}) are typically higher in sulfides, although chalcopyrite from the Candelaria-Punta del Cobre district display the more enriched signals (I_{Sr-cpy} = 0.70155–0.70864, average = 0.70535; I_{Sr-po} = 0.70315–0.70437, average = 0.70384) compared to the chalcopyrite from the Mantoverde district (I_{Sr-cpy} = 0.70363–0.7048, average = 0.70385). Similarly, I_{Sr} from magnetite (I_{Sr-mag} = 0.70341–0.70465, average = 0.70421) from Candelaria-Punta del Cobre are more enriched than hematite from Mantoverde district (I_{Sr-hem} = 0.70238). An anomalous I_{Sr} value of 0.69960 in hematite from Mantoverde was discarded, due as abovementioned, values below 0.7 are related to radiogenic Sr input or Rb loss. The $^{87}Sr/^{86}Sr$ ratio for the primitive mantle is 0.70505 at 0.12 Ga, calculated according to the present-day constraints $^{87}Sr/^{86}Sr$ = 0.7052 and $^{87}Rb/^{86}Sr$ = 0.089 for the bulk Earth (***Zindler & Hart, 1989***). Thus, the Sr isotope data points towards depleted sources similar than the primitive mantle for both Cretaceous IOCG districts. A summary of Sr-Sr results for Carajás Mineral Province is provided in **Table 2**. For full detailed Sr-Sr isotope ratios measured, please refer to **ESM – Table 5**. Additionally, our results are compared to published Sr-Nd isotopic data, and are discussed in the next section. Compilation of published data can be found on **ESM – Table 11.**

4. 3. Neodymium isotopes

Carajás Mineral Province: Nd concentrations, as well as Sm/Nd ratios in chalcopyrite and magnetite concentrates, also vary strongly between Neoarchean IOCG (Nd_{cpy} = 126.54–4352.90 ppm, average = 1241.02 ppm; Nd_{mag} = 6.24–442.30 ppm, average = 121.53 ppm; $^{147}Sm/^{144}Nd_{cpy}$ = 0.069–0.154, average = 0.110; $^{147}Sm/^{144}Nd_{mag}$ = 0.031–0.178, average = 0.031) and Orosirian Cu-Au systems (Nd_{cpy} = 0.88–90.67 ppm, average = 50.31 ppm; Nd_{mag} = 60.46–96.39 ppm, average = 78.43 ppm; $^{147}Sm/^{144}Nd_{cpy}$ = 0.091–0.238, average = 0.149; $^{147}Sm/^{144}Nd_{mag}$ = 0.150–0.122, average = 0.136). To avoid errors and the effect of fractionation, values with $^{147}Sm/^{144}Nd$ over 0.15 and below 0.06 were considered as outliers.

Present-day $^{143}Nd/^{144}Nd$ ratios display slightly variations between magnetite compositions from both ore systems, although chalcopyrite concentrates display higher concentrations in Orosirian Cu-Au systems ($^{143}Nd/^{144}Nd_{cpy}$ = 0.51086–0.51266, average = 0.51156; $^{143}Nd/^{144}Nd_{mag}$ = 0.51112–0.51152, average = 0.51132) rather than in Neoarchean IOCG deposits ($^{143}Nd/^{144}Nd_{cpy}$ = 0.51032–0.51177, average = 0.51093; $^{143}Nd/^{144}Nd_{mag}$ = 0.51019–0.51219, average = 0.51129). Chalcopyrite and magnetite concentrate from Orosirian Cu-Au systems display enriched initial $^{143}Nd/^{144}Nd$ ratios

(I_{Nd}) ($I_{Nd\text{-}cpy}$ = 0.50970–0.50973, average = 0.50972; $I_{Nd\text{-}mag}$ = 0.50961–0.50967, average = 0.50964) and εNd(t) signals ($εNd_{\text{-}cpy}$ = –11.67 to –10.55, average = –11.11; $εNd_{\text{-}mag}$ = –9.82 to 9.21) than those from Neoarchean IOCG systems ($I_{Nd\text{-}cpy}$ = 0.50852–0.50919, average = 0.50894, and $εNd_{\text{-}cpy}$ = –1.83 to +2.18, average = –0.01; $I_{Nd\text{-}mag}$ = 0.50891 – 0.50996, average = 0.50972, and $εNd_{\text{-}mag}$ = –3.30 to +1.44, average = –1.71). Notwithstanding, one magnetite sample from Neoarchean IOCG deposits also exhibits a long-term enriched reservoir ($εNd_{\text{-}mag}$ = –10.94). Thus, the Nd isotope data exhibit source heterogeneity suggesting mixing between mantle magma and contributions of products related to crustal melting for Neoarchean IOCG and a considerable reworking of pre-existing crust for Orosirian Cu-Au systems.

The fractionation factor $f_{Sm/Nd}$ (***DePaolo, 1988***) for the Neoarchean IOCG ranges from –0.65 to –0.41 in chalcopyrite, and –0.29 to –0.25 in magnetite, while for the Orosirian Cu-Au ores, the $f_{Sm/Nd}$ are –0.54 to –0.39 and in chalcopyrite and –0.31 to –0.24 in magnetite. Thus, fractionation was not significant in the Sm-Nd systems of the ore concentrates. From the fractionation factor against εNd(t), the diagram can be useful to discriminate tectonic setting (***DePaolo & Wasserburg, 1976***; ***McLennan & Hemming, 1992***).

Thus, chalcopyrite and magnetite samples reveal a clear relationship with long-term light REE-enriched sources at the bottom-left quadrant for Orosirian Cu-Au systems and wide distribution for Neoarchean IOCG systems, ranging from primitive compositions at the bottom-right quadrant towards more evolved compositions in the bottom-left quadrant (**Figure 8a**). This may represent that ore samples from Orosirian Cu-Au systems are related to contamination in the sources or assimilation of older continental crust and fractionation processes while Neoarchean IOCG systems were formed by changes between closed and open system processes or by hybrid magmatism.

A summary of Sm-Nd results for Carajás Mineral Province is provided in **Table 2**. For full detailed Sm-Nd isotope ratios measured, please refer to **ESM – Table 5**. Additionally, our results are compared to published isotopic data and are discussed in the next section. Compilation of published data can be found on **ESM – Table 6** and **ESM –Table 7**.

Central Andes IOCG Province: Nd concentrations in chalcopyrite and magnetite concentrates are similar within the Candelaria-Punta del Cobre district (Nd_{cpy} = 9.95–206.67 ppm, average = 73.08 ppm; Nd_{mag} = 2.47–109.75 ppm, average = 28.21 ppm). As mentioned above, to avoid errors and the effect of fractionation, values with $^{147}Sm/^{144}Nd$ over 0.15 and below 0.06 were considered as outliers.

Present-day $^{143}Nd/^{144}Nd$ also display similar range of values for chalcopyrite ($^{143}Nd/^{144}Nd$ = 0.51269–0.51280, average = 0.51273) and magnetite ($^{143}Nd/^{144}Nd$ = 0.51224–0.51280, average = 0.51264). Overall, all the samples display similar initial $^{143}Nd/^{144}Nd$ (I_{Nd}) and εNd (t) values for chalcopyrite (I_{Nd} = 0.51262–0.51266, average = 0.51263, and εNd = +2.68 to +3.39, average = +2.88). For magnetite, these values are slightly different for I_{Nd} and εNd (t), varying from 0.51214 to 0.51269, an average of 0.51251, and from +1.81 to +4.03. This suggests that Nd is derived from primitive sources, similar to the chondrite composition. In addition, it is interesting to highlight an outlier value of εNd (t) = –6.63, which suggest evolved contributions during magnetite crystallization. However, a greater amount of analyses are required to affirm this approach. Another hypothesis could be that they are different generations of magnetite, based on older $T_{DM\text{-}mag}$ value (1.26 Ga) exhibit for the enriched signal in comparison to the $T_{DM\text{-}mag}$ value of the primitive signal (0.53–0.63 Ga). Likewise, T_{DM} values for chalcopyrite suggest that it was incubated at younger time periods than magnetite ($T_{DM\text{-}cpy}$ = 0.43–0.55 Ga). On the other hand, pyrrhotite and hematite compositions obtained for Candelaria-Punta del Cobre district, and Mantoverde district, are highly fractionated, with $^{147}Sm/^{144}Nd$ of 0.19 and 0.18, respectively, although as referential material, both display primitive εNd (t) signals of +2.79 and +8.35, respectively.

The fractionation factor $f_{Sm/Nd}$ (***DePaolo, 1988***) for chalcopyrite samples from Candelaria-Punta del Cobre district vary between –0.27 to –0.57, and those from magnetite vary between –0.26 to –0.50. Thus, fractionation was not significant in the Sm-Nd systems of the ore samples, although it was more differentiated in chalcopyrite samples. From the fractionation factor against εNd(t) diagram (***DePaolo & Wasserburg, 1976***; ***McLennan & Hemming, 1992***), all the samples display a vertical distribution in the bottom-right quadrant (**Figure 8b**), indicating enrichment in light REE shortly before melting by mantle-derived components (**Figure 8b**) (***Zacharia et al., 1997***).
A summary of Sm-Nd results for Central Andes IOCG is provided in **Table 2**. For full detailed Sm-Nd isotope ratios measured, please refer to **ESM – Table 5**. Additionally, our results are compared to published isotopic data and are discussed in the next section. Compilation of published data can be found on **ESM – Table 9** and **ESM –Table 10**.

FIGURE 8 SHOULD BE PLACED HERE OR NEAR HERE

Australian IOCG: the εNd_i values from the ore concentrates of Ernest Henry deposit tend to have slightly more evolved isotopic composition from those, with values between –3.03 to –2.39 for magnetite and chalcopyrite concentrates, respectively. Although these values have no statistical significance, they can represent a reference signal. Further, these typically oscillated between values reported for ore-bearing rocks from Gawler Craton –2.5 (***Johnson & McCullough, 1995***) and –4.2 to –5.8 (***Skirrow et al., 2007***). Most of the samples display high fractionation and/or contamination signals.

TABLE 2. SHOULD BE PLACED HERE OR NEAR HERE

5. Discussion

5. 1. Discrimination diagrams as fingerprints for ore fluids

Over the years, several discrimination diagrams for iron oxides; and scarce for copper sulfides have been proposed to discriminate its origin (e.g., ***Tokel et al., 2011***; ***Dare et al., 2014a***; ***2015***; ***Nadoll et al., 2015***; ***Knipping et al., 2015b***; ***Canil et al., 2016***; ***Makvandi et al., 2016***; ***Wen et al., 2017***; ***Deditius et al., 2018***; ***Duran et al., 2019***) and/or economic classification (e.g., ***Loberg & Horndahl, 1983***; ***Beaudoin & Dupuis, 2007***; ***Dupuis & Beaudoin, 2011***; ***Nadoll et al., 2014***; ***Liu et al., 2015***; ***Makvandi et al., 2016***; ***Meng et al., 2017***; ***Duran et al., 2019***). Although the consensus argues that all of these empirical diagrams tend to fail, and their use is limited (e.g., ***Broughm et al., 2017***; ***Wen et al., 2017***; ***Sun et al., 2019***), several works have indicated that its complementation with textural studies (e.g., ***Hu et al., 2015***; ***2020***; ***Huang & Beaudoin, 2019***; ***Huang et al., 2019***), compositional trends (e.g., ***Nadoll et al., 2014***; ***Deditius et al., 2018***; ***Ovalle et al., 2018***; ***Childress et al., 2020***), and the influence of micro-to nano inclusions (e.g., ***Broughm et al., 2017***; ***Deditius et al., 2018***; ***George et al., 2018***) are factors to consider during their interpretation as a whole.

To test the efficacy of discrimination diagrams, trace element concentrations in iron oxides from the studied deposits were plotted (**Figure 9**). We have ruled out the sulfide compositions within this topic due these vary widely within a single deposit (e.g., ***Dare et al., 2014b***; ***Mansur et al., 2020a***), and the available discrimination diagrams (e.g., ***Duran et al., 2019***) do not provide correct discrimination in our data set. On average, most of the trace element contents in iron oxides drop and scatter outside the defined

IOCG field. However, in selected cases, compositional trends can be positively correlated.

Firstly, based on the (Al + Mn) against (Ti + V) diagram proposed by ***Dupuis & Beaudoin (2011)*** and modified by ***Nadoll et al. (2014)*** (**Figure 9a**), it is possibly suggested that magnetite from the Carajás Mineral Province crystallizes from a descending temperature gradient that evolves from the Southern to Northern Copper Belt, concordant with the tectonothermal evolution in the province as is summarized by ***Trunfull et al. (2020)***. Both Neoarchean and Orosirian ore systems fall in the field of magmatic-hydrothermal aqueous fluids at high-temperatures (>500 °C). Comparatively, individual samples from deposits as Salobo and Alemão also involve the intermediate (500–300 °C) to lower temperature (300–200 °C) conditions, respectively, concordant with those reported for magnetite crystallization in the province (>500°C – Salobo; ***Campo et al., 2019***; ***Campo, 2020***; 550 °C – Sequeirinho; ***Monteiro et al., 2008a***; 400 °C – Sossego/Curral; ***Monteiro et al., 2008a***; 259– 330°C – Igarapé-Bahia/Alemão; ***Tallarico et al., 2000***; ***Dreher et al., 2008***; ***de Melo et al., 2019a***). Nonetheless, the geochemical behavior of V, Al, and Mn does not only depend on temperature due their solubility is highly controlled by the mafic precursors, fluid compositions, and host rock buffering (e.g., ***Meinert et al., 2005***; ***Nadoll et al., 2014***; ***2015***; ***Xie et al., 2017***; ***Huang et al., 2019***). Therefore, although high-temperature magmatic-hydrothermal processes were fundamental for the genesis of Neoarchean IOCG and Orosirian Cu-Au systems in the province, a more significant influence factor that differentiates the magnetite crystallization between Neoarchean IOCG and Orosirian Cu-Au systems may include a more substantial interaction between fluid-rock processes for those first.

Oppositely, the (Al + Mn) against (Ti + V) diagram for the Central Andes IOCG Province suggest that despite magnetite crystallizes (500–300 °C) in temperature ranges below the proposed for magnetite crystallization in the Candelaria-Punta del Cobre district (600–500 °C; ***Marschik et al., 2000***; ***Marschik & Fontboté, 2001a***), magmatic-hydrothermal processes are dominant. Interestingly, our ranges are concordant to those reported for copper sulfide precipitation (552–328 °C; ***Hopf, 1987***; ***Marschik & Fontboté, 2001a***; ***del Real et al., 2020***) as well as to those for iron and sulfide mineralization in the Mantoverde district (530–200 °C; ***Rieger et al., 2012***; ***Childress et al., 2020***), suggesting that Cu and Au follow similar processes.

Towards the Ni against Cr diagram proposed after ***Dare et al. (2014a)*** (**Figure 9b**) can be inferred that ore-forming fluids for both South American IOCG provinces, and for the Ernest Henry, were derived from more mafic precursors, concordant as is evidenced in the literature (e.g., ***del Real et al., 2020***; ***Schutesky & Oliveira, 2020***). However, high Cr and Ni content are not an exclusive requirement for the genesis of the entire spectrum, as evidenced in the variable composition of the magnetite from the Olympic Dam Province (***Goldsmith, 2014***; ***Huang et al., 2019***; ***Verdugo-Ihl et al., 2020***). Alternatively, from the Ti against Al diagram proposed after ***Canil et al. (2016)*** (**Figure 9c**), on average, ore-forming fluids in which magnetite crystallizes are partially concordant with the above mentioned for the (Al + Mn) against (Ti + V) diagram. Notwithstanding, its application is quite limited, similar as is evidenced in the V against Ti (ppm) diagram from ***Nadoll et al. (2015)*** (**Figure 9d**). From all of the above, we agree that these bivariate diagrams seem to be very primitive or simplistic to explain the complex genesis of IOCG systems. Therefore, their use should be done with caution.

FIGURE 9 SHOULD BE PLACED HERE OR NEAR HERE

5. 2. Trace element compositions

For Carajás Cu-Au systems, most of the elements – i.e., Mg, Al, Ti, V, Cr, Ni, and Zn, are preferentially partitioned in magnetite compositions (**Figure 6**) from IOCG brecciated orebodies in the Southern Copper Belt, and its content progressively decreases towards the northern counterpart and into Paleoproterozoic Cu-Au systems, reflecting similar precipitation flow involved in the genesis of IOCG deposits that evolves systematically with the tectonothermal events in the province (e.g., ***Santiago, 2016***; ***Trunfull et al., 2020***). Geochemical differences among magnetite compositions between Neoarchean IOCG systems points to fluids with lower solubility, hottest, more reduced, and partially derived from more mafic precursors for those in the south of the province (***Dare et al., 2014***; ***Nadoll et al., 2014***; ***Wang et al., 2018***; ***Huang et al., 2019***; ***Canill & Lacourse, 2020***) while transpressional regimes in the Paleoproterozoic (***Domingos, 2009***) would have triggered the fraction more primitive magmas ascend of hydrothermal fluids more reduced and sulfur-rich than typical IOCG deposits (***Santiago, 2016***; ***Pollard et al., 2019***).

Titanium, V, and Cr are depleted in chalcopyrite compositions due to the partitioning of sulfur is always dependent on the oxygen fugacity (e.g., ***Sharma & Srisvastava, 2014***) though reported amounts could reflect oxides and silicate impurities (***Duran et al., 2019***).

Cadmium in chalcopyrite also suggests hydrothermal fluids from high-temperature conditions for deposits from the Southern Copper Belt, though differences in the sulfide trace element content – i.e., high Co, Mo, Sn, Pb, U but low As, Cr, Ni, Zn, Th and REE content throughout the Neoarchean IOCG deposits could be favored by local environment patterns than the source of fluid (**Figure 6**) (***Duran et al., 2019***). Chondrite-normalized REE patterns (**Figure 10a**) point towards the derivation of the REE from more than a single source – e.g., volcanic rocks or greenstone belt sequences (smooth LREE/HREE enrichment, Eu anomaly and depletion in MREE), but also involving fluids exsolved during crystallization of collisional granitoids (concave LREE/HREE enrichment, Eu anomaly and depletion in MREE). It also suggests that crustal-scale shear zones that served as channel ways to transport and focus metal-bearing fluids and/or melts from the deep crust and mantle to the site of ore formation (e.g., ***Spandler et al., 2020***) were controlled mainly by transpressional tectonics contemporaneous with volcanism and granitoid emplacement in the Carajás Basin and Canaã dos Carajás domain (e.g., ***Domingos, 2009***).

For the Central Andes IOCG Province, ore-forming fluids from the Candelaria-Punta del Cobre district evolved and advanced upwards over time from transitional transtensional to transpressional tectonism and from stratigraphically to structurally-controlled ore-types, respectively (***del Real et al., 2018***). Interestingly, although modern structural, textural, and geochronological evidence supports that volcanic rocks are likely related to ore precipitation in both structurally and lithological zones (***Marschik et al., 2003b***; ***del Real et al., 2018***; ***Ogata et al., 2019***), the predominant ore-forming fluid responsible for mineralization in both Candelaria-Punta del Cobre as well as the Mantoverde districts are magmatic-hydrothermal in origin (***Johansson et al., 2017***; ***del Real et al., 2018***; ***2020***; ***Childress et al., 2020***).

Magnetite from breccia orebodies in Andean IOCG systems unrelated to the main hydrothermal structural conduit – e.g., Santos and Punta del Cobre (***del Real et al., 2018***), show similar bulk continental chondrite-trace element and chondrite-normalized REE patterns compared to those proximal to major structural zones – e.g., Brecha Flores (***Rieger et al., 2010***), indicating similar ore-forming fluids, though different fluid-structural interactions were involved. Therefore, despite both were leached and transported with increased hydrothermal metasomatism (***Huang et al., 2015***), those from second-order structural elements will show the most REE-poor magnetite. On the other hand, regional tectonic or deformation events also play an important role in the physicochemical changes and chemical-crystallographic controls for the distribution of REE within hydrothermal minerals. Magnetite compositions of Mg, Al, Ca, V, Cr, and Mn for Mantoverde districts have been reported with similar compositions across all depths (***Childress et al., 2020***). Nonetheless, based on trace element compositions reported for this study, magnetite compositions for breccia-orebodies – e.g., Candelaria Norte breccia, Santos, Punta del Cobre, and Brecha Flores, accommodated significant amounts of Mg, Al, Ti, Cr, and Co. However, similar V, Ni, Zn, and Mn than mantos and veins orebodies, indicating that both shares a similar mafic precursor but involving different fluid-rock mechanism, preferentially hottest and more reduced for breccia-orebodies (**Figure 6**) (***Dare et al., 2014***; ***Nadoll et al., 2014***; ***Chen et al., 2015***; ***Wang et al., 2017***, ***2018***; ***Canill & Lacourse, 2020***). Extremely depleted Al, Ti, V, and Cr contents in stratabound mineralization for deep district exploration hole south of the Candelaria deposit (>750 m) suggest fluid pathways more oxidized and coolest to those proximal to regional shear zones such as Candelaria Norte manto and Alcaparrosa deposits. Through chalcopyrite compositions, most of the chalcophile and siderophile elements are relatively similar to those for magnetite, suggesting less competition between sulfide and oxide precipitation and derivation from a similar fluid.

FIGURE 10 SHOULD BE PLACED HERE OR NEAR HERE

5. 2. Carajás Mineral Province

5. 2. 1. Metal sources for the Carajás Metallogenic Province

The source of economic mineralization in Neoarchean and Paleoproterozoic Cu-Au systems of the Carajás Mineral Province has been a controversial topic in the literature. While some authors point towards a magmatic-hydrothermal origin for such fluids (e.g., ***de Melo et al., 2019a***; ***Valadão, 2019***; ***Campo, 2020***; ***Pestilho et al., 2020***; ***Schutesky & Oliveira, 2020***), specialized endogenic sources (e.g., ***Tallarico et al., 2005***; ***Pollard, 2006***; ***Grainger et al., 2008***), and a hybrid hydrothermal system involving externally-derived component are also suggested (e.g., ***Xavier et al., 2008***; ***2012***; ***Torresi et al., 2012***; ***Moreto et al., 2015a***; ***b***; ***de Melo et al., 2019a***).

Published sulfur isotopes ($\delta^{34}S$) reveal that fluids are predominantly of magmatic in origin for sulfur and by inference for several Cu-Au occurrences – i.e., IOCG (Salobo – ***Santiago, 2016***; ***de Melo et al., 2019b***; ***Campo et al., 2019***; ***Campo, 2020***; Igarapé-

Cinzento – ***da Costa Silva et al., 2015***; Igarapé-Bahia/Alemão – ***Dreher et al., 2008***; ***Galarza et al., 2008***; ***Santiago, 2016***; Grota Funda – ***Hunger et al., 2018***; Furnas – ***Alves et al., 2019***; Sequeirinho-Pista-Baiano – ***Monteiro et al., 2008a***; ***Bühn et al., 2012***; ***Santiago, 2016***; Cristalino – ***Ribeiro, 2008***; ***Craveiro et al., 2020***; Borrachudo – ***Previato et al., 2020***; Visconde; ***da Costa e Silva et al., 2015***; ***Pestilho et al., 2020***; Castanha – ***Santiago, 2016***; ***Pestilho et al., 2020***; Bacaba – ***Pestilho et al., 2020***; Bacuri – ***Pestilho et al., 2020***; Pedra Branca – ***Pestilho et al., 2020***; Pantera – ***Lopes, 2018***), granite-related Cu-Au (Gameleira – ***Lindenmayer et al., 2001***; Estrela – ***Lindenmayer et al., 2005***; Sossego-Curral; ***Monteiro et al., 2008a***; ***Bühn et al., 2012***; ***Santiago, 2016***; Breves – ***Botelho et al., 2005***; ***Santiago, 2016***; Alvo 118 – ***Santiago, 2016***; ***Pestilho et al., 2020***), and skarn Cu (***Fernandes, 2020***). Notwithstanding, many of these (***Botelho et al., 2005***; ***Monteiro et al., 2008a***; ***Ribeiro, 2008***; ***Lopes, 2018***; ***de Melo et al., 2019a)*** do not rule out that these components can also get derived from the leaching of magmatic rocks – i.e., volcanic and/or mafic-ultramafic rocks, as previously stated by ***Monteiro et al. (2008a***). Modern and detailed studies such as ***Santiago et al. (2020)*** highlight that for Neoarchean IOCG systems, sulfur is most likely of mantle/magmatic origin although also includes derivation from country rocks via fluid-rock processes, whereas for Orosirian Cu-Au systems, sulfur was probably generated by reduced sulfur species sourced from crustal sources in addition to magmatic sulfur related to ca. 1.88 Ga A-type granite emplacement.

The Sm-Nd isotope variations can serve as a monitor for changes of long-time-scale geologic processes (e.g., ***DePaolo & Wasseburg, 1976; Zachariah et al., 1997***; ***Storey & Smith, 2017***). These variations can be attributed to (1) closed system igneous processes, where igneous rocks form from the crystallization of melts generated by melting of deep crustal and mantle sources, and/or (2) open system processes such as magma mixing, crustal assimilation, zone refining and fluid-rock interaction (***Zachariah et al., 1997***). Our results demonstrate that, although both Neoarchean and Orosirian Cu-Au systems formed synchronously with anorogenic granitoid emplacement (**ESM – Table 7**), Nd isotopes of those Cu-Au and Fe-minerals coincides with the derivation of the REE from more than a single source. Prolongated crustal residence times on magnetite and chalcopyrite concentrates ($T_{DM-IOCG}$ = 3.35–2.74 Ga) and the $\varepsilon Nd_{(t)}$ data (εNd_{IOCG} = –3.30 to +2.19) suggest that initial mineralizing fluids and metals for Neoarchean IOCG (Salobo, Sequeirinho, and Alemão), were probably derived from reworked ancient crust through the leaching of Mesoarchean basement rocks. However, the assimilation or contribution from Neoarchean juvenile mantellic components were also involved in their genesis (**Figure 11a**).

Thus, recognized tectono-thermal events in the province (e.g., 2.74, 2.55, and 1.88 Ga; ***Trunfull et al., 2020***) associated with the generation of specialized magmas throughout the province could have exerted the primary heat source for the regional circulation of previously formed mineralizing fluids, rather than the source of metals. The conclusion in which the anorogenic granitoids represent the source of heat for the province is in agreement with those that as previously indicated for episodes of restricted and generalized granitogenesis in 2.55 Ga (e.g., ***Requia et al., 2003***; ***Galarza et al., 2008; Moreto et al., 2015a***; ***b***) and 1.88 Ga (e.g., ***Lindenmayer et al., 2001***; ***Pimentel et al., 2003***; ***Negrão, 2008***; ***de Melo et al., 2019b***; ***Pollard et al., 2019***; ***Valadão, 2019***; ***Trunfull et al., 2020***; ***Santiago et al., 2020***), respectively (**Figure 11b**). Besides, were obtained crustal residence times with Eoarchean ages ($T_{DM\text{-}IOCG}$ ~ 3.83 Ga; $T_{DM\text{-}Cu\text{-}Au}$ ~3.74 Ga) and evolved isotopic compositions (εNd_{IOCG} = –10.93; $\varepsilon Nd_{Cu\text{-}Au}$ = –10.56); however, no geological events are recorded in the province at those times.

Although our values are consistent with Nd compositions closer to the chondrite composition reported for minerals containing REE (allanite) from the Sequeirinho deposit ($\varepsilon Nd_{(2.71)}$ = –1.87 to –0.7; ***Smith et al., 2018***), the provenance of Cu-Au and Fe minerals point towards heterogeneous components, which can be attributed to (1) Mesoarchean basement rocks such as greenstone belt sequences (T_{DM} = 3.24–2.98 Ga; $\varepsilon Nd_{(2.85\text{–}3.06)}$ = –1.25 to +3.15), gneissified granitoids (T_{DM} = 3.65–2.85 Ga; $\varepsilon Nd_{(2.83\text{–}2.95)}$ = –7.02 to +2.75) or sanukitoids (***Ganade et al., 2020***) (2) Neoarchean volcanic rocks (T_{DM} = 3.47–2.77 Ga; $\varepsilon Nd_{(2.57\text{–}2.81)}$ = –4.11 to +4.60) and mafic-ultramafic magmatism (T_{DM} =3.56–2.56 Ga; $\varepsilon Nd_{(2.58\text{–}2.77)}$ = –4.20 to +5.46), whereas syn-to post-tectonic A-type anorogenic granitoids (T_{DM} = 3.19–2.81 Ga; $\varepsilon Nd_{(2.73\text{–}2.99)}$ = –2.87 to +1.40) were the main leaching and transferring mechanism for metals. ***Justo (2018)*** also concludes that Fe from Neoarchean Iron Formations was derived from Mesoarchean greenstone belts (T_{DM} = 3.39–2.75 Ga; $\varepsilon Nd_{(2.74)}$ = –3.60 to +1.35) (**ESM – Table 6**).

Oppositely, the metal source for magnetite and chalcopyrite in the Orosirian Cu-Au systems, here exemplified by Sossego orebody ($T_{DM\ Cu\text{-}Au}$ = 3.22–2.71 Ga; $\varepsilon Nd_{Cu\text{-}Au}$ = –11.68 to –9.22), were derived essentially from Archean igneous crustal sources, without significant influence of mantle magmas except as a source of heat, which probably remobilized metals from Neoarchean ore deposits via widespread and restricted granitogenesis episodes. This thought is in agreement with the conclusions that ***Teixeira et al. (2019)*** and ***Pollard et al. (2019)*** have appointed for the petrogenesis of Orosirian anorogenic granitoids (T_{DM} = 3.353–2.611; $\varepsilon Nd_{(1.88\text{-}1.89)}$ = –9.7 to –7.9) and the genesis of Orosirian Cu-Au deposits, respectively. Besides, our results are consistent with enriched εNd ($\varepsilon Nd_{(2.74)}$ = –8.8; ***Smith et al., 2018***) reported for minerals containing REE (allanite and apatite) from Sossego orebody, as well as with others Orosirian granite-related Cu-Au deposits (Alvo Estrela, and Gameleira; T_{DM} = 2.71–3.84 Ga; $\varepsilon Nd_{(1.70\text{–}1.86)}$ = –9.2 to –10.7) and Cu-Au-Mo-Co-occurrences (T_{DM} =2.96–3.82 Ga; $\varepsilon Nd_{(1.88)}$ = –13.55 to –10.49) in the province (**Figure 11c**; **ESM – Table 6**).

FIGURE 11 SHOULD BE PLACED HERE OR NEAR HERE

Heterogeneity in the source of metals from the Carajás Mineral Province can be interpreted from the $^{87}Sr/^{86}Sr_i$ against εNd(t) plot (***Fauré, 1986***) (**Figure 12**). IOCG ores are distributed between the Field I and Field IV, in accordance with primitive and evolved sources, as previously mentioned. Unfortunately, there is no broad Sr-Nd data published in the literature for the Carajás Mineral Province (**ESM – Table 8**), however, Cu-Au and Fe minerals from the Field IV span near to Mesoarchean gneissified granitoids and Neoarchean volcanic rocks that have experienced significant crustal contamination. Regardless of the fact that there is no clear association between Field I magnetite with lithotypes from the province, its composition points to relatively primitive sources, although still with some contamination of the crust. On the other hand, Cu-Au and Fe-minerals from Orosirian Cu-Au systems distributed in the Field IV reveal a clear association with crustal composition. Thus, although a more significant amount of Sr-Nd data is necessary to assume genetic relationships between metals and lithotypes in the Carajás Mineral Province, this is evidence of different behavior between Neoarchean IOCG and Orosirian Cu-Au systems.

Therefore, if metals and sulfur were derived from a magmatic source, the isotopic composition of the fluid, as well as the prevailing physicochemical conditions (temperature, Eh, and pH; ***Pestilho et al., 2020***, and references therein), would necessarily have to be similar. However, our data show that although $\delta^{34}S$ from the literature suggest a magmatic source for S, the metal source for those minerals is not exclusively from a magmatic origin, indicating a different behavior from Cu and Fe regarding the S. Our results lean more towards conclusions from ***Santiago et al. (2020).***

FIGURE 12 SHOULD BE PLACED HERE OR NEAR HERE

Alternatively, fluid mixing between endogenic and externally-derived components are also highlighted by sulfur (e.g., ***Torresi et al., 2012***; ***Santiago, 2016***; ***Lopes, 2018***; ***de Melo et al., 2019a***; ***Pestilho et al., 2020***) and oxygen isotopes (***Torresi et al., 2012***; ***da Costa e Silva et al., 2015***; **de Melo et al., 2019a**). However, these non-magmatic fluids are frequently interpreted as the later stages of protracted hydrothermal evolution in the Cu-Au deposits (e.g., ***de Melo et al., 2019a***; ***Valadão, 2019***; ***Pestilho et al., 2020***) or as a representation of the "roof zones" of the Carajás IOCG system (***Schutesky & Oliveira, 2020***). Our Sr–Nd data clearly show that there is no input of surficial fluids for ores from IOCG neither Orosirian Cu-Au systems.

On the other hand, redox variations promoted by the precipitation of hydrothermal magnetite have been recently suggested by ***Schutesky & Oliveira (2020)*** as a plausible hypothesis to explain the wide range of sulfur isotopes in the province. These authors highlighted that magmatic-hydrothermal precipitation of magnetite is the link with the sulfide crystallization, and by inference, with the destabilization of chloride complexes. Chlorine ligands are the leading carrier of primary mineralization (Cu, Au, Fe, Ag, Pd, among others) in both Precambrian Cu-Au systems (***Zang et al., 1992***; ***Chiaradia et al., 2006***; ***Monteiro et al., 2008a***; ***b***; ***Torresi et al., 2012***; ***Santiago, 2016***; ***Craveiro et al., 2020***), and REE-forming hydrothermal fluids are no exception (***Migdisov et al., 2016***). Besides, their deposition is strongly controlled by the precipitation of minerals containing the ligands, fluid-rock interaction, fluid mixing, or a variety of redox processes (***Migdisov et al., 2016***). Therefore, if the above hypothesis is correct, the iron metasomatic processes that lead to the formation of Fe-ores would also act as the main trigger for the destabilization of chloride complexes, promoting changes in the S behavior and favoring the mobilization of metals. In contrast, alternatively, the subsequent reactivation of structural domains in the province would connect mantle-derived components to the upper crust, acting as an essential mechanism for metal inheritance throughout time, such as have been stated by ***Ganade et al. (2020)*** and ***Borba et al. (2020).***

Overall, chloride-rich complexes are the primary REE fractionation process (e.g., ***Migdisov et al., 2009***; ***Williams-Jones et al., 2012***; ***Williams-Jones & Migdisov, 2014***) between IOCG (LREE-dominated) and granite-related deposits (HREE-dominated)

(***Weng et al., 2015***), whereas the participation of other complexes – i.e., fluoride, bisulfide, carbonate, phosphate; likely play an essential role as REE depositional ligands (***Migdisov et al., 2016***; ***Xing et al., 2018***). Thus, although chlorine may behave more conservative during the fluid-rocks interactions (***Chiardia et al., 2006***), it has been noted that high Cl activities were mitigated by a dilute aqueous fluid during the evolution of the system (***Torresi et al., 2012***). In addition, the absence of Ce anomalies, ranging from 0.90 to 1.10, is consistent with limited LREE mobility for the samples (***Polat and Hofmann, 2003***). Therefore, despite is probable that additional ligands are likely to be involved in the partition of metals for Orosirian Cu-Au mineralization, a discussion of their ligands is beyond the scope of this study.

5. 2. 2. Regional implications for the Carajás IOCG System

Relation of the timing and metal source within the Carajás Mineral Province requires a brief review of the evolution in the province through this time period. Although there is no consensus regarding the processes that domain the Mesoarchean (ca. 3.1–2.83 Ga), the current train of thought has cited an evolution through vertical drip-tectonics (***Ganade et al., 2020***; ***Lacasse et al., 2020***; ***Costa et al., 2020***) as a more plausible scenario rather than modern-style tectonism of a continent-continent collision (e.g., ***Martins et al.., 2017***; ***Tavares et al., 2018***; ***Marangoanha et al., 2019***; ***Trunfull et al., 2020***). Tectonic quiescence (ca. 2.83–2.76 Ga) by lithospheric stagnation is suggested as a transition between Mesoarchean drip tectonics to Neoarchean, modern-style linear belts (***Costa et al., 2020***). Regardless the controversy continues in the Neoarchean, the strike-slip regime characterized by pulsed transtensional to transpressional is highlighted as triggers for the widespread emplacement of basaltic volcanism and coevally formed bimodal magmatism in the time of period ca. 2.76–2.73 Ga (***Pinheiro & Holdsworth, 1997***; ***Holdsworth & Pinheiro, 2000***; ***Costa et al. 2020***), whereas its subsequent reactivation in the time of period ca. 2.60–2.50 Ga have been pointed as a trigger for the restringed tectonothermal episode in the northern of the province in response a rift setting (e.g., ***Salgado et al., 2019***; ***Motta et al., 2019***; ***Costa et al., 2020***; ***Trunfull et al., 2020***). Towards Paleoproterozoic, craton wide magmatism is linked with the disruption of the Atlantica Supercontinent, triggered by SLIP magmatism (ca. 1.89–1.86; ***Teixeira et al., 2019***) in the Transamazonian event (ca. 2.0–1.89 Ga; ***Salgado et al., 2019***; ***Motta et al., 2019***; ***Teixeira et al., 2019***) during a late-to post-collisional setting (***Roverato et al., 2019***).

In terms of mineralization, at the same time that strike-slip fault systems act, hydrothermal activity related to the mantle and crustal magmatism mobilized and concentrated iron, copper, and gold into economic deposits (ca. 2.76–2.73; ***Schutesky & Oliveira, 2020***), whereas the subsequent reactivation of these structures during the period of ~2.55 Ga serves as fluid channels (e.g., ***Borba et al., 2020***) for hydrothermal circulation related to the second episode of IOCG mineralization (e.g., ***Trunfull et al., 2020***; ***Costa et al., 2020***). There is no consensus regarding the relationship between Neoarchean IOCG and Orosirian Cu-Au and mineralization. However, ***Pollard et al. (2019)*** have proposed that some components can be derived from those.

We postulate that regardless of Neoarchean IOCG deposits were formed by the onset of modern-style tectonics (***Lacasse et al., 2020***; ***Costa et al., 2020***), prolongated incubation periods previous to the main ore-depositional event were primordial for metal endowment, as previously stated in Paleoproterozoic IOA-IOCG deposits at Kiruna, Sweden, by ***Storey & Smith (2017)***. Furthermore, our data in combination with the modern tectonic scenario (**Figure 11**) proposed in the literature (***Ganade et al., 2020***; ***Lacasse et al., 2020***; ***Costa et al., 2020***) show that although the tectonic changes related to the movement of disruption and cyclic aggregation of plates represents the main trigger for mineralization worldwide, for older Archean environments, changes between primitive and modern environments can also be a trigger for ore mineralization. Alternatively, the heat was a fundamental pathway for remobilization of metals throughout the Archaic to Paleoproterozoic, as evidenced by the isotopic signals for Nd-Sr and the generalized model ages for Orosirian Cu-Au. For this latest ore system, the derivation from crustal Mesoarchean sources is similar to the Neoarchean IOCG mineralization, and its formation can be explained in the context of a supercontinent cycle. Furthermore, remobilization from 2.5 Ga sources was triggered by a shift in tectonics, although more analysis is required to elucidate such a relationship.

5. 3. Chilean Iron Belt

5. 3. 1. Metal sources and tectonic implications for the Candelaria-Punta del Cobre district

Robust evidence has demonstrated that ore-forming fluid responsible for IOCG mineralization in the Andean deposits are magmatic-hydrothermal in origin, whereas external fluid incursion occurred late in the evolution of the system (e.g., ***Sillitoe, 2003***;

Rieger et al., 2010; ***2012***; ***Tornos et al., 2010***; ***2012***; ***Richards & Mumin, 2013a***; ***b***; ***Richards et al., 2017***; ***Childress et al., 2020***; ***del Real et al., 2018***; ***2020***). However, until the date for the Candelaria-Punta del Cobre district, there is no consensus if magmatic components of the hydrothermal fluids were derived from specialized components of the Copiapó Batholith (e.g., ***Marschik et al., 2003a***; ***b***; ***Mathur et al., 2002***) or if were derived from mafic magmas (***Chiaradia et al., 2006***; ***del Real et al., 2020***).

Our data show that although Cretaceous IOCG deposits from the Candelaria-Punta del Cobre district overlap in age the emplacement of a volcanic arc, I-type granitoids from the Copiapó Batholith (**ESM – Table 10**), the Nd isotopic composition of chalcopyrite and magnetite (εNd = +1.81 to +4.03) point towards the derivation of the REE from mantle-derived magmas with less primitive compositions than those granitoids ($\varepsilon Nd_{(0.118-0.110)}$ = +3.21 to 4.32; ***Marschik et al., 2003b***) (**Figure 13**). In fact, whole-rock results from this work also show that granitoids from the Copiapó Batholith are highly depleted in comparison to the IOCG ore ($\varepsilon Nd_{i\text{-batholith}}$ = +6.45 to +7.09; **ESM – Table 11**). Alternatively, variable contributions from the basement and/or volcanic host rocks have been previously suggested by Re-Os isotopes (***Mathur et al., 2002***; ***Barra et al., 2017***); however, recent studies as ***del Real et al. (2020)*** highlight that volcanic host rocks are an unlikely source for metals in the district based on Co-Ni compositions. Our results display that volcanic rocks are they are also not the direct source for IOCG genesis in the district, due most of the volcanic and volcanic sedimentary members of Punta del Cobre Formation display variable primitive signals and younger T_{DM} ($\varepsilon Nd_{(0.135-0.110)}$ = +4.41 to +7.84; T_{DM} = 0.15–0.40 Ga; **ESM – Table 11**) than IOCG deposits from the Candelaria-Punta del Cobre district ($T_{DM\text{-IOCG}}$ = 0.43 to 0.65 Ga). In fact, positive εNd_i has also been reported by ***Tornos et al. (2020)*** for the dacitic volcanic host ($\varepsilon Nd_{i\text{-albitophyre}}$ = +2.0) of the Punta del Cobre Formation. Based on this, it is possible to suggest that although Nd from coevally formed regional materials from the Candelaria-Punta del Cobre district shares a primitive magmatic source for the IOCG-type mineralization, it is likely that mantellic or asthenospheric disturbances product of terrane accommodation during the Famatinian and Pampean cycle have influenced in the enrichment of metals during prolonged incubation periods before the Cretaceous metallogenetic event (**Figure 13**) (***Ramos, 2008***; ***Oliveros et al., 2020***). In fact, according to ***Creixell (2007),*** differences or heterogeneities in the mantle source, or mixing between isotopically enriched lithospheric and depleted asthenospheric mantle source may lead to the production of depleted isotopic compositions associated with Proterozoic T_{DM}, while the progressive removal of the old lithospheric mantle during the Mesozoic due to a process of lithospheric delamination would explain the profound change in the subcrustal source, as well as the melting and modification towards a more refractory nature of the continental crust for the Paleocene T_{DM} (***Parada et al., 1999***). Moreover, a crustal-derived source from the Andean basement is unlikely due to the active continental margin of the Central Andes has been the site of magma genesis since at least 0.3 Ga (***Miller & Harris, 1989***; ***Girardi, 2014***). This has also been elucidated by ***Tornos et al. (2020***) for the genesis of Chilean magnetite-apatite deposits. ***Richards et al. (2017)*** have also proposed that the composition of the basement has little influence on the genesis of the Chilean IOCG deposits, similar as is evidenced in Nd signals reported for the Tropezón IOCG deposit (εNd_i = –2.9; ***Tornos et al., 2010***; ***2012***) or as ***Babiak et al. (2017)*** concludes for the genesis of Lower Cretaceous (εNdi between –0.3 to +0.8; ***Velasco & Tornos, 2009***; ***Palma et al., 2019***; ***Tornos et al., 2020***) to Pliocene IOA systems (εNdi between –5.4 to –4.6; ***Tornos et al., 2017***). However, our results suggest that for the genesis of IOCG deposits in the Candelaria-Punta del Cobre district, they were not important. Besides, magnetite-apatite systems display short residence periods suggest compared to IOCG systems, which suggest a different pathway in the processes involved between the genesis of each ore system (**Figure 13**).

FIGURE 13 SHOULD BE PLACED HERE OR NEAR HERE

Towards the $^{87}Sr/^{86}Sr_i$ against εNd(t) plot (***Fauré, 1986***) (**Figure 14**) most of the analyzed ore samples fall in the Field I and Field II throughout the mantle array wedge and show strong proximity with the albitophyre composition (***Tornos et al., 2020***). This suggests derivation from similar magmatic components. Nonetheless, our Sr-Nd analyses from whole-rock samples of the volcanic and volcanic sedimentary members of the Punta del Cobre display seawater modification patterns that odds with the Sr-Nd composition of chalcopyrite and magnetite of IOCG deposits. Similar behavior is displayed for the Sr-Nd compositions of the Copiapó Batholith (***Marschik et al., 2003a***), suggesting that ore-forming fluids related to the IOCG mineralization were driven by magmatic components derived from subduction processes with more primitive compositions than those of the Copiapó Batholith.

FIGURE 14 SHOULD BE PLACED HERE OR NEAR HERE

6. Concluding remarks

This study provided new clues on the source of metals from IOCG systems through the combination of Nd–Sr isotopes and trace elements applied on Cu-Au and Fe minerals together with an extensive data compilation from literature. Based on this view, we can conclude that:

- Heterogeneity in the source of metals from the Carajás Mineral Province can be interpreted from the $^{87}Sr/^{86}Sr_i$ against εNd(t) plot.
- Prolongated crustal residence times on magnetite and chalcopyrite concentrates ($T_{DM-IOCG}$ = 3.35–2.74 Ga) and the $εNd_{(t)}$ data ($εNd_{IOCG}$ = –3.30 to +2.19) suggest that initial mineralizing fluids and metals for Neoarchean IOCG (Salobo, Sequeirinho, and Alemão), were probably derived from reworked ancient crust through the leaching of Mesoarchean basement rocks, although the assimilation and/or contribution from Neoarchean juvenile mantellic components were also involved in their genesis.
- The generation of specialized magmas throughout the province could have exerted the main heat source for regional circulation of previously formed mineralizing fluids, rather than the source of metals.
- The metal source for magnetite and chalcopyrite in the Orosirian Cu-Au systems ($T_{DM\ Cu-Au}$ = 3.22–2.71 Ga; $εNd_{Cu-Au}$ = –11.68 to –9.22) involves derivation from Archean igneous crustal sources.
- Cretaceous IOCG deposits from the Candelaria-Punta del Cobre district derived metals from primitive sources compositionally similar to the arc-volcanic rocks, probably by heterogeneities in the mantle source, rather than a single specialized source.
- Trace element and REE data suggest more mafic compositions in Carajás IOCG and Cu-Au deposits rather than Andean IOCG deposits.
- Long periods of incubations for metals are a requirement for Cu-Au precipitation during tectonic shifts.

7. Acknowledgment

This study was financed in part by the Coordenação de Aperfeiçoamento de Pessoal de Nível Superior – Brasil (CAPES) – Finance Code 001. The authors appreciate all the logistical support provided by Lundin Mining Corporation, Mantos Copper S. A., Sociedad Punta del Cobre S. A., and VALE S. A. during sampling and collection stages in Chile and Brazil. Thanks to Carla Sepulveda for their help with all the logistics concerning fieldwork in the Candelaria-Punta del Cobre district. Special thanks to Lila Avila, Christopher Richings, and Patricio Calderón from the Compañía Contractual Minera Candelaria and Mauricio Arce from the Minera Mantoverde for their help in the field campaign. We acknowledge the constructive commentaries by Fernando Tornos and Elton Dantas, which significantly improved the manuscript. Additionally, Eduardo thanks Juan Fritis, Lidia Pérez, and Cristian Kienteca for their useful help in sending samples.

References

Acosta-Góngora, P., Gleeson, S., Samson, I.M., Corriveau, L., Ootes, L., Jackson, S.E., Taylor, B.E., Girard, I., 2018. Origin of sulfur and crustal recycling of copper in polymetallic (Cu-Au-Co-Bi-U ± Ag) iron-oxide-dominated systems of the Great Bear Magmatic Zone, NWT, Canada. Miner Deposita 53, 353–376. https://doi.org/10.1007/s00126-017-0736-6

Alves, M.A., Monteiro, L.V.S., Zarelli, A.V., 2019. The Cu-Au Furnas Deposit Metallogeny and Ore Typology, Carajás Province, Pará, Brazil. SEG 2019 Conference Proceedings, Santiago, Chile.

Arévalo, C. 2005a. Carta Los Loros, Región de Atacama. Servicio Nacional de Geología y Minería. Carta Geológica de Chile. Serie Geología Básica, 92, 53, 1. Mapa escala 1:100.000.

Arévalo, C. 2005b. Carta Copiapó, Región de Atacama. Servicio Nacional de Geología y Minería. Carta Geológica de Chile, Serie Geología Básica, 92, 53, 1. Mapa escala 1:100.000.

Arévalo, C., Grocott, J., Martin, W., Pringle, M., Taylor, G., 2006. Structural Setting of the Candelaria Fe Oxide Cu-Au Deposit, Chilean Andes (27° 30′ S). Econ. Geol. 101, 819–841. https://doi.org/10.2113/gsecongeo.101.4.819

Austin, J., Björk, A., Patterson, B., 2019. Structural controls of the Ernest Henry IOCG deposit: Insights from integrated structural, geophysical and mineralogical analyses. ASEG Extended Abstracts, 1-5. https://doi.org/10.1080/22020586.2019.12073161

Baker, T., Mustard, R., Fu, B., Williams, P.J., Dong, G., Fisher, L., Mark, G., Ryan, C.G., 2008. Mixed messages in iron oxide–copper–gold systems of the Cloncurry district, Australia: insights from PIXE analysis of halogens and copper in fluid inclusions. Miner Deposita 43, 599–608. https://doi.org/10.1007/s00126-008-0198-y

Babiak, R.N., Delgaudio, S., Hanchar, J.M., Tornos, F., Whitehouse, M.J., 2018. Geochemistry and geochronology of apatite and zircon from MtAp and IOCG deposits, Atacama desert, Chile. XIX Congreso Peruano de Geologia, Lima, Peru

Barra, F., Reich, M., Selby, D., Rojas, P., Simon, A., Salazar, E., Palma, G., 2017. Unraveling the origin of the Andean IOCG clan: A Re-Os isotope approach. Ore Geol. Rev. 81, 62–78. https://doi.org/10.1016/j.oregeorev.2016.10.016

Barton, M.D., 2014. Iron Oxide (-Cu-Au-REE-P-Ag-U-Co) Systems, in: Turekian, K., Holland, H. (Eds.), Treatise on Geochemistry: Second Edition. Elsevier Inc., Amsterdam, pp. 515–541. https://doi.org/10.1016/B978-0-08-095975-7.01123-2

Barton, M.D., Johnson, D.A., 1996. Evaporitic-source model for igneous-related Fe oxide–(REE-Cu-Au-U) mineralization. Geology 24, 259–262. https://doi.org/10.1130/0091-7613(1996)024<0259:ESMFIR>2.3.CO;2

Barton, M.D., Johnson, D.A., 2000. Alternative brine sources for Fe-oxide (Cu-Au) systems: Implications for hydrothermal alteration and metals, in: Porter, T.M. (Ed.), Hydrothermal Iron Oxide Copper-Gold & Related Deposits: A Global Perspective, First Edition. PGC Publishing, Adelaide, pp. 43–60.

Beaudoin, G., Dupuis, C., Gosselin, P., Jébrak, M., 2007. Mineral chemistry of iron oxides: application to mineral exploration. Proceedings of the 9th Biennial SGA meeting, Dublin, Ireland, 497–500.

Benavides, J., Kyser, T.K., Clark, A.H., Oates, C.J., Zamora, R., Tarnovschi, R., Castillo, B., 2007. The Mantoverde Iron Oxide-Copper-Gold District, III Región, Chile: The Role of Regionally Derived, Nonmagmatic Fluids in Chalcopyrite Mineralization. Econ. Geol.102, 415–440. doi: https://doi.org/10.2113/gsecongeo.102.3.415

Betts, P.G., Giles, D., Foden, J., Schaefer, B.F., Mark, G., Pankhurst, M.J., Forbes, C.J., Williams, H.A., Chalmers, N.C., Hills, Q., 2009. Mesoproterozoic plume-modified orogenesis in eastern Precambrian Australia. Tectonics 28, 1–28. https://doi.org/10.1029/2008TC002325

Blenkinsop, T.G., Huddlestone-Holes, C.R., Foster, D.R.W., Edmiston, M.A., Lepong, P., Mark, G., Austin, J.R., Murphy, F.C., Ford, A., Rubenasch, M.J., 2008. The crustal scale architecture of the Eastern Succession, Mount Isa: The influence of inversion. Precambrian Res. 163, 31–49. https://doi.org/10.1016/j.precamres.2007.08.011

Borba, M.L., Tassinari, C.C., Matos, F.M., Sato, K., Huhn, S., Ferreira, S.N., Medeiros, C.A., 2020. Tracking hydrothermal events using zircon REE geochemistry from the Carajás Mineral Province, Brazil. J. Geochem. Explor. 106679. https://doi.org/10.1016/j.gexplo.2020.106679

Botelho, N.F., Moura, M.A., Teixeira, L.M., Olivo, G.R., Cunha, L.M., Santana, U.M., 2005. Caracterização geológica e metalogenética do depósito de Cu ± (Au, W, Mo, Sn) Breves, Carajás, in: Marini, O.J., Queiroz, E.T., Ramos, B.W. (Eds.), Caracterização de depósitos minerais em Distritos Mineiros da Amazônia, Second edition. Brasília, ADIMB, pp. 335–389

Broughm, S.G., Hanchar, J.M., Tornos, F., Westhues, A., Attersley, S., 2017. Mineral chemistry of magnetite from magnetite-apatite mineralization and their host rocks: examples from Kiruna, Sweden, and El Laco, Chile. Miner. Deposita 52, 1223–1244. https://doi.org/10.1007/s00126-017-0718-8

Bühn, B., Santos, R.V., Dardenne, M.A., Oliveira, C.G., 2012. Mass-dependent and mass-independent sulfur isotope fractionation (δ34S and δ33S) from Brazilian Archean and Proterozoic sulfide deposits by laser ablation multi-collector ICP-MS. Chemical Geology, 312-313, 163–176 https://doi.org /10.1016/j.chemgeo.2012.04.003

Campo, R.Y.T., 2020. Química mineral de magnetita e assinatura isotópica de enxofre em sulfetos de Cu-Fe: implicações para o modelo evolutivo do depósito tipo IOCG metamorfizado do salobo, província mineral de Carajás. MSc. dissertation. University of Brasilia, Brazil.

Campo, R.Y.T., Giustina, M.E.S.D., Oliveira, C., 2019. The giant metamorphosed IOCG salobo deposit, Carajás Mineral Province: magnetite trace elements constraints and implications for a multi-stage evolutionary model. SEG 2019 Conference Proceedings, Santiago, Chile.

Canil, D., Lacourse, T., 2020. Geothermometry using minor and trace elements in igneous and hydrothermal magnetite. Chem. Geol. 541, 119576. https://doi.org/10.1016/j.chemgeo.2020.119576

Canil, D., Grondahl, C., Lacourse, T., Pisiak, L.K., 2016. Trace elements in magnetite from porphyry Cu–Mo–Au deposits in British Columbia, Canada. Ore Geol. Rev. 72, 1116–1128. https://doi.org/10.1016/j.oregeorev.2015.10.007

Cawood, P.A., Hawkesworth, C.J., 2013. Temporal relations between mineral deposits and global tectonic cycles. Geol. Soc. Spec. Publ. 393, 9–21. https://doi.org/10.1144/sp393.1

Cembrano, J., Gonzalez, G., Arancibia, G., Ahumada, I., Olivares, V., Herrera, V., 2005. Fault zone development and strain partitioning in an extensional strike-slip duplex: a case study from the Mesozoic Atacama fault system, Northern Chile. Tectonophysics 400, 105–125. https://doi.org/10.1016/j.tecto.2005.02.012

Cembrano, J., Garrido, I., Marquardt, M., 2009. Tectonic setting of IOCG deposits in the Central Andes: Strike-slip-dominated deformation. XII Congreso Geológico Chileno, Santiago, Chile.

Champion, D.C., Huston, D.L., 2016. Radiogenic isotopes, ore deposits and metallogenic terranes: Novel approaches based on regional isotopic maps and the mineral systems concept. Ore Geol. Rev. 76, 229–256. https://doi.org/10.1016/j.oregeorev.2015.09.025

Chen, H., 2013. External sulphur in IOCG mineralization: Implications on definition and classification of the IOCG clan. Ore Geol. Rev. 51, 74–78. https://doi.org/10.1016/j.oregeorev.2012.12.002

Chen, H., Clark, A.H., Kyser, T.K., Ullrich, T.D., Baxter, R., Chen, Y., Moody, T.C., 2010. Evolution of the giant Marcona-Mina Justa iron oxide-copper-gold district, south-central Peru. Econ. Geol. 105, 155–185. https://doi.org/10.2113/gsecongeo.105.1.155

Chen, H., Kyser, T.K., Clark, A.H., 2011. Contrasting fluids and reservoirs in the contiguous Marcona and Mina Justa iron oxide–Cu (–Ag–Au) deposits, south-central Perú. Miner. Deposita 46, 677–706. https://doi.org/10.1007/s00126-011-0343-x

Chen, W.T., Zhou, M.F., 2012. Paragenesis, stable isotopes, and molybdenite Re-Os isotope age of the Lala Iron-Copper Deposit, Southwest China. Econ. Geol. 107, 459–480. https://doi.org/10.2113/econgeo.107.3.459

Chen, H., Cooke, D.R., Baker, M.J., 2013. Mesozoic iron oxide copper-gold mineralization in the central Andes and the Gondwana Supercontinent breakup. Econ. Geol. 108, 37–44. https://doi.org/10.2113/econgeo.108.1.37

Cherry, A.R., Ehrig, K., Kamenetsky, V.S., McPhie, J., Crowley, J.L., Kamenetsky, M.B., 2018. Precise geochronological constraints on the origin, setting and incorporation of ca. 1.59 Ga surficial facies into the Olympic Dam Breccia Complex, South Australia. Precambrian Res. 315, 162–178. https://doi.org/10.1016/j.precamres.2018.07.012

Chiaradia, M., Banks, D., Cliff, R., Marschik, R., De Haller, A., 2006. Origin of fluids in iron oxide–copper–gold deposits: constraints from δ 37 Cl, 87 Sr/86 Sri and Cl/Br. Miner. Deposita 41, 565–573. https://doi.org/10.1007/s00126-006-0082-6Childress, T.M., Simon, A.C., Reich, M., Barra, F., Arce, M., Lundstrom, C.C., Bindeman, I.N., 2020. Formation of the Mantoverde iron oxide-copper-gold (IOCG) deposit, Chile: insights from Fe and O stable isotopes and comparisons with iron oxide-apatite (IOA) deposits. Miner. Deposita 55, 1489–1504. https://doi.org/10.1007/s00126-019-00936-x

Childress, T.M., Simon, A.C., Reich, M., Barra, F., Arce, M., Lundstrom, C.C., Bindeman, I.N., 2020. Formation of the Mantoverde iron oxide-copper-gold (IOCG) deposit, Chile: insights from Fe and O stable isotopes and comparisons with iron oxide-apatite (IOA) deposits. Miner. Deposita 55, 1489–1504. https://doi.org/10.1007/s00126-019-00936-x

Cordani, U.G., Teixeira, W., Tassinari, C.C., Coutinho, J.M., Ruiz, A.S., 2010. The Rio Apa Craton in Mato Grosso do Sul (Brazil) and northern Paraguay: geochronological evolution, correlations and tectonic implications for Rodinia and Gondwana. Am. J. Sci. 310, 981–1023. https://doi.org/10.2475/09.2010.09

Corriveau., L., Montreuil., J.F., Potter., E.G., 2016. Alteration facies linkages among iron oxide copper-gold, iron oxide-apatite, and affiliated deposits in the Great Bear magmatic zone, Northwest Territories, Canada. Econ. Geol. 111, 2045–2072. https://doi.org/10.2113/econgeo.111.8.2045

Courtney-Davies, L., Ciobanu, C. L., Tapster, S. R., Cook, N. J., Ehrig, K., Crowley, J. L., Verdugo-Ihl, M.R., Wade, B.P., Condon, D.J., 2020b. Opening the magmatic-hydrothermal window: High-precision U-Pb geochronology of the Mesoproterozoic Olympic Dam Cu-U-Au-Ag deposit, South Australia. Econ. Geol. https://doi.org/10.5382/econgeo.4772

Costa, F.G., Santos, P.A., Serafim, I.C.C.O., Costa, I.S.L., Roopnarain, S. 2020. From Mesoarchean drips to modern-style tectonics in the Carajás Mineral Province, Amazonian Craton. J. S. Am. Earth Sci. 104, 10281. https://doi.org/10.1016/j.jsames.2020.102817

Craveiro, G.S., Xavier, R.P., Villas, R.N.N., 2019. The Cristalino IOCG deposit: an example of multi-stage events of hydrothermal alteration and copper mineralization. Braz. J. Geol. 49. 1–18. https://doi.org/10.1590/2317-4889201920180015

Craveiro, G.S., Villas, R.N.N., Xavier, R.P., 2020. A Fluid Inclusion and Stable Isotope (O, H, S and C) study of the Archean IOCG Cristalino deposit, Carajás Mineral Province, Brazil: Implications to ore genesis. Ore Geol. Rev. 103822. https://doi.org/10.1016/j.oregeorev.2020.103822

Creixell, C., 2007. Petrogénesis y emplazamiento de enjambre de diques máficos Mesozoicos de Chile Central: Implicancias tectónicas en el desarrollo del arco Jurásico-Cretácico temprano. PhD. thesis. University of Chile, Chile.

Creixell, C., Arevalo, C., Fanning, M., 2009. Geochronology of the Cretaceous magmatism from the Coastal Cordillera of north-central Chile (29°15' to 29°30' S): Metallogenic implications. XII Congreso Geológico Chileno, Santiago, Chile, 1–3.

Curtis, S., Thiel, S., 2019. Identifying lithospheric boundaries using magnetotellurics and Nd isotope geochemistry: An example from the Gawler Craton, Australia. Precambrian Res. 320, 403–423. https://doi.org/10.1016/j.precamres.2018.11.013

da Costa Silva, A.R., Villas, R.N.N., Lafon, J.M., Craveiro, G.S., Ferreira, V.P., 2015. Stable isotope systematics and fluid inclusion studies in the Cu–Au Visconde deposit, Carajás Mineral Province, Brazil: implications for fluid source generation. Miner. Deposita 50, 547–569. https://doi.org/10.1007/s00126-014-0558-8

Dall'Agnol, R., Teixeira, N.P., Rämö, O.T., Moura, C.A., Macambira, M.J.B., de Oliveira, D.C., 2005. Petrogenesis of the Paleoproterozoic rapakivi A-type granites of the

Archean Carajás metallogenic province, Brazil. Lithos 80, 101–129. https://doi.org/10.1016/j.lithos.2004.03.058

Daly, S.J., Fanning, C.M., Fairclough, M.C., 1998. Tectonic evolution and exploration potential of the Gawler Craton, South Australia. AGSO J. Aust. Geol. Geophys. 17, 145–168.

Dardenne, M.A., Ferreira Filho, C.F., Meirelles, M.R., 1988. The role of shoshonitic and calc- alkaline suites in the tectonic evolution of the Carajás District, Brazil. J. S. Am. Earth Sci. 1, 363–372. https://doi.org/10.1016/0895-9811(88)90023-5

Dare, S.A.S., Barnes, S., Beaudoin, G., Méric, J., Boutroy, E., Potvin-Doucet, C., 2014a. Trace elements in magnetite as petrogenetic indicators. Miner. Deposita 49, 785–796. https://doi.org/10.1007/s00126-014-0529-0

Dare, S.A., Barnes, S., Prichard, H.M., Fisher, P.C., 2014b. Mineralogy and geochemistry of Cu-rich ores from the McCreedy East Ni-Cu-PGE deposit (Sudbury, Canada): implications for the behavior of platinum group and chalcophile elements at the end of crystallization of a sulfide liquid. Econ. Geol.109, 343–36. https://doi.org/10.2113/econgeo.109.2.343

Davidson, G.J., Dixon, G.H., 1992. Two sulphur isotope provinces deduced from ores in the Mount Isa Eastern Succession, Australia. Miner. Deposita 27, 30–41. https://doi.org/10.1007/BF00196078

Davidson, G.J., 2002. The shallow to mid-crustal family of iron oxide copper-gold deposits: size, alteration and mechanisms of formation, in: Cooke, D.R., Pongratz, J. (Eds.), Giant Ore Deposits: characteristics, genesis and exploration. CODES Special Publication 4, Hobart, pp. 79–102.

de Souza, Z.S., Potrel, A., Lafon, J.M., Althoff, F.J., Pimentel, M.M., Dall'Agnol, R., de Oliveira, C. G., 2001. Nd, Pb and Sr isotopes in the Identidade Belt, an Archaean greenstone belt of the Rio Maria region (Carajás Province, Brazil): implications for the Archaean geodynamic evolution of the Amazonian Craton. Precambrian Res. 109, 293–315.

Deditius, A.P., Reich, M., Simon, A.C., Suvorova, A., Knipping, J., Roberts, M.P., Rubanov, S., Dodd, A., Saunders, M., 2018. Nanogeochemistry of hydrothermal magnetite. Contrib Mineral Petrol. 173, 46. https://doi.org/10.1007/s00410-018-1474-1 de Haller, A., Zuñiga, A.J., Corfu, F., Fontboté, L., 2002. The iron oxide-Cu-Au deposit of Raul-Condestable, Mala, Lima, Peru. XI Congreso Peruano de Geología, Lima, Peru, 1.

de Haller, A., Corfu, F., Fontboté, L, Schaltegger, U, Barra, F., Chiaradia, M., Frank, M., Alvarado, J.Z., 2006. Geology, geochronology, and Hf and Pb isotope data of the Raúl-Condestable iron oxide-copper-gold deposit, central coast of Perú. Econ. Geol. 101, 281–310. https://doi.org/10.2113/gsecongeo.101.2.281

de Haller, A., and Fontboté, L., 2009. The Raúl-Condestable iron oxide copper-gold deposit, central coast of Peru: Ore and related hydrothermal alteration, sulfur isotopes, and thermodynamic constraints. Econ. Geol. 104, 365–384. https://doi.org/10.2113/gsecongeo.104.3.365

de Melo, G.H., Monteiro, L.V.S., Xavier, R.P., Moreto, C.P.N., Santiago, E.S.B., Dufrane, S.A., Aires, B., Santos, A.F.F., 2017. Temporal evolution of the giant Salobo IOCG deposit, Carajás Province (Brazil): constraints from paragenesis of hydrothermal alteration and U-Pb geochronology. Miner. Deposita 52, 709–732. https://doi.org/10.1007/s00126-016-0693-5

de Melo, G.H., Monteiro, L.V., Xavier, R.P., Moreto, C.P., Santiago, E., 2019a. Tracing Fluid Sources for the Salobo and Igarapé Bahia Deposits: Implications for the Genesis of the Iron Oxide Copper-Gold Deposits in the Carajás Province, Brazil. Econ. Geol. 114, 697–718. https://doi.org/10.5382/econgeo.4659

de Melo, G.H., Monteiro, L.V., Xavier, R.P., Moreto, C.P., Arquaz, R.M., Silva, M.A.D., 2019b. Evolution of the Igarape Bahia Cu-Au deposit, Carajas Province (Brazil): Early syngenetic chalcopyrite overprinted by IOCG mineralization. Ore Geol. Rev. 111, 102993. https://doi.org/10.1016/j.oregeorev.2019.102993

de Souza, Z.S., Potrel, A., Lafon, J.M., Althoff, F.J., Pimentel, M.M., Dall'Agnol, R., de Oliveira, C. G., 2001. Nd, Pb and Sr isotopes in the Identidade Belt, an Archaean greenstone belt of the Rio Maria region (Carajás Province, Brazil): implications for the Archaean geodynamic evolution of the Amazonian Craton. Precambrian Res. 109, 293–315. https://doi.org/10.1016/S0301-9268(01)00164-4 del Real, I., Thompson, J.F., Carriedo, J., 2018. Lithological and structural controls on the genesis of the Candelaria-Punta del Cobre Iron Oxide Copper Gold district, Northern Chile. Ore Geol. Rev. 102, 106–153. https://doi.org/10.1016/j.oregeorev.2018.08.034

del Real, I., Thompson, J.F., Simon, A.C., Reich, M., 2020. Geochemical and Isotopic Signature of Pyrite as a Proxy for Fluid Source and Evolution in the Candelaria-Punta del Cobre Iron Oxide Copper-Gold District, Chile. Econ. Geol. 115, 1493–1518. https://doi.org/10.5382/econgeo.4765

DePaolo, D.J., Wasserburg, G.J., 1976. Nd isotopic variations and petrogenetic models. Geophys. Res. Lett. 3, 249–252. https://doi.org/10.1029/GL003i005p00249

DePaolo, D.J., 1981. Neodymium isotopes in the Colorado Front Range and crust-mantle evolution in the Proterozoic. Nature 291, 193–196. https://doi.org/10.1038/291193a0

DePaolo, D.J., 1988. Neodymium Isotope Geochemistry. An Introduction, first ed. Springer, Berlin.

DOCEGEO., 1988. Revisão litoestratigráfica da Província Mineral de Carajás—Litoestratigrafia e principais depósitos minerais. 35th Congresso Brasileiro de Geologia, Belém, 11–56 (Proceedings).

Domingos, F., 2009. The structural setting of the Canaã dos Carajás region and Sossego-Sequeirinho deposits, Carajás, Brazil. Doctoral dissertation, Durham University, England.

Dreher, A.M., Xavier, R.P., Taylor, B.E., Martini, S.L., 2008. New geologic, fluid inclusion and stable isotope studies on the controversial Igarapé Bahia Cu–Au deposit, Carajás Province, Brazil. Miner. Deposita 43, 161–184. https://doi.org/10.1007/s00126-007-0150-6

Dupuis, C., Beaudoin, G., 2011. Discriminant diagrams for iron oxide trace element fingerprinting of mineral deposit types. Miner. Deposita 46, 319–335. https://doi.org/10.1007/s00126-011-0334-y

Duran, C.J., Dubé-Loubert, H., Pagé, P., Barnes, S.J., Roy, M., Savard, D., Cave, B.J., Arguin, J-P., Mansur, E.T., 2019. Applications of trace element chemistry of pyrite and chalcopyrite in glacial sediments to mineral exploration targeting: Example from the

Churchill Province, northern Quebec, Canada. J. Geochem. Explor. 196, 105–130. https://doi.org/10.1016/j.gexplo.2018.10.006

Eilu, P., Lahtinen, R., 2013. Fennoscandian metallogeny and supercontinent cycles. Proceedings of the 12th Biennial SGA Meeting, Uppsala, Sweden, 1632–1634.

Escolme, A., Cooke, D.R., Hunt, J., Berry, R.F., Maas, R., Creaser, R.A., 2020. The Productora Cu-Au-Mo Deposit, Chile: A Mesozoic Magmatic-Hydrothermal Breccia Complex with Both Porphyry and Iron Oxide Cu-Au Affinities. Econ. Geol. 115, 534–580. https://doi.org/10.5382/econgeo.4718

Fauré, G., 1986. Principles of isotope geology. Wiley & Sons, New York.

Feio, G.R.L., Dall'Agnol, R., Dantas, E.L., Macambira, M.J.B., Santos, J.O.S., Althoff, F.J., Soares, J.E.B., 2013. Archean granitoid magmatism in the Canaã dos Carajás area: Implications for crustal evolution of the Carajás province, Amazonian craton, Brazil. Precambrian Res. 227, 157–185. https://doi.org/10.1016/j.precamres.2012.04.007

Fernandes, K.G., 2020. O depósito Alvo Açaí: um exemplo de skarn de cobre no Domínio Carajás. MSc. dissertation. University of Campinias, Brazil.

Fernandes, C.M.D., Juliani, C., 2019. The tectonic controls on the Paleoproterozoic volcanism and the associated metallogeny in the South Amazonian craton, Brazil: Sr–Nd–Pb isotope constraints. Precambrian Res. 331, 105354. https://doi.org/10.1016/j.precamres.2019.105354

Figuereido e Silva, R.C., Lobato, L.M., Zucchetti, M., Hagemann, S., Venemann, T., 2020. Geotectonic signature and hydrothermal alteration of metabasalts under- and overlying the giant Serra Norte iron deposits, Carajás Mineral Province. Ore Geol. Rev. 120, 103407. https://doi.org/10.1016/j.oregeorev.2020.103407

Fisher, L.A., Kendrick, M.A., 2008. Metamorphic fluid origins in the Osborne Fe oxide–Cu–Au deposit, Australia: evidence from noble gases and halogens. Miner. Deposita 43, 483–497. https://doi.org/10.1007/s00126-008-0178-2

Foster, D.R.W., Austin, J.R., 2008. The 1800-1610 Ma stratigraphic and magmatic history of the Eastern Succession, Mount Isa Inlier, and correlations with adjacent Paleoproterozoic terranes. Precambrian Res. 163, 7–30. https://doi.org/10.1016/j.precamres.2007.08.010

Galarza, M.A., Macambira, M.J.B., Villas, R.N., 2008. Dating and isotopic characteristics (Pb and S) of the Fe oxide–Cu–Au–U–REE Igarapé Bahia ore deposit, Carajás mineral province, Pará state, Brazil. J. S. Am. Earth Sci. 25, 377–397.

Ganade, C.E., Griffin, W.L., Weinberg, R.F., Belousova, E., Takenaka, L.B., Lopes, L.L., Lacasse, C.M., Campos, L.D., 2020. On the origin of oldest Iron-Oxide-Copper-Gold (IOCG) deposits at the transition from Archean drip to plate tectonics. Research Square, 1–21. https://doi.org/10.21203/rs.3.rs-50946/v1

Garcia, V.B., Schutesky, M.E., Oliveira, C.G., Whitehouse, M.J., Huhn, S.R., Augustin, C.T., 2020. The Neoarchean GT-34 Ni deposit, Carajás Mineral Province, Brazil: an atypical IOCG-related Ni sulfide mineralization. Ore Geol. Rev. 103773. https://doi.org/10.1016/j.oregeorev.2020.103773

George, L.L., Cook, N.J., Crowe, B.B., Ciobanu, C.L., 2018. Trace elements in hydrothermal chalcopyrite. Mineral. Mag. 82, 59–88. https://doi.org/10.1180/minmag.2017.081.021

Gibbs, A.K., Wirth, K.R., Hirata, W.K., Olszewski Jr., W.J., 1986. Age and composition of the Grão Pará Group volcanics, Serra dos Carajás. Braz. J. Geol. 16, 201–211

Giles, C.W., 1988. Petrogenesis of the Proterozoic Gawler Range volcanics, South Australia. Precambrian Res. 40, 407–427. https://doi.org/10.1016/0301-9268(88)90078-2

Gioia, S.M.C.L., Pimentel, M.M., 2000. The Sm-Nd isotopic method in the geochronology laboratory of the University of Brasília. An. Acad. Bras. Ciênc. 72, 219–245. https://doi.org/10.1590/S0001-37652000000200009

Girardi, J.D., 2014. Comparison of Mesozoic magmatic evolution and iron oxide (-copper-gold) ('IOCG') mineralization, Central Andes and western North America. PhD. thesis dissertation. The University of Arizona, USA.

Gleason, J.D., Marikos, M.A., Barton, M.D., Johnson, D.A., 2000. Neodymium isotopic study of rare earth element sources and mobility in hydrothermal Fe oxide (Fe-P-REE) systems. Geochim. Cosmochim. Acta 64, 1059–1068. https://doi.org/10.1016/S0016-7037(99)00325-7

Gleeson, S.A., Smith, M.P., 2009. The sources and evolution of mineralising fluids in iron oxide–copper–gold systems, Norrbotten, Sweden: Constraints from Br/Cl ratios and stable Cl isotopes of fluid inclusion leachates. Geochimica et Cosmochimica Acta, 73(19), 5658–5672. https://doi.org/10.1016/j.gca.2009.06.005

Goldsmith, S. D., 2014. The Samphire Project: A distal IOCG and evidence for Mesoarchean crust in the Gawler Craton. PhD. Dissertation, University of Adelaide, Australia.

Grainger, C.J., Groves, D.I., Tallarico, F.H.B., Fletcher, I.R., 2008. Metallogenesis of the Carajás Mineral Province, Southern Amazon Craton, Brazil: Varying styles of Archean through Paleoproterozoic to Neoproterozoic base- and precious-metal mineralisation. Ore Geol. Rev. 33, 451–489. https://doi.org/10.1016/j.oregeorev.2006.10.010

Groves, D.I., Vielreicher, R.M., Goldfarb, R.J., Condie, K.C., 2005. Controls on the heterogeneous distribution of mineral deposits through time. Geol. Soc. Spec. Publ. 248, 71–101. https://doi.org/10.1144/gsl.sp.2005.248.01.04

Groves, D.I., Bierlein, F.P., Meiner, L.D., Hitzman, M.W., 2010. Iron Oxide Copper-Gold (IOCG) Deposits through Earth History: Implications for Origin, Lithospheric Setting, and Distinction from Other Epigenetic Iron Oxide Deposits. Econ. Geol. 105, 641–654. https://doi.org/10.2113/gsecongeo.105.3.641

Haynes, D.W., 2000, Iron oxide copper (-gold) deposits: Their position in the ore deposit spectrum and modes of origin, in: Porter, T.M. (Ed.), Hydrothermal Iron Oxide Copper-Gold & Related Deposits: A Global Perspective, First Edition. PGC Publishing, Adelaide, pp. 43–60.

Haynes, D.W., Cross, K.C., Bills, R.T., Reed, M.H., 1995. Olympic Dam ore deposit: a fluid mixing model. Econ. Geol. 90, 281–307. https://doi.org/10.2113/gsecongeo.90.2.281

Heuser, G., Arancibia, G., Veloso, E.E., Cembrano, J., Cordeiro, P.F.O., Nehler, M., Bracke, R., 2020. The evolution of the Dominga Fe-Cu deposit (northern Chile): Insights from mineral textures and micro-CT analysis. Ore Geol. Rev. 119, 103316. https://doi.org/10.1016/j.oregeorev.2020.103316

Hickson, C.J., Juras, S.J., 1986. Sample contamination by grinding. Can. Mineral. 24, 585–589.

Hitzman, M.W., 2000. Iron-oxide-Cu-Au deposits: what, where, when, and why, in: Porter, T.M. (Ed.), Hydrothermal Iron Oxide Copper-Gold & Related Deposits: A Global Perspective, First Edition. PGC Publishing, Adelaide, pp. 9–25.

Holdsworth, R.E., Pinheiro, V.L., 2000. The anatomy of shallow-crustal transpressional structures: insights from the Archaean Carajás fault zone, Amazon, Brazil. J. Struct. Geol. 22, 1105-1123. https://doi.org/10.1016/S0191-8141(00)00036-5

Hopf, S., 1987. Petrographische, mineralogische und geochemische Beobachtungen an der Cu-Lagerstätte Agustina/Distrikt Punta del Cobre/Chile. Unpublished Diplomarbeit. Universität Heidelberg, Germany.

Hu, H., Lentz, D., Li, J.W., McCarron, T., Zhao, X.F., Hall, D., 2015. Reequilibration processes in magnetite from iron skarn deposits. Econ. Geol. 110, 1–8. https://doi.org/10.2113/econgeo.110.1.1

Hu, X., Chen, H., Beaudoin, G., Zhang, Y., 2020. Textural and compositional evolution of iron oxides at Mina Justa (Peru): Implications for mushketovite and formation of IOCG deposits. Am. Mineral. 105, 397–408. https://doi.org/10.2138/am-2020-7024

Huang, X.W., Beaudoin, G., 2019. Textures and chemical compositions of magnetite from iron oxide copper-gold (IOCG) and kiruna-type iron oxide-apatite (IOA) deposits and their implications for ore genesis and magnetite classification schemes. Econ. Geol. 114, 953–979. https://doi.org/10.5382/econgeo.4651

Huang, X.-W., Zhou, M.-F., Qiu, Y.-Z., Qi, L., 2015. In-situ LA-ICP-MS trace elemental analyses of magnetite: The Bayan Obo Fe-REE-Nb deposit, North China. Ore Geol. Rev. 65, 884–899. https://doi.org/10.1016/j.oregeorev.2014.09.010

Huang, X.W., Boutroy, É., Makvandi, S., Beaudoin, G., Corriveau, L., De Toni, A.F., 2019. Trace element composition of iron oxides from IOCG and IOA deposits: relationship to hydrothermal alteration and deposit subtypes. Miner. Deposita 54, 525–552. https://doi.org/10.1007/s00126-018-0825-1

Hunger, R.B., Xavier, R.P., Moreto, C.P.N., Gao, J.F., 2018. Hydrothermal Alteration, Fluid Evolution, and Re-Os Geochronology of the Grota Funda Iron Oxide Copper-Gold Deposit, Carajás Province (Pará State), Brazil. Econ. Geol. 113, 1769–1794.https://doi.org/10.5382/econgeo.2018.4612

Hunt, J., Baker, T. Thorkelson, D., 2005. Regional-scale Proterozoic IOCG-mineralized breccia systems: examples from the Wernecke Mountains, Yukon, Canada. Miner. Deposita 40, 492–514. https://doi.org/10.1007/s00126-005-0019-5

Jacobsen, S.B., Wasserburg, G.J., 1980. Sm-Nd isotopic evolution of chondrites. Earth Planet. Sci. Lett. 50, 139–155. https://doi.org/10.1016/0012-821X(80)90125-9

Jaireth, S., Hoatson, D.M., Miezitis, Y., 2014. Geological setting and resources of the major rare-earth-element deposits in Australia. Ore Geol. Rev. 62, 72–128. https://doi.org/10.1016/j.oregeorev.2014.02.008

Janoušek, V., Moyen, J.F., Martin, H., Erban, V., Farrow, C., 2016. Geochemical modelling of igneous processes–principles and recipes in R language. Springer, Berlin.

Jesus, S.S.G.P., 2016. Múltiplos estágios de alteração hidrotermal do depósito de óxido de ferro-cobre-ouro Furnas, Província Carajás: Evolução paragenética e química mineral: MSc. thesis. University of São Paulo, Brazil.

Johansson, C., Barra, F., Reich, M., Deditius, A.P., Simon, A.C., Rojas, P., 2017. The Co-Ni signature of sulfide minerals from the Mantoverde IOCG deposit, northern Chile. Goldschmidt Abstracts, Paris, France, 1871.

Johnson, J.P., McCulloch, M.T., 1995. Sources of mineralising fluids for the Olympic Dam deposit (South Australia): Sm-Nd isotopic constraints. Chem. Geol. 121, 177–199. https://doi.org/10.1016/0009-2541(94)00125-R

Justo, A.P., 2018. As formações ferríferas bandadas (BIFs) e a evolução paleoambiental e geodinâmica da Bacia de Carajás. Phd. thesis. University of Brasilia, Brazil.

Kaur, P., Chaudhri, N., 2014. Metallogeny associated with the Palaeo-Mesoproterozoic Columbia supercontinent cycle: A synthesis of major metallic deposits. Ore Geol. Rev. 56, 415–422. https://doi.org/10.1016/j.oregeorev.2013.03.005

Kendrick, M.A., Mark, G., Phillips, D., 2007. Mid-crustal fluid mixing in a Proterozoic Fe oxide-Cu-Au deposit, Ernest Henry, Australia: evidence from Ar, Kr, Xe, Cl, Br and I. Earth Planet. Sci. Lett. 256, 328–343. https://doi.org/10.1016/j.epsl.2006.12.032

Kerrich, R., Goldfarb, R.J., Richards, J.P., 2005. Metallogenic provinces in an evolving geodynamic framework, in: Hedenquist, J.W., Thompson, J.F.H., Goldfarb, R.J., Richards, J.P. (Eds.), One Hundredth Anniversary Volume 1905–2005. Society of

Economic Geologists, Inc. Littleton, Colorado, pp. 1097–1136. https://doi.org/10.5382/AV100.33

Knipping, J.L., Bilenker, L.D., Simon, A.C., Reich, M., Barra, F., Deditius, A.P., Lundstrom, C., Bindeman, I., Munizaga, R., 2015a. Giant Kiruna-type deposits form by efficient flotation of magmatic magnetite suspensions. Geology 43, 491–594. https://doi.org/10.1130/G36650.1

Knipping, J.L., Bilenker, L.D., Simon, A.C., Reich, M., Barra, F., Deditius, A.P., Wälle, M., Heinrich, C.A., Holtz, F., Munizaga, R. 2015b. Trace elements in magnetite from massive iron oxide-apatite deposits indicate a combined formation by igneous and magmatic hydrothermal processes. Geochim. Cosmochim. Acta 171, 15–38. https://doi.org/10.1016/j.gca.2015.08.010

Lacasse, C.M., Ganade, C.E., Mathieu, L., Teixeira, N.A., Lopes, L.B.L., Monteiro, C.F., 2020. Restoring original composition of hydrothermally altered Archean metavolcanic rocks of the Carajás Mineral Province (Brazil): Geodynamic implications for the transition from lid to mobile tectonics. Lithos 372, 105647. https://doi.org/10.1016/j.lithos.2020.105647

Li, X.-C., Zhou, M.-F., Yang, Y.-H., Zhao, X.-F., Gao, J.-F., 2018. Disturbance of the Sm-Nd isotopic system by metasomatic alteration: A case study of fluorapatite from the Sin Quyen Cu-LREE-Au deposit, Vietnam. Amer. Miner. 103, 1487–1496. https://doi.org/10.2138/am-2018-650

Li, X.-C., Zhou, M.-F-, Williams-Jones, A.E., Yang, Y.-H., Gao, J.-F., 2019. Timing and genesis of Cu–(Au) mineralization in the Khetri Copper Belt, northwestern India: constraints from in situ U–Pb ages and Sm–Nd isotopes of monazite-(Ce). Miner. Deposita 54, 553–568. https://doi.org/10.1007/s00126-018-0823-3

Lindenmayer, Z.G., 1990. Salobo Sequence, Carajás, Brazil: geology, geochemistry and metamorphism. PhD. thesis. University of Western Ontario, Canada.

Lindenmayer, Z.G., Pimentel, M.M., Ronchi, L.H., Althoff, F.J., Laux, J.H., Araújo, J.C., Fleck, A., Bortowski, D.C., Nowatzki, A.C., 2001. Geologia do depósito de Cu-Au do Gameleira, Serra dos Carajás, Pará. In: Jost, H., Brod, J.A., Quieroz, E.T. (Eds.), Caracterização de Depósitos Auríferos Brasileiros, ADIMB-DNPM, Brasília, pp. 79–139.

Lindenmayer, Z.G., Fleck, A., Gomes, C.H., Santos, A.B.S., Caron, R., Paula, F. de C., Laux, J.H., Pimentel, M.M., Sardinha, A.S., 2005. Caracterização geológica do Alvo Estrela (Cu-Au), Serra dos Carajás, Pará, in: Marini, O.J., Ramos, B.W., Queiroz, E.T. (Eds.), Caracterização de Depósitos Minerais de Distritos Mineiros da Amazônia. DNPM-CT-Mineral FINEP-ADIMB, Brasilia, pp. 137–205.

Liu, P.P., Zhou, M.F., Chen, W.T., Gao, J.F., Huang, X.W., 2015. In-situ LA-ICP-MS trace elemental analyses of magnetite: Fe–Ti–(V) oxide-bearing mafic–ultramafic layered intrusions of the Emeishan Large Igneous Province, SW China. Ore Geol. Rev. 65, 853–871. https://doi.org/10.1016/j.oregeorev.2014.09.002

Liu, C., Runyon, S.E., Knoll, A.H., Hazen, R.M., 2019. The same and not the same: Ore geology, mineralogy and geochemistry of Rodinia assembly versus other supercontinents. Earth-Sci. Rev. 196, 102860. https://doi.org/10.1016/j.earscirev.2019.05.004

Lobato, L. M., Rosière, C.A., Figuereido e Silva, R.C., Zucchetti, M., Baars, F.J., Seoane, J.C., Rios, F.J., Pimentel, M., Mendes, G.E., Monteiro, A.M., 2005. A mineralização hidrotermal de ferro da Província Mineral de Carajás-Controle estrutural e contexto na evolução metalogenética da província, in: Marini, O.J., de Queiroz, E.T., Ramos, B.W. (Eds.), Caracterização em depósitos minerais em distritos mineiros da Amazônia. DNPM, ADIMB, Brasilia, pp. 25–92.

Loberg, B.E., Horndahl, A.K., 1983. Ferride geochemistry of Swedish Precambrian iron ores. Miner. Deposita18, 487–504. https://doi.org/10.1007/BF00204493

Lugmair, G.W., Marti, K., 1978. Lunar initial 143Nd/l44Nd: Differential evolution of the lunar crust and mantle. Earth Planet. Sci. Lett. 39, 349–357. https://doi.org/10.1016/0012-821X(78)90021-3

Lopez, G.P., Hitzman, M.W., Nelson, E.P., 2014. Alteration patterns and structural controls of the El Espino IOCG mining district, Chile. Miner. Deposita 49, 235–259. https://doi.org/10.1007/s00126-013-0485-0

Lopes, A.M., 2018. Caracterização geológica e metalogenética do depósito IOCG Pantera, domínio Rio Maria, Carajás-PA. MSc. dissertation. University of Campinias, Brazil.

Maas, R., Apukhtina, O.B., Kamenetsky, V.S., Ehrig, K., Sprung, P., Münker, C., 2020. Carbonates at the supergiant Olympic Dam Cu-U-Au-Ag deposit, South Australia Part 2:

Sm-Nd, Lu-Hf and Sr-Pb isotope constraints on the chronology of carbonate deposition. Ore Geol. Rev. 103745. https://doi.org/10.1016/j.oregeorev.2020.103745

Macambira, J.B., 2003. O ambiente deposicional da Formação Carajás e uma proposta de modelo evolutivo para a Bacia Grão Pará. Ph.D. thesis. University of Campinas, Brazil.

Makvandi, S., Ghasemzadeh-Barvarz, M., Beaudoin, G., Grunsky, E.C., McClenaghan, M.B., Duchesne, C., Boutroy, E., 2016. Partial least squares-discriminant analysis of trace element compositions of magnetite from various VMS deposit subtypes: Application to mineral exploration. Ore Geol. Rev. 78, 388–408. https://doi.org/10.1016/j.oregeorev.2016.04.014

Mansur, E.T., Barnes, S.J., Duran, C.J., Sluzhenikin, S.F., 2020a. Distribution of chalcophile and platinum-group elements among pyrrhotite, pentlandite, chalcopyrite and cubanite from the Noril'sk-Talnakh ores: Implications for the formation of platinum-group minerals. Miner. Deposita, 55, 1215–1232. https://doi.org/10.1007/s00126-019-00926-z

Marangoanha, B., de Oliveira, D.C., de Oliveira, V.E.S., Galarza, M.A., Lamarão, C.N., 2019. Neoarchean A-type granitoids from Carajás province (Brazil): New insights from geochemistry, geochronology and microstructural analysis. Precambrian Res. 324, 86–108. https://doi.org/10.1016/j.precamres.2019.01.010

Mark, G., De Jong, G., 1996. Synchronous granitoid emplacement and episodic sodic-calcific alteration in the Cloncurry district: Styles, timing and metallogenic significance, in: Baker, T., Rotherham, J., Richmond, J., Mark, G., Williams, P.J. (Eds.), New developments in metallogenic research: The McArthur, Mt Isa, Cloncurry minerals province. James Cook University of North Queensland Economic Geology Research Unit, Townsville, pp. 81–84.

Mark, G., Foster, D.R.W., Pollard, P.J., Williams, P.J., Tolman, J., Darvall, M., Blake, K. L., 2004. Stable isotope evidence for magmatic fluid input during large-scale Na-Ca alteration in the Cloncurry Fe oxide Cu-Au district, NW Queensland, Australia. Terra Nova 16, 54–61. https://doi.org/10.1111/j.1365-3121.2004.00527.x

Mark, G., Oliver, N.H., Williams, P.J., 2006. Mineralogical and chemical evolution of the Ernest Henry Fe oxide–Cu–Au ore system, Cloncurry district, northwest Queensland, Australia. Miner. Deposita 40, 769–801. https://doi.org/10.1007/s00126-005-0009-7

Marschik, R., Fontboté, L., 2001a. The Candelaria-Punta del Cobre Iron Oxide Cu-Au(-Zn-Ag) Deposits, Chile. Econ. Geol. 96, 1799–1826. https://doi.org/10.2113/gsecongeo.96.8.1799

Marschik, R., Fontboté, L., 2001b. The Punta del Cobre Formation, Punta del Cobre–Candelaria area, northern Chile. J. S. Am. Earth Sci. 14, 401–403. https://doi.org/10.1016/S0895-9811(01)00036-0

Marschik, R., Söllner, F., 2006. Early Cretaceous U–Pb zircon ages for the Copiapó plutonic complex and implications for the IOCG mineralization at Candelaria, Atacama Region, Chile. Miner. Deposita 41, 785–801. https://doi.org/10.1007/s00126-006-0099-x

Marschik, R., Kendrick, M.A. 2015. Noble gas and halogen constraints on fluid sources in iron oxide-copper-gold mineralization: Mantoverde and La Candelaria, Northern Chile. Miner. Deposita 50, 357–371. https://doi.org/10.1007/s00126-014-0548-x

Marschik, R., Leveille, R.A., Martin, W., 2000. La Candelaria and the Punta del Cobre district, Chile: Early Cretaceous iron oxide Cu-Au(-Zn-Ag) mineralization, in: Porter, T.M. (Ed.), Hydrothermal Iron Oxide Copper-Gold & Related Deposits: A Global Perspective, First Edition. PGC Publishing, Adelaide, pp. 163–175.

Marschik, R., Chiaradia, M., Fontboté, L., 2003a. Implications of Pb isotope signatures of rocks and iron oxide Cu-Au ores in the Candelaria-Punta del Cobre district, Chile. Miner. Deposita, 38, 900–912. https://doi.org/10.1007/s00126-003-0385-9

Marschik, R., Fontignie, D., Chiaradia, M., Voldet, P., 2003b. Geochemical and Sr–Nd–Pb–O isotope composition of granitoids of the Early Cretaceous Copiapó plutonic complex (27° 30′ S), Chile. J. S. Am. Earth Sci. 16, 381–398. https://doi.org/10.1016/S0895-9811(03)00104-4

Marschik, R., Mathur, R., Ruiz, J., Leveille, R.A., Almeida, A.J., 2005. Late archean Cu-Au-Mo mineralization at Gameleira and Serra verde, Carajás Mineral Province, Brazil: constraints from re-os molybdenite ages. Miner. Deposita 39, 983–991. https://doi.org/10.1007/s00126-004-0450-z

Martins, P.L.G., Toledo, C.L.B., Silva, A.M., Chemale Jr, F., Santos, J.O.S., Assis, L.M., 2017. Neoarchean magmatism in the southeastern Amazonian Craton, Brazil:

Petrography, geochemistry and tectonic significance of basalts from the Carajás Basin. Precambrian Res. 302, 340–357. https://doi.org/10.1016/j.precamres.2017.10.013

Mathur, R., Marschik, R., Ruiz, J., Munizaga, F., Leveille, R.A., Martin, W., 2002. Age of mineralization of the Candelaria Fe oxide Cu-Au deposit and the origin of the Chilean iron belt, based on Re-Os isotopes." Econ. Geol. 97, 59–71. https://doi.org/10.2113/gsecongeo.97.1.59

McLennan, S.M., Hemming, S., 1992. Samarium/neodymium elemental and isotopic systematics in sedimentary rocks. Geochim. Cosmochim. Acta 56, 887–898. https://doi.org/10.1016/0016-7037(92)90034-G

Meinert, L.D., Dipple, G.M., Nicolescu, S., 2005. World skarn deposits, in: Hedenquist, J.W., Thompson, J.F.H., Goldfarb, R.J., Richards, J.P. (Eds.), One Hundredth Anniversary Volume 1905–2005. Society of Economic Geologists, Inc. Littleton, Colorado, pp. 299–336. https://doi.org/10.5382/AV100.11

Meirelles, M.R., Dardenne, M.A., 1991. Vulcanismo basáltico de afinidade shoshonítica e ambiente de arco arqueano, Grupo Grão-Pará, Serra dos Carajás, Pará. Braz. J. Geol. 21, 41–50.

Meng, Y., Hu, R., Huang, X., Gao, J., 2017. Germanium in magnetite: A preliminary review. Acta Geol. Sin. 91, 711–726. https://doi.org/10.1111/1755-6724.13127

Migdisov, A.A., Williams-Jones, A.E., Wagner, T., 2009. An experimental study of the solubility and speciation of the Rare Earth Elements (III) in fluoride- and chloride-bearing aqueous solutions at temperatures up to 300°C. Geochim Cosmochim Acta 73:7087–7109. https://doi.org/10.1016/j.gca.2009.08.023

Migdisov, A., Williams-Jones, A.E., Brugger, J., Caporuscio, F.A., 2016. Hydrothermal transport, deposition, and fractionation of the REE: Experimental data and thermodynamic calculations. Chem. Geol. 439, 13–42. https://doi.org/10.1016/j.chemgeo.2016.06.005

Miller, J.F., Harris, N.B.W., 1989. Evolution of continental crust in the Central Andes; constraints from Nd isotope systematics. Geology 17, 615–617. https://doi.org/10.1130/0091-7613(1989)017<0615:EOCCIT>2.3.CO;2

Montañez, I.P., Osleger, D.A., Banner, J.L., Mack, L.E., Musgrove, M., 2000. Evolution of the Sr and C isotope composition of Cambrian oceans. GSA today, 10, 1–7.

Monteiro, L.V.S., Xavier, R.P., de Carvalho, E.R., Hitzman, M.W., Johnson, C.A., de Souza, C.R., Torresi, I., 2008a. Spatial and temporal zoning of hydrothermal alteration and mineralization in the Sossego iron oxide-copper–gold deposit, Carajás Mineral Province, Brazil: paragenesis and stable isotope constraints. Miner. Deposita 43, 129–159. https://doi.org/10.1007/s00126-006-0121-3

Monteiro, L.V.S., Xavier, R.P., Hitzman, M.W., Juliani, C., de Souza Filho, C.R., Carvalho, E.D. R., 2008b. Mineral chemistry of ore and hydrothermal alteration at the Sossego iron oxide–copper–gold deposit, Carajás Mineral Province, Brazil. Ore Geol. Rev. 34, 317–336. https://doi.org/10.1016/j.oregeorev.2008.01.003

Moreto, C.P.N., Monteiro, L.V.S., Xavier, R.P., Creaser, R.A., DuFrane, S.A., Tassinari, C.C.G., Sato, K., Kemp, A.I.S., Amaral, W.S., 2015a. Neoarchean and Paleoproterozoic Iron Oxide-Copper-Gold Events at the Sossego Deposit Carajás Province, Brazil: Re-Os and U-Pb Geochronological Evidence. Econ. Geol. 110, 809–835. https://doi.org/10.2113/econgeo.110.3.809

Moreto, C.P., Monteiro, L.V.S., Xavier, R.P., Creaser, R.A., DuFrane, S.A., Melo, G.H., da Silva, M.A.D., Tassinari, C.C.G., Sato, K., 2015b. Timing of multiple hydrothermal events in the iron oxide–copper–gold deposits of the Southern Copper Belt, Carajás Province, Brazil. Miner. Deposita 50, 517–546. https://doi.org/10.1007/s00126-014-0549-9

Motta, J.G., de Souza Filho, C.R., Carranza, E.J.M., Braitenberg, C., 2019. Archean crust and metallogenic zones in the Amazonian Craton sensed by satellite gravity data. Sci. Rep. 9, 1–10. https://doi.org/10.1038/s41598-019-39171-9

Mumin, A.H., Corriveau, L. Somarin, A.K. Ootes, L., 2007. Iron oxide copper-gold-type polymetallic mineralization in the Contact Lake Belt, Great Bear Magmatic Zone, Northwest Territories, Canada. Explor. Min. Geol. 16, 187–208. https://doi.org/10.2113/gsemg.16.3-4.187

Nadoll, P., Angerer, T., Mauk, J.L., French, D., Walshe, J., 2014. The chemistry of hydrothermal magnetite: a review. Ore Geol. Rev. 61, 1–32. https://doi.org/10.1016/j.oregeorev.2013.12.013.

Nadoll, P., Mauk, J.L., Leveille, R.A., Koenig, A.E., 2015. Geochemistry of magnetite from porphyry Cu and skarn deposits in the southwestern United States. Miner. Deposita 50, 493–515.

Neves, M.P., 2006. Estudos isotópicos (Pb-Pb, Sm-Nd, C e O) do depósito Cu-Au do Sossego, Província Mineral de Carajás. M.Sc. dissertation thesis, Federal University of Pará, Brazil.

Negrão, M.M., 2008. Caracterização Geológica e Metalogenética da Ocorrência de Cu-Au (Mo-Co), do Grupo Rio Novo, no contato S-SE com o granito Cigano, Provincia Mineral de Carajás. MSc. dissertation. University of Brasilia, Brazil.

Ngo, X.D., Zhao, X.-F., Thanh Hai, T., Deng, X.-D., Li, J.-W., 2020. Two episodes of REEs mineralization at the Sin Quyen IOCG deposit, NW Vietnam. Ore Geology Reviews, 103676. https://doi.org/10.1016/j.oregeorev.2020.103676

Ogata, T., Ichii, Y., Erdenebayar, J., Nozaki, T., Takaya, Y., 2019. U-Pb Zircon and Tentatively Determined Re-Os Isotope Geochronology for the Atacama Kozan Mine and Sol Nasciente Mine, Region III, Chile. SEG 2019 Conference Proceedings, Santiago, Chile.

Oliveira, R.G., 2018. Insights on the framework of the Carajás Province, Amazonian Craton, Brazil, and on the three-dimensional shape of the Carajás Basin, based on gravity data. JGSB 1, 101–112. https://doi.org/10.29396/jgsb.2018.v1.n3.1.

Oliver, N.H.S., Butera, K.M., Rubenach, M.J., Marshall, L.J., Cleverley, J.S., Mark, G., Tullemans, F., Esser, D., 2008. The protacted hydrothermal evolution of the Mount Isa Eastern Sucessions: A review and tectonic implications. Precambrian Res. 163, 108–130. https://doi.org/10.1016/j.precamres.2007.08.019

Oliveros, V., Vásquez, P., Creixell, C., Lucassen, F., Ducea, M.N., Ciocca, I., González, J., Espinoza, M., Salazar, E., Coloma, F., Kasemann, S.A., 2020. Lithospheric evolution of the Pre- and Early Andean convergent margin, Chile. Gondwana Res. 80, 202–227. https://doi.org/10.1016/j.gr.2019.11.002

Olszewski, W.J., Wirth, K.R., Gibbs, A.K. and Gaudette, H.E., 1989. The age, origin and tectonics of the GrZo Para Group and associated rocks, Serra dos Carajas, Brazil. Precambrian Res. 42, 229–254. https://doi.org/10.1016/0301-9268(89)90013-2

Oreskes, N., Einaudi, M.T., 1992. Origin of hydrothermal fluids at Olympic Dam: preliminary results from fluid inclusion and stable isotopes. Econ. Geol. 87, 64–90. https://doi.org/10.2113/gsecongeo.87.1.64

Orlandea, E., Vlad, Ş.N., 2020. A novel conceptual model of intrusion related gold bearing systems and exploration tools. Studia UBB Geologia 63, 1–12. https://doi.org/10.5038/1937-8602.63.1.1304

Ovalle, J.T., La Cruz, N.L., Reich, M., Barra, F., Simon, A.C., Konecke, B.A., Rodriguez-Mustafa, M.A, Deditius, A.P., Childress, T.M., Morata, D., 2018. Formation of massive iron deposits linked to explosive volcanic eruptions. Sci. Rep. 8, 1–11. https://doi.org/10.1038/s41598-018-33206-3

Oyunjargal, L., Hayashi, K.I., Maruoka, T., 2020. Geological, mineralogical, and oxygen isotope studies of the Chandmani Uul iron oxide–copper–gold deposit in Dornogobi Province, Southeastern Mongolia. Resour. Geol. 70, 233–253. https://doi.org/10.1111/rge.12232

Page, R.W., Stevens, B.P.J., Gibson, G.M., 2005. Geochronology of the sequence hosting the Broken Hill Pb-Zn-Ag orebody, Australia. Econ. Geol. 100, 633–661. https://doi.org/10.2113/gsecongeo.100.4.633

Palma, G., Barra, F., Reich, M., Valencia, V., Simon, A.C., Vervoort, J. Leisen, M., Romero, R., 2019. Halogens, trace element concentrations, and Sr-Nd isotopes in apatite from iron oxide-apatite (IOA) deposits in the Chilean iron belt: Evidence for magmatic and hydrothermal stages of mineralization. Geochim. Cosmochim. Acta 246, 515–540. https://doi.org/10.1016/j.gca.2018.12.019

Palme, H., O'Neill, H.S.C., Heinrich, D.H., Karl, K.T., 2007. Cosmochemical estimates of mantle composition, in: Holland, H.D., Turekian, K.K. (Eds.), Treatrise on Geochemistry, First Edition. Elsevier, Oxford, England, pp. 1–38.

Papanastassiou, D.A., Wasserburg, G.J., 1969. Initial strontium isotopic abundances and the resolution of small time differences in the formation of planetary objects. Earth Planet. Sci. Lett. 5, 361–376. https://doi.org/10.1016/S0012-821X(68)80066-4

Parada, M.A., Nyström, J.O., Levi, B., 1999. Multiple sources for the Coastal batholith of central Chile (31–34°S): Geochemical and Sr-Nd isotopic evidence and tectonic implications: Lithos 46, 505–521. https://doi.org/10.1016/s0024-4937(98)00080-2

Pestilho, A.L.S., Monteiro, L.V.S., de Melo, G.H.C., Moreto, C.P.N., Juliani, C., Fallick, A.E., Xavier, R.P., 2020. Stable isotopes and fluid inclusion constraints on the fluid evolution in the Bacaba and Castanha iron oxide-copper-gold deposits, Carajás Mineral Province, Brazil. Ore Geol. Rev. 103738. https://doi.org/10.1016/j.oregeorev.2020.103738

Pinheiro, R.V.L., Holdsworth, R.E., 1997. Reactivation of Archaean strike-slip fault systems, Amazon region, Brazil. J. Geol. Soc. London 154, 99–103. http://dx.doi.org/10.1144/gsjgs.154.1.0099

Pinheiro, R.S.D.C., 2019. Evolução paragenética e regime de fluidos no sistema Cu-Co Tarzan, Província Carajás. MSc. dissertation. University of Campinas, Brazil.

Pimentel, M.M., Lindenmayer, Z.G., Laux, J.H., Armstrong, R., de Araújo, J.C., 2003. Geochronology and Nd isotope geochemistry of the Gameleira Cu–Au deposit, Serra dos Carajás, Brazil: 1.8–1.7 Ga hydrothermal alteration and mineralization. J. S. Am. Earth Sci. 15, 803–813. https://doi.org/10.1016/S0895-9811(02)00127-X

Pirajno, F., Santosh, M., 2015. Mantle plumes, supercontinents, intracontinental rifting and mineral systems. Precambrian Res. 259, 243–261.https://doi.org/10.1016/j.precamres.2014.12.016

Polat, A., Hofmann, A.W., 2003. Alteration and geochemical patterns in the 3.7–3.8 Ga Isua greenstone belt, West Greenland. Precambrian Res. 126, 197–218. https://doi.org/10.1016/S0301-9268(03)00095-0

Pollard, P.J., 2000. Evidence of a magmatic fluid and metal source for Fe-oxide Cu-Au mineralization, in: Porter, T.M. (Ed.), Hydrothermal Iron Oxide Copper-Gold & Related Deposits: A Global Perspective, First Edition. PGC Publishing, Adelaide, pp. 27–41.

Pollard, P.J., 2006. An intrusion-related origin for Cu–Au mineralization in iron oxide–copper–gold (IOCG) provinces. Miner. Deposita 41, 179–187. https://doi.org/10.1007/s00126-006-0054-x

Pollard, P.J., Taylor, R.G., Peters, L., Matos, F., Freitas, C., Saboia, L., Hunh, S., 2019. 40Ar-39Ar dating of Archean iron oxide Cu-Au and Paleoproterozoic granite-related Cu-Au deposits in the Carajás Mineral Province, Brazil: implications for genetic models. Miner. Deposita 54, 329–346. https://doi.org/10.1007/s00126-018-0809-1

Porter, T.M., 2010. Current Understanding of Iron Oxide Associated-Alkali Altered Mineralised Systems: Part I – An Overview, in: Porter, T.M. (Ed.), Hydrothermal iron oxide copper-gold and related deposits: A Global Perspective, Third Edition. PGC Publishing, Adelaide, pp. 5–32.

Previato, M., Monteiro, L.V.S., da Silveira Bello, R.M., Gonçales, L.C.G., 2020. Evolution of brines and CO2-rich fluids and hydrothermal overprinting in the genesis of the Borrachudo Copper deposit, Carajás Province. Ore Geol. Rev. 121, 103561. https://doi.org/10.1016/j.oregeorev.2020.103561

Ramos, V.A., 2008. The Basement of the Central Andes: The Arequipa and Related Terranes. Annu. Rev. Earth Planet. Sci. 36, 289–324. https://doi.org/10.1146/annurev.earth.36.031207.124304

Reich, M., Simon, A.C., Deditius, A., Barra, F., Chryssoulis, S., Lagas, G., Tardani, D., Knipping, J., Bilenker, L., Sánchez-Alfaro, P., Roberts, M.P., Munizaga, R., 2016. Trace element signature of pyrite from the Los Colorados iron oxide-apatite (IOA) deposit, Chile: A missing link between Andean IOA and iron oxide copper-gold systems?. Econ. Geol. 111, 743–761. https://doi.org/10.2113/econgeo.111.3.743

Reid, A.J., Swain, G.S., Mason, D., Maas, R., 2011. Nature and timing of Cu-Au-Zn-Pb mineralisation at Punt Hill, eastern Gawler Craton. MESA Journal 60, 7–17.

Reid, A., 2019. The Olympic Cu-Au Province, Gawler Craton: A Review of the Lithospheric Architecture, Geodynamic Setting, Alteration Systems, Cover Successions and Prospectivity. Minerals 9, 371. http://doi.org/10.3390/min9060371

Réquia K.C.M., 1995. O papel do metamorfismo e fases fluidas na gênese da mineralização de cobre do Salobo, Província Mineral de Carajás, Pará. MSc. dissertation. University of Campinas, Brazil.

Requia, K., Stein, H., Fontboté, L., Chiaradia, M., 2003. Re–Os and Pb–Pb geochronology of the Archean Salobo iron oxide copper–gold deposit Carajás mineral province, northern Brazil. Miner. Deposita 38, 727–738. https://doi.org/10.1007/s00126-003-0364-1

Ribeiro, A.A., 2008. Geoquímica de isótopos estáveis (C, S e O) das rochas encaixantes e do minério de Cu (Au) do depósito Cristalino, província mineral de Carajás, Pará. MSc. dissertation. University of Ouro Preto, Brazil.

Richards, J.P., Mumin, A.H., 2013a. Magmatic-hydrothermal processes within an evolving Earth: Iron oxide-copper-gold and porphyry Cu ± Mo ± Au deposits. Geology 41, 767–770. https://doi.org/10.1130/G34275.1

Richards, J.P., Mumin, A.H., 2013b. Lithospheric Fertilization and Mineralization by Arc Magmas: Genetic Links and Secular Differences Between Porphyry Copper ± Molybdenum ± Gold and Magmatic-Hydrothermal Iron Oxide Copper-Gold Deposits, in: Colpron, M., Bissig, T., Rusk, B.G., Thompson, J.F.H. (Eds.), Tectonics, Metallogeny, and Discovery: The North American Cordillera and Similar Accretionary Settings. Society of Economic Geologist, Inc. Special Publications 17, Littleton, Colorado, pp. 277–299. https://doi.org/10.5382/SP.17.09

Richards, J.P., López, G.P., Zhu, J.J., Creaser, R.A., Locock, A.J., Mumin, A.H., 2017. Contrasting tectonic settings and sulfur contents of magmas associated with Cretaceous porphyry Cu±Mo±Au and intrusion-related iron oxide Cu-Au deposits in northern Chile. Econ. Geol. 112, 295–318. https://doi.org/10.2113/econgeo.112.2.295

Rieger, A.A., Marschik, R., Díaz, M., Hölzl, S., Chiaradia, M., Akker, B., Spangenberg, J.E., 2010. The hypogene iron oxide copper–gold mineralization in the Mantoverde district, Northern Chile. Econ. Geol. 105, 1271–1299. https://doi.org/10.2113/econgeo.105.7.1271

Rieger, A.A., Marschik, R., Díaz, M., 2012. The evolution of the hydrothermal IOCG system in the Mantoverde district, northern Chile: new evidence from microthermometry and stable isotope geochemistry. Miner. Deposita 47, 359–369. https://doi.org/10.1007/s00126-011-0390-3

Riehl, W., Cabral, A.R., 2018. Meta-evaporite in the Carajás mineral province, northern Brazil. Miner. Deposita 53, 895–902. https://doi.org/10.1007/s00126-018-0810-8

Ripley, E.M., Ohmoto, H., 1977. Mineralogic, sulfur isotope, and fluid inclusion studies of the strata-bound copper deposits at the Raúl Mine, Perú. Econ. Geol. 72, 1017–1041. https://doi.org/10.2113/gsecongeo.72.6.1017

Rodriguez-Mustafa, M.A., Simon, A., del Real, I., Thompson, J.F., Bilenker, L.D., Barra, F., Bindeman, I., Cadwell, D., 2020. A Continuum from Iron Oxide Copper-Gold to Iron Oxide-Apatite Deposits: Evidence from Fe and O Stable Isotopes and Trace Element

Chemistry of Magnetite. Econ. Geol. 115, 1443–1459. https://doi.org/10.5382/econgeo.4752

Roverato, M., Giordano, D., Giovanardi, T., Juliani, C., Polo, L., 2019. The 2.0–1.88 Ga Paleoproterozoic evolution of the southern Amazonian Craton (Brazil): An interpretation inferred by lithofaciological, geochemical and geochronological data. Gondwana Res. 70, 1–24. https://doi.org/10.1016/j.gr.2018.12.005

Rusk, B., 2010. Exploring for Iron Oxide Copper-Gold Deposits: Canada and Global Analogues. Geological Association of Canada Short Course Notes 20. Econ. Geol. 107, 1077.https://doi.org/10.2113/econgeo.107.5.1077

Salgado, S.S., de Andrade Caxito, F., e Silva, R.C.F., Lana, C., 2019. Provenance of the Buritirama Formation reveals the Paleoproterozoic assembly of the Bacajá and Carajás blocks (Amazon Craton) and the chronocorrelation of Mn-deposits in the Transamazonian/Birimian system of northern Brazil/West Africa. J. S. Am. Earth Sci. 96, 102364. https://doi.org/10.1016/j.jsames.2019.102364

Santiago, E.S.B., 2016. Elementos traço (in situ LA-ICP-MS) e isótopos estáveis (Δ33S, Δ34S, δ56Fe e δ18O) em magnetita e sulfetos: origem e evolução de sistemas de Cu-Au Neoarqueanos e Paleoproterozoicos da Província Mineral de Carajás, Brasil. PhD. thesis. University of Campinas, Brazil.

Santiago, E.S.B., Xavier, R.P., Hagemann, S.G., Monteiro, L.V.S., Cliff, J., 2020. Multiple sulfur isotopes constraints on origin and evolution of the Neoarchean and Paleoproterozoic Cu-Au systems from the Carajás Domain, Amazonian Craton, Brazil. Ore Geol. Rev. https://doi.org/10.1016/j.oregeorev.2020.103872

Santos, J.O.S., 2003. Geotectônica do Escudo das Guianas e Brasil-Central, in: Bizzi, L.A., Schobbenhaus, C., Vidotti, R.M., Gonçalves, J.H., (Eds.), Geologia, Tectônica e Recursos Minerais do Brasil. CPRM – Serviço Geológico do Brasil, Brasília, pp. 169–226.

Schenk, C.J., Viger, R.J., Anderson, C.P., 1999. Map Showing Oil and Gas Fields and Geological Provinces of South America, scale 1:7.500.000. U.S. Geological Survey Open-File Report 97-470D

Schlegel, T.U., Wagner, T., Fusswinkel, T., 2020. Fluorite as indicator mineral in iron oxide-copper-gold systems: Explaining the IOCG deposit diversity. Chem. Geol. 548, 119674. https://doi.org/10.1016/j.chemgeo.2020.119674

Schutesky, M.E., Oliveira, C.G., 2020. From the roots to the roof: an integrated model for the Neoarchean Carajás IOCG System, Brazil. Ore Geology Reviews, 103833. https://doi.org/10.1016/j.oregeorev.2020.103833

Seymour, N.M., Singleton, J.S., Mavor, S.P., Gomila, R., Stockli, D.F., Heuser, G., Arancibia, G., 2020. The relationship between magmatism and deformation along the intra-arc strike-slip Atacama fault system, northern Chile. Tectonics 39, e2019TC005702. https://doi.org/10.1029/2019TC005702

Sharma, R.,Srivastava, P.K., 2014. Hydrothermal fluids of magmatic origin, in: Kumar, S., Narain, S.R. (Eds.), Modelling of magmatic and allied processes, Springer, Cham, pp. 181-208.

Shirey, S.B., Hanson, G.N., 1986. Mantle heterogeneity and crustal recycling in Archean granite-greenstone belts: evidence from Nd isotopes and trace elements in the Rainy Lake area, Superior Province, Ontario, Canada. Geochim. Cosmochim. Acta 50, 2631–2651.

Sillitoe, R.H., 2003. Iron oxide-copper-gold deposits: an Andean view. Miner. Deposita 38, 787–812. https://doi.org/10.1007/s00126-003-0379-7

Simon, A.C., Knipping, J., Reich, M., Barra, F., Deditius, A.P., Bilenker, L. Childress, T., 2018. Kiruna-Type Iron Oxide-Apatite (IOA) and Iron Oxide Copper-Gold (IOCG) Deposits Form by a Combination of Igneous and Magmatic-Hydrothermal Processes: Evidence from the Chilean Iron Belt, in: Arribas, R.A.M., Mauk, J.L. (Eds.), Metals, Minerals, and Society, Society of Economic Geologist, Inc. Special Publications 21, Keystone, Colorado, pp. 89–114. https://doi.org/10.5382/SP.21.06

Skirrow, R.G., 2010. "Hematite-group" IOCG ± U ore systems: Tectonic settings, hydrothermal characteristics, and Cu-Au and U mineralizing processes, in: Corriveau, L., Mumin, H. (Eds.), Exploring for Iron Oxide Copper-Gold Deposits: Canada and Global Analogues. Geological Association of Canada Short Courses Notes 20, Washington, pp. 39–58.

Skirrow, R.G., Bastrakov, E.N., Barovich, K., Fraser, G.L., Creaser, R. A., Fanning, C.M., Raymond, O., Davidson, G.J., 2007. Timing of Iron Oxide Cu-Au-(U)

Hydrothermal Activity and Nd Isotope Constraints on Metal Sources in the Gawler Craton, South Australia. Econ. Geol. 102, 1441–1470. https://doi.org/10.2113/gsecongeo.102.8.1441

Skirrow, R.G., Van Der Wielen, S.E., Champion, D.C., Czarnota, K., Thiel, S., 2018. Lithospheric architecture and mantle metasomatism linked to iron oxide Cu-Au ore formation: Multidisciplinary evidence from the Olympic Dam Region, South Australia. Geochem. Geophy. Geosy. 19, 2673–2705. https://doi.org/10.1029/2018GC007561

Smith, E., Kemp, A., Hagemann, S., Xavier, R., Moreto, C., 2018. The Sossego IOCG Deposit, Carajás Mineral Province, Brazil: Two Mineralization Ages, One Archean Source. SEG 2018 Conference Proceedings, Keystone, USA.

Souza, S.R.C., Botelho, N.F., Dantas, E.L., Cuadros Jiménez, F.A., Reis, M.A., Viana, C.S., 2020. Geochemistry and isotopic geology of the Lagoa Seca gold deposit in the Andorinhas greenstone-belt, Carajás Province, Brazil. Journal of South American Earth Sciences, 102523. https://doi.org/10.1016/j.jsames.2020.102523

Spandler, C., Slezak, P., Nazari-Dehkordi, T., 2020. Tectonic significance of Australian rare earth element deposits. Earth-Sci. Rev. 207, 103219.https://doi.org/10.1016/j.earscirev.2020.103219

Steiger, R. H., Jäger, E., 1977. Subcommission on geochronology: convention on the use of decay constants in geo-and cosmochronology. Earth Planet. Sci. Lett. 36, 359–362.

Storey, C.D., Smith, M.P., 2017. Metal source and tectonic setting of iron oxide-copper-gold (IOCG) deposits: Evidence from an in situ Nd isotope study of titanite from Norrbotten, Sweden. Ore Geol. Rev. 81, 1287–1302. https://doi.org/10.1016/j.oregeorev.2016.08.035

Sun, W., Yuan, F., Jowitt, S.M., Zhou, T., Liu, G., Li, X., Wang, F., Troll, V.R., 2019. In situ LA–ICP–MS trace element analyses of magnetite: genetic implications for the Zhonggu orefield, Ningwu volcanic basin, Anhui Province, China. Miner. Deposita 54, 1243–1264. https://doi.org/10.1007/s00126-019-00872-w

Tallarico, F.H.B., 2003. O cinturão cupro-aurifero de Carajas, Brasil. PhD. dissertation thesis. University of Campinas, Brazil.

Tallarico, F.H.B., Oliveira, C.G., Figueiredo, B.R., 2000. The Igarapé Bahia Cu-Au mineralization, Carajás Province. Braz. J. Geol. 30, 230–233.

Tallarico, F.H.B., Figueiredo, B.R., Groves, D.I., Kositcin, N., McNaughton, N.J., Fletcher, I.R., Rego, J.L., 2005. Geology and SHRIMP U-Pb geochronology of the igarapé bahia deposit, carajás copper-gold belt, brazil: an archean (2.57 Ga) example of Iron-Oxide Cu-Au-(U-REE) mineralization. Econ. Geol. 100, 7–28. https://doi.org/10.2113/100.1.0007

Tavares, F.M., 2015. Evolução geotectônica do nordeste da Província Carajás. PhD. thesis. Federal University of Rio de Janeiro, Brazil.

Tavares, F.M., Trouw, R.A.J., da Silva, C.M.G., Justo, A.P., Oliveira, J.K.M., 2018. The multistage tectonic evolution of the northeastern Carajás Province, Amazonian Craton, Brazil: Revealing complex structural patterns. J. S. Am. Earth Sci. 88, 238–252. https://doi.org/10.1016/j.jsames.2018.08.024.

Teixeira, J.B.G., 1994. Geochemistry, Petrology, and Tectonic Setting of Archean Basaltic and Dioritic Rocks from the N4 Iron Deposit, Serra dos Carajás, Pará, Brazil. PhD. thesis. Penn State University, USA.

Teixeira, J.B.G., Eggler, D.H., 1994. Petrology, geochemistry, and tectonic setting of Archean basaltic and dioritic rocks from the N4 iron deposit, Serra dos Carajás, Pará, Brazil. Acta Geologica Leopoldensia 17, 71–114.

Teixeira, N.A., Matos, F.M.V., Ganade, C.E., Klein, E.L., Dreher, A.M., Tavares, F.M., Leandro, D.C., Porto, F., 2015b. Carajás and Tapajós Mineral Province: Cratonic and pericratonic Lithosphere keel metallogeny. XIV Simpósio de Geologia da Amazônia, Belém, Pará, Brazil.

Teixeira, M.F.B., Dall'Agnol, R., Santos, J.O.S., Kemp, A., Evans, N., 2019. Petrogenesis of the Paleoproterozoic (Orosirian) A-type granites of Carajás Province, Amazon Craton, Brazil: Combined in situ HfO isotopes of zircon. Lithos, 332, 1-22. https://doi.org/10.1016/j.lithos.2019.01.024

Tokel, S., Köprübaşi, N., Uysal, I., Van, A., 2011. Occurrences and genesis of Fe-skarn in relation to tectonic environment in E-NE Anatolia: geochemical consideration. N. Jb. Miner. Abh. 188, 141–149. https://doi.org/10.1127/0077-7757/2011/0185

Toledo, F.P.I., Moreto, C.P.N., Xavier, R. P., Gao, J., de Matos, J.H.S.N., de Melo, G.H.C., 2019. Multistage Evolution of the Neoarchean (ca. 2.7 Ga) Igarapé Cinzento (GT-46) Iron Oxide Copper-Gold Deposit, Cinzento Shear Zone, Carajás Province, Brazil. Econ. Geol. 114, 1–34. https://doi.org/10.5382/econgeo.2019.4617

Torresi, I., Xavier, R.P., Bortholoto, D.F.A., Monteiro, L.V.S., 2012. Hydrothermal alteration, fluid inclusions and stable isotope systematics of the Alvo 118 iron oxide–copper–gold deposit, Carajás Mineral Province (Brazil): Implications for ore genesis. Miner. Deposita 47, 299–323. https://doi.org/10.1007/s00126-011-0373-4

Tornos, F., Velasco, F., Barra, F., Morata, D., 2010. The Tropezón Cu–Mo–(Au) deposit, Northern Chile: the missing link between IOCG and porphyry copper systems?. Minera. Deposita 45, 313–321. https://doi.org/10.1007/s00126-010-0277-8

Tornos, F., Wiedenbeck, M., Velasco, F., 2012. The boron isotope geochemistry of tourmaline-rich alteration in the IOCG systems of northern Chile: implications for a magmatic-hydrothermal origin. Miner. Deposita 47, 483–499. https://doi.org/10.1007/s00126-011-0383-2

Tornos, F., Velasco, F., Hanchar, J.M., 2017. The magmatic to magmatic-hydrothermal evolution of the El Laco deposit (Chile) and its implications for the genesis of magnetite-apatite deposits. Econ. Geol. 112, 1595–1628. https://doi.org/10.5382/econgeo.2017.4523

Tornos, F., Hanchar, J.M., Munizaga, R., Velasco, F., Galindo, C., 2020. The role of the subducting slab and melt crystallization in the formation of magnetite-(apatite) systems, Coastal Cordillera of Chile. Miner. Deposita 1–26. https://doi.org/10.1007/s00126-020-00959-9

Trunfull, E.F., Hagemann, S.G., Xavier, R.P., Moreto, C.P., 2020. Critical assessment of geochronological data from the Carajás Mineral Province, Brazil: implications for metallogeny and tectonic evolution. Ore Geol. Rev. 121, 103556. https://doi.org/10.1016/j.oregeorev.2020.103556

Ullrich, T.D., Clark, A.H., Kyser, T.K., 2001. The Candelaria Cu-Au deposit, III Region, Chile: product of long-term mixing of magmatic-hydrothermal and evaporite-sourced fluids. Proceedings of the 33th Annual GSA Meeting, Boston, Massachusetts, USA, A-3.

Valadão, L.V., 2019. Mineralogia e relação textural e microestrutural do minério tipo IOCG da mina do Salobo, Província Mineral de Carajás: revisão da sequência paragenética. MSc. dissertation, University of Brasilia, Brazil.

Vasquez, M.L., Sousa, C.S., Carvalho, J.M.A., 2008. Mapa Geológico e de Recursos Minerais do Estado do Pará, escala 1:100.000. Programa Geologia do Brasil (PGB), Integração, Atualização e Difusão de Dados da Geologia do Brasil, Mapas Geológicos Estaduais. CPRM-Serviço Geológico do Brasil, Superintendência Regional de Belém.

Velasco, F., Tornos, F., 2009. Pegmatite-like magnetite-apatite deposits of northern Chile: a place in the evolution of immiscible iron oxide melts?, in: Williams P.J. et al. (Eds.) Proceedings 10th SGA Meeting, Townsville, Australia, pp. 665–667.

Verdugo-Ihl, M.R., Ciobanu, C.L., Cook, N.J., Ehrig, K.J., Courtney-Davies, L., 2020. Defining early stages of IOCG systems: Evidence from iron oxides in the outer shell of the Olympic Dam deposit, South Australia. Miner. Deposita 55, 429–452. https://doi.org/10.1007/s00126-019-00896-2

Vila, T., Lindsay, N., Zamora, R., 1996. Geology of the Mantoverde copper deposit, northern Chile: a specularite-rich hydrothermal tectonic breccia related to the Atacama fault zone. Geol. Soc. Spec. Publ. 5, 157–170. https://doi.org/10.5382/SP.05.11

Wade, B., Barovich, K., Hand, M., Scrimgeour, I.R., Close, D.F., 2006. Evidence for early Mesoproterozoic arc-related magmatism in the Musgrave Block, central Australia: Implications for Proterozoic crustal growth and tectonic reconstructions of Australia. J. Geol. 114, 43–63. https://doi.org/10.1086/498099

Wade, C.E., Payne, J.L., Barovich, K.M., Reid, A.J., 2019. Heterogeneity of the sub-continental lithospheric mantle and ‘non-juvenile’ mantle additions to a Proterozoic silicic large igneous province. Lithos 340–341, 87–107. https://doi.org/10.1016/j.lithos.2019.05.005

Wang, C., Shao, Y., Zhang, X., Dick, J., Liu, Z., 2018. Trace element geochemistry of magnetite: implications for ore genesis of the Huanggangliang Sn-Fe deposit, Inner Mongolia, northeastern China. Minerals 8, 195. https://doi.org/10.3390/min8050195

Wen, G., Li, J.W., Hofstra, A.H., Koenig, A.E., Lowers, H.A., Adams, D., 2017. Hydrothermal reequilibration of igneous magnetite in altered granitic plutons and its implications for magnetite classification schemes: Insights from the Handan-Xingtai iron district, North China Craton. Geochim. Cosmochim. Acta 213, 255–270. https://doi.org/10.1016/j.gca.2017.06.043

Weng, Z., Jowitt, S.M., Mudd, G.M., Haque, N., 2015. A detailed assessment of global rare earth element resources: opportunities and challenges. Econ. Geol. 110, 1925–1952. https://doi.org/10.2113/econgeo.110.8.1925

Williams, P.J., Barton, M.D., Johnson, D.A., Fontboté, L., De Haller, A., Mark, G., Oliver, N.H.S., Marschik, R., 2005. Iron Oxide Copper-Gold Deposits: Geology, Space-Time Distribution, and Possible Modes of Origin, in: Hedenquist, J.W., Thompson, J.F.H., Goldfarb, R.J., Richards, J.P. (Eds.), One Hundredth Anniversary Volume 1905–2005. Society of Economic Geologists, Inc. Littleton, Colorado, pp. 371–405. https://doi.org/10.5382/AV100.13

Williams, M.R., Holwell, D.A., Lilly, R.M., Case, G.N.D., McDonald, I., 2015. Mineralogical and fluid characteristics of the fluorite-rich Monakoff and E1 Cu–Au deposits, Cloncurry region, Queensland, Australia: Implications for regional F–Ba-rich IOCG mineralisation. Ore Geol. Rev. 64, 103–127. https://doi.org/10.1016/j.oregeorev.2014.05.021

Williams-Jones, A.E., Migdisov, A.A., 2014. Experimental constraints on the transport and deposition of metals in ore-forming hydrothermal systems. Geol. Soc. Spec. Publ. 18, 77–96. https://doi.org/10.5382/SP.18.05

Williams-Jones, A.E., Migdisov, A.A., Samson, I.M., 2012. Hydrothermal mobilisation of the rare earth elements - a tale of “ceria” and “Yttria”. Elements 8, 355–360. https://doi.org/10.2113/gselements.8.5.355

Wirth, K.R., Gibbs, A.K., Olszewski Jr., W.J., 1986. U-Pb ages of zircons from the Grão Pará Group and Serra dos Carajás granite Pará, Brasil. Braz. J. Geol. 16, 195–200.

Xavier, R.P., Wiedenbeck, M., Trumbull, R.B., Dreher, A.M., Monteiro, L.V.S., Rhede, D., Araujo, C.E.G., Torresi, I., 2008. Tourmaline B-isotopes fingerprint marine evaporites as the source of high-salinity ore fluids in iron-oxide-copper gold deposits, Carajas Mineral Province (Brazil). Geology 36, 743–746. https://doi.org/10.1130/G24841A.1

Xavier, R.P., Monteiro, L.V.S., Moreto, C.P.N., Pestilho, A.L.S., de Melo, G.H.C., da Silva, M.A.D., Aires, B., Ribeiro, C., Freitas e Silva F.H., 2012. The Iron Oxide Copper-

Gold Systems of the Carajás Mineral Province, Brazil, in: Hedenquist, J.W., Harris, M., Camus, F. (Eds.), Geology and Genesis of Major Copper Deposits and Districts of the World: A Tribute to Richard H. Sillitoe, Volume 16. Society of Economic Geologists, Inc. Littleton, Colorado, pp. 433–453. https://doi.org/10.5382/SP.16.17

Xavier, R.P., Moreto, C.P.N., de Melo, G.H.C., Toledo, P., Hunger, R., Deminardo, M., Faustinoni, J., Lopes, A., 2017. Geology and metallogeny of Neoarchean and Paleoproterozoic copper systems of the Carajás Domain, Amazonian Craton, Brazil. Proceedings of the 14th Biennial SGA meeting, Quebec, Canada, 3, 899–902.

Xie, Q.H., Zhang, Z.C., Hou, T., Jin, Z.L., Santosh, M., 2017. Geochemistry and oxygen isotope composition of magnetite from the Zhangmatun deposit, North China Craton: Implications for the magmatic-hydrothermal evolution of Cornwall-type iron mineralization. Ore Geol. Rev. 88, 57–70. https://doi.org/10.1016/j.oregeorev.2017.04.014

Xing, Y., Mei, Y., Etschmann, B., Liu, W., Brugger, J., 2018. Uranium transport in F-Cl-bearing fluids and hydrothermal upgrading of U-Cu ores in IOCG deposits. Geofluids 2018,1–22. https://doi.org/10.1155/2018/6835346

Zachariah, J.K., Balakrishnan, S., Rajamani, V., 1997. Significance of Sm-Nd isotope systematics in crustal genesis: a case study of Archaean metabasalts of the Eastern Dharwar Craton. Proc. Indian Acad. Sci. (Earth and Planetary Sciences) 106,361–367. https://doi.org/10.1007/BF02843460

Zang, W., Fyfe, W.S.,Barnett, R.L., 1992. A silver-palladium alloy from the Bahia lateritic gold deposit, Carajas, Brazil. Mineral. Mag. 56, 47–51. https://doi.org/10.1180/minmag.1992.056.382.06

Zhang, Z., Zuo, R., 2014. Sr–Nd–Pb isotope systematics of magnetite: implications for the genesis of Makeng Fe deposit, southern China. Ore Geology Rev. 57, 53-60. https://doi.org/10.1016/j.oregeorev.2013.09.009

Zhimin, Z., Yali, S., 2013. Direct Re-Os dating of chalcopyrite from the Lala IOCG deposit in the Kangdian copper belt, China. Econ. Geol., 108, 871–882. https://doi.org/10.2113/econgeo.108.4.871

Zhou, M.-F., Zhao, X.-F., Chen, W.T., Li, X.-C., Wang, W., Yan, D.-P., Qiu, H.-N., 2014. Proterozoic Fe–Cu metallogeny and supercontinental cycles of the southwestern

Yangtze Block, southern China and northern Vietnam. Earth-Sci. Rev. 139, 59–82. https://doi.org/10.1016/j.earscirev.2014.08.013

Zhu, Z., Tan, H., Liu, Y., Li, C., 2017. Multiple episodes of mineralization revealed by Re-Os molybdenite geochronology in the Lala Fe-Cu deposit, SW China. Miner. Deposita 53, 311–322. https://doi.org/10.1007/s00126-017-0740-x

Zhu, L., Liu, J., Bagas, L., Zhai, D., Meng, G., Verrall, M., 2020. New insights into the genesis of IOCG deposits: From a case study of the Yinachang deposit in SW China. Ore Geol. Rev. 103664. https://doi.org/10.1016/j.oregeorev.2020.103664

Zindler, A., Hart, S., 1986. Chemical geodynamics. Annu. Rev. Earth Planet. Sci. 14, 493–571.

Zuchetti, M., 2007. Rochas máficas do Supergrupo Grão Pará e sua relação com a mineralização de ferro dos depósitos N4 e N5, Carajás, PA. PhD. thesis. Federal University of Minas Gerais, Brazil.

Highlights

• Sr-Nd isotope data from chalcopyrite and magnetite gives insight into the source of the metals.

• Trace element data suggest more mafic compositions in Carajás IOCG and Cu-Au deposits rather than Andean IOCG deposits.

• The source of metals in Neoarchean IOCG systems from the Carajás Mineral Province derived from more than a single source, probably from basement rocks and coevally formed volcanic rocks and mafic-ultramafic components.

• The source of metals in Orosirian Cu-Au systems from the Carajás Mineral Province derived from evolved crustal components, through the derivation from Mesoarchean to Neoarchean processes.

• The source of metals in Candelaria-Punta del Cobre IOCG district was derived from mantle-components with arc-affinities less primitive than coevally formed subduction granitoids

Figures

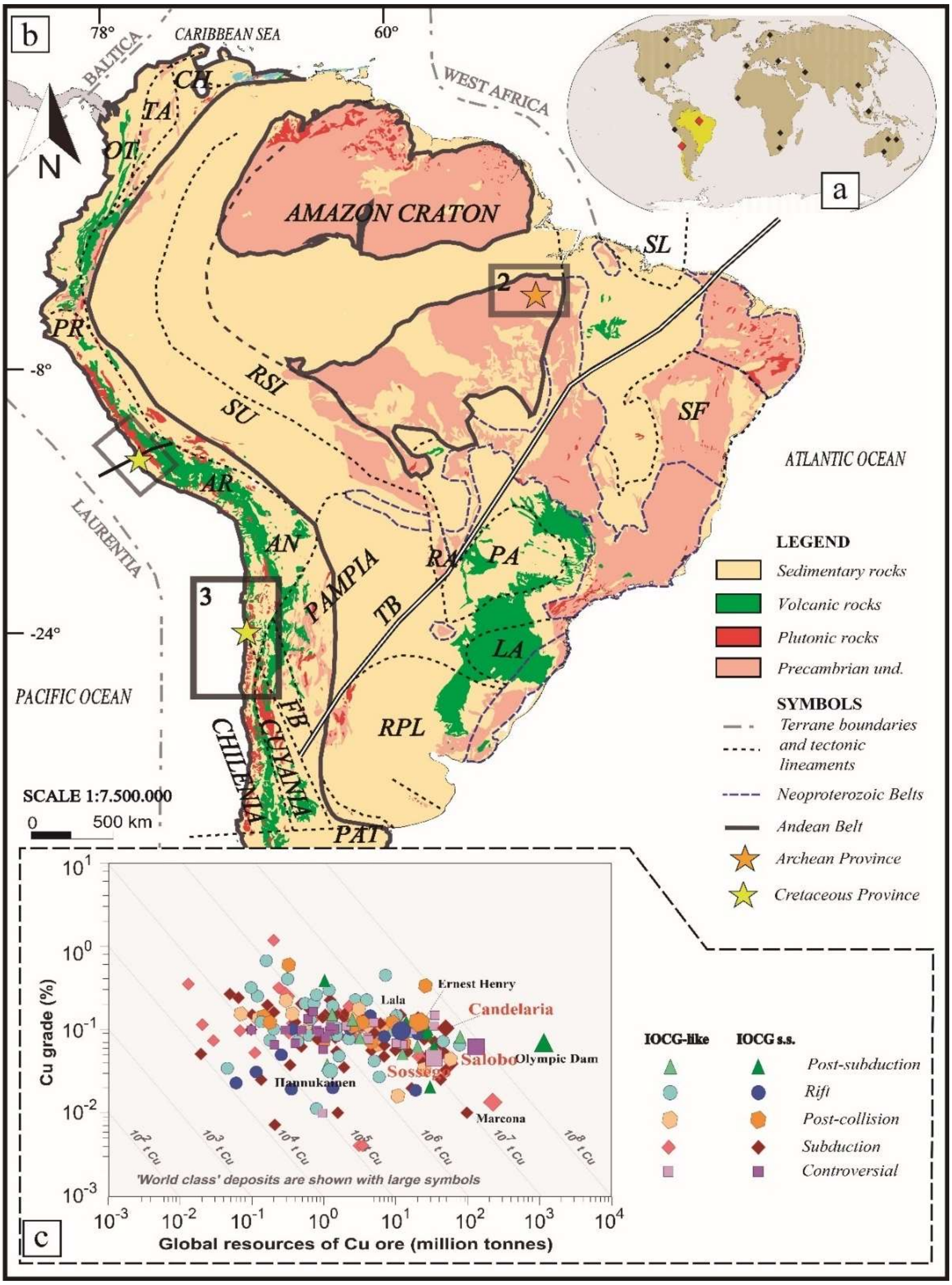

Paper – Figure 10. (A) Distribution of the main provinces with occurrence of the IOCG type, either sensu-stricto or -like (in red symbols and a yellow background the systems are represented the provinces of this study). (B) Geotectonic sketch map of South America with the main basement blocks and lithotypes that composed their architecture. Adapted from ***Schenk et al. (1999)*** and ***Cordani et al. (2010)***. (C) Logarithmic plot of copper grade (wt%) versus global resources of copper ore (million tonnes) for the major IOCG mineralization systems in the world (sensu stricto or -like) with its associated tectonic environment. World-class deposits are shown with large symbosl. Full data is provided in **ESM-Table 7.**

Abbreviations: *RSI – Rondonian-San Ignacio; SU – Sunsas; TB – Transbrasiliano Lineament; SL – São Luiz; SF – São Francisco; PA – Paranapanema; LA – Luiz Alves; RPL – Rio de la Plata; AR – Arequipa; AN – Antofalla; PAT – Patagonia.*

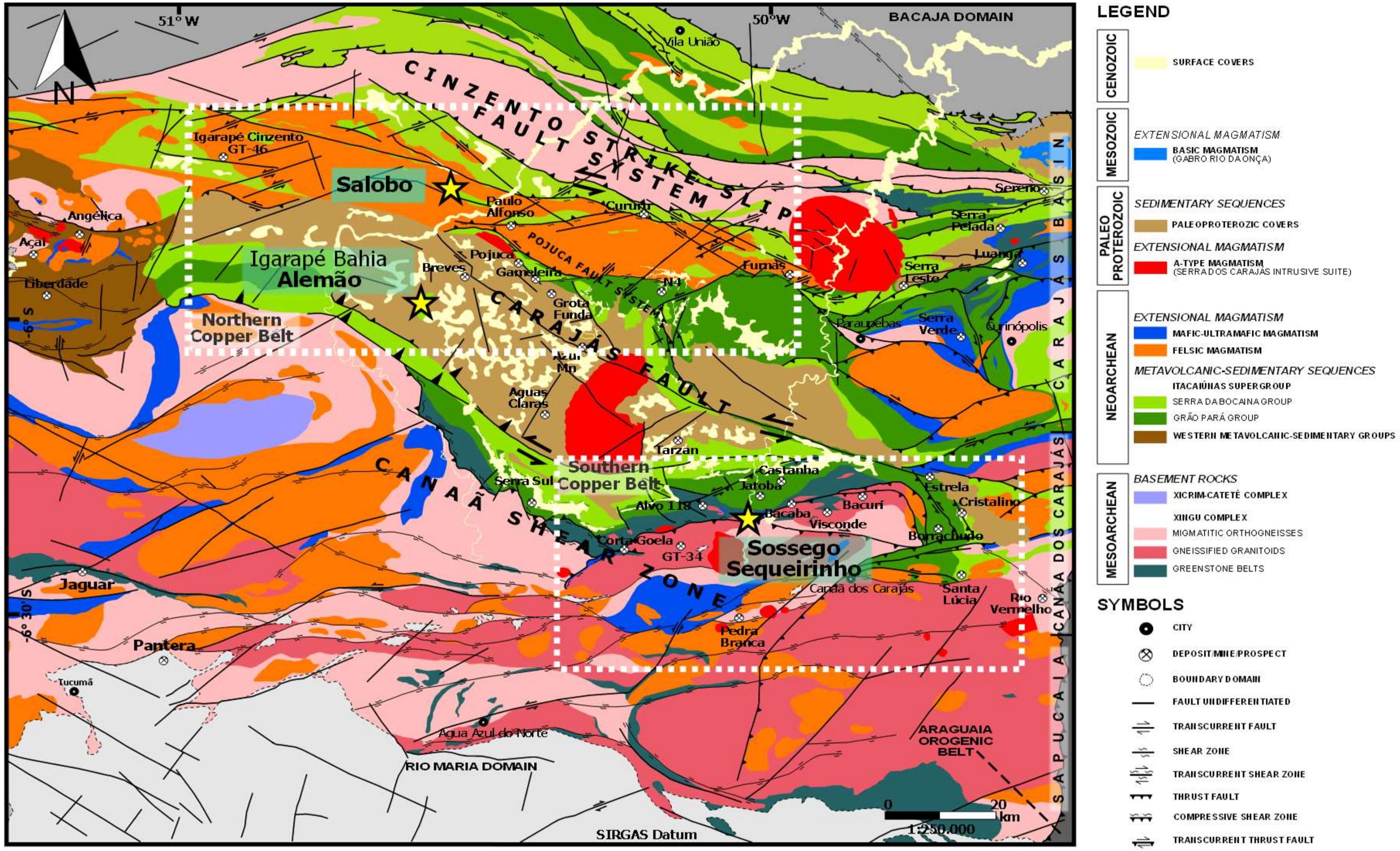

Paper – Figure 11. Simplified geological map of the Carajás Domain and surroundings, Amazonian Craton, Northern Brazil. Modified from ***Vasquez et al. (2008)***. Deposits included in this study were marked with stars symbols.

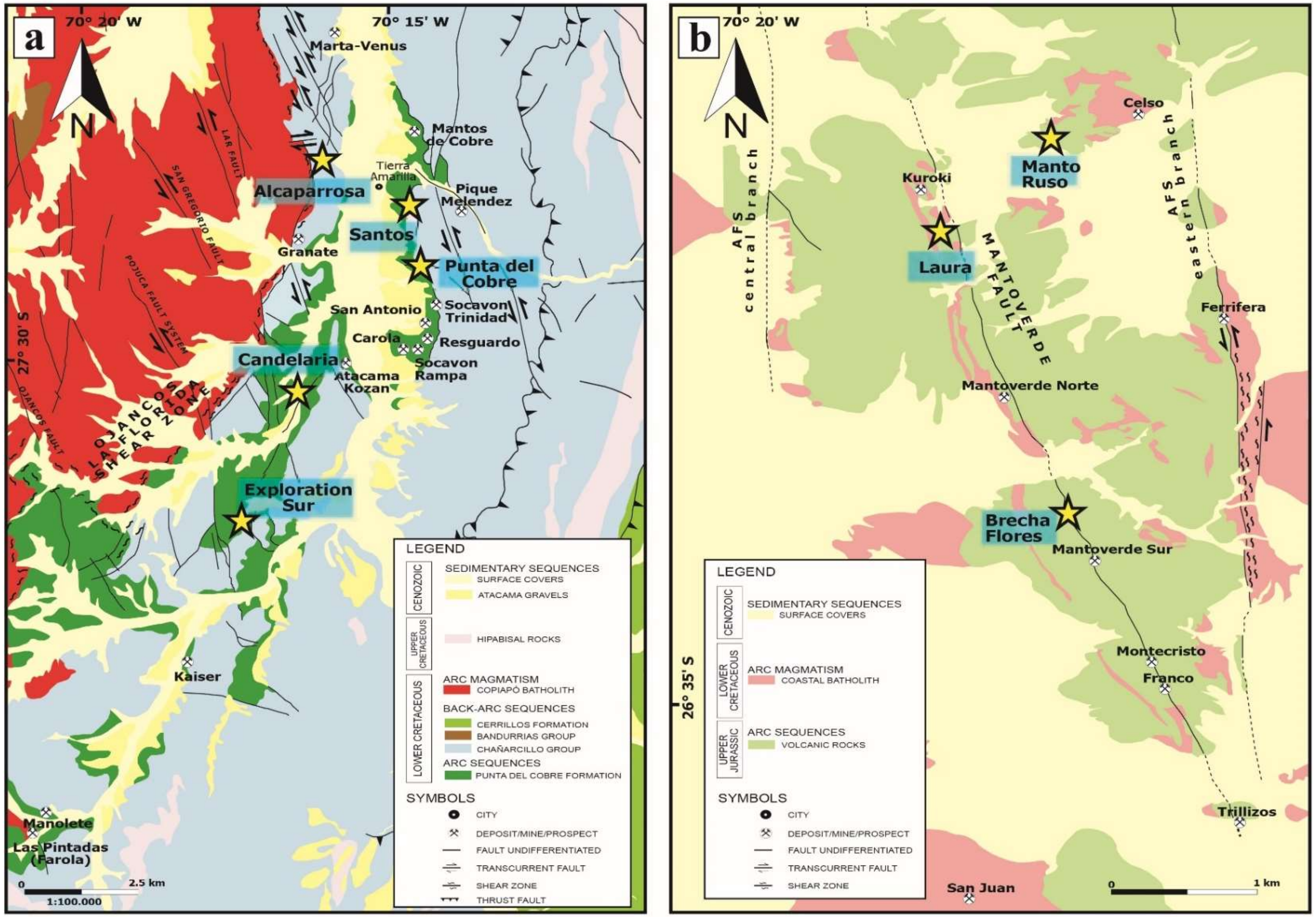

Paper – Figure 12. (a) Simplified geológical map of the Candelaria-Punta del Cobre district. Modified from ***Arévalo (2005a***; ***b)***. (b) Simplified geological map of the Mantoverde district and its metallogenetic deposit. Modified from **Rieger et al. (2012)**. Deposits included in this study were marked with stars symbols.

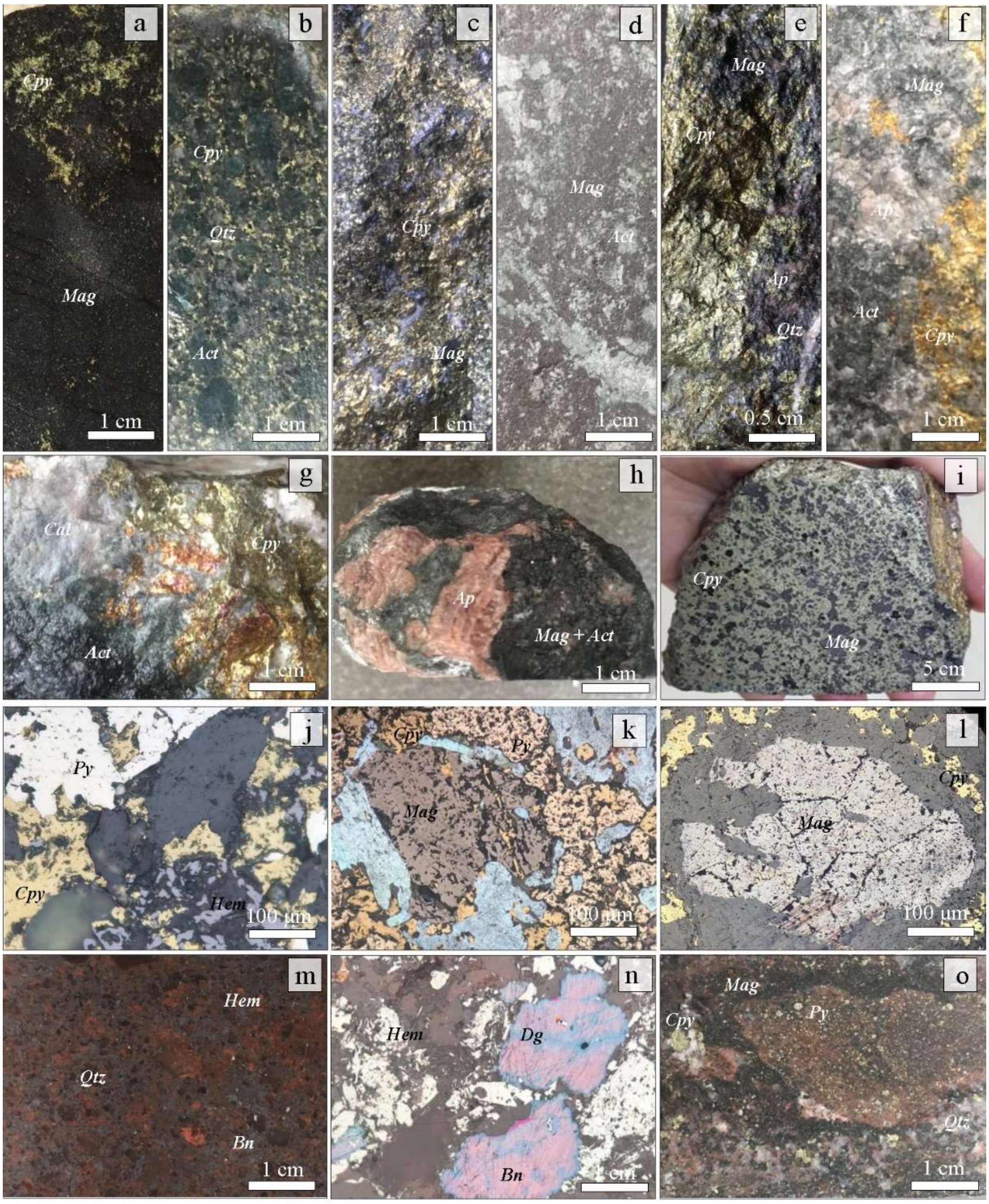

Act = actinolite; Ap= apatite; Bn= bornite; Cpy = chalcopyrite; Dg = digenite; Hem = hematite; Mag = magnetite; Py = pyrite; Qtz = quartz.

Paper – Figure 13. Photographs of mineralized samples from the Carajás Mineral Province, Olympic Dam and Ernest Henry deposits. (a) Alemão orebody: massive magnetite with dissemination of chalcopyrite. (b) Sequeirinho orebody: magnetite-chalcopyrite dissemination in sodic-calcic groundmass (c) Sequeirinho orebody: massive magnetite with strong dissemination of chalcopyrite. (d) Sequeirinho orebody: massive magnetite-actinolite. (e–h) Sossego orebody: magnetite-rich breccias in association with veins and dissemination of chalcopyrite; calcic-ferric groundmass with apatite grains. (i) Salobo: clast supported magnetite breccia with chalcopyrite matrix. Reflected light photomicrographs: hematite overgrowth on interstitial chalcopyrite for Sossego orebody (j) and Sequeirinho orebody (k, l). (m) Olympic Dam: hematite-bornite dissemination in potassic feldspar-ferric groundmass with intense dissemination of silicates. (n) Reflected light photomicrographs: digenite and hematite intergrown in bornite and chalcopyrite crystals, respectively. (o) Ernest Henry: strong dissemination of chalcopyrite-pyrite in potassic feldspar-ferric groundmass with intensive magnetite dissemination.

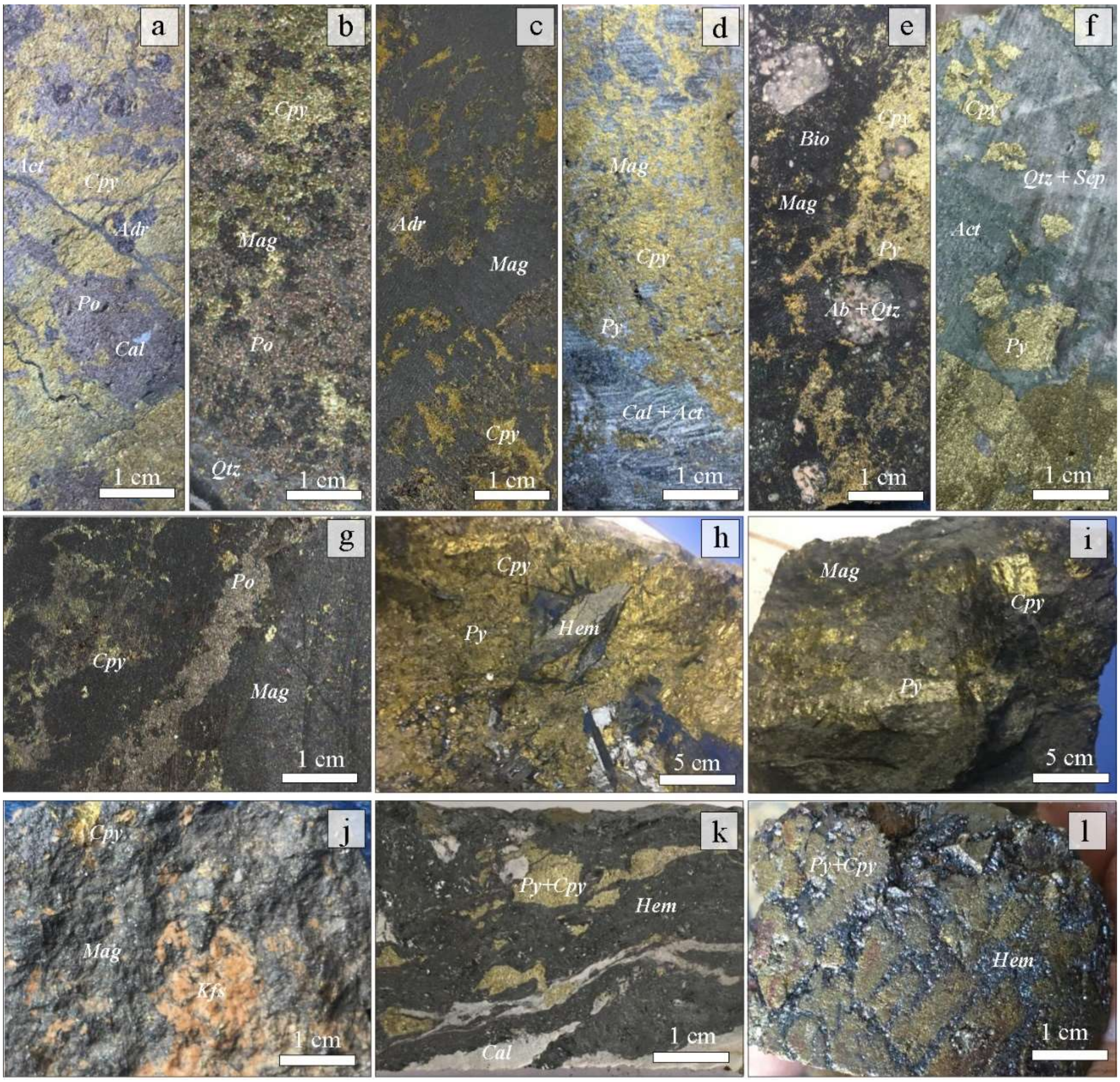

Ab= albite; Act = actinolite; Adr = andradite; Cal = calcite; Cpy = chalcopyrite; Scp = Scapolite; Hem = hematite; Kfs = K-feldspar; Mag = magnetite; Po = pyrrhotite; Py = pyrite; Qtz = quartz.

Paper – Figure 14. Photographs of mineralized samples from the Candelaria–Punta del Cobre and Mantoverde districts. (a) Candelaria Norte: Massive sulfide-rich vein related actinolite-veinlets and grossular andradite and associated calcite dissemination. (b) Exploration Sur: Massive sulfide-rich stratabound orebody associated to slightly andradite dissemination. (c) Candelaria Norte: Massive magnetite-rich manto associated to sulfide brecciation. (d) Alcaparrosa: Chalcopyrite patches with abundant cacite-actinolite veinlets; magnetite typically disseminated. e) Santos: Chalcopyrite-magnetite patches in a pervasive biotite altered andesite. (f) Santos: Chalcopyrite–pyrite patches in a pervasive actinolite and scapolite-albite altered groundmass. (g) Candelaria Norte: Massive magnetite manto orebody intersected by ore-veins, chalcopyrite mainly disseminated and pyrrhotite as veinlets. (h) Punta del Cobre: Massive chalcopyrite patches with associated hematite mineralization. (i) Punta del Cobre: Massive magnetite skarn associated to chalcopyrite-pyrite bands. (j) Brecha Flores: Magnetite-rich breccia with sulfide clasts. (k) Laura: Deformed hematite-rich breccia with calcite and sulfides associated. (l) Manto Ruso: Hematite-rich breccia with associated sulfide clasts.

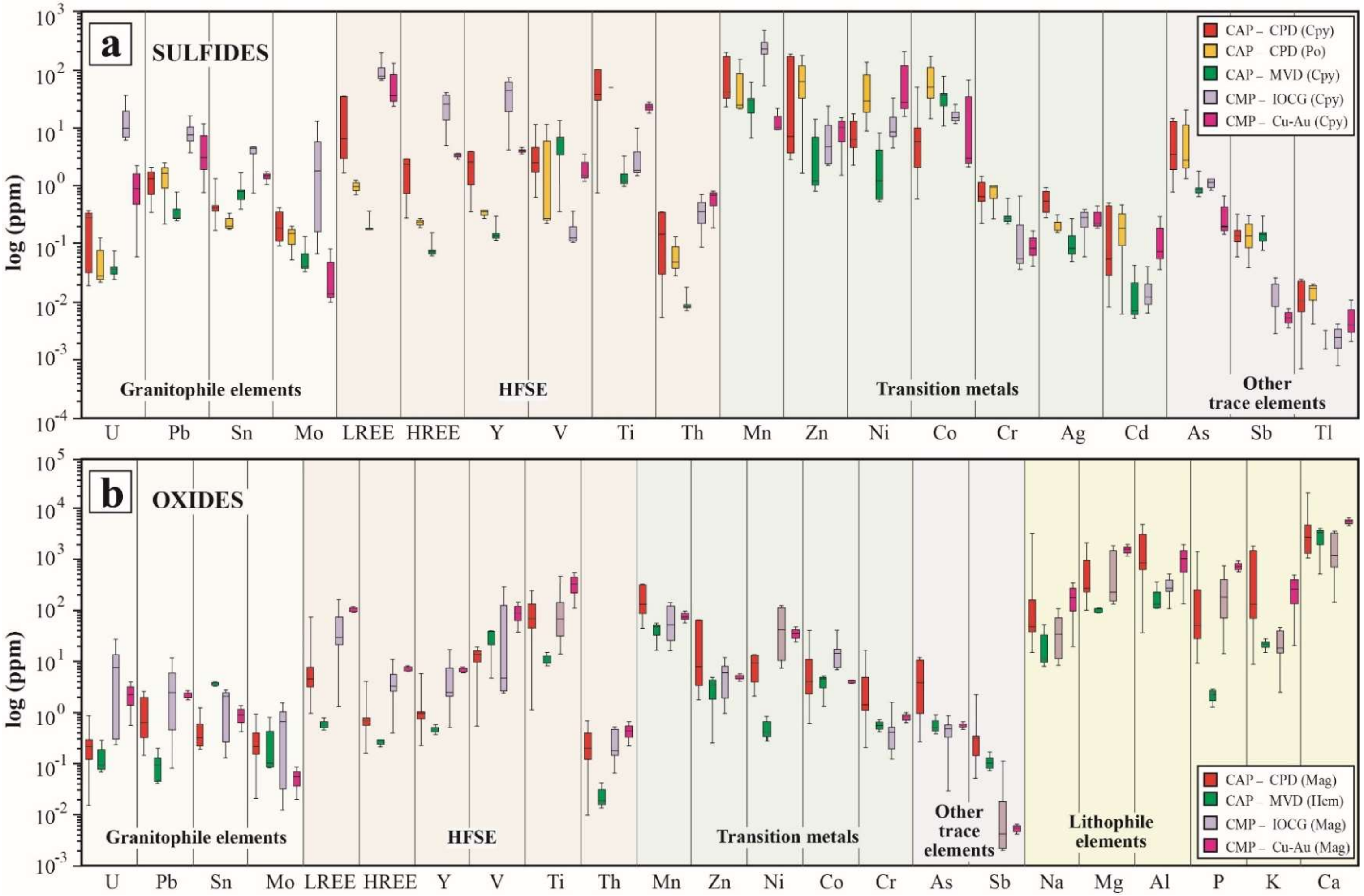

Paper – Figure 15. Multi-element box and whisker plots for ICP-MS trace element data of ore-bearing samples from the studied IOCG systems. (a) Sulfides. (b) Iron oxides. **Abbreviations:** CAP – Central Andes IOCG Province; CMP – Carajás Mineral Province; CPD – Candelaria-Punta del Cobre district; MV – Mantoverde district.

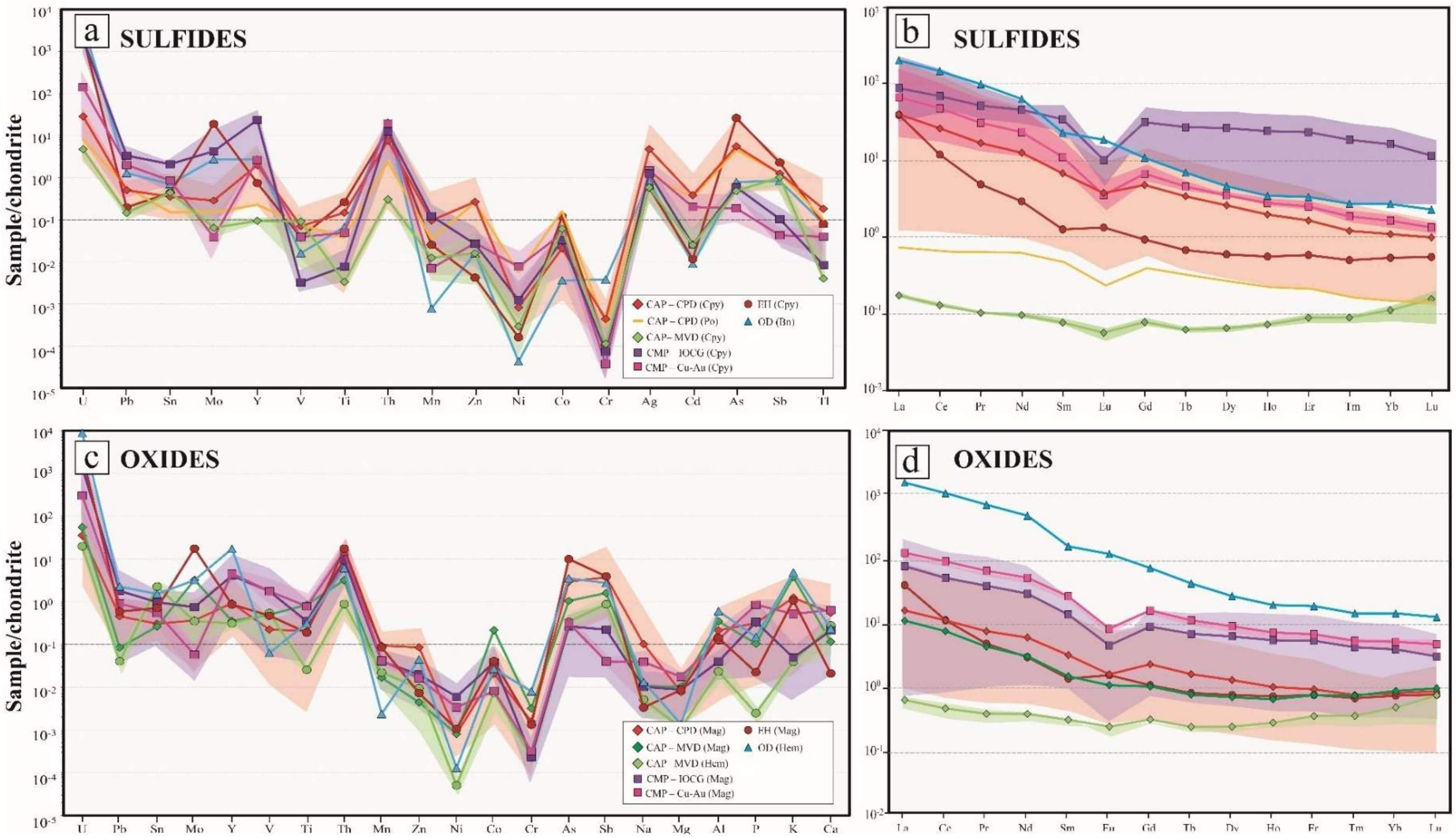

Paper – Figure 16. (a, c) Multi-element diagrams of average major, minor and trace element compositions of sulfides and oxides of IOCG provinces, respectively. (b, d) REE distribution patterns for sulfides and iron-oxides of IOCG provinces, respectively. The whole ICP-MS data-set is normalized to chondrite (***Palme & O'neill, 2007***). Polygons summarizes the composition for Carajás Mineral Province and districts from the Central Andes IOCG Province, respectively. **Abbreviations:** *CAP – Central Andean IOCG Province; CMP – Carajás Mineral Province; CPD – Candelaria-Punta del Cobre district; EH – Ernest Henry; MVD – Mantoverde district.*

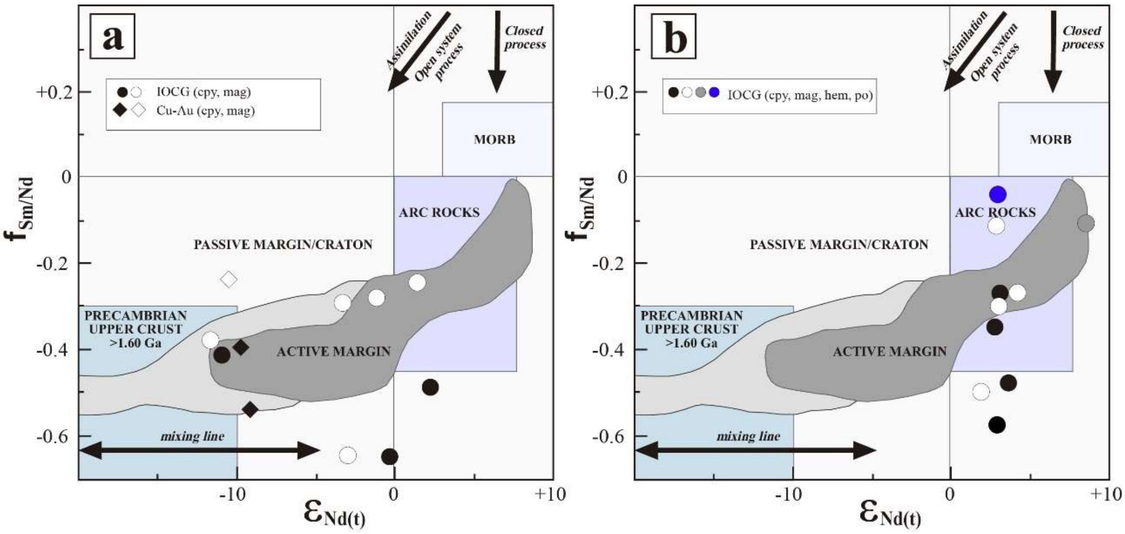

Paper – Figure 17. Fractionation factor ($f_{Sm/Nd}$) vs. εNd(t) diagram (**DePaolo & Wasserbur, 1976**; **Shirey & Hanson, 1986**) for the Cu-Au and Fe minerals studied for (a) Carajás Mineral Province, and (b) Central Andes IOCG Belt. The modeled vectors show open-and-closed system processes (**Zachariah et al., 1997**).

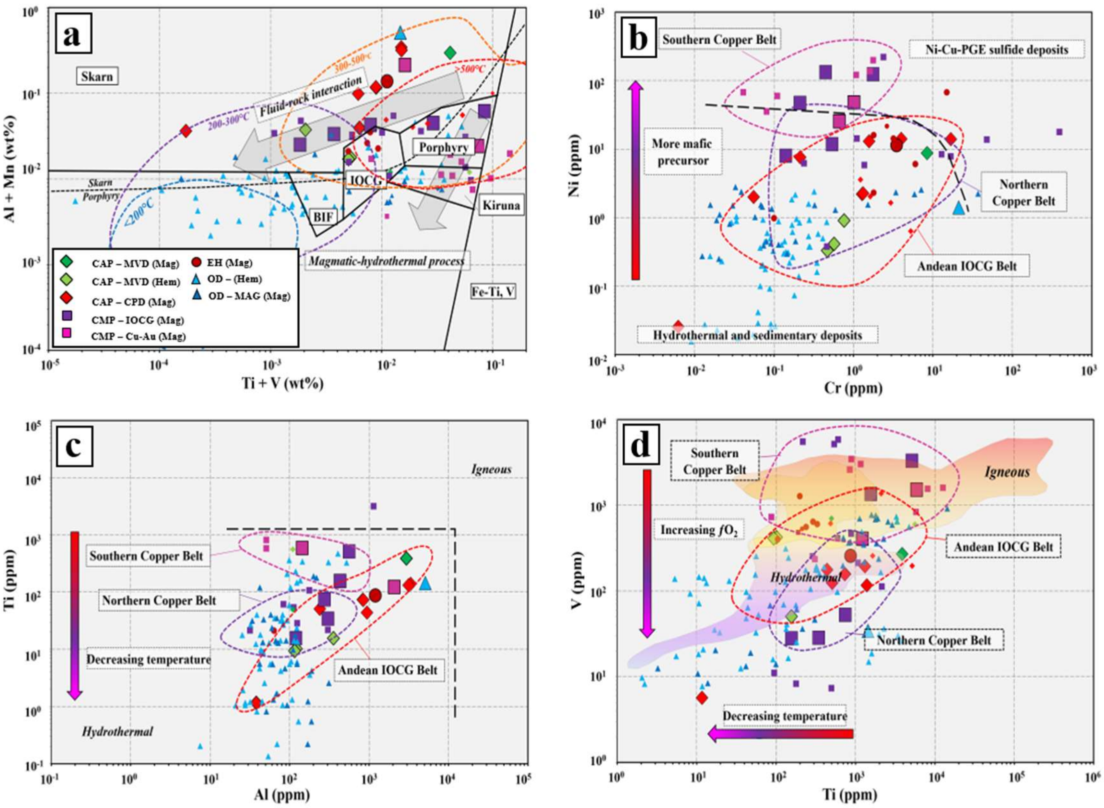

Paper – Figure 18. Plot of ICP-MS Fe-oxide data of IOCG deposits analyzed in this study in different discriminant diagrams. (a) Al+Mn vs. Ti+V (wt%) discriminant plot for distinct mineral deposits proposed by ***Dupuis & Beaudoin (2011)*** and modified by ***Nadoll et al. (2014)***. (b) Ni vs. Cr (after ***Dare et al., 2014a***). (c) Ti vs. Al (ppm) (after Canil et al., 2016). (d) V vs. Ti (ppm) (***Nadoll et al., 2015***). Additional data from previous works are shown with minor symbols (source of LA-ICP-MS data: ***Zhang et al. (2009)***, ***Dare et al. (2014a)***, ***Goldsmith (2014)***, ***Santiago (2016)***, ***Huang et al. (2019***), ***Verdugo-Ihl et al. (2020)***. Source of EPMA data: ***Childress et al. (2020)***.

Abbreviations*: CAP – Central Andean IOCG Province; CP – Carajás Mineral Province; CPD – Candelaria-Punta del Cobre district; EH – Ernest Henry; Hem – hematite; Mag – magnetite; Cu-Au – Orosirian Cu-Au; MVD – Mantoverde district; OD – Olympic Dam.*

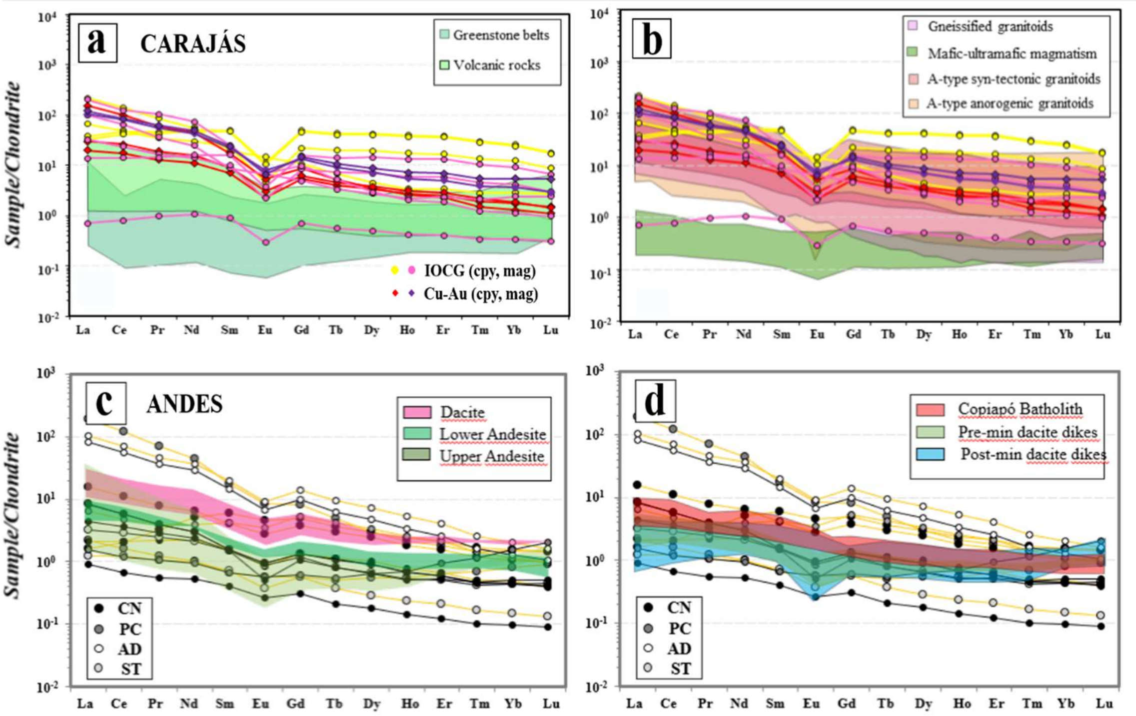

Paper – Figure 19. REE diagrams normalized to chondrite values (***Palme & O'neill, 2007***) of the chalcopyrite and magnetite compared to regional lithologies of each province (a) Carajás ores against supracrustal rocks (***de Souza et al., 2001***; ***Martins et al., 2017***; ***Figuereido e Silva et al., 2020***). (b) Carajás ores against granitoids (***Dall'Agnol et al., 2005***; ***Feio et al., 2013***; ***Marangoanha et al., 2019***; ***Mansur, 2017***). (c) Candelaria-Punta del Cobre district ores against volcanic rocks from the Punta del Cobre Formation (***del Real et al., 2018***); (d) Candelaria-Punta del Cobre district ores against Copiapó batholith (***Marschik et al., 2003a***; ***del Real et al., 2018***). **Note:** yellow and black lines in Andean deposits means chalcopyrite and magnetite compositions, respectively.

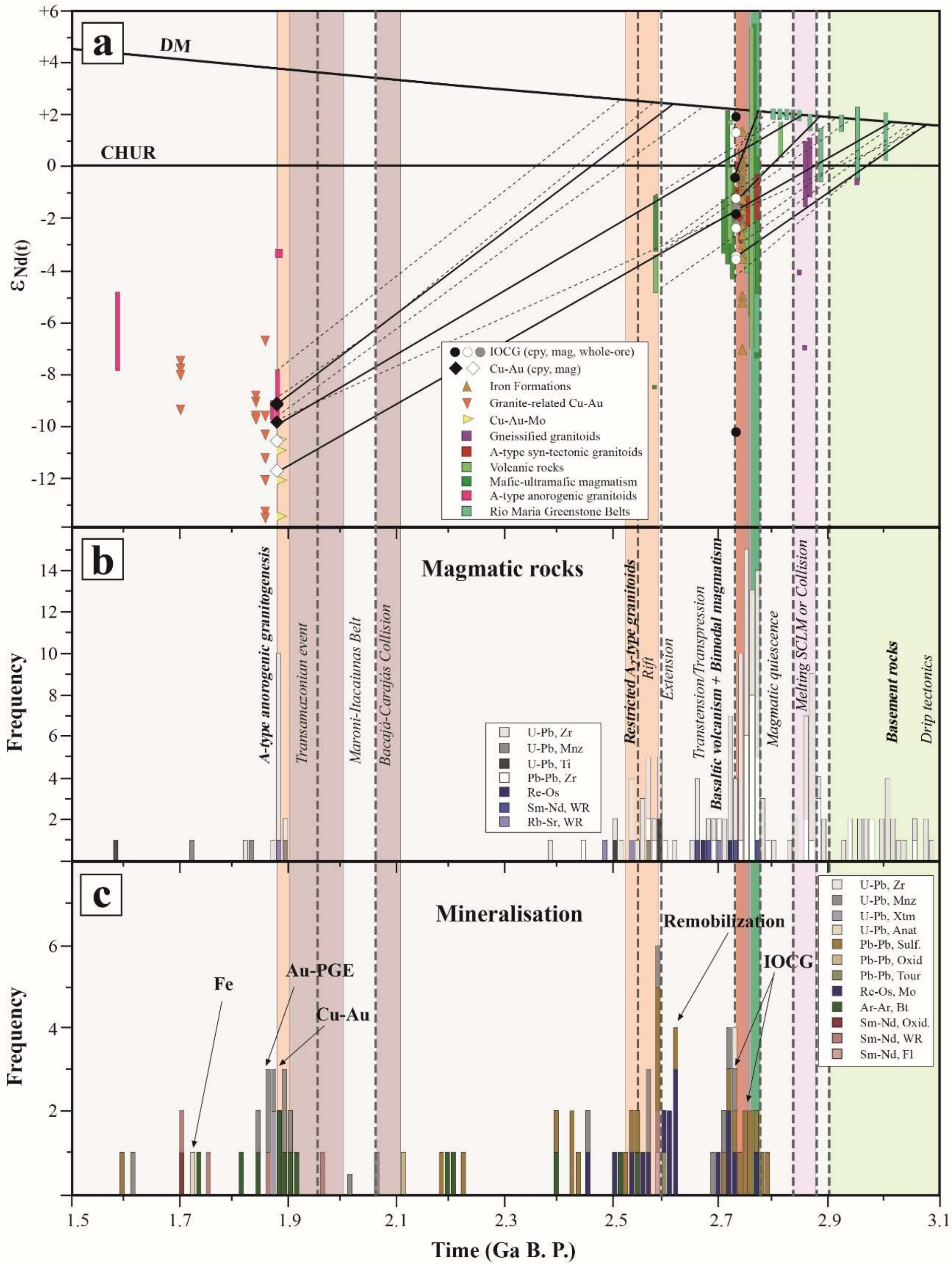

Paper – Figure 20. (a) Evolution trends of εNd(t) for crustal reservoirs in the Carajás Domain, compared with the composition of magnetite and chalcopyrite εNd(t) from this study. (b) Histogram of magmatic rocks from the Carajás Domain. (c) Histogram of mineralized events in the Carajás Domain. Lithotypes and mineralization from other ore systems were previously collected from literature and are presented in **ESM-Table 6** and **ESM-Table 7**, respectively. Tectonic evolution and lithotypes ranges were selected from ***Salgado et al. (2019)***, ***Tavares et al. (2018)***, ***Costa et al. (2020)***, ***Ganade et al. (2020)*** and ***Lacasse et al. (2020)***.

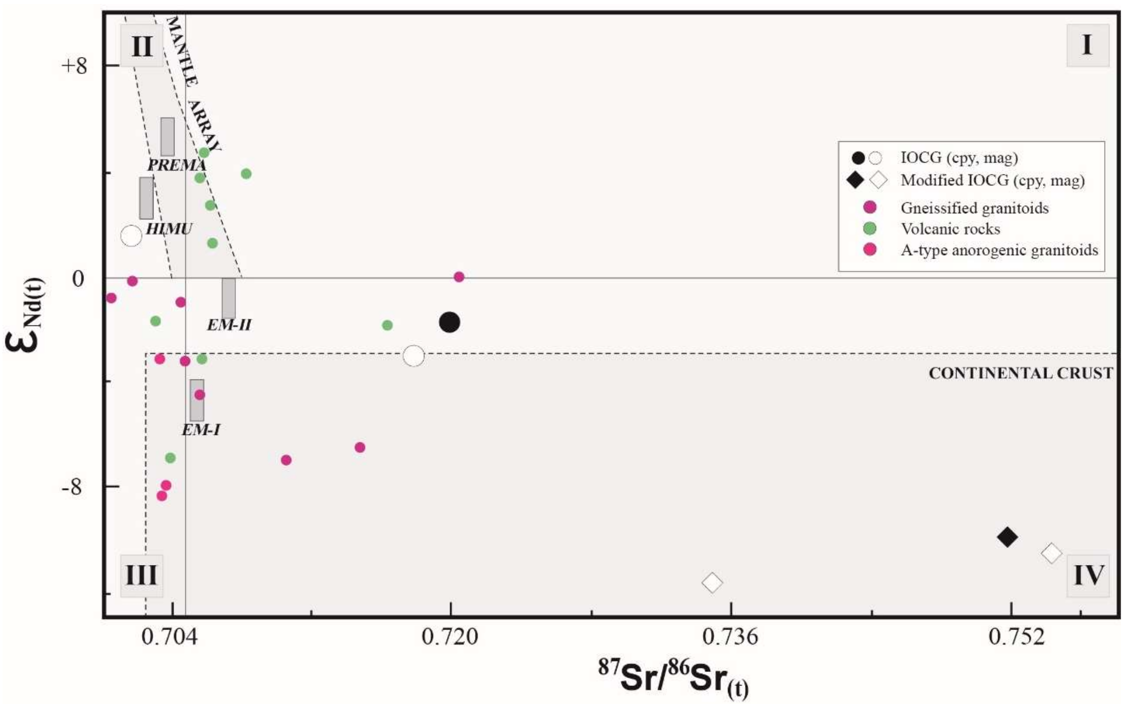

Paper – Figure 21. I_{Sr} and εNd_i signatures of the chalcopyrite and magnetite from Neoarchean IOCG and Orosirian Cu-Au depositis from the Carajás Mineral Province compared with published data from literature. Full compilation values are presented in **ESM-Table 8**. Reservoirs and Fields (I to IV) are from ***Faure (1986)***.

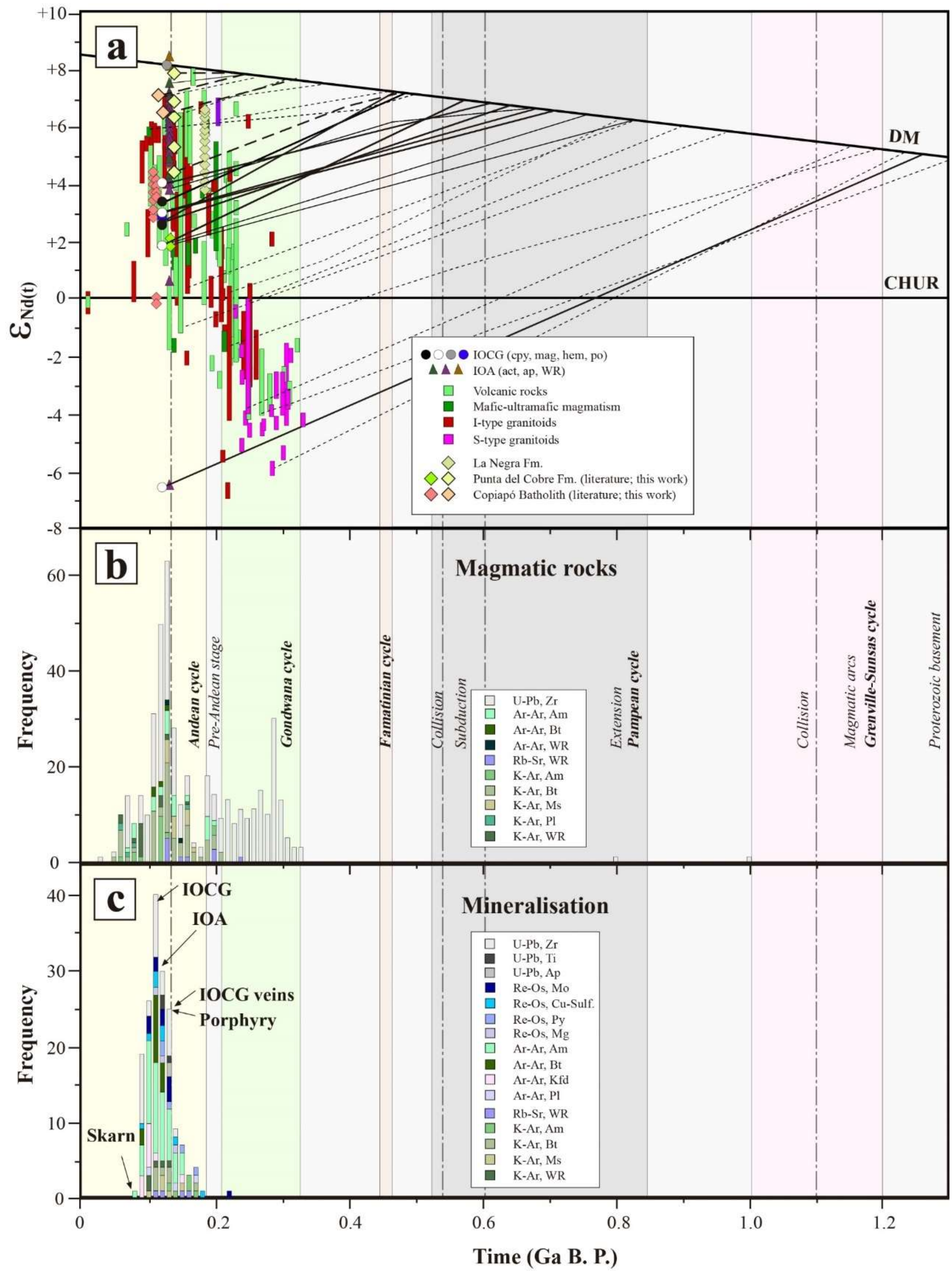

Paper – Figure 22. (a) Evolution trends of εNd(t) for crustal reservoirs in the Central Andes Belt, compared with the composition of magnetite, chalcopyrite, hematite and pyrrhotite εNd(t) from this study. (b) Histogram of magmatic rocks from the Andes Belt. (c) Histogram of mineralized events in the Andes Belt. Lithotypes and mineralization from other ore systems were previously collected from literature and are presented in **ESM-Table 9** and **ESM-Table 10**, respectively. Tectonic evolution ranges were selected from ***Ramos (2008)*** and ***Oliveros et al. (2020)***.

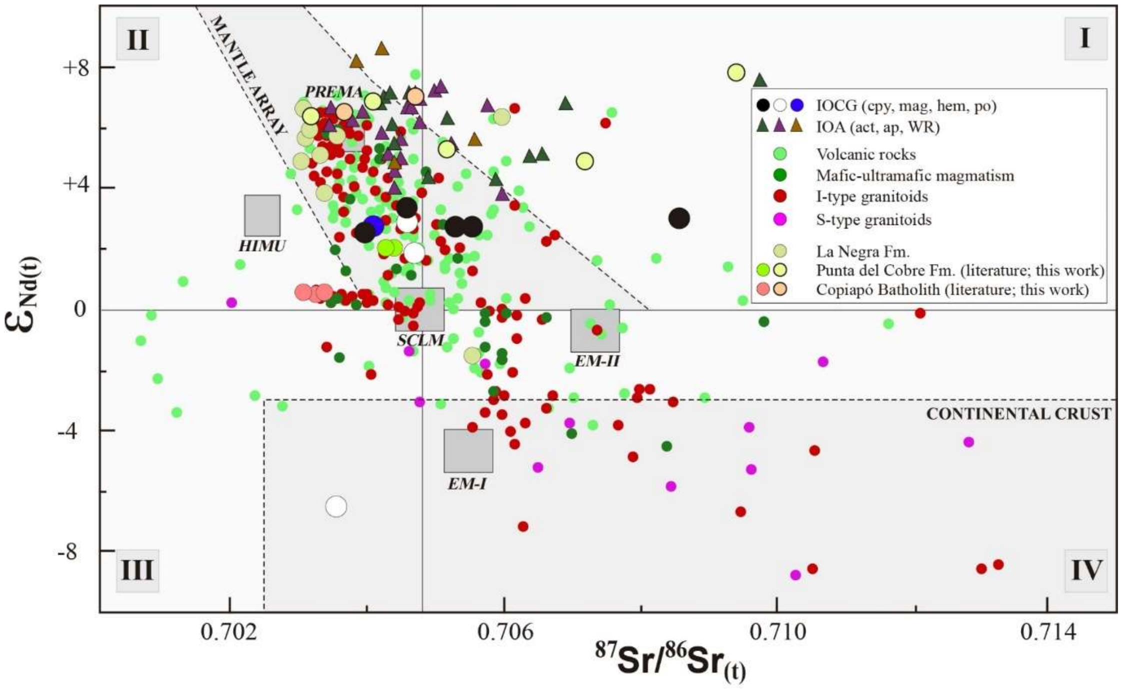

Paper – Figure 234. I_{Sr} and εNd_i signatures of the chalcopyrite, magnetite and pyrrhotite from the Candelaria-Punta del Cobre district compared with published data from literature. Full compilation values are presented in **ESM-Table 11**. Reservoirs and Fields (I to IV) are from ***Faure (1986)***.

Tables

Paper – Table 5. A summarized characteristic from the IOCG provinces included in this study.

Province	Age	Classification	Tectonic setting	Main deposits
Carajás Mineral Province, Brazil	2.76–2.73 Ga[a]	Magnetite[c]–IOCG	Controversial	**Northern Copper Belt:** Salobo, Grota Funda[a] **Central Carajás:** Igarapé-Bahia/Alemão[a] **Southern Copper Belt:** Cristalino, Sequeirinho, GT-34, Castanha, Bacaba, Jatobá[a]
	~1.88 Ga[b]	Magnetite[c]–Remobilized IOCG[a,b] or granite-related Cu-Au[b]	Controversial	**Northern Copper Belt:** Gameleira[b] **Central Carajás:** Estrela, Breves[b] **Southern Copper Belt:** Sossego-Curral, Alvo 118[b]
Olympic Cu-Au Province	1.59–1.57 Ga[d]	Hematite[c]–IOCG	Post-subduction[e]	Olympic Dam, Cairn Hill, Prominent Hill, Moonta-Wallaroo[d]
Mt. Isa Inlier, Australia	1.53–1.51 Ga[f]	Magnetite[c]–IOCG	Post-collision[c]	Ernest Henry, Ernie Junior, E1, Monakoff, Great Australia
Central Andes IOCG Province, Peru-Chile	0.12–0.10[g]	Magnetite-to hematite[c]–IOCG	Subduction[g]	**Northern Chile:** Candelaria, Mantoverde, El Espino[g] **Southern Peru:** Raúl-Condestable, Mina Justa[g]

References: (a) ***Schutesky & Oliveira (2020)***; (b) ***Pollard et al. (2019)***; (c) ***Chen (2013)***; (d) ***Reid (2019)***; (e) ***Skirrow et al. (2018)***; (f) ***Oliver et al. (2008)***; (g) ***Chen et al. (2013)***.

Paper – Table 6. Summarized isotopic and geochemical features of ore samples analyzed in this study.

Province	Type	n	I_{Sr}	n	I_{Nd}	εNd_i	TDM (Ga)	n	∑REE (ppm) [a]	LREE/HREE	La_N/Yb_N [b]	δEu [c]	Trace signature
Carajás Mineral Province													
IOCG													
(Alemão, Salobo,	Cpy	2	0.61617*–0.71973	3	0.508525–0.509193	−10.39 to +2.19	2.74–2.88	4	1214.05	11.31	20.92	0.41	Mg-P-Ca-Mn-Ni-Y-Mo-Sn-Pb-U-REE (LREE>HREE)
Sequeirinho)	Mag	4	0.70159–0.71761	4	0.508913–0.509154	−3.30 to +1.43	2.82–3.35	5	685.38	17.94	46.63	0.44	V-Ni-Y-Pb-REE (LREE>HREE)
Remobilized IOCG or granite-related Cu-Au													
(Sossego)	Cpy	2	0.71802–0.75171	2	0.509705–0.509736	−9.83 to −9.22	3.22	3	665.52	18	48.44	0.39	P-Ti-V-Co-Ni-Cd-Pb-U-REE (LREE>HREE)
	Mag	2	0.68975*–0.72331	2	0.509610–0.509667	−11.68 to −10.56	2.71–3.02	2	1192.96	14.89	25.73	0.39	Mg-P-Ti-V-REE (LREE>HREE)
Olympic Dam Cu-Au Province													
IOCG													
(Olympic Dam)	Bn	1	0.69691*	1	*0.513040	*48.15	-	1	1930.52	37.76	75.05	1.1	Al-K-Cr-Ba-Th-U-REE (LREE>HREE)
	Hem	-	-	-	-	-	-	1	12967.65	47	113.31	1.04	Al-K-Cr-Zn-As-Y-Ag-Ba-Pb-Th-U-REE (LREE>HREE)
Mt. Isa Inlier													
IOCG													
(Ernest Henry)	Cpy	1	0.64701*	1	0.510538	−2.39	1.94	1	200.54	31.83	73.4	1.22	Mg-Al-K-Ti-V-Co-As-Mo-Sb-U
	Mag	1	0.65748*	1	0.510505	−3.03	2	1	174.2	25.05	54.5	1.27	Mn-As-Mo-Sb-Ba-Th-U-REE (LREE>HREE)
Central Andes IOCG Province													
IOCG													
Candelaria-Punta del Cobre district	Cpy	8	0.70155–0.70864	6	0.51262–0.51266	+2.68 to +3.39	0.43–0.55	8	379.57	10.92	26.76	0.69	Na-Mg-Al-K-Ca-V-Cr-Mn-Ni-Zn-As-Ag-Cd-Sb-Cs-Tl
	Mag	6	0.70341–0.70465	5	0.51214–0.51269	+1.81 to +4.03 (−6.63)	0.53–0.63 (1.26)	8	143.9	8.48	16.43	0.64	Na-Al-Ca-Mn-Zn-Ag-Cd-Cs
	Po	3	0.70315–0.70437	1	*0.512633	*2.79	-	3	12.75	4.3	4.91	0.52	V-Cr-Mn-Co-Ni-Zn-As-Sb
Mantoverde district	Cpy	2	0.70363–0.70408	-	-	-	-	3	2.74	2.54	1.64	0.73	V-Co-Sb
	Mag	1	0.70832	-	-	-	-	1	91.49	12.74	12.75	0.85	Al-K-Ti-Cr-Co-Ba
	Hem	2	0.69682*–0.70238	1	*0.512912	*8.35	-	3	9.1	2.41	1.55	0.78	Sn

Abbreviations: Bn – bornite; Cpy – chalcopyrite; Hem – hematite; Mag – magnetite. Note: Sm/Nd>0.15 and Rb/Sr<0.8 were not considered for the Carajás Mineral Province and Candelaria-Punta del Cobre district. *Fractionated or eccentric values only displayed as referential information. Full data sample is available on **ESM - Table 4** and **ESM - Table 5**. [a] ∑REE = ∑(La-Lu). [b] $La_N/Yb_N = (La/La_N)/(Yb/Yb_N)$. [c] $\delta Eu = Eu_N/(0.5Sm_N+0.5Gd_N)$ (Bau & Dulski, 1996). Normalized values from ***Palme & O'neill, 2007***.

Electronic Supplementary Material (ESM)

ESM - Table 7. Compilation of tonnage and grade of selected world-wide IOCG systems and its related tectonic environments.

Deposit	Classification	Tonnage (Mt)	Cu (%)	Au (g/t)	Reference
SOUTH AMERICA					
Carajás Mineral Province, Brazil – Controversial [a]					
Águas Claras	IOCG-like	9.5	<0.1	2.43	Silva & Villas (1998)
Alvo 118	IOCG-like	170	1	0.3	Torresi et al. (2012)
Alvo 118	IOCG-like.	170	1	0.3	Rigon et al. (2000)
Antas North	IOCG-like	19.84	1.1	0.2	Hunger et al. (2018)
Breves	IOCG-like	50	1.22	2.4	Nunes et al. (2001)
Cristalino	IOCG s.s.	379	0.66	0.3	Pinto (2012)
Cristalino	IOCG s.s.	500	1	0.3	Huhn et al. (1999a)
Furnas	IOCG s.s.	500	0.7	-	Jesus (2016)
Gameleira	IOCG-like	100	0.7		Rigon et al. (2000); Lindenmayer et al. (2001)
Grota Funda	IOCG s.s.	15-40	0.8-1.2	-	Hunger et al. (2018)
Igarapé-Bahia/Alemão	IOCG s.s.	219	1.4	0.86	Tallarico et al. (2005)
Jatobá	IOCG-like	355	1.5	0.28	Lancaster-Oliveira et al. (2000); Monteiro et al. (2008a)
Pantera	IOCG s.s.	20.8	1.7	0.2	AVANCOCOPPER (2018)
Paulo Alfonso	IOCG s.s.	200	1	-	de Melo et al. (2019c)
Pedra Branca	IOCG s.s.	22..4	0.94	0.27	Mizuno (2009)
Salobo	IOCG s.s.	1,193.4	0.61	0.3	VALE (2018)
Salobo	IOCG s.s.	1,112	0.69	0.43	de Melo et al. (2019a)
Salobo	IOCG s.s.	986	0.82	0.49	Porter (2010)
Salobo	IOCG s.s.	789	0.96	0.52	Souza & Vieira (2000)
Sequeirinho-Pista-Baiano (Sossego)	IOCG s.s.	245	1.1	0.28	Lancaster-Oliveira et al. (2000)
Sossego	IOCG-like	120.1	0.68	0.2	Hunger et al. (2018)
Sossego-Curral (Sossego)	IOCG-like	110	1.1	0.28	Lancaster-Oliveira et al. (2000)
Visconde	IOCG s.s.	35	1	0.28	da Costa Silva et al. (2015)
Borborema Mineral Province, Brazil – Subduction [b]					
Aurora	IOCG-like	22	0.8	-	Huhn et al. (2011)
Caraibe mine	IOCG-like	24	1.8	-	Huhn & Silva (2018)
Riacho Seco Copper Proyect	IOCG-like	5	0.8	-	Huhn et al. (2014)
Central Andes IOCG Province, Peru-Chile – Subduction [c]					
Alcaparrosa	IOCG s.s.	10	1.4	-	Marschik & Fontboté (2001a)
Alcaparrosa	IOCG s.s.	10.215	0.77	-	Couture et al. (2017)
Amolanas	IOCG-like	3	2.5–3.0	-	Chen (2008)
Atacama Kozan	IOCG s.s.	30	1.5	-	Ichii et al. (2007)
Barreal Seco	IOCG s.s.	54	0.65	-	Simón et al. (2007)
Candelaria	IOCG s.s.	315.892	0.53	0.53	Couture et al. (2017)
Candelaria	IOCG s.s.	470	0.95	0.22	Marschik & Fontboté (2001a)
Candelaria Norte	IOCG s.s.	65.697	0.89	-	Couture et al. (2017)
Candelaria Open Pit + Española Project	IOCG s.s.	415	0.48	0.11	Couture et al. (2018)
Carmen de Cobre	IOCG s.s.	71	0.65	-	Herrera et al. (2008)
Carola	IOCG s.s.	20	1.4	-	Marschik & Fontboté (2001a)
Carola	IOCG s.s.	60.7	1.16	-	del Real et al. (2018)
Casualidad	IOCG s.s.	300	0.5	-	Rivera et al. (2009)
Cerro Negro	IOCG s.s.	249	0.4	0.15	Sillitoe (2003)
Diego de Almagro	IOCG s.s.	70	0.65	0.05	Herrera et al. (2008)
Dominga	IOCG s.s.	2.082	0.07	-	Veloso et al. (2015)
El Espino	IOCG s.s.	145	0.55	0.24	Lopez et al. (2014)
El Soldado	IOCG s.s.	200	1.4	-	Boric et al. (2002)
Franke	IOCG-like	26.665	0.82	-	Leszcyński et al. (2015)
Granate	IOCG s.s.	15	0.8	-	del Real et al. (2018)
La Africana	IOCG-like	3.3	2.5	-	Sillitoe (2003)
Las Pintadas	IOCG s.s.	4	1.0–1.5	-	Marschik & Fontboté (2001a)
Manto Ruso	IOCG s.s.	15.1	0.56	-	Rieger et al. (2010)
Mantos de Cobre	IOCG s.s.	16	0.85	-	del Real et al. (2018)
Mantos de Cobre	IOCG s.s.	1.5	1.45	-	Marschik & Fontboté (2001a)
Mantoverde	IOCG s.s.	1.5	1.5	-	Marschik & Fontboté (2001a)
Mantoverde	IOCG s.s.	400	0.52	0.11	Benavides et al. (2007)
Mantoverde (sulfides)	IOCG s.s.	440	0.56	0.12	Rieger et al. (2010; 2012)
Mantoverde Norte	IOCG s.s.	101.6	0.56	-	Rieger et al. (2010)
Mantoverde Sur	IOCG s.s.	46.8	0.56	-	Rieger et al. (2010)

ESM – Table 1. (continued)

Deposit	Classification	Tonnage (Mt)	Cu (%)	Au (g/t)	Reference
Montecristo	IOCG-like	15	1.6	0.6	Sillitoe (2003)
Ojancos Viejo	IOCG s.s.	15	0.3-0.5	-	Barton et al. (2013)
Panulcillo	IOCG s.s.	10.4	1.45	0.1	Sillitoe (2003)
Panulcillo	IOCG s.s.	15	0.1	-	Hopper & Correa (2000)
Productora	IOCG-like	214.3	0.48	0.1	Escolme et al. (2015)
Productora + Alice Cu-Mo	IOCG-like	236	0.48	0.1	Escolme et al. (2020)
Punta del Cobre	IOCG s.s.	180	0.9	-	del Real et al. (2018)
Punta del Cobre	IOCG s.s.	120	1.5	0.2-0.6	Marschik & Fontboté (2001a)
Resguardo	IOCG s.s.	6	1.8	0.4	Marschik & Fontboté (2001a)
San Antonio	IOCG-like	1.09	0.52	-	SERNAGEOMIN (personal communication, 2019)
Santo Domingo	IOCG s.s.	417	0.25	0.032	Daroch et al. (2015)
Santo Domingo Sur	IOCG s.s.	486	0.32	0.043	Daroch & Barton (2011)
Santos	IOCG s.s.	13.295	0.94	0.4	Couture et al. (2017)
Santos	IOCG s.s.	20	1.5	0.4-0.5	Marschik & Fontboté (2001a)
Socavon Rampa	IOCG s.s.	25	1.2	0.2	Ichii et al. (2007)
Socavon Rampa	IOCG s.s.	25	1.2	0.2-0.3	Marschik & Fontboté (2001a)
Tamaya	IOCG-like	2	12	-	Sillitoe (2003)
Teresa de Colmo	IOCG s.s.	70	0.8	-	Hopper & Correa (2000)
Tocopilla	IOCG-like	2.4	3.1	-	Injoque (2002)
Trinidad	IOCG s.s.	15	1.5	0.2	Marschik & Fontboté (2001a)
Tropezon	IOCG s.s.	1	1	-	Tornos et al. (2010)
Cata Cañete	IOCG s.s.	1	1.5	-	Injoque (2002)
Cobrepampa	IOCG s.s.	5	2	-	Injoque (2002)
Cobriza	IOCG-like	100	1.5	-	Injoque (2002)
Eliana	IOCG s.s.	0.5	2.7	-	Injoque (2002)
Marcona	IOCG s.s.	1,940	0.12	-	Chen et al. (2010)
Mina Justa	IOCG s.s.	346.6	0.71	0.03	Chen et al. (2010)
Monterrosas	IOCG s.s.	1.9	1.6	-	Injoque (2002)
Pampa de Pongo	IOCG s.s.	953	<0.1	-	Chen et al. (2010)
Raúl-Condestable	IOCG s.s.	32	1.7	0.3	de Haller et al. (2006)
Raúl-Condestable	IOCG s.s.	25	1.7	0.9	de Haller et al. (2002)
Santiago (Veta Gallinazos)	IOCG-like	0.001	5.09	-	Acosta (2006)
Valparaiso (Veta Mina Antigua)	IOCG-like	0.13	3.5	-	Acosta (2006)
NORTH AMERICA					
Great Bear Magmatic Zone, Canada – Subduction [d]					
NICO	IOCG-like	33	1.02	0.04	Acosta-Góngora et al. (2018)
NICO	IOCG-like	33.077	0.04	1.07	Burgess et al. (2014)
NICO	IOCG-like	31	0.04	0.91	Montreuil et al. (2013)
Sue Dianne	IOCG s.s.	8.4	0.8	0.07	Hennessey & Puritch (2008)
SE Missouri Fe Metallogenetic Province, USA – Controversial [e]					
Boss-Bixby	IOCG-like	40	0.8	-	Day et al. (2011)
Pea Ridge	IOCG-like	40	0.83	-	Mercer et al. (2020)
Pumpkin Hollow	IOCG-like	312	0.44	-	Gander et al. (2007)
OCEANIA					
Gawler Craton, Australia – Post-Subduction [f]					
Olympic Dam	IOCG s.s.	10,892	0.73	0.31	Courtney-Davies et al. (2020)
Olympic Dam	IOCG s.s.	9,576	0.82	0.31	Zhu (2016)
Olympic Dam	IOCG s.s.	10,100	0.78	1	Cherry et al. (2018)
Prominent Hill	IOCG s.s.	140	1.2	0.5	Baudet et al. (2020)
Prominent Hill	IOCG s.s.	283	0.89	0.81	Hayward & Skirrow (2010)
Prominent Hill	IOCG s.s.	278	0.98	0.75	Freeman & Tomkinson (2010)
Cairn Hill	IOCG-like	11.4	0.37	0.11	Hayward & Skirrow (2010)
Oak Dam	IOCG s.s.	300	0.2	-	COHIBA (2018); INVESTSA (2016)
Khamsin	IOCG-like	206	0.6	-	COHIBA (2018); INVESTSA (2016)
Carrapateena	IOCG-like	800	0.8	0.3	COHIBA (2018); INVESTSA (2016)
Hillside	IOCG s.s.	337	0.6	0.14	INVESTSA (2016)
Moonta-Wallaroo	IOCG s.s.	10.1	3.7	0.42	Ehrig et al. (2012)
Emmie Bluff	IOCG-like	25	1.3	-	Argoexploration, 2006
Mutooroo	IOCG-like	13.1	1.48	-	INVESTSA (2016)
Kalkaroo	IOCG-like	124	0.5	0.39	INVESTSA (2016)

ESM – Table 1. (continued)

Deposit	Classification	Tonnage (Mt)	Cu (%)	Au (g/t)	Reference
North Portia	IOCG-like	11.3	0.899	0.64	INVESTSA (2016)
Kanmantoo	IOCG-like	31.3	0.78	0.2	INVESTSA (2016)
Mt. Isa Inlier, Australia – Post-collision [g]					
Mt. Isa	IOCG s.s.	250	3.3	-	Maiden & Hughes (2000)
Ernest Henry	IOCG s.s.	167	1.1	0.54	Mark et al. (2006)
Ernest Henry	IOCG s.s.	89.8	1.17	0.6	Valenta (2018)
Turpentine	IOCG-like	5.6	0.94	0.2	EXCO Resource (2012a)
E1	IOCG s.s.	10.1	0.73	0.22	Case et al. (2017)
E1	IOCG s.s.	47	0.71	0.21	Williams et al. (2015)
Monakoff	IOCG s.s.	1.5	1.39	0.44	Williams et al. (2015)
Eloise	IOCG s.s.	3.2	5.8	1.5	William & Skirrow (2000)
Roseby Corredor	IOCG s.s.	132	0.7	0.06	Porter (2010)
Starra/Selwvn	IOCG s.s.	253	0.34	0.48	Zhu (2016)
Starra	IOCG s.s.	37.4	1.2	1.2	Duncan et al. (2011)
Trekelano	IOCG-like	3.1	2.1	0.64	GBM Resources Limited (2006)
Osborne	IOCG-like	27	1.4	0.8	Porter (2010)
Mount Elliot	IOCG-like	570	0.44	0.26	Duncan et al. (2014)
Mount Dore	IOCG s.s.	26	1.1	5.5	William & Skirrow (2000)
Greenmount	IOCG-like	3.6	1.5	0.78	William & Skirrow (2000)
Rocklands	IOCG-like	55.4	0.64	0.15	Cudeco (2017)
Great Australia	IOCG s.s.	1.7	1.2	-	William & Skirrow (2000)
Lady Ella	IOCG-like	0.7	1.5	1.3	Duncan et al. (2011)
SWAN	IOCG-like	340	0.5	0.3	Duncan et al. (2011)
Kangaroo rat	IOCG-like	1.26	1.29	-	EXCO Resource (2012b)
Mayfield	IOCG-like	3.1	2.1	0.64	GBM Resources Limited (2006)
Tennant Creek Inlier, Australia – Rift [h]					
Juno	IOCG-like	0.45	0.33	56.1	Porter (2010)
Peko	IOCG-like	3.2	4	-	Haynes et al. (2020)
Warrego	IOCG-like	6.95	2	6.6	Porter (2010)
Aileron Province, Australia – Subduction [i]					
Bellbird	IOCG-like	3.9	1.2	0.08	Huston et al. (2012)
Bellbird North	IOCG-like	0.305	0.72	0.27	Huston et al. (2012)
Green Parrot	IOCG-like	0.689	0.97	0.94	Huston et al. (2012)
Reward	IOCG-like	7	1.3	0.28	Huston et al. (2012)
EUROPE					
Fennoscandian Shield, Sweden – Subduction [j]					
Aitik	IOCG s.s.	606	0.38	0.21	Edfelt et al. (2004)
Gruvberget Cu	IOCG s.s.	0.2	0.5	-	Edfelt et al. (2005)
Hannukainen	IOCG s.s.	170.7	0.2	0.1	Edfelt et al. (2004)
Kiskamavaara	IOCG s.s.	3.4	0.37	-	Edfelt et al. (2005)
Minto	IOCG s.s.	19.3	1.42	0.51	Hood et al. (2009)
Nautanen	IOCG s.s.	0.63	2.4	1.3	Martinson & Aaltonen (2004)
Pahtohavare	IOCG s.s.	1.68	1.89	0.88	Edfelt et al. (2005)
Pikkujãrvi	IOCG s.s.	5	0.61	-	Edfelt et al. (2005)
Rakkurijärvi-Cu	IOCG s.s.	1.4	0.25	-	Smith et al. (2007)
Slab	IOCG s.s.	20	0.35	0.17	Thorkelson et al. (2003)
Tjårrojåkka Cu	IOCG-like	3.23	0.87	-	Edfelt et al. (2005)
Viscaria	IOCG s.s.	12.54	2.29	-	Measurel (2011)
Lapland Greenstone Belt, Finland – Rift [k]					
Hannukainen (Laurinoja)	IOCG s.s.	187	0.18	-	Niiranen et al. (2007)
Rautavaara	IOCG s.s.	13.3	0.2	-	Niiranen et al. (2007)
Rautavaara Cu	IOCG s.s.	2.6	0.48	-	Niiranen et al. (2007)
Kuervitikko	IOCG s.s.	1.2	0.3	-	Niiranen et al. (2007)
Rautuoja	IOCG s.s.	1.9	0.19	-	Niiranen et al. (2007)
Lauttaselkä	IOCG s.s.	0.6	0.23	-	Niiranen et al. (2007)
Turkish Tethyan Collage, Turkey – Subduction [l]					
Bakirlik Hill (Şamlı)	IOCG-like	0.096	1	-	Kuşcu et al. (2010)
Divritji A-B Kafa (Sivas)	IOCG-like	133.8	0.5	-	Kuşcu et al. (2010)
Hasangelebi (Malatya)	IOCG-like	94.8	1.775	0.04	Kuşcu et al. (2010)
Variscan Iberian Massif, Spain – Rift [m]					
Bilbaina	IOCG-like	7.85	0.11	-	Tornos et al. (2004)
Boleo	IOCG-like	445	0.71	-	Conly et al. (2001)
Cala	IOCG-like	50	0.4	-	Tornos et al. (2005)
Cala	IOCG-like	60	0.27	-	Tomé et al. (2009)

ESM – Table 1. (continued)

Deposit	Classification	Tonnage (Mt)	Cu (%)	Au (g/t)	Reference
Herrerias	IOCG-like	12	0.3	-	Tornos et al. (2005)
Aguablanca	IOCG-like	17	0.47	-	Tornos et al. (2005)
Sultana	IOCG-like	1	3	-	Tornos et al. (2005)
Srednogorie Belt, Bulgaria – Rift [n]					
Rosen	IOCG-like	15	1.04	-	Sillitoe et al. (2020)
AFRICA					
Pan-African Mauritanides Belt, Mauritania – Rift [o]					
Guelb Moghrein	IOCG-like	33.4	1.12	1.41	Kolb et al. (2010)
Kaapval Craton, South Africa – Post-collision [p]					
Phalaborwa	IOCG-like	1200	0.59	-	Porter (2010)
Damara-Lufilian-Zambezi Orogenic System, Namibia-Zambia – Rift [q]					
Kitumba	IOCG-like	27.9	2.2	0.03	Milani et al. (2019)
Chimiwungo	IOCG-like	761	0.64	-	Zhu (2016)
Malundwe	IOCG-like	162	0.89	-	Zhu (2016)
Kitumba	IOCG-like	38.8	2.19	-	Woolrych et al. (2015)
Mumbwa	IOCG-like	87	0.94	0.05	Porter (2010)
Kombat	IOCG-like	12	2.94	-	Maiden & Hughes (2000)
Kalengwa	IOCG-like	1.6	6.5	-	Nisbet et al. (2000)
Sassare	IOCG-like	1.4	1.2	-	Nisbet et al. (2000)
Nampundwe	IOCG-like	23	0.79	-	Lobo-Guerrero (2004)
Witvlei	IOCG-like	13	1.85	-	Diggers & Dealers (2010)
Shituru	IOCG-like	0.085	2	-	Lobo-Guerrero (2004)
Luiswishi	IOCG-like	8	2.5	-	Lobo-Guerrero (2004)
Kamoya	IOCG-like	1.2	2.5	-	Lobo-Guerrero (2004)
Oamites	IOCG-like	6.5	1.3	-	Diggers & Dealers (2010)
Tsumeb	IOCG-like	72	4.3	-	Diggers & Dealers (2010)
Boseto	IOCG-like	103	1.4	-	Diggers & Dealers (2010)
Dorbadis	IOCG-like	2	0.98	-	Diggers & Dealers (2010)
Klein	IOCG-like	5.5	2	-	Diggers & Dealers (2010)
ASIA					
Yangtze Block, Vietnam – Subduction [r]					
Sin Quyen	IOCG-s.s.	52.8	0.91	-	Ngo et al. (2020)
Sin Quyen	IOCG-s.s.	52.8	0.91	-	Zhimin & Yali (2013)
Kangdian Belt, China – Rift [s]					
Yinachang	IOCG-s.s.	3.74	1	-	Zhu et al. (2020)
Dahongshan	IOCG s.s.	192	0.9	0.18	McLean & Porter (2001)
Lala	IOCG-s.s.	106	0.87	0.19	Zhao & Zhou (2010)
Luodang (Lala)	IOCG-s.s.	73.55	0.83	0.16	Zhu et al. (2017)
Laoyanghantan (Lala)	IOCG-s.s.	24.72	1	0.29	Zhu et al. (2017)
Shilong (Lala)	IOCG-like	6.33	0.84	-	Zhu et al. (2017)
Laohushan(Lala)	IOCG-like	1.85	0.73	-	Zhu et al. (2017)
Changpuqing (Lala)	IOCG-like	4.33	0.7	-	Zhu et al. (2017)
Hongnipo (Lala)	IOCG-s.s.	44.37	1.42	0.1	Zhu et al. (2017)
Yinachang-Cu	IOCG-like	15	0.85	-	Li et al. (2015)
Bastar Craton, India – Post-collision [t]					
Thanewasna	IOCG-like	6.64	0.89	-	Dora et al. (2017)
Khetri Copper Belt, India – Post-collision [u]					
Khetri	IOCG-like	140	1.1	0.5	Knight et al. (2002)
Madhan Kudhan (Khetri)	IOCG-like	66	1.12	0.2	Knight et al. (2002)
Kolihan-Chandmari (Khetri)	IOCG-like	40	1.14	0.2	Knight et al. (2002)
Banwas (Khetri)	IOCG-like	30	1.7	0.5	Knight et al. (2002)
Bhukia	IOCG-like	105.81	0.15	1.97	Mukherjee & Venkatesh (2017)

Tectonic environment references: **a.** Mentioned in the text. **b.** Huhn et al. (2011); **c.** Sillitoe (2003); **d.** Ootes et al. (2017); **e.** Skirrow et al. (2018); **f.** Nold et al. (2014); **g.** Chen (2013); **h.** Duggan & Jaques (1996); **i.** Champion (2013); j. Weihed et al. (2005); **k.** Niiranen (2005); **l.** Kuşcu et al. (2010); **m.** Bellido et al. (2010); **n.** Sillitoe et al. (2020); **o.** Meyer et al. (2006); **p.** Vielreicher et al. (2000); **q.** Sanz (20005); **r.** Ngo et al. (2020); **s.** Zhu et al. (2020); **t.** Dora et al. (2017); **u.** Knight et al. (2002)

Supplementary 1 – References

Acosta, J.A., 2006. Características Metalogéneticas de los Yacimientos Asociados a los Arcos Magmáticos Mesozoicos y Cenozoicos del Sur del Perú (Latitudes 16°-18°30′). Instituto geológico minero y metalúrgico dirección de geología económica y prospección. Republica del Perú, sector energia y minas, pp. 1-32.

Acosta-Góngora, P., Gleeson, S.A., Samson, I.M., Corriveau, L., Ootes, L., Jackson, S.E., Taylor, B.E., Girard, I., 2018. Origin of sulfur and crustal recycling of copper in polymetallic (Cu-Au-Co-Bi-U ± Ag) iron-oxide-dominated systems of the Great Bear Magmatic Zone, NWT, Canada. Miner. Deposita 53, 353–376. https://doi.org/10.1007/s00126-017-0736-6

Argoexploration (2006), prospectus. 1-41

AVANCOCOPPER., 2018. Techinal Report, Maiden Pantera MRE pushes Avanco's Carajás Resource Base Beyond 1 Mt of Contained Copper. 1-23.

Barton, M.D., Johnson, D.A., Kreiner, D.C., Jensen, E.P., 2013. Vertical zoning and continuity in Fe oxide (-Cu-Au-Ag-Co-UP-REE)(or 'IOCG') systems: Cordilleran insights. Proceedings of the 12th SGA Biennial Meeting, Uppsala, Sweden, 1348–1351.

Baudet, E., Giles, D., Tiddy, C., Asamoah, R., Hill, S., 2020. Mineralogy as a proxy to characterise geochemical dispersion processes: A study from the Eromanga Basin over the Prominent Hill IOCG deposit, South Australia. J. Geochem. Explor. 210, 106447. https://doi.org/10.1016/j.gexplo.2019.106447

Bellido, F., Díez-Montes, A., Sánchez-García, T., 2010. Caracterización geoquímica y estudio comparativo de plagiogranitos de las Zonas Surportuguesa y Ossa-Morena (SO del Macizo Ibérico, España). Estudios Geológicos 66, 3-23.

Benavides, J., Kyser, T.K., Clark, A.H., Oates, C.J., Zamora, R., Tarnovschi, R., Castillo, B., 2007. The Mantoverde Iron Oxide-Copper-Gold District, III Región, Chile: The Role of Regionally Derived, Nonmagmatic Fluids in Chalcopyrite Mineralization. Econ. Geol.102, 415–440. doi: https://doi.org/10.2113/gsecongeo.102.3.415

Boric, R., Holmgren, C., Wilson, N.S.F., Zentilli, M. 2002. The Geology of El Soldado Manto Type Cu (Ag) Deposit, Central Chile, in: Porter, T.M. (Ed.), Hydrothermal Iron Oxide Copper-Gold & Related Deposits: A Global Perspective, Second Edition. PGC Publishing, Adelaide, pp. 163–184.

Burgess, H., Gowans, R.M., Hennessey, B.T., Lattanzi, C.R., Puritch, E. 2014. Technical report on the feasibility study for the NICO gold–cobalt–bismuth–copper deposit, Northwest Territories, Canada. Fortune Minerals Ltd., NI 43-101 Technical Report No. 1335.

Case, G., Blenkinsop, T., Chang, Z., Huizenga, J.M., Lilly, R., McLellan, J., 2018. Delineating the structural controls on the genesis of iron oxide–Cu–Au deposits through implicit modelling: a case study from the E1 Group, Cloncurry District, Australia. Geol. Soc. Spec. Publ. 453, 349–384. https://doi.org/10.1144/SP453.4

Champion, D.C. 2013. Neodymium depleted mantle model age map of Australia: explanatory notes and user guide. Record 2013/44. Geoscience Australia, Canberra. https://doi.org/10.11636/Record.2013.044

Chen, H., 2008. The Marcona-Mina Justa district, south-central Peru: Implications for the genesis and definition of the iron oxide-copper (-gold) ore deposit clan. PhD. dissertation. Queen's University, Canada.

Chen, H., 2013. External sulphur in IOCG mineralization: Implications on definition and classification of the IOCG clan. Ore Geol. Rev. 51, 74–78. https://doi.org/10.1016/j.oregeorev.2012.12.002

Chen, H., Clark, A.H., Kyser, T.K., Ullrich, T.D., Baxter, R., Chen, Y., Moody, T.C., 2010. Evolution of the giant Marcona-Mina Justa iron oxide-copper-gold district, south-central Peru. Econ. Geol. 105, 155–185. https://doi.org/10.2113/gsecongeo.105.1.155

Cherry, A.R., Ehrig, K., Kamenetsky, V.S., McPhie, J., Crowley, J.L., Kamenetsky, M.B., 2018. Precise geochronological constraints on the origin, setting and incorporation of ca. 1.59 Ga surficial facies into the Olympic Dam Breccia Complex, South Australia. Precambrian Res. 315, 162–178. https://doi.org/10.1016/j.precamres.2018.07.012

COHIBA., 2018. Commencement of Exploration Program & Appointment of Geophysical Consultant, COMPANY ANNOUNCEMENTS OFFICE ASX LIMITED, 1-6.

Conly, A.G., Scott, S.D., Bellón, H., Beaudoin, G., 2001. The Boléo Cu-Co-Zn deposit, Baja California sur, Mexico: The role of magmatic fluids in the genesis of synsedimentary deposit. In: Piestrzyñski (Eds.), Mineral Deposits at the Beginning of the 21st Century, Krakóv, 223–226.

Courtney-Davies, L., Ciobanu, C.L., Tapster, S.R., Cook, N.J., Ehrig, K., Crowley, J.L., Verdugo-Ilh, M.R., Wade, B.P., Condon, D.J., 2020. Opening the magmatic-hydrothermal window: High-precision U-Pb geochronology of the Mesoproterozoic Olympic Dam Cu-U-Au-Ag deposit, South Australia. Econ. Geol, 1–16. https://doi.org/10.5382/econgeo.4772

Couture, J.-F., Cole, G., Zhang, B., Nilsson, J., Dance, A., Scott, C., Vidal, M.I., 2017. Technical Report for the Candelaria Copper Mining Complex, Atacama Province, Region III, Chile, pp. 43–101 Report. Prepared for Lundin Mining Corporation.

Couture, J.-F., Cole, G., Zhang, B., Scott, C.C., Kautzman, S., Nilsson, J., Dance, A., Vidal, M.I., 2018. Technical Report for the Candelaria Copper mining complex, Atacama region, Region III, Chile. SRK Consulting 3CL014.002.

Cudeco, 2017, Annual Rocklands resource update – 2017: Market release 31 October 2017.

da Costa Silva, A.R., Villas, R.N.N., Lafon, J.M., Craveiro, G.S., Ferreira, V.P., 2015. Stable isotope systematics and fluid inclusion studies in the Cu–Au Visconde deposit, Carajás Mineral Province, Brazil: implications for fluid source generation. Miner. Deposita 50, 547–569. https://doi.org/10.1007/s00126-014-0558-8

Daroch, G., Anguita, N., Cortes, M., 2015. Geología y zonación hidrotermal del depósito Fe (-Cu-Au) Santo Domingo, Región de Atacama-Chile. In XIV Congreso Geológico Chileno, La Serena, Chile, 433–436.

Daroch, G.A., Barton, M.D., 2011. Hydrothermal alteration and mineralization in Santo Domingo Sur iron oxide (-Cu-Au)(IOCG) deposit, Atacama Region, Chile. Proceedings of the 11th SGA Biennial meeting, Antofagasta, Chile, 488–490.

Day, W.C., Seeger, C.M., Rye, R.O., 2001. Review of the iron oxide deposits of Missouri; magmatic end members of the iron oxide–Cu–Au–U–REE deposit family. Proceedings of the 33th GSA annual meeting, Boston, USA, 4.

de Haller, A., Corfu, F., Fontboté, L, Schaltegger, U, Barra, F., Chiaradia, M., Frank, M., Alvarado, J.Z., 2006. Geology, geochronology, and Hf and Pb isotope data of the Raúl-Condestable iron oxide-copper-gold deposit, central coast of Perú. Econ. Geol. 101, 281–310. https://doi.org/10.2113/gsecongeo.101.2.281

de Haller, A., Zúñiga, A. J., Corfu, F., and Fontboté, L., 2002. The iron oxide-Cu-Au deposit of Raúl-Condestable, Mala, Lima, Peru. XI Congreso Geológico Peruano, Lima, Peru, 80.

de Melo, G.H., Monteiro, L.V., Xavier, R.P., Moreto, C.P., Santiago, E., 2019a. Tracing Fluid Sources for the Salobo and Igarapé Bahia Deposits: Implications for the Genesis of the Iron Oxide Copper-Gold Deposits in the Carajás Province, Brazil. Econ. Geol. 114, 697–718. https://doi.org/10.5382/econgeo.4659

de Melo, G.H.C., Xavier, R.P., Toledo, P.I.F., 2019c. IOCG Systems of the Carajás Province, Amazon Craton, Northern Brazil. Guidebook SEG Conference Field Trip September 29–October 4.

del Real, I., Thompson, J.F., Carriedo, J., 2018. Lithological and structural controls on the genesis of the Candelaria-Punta del Cobre Iron Oxide Copper Gold district, Northern Chile. Ore Geol. Rev. 102, 106–153. https://doi.org/10.1016/j.oregeorev.2018.08.034

Diggers & Dealers., 2010. Copper-REE Namibia Africa. Cullen Resources Limited.

Dora, M.L., Randive, K.R., Ramachandra, H.M., Suresh, G., 2017. Iron oxide–copper–gold mineralization at Thanewasna, Western Bastar Craton. Curr. Sci 112, 10. 1045–1050.

"Duggan, M.B., Jaques, A.L., 1996. Mineralogy and geochemistry of Proterozoic shoshonitic lamprophyres from the Tennant Creek Inlier, northern territory. Aust. J. Earth Sci. 43, 269–278. https://doi.org/10.1080/08120099608728254 "

Duncan, R.J., Hitzman, M.W., Nelson, E.P., Togtokhbayar, O., 2014. Structural and Lithological Controls on Iron Oxide Copper-Gold Deposits of the Southern Selwyn-Mount Dore Corridor, Eastern Fold Belt, Queensland, Australia. Econ. Geol.109, 419–456. https://doi.org/10.2113/econgeo.109.2.419

Duncan, R.J., Stein, H.J., Evans, K.A., Hitzman, M.W., Nelson, E.P., Kirwin, D.J., 2011. A new geochronological framework for mineralization and alteration in the Selwyn-Mount Dore corridor, Eastern fold belt, Mount Isa inlier, Australia: Genetic implications for iron oxide copper-gold deposits. Econ. Geol. 106, 169–192. https://doi.org/10.2113/econgeo.106.2.169

Edfelt, Å., Armstrong, R.N., Smith, M., Martinsson, O., 2005. Alteration paragenesis and mineral chemistry of the Tjårrojåkka apatite–iron and Cu (-Au) occurrences, Kiruna area, northern Sweden. Miner. Deposita, 40, 409–434. https://doi.org/10.1007/s00126-005-0005-y

Edfelt, A., Eilu, P., Martinsson, O., Niiranen, T., Weihed, P., 2004. The Northern Fennoscandia IOGC-province. SGA News 18, 4–9.

Ehrig, K., McPhie, J., Kamenetsky, V.S., 2012.Geology and mineralogical zonation of the Olympic Dam Iron Oxide Cu-U-Au-Ag deposit, South Australia, in: Hedenquist, J.M., Harris, M., Camus, F. (Eds.), Geology and Genesis of Major Copper Deposits and Districts of the World: A Tribute to Richard H. Sillitoe, Volume 16. Society of Economic Geologists, Inc. Littleton, Colorado, pp. 237–267.

Escolme, A., Cooke, D.R., Hunt, J., Berry, R.F., Maas, R., Creaser, R.A., 2020. The Productora Cu-Au-Mo Deposit, Chile: A Mesozoic Magmatic-Hydrothermal Breccia Complex with Both Porphyry and Iron Oxide Cu-Au Affinities. Econ. Geol. 115, 534–580. https://doi.org/10.5382/econgeo.4718

Escolme, A., Halley, S., Potma, W., 2015. The Productora Cu-Au-Mo Deposit, Chile. Proceedings of the 16th Biennial SGA meeting, Nancy, France, 287–290.

EXCO Resource., 2012b. KANGAROO RAT PROJECT UPDATE, pp. 1-11.

EXCO Resources., 2012a. TURPENTINE RESOURCE UPDATE, pp. 1–10.

Freeman, H., Tomkinson, M., 2010. Geological setting of iron oxide related mineralisation in the southern Mount Woods domain, South Australia, in: Porter, T.M. (Ed.), Hydrothermal Iron Oxide Copper-Gold and Related Deposits: A Global Perspective, Third Edition. PGC Publishing, Adelaide, PGC Publishing, pp. 171–190.

Gander, M.J., French, G.M., Ohlin, H., 2007. The geology and mineralization of the Pumpkin Hollow Cu-Fe-Au deposit, Yerington, Lyon County, Nevada. Proceedings of the 39th SGA annual meeting, Denver, USA, 626.

GBM Resources Limited., 2006. Other projects, pp. 1-4.

Haynes, M., Walsh, S.D.C., Czarnota, K., Northey, S.A., Yellishetty, M., 2020. Economic fairways assessments across northern Australia. Exploring for the Future. Extended abstracts, Geoscience Australia, Canberra, Australia, 1–4.

Hayward, N., Skirrow, R., 2010. Geodynamic setting and controls on iron oxide Cu–Au (±U) ore in the Gawler Craton, South Australia, in: Porter, T.M. (Ed.), Hydrothermal Iron Oxide Copper-Gold and Related Deposits: A Global Perspective, Third Edition. PGC Publishing, Adelaide, pp. 119–146.

Hennessey, B.T., Puritch, E., 2008. A technical report on a mineral resource estimate for the Sue-Dianne deposit, Mazenod Lake area, Northwest Territories, Canada. Fortune Minerals Limited, Technical Report.

Herrera, V., Garmendia, P., Pizarro, R., 2008. Proyecto Diego de Almagro: Geología y mineralización tipo IOCG, Región de Atacama, Norte de Chile. XIII Congreso Latinoamericano de Geología, Lima, Peru, 1–6.

Hood, S., Hickey, K., Colpron, M. Mercer, B., 2009. High-grade hydrothermal copper-gold mineralization in foliated granitoids at the Minto mine, central Yukon, in: Weston, L.H., Blackburn, L.R., Lewis, L.L. (Eds.), Yukon Exploration and Geology. Yukon Geological Survey, pp. 137–146.

Hopper, D., Correa, A., 2000. The Panulcillo and Teresa de Colmo copper deposits: two contrasting examples of Fe-ox-Cu-Au mineralisation from the Coastal Cordillera of Chile, in: Porter, T.M. (Ed.), Hydrothermal Iron Oxide Copper-Gold & Related Deposits: A Global Perspective, First Edition. PGC Publishing, Adelaide, pp. 179–189.

Huhn, S.R.B., Macambira, M.J.B., Dall'Agnol, R., 1999a. Geologia e geocronologia Pb-Pb do granito alcalino arqueano Planalto, região da Serra do Rabo, Carajás-PA. VI Simpósio de Geologia da Amazônia, Belém, Brazil, 463–466.

Huhn, S.R.B., Justo, A.P., de Souza Filho, C.R., Monteiro, L.V.S., 2011. Caracterização geológica do prospecto de óxido de ferro-cobre-ouro (IOCG) Aurora, Ceará, Brasil. Braz. J. Geol. 41, 525–538.

Huhn, S.R.B., Silva, A.M., 2018. Favorability potential for IOCG type deposits in the Riacho do Pontal Belt: new insights for identifying prospects of IOCG-type deposits in NE Brazil. Braz. J. Geol. 48, 703–719. https://doi.org/10.1590/2317-4889201820180029

Huhn, S.R.B., Sousa, M.J., Souza Filho, C.R.D., Monteiro, L.V.S., 2014. Geology of the Riacho do Pontal iron oxide copper-gold (IOCG) prospect, Bahia, Brazil: hydrothermal alteration approached via hierarchical cluster analysis. Braz. J. Geol. 44, 309–324. https://doi.org/10.5327/Z2317-4889201400020010

Hunger, R.B., Xavier, R.P., Moreto, C.P.N., Gao, J.F., 2018. Hydrothermal Alteration, Fluid Evolution, and Re-Os Geochronology of the Grota Funda Iron Oxide Copper-Gold Deposit, Carajás Province (Pará State), Brazil. Econ. Geol. 113, 1769–1794.https://doi.org/10.5382/econgeo.2018.4612

Huston, D.L., Whelan, J.A., Schofield, A., Chopping, R.G., Gallagher, R.G., 2012. Uranium-rich Iron oxide copper-gold systems, in: Schofield, A. (Ed.), An assessment of the uranium and geothermal prospectivity of the southern Northern Territory. Geoscience Australia, Canberra, pp. 45–156.

Ichii, Y., Abe, A., Ichige, Y., Matsunaga, J., Miyoshi, M., 2007. Copper exploration of the Atacama Kozan Mine, Region III. 資源地質 57, 1–14. https://doi.org/10.11456/shigenchishitsu1992.57.1

Injoque, J., 2002, Fe oxide-Cu-Au deposits in Peru: An integrated view, in: Porter, T.M. (Ed.), Hydrothermal Iron Oxide Copper-Gold & Related Deposits: A Global Perspective, Second Edition. PGC Publishing, Adelaide, pp. 97–113.

INVESTSA., 2016. Copper in South Australia, pp. 48. http://australiaminerals.gov.au/__data/assets/pdf_file/0004/47623/Copper-in-South-Australia.pdf

Jesus, S.S.G.P., 2016. Múltiplos estágios de alteração hidrotermal do depósito de óxido de ferro-cobre-ouro Furnas, Província Carajás: Evolução paragenética e química mineral: MSc. thesis. University of São Paulo, Brazil.

Knight, J., Joy, S., Cameron, J., Merrillees, J., Nag, S., Shah, N., Dua, G., Jhala., 2002. The Khetri Copper Belt, Rajasthan. Iron Oxide Copper-Gold Terrane in the Proterozoic of NW India, in: Porter, T.M. (Ed.), Hydrothemal Iron Oxide Copper-Gold & Related Depoits, Second Edition. PGC Publishing, Adelaide, pp .321–341.

Kolb, J., Meyer, F.M., Vennemann, T.S., Sindern, S., Prantl, S., Bottcher, M.E., Sakellaris, G.A., 2010. Characterisation of the hydrothermal fluids of the Guelb Moghrein Iron Oxide-Cu-Au-Co deposits, Mauritania: ore mineral chemistry, Fluid inclusions and isotope geochemistry, in: Porter, T.M. (Ed.), Hydrothermal iron oxide copper-gold and related deposits: A global perspective, fourth edition. PGC Publishing, Adelaide, pp. 553–572.

Kuşcu, İ., Yılmazer, E., Demirela, G., Gençalioğlu-Kuşcu, G., Güleç, N., 2010. Iron oxide-(copper±gold) mineralisation in the Turkish Tethyan collage, in: Porter, T.M. (Ed.), Hydrothermal iron oxide copper-gold and related deposits: A Global Perspective, Third Edition. PGC Publishing, Adelaide, pp. 1–23.

Lancaster-Oliveira, J.A., Fanton, J., Almeida, A.J., Leveille, R.A., Vieira, S., 2000. Discovery and geology of the Sossego copper–gold deposit, Carajás District, Pará State, Brazil. IUGS, Intern. Geol. Congr., 31 [CD-ROM].

Leszcyński, R., Hardy, S., Lipień, G., 2015. Mineral resources and reserves report. KGHM Polska Miedź, 1–38.

Li, X., Zhao, X., Zhou, M.F., Chen, W. T., Chu, Z., 2015. Fluid inclusion and isotopic constraints on the origin of the Paleoproterozoic Yinachang Fe-Cu-(REE) Deposit, Southwest China. Econ. Geol. 110, 1339–1369. https://doi.org/10.2113/econgeo.110.5.1339

Lindenmayer, Z.G., Pimentel, M.M., Ronchi, L.H., Althoff, F.J., Laux, J.H., Araújo, J.C., Fleck, A., Bartowski, D.C., Nowatzski, A.C., 2001.Geologia do depósito de Cu–Au de Gameleira, Serra dos Carajás, Pará, in: Jost, H., Brod, J.A., Queiroz, E.T. (Eds.), Caracterização de depósitos Auríferos Brasileiros. ADIMB-DNPM, Brasília, pp. 79–139.

Lobo-Guerrero, A., 2004. Granitoid-related iron-oxide-copper-gold mineralisation, Greater Lufilian Arc, Zambia and Namibia. Proceedings of SEG Conference, Perth, Australia.

Lopez, G.P., Hitzman, M.W., Nelson, E.P., 2014. Alteration patterns and structural controls of the El Espino IOCG mining district, Chile. Miner. Deposita, 49, 235–259. https://doi.org/10.1007/s00126-013-0485-0

Maiden, K., Hughes, M., 2000. Mount Isa and Tsumeb: a comparative metallogenic study. Communications, Geological Survey of Namibia 12, 167–177.

Mark, G., Oliver, N.H., Williams, P.J., 2006. Mineralogical and chemical evolution of the Ernest Henry Fe oxide–Cu–Au ore system, Cloncurry district, northwest Queensland, Australia. Miner. Deposita 40, 769–801. https://doi.org/10.1007/s00126-005-0009-7

Marschik, R., Fontboté, L., 2001a. The Candelaria-Punta del Cobre Iron Oxide Cu-Au(-Zn-Ag) Deposits, Chile. Econ. Geol. 96, 1799–1826. https://doi.org/10.2113/gsecongeo.96.8.1799

Martinsson, O., Aaltonen, R., 2004. Locality 4. Gällivare, in: Eilu, P. (Ed.), Iron oxide-copper gold excursion and workshop to Northern Finland and Sweden 31.5.–4.6.2004. Geological Survey of Finland Report M10.3/2004/1/10. 75-84.

Masurel, Q., 2011. Volcanic and volcano-sedimentary facies analysis of the Viscaria D-zone Fe-Cu occurrence, Kiruna district, northern Sweden. MSc. thesis. Luleå University of Technology, Sweden.

McLean, R.N., Porter, T.M., 2001. The Sin Quyen iron oxide-copper-gold-rare earth oxide mineralization of North Vietnam, in: Porter, T.M. (Ed.), Hydrothermal iron oxide copper-gold & related deposits: A global perspective, Second Edition. PGC Publishing, Adelaide, 293–301.

Mercer, C.N., Watts, K.E., Gross, J., 2020. Apatite trace element geochemistry and cathodoluminescent textures—A comparison between regional magmatism and the Pea Ridge IOA-REE and Boss IOCG deposits, southeastern Missouri iron metallogenic province, USA. Ore Geology Rev. 116, 103129. https://doi.org/10.1016/j.oregeorev.2019.103129

Meyer, F.M., Kolb, J., Sakellaris, G.A., Gerdes, A., 2006. New ages from the Mauritanides Belt: recognition of Archean IOCG mineralization at Guelb Moghrein, Mauritania. Terra Nova 18, 345–352. https://doi.org/10.1111/j.1365-3121.2006.00698.x

Milani, L., Lehmann, J., Naydenov, K.V., Saalmann, K., Nex, P.A.M., Kinnaird, J.A., Friedman, I.S., Woolrych, T., Selley, D., 2019. Geology and mineralization of the Cu-rich Mumbwa district, a potential IOCG-type system at the eastern margin of the Pan-African Hook batholith, Zambia. J. Afr. Earth Sci. 158, 103513. https://doi.org/10.1016/j.jafrearsci.2019.103513

Mizuno, T.A., 2009. Alteração hidrotermal e paragênese de minério do depósito de óxido de Fe–Cu–Au (IOCG) Pedra Branca, Província Mineral de Carajás. Honour thesis. University of Campinas, Brazil.

Monteiro, L.V.S., Xavier, R.P., de Carvalho, E.R., Hitzman, M.W., Johnson, C.A., de Souza, C.R., Torresi, I., 2008a. Spatial and temporal zoning of hydrothermal alteration and mineralization in the Sossego iron oxide-copper–gold deposit, Carajás Mineral Province, Brazil: paragenesis and stable isotope constraints. Miner. Deposita 43, 129–159. https://doi.org/10.1007/s00126-006-0121-3

Montreuil, J.-F., Corriveau, L., Grunsky, E.C., 2013. Compositional data analysis of hydrothermal alteration in IOCG systems, Great Bear magmatic zone, Canada: to each alteration type its own geochemical signature. GEEA 13, 229–247. https://doi.org/10.1144/geochem2011-101

Mukherjee, R., Venkatesh, A.S., 2017. Chemistry of magnetite-apatite from albitite and carbonate-hosted Bhukia Gold Deposit, Rajasthan, western India–An IOCG-IOA analogue from Paleoproterozoic Aravalli Supergroup: Evidence from petrographic, LA-ICP-MS and EPMA studies. Ore Geol. Rev. 91, 509–529. https://doi.org/10.1016/j.oregeorev.2017.09.005

Ngo, X.D., Zhao, X.-F., Thanh Hai, T., Deng, X.-D., Li, J.-W., 2020. Two episodes of REEs mineralization at the Sin Quyen IOCG deposit, NW Vietnam. Ore Geology Reviews, 103676. https://doi.org/10.1016/j.oregeorev.2020.103676

Niiranen, T., 2005. Iron Oxide-Copper-Gold Deposits in Finland: case studies from the Peräpohja schist belt and the Central Lapland greenstone belt. Academic dissertation, University of Helsinki, Finland.

Niiranen, T., Poutiainen, M., Mänttäri, I., 2007. Geology, geochemistry, fluid inclusion characteristics, and U–Pb age studies on iron oxide–Cu–Au deposits in the Kolari region, northern Finland. Ore Geol. Rev. 30, 75–105. https://doi.org/10.1016/j.oregeorev.2005.11.002

Nisbet, B., Cooke, J., Richards, M., Williams, C., 2000. Exploration for iron oxide-copper-gold deposits in Zambia and Sweden: comparison with Australian experience, in Porter, T.M., ed., Hydrothermal Iron Oxide Copper-Gold and Related Deposits: A Global Perspective, First Edition. PGC Publishing, Adelaide, pp. 297–308.

Nold, J.L., Dudley, M.A., Davidson, P., 2014. The Southeast Missouri (USA) Proterozoic iron metallogenic province—Types of deposits and genetic relationships to magnetite–apatite and iron oxide–copper–gold deposits. Ore Geol. Rev. 57, 154–171. https://doi.org/10.1016/j.oregeorev.2013.10.002

Nunes, A.R., Rego, J.L., Meireles, H.P., Carvalho, J.B., Lima da Silva, P.E., Siqueira, J.B., Ferreira, F.J.F., 2001, A descoberta do depósito Breves na Província Mineral de Carajás. VII Simpósio de Geologia da Amazônia, Manaus, Brazil, 72–74.

Ootes, L., Snyder, D., Davis, W. J., Acosta-Góngora, P., Corriveau, L., Mumin, A.H., Gleeson, S.A., Samson, I.A., Montreuil, J-F-., Potter, E., Jackson, V. A., 2017. A Paleoproterozoic Andean-type iron oxide copper-gold environment, the Great Bear magmatic zone, Northwest Canada. Ore Geol. Rev. 81, 123–139. https://doi.org/10.1016/j.oregeorev.2016.09.024

Pinto A. 2012. Salobo Copper Mine Feasibility in Carajás, Pará State. V Brazilian Symposium on Mineral Exploration, Ouro Preto, Brazil.

Porter, T.M., 2010. Current understanding of iron oxide associated-alkali altered mineralised systems. Part 1—An overview, in: Porter, T.M. (Ed.), Hydrothermal Iron Oxide Copper–Gold and Related Deposits: A Global Perspective, Third Edition. PGC Publishing, Adelaide, pp. 5–32.

Rieger, A.A., Marschik, R., Díaz, M., 2012. The evolution of the hydrothermal IOCG system in the Mantoverde district, northern Chile: new evidence from microthermometry and stable isotope geochemistry. Miner. Deposita 47, 359–369. https://doi.org/10.1007/s00126-011-0390-3

Rieger, A.A., Marschik, R., Díaz, M., Hölzl, S., Chiaradia, M., Akker, B., Spangenberg, J.E., 2010. The hypogene iron oxide copper–gold mineralization in the Mantoverde district, Northern Chile. Econ. Geol. 105, 1271–1299. https://doi.org/10.2113/econgeo.105.7.1271

Rigon, J.C., Munaro, P., Santos, L.A., Nascimento, J.A.S., Barreira, C.F., 2000. Alvo 118 copper-gold deposit: Geology and mineralization, Serra dos Carajás. Proceedings of the XXXI International Geology Congress, Rio de Janeiro.

Rivera, S., Cerda, A., Garay, B., Kovacic, P.V., Villegas, P., 2009. Descubrimiento y Geología del Yacimiento tipo IOCG Casualidad. Distrito Sierra Overa, II Región de Antofagasta, Chile. In XII Congreso Geológico Chileno, Santiago, Chile 11–39.

Sanz, A.L.G., 2005. Pre-and post-Katangan granitoids of the Greater Lufilian Arc-geology, geochemistry, geochronology and metallogenic significance. PhD. dissertation. University of the Witwatersrand, South Africa.

Sillitoe, R.H., 2003. Iron oxide-copper-gold deposits: an Andean view. Miner. Deposita 38, 787–812. https://doi.org/10.1007/s00126-003-0379-7

Sillitoe, R.H., Magaranov, G., Mladenov, V., Creaser, R.A., 2020. Rosen, Bulgaria: A Newly Recognized Iron Oxide-Copper-Gold District. Econ. Geol. 115, 481–488. https://doi.org/10.5382/econgeo.4731

Silva, C.M.G., Villas, N.R., 1998. The Águas Claras Cu-sulfide ± Au deposit, Carajás region, Pará, Brazil: geological setting, wall-rock alterationand mineralizing fluids. Braz. J. Geol. 28, 315–326.

Simón, A., Marinho, R., Maycock, J., 2007. Barreal Seco Project II Region, Chile. 43-101 Technical Report and Qualified Person's Review (Update - 28 February 2007).

Skirrow, R.G., Van Der Wielen, S.E., Champion, D.C., Czarnota, K., Thiel, S., 2018. Lithospheric architecture and mantle metasomatism linked to iron oxide Cu-Au ore formation: Multidisciplinary evidence from the Olympic Dam Region, South Australia. Geochem. Geophys. Geosyst. 19, 2673–2705. https://doi.org/10.1029/2018GC007561

Smith, M., Coppard, J., Herrington, R., Stein, H., 2007. The geology of the Rakkurijarvi Cu-(Au) prospect, Norrbotten: A new iron oxide-copper-gold deposit in northern Sweden. Econ. Geol. 102, 393–414. https://doi.org/10.2113/gsecongeo.102.3.393

Souza, L.J., Vieira, E.A., 2000. Salobo 3 Alpha deposit: geology and mineralization, in: Porter, T.M. (Ed.), Hydrothermal Iron Oxide Copper-Gold & Related Deposits: A Global Perspective, First Edition. PGC Publishing, Adelaide, pp. 213–224.

Tallarico, F.H.B., Figueiredo, B.R., Groves, D.I., Kositcin, N., McNaughton, N.J., Fletcher, I.R., Rego, J.L., 2005. Geology and SHRIMP U-Pb geochronology of the igarapé bahia deposit, carajás copper-gold belt, brazil: an archean (2.57 Ga) example of Iron-Oxide Cu-Au-(U-REE) mineralization. Econ. Geol. 100, 7–28. https://doi.org/10.2113/100.1.0007

Thorkelson, D.J., Laughton, J.R., Hunt, J.A., Baker, T., 2003. Geology and mineral occurrences of the Quartet Lakes map area (NTS 106E/1), Wernecke and Mackenzie mountains, Yukon, in: Emond, D.S., Lewis, L.L. (Eds.), Yukon Exploration and Geology 2002. Exploration and Geological Services Division, Yukon Region, Indian and Northern Affairs Canada, pp. 223–239.

Tomé, C.M., Tornos, F., Carriedo, J., Velasco, F. 2009. Hydrothermal Evolution of the IOCG-like Cala Deposit, SW Spain.Proceedings of the 10th Biennial SGA Meeting, Townsville, Australia, 659–661.

Tornos, F., Casquet, C., Rodriguez, P.L., Velasco, F., 2005. 4-2: The iron oxide –(Cu–Au) Deposits of SW Iberia: Fregenal–Burguillos–Cala District: Lat. 38°18' N, Long. 6°40' W, in: Blundell, D., Arndt, N., Cobbold, P.R., Heinrich, C. (Eds.), Geodynamics and Ore Deposit Evolution in Europe, first edition. Ore Geology Reviews. Elsevier Science, Amsterdam, pp. 166–167.

Tornos, F., Oliveira, V., Inverno, C.M.C., Casquet, C., Mateus, A., Ortiz, G., 2004. The metallogenic evolution of the Ossa-Morena Zone. J. Iber. Geol. 30, 143–181.

Tornos, F., Velasco, F., Barra, F., Morata, D., 2010. The Tropezón Cu–Mo–(Au) deposit, Northern Chile: the missing link between IOCG and porphyry copper systems?. Minera. Deposita 45, 313–321. https://doi.org/10.1007/s00126-010-0277-8

Torresi, I., Xavier, R.P., Bortholoto, D.F.A., Monteiro, L.V.S., 2012. Hydrothermal alteration, fluid inclusions and stable isotope systematics of the Alvo 118 iron oxide–copper–gold deposit, Carajás Mineral Province (Brazil): Implications for ore genesis. Miner. Deposita 47, 299–323. https://doi.org/10.1007/s00126-011-0373-4

Valenta, R., 2018. NW Queensland Mineral Province Deposit Atlas Prototype Report – the Mount Isa and Ernest Henry Deposits. DNRME-GSQ Commissioned study and report. https://smi.uq.edu.au/files/36554/Atlas_Prototype_Ch3_ErnestHenry.pdf

Veloso, E., Neira, S., Siña, A., Vivanco, M., Cembrano, J., Heuser, G., Garrido, I., 2015. Etapas de alteración/mineralización en el depósito de Dominga (Fe-Cu), Región de Coquimbo. In XIV Congreso Geológico Chileno, La Serena, Chile, 390–393.

Vielreicher, N.M., Groves, D.I., Vielreicher, R.M., 2000. The Phalaborwa (Palabora) Deposit and its Potential Connection to Iron-Oxide Copper-Gold Deposit of Olympic Dam Type, in: Porter, T.M. (Ed.), Hydrothermal Iron Oxide Copper-Gold and Related Deposits, First Edition. PGC Publishing, Adelaide, pp. 321–329.

Weihed, P., Arndt, N., Billström, K., Duchesne, J.-C., Eilu, P., Martinsson, O., Papunen, H., Lahtinen, R., 2005. 8: Precambrian geodynamics and ore formation: The Fennoscandian Shield. Ore Geol. Rev. 27, 273–322. https://doi.org/10.1016/j.oregeorev.2005.07.008

Williams, M.R., Holwell, D.A., Lilly, R.M., Case, G.N., McDonald, I., 2015. Mineralogical and fluid characteristics of the fluorite-rich Monakoff and E1 Cu–Au deposits, Cloncurry region, Queensland, Australia: Implications for regional F–Ba-rich IOCG mineralisation. Ore Geology Reviews, 64, 103–127.https://doi.org/10.1016/j.oregeorev.2014.05.021

Williams, P.J., Skirrow, R.G., 2000. Overview of iron oxide copper-gold deposits in the Curnamona province and Cloncurry district (Eastern Mt Isa Block), Australia, in: Porter, T.M. (Ed), Hydrothermal Iron-Oxide Copper Gold and Related Deposits: A Global Perspective, First Edition. PGC Publishing, Adelaide, pp. 105–122.

Woolrych, T.R., Christensen, A.N., McGill, D.L., Whiting, T., 2015. Geophysical methods used in the discovery of the Kitumba iron oxide copper gold deposit. Interpretation 3, SL15–SL25. https://doi.org/10.1190/INT-2014-0201.1

Zhao, X.F. Zhou M.F., 2011. Fe–Cu deposits in the Kangdian region, SW China: a Proterozoic IOCG (iron-oxide–copper–gold) metallogenic province. Miner. Deposita 46, 731–747. https://doi.org/10.1007/s00126-011-0342-y

Zhimin, Z., Yali, S., 2013. Direct Re-Os dating of chalcopyrite from the Lala IOCG deposit in the Kangdian copper belt, China. Econ. Geol. 108, 871–882. https://doi.org/10.2113/econgeo.108.4.871

Zhu, L., Liu, J., Bagas, L., Zhai, D., Meng, G., Verrall, M., 2020. New insights into the genesis of IOCG deposits: From a case study of the Yinachang deposit in SW China. Ore Geol. Rev. 124, 103664. https://doi.org/10.1016/j.oregeorev.2020.103664

Zhu, Z. 2016. Gold in Iron Oxide Copper-Gold Deposits. Ore Geol. Rev. 72, 37–42. https://doi.org/10.1016/j.oregeorev.2015.07.001

Zhu, Z., Tan, H., Liu, Y., Li, C., 2017. Multiple episodes of mineralization revealed by Re-Os molybdenite geochronology in the Lala Fe-Cu deposit, SW China. Miner. Deposita 53, 311–322. https://doi.org/10.1007/s00126-017-0740-x

ESM – Table 8. Main geological features of the studied deposits.

Deposit	Host rocks	Ore control	Ore morphology	Main opaque hypogene	Hydrothermal alteration
<u>Carajás Mineral Province, Brazil</u>					
Sequeirinho orebody	Sequeirinho granite, gabbronorite, Pista felsic metavolcanic rock, gneiss (Xingu Complex) (1–3)	Canaã shear zone (4)	Tabular, breccia, disseminations along the mylonitic foliation, veins, and stockwork breccias (2–4)	Cpy, Py, Po, Mag (3)	1°: Intense Na 2°: Intense Na-Ca (+Fe-P) 3°: Poorly K (2)
Sossego orebody	Sossego granophyric granite, Curral granite (1–3)	Canaã shear zone (4)	Subvertical breccia pipes, veins (2, 3)	Cpy, Py, Mag (3)	1°: Poorly Na 2°: Poorly Na-Ca 3°: Intense K 4°: Intense Chl (2)
Salobo	Orthogneiss (Xingu Complex), Igarapé Gelado Suite (5)	Cinzento shear zone (5)	Massive, steeply dipping lenses along the mylonitic foliation (5)	Bn, Cc, Cpy, Mag (5, 6)	1°: Na 2°: Ca-Fe (6)
Alemão orebody	Metavolcanosedimentary sequence of Igarapé Bahia Group, metasedimentary rocks of the Águas Claras Fm. (7)	Carajás fault (7)	Massive lenses, hydrothermal breccias (7)	Cpy, Mag, Py (7)	1°: Na-Ca 2°: K-Fe 3°: Tour+Cb 4°: Chl (7)
<u>Olympic Dam Cu-Au Province, Australia</u>					
Olympic Dam	Olympic Dam Breccia Complex (derived from Roxby Downs Granite), felsic volcanic rocks, and bedded clastic facies (8)	NE-striking fault zone (8–10)	Breccias (8)	Bn, Hem, Cpy, Py, Cc, Dg, Mag (11)	1°: Redox Fe-oxide 2°: Ser 3°: Qtz 4°: Chl (11)
<u>Mt. Isa Inlier, Australia</u>					
Ernest Henry	Metandesites from Mt. Fort Constantine Volcanics equivalents, metasediments intercalations (12)	NE-trending shear zones (13)	Breccia pipe-like, veins, lenses (14)	Cpy, Mag, Py (12)	1°: Na-Ca 2°: K+Ser (12)
<u>Central Andes IOCG Province, Chile</u>					
<u>Mantoverde district</u>					
Laura orebody	Basaltic andesite, andesite flows, volcanic rocks from La Negra Fm. (15)	Mantoverde fault (15)	Tabular breccia, veins, cataclasite breccia (15)	Py, Cpy, Hem, Dg (16)	1°: Strong Fe-K 2°: Chl-Ser-Qtz-Kfd (16, 17)
Brecha Flores orebody	Basaltic andesite, andesite flows, volcanic rocks from La Negra Fm. (15)	Mantoverde fault (15)	Tabular breccia, veins, cataclasite breccia (15)	Py, Cpy, Hem, Dg (16)	1°: Strong Fe-K 2°: Chl-Ser-Qtz-Kfd (16, 17)
Manto Ruso	Contact between volcanic rocks from La Negra Fm. and granitoids from the Coastal Batholith (15)	NW fault systems at the east of Mantoverde fault (15)	Subvertical breccia, dissemination, veinlets (15)	Py, Cpy, Hem, Bn, Dg (16)	1°: Strong Fe-K 2°: Chl-Qtz (16, 17)

ESM – Table 2. (continued)

Deposit	Host rocks	Ore control	Ore morphology	Main opaque hypogene	Hydrothermal alteration
Candelaria-Punta del Cobre district					
Candelaria	Metavolcanic and metavolcanic-sedimentary rocks of Punta del Cobre Fm. [18]	NW-NNW fault systems, Candelaria shear zone [18, 19]	Mantos, stockwork, breccia, veins [18]	Cpy, Mag, Py, Po, Hem [18]	1°: Na 2°: Na-Ca 3°: Ca-Fe 4°: Strong K-Fe+Ca-Chl 5°: Ca-Fe-Mg [18]
Alcaparrosa	Metavolcanic and brecciated dacitic dome of Punta del Cobre Fm. [18]	NW-NNW fault systems, Candelaria shear zone [18, 19]	Disseminated patches, breccia filling, veins [18]	Cpy, Mag, Py, Hem [18]	1°: Na 2°: Na-Ca 3°: Ca-Fe 4°: K-Fe± Ca 5°: Ca-Fe-Mg [18]
Santos	Metavolcanic and brecciated dacitic dome of Punta del Cobre Fm. [18]	NW-NNW fault systems [18]	Veins, disseminated, breccia filling, irregular pipe-like body [18]	Cpy, Mag, Py, Hem [18]	1°: Na 2°: Na-Ca 3°: Ca-Fe 4°: Strong K-Fe 5°: Ca-Fe-Mg [18]
Punta del Cobre	Metavolcanic and brecciated dacitic dome of Punta del Cobre Fm.	NW-NNW fault systems [18]	Patches, breccia filling, veins [18]	Cpy, Mag, Py, Hem [18]	1°: K-Na 2°: Chl-Fe [20]

Abbreviations: *Bn – bornite; Ca – calcic; Cb – carbonate; Cc – chalcocite; Chl – chloritic; Cpy – chalcopyrite; Dg – digenite; Fe – ferric; Hem – hematite; K – potassic; Kfd – potassic feldspar; Mag – magnetite; Na – sodic; P – phosphatic; Po – pyrrhotite; Py – pyrite; Ser – sericitic; Tour – tourmaline.*

References: (1) Monteiro et al. (2008a); (2) Monteiro et al. (2008b); (3) Moreto et al. (2015a); (4) Domingos (2009); (5) de Melo et al. (2017); (6) Valadão (2019); (7) de Melo et al. (2019b); (8) Cherry et al. (2018); (9) Hayward & Skirrow (2010); (10) McPhie et al. (2016); (11) Ehrig et al. (2012); (12) Mark et al. (2006); (13) Austin et al. (2019); (14) Cave et al. (2018); (15) Rieger et al. (2010); (16) Childress et al. (2020); (17) Johansson et al. (2018); (18) del Real et al. (2018); (19) Arévalo et al. (2006); (20) Marschik & Fontboté (2001b).

Supplementary 2 – References

Arévalo, C., Grocott, J., Martin, W., Pringle, M., Taylor, G., 2006. Structural Setting of the Candelaria Fe Oxide Cu-Au Deposit, Chilean Andes (27° 30′ S). Econ. Geol. 101, 819–841. https://doi.org/10.2113/gsecongeo.101.4.819

Austin, J., Björk, A., Patterson, B., 2019. Structural controls of the Ernest Henry IOCG deposit: Insights from integrated structural, geophysical, and mineralogical analyses. ASEG Extended Abstracts, 1-5. https://doi.org/10.1080/22020586.2019.12073161

Cave, B.W., Lilly, R., Glorie, S., Gillespie, J., 2018. Geology, apatite geochronology, and geochemistry of the Ernest Henry inter-Lens: implications for a re-examined deposit model. Minerals 8, 405. https://doi.org/10.3390/min8090405

Cherry, A.R., Ehrig, K., Kamenetsky, V.S., McPhie, J., Crowley, J.L., Kamenetsky, M.B., 2018. Precise geochronological constraints on the origin, setting and incorporation of ca. 1.59 Ga surficial facies into the Olympic Dam Breccia Complex, South Australia. Precambrian Res. 315, 162–178. https://doi.org/10.1016/j.precamres.2018.07.012

Childress, T.M., Simon, A.C., Reich, M., Barra, F., Arce, M., Lundstrom, C.C., Bindeman, I.N., 2020. Formation of the Mantoverde iron oxide-copper-gold (IOCG) deposit, Chile: insights from Fe and O stable isotopes and comparisons with iron oxide-apatite (IOA) deposits. Miner. Deposita 55, 1489–1504. https://doi.org/10.1007/s00126-019-00936-x

de Melo, G.H., Monteiro, L.V.S., Xavier, R.P., Moreto, C.P.N., Santiago, E.S.B., Dufrane, S.A., Aires, B., Santos, A.F.F., 2017. Temporal evolution of the giant Salobo IOCG deposit, Carajás Province (Brazil): constraints from paragenesis of hydrothermal alteration and U-Pb geochronology. Miner. Deposita 52, 709–732. https://doi.org/10.1007/s00126-016-0693-5

de Melo, G.H., Monteiro, L.V., Xavier, R.P., Moreto, C.P., Arquaz, R.M., Silva, M.A.D., 2019b. Evolution of the Igarape Bahia Cu-Au deposit, Carajas Province (Brazil): Early syngenetic chalcopyrite overprinted by IOCG mineralization. Ore Geol. Rev. 111, 102993. https://doi.org/10.1016/j.oregeorev.2019.102993

del Real, I., Thompson, J.F., Carriedo, J., 2018. Lithological and structural controls on the genesis of the Candelaria-Punta del Cobre Iron Oxide Copper Gold district, Northern Chile. Ore Geol. Rev. 102, 106–153. https://doi.org/10.1016/j.oregeorev.2018.08.034

Domingos, F., 2009. *The structural setting of the Canaã dos Carajás region and Sossego-Sequeirinho deposits, Carajás, Brazil*. PhD. dissertation. Durham University, England.

Ehrig, K., McPhie, J., Kamenetsky, V.S., 2012.Geology and mineralogical zonation of the Olympic Dam Iron Oxide Cu-U-Au-Ag deposit, South Australia, in: Hedenquist, J.M., Harris, M., Camus, F. (Eds.), Geology and Genesis of Major Copper Deposits and Districts of the World: A Tribute to Richard H. Sillitoe, Volume 16. Society of Economic Geologists, Inc. Littleton, Colorado, pp. 237–267.

Hayward, N., Skirrow, R., 2010. Geodynamic setting and controls on iron oxide Cu–Au (±U) ore in the Gawler Craton, South Australia, in: Porter, T.M. (Ed.), Hydrothermal Iron Oxide Copper-Gold and Related Deposits: A Global Perspective, Third Edition. PGC Publishing, Adelaide, pp. 119–146.

Johansson, C., Barra, F., Reich, M., Deditius, A.P., Simon, A.C., Rojas, P., 2017. The Co-Ni signature of sulfide minerals from the Mantoverde IOCG deposit, northern Chile. Goldschmidt Abstracts, Paris, France.

Marschik, R., Fontboté, L., 2001b. The Punta del Cobre Formation, Punta del Cobre–Candelaria area, northern Chile. J. S. Am. Earth Sci., 14, 401–433. https://doi.org/10.1016/S0895-9811(01)00036-0

Mark, G., Oliver, N.H., Williams, P.J., 2006. Mineralogical and chemical evolution of the Ernest Henry Fe oxide–Cu–Au ore system, Cloncurry district, northwest Queensland, Australia. Miner. Deposita 40, 769–801. https://doi.org/10.1007/s00126-005-0009-7

McPhie, J., Orth, K., Kamenetsky, V., Kamenetsky, M., Ehrig, K., 2016. Characteristics, origin and significance of Mesoproterozoic bedded clastic facies at the Olympic Dam Cu–U–Au–Ag deposit, South Australia. Precambr. Res. 276, 85–100. https://doi.org/10.1016/j.precamres.2016.01.029

Monteiro, L.V.S., Xavier, R.P., de Carvalho, E.R., Hitzman, M.W., Johnson, C.A., de Souza, C.R., Torresi, I., 2008a. Spatial and temporal zoning of hydrothermal alteration and mineralization in the Sossego iron oxide-copper–gold deposit, Carajás Mineral Province, Brazil: paragenesis and stable isotope constraints. Miner. Deposita 43, 129–159. https://doi.org/10.1007/s00126-006-0121-3

Monteiro, L.V.S., Xavier, R.P., Hitzman, M.W., Juliani, C., de Souza Filho, C.R., Carvalho, E.D. R., 2008b. Mineral chemistry of ore and hydrothermal alteration at the Sossego iron oxide–copper–gold deposit, Carajás Mineral Province, Brazil. Ore Geol. Rev. 34, 317–336. https://doi.org/10.1016/j.oregeorev.2008.01.003

Moreto, C.P.N., Monteiro, L.V.S., Xavier, R.P., Creaser, R.A., DuFrane, S.A., Tassinari, C.C.G., Sato, K., Kemp, A.I.S., Amaral, W.S., 2015a. Neoarchean and Paleoproterozoic Iron Oxide-Copper-Gold Events at the Sossego Deposit Carajás Province, Brazil: Re-Os and U-Pb Geochronological Evidence. Econ. Geol. 110, 809–835. https://doi.org/10.2113/econgeo.110.3.809

Rieger, A.A., Marschik, R., Díaz, M., Hölzl, S., Chiaradia, M., Akker, B., Spangenberg, J.E., 2010. The hypogene iron oxide copper–gold mineralization in the Mantoverde district, Northern Chile. Econ. Geol. 105, 1271–1299. https://doi.org/10.2113/econgeo.105.7.1271

Valadão, L.V., 2019. Mineralogia e relação textural e microestrutural do minério tipo IOCG da mina do Salobo, Província Mineral de Carajás: revisão da sequência paragenética. MSc. dissertation, University of Brasilia, Brazil.

ESM – Table 9. Ore-bearing sample description.

Location	Sample	Lithology	Radiogenic isotope analysis (MC-TIMS) Sm-Nd	Radiogenic isotope analysis (MC-TIMS) Sr-Sr	Geochemical analysis (ICP-MS) T. E. + REE	Description
Carajás Mineral Province, Brazil						
Sequeirinho orebody	SQ01	Sequeirinho granite	Cpy, Mag	Cpy, Mag	-	Chalcopyrite-magnetite dissemination in sodic-calcic groundmass with abundant actinolite and grains of apatite and quartz
	SQ02	Sequeirinho granite	Mag	Cpy, Mag	Mag	Magnetite breccia with strong dissemination of chalcopyrite and associated quartz-actinolite-apatite
	SQ04	Sequeirinho granite	Mag	Mag	Mag	Massive magnetite-actinolite with moderate dissemination of silicates and traces of sulfides
Sossego orebody	SS01	Sossego granophyric granite	Mag	Cpy, Mag	Cpy, Mag	Magnetitte-actinolite breccia with slight dissemination of chalcopyrite; frequent occurrence of apatite
	SS02	Sossego granophyric granite	Cpy, Mag	Mag	Cpy, Mag	Magnetite-actinolite breccias with moderate dissemination of chalcopyrite; abundant apatite
	SS03	Sossego granophyric granite	Cpy	Cpy	-	Magnetite-chalcopyrite breccia in calcic-ferric groundmass with actinolite-apatite-quartz grains
	SS04	Sossego granophyric granite	Cpy	Cpy	Cpy	Massive magnetite with strong dissemination of chalcopyrite and associated quartz-actinolite
Salobo	103	Old Salobo granite	Cpy, Mag	Cpy, Mag	Cpy, Mag	Clast supported hydrothermal breccia with chalcopyrite matrix; slight dissemination of actinolite-quartz
	104	Old Salobo granite	Mag	-	Cpy, Mag	Clast supported hydrothermal breccia with chalcopyrite matrix; slight dissemination of actinolite-quartz
	105	Old Salobo granite	Cpy	-	-	Clast supported hydrothermal breccia with chalcopyrite matrix; slight dissemination of actinolite-quartz
Alemão orebody	AM	Metavolcanic rock	Cpy, Mag	Cpy, Mag	Cpy, Mag	Massive magnetite with strong dissemination of chalcopyrite and traces of pyrite
Olympic Dam Cu-Au Province						
Olympic Dam	OD	Roxby Downs grantie	Bn	Bn	Bn, Hem	Moderate hematite and bornite dissemination in pervasive feldspar potassic-ferric altered granite; abundant quartz grains
Mt. Isa Inlier						
Ernest Henry	EH	Metandesite	Cpy, Mag	Cpy, Mag	Cpy, Mag	Strong dissemination of chalcopyrite-pyrite-magnetite in the potassic feldspar-ferric groundmass

ESM – Table 3. (continued)

Location	Sample	Lithology	Radiogenic isotope analysis (MC-TIMS)		Geochemical analysis (ICP-MS)	Description
			Sm-Nd	Sr-Sr	T. E. + REE	
Central Andes IOCG Province						
Mantoverde district						
Laura orebody	L2	Metandesite	Cpy, Hem	Cpy	Cpy, Hem	Deformed specular-hematite breccia with abundant chalcopyrite-pyrite clasts and veins of calcite
Brecha Flores orebody	BF	Metandesite	-	Mag	Mag	Magnetite breccia with clasts of pervasive potassic-feldspar alteration; minor chalcopyrite-pyrite dissemination
Manto Ruso	MR	Metandesite	-	Cpy, Hem	Cpy, Hem	Specular-hematite breccia with abundant chalcopyrite-pyrite clasts and chlorite-quartz-hornblende dissemination
Candelaria-Punta del Cobre district						
Candelaria	LS1455-11a	Volcanic-sedimentary unit	Cpy, Mag	Cpy, Mag	Cpy, Mag	Sample from manto. Massive magnetite with chalcopyrite-pyrite-andradite stockwork
	LS1257-5b	Volcanic-sedimentary unit	Cpy	Cpy, Po	Cpy, Po	Chalcopyrite-pyrrhotite-pyrite vein with abundant dissemination of magnetite and minor calcite-actinolite-biotite
	LS1257-6b	Volcanic-sedimentary unit	Cpy, Mag	Cpy, Mag, Po	Cpy, Mag, Po	Vein intersecting manto horizon. Chalcopyrite-pyrrhotite-pyrite vein associated with magnetite-actinolite veinlets; abundant andradite and calcite dissemination
Exploration Sur	ES082-10	Volcanic-sedimentary unit	Po	Cpy, Po	Mag, Po	Sample from the deep manto mineralization (>750 m depth). Massive magnetite-chalcopyrite-pyrrhotite-pyrite with slight dissemination of actinolite, andradite, quartz, and calcite; pyrrhotite is the main sulfide in the sample
Alcaparrosa	AD689-4	Volcanic-sedimentary unit	Cpy, Mag	Cpy, Mag	Cpy, Mag	Chalcopyrite patches with abundant calcite-actinolite veinlets; magnetite typically disseminated
Santos	DH-1	Lower andesite	Cpy	Cpy	Cpy	Chalcopyrite patches in a pervasive scapolite-albite-actinolite andesite
	DH-1546-7	Lower andesite	Mag	Cpy, Mag	Cpy, Mag	Chalcopyrite-magnetite patches in a pervasive biotite altered andesite
Punta del Cobre	PdC	Lower andesite	Cpy	Cpy	Cpy, Mag	Massive chalcopyrite-pyrite with abundant specular-hematite stains
	PdC-2	Lower andesite	Mag	Cpy, Mag	Cpy, Mag	Intercalation of magnetite-chalcopyrite-pyrite bands

Abbreviations: *Bn – bornite; Cpy – chalcopyrite; Hem – hematite; Mag – magnetite; Po – pyrrhotite; T. E. – trace elements.*

ESM – Table 10. Full ICP-MS analytical results (in ppm) of samples included in this study.

Carajás Mineral Province									
Deposit	Alemão		Salobo					Sequeirinho	
Sample	AM-Cpy	AM-Mgt	C103	C104	C104*	M103	M104	MSQ02	MSQ04
Material	Cpy	Mag	Cpy	Cpy	Cpy	Mag	Mag	Mag	Mag
Traces									
Li	-	0.55	-	-	-	0.25	0.22	0.65	2.91
B	2.95	-	17.39	54.63	65.51	7.54	44.14	2.98	-
Na	367.36	123.68	1984.46	117.35	130.78	374.38	94.19	784.90	1169.08
Mg	4694.51	1519.29	5968.25	3953.59	4064.59	1716.72	2491.57	16126.37	20333.31
Al	2995.89	1201.83	7428.63	1416.27	1420.62	3038.84	2753.88	4322.72	5601.66
P	5719.60	792.10	5437.71	16083.07	14597.38	1964.86	4400.55	8213.07	155.97
K	1704.19	512.53	935.14	32.48	28.36	200.11	27.59	165.17	428.52
Ca	15562.13	1685.21	30522.70	41492.77	38870.24	8202.94	13366.66	40501.30	35122.45
Ti	91.99	156.30	18.77	14.70	17.14	345.02	742.37	1562.67	5138.30
V	3.51	28.02	1.33	1.13	1.07	28.37	52.71	1356.22	3304.21
Cr	6.35	1.40	0.48	0.37	0.60	2.12	5.38	4.46	17.65
Mn	4449.38	1309.45	515.63	2237.46	2236.85	293.77	1522.49	177.00	580.15
Fe	-	-	-	-	-	-	-	-	-
Co	117.45	83.97	244.56	154.58	138.33	451.57	182.87	157.62	79.53
Ni	43.76	80.16	309.13	90.06	78.60	471.01	118.26	1328.15	1237.79
Cu	-	-	-	-	-	-	-	-	-
Zn	68.10	10.22	226.35	23.59	23.70	65.65	20.87	87.55	135.20
As	9.48	5.29	12.60	12.53	8.18	3.53	6.05	8.82	0.31
Rb	11.67	3.56	1.68	0.52	0.51	0.53	-	0.57	1.30
Sr	22.29	1.81	8.78	4.71	4.40	1.00	1.49	62.48	15.66
Y	40.71	26.48	235.97	617.31	570.81	80.08	181.87	22.87	5.55
Mo	32.76	7.19	122.15	1.90	0.66	11.11	15.84	0.13	0.35
Ag	2.28	1.56	3.81	0.62	3.15	2.47	0.55	3.51	-
Cd	0.13	0.04	0.39	0.10	0.06	0.15	0.05	0.26	0.04
Sn	7.28	2.83	44.83	44.73	43.82	22.02	28.75	26.77	1.41
Sb	0.24	1.20	0.03	0.10	0.18	0.02	0.19	0.04	0.02
Cs	2.20	0.74	0.03	0.02	0.03	0.04	0.02	0.01	0.02
Ba	146.49	134.98	4.62	-	-	1.09	-	2.49	12.23
Tl	0.04	0.07	-	-	0.01	0.06	0.09	0.01	0.03
Pb	80.70	25.36	38.60	64.00	154.42	64.02	130.54	4.99	0.87
Th	0.90	0.69	2.63	4.30	6.98	1.71	5.43	1.60	4.89
U	64.29	83.46	67.37	130.19	353.23	144.80	299.89	2.52	3.30
Ni/Co	0.37	0.95	1.26	0.58	0.57	1.04	0.65	8.43	15.56
Ni/Cr	6.89	57.17	648.69	243.46	131.90	222.05	21.97	297.79	70.12
Th/U	0.01	0.01	0.04	0.03	0.02	0.01	0.02	0.64	1.48
REE									
La	530.48	242.00	161.41	91.69	78.99	79.92	33.32	493.99	1.74
Ce	901.99	409.21	308.77	294.57	263.37	151.38	88.82	792.01	5.07
Pr	82.38	34.89	33.21	44.00	40.73	15.96	13.90	99.32	0.94
Nd	261.29	116.41	142.36	241.10	225.21	66.77	75.05	347.42	5.01
Sm	29.93	13.35	36.11	75.77	71.65	15.22	24.50	38.50	1.41
Eu	8.41	3.81	2.65	6.49	6.06	1.28	2.14	4.09	0.17
Gd	21.49	9.88	44.73	98.61	93.05	16.98	31.86	19.66	1.43
Tb	2.51	1.25	7.41	15.99	15.12	2.67	5.22	1.94	0.21
Dy	11.41	6.86	48.83	107.06	101.73	17.42	36.51	7.36	1.27
Ho	1.93	1.25	9.84	22.20	20.93	3.37	7.52	1.15	0.24
Er	5.56	3.86	27.45	63.36	59.79	9.55	21.72	3.05	0.67
Tm	0.72	0.54	3.48	7.67	7.28	1.15	2.63	0.32	0.09
Yb	4.73	3.97	20.32	42.56	40.04	6.80	15.12	1.84	0.56
Lu	0.70	0.61	2.24	4.56	4.31	0.76	1.69	0.25	0.08
[a] ∑REE	1863.53	847.90	848.81	1115.62	1028.26	389.24	360.00	1810.89	18.87
[b] ∑LREE	1814.48	819.67	684.51	753.62	686.00	330.53	237.72	1775.32	14.35
[c] ∑HREE	49.04	28.23	164.30	362.00	342.26	58.71	122.27	35.56	4.53
[d] ∑REY	1904.23	874.38	1084.78	1732.93	1599.07	469.32	541.87	1833.75	24.42
LREE/HREE	37.00	29.03	4.17	2.08	2.00	5.63	1.94	49.92	3.17
[e] La_N/Yb_N	75.57	41.09	5.35	1.45	1.33	7.91	1.48	180.58	2.11
[f] La_N/Sm_N	469.71	480.55	118.47	32.07	29.22	139.20	36.05	340.09	32.65
[g] Sm_N/Yb_N	6.78	3.61	1.90	1.91	1.92	2.40	1.74	22.39	2.72
[h] δCe	0.94	0.95	0.96	1.11	1.11	0.96	0.99	0.81	0.94
[i] δEu	0.97	0.97	0.20	0.23	0.23	0.24	0.23	0.41	0.36

ESM – Table 4. (continued)

	Carajás Mineral Province					Australian IOCG			
Deposit			Sossego			Olympic Dam		Ernest Henry	
Sample	CSS01	CSS02	CSS04	MSS01	MSS02	OD-Bn	OD-Hmt	EH-Cpy	EH-Mgt
Material	Cpy	Cpy	Cpy	Mag	Mag	Bn	Hem	Cpy	Mag
Traces									
Li	0.95	-	2.07	3.97	4.25	6.57	26.15	6.75	8.22
B	-	-	-	-	-	6.69	30.14	2.79	14.39
Na	256.75	279.93	150.16	209.69	3664.52	321.27	663.96	186.92	167.01
Mg	3198.22	13406.19	3987.46	12923.55	20826.67	343.29	1315.60	7200.11	8382.34
Al	570.28	1761.64	2150.42	1439.38	20729.21	12200.45	51190.19	13333.98	12064.50
P	4995.81	20392.17	5494.30	9628.88	6099.94	357.74	1380.27	484.77	207.80
K	128.30	74.82	55.22	222.20	5393.93	6004.71	26377.08	9655.90	5787.80
Ca	14661.63	56202.34	33508.26	56562.29	62179.66	9744.99	22025.95	3483.07	1959.02
Ti	177.19	225.26	271.63	5884.67	1225.05	307.78	1440.42	1202.70	866.97
V	15.11	35.07	13.06	1509.64	403.61	8.70	34.14	20.80	256.02
Cr	0.86	0.43	1.67	10.16	6.65	100.98	212.26	2.77	34.94
Mn	94.43	96.18	214.17	973.94	653.70	15.02	46.08	489.11	1646.33
Fe	-	-	-	-	-	-	-	-	-
Co	21.39	661.75	29.40	39.71	43.28	18.20	136.50	603.87	205.13
Ni	161.38	2031.86	271.22	477.48	252.82	4.60	13.98	17.23	113.57
Cu	-	-	-	-	-	-	-	-	-
Zn	151.70	102.48	15.36	46.65	56.95	51.31	144.61	13.54	23.54
As	1.98	6.63	1.52	5.32	6.11	14.28	64.20	473.93	179.73
Rb	1.34	0.27	0.49	3.18	31.41	23.63	97.71	24.73	15.80
Sr	7.64	37.35	23.39	36.51	64.33	130.86	451.33	23.18	16.84
Y	45.54	39.05	38.51	76.64	64.96	42.64	268.92	11.60	13.41
Mo	0.10	0.14	0.83	0.86	0.21	25.14	29.54	174.72	161.47
Ag	4.61	1.90	2.27	0.86	0.19	1.65	4.26	1.14	1.31
Cd	2.97	0.74	0.38	0.39	0.08	0.06	0.06	0.08	0.11
Sn	15.74	10.72	16.50	14.03	4.30	11.80	25.45	7.34	11.99
Sb	0.04	0.05	0.08	0.06	0.04	1.11	3.62	3.03	5.20
Cs	0.04	0.01	0.04	0.05	0.08	0.54	2.28	0.05	0.05
Ba	4.05	0.84	3.19	3.47	147.90	447.94	2537.63	91.18	1360.74
Tl	0.11	0.04	0.02	0.07	0.07	0.12	0.47	0.11	0.09
Pb	113.72	7.80	30.77	26.27	19.35	32.41	57.27	4.97	14.86
Th	7.92	7.37	1.94	6.65	2.35	6.11	1.81	3.98	5.20
U	9.02	0.60	23.06	40.82	6.29	344.16	685.40	172.38	213.10
Ni/Co	7.54	3.07	9.22	12.02	5.84	0.25	0.10	0.03	0.55
Ni/Cr	188.56	4737.41	162.31	47.01	38.03	0.05	0.07	6.22	3.25
Th/U	0.88	12.27	0.08	0.16	0.37	0.02	0.00	0.02	0.02
REE									
La	72.78	373.86	48.32	256.14	297.08	497.32	3506.19	96.77	85.75
Ce	168.40	639.72	111.20	519.38	533.62	939.88	6240.75	76.32	62.85
Pr	18.32	58.92	12.47	54.11	59.31	95.72	619.07	4.70	4.05
Nd	73.44	207.69	52.98	205.82	229.28	301.37	2049.52	13.92	12.26
Sm	13.64	26.70	10.96	34.67	37.06	35.56	219.35	1.95	1.83
Eu	1.76	3.09	1.32	4.61	3.80	10.86	62.64	0.77	0.78
Gd	12.60	17.68	10.96	27.11	30.11	22.15	132.57	1.90	1.91
Tb	1.72	1.94	1.49	3.42	3.94	2.61	13.96	0.25	0.27
Dy	9.67	8.77	8.34	18.15	22.13	11.77	59.85	1.51	1.68
Ho	1.77	1.46	1.53	3.09	4.07	1.97	9.66	0.32	0.35
Er	4.69	3.73	4.10	8.35	11.33	5.56	27.23	0.97	1.10
Tm	0.56	0.39	0.49	0.99	1.39	0.70	3.24	0.13	0.15
Yb	3.09	2.13	2.89	5.93	8.94	4.46	20.84	0.89	1.06
Lu	0.36	0.28	0.38	0.74	1.35	0.58	2.81	0.14	0.17
[a] ∑REE	382.79	1346.35	267.42	1142.51	1243.42	1930.52	12967.65	200.54	174.20
[b] ∑LREE	348.33	1309.98	237.24	1074.73	1160.16	1880.71	12697.50	194.43	167.51
[c] ∑HREE	34.45	36.37	30.18	67.78	83.27	49.81	270.15	6.11	6.69
[d] ∑REY	428.33	1385.40	305.93	1219.15	1308.38	1973.16	13236.57	212.13	187.61
LREE/HREE	10.11	36.02	7.86	15.86	13.93	37.76	47.00	31.83	25.05
[e] La_N/Yb_N	15.87	118.19	11.25	29.10	22.37	75.05	113.31	73.40	54.50
[f] La_N/Sm_N	141.41	371.06	116.90	195.81	212.48	370.67	423.66	1316.99	1240.02
[g] Sm_N/Yb_N	4.73	13.43	4.06	6.27	4.44	8.54	11.28	2.35	1.85
[h] δCe	1.08	0.94	1.07	1.01	0.92	0.97	0.94	0.54	0.50
[i] δEu	0.40	0.41	0.36	0.44	0.34	1.10	1.04	1.22	1.27

ESM – Table 4. (continued)

	Central Andes IOCG Province							
Daposit	Candelaria							
Sample	LS1257-5b-Cpy	LS1257-6b-Cpy	LS1455-11a-Cpy	LS1455-11a-Mgt	LS1455-11a-Mgt*	LS1257-6b-Mgt	LS1257-5b-Po	LS1257-6b-Po
Traces								
Li	-	2.28	3.88	2.74	3.33	3.62	-	3.55
B	100.00	8.72	22.41	11.03	7.33	10.22	54.07	11.51
Na	242.13	294.35	575.84	389.08	410.97	545.88	143.57	511.78
Mg	404.63	2487.44	5654.83	2432.97	2473.59	1074.93	299.82	1222.64
Al	607.93	9213.08	19814.34	8327.93	8466.54	2397.43	319.58	2506.00
P	653.17	346.17	1658.91	535.65	542.89	94.09	265.67	104.29
K	64.04	386.19	654.06	738.41	743.11	803.41	46.64	852.08
Ca	12626.61	110298.87	151535.74	49474.28	49376.78	11238.17	5306.64	12915.98
Ti	8.06	387.43	910.61	735.33	731.15	507.33	-	508.78
V	6.61	76.41	103.52	157.04	156.18	124.07	2.89	120.16
Cr	2.30	6.19	6.57	12.87	13.20	15.76	2.87	10.33
Mn	344.88	4369.09	7866.68	3321.83	3306.70	1550.48	239.64	1550.80
Fe	-	-	-	-	-	-	-	-
Co	61.68	55.56	80.75	26.55	26.43	224.40	538.80	157.58
Ni	190.42	23.95	55.98	21.90	22.56	130.30	1400.53	93.62
Cu	-	-	-	-	-	-	-	-
Zn	3085.38	1726.47	1812.03	644.45	638.16	680.15	1813.14	640.36
As	193.83	47.60	380.38	108.04	103.59	31.99	205.25	28.90
Rb	0.43	1.21	3.95	2.91	2.92	2.84	0.39	2.97
Sr	9.61	4.24	13.31	8.27	8.13	10.04	2.93	7.03
Y	11.87	38.80	24.86	10.53	10.31	2.42	3.83	2.90
Mo	3.23	5.81	1.15	2.81	1.64	2.39	1.58	2.09
Ag	7.82	9.39	36.14	0.56	6.69	2.93	1.79	1.79
Cd	8.52	6.26	4.17	1.39	1.39	1.88	4.84	1.97
Sn	4.24	4.61	4.30	1.95	2.39	2.22	2.04	1.91
Sb	1.51	0.62	1.59	3.45	3.42	3.55	1.44	3.20
Cs	0.31	0.42	4.03	1.94	1.88	0.88	0.26	0.91
Ba	1.27	9.49	8.38	20.37	18.88	21.80	1.41	21.70
Tl	0.20	0.35	1.17	0.23	0.21	0.17	0.21	0.18
Pb	18.75	3.73	17.45	27.20	25.98	18.19	25.48	17.14
Th	0.06	0.32	2.06	2.03	1.98	0.22	0.30	0.50
U	0.34	3.28	3.39	2.32	2.18	1.39	0.23	1.35
Ni/Co	3.09	0.43	0.69	0.82	0.85	0.58	2.60	0.59
Ni/Cr	82.65	3.87	8.52	1.70	1.71	8.27	487.72	9.07
Th/U	0.17	0.10	0.61	0.87	0.91	0.16	1.30	0.37
REE								
La	5.12	3.93	37.94	20.80	20.21	2.24	1.93	2.08
Ce	13.57	13.12	70.26	37.35	36.34	4.19	5.57	3.93
Pr	2.11	3.17	7.56	3.83	3.75	0.53	0.86	0.52
Nd	10.31	24.43	30.27	14.09	13.91	2.52	4.12	2.64
Sm	2.46	9.10	6.31	2.38	2.35	0.63	0.89	0.69
Eu	0.49	2.62	1.62	0.56	0.55	0.15	0.17	0.18
Gd	2.68	10.07	7.57	2.74	2.68	0.63	0.92	0.74
Tb	0.43	1.38	1.14	0.41	0.40	0.08	0.14	0.10
Dy	2.57	7.63	6.25	2.32	2.26	0.46	0.83	0.55
Ho	0.45	1.36	1.04	0.39	0.38	0.08	0.14	0.10
Er	1.09	3.53	2.57	0.99	0.98	0.21	0.36	0.26
Tm	0.13	0.43	0.30	0.12	0.11	0.03	0.04	0.03
Yb	0.80	2.61	1.77	0.74	0.72	0.16	0.26	0.20
Lu	0.10	0.38	0.24	0.10	0.10	0.02	0.03	0.03
[a] ∑REE	42.30	83.76	174.84	86.81	84.75	11.92	16.28	12.05
[b] ∑LREE	34.05	56.36	153.96	79.00	77.10	10.25	13.54	10.05
[c] ∑HREE	8.25	27.40	20.88	7.81	7.65	1.66	2.74	2.01
[d] ∑REY	54.18	122.56	199.71	97.34	95.06	14.34	20.11	14.95
LREE/HREE	4.13	2.06	7.37	10.12	10.08	6.16	4.95	5.01
[e] La_N/Yb_N	4.30	1.01	14.43	18.92	18.89	9.45	5.03	7.09
[f] La_N/Sm_N	55.24	11.44	159.40	231.49	227.72	94.26	57.19	79.78
[g] Sm_N/Yb_N	3.28	3.73	3.82	3.45	3.50	4.23	3.71	3.75
[h] δCe	0.99	0.84	0.94	0.94	0.94	0.90	1.04	0.89
[i] δEu	0.58	0.83	0.72	0.66	0.67	0.73	0.58	0.79

ESM – Table 4. (continued)

Central Andes IOCG Province									
Deposit	Punta del Cobre				Alcaparrosa		Santos		
Sample	PdC-Cpy	PdC-2-Cpy	PdC-Mgt	PdC-2-Mgt	AD689-4-Cpy	AD689-4-Mgt	DH1546-7-Cpy	DH1	DH1546-7-Mgt
Material	Cpy	Cpy	Mag	Mag	Cpy	Mag	Cpy	Cpy	Mag
Traces									
Li	13.68	10.53	11.29	4.13	7.83	6.73	4.73	5.27	15.78
B	12.59	-	2.41	3.07	97.43	94.19	19.67	4.34	55.55
Na	40064.57	2866.25	4643.37	33528.24	545.66	427.29	299.86	787.68	624.10
Mg	10165.49	21779.73	21537.93	2816.28	8524.59	6738.01	6155.82	5174.58	19449.74
Al	67869.36	27477.90	31353.46	51146.57	11240.34	9444.34	7776.22	6906.96	33405.43
P	895.73	1607.15	1828.13	338.55	25121.32	15084.59	3540.45	675.62	4803.39
K	10724.92	14094.72	15798.83	14899.55	2614.26	2016.80	2602.23	505.53	18828.09
Ca	21247.27	16306.64	11448.11	23344.79	57501.64	34299.49	9561.23	8288.17	14295.03
Ti	1922.86	1269.47	1317.18	2448.04	382.13	439.92	393.99	97.77	1388.15
V	35.89	25.93	193.75	40.12	20.32	176.24	11.21	25.86	116.42
Cr	36.11	20.53	168.68	75.20	4.43	7.18	7.13	9.07	40.04
Mn	831.66	432.74	474.51	1046.05	408.71	457.27	324.93	248.47	1089.96
Fe	-	-	-	-	-	-	-	-	-
Co	10.89	441.75	54.53	6.27	5.99	16.26	158.38	25.54	73.53
Ni	28.41	154.66	139.31	47.59	76.86	117.83	123.90	55.33	141.31
Cu	-	-	-	-	-	-	-	-	-
Zn	31.77	42.09	53.87	35.39	30.94	35.04	80.17	67.65	108.42
As	20.78	8.21	3.89	2.84	16.55	11.93	112.24	24.80	46.66
Rb	23.14	45.26	53.99	14.99	11.42	8.41	8.37	1.67	33.99
Sr	42.37	40.36	44.06	28.34	56.34	37.61	10.24	32.89	31.83
Y	28.72	7.98	10.28	5.61	91.00	58.21	3.71	40.29	8.78
Mo	4.87	2.40	7.24	9.54	1.54	1.45	0.99	1.18	1.93
Ag	2.97	3.08	1.06	0.50	4.01	1.66	5.61	5.71	6.07
Cd	0.09	0.68	0.13	0.05	0.24	0.16	0.32	0.49	0.16
Sn	2.52	4.93	2.91	4.40	4.29	3.55	20.80	1.77	12.31
Sb	1.31	0.68	0.53	0.72	1.39	1.77	2.23	3.96	3.11
Cs	0.34	1.97	2.47	0.09	0.41	0.35	0.31	0.15	0.78
Ba	205.29	101.56	129.40	208.63	35.39	33.59	84.36	20.86	255.05
Tl	0.10	0.12	0.18	0.15	0.06	0.10	0.08	0.01	0.10
Pb	21.75	3.74	2.45	3.76	10.29	7.55	8.76	17.18	5.74
Th	7.01	3.50	6.86	3.84	3.75	4.49	0.31	1.04	1.61
U	3.94	3.76	8.94	2.69	2.52	3.54	0.20	0.33	0.86
Ni/Co	2.61	0.35	2.55	7.59	12.83	7.25	0.78	2.17	1.92
Ni/Cr	0.79	7.53	0.83	0.63	17.33	16.40	17.37	6.10	3.53
Th/U	1.78	0.93	0.77	1.43	1.49	1.27	1.56	3.15	1.87
REE									
La	469.29	5.45	3.87	9.14	248.70	200.04	3.02	15.84	7.99
Ce	757.46	10.21	7.65	20.37	442.12	350.83	7.73	30.46	18.66
Pr	66.58	1.17	1.02	1.83	44.77	34.89	1.03	3.81	2.35
Nd	211.29	4.75	4.45	6.60	175.47	135.85	4.65	18.58	10.22
Sm	27.27	1.04	1.01	1.09	29.76	22.20	1.13	6.58	2.32
Eu	4.81	0.33	0.33	0.20	5.37	3.87	0.22	2.00	0.50
Gd	16.26	1.16	1.27	0.99	28.38	19.75	1.18	10.99	2.45
Tb	1.83	0.19	0.21	0.15	3.56	2.34	0.14	1.57	0.31
Dy	7.66	1.40	1.62	1.06	18.23	11.95	0.74	8.43	1.67
Ho	1.18	0.31	0.39	0.25	3.00	1.90	0.13	1.47	0.30
Er	3.07	1.09	1.57	0.95	6.79	4.31	0.35	3.47	0.85
Tm	0.37	0.17	0.29	0.16	0.66	0.41	0.04	0.36	0.11
Yb	2.48	1.33	2.55	1.40	3.35	2.15	0.24	1.88	0.73
Lu	0.37	0.23	0.51	0.27	0.41	0.27	0.03	0.25	0.11
[a] ∑REE	1569.91	28.84	26.74	44.46	1010.57	790.77	20.65	105.70	48.58
[b] ∑LREE	1536.70	22.96	18.33	39.22	946.19	747.69	17.78	77.27	42.05
[c] ∑HREE	33.22	5.88	8.41	5.24	64.38	43.07	2.87	28.43	6.53
[d] ∑REY	1598.63	36.82	37.02	50.07	1101.58	848.98	24.36	145.99	57.36
LREE/HREE	46.26	3.91	2.18	7.49	14.70	17.36	6.20	2.72	6.43
[e] La_N/Yb_N	127.49	2.76	1.02	4.41	50.05	62.66	8.34	5.67	7.41
[f] La_N/Sm_N	456.12	138.85	101.55	223.01	221.51	238.79	71.21	63.78	91.06
[g] Sm_N/Yb_N	11.79	0.84	0.43	0.83	9.53	11.06	4.94	3.75	3.43
[h] δCe	0.91	0.93	0.91	1.13	0.94	0.93	1.05	0.92	1.03
[i] δEu	0.65	0.92	0.89	0.58	0.56	0.55	0.58	0.71	0.63

ESM – Table 4. (continued)

	Central Andes IOCG Province								
Deposit	Exploration Sur		Laura				Brecha Flores	Manto Ruso	
Sample	ES082-10-Mgt	ES082-10 Po	L2-Cpy	L2-Cpy*	L2-Hmt	L2-Hmt*	BF4	MR-Cpy	MR-Hmt
Material	Mag	Po	Cpy	Cpy	Hem	Hem	Mag	Cpy	Hem
Traces									
Li	0.46	-	-	-	0.08	0.13	25.14	-	2.12
B	38.94	-	3.23	-	-	-	186.89	-	12.61
Na	165.19	132.34	153.27	159.98	96.84	113.48	534.97	318.39	559.89
Mg	2522.94	278.62	1106.12	1074.65	1129.70	1098.25	9833.71	55.23	1022.11
Al	380.10	490.61	207.66	271.91	1212.61	1159.03	29416.67	319.61	3571.35
P	198.38	916.86	-	45.23	13.27	23.80	969.73	13.76	31.69
K	94.19	94.85	77.25	81.51	229.35	248.78	20561.05	54.36	164.05
Ca	215024.81	15501.37	6642.12	6425.04	36570.29	35707.28	10792.63	325.32	5797.06
Ti	11.60	-	11.95	22.38	101.49	93.55	3880.54	11.37	155.93
V	5.68	2.50	73.40	69.97	424.04	411.00	270.09	3.89	50.16
Cr	2.13	10.19	2.47	3.53	4.69	5.71	84.44	2.88	7.61
Mn	3261.51	230.75	336.13	318.82	563.02	546.86	323.14	69.40	175.44
Fe	-	-	-	-	-	-	-	-	-
Co	408.93	1734.51	411.41	393.87	49.65	49.08	1094.99	112.22	14.64
Ni	75.51	304.17	6.18	6.23	3.30	4.12	87.33	81.28	9.03
Cu	-	-	-	-	-	-	-	-	-
Zn	18.77	17.67	12.84	132.58	2.70	51.74	14.35	8.90	37.68
As	119.59	14.02	9.71	9.43	4.63	4.38	18.93	6.98	9.53
Rb	0.50	0.86	0.23	0.30	0.71	0.60	20.38	0.33	0.67
Sr	71.57	4.33	5.80	5.69	19.10	18.15	15.96	3.49	26.50
Y	9.13	3.87	1.51	1.67	5.40	5.11	5.53	1.21	4.08
Mo	0.22	0.56	0.37	0.46	0.94	0.91	29.97	0.97	7.88
Ag	2.32	3.14	0.54	0.90	0.09	0.10	0.72	2.01	2.83
Cd	0.09	0.07	0.08	0.06	0.03	0.01	0.06	0.38	0.11
Sn	11.17	3.63	8.54	9.41	41.94	37.85	4.41	4.24	34.18
Sb	22.89	0.42	1.57	1.66	0.81	0.91	2.12	0.84	1.76
Cs	0.19	0.28	0.06	0.05	0.03	0.04	0.29	0.11	0.07
Ba	17.17	14.27	3.11	3.36	1.91	1.05	461.78	20.38	14.08
Tl	0.02	0.04	-	-	0.03	0.01	0.07	0.02	0.04
Pb	1.56	2.34	2.74	2.94	0.49	0.47	2.14	5.34	2.12
Th	0.10	1.33	0.08	0.10	0.20	0.14	0.95	0.09	0.45
U	0.15	0.29	0.26	0.41	0.83	0.79	4.31	0.43	3.00
Ni/Co	0.18	0.18	0.02	0.02	0.07	0.08	0.08	0.72	0.62
Ni/Cr	35.42	29.85	2.51	1.77	0.70	0.72	1.03	28.23	1.19
Th/U	0.62	4.59	0.31	0.24	0.24	0.18	0.22	0.21	0.15
REE									
La	10.90	1.26	0.45	0.40	1.16	1.13	23.78	0.42	1.75
Ce	23.21	3.00	0.84	0.78	2.12	2.02	42.21	0.86	3.61
Pr	2.76	0.42	0.10	0.10	0.27	0.26	3.65	0.10	0.43
Nd	11.42	2.07	0.47	0.48	1.44	1.38	12.66	0.42	1.90
Sm	2.29	0.61	0.11	0.13	0.39	0.37	2.00	0.11	0.48
Eu	0.29	0.05	0.04	0.04	0.14	0.13	0.54	0.03	0.09
Gd	2.14	0.79	0.16	0.18	0.57	0.55	1.83	0.14	0.55
Tb	0.30	0.12	0.02	0.02	0.08	0.07	0.25	0.02	0.08
Dy	1.62	0.66	0.15	0.18	0.52	0.50	1.54	0.17	0.58
Ho	0.29	0.13	0.04	0.04	0.14	0.14	0.32	0.04	0.13
Er	0.88	0.39	0.15	0.16	0.57	0.54	1.09	0.13	0.42
Tm	0.12	0.05	0.02	0.02	0.09	0.09	0.16	0.02	0.06
Yb	0.84	0.33	0.20	0.21	0.84	0.82	1.26	0.13	0.43
Lu	0.13	0.05	0.05	0.05	0.22	0.21	0.21	0.02	0.06
[a] ∑REE	57.19	9.93	2.80	2.80	8.53	8.21	91.49	2.60	10.57
[b] ∑LREE	50.87	7.40	2.01	1.93	5.51	5.30	84.83	1.93	8.27
[c] ∑HREE	6.32	2.53	0.79	0.87	3.03	2.91	6.66	0.67	2.30
[d] ∑REY	66.32	13.79	4.31	4.47	13.94	13.32	97.03	3.82	14.65
LREE/HREE	8.05	2.93	2.54	2.20	1.82	1.82	12.74	2.87	3.59
[e] La_N/Yb_N	8.70	2.59	1.50	1.26	0.93	0.93	12.75	2.15	2.77
[f] La_N/Sm_N	126.36	55.06	104.78	80.77	79.42	80.32	315.72	103.05	96.73
[g] Sm_N/Yb_N	2.90	1.98	0.60	0.66	0.50	0.49	1.70	0.88	1.21
[h] δCe	1.00	0.99	0.91	0.92	0.88	0.86	0.98	0.98	0.98
[i] δEu	0.40	0.21	0.84	0.71	0.89	0.91	0.85	0.64	0.56

Abbreviations: *Bn – bornite; Cpy – chalcopyrite; Hem – hematite; Mag – magnetite; Po – pyrrhotite. UA – Upper andesite member; VM – Volcanic sedimentary member; LA; Lower andesite member; BP – La Brea phase; LP – Los Lirios phase.* * Repeated analyses; $_N$ – normalized values from Palme et al. (2007); [a] ∑REE = ∑(La-Lu); [b] ∑LREE = ∑(La-Eu); [c] ∑HREE = ∑(Gd-Lu); [d] ∑REY = ∑(REE+Y); [e] $La_N/Yb_N = (La/La_N)/(Yb/Yb_N)$; [f] $La_N/Sm_N = (La/La_N)/(Sm/Sm_N)$; [g] $Sm_N/Yb_N = (Sm/Sm_N)/(Yb/Yb_N)$; [h] $\delta Ce = Ce_N/(0.5La_N+0.5Pr_N)$; [i] $\delta Eu = Eu_N/(0.5Sm_N+0.5Gd_N)$ (Bau & Dulski, 1996).

Supplementary 4 – References

Palme, H., O'Neill, H.S.C., Heinrich, D.H., Karl, K.T., 2007. Cosmochemical estimates of mantle composition, in: Holland, H.D., Turekian, K.K. (Eds.), Treatrise on Geochemistry, First Edition. Elsevier, Oxford, England, pp. 1–38.

Bau, M., Dulski, P., 1996. Distribution of yttrium and rare-earth elements in the Penge and Kuruman iron-formations, Transvaal Supergroup, South Africa. Precambrian Res. 79, 37–55. https://doi.org/10.1016/0301-9268(95)00087-9

ESM – Table 11. Sr-Nd isotopic data for ore-samples included in this study.

Deposit	Type	Sample	Material	Age (Ga)*	Rb (ppm)**	Sr (ppm)**	Rb/Sr**	$^{87}Rb/^{86}Sr$**	$^{87}Sr/^{86}Sr$	I_{Sr}	Sm (ppm)	Nd (ppm)	$^{147}Sm/^{144}Nd$	$^{143}Nd/^{144}Nd$	fSm/Nd	I_{Nd}	± 2σ	εNd	$εNd_i$	T_{DM} (Ga)
Carajás Mineral Province																				
Alemão	Mag IOCG	AM-Cpy	Cpy	2.74 [a]	16.16	18.40	0.88	2.54428	0.71711	0.61617	36.09	314	0.0695	0.510319	-0.65	0.509063	1.90E-05	-45.23	-0.37	2.88
		AM-Mgt	Cpy	2.74 [a]	4.93	1.49	3.30	9.57652	0.72399	0.34404	5.59	107.83	0.0313	0.510531	-0.84	0.509964	1.40E-05	-41.1	17.34	2.09
Salobo	Mag IOCG	C103	Cpy	2.74 [a]	2.32	7.25	0.32	0.93170	0.75670	0.71973	32.16	126.54	0.1536	0.511766	-0.22	0.508989	4.00E-06	-17.01	-1.82	3.29
		C105	Cpy	2.74 [a]	-	-	-	-	-	-	834.23	4352.9	0.1158	0.510619	-0.411	0.508525	7.00E-06	-39.38	-10.93	3.83
		M103	Mag	2.74 [a]	0.73	0.82	0.89	2.58734	0.75807	0.65542	15.35	65.46	0.1418	0.511583	-0.28	0.509019	1.40E-05	-20.58	-1.22	3.12
		M104	Mag	2.74 [a]	-	1.23	-	-	-	-	16.61	56.27	0.1785	0.512187	-0.09	0.50896	1.20E-05	-8.79	-2.39	3.95
Sequeirinho	Mag IOCG	CSQ01	Cpy	2.74 [a]	-	-	-	-	0.71355	-	28.69	170.64	0.1016	0.51103	-0.48	0.509193	1.40E-05	-31.38	2.19	2.74
		CSQ02	Cpy	2.74 [a]	-	-	-	-	0.71818	-	-	-	-	-	-	-	-	-	-	-
		MSQ01	Mag	2.74 [a]	-	-	-	-	0.71405	-	11.82	51.07	0.1399	0.511443	-0.29	0.508913	5.00E-06	-23.3	-3.3	3.35
		MSQ02	Mag	2.74 [a]	0.79	51.59	0.02	0.04432	0.71937	0.71761	51.06	442.3	0.0698	0.510185	-0.65	0.508923	1.30E-05	-47.86	-3.11	3.03
		MSQ04	Mag	2.74 [a]	1.80	12.93	0.14	0.40334	0.71759	0.70159	1.53	6.24	0.1482	0.511834	-0.25	0.509154	6.00E-06	-15.68	1.43	2.82
Sossego	Mag Remobilized IOCG[1,2] or granite-related Cu-Au[2]	CSS01	Cpy	1.88 [b]	1.86	6.31	0.30	0.85720	0.74121	0.71802	-	-	-	-	-	-	-	-	-	-

ESM – Table 5. (continued)

Deposit	Type	Sample	Material	Age (Ga)*	Rb (ppm)*	Sr (ppm)*	Rb/Sr **	$^{87}Rb/^{86}Sr$	$^{87}Sr/^{86}Sr$	I_{Sr}	Sm (ppm)	Nd (ppm)	$^{147}Sm/^{144}Nd$	$^{143}Nd/^{144}Nd$	fSm/Nd	I_{Nd}	± 2σ	εNd	$εNd_i$	T_{DM} (Ga)
		CSS02	Cpy	1.88 [b]	0.38	30.84	0.01	-	-	-	13.67	90.68	0.0911	0.510862	-0.54	0.509736	1.00E-05	-34.64	-9.22	2.71
		CSS03	Cpy	1.88 [b]	-	-	-	-	0.74808	-	0.35	0.88	0.2378	0.512656	0.21	0.509716	2.70E-05	0.34	-9.61	-
		CSS04	Cpy	1.88 [b]	0.68	19.31	0.04	0.1028	0.75449	0.75171	11.69	59.37	0.119	0.511176	-0.39	0.509705	1.20E-05	-28.52	-9.83	3.02
		MSS01	Mag	1.88 [b]	4.41	30.15	0.15	0.4241	0.73479	0.72331	12.22	60.47	0.1222	0.511121	-0.38	0.50961	1.00E-05	-29.58	-11.68	3.22
		MSS02	Mag	1.88 [b]	43.50	53.13	0.82	2.3806	0.75416	0.68975	23.93	96.4	0.1501	0.511523	-0.24	0.509667	1.50E-05	-21.75	-10.56	3.74
<u>Australian IOCG</u>																				
Olympic Dam	Hem IOCG	OD-Bn	Bn	1.59 [c]	32.73	108.06	0.30	0.8775	0.71695	0.69691	45.26	1212.58	0.0226	0.513276	-0.86	0.51304	1.80E-05	12.45	48.15	-0.16
Ernest Henry	Mag IOCG	EH-Cpy	Cpy	1.53 [d]	34.25	19.14	1.79	5.2050	0.76133	0.64701	5.33	38.64	0.0834	0.511377	-0.58	0.510538	8.00E-06	-24.59	-2.39	1.94
		EH-Mgt	Mag	1.53 [d]	21.89	13.91	1.57	4.5784	0.75804	0.65748	1.8	11.94	0.0912	0.511422	-0.54	0.510505	7.00E-06	-23.72	-3.03	2
<u>Central Andes IOCG Province</u>																				
Candelaria	Mag IOCG	LS1257-5b-Cpy	Cpy	0.12 [e]	0.60	7.94	0.08	0.2196	0.70901	0.70864	2.75	11.55	0.1438	0.51275	-0.27	0.512637	1.90E-05	2.18	3	0.65
		LS1257-5b-Po	Po	0.12 [e]	0.54	2.42	0.22	0.6419	0.70546	0.70437	-	-	-	-	-	-	-	-	-	
		LS1257-6b-Cpy	Cpy	0.12 [e]	1.68	3.50	0.48	1.3870	0.70788	0.70551	8.82	23.5	0.2269	0.512797	0.15	0.512619	1.40E-05	3.1	2.64	-
		LS1257-6b-Po	Po	0.12 [e]	4.12	5.80	0.71	2.0533	0.70665	0.70315	-	-	-	-	-	-	-	-	-	
		LS1455-11a-Cpy	Cpy	0.12 [e]	5.47	11.00	0.50	1.4384	0.70638	0.70393	6.27	29.46	0.1286	0.512722	-0.35	0.512621	1.50E-05	1.64	2.68	0.59
		LS1455-11a-Mgt	Mag	0.12 [e]	4.03	6.83	0.59	1.7086	0.70632	0.70341	3.32	17.25	0.1163	0.512235	-0.41	0.512144	1.10E-05	-7.87	-6.63	1.26
		LS1257-6b-Mgt	Mag	0.12 [e]	3.94	8.29	0.48	1.3748	0.70693	0.70459	0.71	2.47	0.1747	0.512761	-0.11	0.51263	2.00E-05	2.41	2.72	-
Punta del Cobre	Magnetite IOCG	PdC-Cpy	Cpy	0.12 [e]	32.05	34.99	0.92	2.6517	0.70981	0.70529	28.49	204.03	0.0844	0.512687	-0.57	0.512621	1.90E-05	0.96	2.68	0.43
		PdC-Mgt	Cpy	0.12 [e]	20.77	23.40	0.89	2.5695	0.71205	0.70767	-	9.95	-	0.512712	-	-	2.10E-05	1.45	-	-

ESM – Table 5. (continued)

Deposit	Type	Sample	Material	Age (Ga) *	Rb (ppm) **	Sr (ppm) **	Rb/Sr	$^{87}Rb/^{86}Sr$ **	$^{87}Sr/^{86}Sr$	I_{sr}	Sm (ppm)	Nd (ppm)	$^{147}Sm/^{144}Nd$	$^{143}Nd/^{144}Nd$	fSm/Nd	I_{Nd}	± 2σ	εNd	$εNd_i$	T_{DM} (Ga)
		PdC-2-Cpy	Cpy	0.12 [e]	62.69	33.33	1.88	5.4490	0.71734	0.70805	-	-	-	-	-	-	-	-	-	-
		PdC-2-Mgt	Mag	0.12 [e]	74.78	36.39	2.06	5.9492	0.70915	0.69900	1.60	6.66	0.1451	0.512804	-0.26	0.512690	8.00E-06	3.24	4.03	0.55
Alcaparrosa	Mag IOCG	AD 689-4-Cpy	Cpy	0.12 [e]	15.82	46.53	0.34	0.9838	0.70621	0.70453	35.07	206.67	0.1026	0.512738	-0.48	0.512657	4.00E-06	1.96	3.39	0.44
		AD 689-4-Mgt	Mag	0.12 [e]	11.65	31.06	0.38	1.0854	0.70650	0.70465	17.92	109.75	0.0987	0.512654	-0.50	0.512577	5.00E-06	0.32	1.81	0.53
Santos	Mag IOCG	DH1	Cpy	0.12 [e]	2.31	27.16	0.09	0.2465	0.70571	0.70529	8.37	26.41	0.1915	0.513187	-0.03	0.513037	1.70E-05	10.71	10.79	0.44
		DH1546-7-Cpy	Cpy	0.12 [e]	11.59	8.45	1.37	3.9680	0.70832	0.70155	-	-	-	-	-	-	-	-	-	-
		DH1546-7-Mgt	Mag	0.12 [e]	47.08	26.29	1.79	5.1837	0.70803	0.69919	1.14	4.94	0.1391	0.512744	-0.29	0.512635	1.90E-05	2.07	2.95	0.63
Exploration Sur	Mag IOCG	ES082-10-Cpy	Cpy	0.12 [f]	-	-	-	-	-	-	-	-	-	-	-	-	-	-	-	-
		ES082-10-Po	Po	0.12 [f]	1.19	3.58	0.33	0.9641	0.70566	0.70402	0.65	2.08	0.1888	0.512775	-0.04	0.512633	5.00E-06	2.67	2.69	-
Brecha Flores	Hem IOCG	BF4	Mag	0.12 [f]	28.22	13.18	2.14	6.2067	0.71890	0.70831	-	-	-	-	-	-	-	-	-	-
Laura	Hem IOCG	L2-Cpy	Cpy	0.12 [f]	0.32	4.79	0.07	0.1940	0.70396	0.70363	-	-	-	-	-	-	-	-	-	-
		L2-Hmt	Hem	0.12 [f]	0.98	15.77	0.06	0.1793	0.70393	0.69682	0.42	1.44	0.1764	0.513050	-0.10	0.512912	9.00E-06	8.04	8.35	-
Manto Ruso	Hem IOCG	MR-Cpy	Cpy	0.12 [f]	0.46	2.88	0.16	0.4586	0.70486	0.70408	-	-	-	-	-	-	-	-	-	-
		MR-Hmt	Hem	0.12 [f]	0.93	21.89	0.04	0.1233	0.70727	0.70238	-	-	-	-	-	-	-	-	-	-

Note: The present-day CHUR (chondritic uniform reservoir) values are $^{147}Sm/^{144}Nd = 0.1967$ and $^{143}Nd/^{144}Nd = 0.512638$, $\lambda Sm = 6.54 \times 10^{-12}$/year (Jacobsen & Wasserburg, 1980). T_{DM} values were calculated using the model of DePaolo (1981). (1) Pollard et al. (2019); (2) Schutesky & Oliveira (2020) * Calculated at Age (Ga): [a] Referential value; [b] Moreto et al. (2015b); [c] Cherry et al. (2018); [d] Mark et al. (2006); [e] del Real et al. (2018); [f] Vila et al. (1996). ** Values recalculated from ICP-MS data, formulas avaliable on Janoušek et al. (2016). Abbreviations: Bn – bornite; Cpy – chalcopyrite; Hem – hematite; Mag – magnetite; Po – pyrrhotite.

Supplementary 5 - References

Cherry, A.R., Ehrig, K., Kamenetsky, V.S., McPhie, J., Crowley, J.L., Kamenetsky, M.B., 2018. Precise geochronological constraints on the origin, setting and incorporation of ca. 1.59 Ga surficial facies into the Olympic Dam Breccia Complex, South Australia. Precambrian Res. 315, 162–178. https://doi.org/10.1016/j.precamres.2018.07.012

del Real, I., Thompson, J.F., Carriedo, J., 2018. Lithological and structural controls on the genesis of the Candelaria-Punta del Cobre Iron Oxide Copper Gold district, Northern Chile. Ore Geol. Rev. 102, 106–153. https://doi.org/10.1016/j.oregeorev.2018.08.034.

DePaolo, D.J., 1981. Neodymium isotopes in the Colorado Front Range and crust-mantle evolution in the Proterozoic. Nature 291, 193–196. https://doi.org/10.1038/291193a0

Jacobsen, S.B., Wasserburg, G.J., 1980. Sm-Nd isotopic evolution of chondrites. Earth Planet. Sci. Lett. 50, 139–155. https://doi.org/10.1016/0012-821X(80)90125-9

Janoušek, V., Moyen, J.F., Martin, H., Erban, V., Farrow, C., 2016. Geochemical modelling of igneous processes–principles and recipes in R language. Springer, Berlin.

Mark, G., Oliver, N.H.S., Williams, P.J., 2006. Mineralogical and chemical evolution of the Ernest Henry Fe oxide–Cu–Au ore system, Cloncurry district, northwest Queensland, Australia. Miner. Deposita 40, 769–801. https://doi.org/10.1007/s00126-005-0009-7

Moreto, C.P., Monteiro, L.V.S., Xavier, R.P., Creaser, R.A., DuFrane, S.A., Melo, G.H., da Silva, M.A.D., Tassinari, C.C.G., Sato, K., 2015b. Timing of multiple hydrothermal events in the iron oxide-copper-gold deposits of the Southern Copper Belt, Carajás Province, Brazil. Miner. Deposita 50, 517-546. https://doi.org/10.1007/s00126-014-0549-9

Pollard, P.J., Taylor, R.G., Peters, L., Matos, F., Freitas, C., Saboia, L., Hunh, S., 2019. ^{40}Ar-^{39}Ar dating of Archean iron oxide Cu-Au and Paleoproterozoic granite-related Cu-Au deposits in the Carajás Mineral Province, Brazil: implications for genetic models. Miner. Deposita 54, 329–346. https://doi.org/10.1007/s00126-018-0809-1

Schutesky, M.E., Oliveira, C.G., 2020. From the roots to the roof: an integrated model for the Neoarchean Carajás IOCG System, Brazil. Ore Geology Reviews, 103833. https://doi.org/10.1016/j.oregeorev.2020.103833

Vila, T., Lindsay, N., Zamora, R., 1996. Geology of the Mantoverde copper deposit, northern Chile: a specularite-rich hydrothermal tectonic breccia related to the Atacama fault zone. Geol. Soc. Spec. Publ. 5, 157–170. https://doi.org/10.5382/SP.05.11

ESM – Table 12. Compiled Sm-Nd isotopic data from the Carajás Mineral Province, Brazil.

Sample	Unit	Petrography	Age (Ma)	Sm (ppm)	Nd (ppm)	$^{147}Sm/^{144}Nd$	± σ	$^{143}Nd/^{144}Nd$	± σ	εNd	I_{Nd}	$εNd_i$	T_{DM} (Ga)	Reference
Greenstone Belts														
381	Identidade Greenstone Belt - RMD	Dac.	3064	4661	29240	0.0963	1.0E-4	0.510746	1.1E-5	-	-	1.9	3.1	de Souza et al. (2001)
178E	Identidade Greenstone Belt - RMD	Dac.	3064	1288	6998	0.1114	1.0E-4	0.510959	1.0E-5	-	-	0.22	3.24	de Souza et al. (2001)
173Z	Identidade Greenstone Belt - RMD	Dac.	3064	0.855	4404	0.1173	1.0E-4	0.511169	1.7E-5	-	-	2.04	3.11	de Souza et al. (2001)
105C	Identidade Greenstone Belt - RMD	Dac.	3064	0.84	3980	0.1276	1.0E-4	0.511331	1.2E-5	-	-	1.24	3.2	de Souza et al. (2001)
173C	Identidade Greenstone Belt - RMD	Dac.	3064	5909	21.05	0.1697	2.0E-4	0.512263	5.0E-6	-	-	3.15	3.05	de Souza et al. (2001)
57A	Identidade Greenstone Belt - RMD	Bas.	3064	2004	6230	0.1945	2.0E-4	0.51271	3.1E-5	-	-	2.28	-	de Souza et al. (2001)
168	Identidade Greenstone Belt - RMD	Bas.	3064	1709	5093	0.2029	2.0E-4	0.512889	9.0E-6	-	-	2.53	-	de Souza et al. (2001)
270C	Identidade Greenstone Belt - RMD	Bas.	3064	1664	4953	0.2031	2.0E-4	0.512862	1.4E-5	-	-	1.9	-	de Souza et al. (2001)
478	Identidade Greenstone Belt - RMD	Bas.	3064	2077	6181	0.2032	2.0E-4	0.512874	1.4E-5	-	-	2.12	-	de Souza et al. (2001)
32A	Identidade Greenstone Belt - RMD	Bas.	3064	2.05	6086	0.2037	2.0E-4	0.512863	2.9E-5	-	-	1.72	-	de Souza et al. (2001)
9	Identidade Greenstone Belt - RMD	Bas.	3064	1957	5777	0.2048	2.0E-4	0.512881	6.0E-5	-	-	1.62	-	de Souza et al. (2001)
123	Identidade Greenstone Belt - RMD	Gab.	3064	2546	8098	0.1901	2.0E-4	0.512567	2.3E-5	-	-	1.11	-	de Souza et al. (2001)
39X	Identidade Greenstone Belt - RMD	Gab.	3064	2482	7640	0.1964	2.0E-4	0.512719	2.5E-5	-	-	1.63	-	de Souza et al. (2001)
24	Identidade Greenstone Belt - RMD	Gab.	3064	2606	7802	0.2019	2.0E-4	0.512836	1.3E-5	-	-	1.85	-	de Souza et al. (2001)
266B	Identidade Greenstone Belt - RMD	Gab.	3064	1973	5780	0.2064	2.0E-4	0.512949	1.8E-5	-	-	2.26	-	de Souza et al. (2001)
PP05A	Greenstone Belts	Gneiss	2850	5553	50242	0.066835	-	0.510149	-	-	-	-1.25	3.02	Sato & Tassinari (1997)
PP05H	Greenstone Belts	Ton.	2850	1175	7919	0.089724	-	0.510641	-	-	-	-0.05	2.98	Sato & Tassinari (1997)
Gneissified granitoids														
AER-27	Serra Dourada Granite	Mgr.	2830	3.02	16.58	0.1084	-	0.510996	1.6E-5	-32.03	-	0.15	3.00	Feio et al. (2013)
AER-59	Serra Dourada Granite	Mgr.	2830	3.47	22.22	0.1025	-	0.510925	1.1E-5	-33.42	-	0.92	2.94	Feio et al. (2013)
AE-47	Bom Jesus Orthogneiss	Mgr.	2850	1.45	12.04	0.0729	-	0.510337	1.9E-5	-44.9	-	0.55	2.96	Feio et al. (2013)
ARC-116	Bom Jesus Orthogneiss	Mgr.	2850	2.6	31	0.0508	-	0.509899	1.7E-5	-53.4	-	0.12	2.97	Feio et al. (2013)
ARC-113	Cruzadão Granite	Sgr.	2850	7.68	70.78	0.0655	-	0.510217	1.4E-5	-47.2	-	2.31	2.93	Feio et al. (2013)
GRD-58A	Cruzadão Granite	Sgr.	2850	13.33	82.55	0.0976	-	0.510793	1.0E-6	-36	-	0.38	2.99	Feio et al. (2013)
AER-29A	Campina Verde Comp.	Ton.	2850	3.21	17.47	0.1111	-	0.511008	8.0E-6	-31.8	-	-0.38	3.06	Feio et al. (2013)
ARC-65A	Campina Verde Comp.	Ton.	2850	4.98	31.65	0.0951	-	0.510651	9.0E-6	-38.76	-	-1.48	3.11	Feio et al. (2013)
ARC-95A	Campina Verde Comp.	Ton.	2850	4.44	23.74	0.1131	-	0.511033	1.3E-5	-31.31	-	-0.63	3.09	Feio et al. (2013)
ERF-113	Campina Verde Comp.	Grd.	2850	3.75	19.03	0.1192	-	0.511178	1.4E-5	-28.48	-	-0.04	3.05	Feio et al. (2013)
ERF-07C	Campina Verde Comp.	Grd.	2850	2.48	16.47	0.091	-	0.510697	2.2E-5	-37.86	-	0.94	2.94	Feio et al. (2013)
ERF-134	Campina Verde Comp.	Grd.	2850	4.9	29.04	0.1021	-	0.51065	2.6E-4	-38.78	-	-4.09	3.32	Feio et al. (2013)
GRD-79C	Rio Verde Trondhjemite	Grd.	2860	1.21	10.08	0.0723	-	0.510421	1.2E-5	-43.2	-	2.75	2.85	Feio et al. (2013)
AER-11	Rio Verde Trondhjemite	Trond.	2930	1.78	18.7	0.0572	-	0.509949	2.2E-5	-52.5	-	0.19	3.04	Feio et al. (2013)
AER-77B	Rio Verde Trondhjemite	Trond.	2930	2.55	21.17	0.0741	-	0.510399	1.7E-5	-43.7	-	2.61	2.91	Feio et al. (2013)
AMR-102	Canaã dos Carajás Granite	Mgr.	2950	1.94	11.14	0.105	-	0.51082	6.0E-5	-35.46	-	-0.66	3.16	Feio et al. (2013)
AMR-213	Canaã dos Carajás Granite	Mgr.	2950	3.84	23.49	0.0988	-	0.510691	5.0E-6	-37.98	-	-0.51	3.16	Feio et al. (2013)
F24/251.4	Xingu Comp.	Ton. Gneiss	2859	3711	18877	0.1189	4.1E-4	0.51082	4.0E-4	-35.4	-	-7.02	3.65	Mellito (1998)
F147/32.7	Xingu Comp.	Ton. Gneiss	2859	3027	23302	0.0785	2.6E-4	0.510431	4.0E-5	-43.05	-	0.04	2.98	Mellito (1998)
F19/259.06	Xingu Comp.	Ton. Gneiss	2859	60372	36111	0.1067	3.5E-4	0.510953	3.6E-5	-32.87	-	-0.05	3.01	Mellito (1998)
F19/258.0	Xingu Comp.	Ton. Gneiss	2859	4167	22099	0.1140	3.8E-4	0.511037	4.6E-5	-31.23	-	-1.08	3.11	Mellito (1998)

ESM – Table 6. (continued)

Sample	Unit	Petrography	Age (Ma)	Sm (ppm)	Nd (ppm)	$^{147}Sm/^{144}Nd$	± σ	$^{143}Nd/^{144}Nd$	± σ	εNd	I_{Nd}	$εNd_i$	T_{DM} (Ga)	Reference
F12/498.3	Xingu Comp.	Ton. Gneiss	2859	9302	65635	0.0857	2.8E-4	0.510605	3.6E-5	-39.66	-	0.82	2.93	Mellito (1998)
F143/303.3	Xingu Comp.	Ton. Gneiss	2859	5508	39799	0.0837	2.8E-4	0.510578	4.2E-5	-40.18	-	1.03	2.92	Mellito (1998)
<u>Volcanic rocks</u>														
A37	Igarapé-Bahia Group	Metavolc. maf.	2745	4.72	27.19	0.1049	-	0.5109	7.0E-5	-33.3	-	-0.85	2.99	Galarza (2002)
A62	Igarapé-Bahia Group	Metavolc. maf.	2745	0.64	3.68	0.1060	-	0.5109	3.0E-5	-33.77	-	-1.71	3.06	Galarza (2002)
A44	Igarapé-Bahia Group	Metavolc. maf.	2745	5.12	27.75	0.1116	-	0.5110	1.1E-4	-31.09	-	-1.03	3.02	Galarza (2002)
A24	Igarapé-Bahia Group	Metavolc. maf.	2745	2.63	12.28	0.1293	-	0.5113	9.0E-5	-25.4	-	-1.59	3.13	Galarza (2002)
A61	Igarapé-Bahia Group	Metavolc. maf.	2745	1.87	6.79	0.1662	-	0.5120	1.1E-4	-12.37	-	-1.62	3.47	Galarza (2002)
A50	Igarapé-Bahia Group	Metapiroc.	2747	3.21	30.21	0.0943	-	0.5107	1.0E4	-37.78	-	-1.59	3.02	Galarza (2002)
A54	Igarapé-Bahia Group	Metapiroc.	2747	4.33	22.11	0.0985	-	0.5108	1.1E-04	-36.83	-	-2.12	3.07	Galarza (2002)
A31	Igarapé-Pojuca Group	Metavolc. maf.	2757	7.19	32.64	0.1332	-	0.5114	9.0E-6	-24.73	-	-2.2	3.23	Galarza (2002)
A5	Igarapé-Pojuca Group	Metavolc. maf.	2757	2.01	8.84	0.1372	-	0.5115	2.4E-5	-22.53	-	-1.42	3.17	Galarza (2002)
A6	Igarapé-Pojuca Group	Metavolc. maf.	2757	2.52	10.93	0.1391	-	0.5115	1.4E-5	-21.34	-	-0.89	3.12	Galarza (2002)
GB-67	Grão Pará Group	Bas. Trach.	2758	2.7	11.97	0.1364	-	0.5118	-	-	-	3.6	-	Gibbs et al. (1986)
GB-82-a	Grão Pará Group	Bas.	2758	3.55	12.23	0.1755	-	0.5125	-	-	-	4.6	-	Gibbs et al. (1986)
GB-82-b	Grão Pará Group	Bas.	2758	3.55	11.82	0.1813	-	0.5121	-	-	-	-7	-	Gibbs et al. (1986)
GB-85	Grão Pará Group	Rhy.	2758	13.61	75.73	0.1087	-	0.5113	-	-	-	3.8	-	Gibbs et al. (1986)
GB-86	Grão Pará Group	Bas. Trach.	2758	2.76	12.34	0.1352	-	0.5117	-	-	-	2.6	-	Gibbs et al. (1986)
GB-87	Grão Pará Group	Bas.	2758	2.94	12.84	0.1387	-	0.5115	-	-	-	-1.9	-	Gibbs et al. (1986)
GB-93	Grão Pará Group	Bas. Trach.	2758	3.03	13.58	0.1351	-	0.5116	-	-	-	1.2	-	Gibbs et al. (1986)
GB-94	Grão Pará Group	Rhy.	2758	3.25	15.82	0.1244	-	0.5114	-	-	-	-0.6	-	Gibbs et al. (1986)
GB-102	Grão Pará Group	Bas. Trach.	2758	2.7	11.86	0.1378	-	0.5118	-	-	-	-3.2	-	Gibbs et al. (1986)
GB-104	Grão Pará Group	Bas. Trach.	2758	2.9	12.99	0.1370	-	0.5115	-	-	-	-1.8	-	Gibbs et al. (1986)
AND137,70	Grão Pará Group	And.	2579	9.17	41.93	0.1323	-	0.5114	6.0E-6	-25.02	-	-	3.18	Lindenmayer et al. (2005)
AND 201,80	Grão Pará Group	And.	2579	4931	17152	0.1738	-	0.5120	7.0E-6	-12.4	-	-	4.26?	Lindenmayer et al. (2005)
AND 153,70	Grão Pará Group	And.	2579	21.83	98.9	0.1334	-	0.5114	7.0E-6	-24.43	-	-	3.17	Lindenmayer et al. (2005)
F1100/172	Parauapebas Fm.	Bas.	2749	6961	36252	0.1161	-	0.5111	6.0E-6	-30	-	-1.53	3.02	Martins et al. (2017)
F1279/Z	Parauapebas Fm.	Bas.	2749	5365	23.04	0.1408	-	0.5114	2.7E-5	-23.8	-	-4.11	3.36	Martins et al. (2017)
F1279/D	Parauapebas Fm.	Bas.	2749	3.67	16601	0.1337	-	0.5114	2.3E-5	-24.22	-	-1.95	3.16	Martins et al. (2017)
F1398/151	Parauapebas Fm.	Bas.	2749	3602	14525	0.1499	-	0.5116	1.4E-5	-19.5	-	-2.99	3.31	Martins et al. (2017)
GB102	Grão Para Group	Rhy.	2573	2.7	11.86	0.1378	-	0.5118	-	-	-	4.09	2.55	Olszewski et al. (1989)
GB104	Grão Para Group	Rhy.	2760	2.9	12.99	0.1377	-	0.5115	-	-	-	-0.96	3.08	Olszewski et al. (1989)
GB67	Grão Para Group	Bas.	2760	2.7	11.97	0.1342	-	0.5118	-	-	-	4.39	2.52	Olszewski et al. (1989)
GB82A	Grão Para Group	Bas.	2760	3.55	12.23	0.1755	-	0.5125	-	-	-	5.3	2.07	Olszewski et al. (1989)
GB82B	Grão Para Group	Bas.	2760	3.55	11.82	0.1813	-	0.5121	-	-	-	-6.31	5.70?	Olszewski et al. (1989)
GB85	Grão Para Group	Bas.	2760	13.61	75.73	0.1087	-	0.5113	-	-	-	4.58	2.57	Olszewski et al. (1989)
GB86	Grão Para Group	Bas.	2760	2.76	12.34	0.1352	-	0.5117	-	-	-	3.43	2.63	Olszewski et al. (1989)
GB87	Grão Para Group	Bas.	2760	2.94	12.84	0.1387	-	0.5115	-	-	-	-1	3.10	Olszewski et al. (1989)
GB93	Grão Para Group	Bas.	2760	3.03	13.58	0.1351	-	0.5116	-	-	-	2.03	2.77	Olszewski et al. (1989)

ESM – Table 6. (continued)

Sample	Unit	Petrography	Age (Ma)	Sm (ppm)	Nd (ppm)	$^{147}Sm/^{144}Nd$	± σ	$^{143}Nd/^{144}Nd$	± σ	εNd	I_{Nd}	$εNd_i$	T_{DM} (Ga)	Reference
GB94	Grão Para Group	Bas.	2760	3.25	15.82	0.1244	-	0.5114	-	-	-	0.32	2.92	Olszewski et al. (1989)
FSAL01316,47	Salobo-Pojuca Group	Amp.	2812	5008	19.01	0.1701	-	0.5122	4.1E-5	-	-	-	-	Pimentel et al. (2003)
FSAL01322,16	Salobo-Pojuca Group	Amp.	2812	2835	9101	0.1883	-	0.5126	1.4E-5	-	-	-	-	Pimentel et al. (2003)
FSAL01390,55	Salobo-Pojuca Group	Amp.	2812	5151	17.23	0.1807	-	0.5124	1.0E-5	-	-	-	-	Pimentel et al. (2003)
F20/763,87	Salobo-Pojuca Group	Sch.	2812	8289	44.81	0.1124	-	0.5111	1.9E-5	-	-	-	2.79	Pimentel et al. (2003)
F20/786,72	Salobo-Pojuca Group	Sch.	2812	6001	27.93	0.1305	-	0.5114	1.8E-5	-	-	-	2.91	Pimentel et al. (2003)
F20/788,52	Salobo-Pojuca Group	Sch.	2812	9393	48.95	0.1160	-	0.5111	1.1E-5	-	-	-	3.01	Pimentel et al. (2003)
F20/731,40	Salobo-Pojuca Group	Sch.	2812	22.3	140.79	0.0962	-	0.5109	1.6E-5	-	-	-	2.79	Pimentel et al. (2003)
F20/661,60	Salobo-Pojuca Group	And.	2719	8318	41.49	0.1218	-	0.5112	1.3E-5	-	-	-	3.06	Pimentel et al. (2003)
F20/683,37	Salobo-Pojuca Group	And.	2719	10.43	56.07	0.1131	-	0.5110	1.9E-5	-	-	-	3.04	Pimentel et al. (2003)
F20/691,45	Salobo-Pojuca Group	And.	2719	26.01	138.05	0.1145	-	0.5111	1.5E-5	-	-	-	2.99	Pimentel et al. (2003)
F20/149,60	Salobo-Pojuca Group	And.	2719	3514	11.78	0.1812	-	0.5124	1.7E-5	-	-	-	-	Pimentel et al. (2003)
F20/153,45	Salobo-Pojuca Group	And.	2719	2155	5913	0.2216	-	0.5129	5.5E-5	-	-	-	-	Pimentel et al. (2003)
LUSL 19	Itacaiunas Supergroup	Bas.	2742	2386	7239	0.1992	-	0.5128	2.4E-5	2.56	0.508997	1.68	-	Teixeira (2013)
Mafic-ultramafic magmatism														
A58	Dike at Ig. Bahia dep.	Intrus. maf.	2765	6.35	32.22	0.12324		0.51128	1.1E-4	-26.51	-	-0.36	3.01	Galarza (2002)
A47	Dike at Ig. Bahia dep.	Intrus. maf.	2765	3.66	18.07	0.12248		0.51121	1.2E-4	-27.89	-	-1.49	3.01	Galarza (2002)
A33	Gameleira dep.	Intrus. maf.	2705	7.12	31.35	0.13736	-	0.511413	-	-23.9	-	-3.26	3.33	Galarza & Macambira (2002)
A11	Gameleira dep.	Intrus. maf.	2705	1.6	6.68	0.14473	-	0.511638	-	-19.51	-	-1.42	3.17	Galarza & Macambira (2002)
GB 193,30	Alvo Estrela dep.	Gab.	2579	10161	14681	0.4184	-	0.515974	1.0E-5	65.08	-	-	-	Lindenmayer et al. (2005)
GB 290,40	Alvo Estrela dep.	Gab.	2579	2679	8157	0.1986	-	0.512554	6.0E-6	-2.23	-	-	-	Lindenmayer et al. (2005)
GB 229,40	Alvo Estrela dep.	Gab.	2579	3813	18.15	0.127	-	0.511291	6.0E-6	-26.28	-	-	3.10	Lindenmayer et al. (2005)
GB 294,10	Alvo Estrela dep.	Gab.	2579	3803	14784	0.1555	-	0.511876	9.0E-6	-14.87	-	-	3.10	Lindenmayer et al. (2005)
LUFD120B	Luanga Comp.	Nor.	2763	0.598	2416	0.1498	-	0.51176	1.0E-5	-17.13	-	-0.47	3.09	Mansur (2017)
LUFD120A	Luanga Comp.	Nor.	2763	1014	4231	0.1448	-	0.511681	6.0E-6	-18.67	-	-0.23	3.04	Mansur (2017)
LUFD93-103	Luanga Comp.	Nor.	2763	0.209	0.986	0.1279	-	0.511338	1.4E-5	-25.36	-	-0.92	3.05	Mansur (2017)
LUFD120B	Luanga Comp.	Nor.	2763	0.598	2416	0.1498	-	0.51176	1.0E-5	-17.13	-	-0.47	3.09	Mansur (2017)
LUFD120A	Luanga Comp.	Nor.	2763	1014	4231	0.1448	-	0.511681	6.0E-6	-18.67	-	-0.23	3.04	Mansur (2017)
LUFD93-103	Luanga Comp.	Nor.	2763	0.209	0.986	0.1279	-	0.511338	1.4E-5	-25.36	-	-0.92	3.05	Mansur (2017)
LUFD79-143	Luanga Comp.	Nor.	2763	0.33	2073	0.0963	-	0.510855	9.0E-6	-34.78	-	0.9	2.84	Mansur (2017)
LUFD78-206	Luanga Comp.	Opx.	2763	0.157	0.763	0.124	-	0.51141	2.0E-5	-23.95	-	1.89	2.78	Mansur (2017)
LUFD78-55	Luanga Comp.	Nor.	2763	0.246	1.79	0.093	-	0.510845	2.9E-5	-34.98	-	5.46	2.56	Mansur (2017)
LUFD69-111	Luanga Comp.	Opx.	2763	0.176	0.835	0.1276	-	0.51152	1.2E-5	-21.8	-	2.76	2.70	Mansur (2017)
LUFD69-115	Luanga Comp.	Opx.	2763	0.346	1466	0.1426	-	0.512242	5.3E-5	-7.72	-	11.58	1.70	Mansur (2017)
LUFD141-209	Luanga Comp.	Serp.	2763	0.67	1888	0.2145	-	0.513193	1.6E-5	10.83	-	4.53	-	Mansur (2017)
F266/634m	Sossego dep.	Gab.	2739	13.25	62.27	0.1286	-	0.511338	-	-23.35	-	-1.26	3.07	Neves (2006)
F69/350,20	Gameleira dep.	Gab.	2757	12.58	40.01	0.1934	-	0.512461	1.7E-5	-	-	-	-	Pimentel et al. (2003)
F69/41	Gameleira dep.	Gab.	2757	2263	10.16	0.1353	-	0.511483	3.4E-5	-	-	-	2.85	Pimentel et al. (2003)
F69/305,70	Gameleira dep.	Gab.	2757	16.99	50.86	0.1578	-	0.511637	1.1E-5	-	-	-	-	Pimentel et al. (2003)

ESM – Table 6. (continued)

Sample	Unit	Petrography	Age (Ma)	Sm (ppm)	Nd (ppm)	$^{147}Sm/^{144}Nd$	± σ	$^{143}Nd/^{144}Nd$	± σ	εNd	I_{Nd}	$εNd_i$	T_{DM} (Ga)	Reference
F69/350,20	Gameleira deposit - host rocks	Gab.	2757	12.58	40.01	0.1934	-	0.512461	1.7E-5	-	-	-	-	Pimentel et al. (2003)
F69/403,74	Gameleira deposit - host rocks	Gab.	2757	2649	10.37	0.1578	-	0.511637	1.7E-5	-	-	-	-	Pimentel et al. (2003)
F72/374	Gameleira deposit - host rocks	Gab.	2757	2655	8261	0.1953	-	0.512655	2.0E-5	-	-	-	-	Pimentel et al. (2003)
F07/53,15	Gameleira deposit - host rocks	Gab.	2757	3282	14.18	0.1406	-	0.511465	2.0E-5	-	-	-	-	Pimentel et al. (2003)
F07/115,15	Gameleira deposit - host rocks	Gab.	2757	2371	11.27	0.1278	-	0.511351	1.3E-5	-	-	-	3.02	Pimentel et al. (2003)
F07/136,20	Gameleira deposit - host rocks	Gab.	2757	3109	10.75	0.1757	-	0.512322	7.7E-5	-	-	-	-	Pimentel et al. (2003)
F07/169,65	Gameleira deposit - host rocks	Gab.	2757	2361	10.34	0.1387	-	0.511623	3.0E-5	-	-	-	2.90	Pimentel et al. (2003)
F07/184,50	Gameleira deposit - host rocks	Gab.	2757	1752	7464	0.1426	-	0.511664	1.9E-5	-	-	-	-	Pimentel et al. (2003)
SC33A	Serra do Puma Comp.	Gab.	2713	0.78	2793	0.1689	-	0.512201	1.0E-5	-8.52	0.509114	1.38	-	Rosa (2014)
SC34B	Serra do Puma Comp.	Perid.	2713	0.665	1957	0.2056	-	0.512699	1.2E-5	1.19	0.508941	-2.02	-	Rosa (2014)
SC35B	Serra do Puma Comp.	Gab.	2713	2124	8419	0.1525	-	0.511955	9.0E-6	-13.32	0.509167	2.41	-	Rosa (2014)
SC37	Serra do Puma Comp.	Perid.	2713	0.464	1665	0.1683	-	0.511984	1.3E-5	-12.76	0.508907	-2.70	-	Rosa (2014)
SC38	Serra do Puma Comp.	Perid.	2713	0.37	1306	0.1711	-	0.511991	1.4E-5	-12.52	0.508863	-3.55	-	Rosa (2014)
SC43	Serra do Puma Comp.	Gab.	2713	0.906	2648	0.2069	-	0.512701	1.2E-5	1.23	0.508918	-2.47	-	Rosa (2014)
SC44	Serra do Puma Comp.	Gab.	2713	0.448	1392	0.1944	-	0.51262	1.6E-5	-0.35	0.509067	0.45	-	Rosa (2014)
SC46	Serra do Puma Comp.	Cpx	2713	0.962	2888	0.2014	-	0.51279	1.7E-5	2.97	0.509107	1.24	-	Rosa (2014)
SC48	Serra do Puma Comp.	Perid.	2713	0.249	0.663	0.2273	-	0.513166	2.0E-5	10.3	0.509011	-0.64	-	Rosa (2014)
SC68	Serra do Puma Comp.	Gab.	2766	1.53	5.8	0.1595	-	0.511956	2.1E-5	-13.3	0.509041	-0.06	-	Rosa (2014)
SC12	Serra da Onça Comp.	Gab.Nor.	2766	0.226	0.795	0.1721	-	0.512021	2.1E-5	-12.04	0.508874	-3.33	-	Rosa (2014)
SC17	Serra da Onça Comp.	Gab.Nor.	2766	0.212	0.764	0.1675	-	0.511965	1.8E-5	-13.13	0.508902	-2.78	-	Rosa (2014)
SC22	Serra da Onça Comp.	Gab.Nor.	2766	0.406	1586	0.1548	-	0.511712	1.4E-5	-18.06	0.508882	-3.17	-	Rosa (2014)
SC25	Serra da Onça Comp.	Gab.Nor.	2766	0.424	1491	0.1719	-	0.512031	1.4E-5	-11.84	0.508889	-3.04	-	Rosa (2014)
SC27	Serra da Onça Comp.	Gab.Nor.	2766	1847	7961	0.1402		0.511499	1.2E-5	-22.22	0.508936	-2.12	-	Rosa (2014)
RDM09B	Diopside-Norite Pium	Gab.Nor.	2743	6.71	38.26	0.106013	-	0.511036	1.6E-5	-34.78	-	-2.78	3.14	Santos et al. (2013)
RDM09A	Diopside-Norite Pium	Gab.Nor.	2743	5.1	27.94	0.110444	-	0.510295	1.4E-5	-32.17	-	-1.72	3.07	Santos et al. (2013)
RDM10	Diopside-Norite Pium	Gab.Nor.	2744	7.38	39.65	0.112544	-	0.510263	5.0E-6	-31.52	-	-1.80	3.09	Santos et al. (2013)
RMD06	Diopside-Norite Pium	Nor.	2745	7.94	45.68	0.105051	-	0.511021	1.0E-5	-34.18	-	-1.80	3.06	Santos et al. (2013)
CP45	Diopside-Norite Pium	Nor.	2745	0.33	1.63	0.120817	-	0.510805	1.4E-5	-28.44	-	-1.64	3.1	Santos et al. (2013)
CP42	Diopside-Norite Pium	Nor.	2745	6.37	33.68	0.114314	-	0.510256	1.8E-5	-30.68	-	-1.58	3.08	Santos et al. (2013)
V2-10	Vermelho Comp.	Gab.	2770	2.95	13.8	0.129	-	0.511232	9.0E-6	-27.4	0.50887	-3.40	3.30	Siepierski (2016)
V2-11	Vermelho Comp.	Gab.	2770	2.1	10.3	0.123	-	0.511199	1.2E-5	-28.1	0.508946	-1.90	3.13	Siepierski (2016)
62	Vermelho Comp.	Pegm. Gab.	2770	1.48	8.6	0.104	-	0.510866	1.2E-5	-34.6	0.508964	-1.50	3.03	Siepierski (2016)
94	Vermelho Comp.	Pegm. Gab.	2770	2.16	8	0.163	-	0.512005	1.0E-5	-12.3	0.509021	-0.40	3.19	Siepierski (2016)
110 (V2FP-425)	Vermelho Comp.	Pegm. Gab.	2770	0.38	2.4	0.096	-	0.510798	9.0E-6	-35.9	0.509048	0.10	2.90	Siepierski (2016)
161	Vermelho Comp.	Harzb.	2770	1.22	6	0.123	-	0.511203	1.2E-5	-28	0.508956	-1.70	3.11	Siepierski (2016)
RAV-62 (DDH-25)	Vermelho Comp.	Harzb.	2770	0.26	1	0.157	-	0.511901	1.3E-5	-14.4	0.509028	-0.30	3.12	Siepierski (2016)
RAV-65 (DDH-25)	Vermelho Comp.	Harzb.	2770	0.09	0.3	0.181	-	0.512299	1.8E-5	-6.6	0.508984	-1.10	-	Siepierski (2016)
V1-04C	Vermelho Comp.	Opx.	2770	0.18	0.4	0.272	-	0.513643	1.6E-5	19.6	0.50867	-7.30	-	Siepierski (2016)
RAV-70 (DDH-25)	Vermelho Comp.	Opx.	2770	0.19	0.6	0.191	-	0.512449	1.5E-5	-3.7	0.50895	-1.80	-	Siepierski (2016)
RAV-72 (DDH-25)	Vermelho Comp.	Opx.	2770	0.98	5.8	0.102	-	0.510751	8.0E-6	-36.8	0.508884	-3.10	3.14	Siepierski (2016)
RAV-74 (DDH-25)	Vermelho Comp.	Opx.	2770	1.09	6.6	0.1	-	0.510732	9.0E-6	-37.2	0.508907	-2.70	3.10	Siepierski (2016)

ESM – Table 6. (continued)

Sample	Unit	Petrography	Age (Ma)	Sm (ppm)	Nd (ppm)	$^{147}Sm/^{144}Nd$	± σ	$^{143}Nd/^{144}Nd$	± σ	εNd	I_{Nd}	$εNd_i$	T_{DM} (Ga)	Reference
297 (DDH-14)	Vermelho Comp.	Harzb.	2770	0.19	0.5	0.23	-	0.513001	1.8E-5	7.1	0.508802	-4.70	-	Siepierski (2016)
306 (DDH-14)	Vermelho Comp.	Harzb.	2770	0.44	1.4	0.19	-	0.512399	1.5E-5	-4.7	0.508926	-2.30	-	Siepierski (2016)
370 (DDH-14)	Vermelho Comp.	Harzb.	2770	0.16	0.7	0.138	-	0.511432	1.2E-5	-23.5	0.508906	-2.70	3.29	Siepierski (2016)
EZ-01	Ézio Comp.	Gab.	2770	3.9	1.18	0.1829	-	0.512401	1.0E-5	-4.62	0.509057	0.30	3.31	Silva (2015)
EZ-06	Ézio Comp.	Serp.	2770	0.3	0.14	0.2821	-	0.513991	1.8E-5	26.39	0.508834	-4.09	-	Silva (2015)
EZ-09	Ézio Comp.	Gab.	2770	2.6	0.77	0.179	-	0.512294	1.2E-5	-6.71	0.509021	-0.41	3.43	Silva (2015)
EZ-10	Ézio Comp.	Gab.	2770	2.8	0.63	0.136	-	0.511498	1.0E-5	-22.24	0.509012	-0.60	3.05	Silva (2015)
EZ-11	Ézio Comp.	Gab.	2770	2.4	0.48	0.1209	-	0.5112	1.2E-5	-28.05	0.50899	-1.02	3.04	Silva (2015)
EZ-12	Ézio Comp.	Gab.	2770	8.3	1.93	0.1406	-	0.511398	9.0E-6	-24.19	0.508828	-4.20	3.48	Silva (2015)
FD25-198.40	Ézio Comp.	Cpx	2770	7.5	2.62	0.2112	-	0.512859	8.0E-6	4.31	0.508999	-0.85	-	Silva (2015)
FD25-156.25	Ézio Comp.	Perid.	2770	1.1	0.42	0.2308	-	0.513211	2.2E-5	11.18	0.508992	-0.99	-	Silva (2015)
FD25-138.70	Ézio Comp.	Gab.	2770	14	2.87	0.1239	-	0.511109	9.0E-6	-29.83	0.508844	-3.90	3.31	Silva (2015)
FD27-207.90	Ézio Comp.	Gab.	2770	5.3	1.11	0.1266	-	0.511299	1.3E-5	-26.12	0.508985	-1.13	3.07	Silva (2015)
FD27-125.30	Ézio Comp.	Gab.	2770	4	1.15	0.1738	-	0.512152	1.8E-5	-9.48	0.508975	-1.32	3.54	Silva (2015)
LUSL 20B	Lago Grande Comp.	Gab.	2722	0.793	3548	0.1351	-	0.511458	2.0E-5	-23.02	0.509141	-1.14	3.10	Teixeira (2013)
LUSL 79.85	Lago Grande Comp.	Harzb.	2722	0.128	0.409	0.1899	-	0.512697	1.7E-5	-	0.509141	-	-	Teixeira et al. (2015a)
LUSL 99.85	Lago Grande Comp.	Harzb.	2722	0.425	1936	0.1327	-	0.511427	1.2E-5	-23.62	0.50901	-0.89	3.06	Teixeira et al. (2015a)
LUSL 117.45	Lago Grande Comp.	Harzb.	2722	0.233	1040	0.1353	-	0.51147	1.3E-5	-22.78	0.509006	-0.98	3.08	Teixeira et al. (2015a)
LUSL 134.05	Lago Grande Comp.	Harzb.	2722	0.184	0.759	0.1467	-	0.511609	2.1E-5	-20.07	0.508937	-2.32	3.31	Teixeira et al. (2015a)
LUSL 152.90	Lago Grande Comp.	Harzb.	2722	0.275	1230	0.1351	-	0.511467	5.2E-5	-22.84	0.509006	-0.96	3.08	Teixeira et al. (2015a)
LUSL 179.60	Lago Grande Comp.	Harzb.	2722	0.23	0.844	0.1649	-	0.511936	1.8E-5	-13.69	0.508932	-2.41	3.56	Teixeira et al. (2015a)
LUSL 205.00	Lago Grande Comp.	Opx.	2722	0.336	1670	0.1215	-	0.511272	1.0E-5	-26.65	0.509059	-0.07	2.94	Teixeira et al. (2015a)
LUSL 220.00	Lago Grande Comp.	Opx.	2722	0.301	1163	0.1566	-	0.511852	1.0E-5	-33.45	0.509	-3.81	3.23	Teixeira et al. (2015a)
LUSL 240.55	Lago Grande Comp.	Gab.	2722	0.265	1413	0.1132	-	0.510923	1.8E-5	-15.33	0.508861	-1.09	3.23	Teixeira et al. (2015a)
LUSL 260.50	Lago Grande Comp.	Gab.	2722	0.636	3356	0.1146	-	0.511049	6.0E-6	-31	0.508962	-1.84	3.08	Teixeira et al. (2015a)
Syn-to post-tectonic A-type anorogenic granitoids														
PSV-22	Estrela Granite	Mgr.	2763	14.72	87.05	0.10221	2.1E-4	0.510853	6.0E-6	-34.82	-	-1.22	3.03	Barros et al. (2004)
CN-40	Estrela Granite	Mgr.	2763	11.67	67.97	0.10378	5.4E-4	0.510892	3.2E-5	-34.06	-	-1.02	3.02	Barros et al. (2004)
PSV-77	Estrela Granite	Mgr.	2763	5.85	33.67	0.10503	4.2E-4	0.510947	1.6E-5	-32.99	-	-0.38	2.97	Barros et al. (2004)
PSV-62	Estrela Granite	Mgr.	2763	16.17	76.89	0.12716	4.8E-4	0.511265	2.7E-5	-26.78	-	-2.06	3.19	Barros et al. (2004)
PSV-75	Estrela Granite	Mgr.	2763	16.04	76.2	0.12729	1.4E-3	0.511304	3.6E-5	-26.02	-	-1.34	3.12	Barros et al. (2004)
ARC-108	Planalto Suite	Sgr.	2730	6.02	42	0.0867	-	0.510573	9.0E-6	-35.46	-	-0.66	3.16	Feio et al. (2013)
ARC-109	Planalto Suite	Sgr.	2730	11.35	63	0.1089	-	0.511013	7.0E-6	-37.98	-	-0.51	3.16	Feio et al. (2013)
AMR-152	Planalto Suite	Mgr.	2730	13.82	77.83	0.1073	-	0.511098	1.2E-5	-30	-	1.40	2.81	Feio et al. (2013)
AMR-187B	Planalto Suite	Sgr.	2730	17.09	100.52	0.1027	-	0.510901	1.7E-4	-33.9	-	0.90	2.98	Feio et al. (2013)
GRD-77	Planalto Suite	Sgr.	2730	13.4	77.29	0.1048	-	0.510868	2.3E-5	-34.5	-	-2.30	3.08	Feio et al. (2013)
AMR-191A	Pedra Branca Suite	Trond.	2750	1.72	8.94	0.1164	-	0.51107	6.0E-5	-30.59	-	-2.16	3.14	Feio et al. (2013)
ARC-142	Pedra Branca Suite	Trond.	2750	12.84	124.27	0.0625	-	0.510141	7.0E-6	-48.71	-	-1.21	2.95	Feio et al. (2013)

ESM – Table 6. (continued)

Sample	Unit	Petrography	Age (Ma)	Sm (ppm)	Nd (ppm)	$^{147}Sm/^{144}Nd$	± σ	$^{143}Nd/^{144}Nd$	± σ	εNd	I_{Nd}	$εNd_i$	T_{DM} (Ga)	Reference
AMD-02	Vila Cedere III	Mgr.	2732	8.42	49.98	0.10181	-	0.510908	1.0E-5	-33.75	-	-0.38	2.94	Galarza et al. (2017)
CMD-01	Vila Cedere III	Grd.	2733	11.26	60.16	0.11319	-	0.511019	1.1E-5	-31.58	-	-2.22	3.11	Galarza et al. (2017)
FDM-02	Vila Cedere III	Mgr.	2734	34.05	199.92	0.10296	-	0.510941	4.0E-6	-33.1	-	-0.11	2.92	Galarza et al. (2017)
AMD-03	Vila Cedere III	Mgr.	2736	8.07	48.54	0.1005	-	0.510906	2.4E-5	-33.79	-	0.08	2.91	Galarza et al. (2017)
AMD-01B	Vila Cedere III	Sgr.	2737	4.68	36.16	0.07829	-	0.51044	2.0E-5	-42.88	-	-1.18	2.96	Galarza et al. (2017)
CMD-02	Vila Cedere III	Grd.	2739	10.1	55.15	0.10971	-	0.510977	9.0E-6	-32.4	-	-1.73	3.07	Galarza et al. (2017)
TDM-13	Vila Cedere III	Grd.	2740	11.68	67.44	0.10467	-	0.510932	6.0E-6	-33.28	-	-0.83	2.98	Galarza et al. (2017)
TDM-09	Vila Cedere III	Sgr.	2740	9.65	51.24	0.11387	-	0.511085	5.0E-6	-30.29	-	-1.09	3.03	Galarza et al. (2017)
TDM-03	Vila Cedere III	Mgr.	2740	9.72	55.01	0.10686	-	0.510999	7.0E-6	-31.97	-	-0.29	2.95	Galarza et al. (2017)
TDM-02	Vila Cedere III	Mgr.	2740	5.89	33.9	0.10507	-	0.510935	1.1E-5	-33.22	-	-0.91	2.99	Galarza et al. (2017)
AMD-01A	Vila Cedere III	Ton.	2741	11.55	65.17	0.10713	-	0.511033	8.0E-6	-31.31	-	0.30	2.91	Galarza et al. (2017)
TDM-01	Vila Cedere III	Mgr.	2742	7.1	47.02	0.09126	-	0.510687	7.0E-6	-38.06	-	-0.88	2.96	Galarza et al. (2017)
BDE 19-B	Vila União Suite	Grt.	2744	6.49	38.16	0.10281	1.4E-3	0.51089	1.3E-5	-	-	-0.92	2.99	Marangoanha et al. (2020)
BVD 42-B	Vila União Suite	Grt.	2744	11.36	58.17	0.11811	2.7E-4	0.51115	4.0E-6	-	-	-1.31	3.06	Marangoanha et al. (2020)
BVD 15	Vila União Suite	Mgr.	2745.3	6.39	34.47	0.11209	1.7E-4	0.51105	7.0E-6	-	-	-1.16	3.03	Marangoanha et al. (2020)
BVD 21	Vila União Suite	Mgr.	2745.3	5.58	33.87	0.09962	1.5E-4	0.5108	7.0E-6	-	-	-1.62	3.04	Marangoanha et al. (2020)
BVD 42-H	Vila União Suite	Mgr.	2745.3	8.05	45.1	0.10798	1.3E-4	0.51099	4.0E-6	-	-	-0.90	3.00	Marangoanha et al. (2020)
BVD 44	Vila União Suite	Mgr.	2745.3	7.4	46.45	0.09627	2.7E-4	0.51079	5.0E-6	-	-	-0.54	2.95	Marangoanha et al. (2020)
BVD 42-C	Vila União Suite	Ton.	2745.8	11.21	59.24	0.1144	4.3E-4	0.51106	5.0E-6	-	-	-1.69	3.09	Marangoanha et al. (2020)
BVD 12-B	Vila União Suite	Qtz-Dio.	2734.5	11.3	64.92	0.10521	3.5E-4	0.51096	4.0E-6	-	-	-0.51	2.96	Marangoanha et al. (2020)
BDE 38	Vila União Suite	Qtz-Dio.	2734.5	8.89	51.77	0.10378	3.1E-4	0.511	6.0E-6	-	-	0.72	2.86	Marangoanha et al. (2020)
F266/107,7m	Sossego dep.	Qtz-Dio.	2990	4.86	32.3	0.0909	-	0.510579	-	-40.16	-	-2.87	3.06	Neves (2006)
F33/205m	Sossego dep.	Qtz-Dio.	2990	15.58	98.93	0.0952	-	0.51073	-	-37.22	-	-1.30	2.98	Neves (2006)
BIX/Frente_de_lavra	Sossego dep.	Qtz-Dio.	2990	3.84	15.97	0.1454	-	0.511659	-	-19.09	-	-0.94	3.12	Neves (2006)
<u>**A-type anorogenic granitoids**</u>														
F14/395	Pojuca Granite	Grt.	1874	9.08	39.3	0.1397	-	0.51144	1.1E-5	-	-	-9.7	3.35	Dall'Agnol et al. (2005)
CJ-29b	Serra dos Carajás Granite	Grt.	1880	23.62	160.1	0.08917	-	0.510909	7.0E-6	-	-	-7.9	2.61	Dall'Agnol et al. (2005)
CJ-38	Serra dos Carajás Granite	Grt.	1880	16.99	109.9	0.09349	-	0.510894	8.0E-6	-	-	-9.2	2.73	Dall'Agnol et al. (2005)
ECR-CG-59C	Cigano Granite	Bas. Dike	1883	11.97	63.88	0.1133	-	0.511115	1.3E-5	-	-	-9.7	2.94	Dall'Agnol et al. (2005)
ECR-CG-96	Cigano Granite	Grt.	1883	23.53	173.9	0.08177	-	0.510733	1.0E-5	-	-	-9.5	2.67	Dall'Agnol et al. (2005)
CJ-124	Carajás Dyke Swarms	Bas. Dike	1882	4.2	23	0.107903	-	0.511132	7.0E-6	-	-	-8	2.78	Giovanardi et al. (2019)
CJ-126	Carajás Dyke Swarms	Bas. Dike	1882	2.5	12	0.121389	-	0.511284	1.1E-5	-	-	-8.3	2.94	Giovanardi et al. (2019)
CJ-142	Carajás Dyke Swarms	Bas. Dike	1882	6.8	30	0.129078	-	0.51161	9.0E-6	-	-	-3.3	2.60	Giovanardi et al. (2019)
EF2 472	Alvo Estrela dep.	Php. Qtz. Dio.	1881	16581	93.24	0.1075	-	0.511017	2.6E-5	-31.6	-	-	2.91	Lindenmayer et al. (2005)
EF2 467,70	Alvo Estrela dep.	Php. Qtz. Dio.	1881	13.75	81.48	0.102	-	0.51093	2.4E-5	-33.3	-	-	2.89	Lindenmayer et al. (2005)
F19/722	Pojuca Granite	Apl.	1583	4713	8679	0.3301	-	0.513775	1.4E-5	-	-	-	-	Pimentel et al. (2003)
F19/723	Pojuca Granite	Apl.	1583	4030	8580	0.2838	-	0.513237	1.7E-5	-	-	-	-	Pimentel et al. (2003)
F20/689,15	Pojuca Granite	Apl.	1583	5573	12.13	0.2748	-	0.513052	2.4E-5	-	-	-	-	Pimentel et al. (2003)
PFA-22 (BAGrd)	Gogó da Onça Granite	Grd.	1870	13.83	85.1	0.0982	3.0E-4	0.510936	4.0E-6	-	-	-9.48	2.81	Teixeira et al. (2017)

ESM – Table 6. (continued)

Sample	Unit	Petrography	Age (Ma)	Sm (ppm)	Nd (ppm)	$^{147}Sm/^{144}Nd$	± σ	$^{143}Nd/^{144}Nd$	± σ	εNd	I_{Nd}	$εNd_i$	T_{DM} (Ga)	Reference
PFR-18B (BAGrd)	Gogó da Onça Granite	Grd.	1870	13.72	84.86	0.0977	4.0E-4	0.510945	5.0E-6	-	-	-9.18	2.78	Teixeira et al. (2017)
PFR-20 (BAMzg)	Gogó da Onça Granite	Mgr.	1870	17.76	106.79	0.1006	3.0E-4	0.510986	1.0E-6	-	-	-9.07	2.80	Teixeira et al. (2017)
<u>Iron Formations</u>														
CNS-6	N5	BIF	2740	2.72	12.09	0.1015	-	0.511377	1.8E-5	-24.6	-	-3.44	3.30	Dantas et al. (2014)
CNS-10	N5	BIF	2740	0.48	1.87	0.1311	-	0.511928	2.5E-5	-13.85	-	1.15	2.86	Dantas et al. (2014)
N1-0083-02	N1	BIF	2740	0.54	2.22	0.1429	-	0.511489	1.7E-5	-22.42	-	-3.60	3.39	Justo (2018)
N1-0083-11	N1	BIF	2740	0.22	0.63	0.2219	-	0.512989	5.0E-6	6.85	-	1.32	-	Justo (2018)
N4E-1421-08	N4	BIF	2740	0.17	1.22	0.151	-	0.510592	1.2E-5	-39.9	-	-0.54	2.88	Justo (2018)
N4E-1421-09	N4	BIF	2740	0.16	0.9	0.0841	-	0.510944	4.0E-6	-33.05	-	-2.17	3.05	Justo (2018)
N4WN-1103-05	N4	BIF	2740	0.1	0.44	0.1084	-	0.511398	1.8E-5	-24.2	-	-0.69	2.99	Justo (2018)
N4WN-1103-09	N4	BIF	2740	0.16	0.78	0.1295	-	0.511206	6.7E-5	-27.93	-	-2.31	3.12	Justo (2018)
N5W-0576-06	N5	BIF	2740	0.08	0.74	0.1234	-	0.510242	1.2E-5	-46.74	-	-0.38	2.85	Justo (2018)
N5W-0755-05	N5	BIF	2740	0.18	1.05	0.1329	-	0.511001	9.0E-6	-31.93	-	1.35	2.77	Justo (2018)
MNSE-RO-006	N5	Hem.	2740	0.61	2.99	0.1203	-	0.511303	2.1E-5	-26.04	-	-0.06	2.91	Justo (2018)
MNSE-RO-009	N5	BIF	2740	0.1	0.85	0.1224	-	0.510365	1.0E-6	-44.33	-	0.17	2.82	Justo (2018)
PFC-N8-0054-08	N8	BIF	2740	0.09	0.68	0.0694	-	0.510596	3.0E-6	-39.83	-	-0.22	2.86	Justo (2018)
PFC-N8-0054-018	N8	BIF	2740	0.19	0.19	0.0834	-	0.511705	1.3E-5	-18.19	-	-0.79	3.08	Justo (2018)
ALFA-FD01-451	S11A BIF	BIF	2740	0.09	0.53	0.1034	-	0.51081	2.2E-5	-34.66	-	-3.04	3.02	Justo (2018)
ALFA-FD01-459	S11A BIF	BIF	2740	0.09	0.47	0.121	-	0.510917	2.6E-5	-33.57	-	-7.10	3.54	Justo (2018)
ALFA-FD01-460	S11A BIF	BIF	2740	0.11	0.67	0.1006	-	0.51092	1.9E-5	-33.51	-	0.09	2.86	Justo (2018)
GTCH-FD01-540	S11A BIF	BIF	2740	0.34	1.32	0.1544	-	0.51162	2.1E-5	-19.86	-	-5.07	3.76	Justo (2018)
GTCH-FD01-542	S11A BIF	BIF	2740	0.18	0.74	0.1453	-	0.511445	3.0E-5	-23.27	-	-5.30	3.64	Justo (2018)
GTCH-FD01-544	S11A BIF	BIF	2740	0.17	0.84	0.1193	-	0.511162	2.1E-5	-28.79	-	-1.73	3.05	Justo (2018)
GTCH-FD01-545	S11A BIF	BIF	2740	0.15	0.85	0.1049	-	0.510902	1.7E-5	-33.86	-	-1.77	3.01	Justo (2018)
GTCH-FD01-558	S11A BIF	BIF	2740	0.04	0.24	0.097	-	0.51081	1.3E-5	-35.65	-	-0.84	2.92	Justo (2018)
ESTR-FD24-155	Estrela Fe-prospect	BIF	2740	0.04	0.17	0.1579	-	0.511883	2.1E-5	-14.73	-	-1.16	3.22	Justo (2018)
ESTR-FD24-156	Estrela Fe-prospect	BIF	2740	0.05	0.15	0.2004	-	0.512592	2.2E-5	-0.9	-	-2.19	-	Justo (2018)
ESTR-FD24-157	Estrela Fe-prospect	BIF	2740	0.08	0.35	0.1383	-	0.511451	1.8E-5	-23.15	-	-2.74	3.25	Justo (2018)
AP-246A	120 Fe-prospect	BIF	2740	0.37	1.44	0.1557	-	0.51185	7.0E-6	-15.37	-	-1.04	3.21	Justo (2018)
SF18-FD02-562	Serra de São Félix	BIF	2740	0.31	1.55	0.1228	-	0.511222	2.0E-5	-27.62	-	-1.78	3.07	Justo (2018)
SF18-FD02-565	Serra de São Félix	BIF	2740	0.22	1.24	0.1059	-	0.510984	2.7E-5	-32.26	-	-0.52	2.91	Justo (2018)
SF18-FD02-572	Serra de São Félix	BIF	2740	0.36	2.82	0.0765	-	0.510549	1.0E-5	-40.75	-	1.28	2.77	Justo (2018)
SF18-FD02-574	Serra de São Félix	BIF	2740	0.07	0.36	0.1101	-	0.511038	5.0E-6	-31.2	-	-0.93	2.96	Justo (2018)
SF18-FD02-576	Serra de São Félix	BIF	2740	0.2	1.11	0.1092	-	0.511001	7.0E-6	-31.93	-	-1.34	2.98	Justo (2018)
ARQU-DH14-61	Serra Arqueada	BIF	2740	0.13	0.63	0.1201	-	0.51129	7.0E-6	-26.29	-	0.49	2.86	Justo (2018)
ARQU-DH14-68	Serra Arqueada	BIF	2740	0.18	1.01	0.1095	-	0.511097	6.0E-6	-30.07	-	0.43	2.85	Justo (2018)
ARQU-DH14-69	Serra Arqueada	BIF	2740	0.25	1.09	0.1382	-	0.51145	1.3E-5	-23.18	-	-2.72	3.25	Justo (2018)
ARQU-DH14-71	Serra Arqueada	BIF	2740	0.11	0.68	0.0972	-	0.51073	4.9E-5	-37.22	-	-2.43	3.06	Justo (2018)

ESM – Table 6. (continued)

Sample	Unit	Petrography	Age (Ma)	Sm (ppm)	Nd (ppm)	$^{147}Sm/^{144}Nd$	± σ	$^{143}Nd/^{144}Nd$	± σ	εNd	I_{Nd}	$εNd_i$	T_{DM} (Ga)	Reference
Granite-related Cu-Au														
F43 179,0	Alvo Estrela deposit	Sulf. vein	1857	36.72	57.61	0.3853	-	0.514455	-	35.44	-	-	-	Lindenmayer et al. (2005)
E F11 122,0	Alvo Estrela deposit	Gang. vein	1857	17116	61411	0.1685	-	0.511952	-	-13.39	-	-	3.84	Lindenmayer et al. (2005)
E F1 286,10	Alvo Estrela deposit	Sulf. vein	1857	76.9	208.65	0.2228	-	0.512277	-	-7.04	-	-	-	Lindenmayer et al. (2005)
F15 469,0	Alvo Estrela deposit	Sulf. vein	1857	591.9	1377	0.2599	-	0.512711	-	1.43	-	-	-	Lindenmayer et al. (2005)
EF 04 342,90	Alvo Estrela deposit	Sulf. vein	1857	1666	4539	0.2219	-	0.512329	-	-6.93	-	-	-	Lindenmayer et al. (2005)
F14 339,0	Alvo Estrela deposit	Sulf. vein	1857	25831	90.1	0.1733	-	0.511823	-	-15.89	-	-	-	Lindenmayer et al. (2005)
EF 03 332,90	Alvo Estrela deposit	Sulf. vein	1857	25288	48.21	0.3171	-	0.51362	-	19.15	-	-	-	Lindenmayer et al. (2005)
F15-468,50	Alvo Estrela deposit	Gang. vein	1857	14957	67361	0.1342	-	0.511301	-	-26.07	-	-	3.38	Lindenmayer et al. (2005)
F07/130,40	Gameleira deposit	Sulf. vein	1700	7645	10.67	0.433	-	0.514881	1.3E-5	-	-	-	-	Pimentel et al. (2003)
F07/130,85	Gameleira deposit	Sulf. vein	1700	66.69	89.17	0.4521	-	0.515084	2.2E-5	-	-	-	-	Pimentel et al. (2003)
F07/103,95	Gameleira deposit	Sulf. vein	1700	8781	43.38	0.123	-	0.511431	2.3E-5	-	-	-	2.71	Pimentel et al. (2003)
F07/105,60	Gameleira deposit	Sulf. vein	1700	3685	14.3	0.1566	-	0.511713	9.0E-6	-	-	-	-	Pimentel et al. (2003)
F07/146,40	Gameleira deposit	Sulf. vein	1700	4034	15.13	0.162	-	0.511839	5.4E-5	-	-	-	-	Pimentel et al. (2003)
F20/478,55	Gameleira deposit	Qtz-Grun. vein	1839	1728	3125	0.3362	-	0.513865	2.1E-5	-	-	-	-	Pimentel et al. (2003)
F20/480,60	Gameleira deposit	Qtz-Grun. vein	1839	0.627	2015	0.188	-	0.512085	1.6E-5	-	-	-	-	Pimentel et al. (2003)
F20/482,35	Gameleira deposit	Qtz-Grun. vein	1839	1982	11.52	0.1045	-	0.511025	1.4E-5	-	-	-	2.70	Pimentel et al. (2003)
F20/485,60	Gameleira deposit	Qtz-Grun. vein	1839	0.696	2289	0.1848	-	0.512033	5.1E-5	-	-	-	-	Pimentel et al. (2003)
F72/295,35	Gameleira deposit	Qtz-Grun. vein	1839	42.55	61.88	0.4157	-	0.514794	1.2E-5	-	-	-	-	Pimentel et al. (2003)
Cu-Au-Mo-Co occurrences														
RN8-218,75	Alvo RN4	Ore	1883	8056	46242	0.1053	-	0.510891	6.0E-6	-	-	-	3.04	Negrão (2008)
RN10-189,94	Alvo RN4	Ore	1883	1465	6294	0.1407	-	0.511254	1.7E-5	-	-	-	3.82	Negrão (2008)
RN9-47,67	Alvo RN4	Ore	1883	7111	40556	0.106	-	0.510956	1.5E-5	-	-	-	2.96	Negrão (2008)
RN9-172,82	Alvo RN4	Ore	1883	0.946	4482	0.1276	-	0.511248	1.0E-5	-	-	-	3.2	Negrão (2008)

Abbreviations: *Amp – amphibolite; And – andesite; Apl – aplite; Bas – basalt; BIF – banded iron formation; Cpx – clinopyroxenite; Gab – gabbro; Gang – gangue; Grd – granodiorite; Grt – granite; Harzb – harzburguite; Hem – hematite; Intrus – intrusive; Maf – mafic; Metapiroc – metapiroclastic; Metavolc – metavolcanic; Mgr – monzogranite; Nor – norite; Opx – orthopyroxenite; Pegm – pegmatite; Perid – peridotite; Php – porphyry; Qtz-Dio – quartz-diorite; Rhy – rhyolite; Sch – schist; Serp – serpentinite; Sgr – syenogranite; Sulf – sulfide; Trach – trachyandesite; Ton – tonalite; Trond – trondhjemite*

Supplementary 6 - References

Barros, C.E.D.M., Macambira, M.J.B., Barbey, P., Scheller, T., 2004. Dados isotópicos Pb-Pb em zircão (evaporação) e Sm-Nd do Complexo Granítico Estrela, província Mineral de carajás, Brasil: implicações petrológicas e tectônicas. Braz. J. Geol. 34, 531–538. https://doi.org/10.25249/0375-7536.2004344531538

Dall'Agnol, R., Teixeira, N.P., Rämö, O.T., Moura, C.A., Macambira, M.J., de Oliveira, D.C., 2005. Petrogenesis of the Paleoproterozoic rapakivi A-type granites of the Archean Carajás metallogenic province, Brazil. Lithos 80, 101–129. https://doi.org/10.1016/j.lithos.2004.03.058

Dantas E.L., Oliveira C.G. de, Souza V.S., Buhn B., Santos R.V., Justo A.P., Freitas-Silva F.H., 2014. Nd Isotopes in iron and manganese formations of the Carajás region - PA. 9th South American Symposium on Isotope Geology, São Paulo, Brazil.

de Souza, Z.S., Potrel, A., Lafon, J.M., Althoff, F.J., Pimentel, M.M., Dall'Agnol, R., de Oliveira, C. G., 2001. Nd, Pb and Sr isotopes in the Identidade Belt, an Archaean greenstone belt of the Rio Maria region (Carajás Province, Brazil): implications for the Archaean geodynamic evolution of the Amazonian Craton. Precambrian Res. 109, 293–315.

Feio, G.R.L., Dall'Agnol, R., Dantas, E.L., Macambira, M.J.B., Santos, J.O.S., Althoff, F.J., Soares, J.E.B., 2013. Archean granitoid magmatism in the Canaã dos Carajás area: implications for crustal evolution of the Carajás province, Amazonian craton, Brazil. Precambrian Res. 227, 157–185. https://doi.org/10.1016/j.precamres.2012.04.007

Galarza, M.A., 2002. Geocronologia e geoquímica isotópica dos depósitos de Cu-Au Igarapé Bahia e Gameleira, província mineral de Carajás (PA), Brasil. PhD. thesis. Federal University of Pará, Brazil.

Galarza, M.A., Macambira, M.J.B., 2002. Geocronologia e evolução crustal da área do depósito de Cu-Au Gameleira, Província Mineral de Carajás (Pará), Brasil. Geologia USP. Série Científica 2, 143–159. https://doi.org/10.5327/S1519-874X2002000100012

Galarza, M. A., de Oliveira, D.C., Rodrigues, E.A., dos Santos, A.N., Martins, A.C., Marangoanha, B., 2017. Granitoides neoarqueanos (2,73 - 2,74 Ga) intrusivos e associados ao Diopsídio-Norito Pium, Canaã dos Carajás, Província Carajás (PA), in: de Lima, A.M.M., Gorayeb, P.S.S. (Eds.), Contribuições à Geologia da Amazônia, primeira edição. Sociedade Brasileira de Geologia - Núcleo Norte, Belém, pp. 225–246.

Gibbs, A.K., Wirth, K.R., Hirata, W.K., Olszewski Jr, W.J., 1986. Age and composition of the Grão Pará Group volcanics, Serra dos Carajás. Braz. J. Geol. 16, 201–211.

Giovanardi, T., Girardi, V.A., Teixeira, W., Mazzucchelli, M., 2019. Mafic dyke swarms at 1882, 535 and 200 Ma in the Carajás region, Amazonian Craton: Sr-Nd isotopy, trace element geochemistry and inferences on their origin and geological settings. J. S. Am. Earth Sci. 92, 197–208. https://doi.org/10.1016/j.jsames.2019.02.017

Justo, A.P., 2018. As formações ferríferas bandadas (BIFs) e a evolução paleoambiental e geodinâmica da Bacia de Carajás. Phd. thesis. University of Brasilia, Brazil.

Lindenmayer, Z.G., Fleck, A., Gomes, C.H., Santos, A.B.S., Caron, R., Paula, F. de C., Laux, J.H., Pimentel, M.M., Sardinha, A.S., 2005. Caracterização geológica do Alvo Estrela (Cu-Au), Serra dos Carajás, Pará, in: Marini, O.J., Ramos, B.W., Queiroz, E.T. (Eds.), Caracterização de Depósitos Minerais de Distritos Mineiros da Amazônia. DNPM-CT-Mineral FINEP-ADIMB, Brasilia, pp. 137–205.

Mansur, E.T., 2017. Caracterização e metalogênese do depósito de elementos do grupo da platina do Complexo Luanga, província mineral do Carajás. MSc. dissertation. University of Brasilia, Brazil.

Marangoanha, B., de Oliveira, D.C., Galarza, M.A., Marques, G.T., 2020. Crustal anatexis and mantle-derived magmas forming Neoarchean A-type granitoids in Carajás Province, northern Brazil: petrological evidence and tectonic control. Precambrian Res. 338, 105585. https://doi.org/10.1016/j.precamres.2019.105585

Martins, P.L.G., Toledo, C.L.B., Silva, A.M., Chemale Jr, F., Santos, J.O.S., Assis, L.M., 2017. Neoarchean magmatism in the southeastern Amazonian Craton, Brazil: Petrography, geochemistry and tectonic significance of basalts from the Carajás Basin. Precambrian Res. 302, 340–357. https://doi.org/10.1016/j.precamres.2017.10.013

Mellito, K.M., 1998. Aplicação do método Rb-Sr e Pb-Pb à evolução da mineralização cuprífera do depósito de Salobo 3A, Província Mineral de Carajás, Pará. MSc. dissertation. University of São Paulo, Brazil.

Negrão, M.M., 2008. Caracterização geológica e metalogenética da ocorrência de Cu-Au (Mo-Co), do Grupo Rio Novo, no contato S-SE com o Granito Cigano, Província Mineral de Carajás. PhD. thesis. University of Brasilia, Brazil.

Neves, M.P., 2006. Estudos isotópicos (Pb-Pb, Sm-Nd, C e O) do depósito Cu-Au do Sossego, Província Mineral de Carajás. MSc. dissertation. Federal University of Pará, Brazil.

Olszewski, W.J., Wirth, K.R., Gibbs, A.K. and Gaudette, H.E., 1989. The age, origin and tectonics of the GrZo Para Group and associated rocks, Serra dos Carajas, Brazil. Precambrian Res. 42, 229–254. https://doi.org/10.1016/0301-9268(89)90013-2

Pimentel, M.M., Lindenmayer, Z.G., Laux, J.H., Armstrong, R., de Araújo, J.C., 2003. Geochronology and Nd isotope geochemistry of the Gameleira Cu–Au deposit, Serra dos Carajás, Brazil: 1.8–1.7 Ga hydrothermal alteration and mineralization. J. S. Am. Earth Sci. 15, 803–813. https://doi.org/10.1016/S0895-9811(02)00127-X

Rosa, W.D., 2014. Complexos acamados da Serra da Onça e Serra do Puma: geologia e petrologia de duas intrusões máfico-ultramáficas com sequencia de cristalização distinta na Província Arqueana de Carajás, Brasil. MSc. dissertation. University of Brasilia, Brazil.

Santos, R.D., Galarza, M.A.G., de Oliveira, D.C., 2013. Geologia, geoquímica e geocronologia do Diopsídio-Norito Pium, Província Carajás. Bol. Mus. Para. Emílio Goeldi. Cienc. Nat. 8, 355–382.

Sato, K., Tassinari, C.C.G., 1997. Principais eventos de acreção continental no Cráton Amazônico baseados em idade modelo Sm-Nd, calculada em evoluções de estágio único e estágio duplo, in: Costa, M.L. Angélica, R.S. (Eds.), Contribuições à Geologia da Amazônia. Sociedade Brasileira de Geologia, Belém, pp. 91–142.

Siepierski, L., 2016. Geologia, petrologia e potencial para mineralizações magmáticas dos corpos máfico-ultramáficos da região de Canaã dos Carajás, Província Mineral de Carajás. PhD. thesis. University of Brasilia, Brazil.

Silva, K.S., 2015. Geologia, petrologia, geocronologia e mineralizações sulfetadas do complexo ézio, província mineral de carajás, Brasil. MSc. dissertation. University of Brasilia, Brazil.

Teixeira, A.S., 2013. Geologia, petrologia e geocronologia do complexo acamadado lago grande: evidência para uma suíte magmática mineralizada a egp na província mineral de Carajás, Brasil. MSc. dissertation. University of Brasilia, Brazil. https://doi.org/10.1016/S0301-9268(01)00164-4

Teixeira, A.S., Ferreira Filho, C.F., Della Giustina, M.E.S., Araújo, S.M., da Silva, H.H.A.B., 2015a. Geology, petrology and geochronology of the Lago Grande layered complex: evidence for a PGE-mineralized magmatic suite in the Carajás Mineral Province, Brazil. J. S. Am. Earth Sci. 64, 116–138. https://doi.org/10.1016/j.jsames.2015.09.006

ESM – Table 13. Compiled radiometric ages for the Carajás Mineral Province, Brazil.

Age (Ma)	±σ	Unit	Method	Application	Reference
Mesoarchean gneissified granitoids					
2990.9	5.8	Bacaba Tonalite	U-Pb	Zr	Moreto et al. (2011)
2993.1	7.1	Bacaba Tonalite	U-Pb	Zr	Moreto (2010)
2997.2	4.7	Bacaba Tonalite	U-Pb	Zr	Moreto (2010)
3001	3.6	Bacaba Tonalite	U-Pb	Zr	Moreto et al. (2011)
3004.6	9	Bacaba Tonalite	U-Pb	Zr	Moreto et al. (2011)
3004.7	7.8	Bacaba Tonalite	U-Pb	Zr	Moreto (2010)
2833	6	Bom Jesus Granite	U-Pb	Zr	Feio (2011); Feio et al. (2013)
3017	5	Bom Jesus Granite	U-Pb	Zr	Feio et al. (2013)
3074	6	Bom Jesus Granite	U-Pb	Zr	Feio et al. (2013)
2724	15	Campina Verde Tonalite	U-Pb	Zr	Feio (2011); Feio et al. (2013)
2849	18	Campina Verde Tonalite	U-Pb	Zr	Feio (2011); Feio et al. (2013)
2850	7	Campina Verde Tonalite	U-Pb	Zr	Feio (2011); Feio et al. (2013)
2854	2	Campina Verde Tonalite	Pb-Pb	Zr	Feio et al. (2013)
2868	2	Campina Verde Tonalite	Pb-Pb	Zr	Feio et al. (2013)
2871	7.7	Campina Verde Tonalite	U-Pb	Zr	Moreto et al. (2015a)
2872	1	Campina Verde Tonalite	Pb-Pb	Zr	Feio (2011); Feio et al. (2013)
2876	5.4	Campina Verde Tonalite	U-Pb	Zr	Moreto et al. (2015a)
2966	5	Campina Verde Tonalite	Pb-Pb	Zr	Feio et al. (2013)
3002	23	Campina Verde Tonalite	U-Pb	Zr	Feio et al. (2013)
2864	12	Canaã dos Carajás Granite	U-Pb	Zr	Feio et al. (2013)
2928	1	Canaã dos Carajás Granite	Pb-Pb	Zr	Sardinha et al. (2004)
2959	6	Canaã dos Carajás Granite	U-Pb	Zr	Feio (2011); Feio et al. (2013)
3030	15	Canaã dos Carajás Granite	U-Pb	Zr	Feio et al. (2013)
2675	26	Cruzadão Granite	U-Pb	Zr	Feio et al. (2013)
2785	16	Cruzadão Granite	U-Pb	Zr	Feio et al. (2013)
2845	15	Cruzadão Granite	U-Pb	Zr	Feio (2011); Feio et al. (2013)
2857	8	Cruzadão Granite	U-Pb	Zr	Feio (2011); Feio et al. (2013)
2875	12	Cruzadão Granite	U-Pb	Zr	Feio et al. (2013)
3053	8	Cruzadão Granite	U-Pb	Zr	Feio et al. (2013)
2851	2	Felsic gneiss	U-Pb	Zr	Machado et al. (1991)
2733	2	Granitoids at Canaã dos Carajás area	Pb-Pb	Zr	Feio (2011)
2751	15	Granitoids at Canaã dos Carajás area	U-Pb	Zr	Feio (2011)
2762	13	Granitoids at Canaã dos Carajás area	U-Pb	Zr	Feio (2011)
2831	56	Granitoids at Canaã dos Carajás area	U-Pb	Zr	Feio (2011)
2841	9	Granitoids at Canaã dos Carajás area	U-Pb	Zr	Feio (2011)
2853	2	Granitoids at Canaã dos Carajás area	Pb-Pb	Zr	Feio (2011)
2868	6	Granitoids at Canaã dos Carajás area	U-Pb	Zr	Feio (2011)
2879	37	Granitoids at Canaã dos Carajás area	U-Pb	Zr	Feio (2011)
2943	9	Granitoids at Southern Copper Belt	U-Pb	Zr	Borba et al. (2019)
3076	5.3	Xingu Comp. – Sequeirinho ore breccia	U-Pb	Zr	Moreto et al. (2015b)
2959	15	Migmatized gneiss at Xingu Comp.	U-Pb	Zr	Delinardo da Silva (2014)
3066	6	Migmatized gneiss at Xingu Comp.	U-Pb	Zr	Delinardo da Silva (2014)
2974	15	Orthogneiss from Xingu Comp.	Pb-Pb	Zr	Avelar et al. (1999)
2857	6.7	Orthogneiss from Xingu Comp. at Salobo Deposit	U-Pb	Zr	de Melo et al. (2017)
2950	25	Orthogneiss from Xingu Comp. at Salobo Deposit	U-Pb	Zr	de Melo et al. (2017)
2954	52	Pedra Branca Suite	U-Pb	Zr	Feio et al. (2013)
2709	30	Rio Verde Trondhjemite	U-Pb	Zr	Feio et al. (2013)
2820	22	Rio Verde Trondhjemite	U-Pb	Zr	Feio et al. (2013)
2858	6	Rio Verde Trondhjemite	U-Pb	Zr	Feio et al. (2013)
2869	4	Rio Verde Trondhjemite	Pb-Pb	Zr	Feio (2011); Feio et al. (2013)
2923	15	Rio Verde Trondhjemite	U-Pb	Zr	Feio (2011); Feio et al. (2013)
2929	3	Rio Verde Trondhjemite	Pb-Pb	Zr	Feio (2011); Feio et al. (2013)
2989	5.2	Sequeirinho Granite at Sequeirinho orebody	U-Pb	Zr	Moreto et al. (2015b)
3010	21	Sequeirinho Granite at Sequeirinho orebody	U-Pb	Zr	Moreto et al. (2015b)
3014	22	Sequeirinho Granite at Sequeirinho orebody	U-Pb	Zr	Moreto et al. (2015b)
2831	6	Serra Dourada Granite	U-Pb	Zr	Feio et al. (2013)
2848	5.5	Serra Dourada Granite	U-Pb	Zr	Moreto et al. (2015a)
2858	30	Serra Dourada Granite	U-Pb	Zr	Moreto (2010)
2860	22	Serra Dourada Granite	U-Pb	Zr	Moreto et al. (2011)
2935	36	Xenoliths of Deformed Granitoids at Igarapé Bahia Deposit	U-Pb	Zr	de Melo et al. (2019b)
2856	3	Xingu Comp.	Pb-Pb	Zr	Machado et al. (1991)
2859	2	Xingu Comp.	U-Pb	Zr	Machado et al. (1991)
2860	2	Xingu Comp.	U-Pb	Zr	Machado et al. (1991)
2872	10	Granitoid from Carajás Province	Pb-Pb	Zr	Rodrigues et al. (1992)
Mesoarchean granulites					
2735	5	Charnockite associated to Pium Comp.	U-Pb	Zr	Feio (2011)
2859	9	Granulitization event from Pium Comp.	U-Pb	Zr	Pidgeon et al. (2000)
3050	57	Pium Comp. - Granulite	Pb-Pb	Zr	Rodrigues et al. (1992)

ESM – Table 7. (continued)

Age (Ma)	±σ	Unit	Method	Application	Reference
Neoarchean volcanic rocks					
2758	39	Grão Para Group	U-Pb	Zr	Wirth et al. (1986)
2759	2	Grão Para Group	Pb-Pb	Zr	Machado et al. (1991)
2687	54	Grão Para Group	Rb-Sr	WR	Gibbs et al. (1986)
2759	2	Grão Para Group	U-Pb	Zr	Machado et al. (1991)
2743	11	Grão Para Group – Carajás Fm.	U-Pb	Zr	Trendall et al. (1998)
2757	7	Grão Para Group - Parauapebas Fm.	U-Pb	Zr	Trendall et al. (1998)
2760	11	Grão Para Group - Parauapebas Fm.	U-Pb	Zr	Trendall et al. (1998)
2749	6.5	Grão Para Group - Parauapebas Fm.	U-Pb	Zr	Martins et al. (2017)
2745	5	Grão Para Group - Parauapebas Fm.	U-Pb	Zr	Martins et al. (2017)
2661	110	Grão Para Group - Serra Sul BIF Seq.	Re-Os	-	Cabral et al. (2013)
2710	38	Grão Para Group - Serra Sul BIF Seq.	Re-Os	-	Cabral et al. (2013)
2774	19	Grão Para Group at Ig.Cinzento/GT-46 Deposit	U-Pb	Zr	Toledo et al. (2019)
2751	4	Grão Para Group	Pb-Pb	Zr	Krymsky et al. (2002)
2748	34	Igarapé Bahia Group	U-Pb	Zr	Tallarico et al. (2005)
2745	1	Igarapé Bahia Group	Pb-Pb	Zr	Galarza et al. (2001)
2747	1	Igarapé Bahia Group	Pb-Pb	Zr	Galarza et al. (2001)
2758	75	Igarapé Bahia Group	Sm-Nd	WR	Galarza et al. (2003)
2776	12	Igarapé Bahia Group	Pb-Pb	Zr	Galarza et al. (2003)
2751	81	Igarapé Bahia Group	Pb-Pb	Zr	Santos (2002)
2759	24	Igarapé Bahia Group	Sm-Nd	WR	Santos (2002)
2732	2	Igarapé Pojuca Group	U-Pb	Zr	Machado et al. (1991)
2719	80	Igarapé Pojuca Group	Sm-Nd	WR	Pimentel et al. (2003)
2719	80	Meta-andesite at Gameleira Deposit	Sm-Nd	WR	Pimentel et al. (2003)
2555	4	Salobo Group	U-Pb	Mnz	Machado et al. (1988)
2551	2	Salobo Group	Pb-Pb	Zr	Machado et al. (1991)
2761	3	Salobo Group	Sm-Nd	WR	Macambira & Tassinari (1998)
Neoarchean syn-to post-tectonic A-type granitoids					
2743	3	Alvo 118 Tonalite	U-Pb	Zr	Tallarico (2003)
2734	4	Canaã dos Carajás area - Granite	Pb-Pb	Zr	Sardinha et al. (2004)
2763	4.4	Cascata Gneiss correl. to Igarapé Gelado Granite	U-Pb	Zr	de Melo et al. (2017)
2745	4	Castanha quartz-feldspar Porphyry	U-Pb	Zr	Moreto et al. (2015a)
2612	2	Cinzento Granite	U-Pb	Zr	Silva et al. (2005)
2739	4.2	Curral Granite	U-Pb	Zr	Moreto et al. (2015b)
2645	9	Dacitic to rhyolitic porphyry at Alvo 188 Deposit	U-Pb	Zr	Tallarico (2003)
2654	9	Dacitic to rhyolitic porphyry at Alvo 188 Deposit	U-Pb	Zr	Tallarico (2003)
2527	34	Estrela Granite	Rb-Sr	WR	Barros et al. (1992)
2763	7	Estrela Granite	Pb-Pb	Zr	Barros et al. (2009)
2532	26	Foliated tonalite at Igarapé Cinzento/GT-46 Deposit	U-Pb	Zr	Toledo et al. (2019)
2639	16	Foliated tonalite at Igarapé Cinzento/GT-46 Deposit	U-Pb	Zr	Toledo et al. (2019)
2688	11	Geladinho Granite	Pb-Pb	Zr	Barbosa et al. (2001)
2652	98	Granites at Igarapé Cinzento/GT-46 Deposit	Sm-Nd	WR	Silva et al. (2005)
2668	100	Granites at Igarapé Cinzento/GT-46 Deposit	Sm-Nd	WR	Silva et al. (2005)
2732		Granitic vein at Mirim Area	Pb-Pb	Zr	Machado et al. (1991)
2732		Granitic vein at Salobo Group	Pb-Pb	Zr	Machado et al. (1991)
2581	5	Granitic vein at Salobo Group	U-Pb	Ti	Machado et al. (1991)
2584	5	Granitic vein at Salobo Group	U-Pb	Zr	Machado et al. (1991)
2758		Granitic vein at Salobo Group	U-Pb	Zr	Machado et al. (1991)
2497	5	Granitic vein at Salobo Group	U-Pb	Ti	Machado et al. (1991)
2183	31	Granitoids at Southern Copper Belt	Ar-Ar	Amp	Borba et al. (2019)
2288	20	Granitoids at Southern Copper Belt	Ar-Ar	Bt	Borba et al. (2019)
2732	22	Granitoids at Southern Copper Belt	U-Pb	Zr	Borba et al. (2019)
2739	19	Granitoids at Southern Copper Belt	U-Pb	Zr	Borba et al. (2019)
2739	8	Granitoids at Southern Copper Belt	U-Pb	Zr	Borba et al. (2019)
2535	8.4	Old Salobo Granite	U-Pb	Zr	de Melo et al. (2017)
2731	26	Igarapé Gelado Suite	Pb-Pb	Zr	Barbosa (2004)
2508	14	Igarapé Gelado Suite	Pb-Pb	Zr	Barbosa (2004)
2533	7	Igarapé Gelado Suite	Pb-Pb	Zr	Barbosa (2004)
2574	8	Igarapé Gelado Suite	Pb-Pb	Zr	Barbosa (2004)
2576	4	Igarapé Gelado Suite	Pb-Pb	Zr	Barbosa (2004)
2588	5	Igarapé Gelado Suite	Pb-Pb	Zr	Barbosa (2004)
2480	37	Itacaiúnas Granite	Rb-Sr	WR	Montalvão et al. (1984)
2525	38	Itacaiúnas Granite	Pb-Pb	Zr	Souza et al. (1996)
2560	37	Itacaiúnas Granite	Pb-Pb	Zr	Souza et al. (1996)
2701	30	Mylonitised Cascata Gneiss	U-Pb	Zr	de Melo et al. (2017)
2547	5.3	Old Salobo Granite	U-Pb	Zr	de Melo et al. (2017)
2573	2	Old Salobo Granite	U-Pb	Zr	Machado et al. (1991)
2560	37	Itacaiúnas Granite	Pb-Pb	Zr	Souza et al. (1996)

ESM – Table 7. (continued)

Age (Ma)	±σ	Unit	Method	Application	Reference
2701	6	Pedra Branca Suite	U-Pb	Zr	Feio (2011); Feio et al. (2013)
2750	5	Pedra Branca Suite	U-Pb	Zr	Feio (2011); Feio et al. (2013)
2562	39	Pegmatite at Igarapé Cinzento/GT-46 Deposit	U-Pb	Zr	Toledo et al. (2019)
2738	6	Planalto Granite	Pb-Pb	Zr	Huhn et al. (1999a)
2706	5	Planalto Suite	U-Pb	Zr	Feio (2011); Feio et al. (2012)
2710	10	Planalto Suite	U-Pb	Zr	Feio (2011); Feio et al. (2012)
2729	17	Planalto Suite	U-Pb	Zr	Feio (2011); Feio et al. (2012)
2730	5	Planalto Suite	U-Pb	Zr	Feio (2011); Feio et al. (2013)
2731	1	Planalto Suite	Pb-Pb	Zr	Feio (2011); Feio et al. (2012)
2736	4	Planalto Suite	Pb-Pb	Zr	Feio (2011); Feio et al. (2012)
2738	3	Planalto Suite	U-Pb	Zr	Feio (2011); Feio et al. (2013)
2736	24	Plaquê Suite	Pb-Pb	Zr	Avelar et al. (1999)
2560	37	Pojuca Granite	Pb-Pb	Zr	Souza et al. (1996)
2705	2	Quartz diorite at Gameleira Deposit	Pb-Pb	Zr	Galarza & Macambira (2002a)
2741	4.7	Quartz-feldspar Porphyry	U-Pb	Zr	Moreto et al. (2015a)
2743	1.6	Serra do Rabo Granite	U-Pb	Zr	Sardinha et al. (2006)
2740	26	Sossego Granophyric Granite	U-Pb	Zr	Moreto et al. (2015b)
2765	39	Trondhjemite at Canaã dos Carajás Area	U-Pb	Zr	Sardinha et al. (2004)
2557	26	Granite at Igarapé Cinzento/GT-46 Deposit	U-Pb	Zr	Toledo et al. (2019)
2733	2	Velha Canadá Leucogranite	Pb-Pb	Zr	Santos et al. (2010)
2747	2	Velha Canadá Leucogranite	Pb-Pb	Zr	Huh et al. (1999b)
2725	5	Vila Jussara Suite	Pb-Pb	Zr	Dall'Agnol et al. (2017)
2735	4	Vila Jussara Suite	Pb-Pb	Zr	Dall'Agnol et al. (2017)
2743	1	Vila Jussara Suite	Pb-Pb	Zr	Dall'Agnol et al. (2017)
2743	3	Vila Jussara Suite	Pb-Pb	Zr	Dall'Agnol et al. (2017)
2743	9	Vila Jussara Suite	Pb-Pb	Zr	Dall'Agnol et al. (2017)
2748	2	Vila Jussara Suite	Pb-Pb	Zr	Souza et al. (2010)
2749	3	Vila Jussara Suite	Pb-Pb	Zr	Souza et al. (2010)
2749	3	Vila Jussara Suite	Pb-Pb	Zr	Silva et al. (2020a)
2752	5.7	Vila Jussara Suite	Pb-Pb	Zr	Silva et al. (2020a)
2754	2	Vila Jussara Suite	Pb-Pb	Zr	Souza et al. (2010)
2754	2.2	Vila Jussara Suite	Pb-Pb	Zr	Silva et al. (2020a)
2769	10	Vila Jussara Suite	U-Pb	Zr	Dall'Agnol et al. (2017)
2738.8	7.9	Vila União Granitoids	U-Pb	Zr	Marangoanha et al. (2019)
2744.1	5.5	Vila União Granitoids	U-Pb	Zr	Marangoanha et al. (2019)
2745.3	7.1	Vila União Granitoids	U-Pb	Zr	Marangoanha et al. (2020)
2755	15	Vila União Granitoids	U-Pb	Zr	Marangoanha et al. (2020)
2744	5	Visconde Granite	Pb-Pb	Zr	da Costa Silva et al. (2015)
Mafic-ultramafic magmatism					
1874	110	Andesitic Dike	Rb-Sr	WR	Rivalenti et al. (1998)
2766	6	Cateté Intrusive Suite - Serra da Onca	U-Pb	Zr	Lafon et al. (2000)
1882		Dike Swarms - Gabbro	U-Pb	Bdy	Giovanardi et al. (2019)
2442	22	Ézio Comp.	U-Pb	Zr	Silva (2015)
2569	39	Ézio Comp.	U-Pb	Zr	Silva (2015)
2620	14	Ézio Comp.	U-Pb	Zr	Silva (2015)
2770	170	Ézio Comp.	Sm-Nd	WR	Silva (2015)
2645	12	Gabbro Dike	U-Pb	Zr	Dias et al. (1996)
2378	55	Gabbro from Serra da Onça	U-Pb	Zr	Teixeira et al. (2015a)
2553	61	Lago Grande Comp.	U-Pb	Zr	Teixeira et al. (2015a)
2722	53	Lago Grande Comp.	U-Pb	Zr	Teixeira et al. (2015a)
2763	6	Luanga Comp.	U-Pb	Zr	Machado et al. (1991)
2670		Mafic Dike	U-Pb	Zr	Tallarico et al. (2005)
2705	2	Mafic Dikes, Sills, Metagabbro	Pb-Pb	Zr	Galarza & Macambira (2002a)
2708	37	Mafic Dikes, Sills, Metagabbro	U-Pb	Zr	Mougeot et al. (1996b)
2757	81	Mafic Dikes, Sills, Metagabbro	Sm-Nd	WR	Pimentel et al. (2003)
2739	5.9	Mafic Dikes, Sills, Metagabbro	U-Pb	Zr	Moreto et al. (2015b)
2743	109	Metaultramafic host rocks at Lagoa Seca Deposit	Sm-Nd	WR	Souza et al. (2020)
2867	40	Metavolcanic host rocks at Lagoa Seca Deposit	Sm-Nd	WR	Souza et al. (2020)
2744	1	Pium Diopside Norite	Pb-Pb	Zr	Santos et al. (2013)
2745	1	Pium Diopside Norite	Pb-Pb	Zr	Santos et al. (2013)
2744	1	Pium Diopside Norite	Pb-Pb	Zr	Santos et al. (2013)
Orosirian A-type anorogenic granitoids					
1716	9	Aplite at Estrela Deposit	U-Pb	Mnz	Volp et al. (2006)
1827	23	Aplite at Estrela Deposit	U-Pb	Mnz	Volp et al. (2006)
1886	19	Aplite at Estrela Deposit	U-Pb	Mnz	Volp et al. (2006)
1879	6	Breves Granite	U-Pb	Zr	Tallarico et al. (2004)
1883	2	Cigano Granite	U-Pb	Zr	Machado et al. (1991)
1884	4	Cigano Granite	U-Pb	Zr	Teixeira et al. (2018)
1884	3	Cigano Granite	U-Pb	Zr	Teixeira et al. (2018)

ESM – Table 7. (continued)

Age (Ma)	±σ	Unit	Method	Application	Reference
1866	10	Gogó da Onça Granite	U-Pb	Zr	Teixeira et al. (2017)
1869	4	Gogó da Onça Granite	U-Pb	Zr	Teixeira et al. (2017)
1872	13	Gogó da Onça Granite	U-Pb	Ti	Teixeira et al. (2017)
1878	9	Gogó da Onça Granite	U-Pb	Zr	Teixeira et al. (2017)
1879	15	Gogó da Onça Granite	U-Pb	Ti	Teixeira et al. (2017)
1875	1.5	Granite at Estrela Deposit	U-Pb	Mnz	Lindenmayer et al. (2005)
1881	5	Granite at Estrela Deposit	U-Pb	Zr	Lindenmayer et al. (2005)
1927	27	Granitoids at Southern Copper Belt	Ar-Ar	Bt	Borba et al. (2019)
2003	22	Granitoids at Southern Copper Belt	Ar-Ar	Bt	Borba et al. (2019)
1883	5	Musa Granite	U-Pb	Zr	Machado et al. (1991)
1874	2	Pojuca Granite	U-Pb	Zr	Machado et al. (1991)
1820	49	Serra dos Carajás Granite	U-Pb	Zr	Wirth et al. (1986)
1880	2	Serra dos Carajás Granite	U-Pb	Zr	Machado et al. (1991)
1882	10	Serra dos Carajás Granite	U-Pb	Zr	Teixeira et al. (2018)
1886	4.2	Serra Dourada Quartz porphyry	U-Pb	Zr	Moreto et al. (2015b)
1880	80	Young Salobo Granite	Rb-Sr	WR	Cordani (1981)
Au-PGE deposits					
1861	45	Serra Pelada	U-Pb	Mnz	Grainger et al. (2008)
1882	3	Serra Pelada	Ar-Ar	Bt	Grainger et al. (2008)
Cu-Au deposits					
1885	4	Alvo 118	Ar-Ar	Bt	Pollard et al. (2019)
1869	7	Alvo 118	U-Pb	Xen	Tallarico (2003)
1868	7	Alvo 118	U-Pb	Xen	Tallarico (2003)
1886	5	Breves	Ar-Ar	Bt	Pollard et al. (2019)
1872	7	Breves	U-Pb	Mnz	Tallarico et al. (2004)
1883	9	Cu-Au-Mo at Rio Novo Group	Re-Os	Mo	Negrão (2008)
1884	9	Cu-Au-Mo at Rio Novo Group	Re-Os	Mo	Negrão (2008)
1729	420	Cu-Au-Mo at Rio Novo Group	Sm-Nd	WR	Negrão (2008)
1890	8.5	Curral orebody - Sossego	U-Pb	Mnz	Moreto et al. (2015b)
1896	7	Estrela	Ar-Ar	Bt	Pollard et al. (2019)
1857	98	Estrela	Sm-Nd	WR	Lindenmayer et al. (2005)
1839	14	Estrela	U-Pb	Mnz	Volp et al. (2006)
2217	19	Gameleira	Pb-Pb	Cpy	Galarza & Macambira (2002a)
2180	84	Gameleira	Pb-Pb	Cpy	Galarza & Macambira (2002a)
2419	12	Gameleira	Pb-Pb	Cpy	Galarza & Macambira (2002a)
1908	7	Gameleira	Ar-Ar	Bt	Pollard et al. (2019)
2614	14	Gameleira	Re-Os	Mo	Marschik et al. (2005)
1700	31	Gameleira	Sm-Nd	WR	Pimentel et al. (2003)
1734	8	Gameleira	Ar-Ar	Bt	Pimentel et al. (2003)
1839	15	Gameleira	Sm-Nd	WR	Pimentel et al. (2003)
1958	230	Gameleira	Sm-Nd	WR	Pimentel et al. (2003)
2602	13	Garimpo Fernando (Au)	Re-Os	Mo	Marschik et al. (2005)
2592	13	Garimpo Fernando (Au)	Re-Os	Mo	Marschik et al. (2005)
2509	85	Serra Verde	Pb-Pb	Cpy+Mo	Reis et al. (2001)
2362	19	Serra Verde	U-Pb	Ap	Reis et al. (2001)
2609	13	Serra Verde	Re-Os	Mo	Marschik et al. (2005)
1879	4.1	Sossego orebody - Sossego	U-Pb	Mnz	Moreto et al. (2015b)
1904	5.2	Sossego orebody - Sossego	U-Pb	Mnz	Moreto et al. (2015b)
1592	45	Sossego orebody - Sossego	Pb-Pb	Cpy	Neves (2006)
2058	39	Sossego orebody - Sossego	Sm-Nd	Aln	Smith et al. (2018)
Fe deposits					
2786	140	Serra Norte	Sm-Nd	WR	Justo (2018)
1701	97	Serra Norte	Sm-Nd	Hem	Lobato et al. (2005)
2593	260	Serra Norte	Sm-Nd	WR	Lobato et al. (2005)
1717	12	Serra Norte N5E	U-Pb	Ant	Santos et al. (2010)
1613	21	Serra Norte N5E	U-Pb	Mnz	Santos et al. (2010)
2567	180	Serra Sul	Sm-Nd	WR	Justo (2018)
IOCG deposits					
2575	12	Acampamento Sul orebody - Igarapé Bahia/Alemão	U-Pb	Mnz	Tallarico et al. (2005)
2559	34	Alemão	U-Pb	Mnz	de Melo et al. (2019b)
2720	15	Bacaba	U-Pb	Mnz	Moreto et al. (2015a)
2060	9.6	Bacaba	U-Pb	Mnz	Moreto et al. (2015a)
2681	20	Bacaba	U-Pb	Mnz	Moreto et al. (2015a)
2703	6.2	Bacuri	U-Pb	Mnz	Moreto et al. (2015a)
2758	11	Bacuri	Re-Os	Mo	Moreto et al. (2015a)

ESM – Table 7. (continued)

Age (Ma)	±σ	Unit	Method	Application	Reference
2011	6.8	Borrachudo	U-Pb	Ti	Previato et al. (2020)
2193	4	Corta Goela	Ar-Ar	Bt	Pollard et al. (2019)
2388	5	Cristalino	Ar-Ar	Bt	Pollard et al. (2019)
2719	36	Cristalino	Pb-Pb	Cpy-Py	Soares et al. (2001)
2700	29	Cristalino	Pb-Pb	Cpy	Soares et al. (2001)
2530	60	Grota Funda	Re-Os	Mo	Hunger et al. (2018)
2724	4	GT-34	U-Pb	Zr	Garcia (2018); Garcia et al. (2020)
2512	7	GT-34	Ar-Ar	Bt	Pollard et al. (2019)
2385	122	Igarapé Bahia/Alemão	Pb-Pb	Cpy	Galarza et al. (2008)
2417	120	Igarapé Bahia/Alemão	Pb-Pb	Cpy	Galarza et al. (2008)
2744	12	Igarapé Bahia/Alemão	Pb-Pb	Au	Galarza et al. (2008)
2754	36	Igarapé Bahia/Alemão	Pb-Pb	Cpy	Galarza et al. (2008)
2756	24	Igarapé Bahia/Alemão	Pb-Pb	Cpy	Galarza et al. (2008)
2772	46	Igarapé Bahia/Alemão	Pb-Pb	Cpy	Galarza et al. (2008)
2777	22	Igarapé Bahia/Alemão	Pb-Pb	Cpy	Galarza et al. (2001)
2537	6	Igarapé Bahia/Alemão	Ar-Ar	Bt	Pollard et al. (2019)
2539	26	Igarapé Bahia/Alemão	Pb-Pb	Cpy-Au	Santos (2002)
2521	56	Igarapé Bahia/Alemão	Pb-Pb	Sulf.	Santos (2002)
2575	86	Igarapé Bahia/Alemão	Pb-Pb	Au	Santos (2002)
2580	79	Igarapé Bahia/Alemão	Sm-Nd	Fl	Santos (2002)
1752	77	Igarapé Cinzento/GT-46	Sm-Nd	WR	Silva et al. (2005)
1810	15	Igarapé Cinzento/GT-46	Ar-Ar	Bt	Silva et al. (2005)
1858	7	Igarapé Cinzento/GT-46	Ar-Ar	Bt	Silva et al. (2005)
2554	8	Igarapé Cinzento/GT-46	Re-Os	Mo	Silva et al. (2005)
2557	8	Igarapé Cinzento/GT-46	Re-Os	Mo	Silva et al. (2005)
2600	8	Igarapé Cinzento/GT-46	Re-Os	Mo	Silva et al. (2005)
2612	1.5	Igarapé Cinzento/GT-46	Re-Os	Mnz	Silva et al. (2005)
2449	44	Igarapé Cinzento/GT-46	Re-Os	Mo	Toledo et al. (2019)
2503	51	Igarapé Cinzento/GT-46	Re-Os	Mo	Toledo et al. (2019)
2711	9	Igarapé Cinzento/GT-46	Re-Os	Mo	Toledo et al. (2019)
2718	56	Igarapé Cinzento/GT-46	Re-Os	Mo	Toledo et al. (2019)
2685	11	Pista orebody - Sossego	Re-Os	Mo	Moreto et al. (2015b)
2710	11	Pista orebody - Sossego	Re-Os	Mo	Moreto et al. (2015b)
2452	14	Salobo	U-Pb	Mnz	de Melo et al. (2017)
2562	8	Salobo	Re-Os	Mo	Requia et al. (2003)
2576	8	Salobo	Re-Os	Mo	Requia et al. (2003)
2579	71	Salobo	Pb-Pb	Bn-Cpy	Requia et al. (2003)
2112	12	Salobo	Pb-Pb	Mag	Tassinari et al. (2003)
2427	130	Salobo	Pb-Pb	Cpy	Tassinari et al. (2003)
2587	150	Salobo	Pb-Pb	Tourm	Tassinari et al. (2003)
2705	42	Salobo	Pb-Pb	Cc	Tassinari et al. (2003)
2959	310	Sequeirinho orebody - Sossego	Sm-Nd	Aln	Smith et al. (2018)
2097	56	Sequeirinho orebody - Sossego	Sm-Nd	Aln	Smith et al. (2018)
2199	13	Sequeirinho orebody - Sossego	Ar-Ar	Amp	Marschik et al. (2003c)
3076	5.3	Sequeirinho orebody - Sossego	U-Pb	Zr	Moreto et al. (2015b)
2712	4.7	Sequeirinho orebody - Sossego	U-Pb	Mnz	Moreto et al. (2015b)
2530	25	Sequeirinho orebody - Sossego	Pb-Pb	Cpy	Neves (2006)
2608	25	Sequeirinho orebody - Sossego	Pb-Pb	Cpy	Neves (2006)
2578	29	Sequeirinho orebody - Sossego	Sm-Nd	WR	Neves (2006)
2747	140	Visconde	Pb-Pb	Cpy	da Costa Silva et al. (2012)
2729	150	Visconde	Pb-Pb	Cpy	da Costa Silva et al. (2015)
2736	100	Visconde	Pb-Pb	Cpy	da Costa Silva et al. (2015)

Abbreviations: *Aln – allanite; Amp – amphibole; Ant – anatase; Ap – apatite; Au – gold; Bdy – baddeleyite; Bn – bornite; Bt – biotite; Cc – chalcocite; Cpy – chalcopyrite; Fl – fluorite; Hem – hematite; Mag – magnetite; Mnz – monazite; Py – pyrite; Sulf – sulfides; Ti – titanite; Tourm – tourmaline; WR – whole rock; Xen – xenotime; Zr – zircon.*

Supplementary 7 – References

Avelar, V.G., Lafon, J.-M., Correia Jr, F.C., Macambira, B.E.M., 1999. O magmatismo arqueano da região de Tucumã, Província Mineral de Carajás, Amazônia Oriental, Brasil: novos dados geocronológicos. Braz. J. Geol. 29, 453−460.

Barbosa, J.P.O., 2004. Geologia estrutural, geoquímica, petrografia e geocronologia de granitóides da região do Igarapé Gelado, norte da Província Mineral de Carajás. MSc. Dissertation. Federal University of Pará, Brazil.

Barbosa, J.P.O., Barros, C.E.M., Macambira, M.J.B., Vale, A.G., 2001. Geologia e Geocronologia do Stock Granítico Geladinho, região de Parauapebas, Província Mineral de Carajás. VII Simpósio de Geologia da Amazônia, Belém, Brazil, 763–766.

Barros, C.E.M., Dall'Agnoll, R., Lafon, J.M., Teixeira, N.P., Ribeiro, J.W., 1992. Geologia e geocronologia Rb-Sr do Gnaisse Estrela, Curionópolis, PA. Bol. Mus. Para. Emílio Goeldi. Cienc. Hum. 4, 83−104.

Barros, C.E.M., Sardinha, A.S., Barbosa, J.P.O., Macambira, M.J.B., Barbey, P., Boullier, A.-M., 2009. Structure, petrology, geochemistry and zircon U/Pb and Pb/Pb geochronology of the synkinematic Archean (2.7 Ga) A-type granites from the Carajas metallogenic province, northern Brazil. Can. Mineral. 47, 1423–1440. https://doi.org/10.3749/canmin.47.6.1423

Borba, M.L., Matos, F.M., Tassinari, C.C.G., Huhn, S.R.B., Nunes, S., Medeiros, C.A., 2019. Rhyacian-Orosirian Thermal Event in the Carajás Mineral Province, Brazil. SEG 2019 Conference Proceedings, Santiago, Chile

Cabral, A.R., Creaser, R.A., Nägler, T., Lehmann, B., Voegelin, A.R., Belyatsky, B., Pašava, P., Seabra Gomes Jr, A.A., Galbiatti, H., Böttcheri, M.E., Escher, P., 2013. Trace-element and multi-isotope geochemistry of Late-Archean black shales in the Carajás iron-ore district, Brazil. Chem. Geol. 362, 91–104. https://doi.org/10.1016/j.chemgeo.2013.08.041

Cordani, U., 1981. Comentários sobre as determinações geocronológicas da região da Serra dos Carajás. Universidade de São Paulo-Docegeo.

da Costa Silva, A.R.C., Villas, R.N.N., Lafon, J.M., Craveiro, G.S., 2012. Idade da alteração e mineralização do depósito de Cu-Au Visconde, Província Mineral de Carajás (Pará), Brasil. XLVI Congresso Brasileiro de Geologia, Santos, Brazil, 1–2.

da Costa Silva, A.R., Villas, R.N.N., Lafon, J.M., Craveiro, G.S., Ferreira, V.P., 2015. Stable isotope systematics and fluid inclusion studies in the Cu–Au Visconde deposit, Carajás Mineral Province, Brazil: implications for fluid source generation. Miner. Deposita 50, 547–569. https://doi.org/10.1007/s00126-014-0558-8

Dall'Agnol, R., Cunha, I.R.V., Guimarães, F.V., de Oliveira, D.C., Teixeira, M.F.B., Feio, G.R.L., Lamarão, C.N., 2017. Mineralogy, geochemistry, and petrology of Neoarchean ferroan to magnesian granites of Carajás Province, Amazonian Craton: the origin of hydrated granites associated with charnockites. Lithos 277, 3–32. https://doi.org/10.1016/j.lithos.2016.09.032

de Melo, G.H., Monteiro, L.V.S., Xavier, R.P., Moreto, C.P.N., Santiago, E.S.B., Dufrane, S.A., Aires, B., Santos, A.F.F., 2017. Temporal evolution of the giant Salobo IOCG deposit, Carajás Province (Brazil): constraints from paragenesis of hydrothermal alteration and U-Pb geochronology. Miner. Deposita 52, 709–732. https://doi.org/10.1007/s00126-016-0693-5

de Melo, G.H., Monteiro, L.V., Xavier, R.P., Moreto, C.P., Arquaz, R.M., Silva, M.A.D., 2019b. Evolution of the Igarape Bahia Cu-Au deposit, Carajas Province (Brazil): Early syngenetic chalcopyrite overprinted by IOCG mineralization. Ore Geol. Rev. 111, 102993. https://doi.org/10.1016/j.oregeorev.2019.102993

Delinardo da Silva, M. A., 2014, Metatexitos e diatexitos do Complexo Xingu na região de Canaã dos Carajás: implicações para a evolução mesoarqueana do Domínio Carajás. MSc. thesis. University of Campinas, Brazil.

Dias, G.S., Macambira, M.B., Dall'Agnol, R., Soares, A.D.V., Barros, C.E.M., 1996. Datações de zircões de sill de metagabro: comprovação de idade arqueana da Formação Águas Claras, Carajás, Pará. V Simpósio de Geologia da Amazônia, Belém, 376–378.

Feio, G.R.L., 2011. Magmatismo granitóide arqueano da área de Canaã dos Carajás: implicações para a evolução crustal da Província Carajás. PhD. thesis. Federal University of Pará, Brazil.

Feio, G.R.L., Dall'Agnol, R., 2012. Geochemistry and petrogenesis of the Mesoarchean granites from the Canaã dos Carajás area, Carajás Province, Brazil: Implications for the origin of Archean granites. Lithos 154, 33–52. https://doi.org/10.1016/j.lithos.2012.06.022

Feio, G.R.L., Dall'Agnol, R., Dantas, E.L., Macambira, M.J.B., Santos, J.O.S., Althoff, F.J., Soares, J.E.B., 2013. Archean granitoid magmatism in the Canaã dos Carajás area: Implications for crustal evolution of the Carajás province, Amazonian craton, Brazil. Precambrian Res. 227, 157–185. https://doi.org/10.1016/j.precamres.2012.04.007

Galarza, M. A., Macambira, M.J.B., 2002. Geocronologia e evolução crustal da área do depósito de Cu-Au Gameleira, Província Mineral de Carajás (Pará), Brasil. Geol. USP Sér. Cient. 2, 143–159. https://doi.org/10.5327/S1519-874X2002000100012

Galarza, M.A.T., Macambira, M.J.B., Maurity, C.W., Meireles, H.P., 2001. Idade do depósito Igarapé Bahia (Província Mineral de Carajás, Brasil) com base nos isótopos de Pb. VII Simpósio de Geologia da Amazônia, Belém, Brazil, 116–119.

Galarza, M. A., Macambira, M. J. B., and Moura, C. A. V., 2003, Geocronologia Pb–Pb e Sm–Nd das rochas máficas do depósito Igarapé Bahia, Província Mineral de Carajás (PA). VII Simpósio de Geologia da Amazônia, Belém, Brazil.

Galarza, M.A., Macambira, M.J.B., Villas, R.N., 2008. Dating and isotopic characteristics (Pb and S) of the Fe oxide–Cu–Au–U–REE Igarapé Bahia ore deposit Carajás mineral province, Pará state, Brazil. J. S. Am. Earth Sci. 25, 377–397. https://doi.org/10.1016/j.jsames.2007.07.006

Garcia, V.B., 2018. A raiz do Sistema IOCG de Carajás: alterações hidrotermais e mineralização niquelífera neoarqueana no depósito GT-34. MSc. dissertation. University of Brasilia, Brazil.

Garcia, V.B., Schutesky, M.E., Oliveira, C.G., Whitehouse, M.J., Huhn, S.R., Augustin, C.T., 2020. The Neoarchean GT-34 Ni deposit, Carajás Mineral Province, Brazil: an atypical IOCG-related Ni sulfide mineralization. Ore Geol. Rev. 103773. https://doi.org/10.1016/j.oregeorev.2020.103773

Gibbs, A.K., Wirth, K.R., Hirata, W.K., Olszewski Jr., W.J., 1986. Age and composition of the Grão Pará Group volcanics, Serra dos Carajás. Braz. J. Geol. 16, 201–211

Giovanardi, T., Girardi, V.A., Teixeira, W., Mazzucchelli, M., 2019. Mafic dyke swarms at 1882, 535 and 200 Ma in the Carajás region, Amazonian Craton: Sr-Nd isotopy, trace element geochemistry and inferences on their origin and geological settings. J. S. Am. Earth Sci. 92, 197–208. https://doi.org/10.1016/j.jsames.2019.02.017"

Grainger, C.J., Groves, D.I., Tallarico, F.H.B., Fletcher, I.R., 2008. Metallogenesis of the Carajás Mineral Province, Southern Amazon Craton, Brazil: Varying styles of Archean through Paleoproterozoic to Neoproterozoic base- and precious-metal mineralisation. Ore Geol. Rev. 33, 451–489. https://doi.org/10.1016/j.oregeorev.2006.10.010

Huhn, S.R.B., Macambira, M.J.B., Dall'Agnol, R., 1999a. Geologia e geocronologia Pb-Pb do granito alcalino arqueano Planalto, região da Serra do Rabo, Carajás-PA. VI Simpósio de Geologia da Amazônia, Belém, Brazil, 463–466.

Huhn, S.R.B., Souza, C.I.J., Albuquerque, M.C., Leal, E.D., Brustolin, V., 1999b. Descoberta do depósito Cu-(Au) Cristalino: Geologia e mineralização associada região da Serra do Rabo, Carajás, PA. VI Simpósio de Geologia da Amazônia, Belém, Brazil, 140–143.

Hunger, R.B., Xavier, R.P., Moreto, C.P.N., Gao, J.F., 2018. Hydrothermal Alteration, Fluid Evolution, and Re-Os Geochronology of the Grota Funda Iron Oxide Copper-Gold Deposit, Carajás Province (Pará State), Brazil. Econ. Geol. 113, 1769–1794.https://doi.org/10.5382/econgeo.2018.4612

Justo, A.P., 2018. As formações ferríferas bandadas (BIFs) e a evolução paleoambiental e geodinâmica da Bacia de Carajás. PhD. thesis. University of Brasilia, Brazil.

Krymsky, R.S., Macambira, J.B., Macambira, M.J.B., 2002. Geocronologia U-Pb em zircão de rochas vulcânicas da Formação Carajás, Estado do Pará. II Simpósio sobre vulcanismo e ambientes associados, Belém, Brazil, 41.

Lafon, J.M., Macambira, M.J.B., Pidgeon, R.T., 2000. Zircon U-Pb SHRIMP dating of Neoarchean magmatism in the southwestern part of the Carajás province (eastern Amazonian craton, Brazil). 31st International Geological Congress, Rio de Janeiro, Brazil.

Lindenmayer, Z.G., Fleck, A., Gomes, C.H., Santos, A.B.S., Caron, R., Paula, F. de C., Laux, J.H., Pimentel, M.M., Sardinha, A.S., 2005. Caracterização geológica do Alvo Estrela (Cu-Au), Serra dos

Carajás, Pará, in: Marini, O.J., Ramos, B.W., Queiroz, E.T. (Eds.), Caracterização de Depósitos Minerais de Distritos Mineiros da Amazônia. DNPM-CT-Mineral FINEP-ADIMB, Brasilia, pp. 137–205.

Lobato, L. M., Rosière, C.A., Figuereido e Silva, R.C., Zucchetti, M., Baars, F.J., Seoane, J.C., Rios, F.J., Pimentel, M., Mendes, G.E., Monteiro, A.M., 2005. A mineralização hidrotermal de ferro da Província Mineral de Carajás-Controle estrutural e contexto na evolução metalogenética da província, in: Marini, O.J., de Queiroz, E.T., Ramos, B.W. (Eds.), Caracterização em depósitos minerais em distritos mineiros da Amazônia. DNPM, ADIMB, Brasilia, pp. 25–92.

Macambira, E., Tassinari, C.C.G., 1998. Estudos Sm-Nd no complexo máfico ultramáfico da Serra da Onça-sul do Pará: implicações geocronológicas e geotectônicas. XL Congresso Brasileiro de Geologia, Belo Horizonte, Brazil, 463.

Machado, N., Lindenmayer, D., Lindenmayer, Z., 1988. Geocronologia U-Pb da província metalogenética de Carajás, Pará: resultados preliminares. VII Cong. Lattnoamer. Geol. 339–347.

Machado, N., Lindenmayer, Z., Krogh, T.E., Lindenmayer, D., 1991. U-Pb geochronology of Archean magmatism and basement reactivation in the Carajás area Amazon shield, Brazil. Precambrian Res. 49, 329–354. https://doi.org/10.1016/0301-9268(91)90040-h

Marangoanha, B., de Oliveira, D.C., de Oliveira, V.E.S., Galarza, M.A., Lamarão, C.N., 2019. Neoarchean A-type granitoids from Carajás province (Brazil): New insights from geochemistry, geochronology and microstructural analysis. Precambrian Res. 324, 86–108. https://doi.org/10.1016/j.precamres.2019.01.010

Marangoanha, B., de Oliveira, D.C., Galarza, M.A., Marques, G.T., 2020. Crustal anatexis and mantle-derived magmas forming Neoarchean A-type granitoids in Carajás Province, northern Brazil: Petrological evidence and tectonic control. 338, 105585 https://doi.org/10.1016/j.precamres.2019.105585

Marschik, R., Spangenberg, J.E., Leveille, R.A., Almeida, A.J., 2003c. The Sossego iron oxide-Cu-Au deposit, Carajás, Brazil, in: Eliopoulos, D. (Ed.), Mineral Exploration and Sustainable Development, Volume 1. Millpress, Rotterdam, pp. 331–334.

Marschik, R., Mathur, R., Ruiz, J., Leveille, R.A., Almeida, A.J., 2005. Late archean Cu-Au-Mo mineralization at Gameleira and Serra verde, Carajás Mineral Province, Brazil: constraints from re-os molybdenite ages. Miner. Deposita 39, 983–991. https://doi.org/10.1007/s00126-004-0450-z

Martins, P.L.G., Toledo, C.L.B., Silva, A.M., Chemale Jr, F., Santos, J.O.S., Assis, L.M., 2017. Neoarchean magmatism in the southeastern Amazonian Craton, Brazil: Petrography, geochemistry and tectonic significance of basalts from the Carajás Basin. Precambrian Res. 302, 340–357. https://doi.org/10.1016/j.precamres.2017.10.013

Montalvão, R., Tassinari, C., Bezerra, P., Prado, P., 1984. Geocronologia dos granitóides e gnaisses das regiões de Rio Maria, Fazenda Mata Geral e Rio Itacaiúnas, sul do Pará (Distrito Carajás-Cumaru). XXXIII Congresso Brasileiro de Geologia, Rio do Janeiro, Brazil, 2757–2766.

Moreto, C.P.N., 2010. O deposito de oxido de ferro-cobre-ouro bacaba, provincia mineral de Carajas, PA: geocronologia U-Pb das rochas hospedeiras. MSc. dissertation. University of Campinas, Brazil.

Moreto, C.P.N., Monteiro, L.V.S., Xavier, R.P., Amaral, W.S., Santos, T.J.S., Juliani, C., Souza Filho, C.R., 2011. Mesoarchean (3.0 and 2.86 Ga) host rocks of the iron oxide–Cu–Au Bacaba deposit, Carajás Mineral Province: U-Pb geochronology and metallogenetic implications. Miner. Deposita 46, 789–811. https://doi.org/10.1007/s00126-011-0352-9

Moreto, C.P.N., Monteiro, L.V.S., Xavier, R.P., Creaser, R.A., DuFrane, S.A., Tassinari, C.C.G., Sato, K., Kemp, A.I.S., Amaral, W.S., 2015a. Neoarchean and paleoproterozoic iron oxide-copper-gold events at the sossego deposit Carajás Province, Brazil: Re-Os and U-Pb Geochronological Evidence. Econ. Geol. 110, 809–835. https://doi.org/10.2113/econgeo.110.3.809

Moreto, C.P., Monteiro, L.V.S., Xavier, R.P., Creaser, R.A., DuFrane, S.A., Melo, G.H., da Silva, M.A.D., Tassinari, C.C.G., Sato, K., 2015b. Timing of multiple hydrothermal events in the iron oxide–copper–gold deposits of the Southern Copper Belt, Carajás Province, Brazil. Miner. Deposita 50, 517–546. https://doi.org/10.1007/s00126-014-0549-9

Mougeot, R., Respaut, J.P., Briqueu, L., Ledru, P., Milesi, J.P., Macambira, M.J.B., Huhn, S.B., 1996. Geochronological constrains for the age of the Águas Claras Formation (Carajás province, Pará, Brazil). XXXIX Congresso Brasileiro de Geologia, Salvador, 579–581.

Negrão, M.M., 2008. Caracterização Geológica e Metalogenética da Ocorrência de Cu-Au (Mo-Co), do Grupo Rio Novo, no contato S-SE com o granito Cigano, Provincia Mineral de Carajás. MSc. dissertation. University of Brasilia, Brazil.

Neves, M.P., 2006. Estudos isotópicos (Pb-Pb, Sm-Nd, C e O) do depósito Cu-Au do Sossego, Província Mineral de Carajás. MSc. dissertation thesis, Federal University of Pará, Brazil.

Pidgeon, R.T., Macambira, M.J.B., Lafon, J.M., 2000. Th–U–Pb isotopic systems and internal structures of complex zircons from an enderbite from the Pium Complex, Carajás Province, Brazil: evidence for the ages of granulite facies metamorphism and the protolith of the enderbite. Chem. Geol. 166, 159–171. https://doi.org/10.1016/S0009-2541(99)00190-4

Pimentel, M.M., Lindenmayer, Z.G., Laux, J.H., Armstrong, R., de Araújo, J.C., 2003. Geochronology and Nd isotope geochemistry of the Gameleira Cu–Au deposit, Serra dos Carajás, Brazil: 1.8–1.7 Ga hydrothermal alteration and mineralization. J. S. Am. Earth Sci. 15, 803–813. https://doi.org/10.1016/S0895-9811(02)00127-X

Pollard, P.J., Taylor, R.G., Peters, L., Matos, F., Freitas, C., Saboia, L., Huhn, S., 2019. 40Ar-39Ar dating of Archean iron oxide Cu-Au and Paleoproterozoic granite-related Cu-Au deposits in the Carajás Mineral Province, Brazil: implications for genetic models. Miner. Deposita 54, 329–346. https://doi.org/10.1007/s00126-018-0809-1

Previato, M., Monteiro, L.V.S., da Silveira Bello, R.M., Gonçales, L.C.G., 2020. Evolution of brines and CO2-rich fluids and hydrothermal overprinting in the genesis of the Borrachudo Copper deposit, Carajás Province. Ore Geol. Rev. 121, 103561. https://doi.org/10.1016/j.oregeorev.2020.103561

Reis, F.N., Macambira, M.J.B., Villas, R.N., Krymsky, R., 2001. Estudo isotópico do depósito cupro-aurífero de Serra Verde, Província Mineral de Carajás, Pará. VII Simpósio de Geologia da Amazónia, Belém, Brazil, 80–83.

Requia, K., Stein, H., Fontboté, L., Chiaradia, M., 2003. Re–Os and Pb–Pb geochronology of the Archean Salobo iron oxide copper–gold deposit Carajás mineral province, northern Brazil. Miner. Deposita 38, 727–738. https://doi.org/10.1007/s00126-003-0364-1

Rivalenti, G., Mazzucchelli, M., Girardi, V.A.V., Cavazzini, G., Finatti, C., Barbieri, M.A., Teixeira, W., 1998. Petrogenesis of the Paleoproterozoic basalt–andesite–rhyolite dyke association in the Carajás region, Amazonian craton. Lithos 43, 235–265. https://doi.org/10.1016/S0024-4937(98)00015-2

Rodrigues, E.S., Lafon, J.M., Scheller, T., 1992. Geocronologia Pb-Pb da Província Mineral de Carajás: primeiros resultados. XXXVII Congresso Brasileiro de Geologia, São Paulo, Brazil, 183–184.

Santos, M.G.S., 2002. Estudo dos isótopos de Pb e Nd do depósito de Cu-Au (U-ETR) Alemão, Província Mineral de Carajás (PA). MSc. dissertation thesis. Federal University of Pará, Brazil.

Santos, P.J.L., de Oliveira, D.C., Galarza, M.A., Macambira, M.J.B., 2010. Geologia, petrografia e geocronologia das rochas granitoides do Complexo Xingu da região de Nova Canadá, município de Água Azul do Norte – Província Mineral de Carajás. XLV Congresso Brasileiro de Geologia, Belém, Brazil.

Santos, R., Galarza, M., de Oliveira, D.C., 2013. Geologia, geoquímica e geocronologia do Diopsídio-Norito Pium, Província Carajás. Bol. Mus. Para. Emílio Goeldi. Cienc. Hum. 8, 331–337.

Sardinha, A. S., Dall'Agnol, R., Gomes, A. C. B., Macambira, M. J. B., and Galarza, M. A., 2004, Geocronologia Pb-Pb e U-Pb em zircões de granitóides arqueanos da região de Canaã dos Carajás, Província Mineral de Carajás: Congresso Brasileiro de Geologia, 42nd, 2004.Sardinha, A.S., Dall'Agnol, R., Gomes, A.C.B., Macambira, M.J.B., Galarza, M.A., 2004. Geocronologia Pb-Pb e U-Pb em zircões de granitóides arqueanos da região de Canaã dos Carajás, Província Mineral de Carajás. XLII Congresso Brasileiro de Geologia, Araxá, Brazil.

Sardinha, A. S., de Mesquita Barros, C.E., Krymsky, R., 2006. Geology, geochemistry, and U–Pb geochronology of the Archean (2.74 Ga) Serra do Rabo granite stocks, Carajás Metallogenetic Province, northern Brazil. J. South Am. Earth Sci. 20, 327–339. https://doi.org/10.1016/j.jsames.2005.11.001

Silva, K.S., 2015. Geologia, petrologia, geocronologia e mineralizações sulfetadas do complexo ézio, província mineral de carajás, Brasil. MSc. dissertation. University of Brasilia, Brazil.

Silva, M.G., Teixeira, J.B.G., Pimentel, M.M., Vasconcelos, P.M., Arielo, A., Rocha, W.J.S.F., 2005. Geologia e mineralizações de Fe-Cu-Au do Alvo GT46 (Igarapé Cinzento), Carajás, in: Marini, O.J., Queiroz, E.T., Ramos, B.W. (Eds.), Caracterização de Depósitos Minerais em Distritos Mineiros da Amazônia. DNPM, ADIMB, Brasilia, pp. 94–151.

Silva, F.F., de Oliveira, D.C., Dall'Agnol, R., Silva, L.R., Cunha, I.V., 2020a. Lithological and structural controls on the emplacement of a Neoarchean plutonic complex in the Carajás province, southeastern Amazonian craton (Brazil). J. South. Am. Earth Sci. 102, 102696. https://doi.org/10.1016/j.jsames.2020.102696

Smith, E., Kemp, A., Hagemann, S., Xavier, R., Moreto, C., 2018. The Sossego IOCG Deposit, Carajás Mineral Province, Brazil: Two Mineralization Ages, One Archean Source. SEG 2018 Conference Proceedings, Keystone, USA.

Soares, A.D.V., Macambira, M.J.B., Santos, M.G.S., Vieira, E.A.P., Massoti, F.S., Souza, C.I.J., Padilha, J.L., Magni, M.C.V., 2001. Depósito Cu-(Au) Cristalino, Serra dos Carajás, PA: Idade da mineralização com base em análises Pb-Pb em sulfetos (dados preliminares). VII Simpósio de Geologia da Amazônia, Brazil, 108–111.

Souza, S.R.B., Macambira, M.J.B., Scheller, J., 1996. Novos dados geocronológicos para os granitos deformados do Rio Itacaiunas (Serra dos Carajás, PA): implicações estratigráficas. V Simpósio de Geologia da Amazônia, Belém, Brazil, 380–383.

Souza, S.R.C., Botelho, N.F., Dantas, E.L., Cuadros Jiménez, F.A., Reis, M.A., Viana, C.S., 2020. Geochemistry and isotopic geology of the Lagoa Seca gold deposit in the Andorinhas greenstone-belt, Carajás Province, Brazil. Journal of South American Earth Sciences, 102523. https://doi.org/10.1016/j.jsames.2020.102523

Sousa, S.D., de Oliveira, D.C., Gabriel, E.O., Macambira, M.J.B., 2010. Geologia, petrografia e geocronologia das rochas granitoides do Complexo Xingu da porção a leste da cidade de Água Azul do Norte (PA) – PMC. XLV Congresso Brasileiro de Geologia, Belém, Brazil.

Tallarico, F.H.B., 2003. O cinturão cupro-aurifero de Carajas, Brasil. PhD. dissertation thesis. University of Campinas, Brazil.

Tallarico, F.H.B., McNaughton, N.J., Groves, D.I., Fletcher, I.R., Figueiredo, B.R., Carvalho, J.B., Rego, J.L., Nunes, A.R., 2004. Geological and SHRIMP II U-Pb constraints on the age and origin of the Breves Cu-Au-(W-Bi-Sn) deposit Carajás, Brazil. Miner. Deposita 39, 68–86. https://doi.org/10.1007/s00126-003-0383-y

Tallarico, F.H.B., Figueiredo, B.R., Groves, D.I., Kositcin, N., McNaughton, N.J., Fletcher, I.R., Rego, J.L., 2005. Geology and SHRIMP U-Pb geochronology of the igarapé bahia deposit, carajás copper-gold belt, brazil: an archean (2.57 Ga) example of Iron-Oxide Cu-Au-(U-REE) mineralization. Econ. Geol. 100, 7–28. https://doi.org/10.2113/100.1.0007

Tassinari, C.C.G., Mellito, M.K., Babinski, M., 2003. Age and origin of the Cu (Au-Mo-Ag) Salobo 3A ore deposit, Carajás Mineral province, Amazonian craton, northern Brazil. Episodes 26, 2–9. https://doi.org/10.18814/epiiugs/2003/v26i1/001

Teixeira, A.S., Ferreira Filho, C.F., Giustina, M.E.S.D., Araújo, S.M., da Silva, H.H.A.B., 2015a. Geology, petrology and geochronology of the Lago Grande layered complex: evidence for a PGE-mineralized magmatic suite in the Carajás Mineral Province, Brazil. J. S. Am. Earth Sci. 64, 116–138. https://doi.org/10.1016/j.jsames.2015.09.006

Teixeira, M.F.B., Dall'Agnol, R., Santos, J.O.S., de Sousa, L.A.M., Lafon, J.M., 2017. Geochemistry, geochronology and Nd isotopes of the Gogó da Onça Granite: a new Paleoproterozoic A-type granite of Carajás Province, Brazil. J. S. Am. Earth Sci. 80, 47–65. https://doi.org/10.1016/j.jsames.2017.09.017

Teixeira, M.F.B., Dall'Agnol, R., Santos, J.O.S., de Oliveira, D.C., Lamarão, C.N., McNaughton, N.J., 2018. Crystallization ages of Paleoproterozoic A-type granites of Carajás province, Amazon craton: Constraints from U-Pb geochronology of zircon and titanite. J. S. Am. Earth Sci. 88, 312–331. https://doi.org/10.1016/j.jsames.2018.08.020

Toledo, F.P.I., Moreto, C.P.N., Xavier, R. P., Gao, J., de Matos, J.H.S.N., de Melo, G.H.C., 2019. Multistage Evolution of the Neoarchean (ca. 2.7 Ga) Igarapé Cinzento (GT-46) Iron Oxide Copper-Gold Deposit, Cinzento Shear Zone, Carajás Province, Brazil. Econ. Geol. 114, 1–34. https://doi.org/10.5382/econgeo.2019.4617

Trendall, A.F., Basei, M.A.S., de Laeter, J.R., Nelson, D.R., 1998. SHRIMP zircon U-Pb constraints on the age of the Carajás formation, Grão Pará Group, Amazon Craton. J. S. Am. Earth Sci. 11, 265–277. https://doi.org/10.1016/S0895-9811(98)00015-7

Volp, K., Evins, P., Meffre, S., 2006. EPMA and LA-ICPMS dating of hydrothermal REE minerals from the Estrela Copper Deposit Carajás, Brazil. Geochim. Cosmochim. Acta 70, A675. https://doi.org/10.1016/j.gca.2006.06.1262

Wirth, K.R., Gibbs, A.K., Olszewski Jr., W.J., 1986. U-Pb ages of zircons from the Grão Pará Group and Serra dos Carajás granite Pará, Brasil. Braz. J. Geol. 16, 195–200.

ESM – Table 14. Compiled Sr–Nd isotopic data from the Carajás Mineral Province, Brazil.

Sample	Unit	Petrography	Age [Ga]	$^{87}Rb/^{86}Sr$	$^{87}Sr/^{86}Sr$	I_{Sr}	$^{147}Sm/^{144}Nd$	$^{143}Nd/^{144}Nd$	I_{Nd}	εNd_i	Reference
Gneissified granitoids											
F147/32.7	Xingu Complex	Ton. Gneiss	2.86	4.385	0.85995	-	0.07854	0.51043	-	0.04	Mellito (1998)
F19/259.06	Xingu Complex	Ton. Gneiss	2.86	0.958	0.75940	-	0.10671	0.51095	-	-0.05	Mellito (1998)
F19/258	Xingu Complex	Ton. Gneiss	2.86	2.286	0.79791	-	0.11402	0.51104	-	-1.08	Mellito (1998)
F24/251.4	Xingu Complex	Ton. Gneiss	2.86	1.817	0.78467	-	0.11887	0.51082	-	-7.02	Mellito (1998)
Marc10	Gneissic granitoids	-	2.86	4.583	0.88908	-	0.11172	0.51102	-	-	Fernandes & Juliani (2019)
Marc50	Gneissic granitoids	-	2.86	1.159	0.74763	-	0.10196	0.51081	-	-	Fernandes & Juliani (2019)
Marc43	Gneissic granitoids	-	2.86	3.390	0.84331	-	0.07931	0.51026	-	-	Fernandes & Juliani (2019)
Marc52	Gneissic granitoids	-	2.86	1.149	0.76163	-	0.08855	0.51026	-	-	Fernandes & Juliani (2019)
Marc37	Gneissic granitoids	-	2.86	11.062	1.08884	-	0.12012	0.51104	-	-	Fernandes & Juliani (2019)
Marc60	Gneissic granitoids	-	2.86	3.145	0.83419	-	0.08498	0.51030	-	-	Fernandes & Juliani (2019)
Volcanic rocks											
F1100/172	Parauapebas Fm.	Bas.	2.75	-	0.72917	0.70662	0.11610	0.51110	-	-30.00	Martins et al. (2017)
F1279/Z	Parauapebas Fm.	Bas.	2.75	-	0.73192	0.70957	0.14080	0.51142	-	-23.80	Martins et al. (2017)
F1279/D	Parauapebas Fm.	Bas.	2.75	-	0.74213	0.70420	0.13370	0.51140	-	-24.22	Martins et al. (2017)
F1398/151	Parauapebas Fm.	Bas.	2.75	-	0.73131	0.70711	0.14990	0.51164	-	-19.50	Martins et al. (2017)
GB-67	Grão Pará Group	Bas. Trach.	2.76	1.766	0.77515	-	0.13642	0.51178	-	3.60	Gibbs et al. (1986)
GB-82-a	Grão Pará Group	Bas.	2.76	0.734	0.73456	-	0.17551	0.51254	-	4.60	Gibbs et al. (1986)
GB-82-b	Grão Pará Group	Bas.	2.76	0.467	0.72214	-	0.18134	0.51206	-	-7.00	Gibbs et al. (1986)
GB-85	Grão Pará Group	Rhy.	2.76	2.282	0.79817	-	0.10866	0.51129	-	3.80	Gibbs et al. (1986)
GB-86	Grão Pará Group	Bas. Trach.	2.76	0.829	0.73871	-	0.13524	0.51171	-	2.60	Gibbs et al. (1986)
GB-87	Grão Pará Group	Bas.	2.76	0.920	0.75241	-	0.13869	0.51154	-	-1.90	Gibbs et al. (1986)
GB-93	Grão Pará Group	Bas. Trach.	2.76	0.860	0.74011	-	0.13507	0.51163	-	1.20	Gibbs et al. (1986)
GB-94	Grão Pará Group	Rhy.	2.76	22.250	1.48964	-	0.12437	0.51135	-	-0.60	Gibbs et al. (1986)
GB-102	Grão Pará Group	Bas. Trach.	2.76	2.274	0.79519	-	0.13776	0.51179	-	-3.20	Gibbs et al. (1986)
GB-104	Grão Pará Group	Bas. Trach.	2.76	2.270	0.79237	-	0.13700	0.51148	-	-1.80	Gibbs et al. (1986)
Orosirian A-type granitoids											
CJ-124	Carajás Dyke Swarm	Dike	1.88	0.222	0.70951	0.7035	0.10790	0.51113		-8.00	Giovanardi et al. (2019)
CJ-126	Carajás Dyke Swarm	Dike	1.882	0.26735	0.71053	0.7033	0.12139	0.511284		-8.30	Giovanardi et al. (2019)
CJ-142	Carajás Dyke Swarm	Dike	1.882	0.327872	0.71200	0.7031	0.12908	0.51161		-3.30	Giovanardi et al. (2019)

Abbreviations: *Bas – basalt; Grt – granite; Rhy – rhyolite;; Trach – trachyandesite; Ton – tonalite.*

Supplementary 6 - References

Fernandes, C.M.D., Juliani, C., 2019. The tectonic controls on the Paleoproterozoic volcanism and the associated metallogeny in the South Amazonian craton, Brazil: Sr–Nd–Pb isotope constraints. Precambrian Res. 331, 105354. https://doi.org/10.1016/j.precamres.2019.105354

Gibbs, A.K., Wirth, K.R., Hirata, W.K., Olszewski Jr., W.J., 1986. Age and composition of the Grão Pará Group volcanics, Serra dos Carajás. Braz. J. Geol. 16, 201–211

Giovanardi, T., Girardi, V.A., Teixeira, W., Mazzucchelli, M., 2019. Mafic dyke swarms at 1882, 535 and 200 Ma in the Carajás region, Amazonian Craton: Sr-Nd isotopy, trace element geochemistry and inferences on their origin and geological settings. J. S. Am. Earth Sci. 92, 197–208. https://doi.org/10.1016/j.jsames.2019.02.017

Martins, P.L.G., Toledo, C.L.B., Silva, A.M., Chemale Jr, F., Santos, J.O.S., Assis, L.M., 2017. Neoarchean magmatism in the southeastern Amazonian Craton, Brazil: Petrography, geochemistry and tectonic significance of basalts from the Carajás Basin. Precambrian Res. 302, 340–357. https://doi.org/10.1016/j.precamres.2017.10.013

Mellito, K.M., 1998. Aplicação do método Rb-Sr e Pb-Pb à evolução da mineralização cuprífera do depósito de Salobo 3A, Província Mineral de Carajás, Pará. MSc. dissertation. University of São Paulo, Brazil.

ESM – Table 15. Compiled Sm–Nd isotopic data from the Central Andes of Chile between 22°S to 33°S and east of 71°W.

Sample	Unit	Petrography	Age (Ma)	Sm (ppm)	Nd (ppm)	$^{147}Sm/^{144}Nd$	± σ	$^{143}Nd/^{144}Nd$	± σ	εNd	I_{Nd}	$εNd_i$	T_{DM} (Ga)	Reference
Volcanic rocks														
K 51	S. de Candeleros	Bas.	163	8.9	35	0.154	-	0.512847	6.0E-6	4.1	0.51268	5	-	Bartsch (2004)
96–310	C° Blanco	Bas. Trach.	170	5.3	20	0.16	-	0.512997	1.2E-5	7	0.51282	7.8	-	Bartsch (2004)
97-239	C° Blanco	Bas.	154	12	47	0.154403	-	0.512911	6.0E-6	5.3	0.51276	6.16	-	Bartsch (2004)
96–21	C° Difunto	Bas.	194	3.6	12.2	0.178	-	0.5128	1.0E-6	3.2	0.51257	3.6	-	Bartsch (2004)
95–21	C° Difunto	Bas.	154	6.3	26	0.147	-	0.512777	7.0E-6	2.7	0.51263	3.7	-	Bartsch (2004)
95–45	C° Difunto	Bas. Trach.	154	4.3	16	0.163	-	0.512856	1.2E-5	4.3	0.51269	4.9	-	Bartsch (2004)
95–70a	C° Difunto	Bas.	154	5.7	22	0.157	-	0.5128	1.1E-5	3.2	0.51264	3.9	-	Bartsch (2004)
96-68	C° Difunto	Trach.	154	8.8	35	0.152045	-	0.512757	7.0E-6	2.3	0.5126	3.2	-	Bartsch (2004)
96–192	C° Difunto	Bas. Trach.	140	2.8	11	0.154	-	0.512885	6.0E-6	4.8	0.51274	5.6	-	Bartsch (2004)
95-58	C° Difunto	Trach.	154	11	44	0.151183	-	0.512823	9.0E-6	3.6	0.51267	4.51	-	Bartsch (2004)
96-164a	C° Difunto	And.	140	6.3	26	0.1481	-	0.512769	1.2E-5	2.6	0.51263	3.4	-	Bartsch (2004)
96-196	C° Difunto	And.	140	10	2.7	0.148096	-	0.512769	1.2E-5	2.6	0.51263	3.43	-	Bartsch (2004)
K 32	Qda. La Tranquita	Bas.	165	6.6	26	0.154	-	0.51285	9.0E-6	4.1	0.51269	5	-	Bartsch (2004)
K 37	Qda. La Tranquita	Bas. Trach.	161	33	7.3	0.148436	-	0.51287	5.0E-6	4.5	0.51271	5.52	-	Bartsch (2004)
96–77a	Qda. Cachina	Dac.	211	2.9	14	0.125	-	0.512631	6.0E-6	-0.1	0.51246	1.8	-	Bartsch (2004)
K 27	S. Minillas	Trach.	170	6.5	29	0.13554	-	0.51271	1.0E-5	1.4	0.51256	2.73	-	Bartsch (2004)
CaB-079	Falla Poblete volcanics	And.	127.9	4.92	20.78	0.143	-	0.512918	7.0E-6	-	0.5128	6.3	0.312	Girardi (2014)
CaB-287b	Las Animas Fm.	And.	131	6.01	24.51	0.148	-	0.512908	6.0E-6	-	0.51278	6.1	0.356	Girardi (2014)
GUC-05q	Pastos Blancos Fm.	Rhy.	224	4.01	22.5	0.108	-	0.512494	1.9E-6	-	0.51232	-0.5	-	González et al. (2018)
GUC-32q	Pastos Blancos Fm.	And.	224	4.9	22.1	0.134	-	0.512623	3.2E-6	-	0.51253	1.5	-	González et al. (2018)
GUC-33q	Pastos Blancos Fm.	Dac.	224	7.4	36.3	0.123	-	0.512462	1.7E-6	-	0.51228	-1.34	-	González et al. (2018)
GUC-38Bq	Pastos Blancos Fm.	Volc. Breccia	224	4.73	17.4	0.164	-	0.512554	2.5E-6	-	0.51231	-0.72	-	González et al. (2018)
GUC-41q	Pastos Blancos Fm.	Rhy. Tuff	224	8.55	40	0.129	-	0.512586	1.6E-06	-	0.5124	0.91	-	González et al. (2018)
GUC-45q	Pastos Blancos Fm.	Rhy. Tuff	224	6.14	31.8	0.117	-	0.512565	2.3E-6	-	0.51239	0.87	-	González et al. (2018)
GUC-46q	Pastos Blancos Fm.	Rhy. Tuff	224	7.04	34.3	0.124	-	0.512468	3.9E-6	-	0.51229	-1.24	-	González et al. (2018)
GUC-47q	Pastos Blancos Fm.	Dac.	224	4.7	23.5	0.121	-	0.512497	1.9E-6	-	0.51232	-0.58	-	González et al. (2018)
Veta Negra	Veta Negra Fm.	-	120	-	-	-	-	-	-	-	0.51273	4.85	-	Hesler (2007)
Veta Negra	Veta Negra Fm.	-	120	-	-	-	-	-	-	-	0.51262	2.6	-	Hesler (2007)
Yerbas Buenas	Upper member Lo Prado Fm.	-	120	-	-	-	-	-	-	-	0.51264	3	-	Hesler (2007)
Yerbas Buenas	Upper member Lo Prado Fm.	-	120	-	-	-	-	-	-	-	0.51254	2.8	-	Hesler (2007)
Abuelitas	Upper member Lo Prado Fm.	-	120	-	-	-	-	-	-	-	0.51266	3.45	-	Hesler (2007)
Abuelitas	Upper member Lo Prado Fm.	-	120	-	-	-	-	-	-	-	0.51259	2.08	-	Hesler (2007)
Poca Pena	Upper member Lo Prado Fm.	-	130	-	-	-	-	-	-	-	0.51264	3.36	-	Hesler (2007)
Poca Pena	Upper member Lo Prado Fm.	-	130	-	-	-	-	-	-	-	0.51255	1.5	-	Hesler (2007)
AS1	Caleta Agua Salada	-	160	-	-	0.178834	-	0.512945	-	-	0.51276	6.36	-	Lucassen & Franz (1994)
AS5	Caleta Agua Salada	-	160	-	-	0.103991	-	0.512874	-	-	0.51277	6.5	-	Lucassen & Franz (1994)
AS9	Caleta Agua Salada	-	160	-	-	0.136638	-	0.512892	-	-	0.51275	6.18	-	Lucassen & Franz (1994)
AS10	Caleta Agua Salada	-	160	-	-	0.157671	-	0.512937	-	-	0.51277	6.63	-	Lucassen & Franz (1994)
AS72	Caleta Agua Salada	-	160	-	-	0.152742	-	0.512921	-	-	0.51276	6.42	-	Lucassen & Franz (1994)

ESM – Table 9. (continued)

Sample	Unit	Petrography	Age (Ma)	Sm (ppm)	Nd (ppm)	$^{147}Sm/^{144}Nd$	± σ	$^{143}Nd/^{144}Nd$	± σ	εNd	I_{Nd}	$εNd_i$	T_{DM} (Ga)	Reference
164	Qda. La Negra	-	186	3.4	13	0.158	-	0.512946	5.0E-6	-	0.51275	6.9	-	Lucassen et al. (2006)
9	C° del Difunto	-	160	5.92	23.46	0.153	-	0.512857	5.0E-6	-	0.5127	5.2	-	Lucassen et al. (2006)
97–5	S. Fraga	-	160	6.6	25	0.16	-	0.512953	5.0E-6	-	0.51279	7.1	-	Lucassen et al. (2006)
97–213	C° Yumbes	-	211	1.67	7.24	0.139	-	0.512412	5.0E-6	-	0.51222	–2.9	-	Lucassen et al. (2006)
97–218	C° Yumbes	-	211	7.05	35	0.122	-	0.51239	5.0E-6	-	0.51222	–2.8	-	Lucassen et al. (2006)
K 116	Qda. Cachina	-	211	4.34	22.6	0.116	-	0.512597	5.0E-6	-	0.51244	1.4	-	Lucassen et al. (2006)
K 118	Qda. Cachina	-	211	4.35	19.4	0.135	-	0.512721	5.0E-6	-	0.51253	3.3	-	Lucassen et al. (2006)
MARQ-76	Arqueros Fm.	Bas. And.	117	8.89	41.1	-	-	0.512831	-	-	0.51273	4.7	0.47	Morata & Aguirre (2003)
ARQ99-7	Arqueros Fm.	Bas.	117	5.81	22.3	-	-	0.512847	-	-	0.51273	4.7	0.63	Morata & Aguirre (2003)
ARQ99-4	Arqueros Fm.	Bas. And.	115	7.02	34.2	-	-	0.512744	-	-	0.51265	3.1	0.58	Morata & Aguirre (2003)
ARQ00-13	Arqueros Fm.	Bas. And.	115	7.04	36.4	-	-	0.512745	-	-	0.51266	3.3	0.53	Morata & Aguirre (2003)
ARQ00-9	Qda. Marquesa Fm.	Bas. And.	110	6.47	32.2	-	-	0.512805	-	-	0.51272	4.3	0.47	Morata & Aguirre (2003)
ARQ00-19	Andesites	Bas. And.	100	7.35	34.2	-	-	0.512865	-	-	0.51278	5.3	0.41	Morata & Aguirre (2003)
TC00-13	Arqueros Fm. (?)	Bas. And.	115	6.01	29.5	-	-	0.512732	-	-	0.51264	2.9	0.59	Morata & Aguirre (2003)
TC99-2	Intrusive And. (?)	And.	100	4.93	21.6	-	-	0.512873	-	-	0.51278	5.3	0.44	Morata & Aguirre (2003)
111	Pichidangui Fm.	Bas.	220	7.77	28	-	-	0.512787	-	3.72	0.51255	-	0.92	Morata et al. (2000)
124	Pichidangui Fm.	Bas.	220	5.18	18	-	-	0.512859	-	4.95	0.51261	-	0.81	Morata et al. (2000)
114	Pichidangui Fm.	Bas.	220	6.5	23	-	-	0.512761	-	3.12	0.51252	-	1.05	Morata et al. (2000)
118	Pichidangui Fm.	Bas.	220	6.49	24	-	-	0.51278	-	3.7	0.51254	-	0.87	Morata et al. (2000)
113	Pichidangui Fm.	Rhy.	220	7.53	35	-	-	0.51267	-	2.5	0.51248	-	0.74	Morata et al. (2000)
142	Pichidangui Fm.	Rhy.	220	5.76	26	-	-	0.512719	-	3.34	0.51253	-	0.69	Morata et al. (2000)
120	Pichidangui Fm.	Rhy.	220	7.45	32	-	-	0.51264	-	1.61	0.51244	-	0.89	Morata et al. (2000)
110	Pichidangui Fm.	Rhy.	220	13.94	62	-	-	0.512304	-	-4.81	0.51211	-	1.43	Morata et al. (2000)
TC99-5a	Arqueros Fm.	Bas. And.	111.3	5.62	25.133	0.1353	-	0.51275	1.0E-3	-	-	-	-	Morata et al. (2008)
GIS-115	Pastos Blancos Fm.	And.	236	-	-	-	-	0.512479	5.0E-6	-3.1016	0.51227	-1.5002	-	Murillo et al. (2017)
GUM-31	Las Breas Fm.	Bas. And.	219.5	-	-	-	-	0.512752	4.0E-5	2.22379	0.51258	4.35891	-	Murillo et al. (2017)
CPV-14-194	Agua Chica Fm.	Dac. Tuff	200.4	-	-	0.134879	-	0.512647	-	0.17	0.51247	1.75	-	Oliveros et al. (2020)
CPV-14-198	Agua Chica Fm.	And.	200.4	-	-	0.133824	-	0.512557	-	-1.58	0.51238	0.03	-	Oliveros et al. (2020)
CPV-12-26B	Algarrobal Fm.	And.	152.7	-	-	0.159827	-	0.512616	-	-0.43	0.51246	0.29	-	Oliveros et al. (2020)
CPV-12-28x	Algarrobal Fm.	Bas. And.	152.7	-	-	0.153155	-	0.512803	-	3.22	0.51265	4.07	-	Oliveros et al. (2020)
CPV-12-30x	Algarrobal Fm.	And.	152.7	-	-	0.134207	-	0.512637	-	-0.02	0.5125	1.2	-	Oliveros et al. (2020)
CPV-12-90	Canto del Agua Fm.	Tuff	212.75	-	-	0.149829	-	0.512454	-	-3.59	0.51225	−2.32	-	Oliveros et al. (2020)
CPV-14-263	C° Rincones Beds	Dac.	328.3	-	-	0.116623	-	0.512332	-	-5.97	0.51211	−2.97	-	Oliveros et al. (2020)
CPV-14-184	Cifuncho Fm.	And.	212	-	-	0.133138	-	0.512693	-	1.07	0.51251	2.79	-	Oliveros et al. (2020)
CPV-14-187	Cifuncho Fm.	And.	210.1	-	-	0.130071	-	0.512675	-	0.72	0.5125	2.5	-	Oliveros et al. (2020)
CPV-14-190	Cifuncho Fm.	Dac.	212	-	-	0.140619	-	0.512683	-	0.87	0.51249	2.39	-	Oliveros et al. (2020)
SCL-28q	Guanaco Sonso Fm.	Rhy. Tuff	249.1	-	-	0.137724	-	0.512444	-	-3.78	0.51222	−1.91	-	Oliveros et al. (2020)
RCM-150q	Guanaco Sonso Fm.	Rhy. Tuff	252.4	-	-	0.108168	-	0.51241	-	-4.44	0.51223	−1.59	-	Oliveros et al. (2020)
SCL-96	Guanaco Sonso Fm.	Dac. Tuff	248.8	-	-	0.143762	-	0.512637	-	-0.02	0.5124	1.66	-	Oliveros et al. (2020)
CPV-14-176	La Tabla Fm.	Rhy. Tuff	295.1	-	-	0.118763	-	0.512341	-	-5.79	0.51211	−2.85	-	Oliveros et al. (2020)

ESM – Table 9. (continued)

Sample	Unit	Petrography	Age (Ma)	Sm (ppm)	Nd (ppm)	$^{147}Sm/^{144}Nd$	± σ	$^{143}Nd/^{144}Nd$	± σ	εNd	I_{Nd}	$εNd_i$	T_{DM} (Ga)	Reference
CPV-14-249	La Tabla Fm.	Rhy. Tuff	307	-	-	0.13204	-	0.512322	-	-6.16	0.51207	−3.76	-	Oliveros et al. (2020)
CPV-12-23	La Totora Fm.	And.	221	-	-	0.131692	-	0.51263	-	-0.16	0.51244	1.63	-	Oliveros et al. (2020)
CPV-12-24	La Totora Fm.	And.	221	-	-	0.160713	-	0.512789	-	2.95	0.51256	3.94	-	Oliveros et al. (2020)
CPV-12-60	La Totora Fm.	Bas.	221	-	-	0.12278	-	0.512605	-	-0.64	0.51243	1.39	-	Oliveros et al. (2020)
SCL-26q	La Totora Fm.	Rhy. Tuff	217.9	-	-	0.107184	-	0.512568	-	-1.36	0.51242	1.13	-	Oliveros et al. (2020)
CPV-12-105	Llano de Chocolate Beds	Rhy.	318.8	-	-	0.132543	-	0.512329	-	-6.03	0.51205	−3.42	-	Oliveros et al. (2020)
CPV-12-12	Llano de Chocolate Beds	Dac.	303.8	-	-	0.122331	-	0.512325	-	-6.11	0.51208	−3.22	-	Oliveros et al. (2020)
CPV-12-127	Llano de Chocolate Beds	Rhy.	291.4	-	-	0.156505	-	0.512782	-	2.81	0.51248	4.31	-	Oliveros et al. (2020)
RCM-78q	Pastos Blancos Fm.	And.	231.7	-	-	0.129313	-	0.512438	-	-3.9	0.51225	−1.95	-	Oliveros et al. (2020)
CPV-14-245	Qda. del Salitre Fm.	Bas. And.	212	-	-	0.162681	-	0.512677	-	0.76	0.51245	1.68	-	Oliveros et al. (2020)
CPV-14-247	Qda. del Salitre Fm.	Tuff	212	-	-	0.136957	-	0.512512	-	-2.46	0.51232	−0.84	-	Oliveros et al. (2020)
CPV-14-253	Qda. del Salitre Fm.	Bas.	212	-	-	0.163548	-	0.512676	-	0.74	0.51245	1.64	-	Oliveros et al. (2020)
CPV-14-256	Qda. del Salitre Fm.	Bas. And.	233	-	-	0.156501	-	0.512739	-	1.97	0.5125	3.17	-	Oliveros et al. (2020)
CPV-15-303	Qda. del Salitre Fm.	Bas. And.	232.9	-	-	0.153351	-	0.512704	-	1.29	0.51249	2.46	-	Oliveros et al. (2020)
CPV-15-310	Qda. del Salitre Fm.	Rhy.	232.9	-	-	0.14335	-	0.512672	-	0.66	0.51247	2.11	-	Oliveros et al. (2020)
CPV-15-311	Qda. del Salitre Fm.	Bas.	232.9	-	-	0.158989	-	0.512814	-	3.43	0.51257	4.56	-	Oliveros et al. (2020)
CPV-15-312	Qda. del Salitre Fm.	And.	232.9	-	-	0.126051	-	0.512519	-	-2.32	0.51233	−0.22	-	Oliveros et al. (2020)
CPV-15-314	Qda. del Salitre Fm.	Rhy.	232.9	-	-	0.133384	-	0.512614	-	-0.47	0.51241	1.42	-	Oliveros et al. (2020)
CPV-15-319	Qda. del Salitre Fm.	Dac.	232.9	-	-	0.134681	-	0.512638	-	0	0.51245	1.68	-	Oliveros et al. (2020)
CPV-15-322	Qda. del Salitre Fm.	And.	232.9	-	-	0.16718	-	0.51293	-	5.7	0.51269	6.54	-	Oliveros et al. (2020)
CPV-12-38	San Félix Fm.	Tuff	252	-	-	0.116632	-	0.512308	-	-6.44	0.51212	−3.94	-	Oliveros et al. (2020)
CPV-12-49b	San Félix Fm.	Tuff	252	-	-	0.124326	-	0.512363	-	-5.36	0.51216	−3.11	-	Oliveros et al. (2020)
CHY-01	Los Tilos Fm.	Rhy.	224	8.53	42.1	0.12252	-	0.512422	-	-4.2	-	-2.1	-	Parada (2013)
CHY-02	Los Tilos Fm.	Tuff	221	7.89	39	0.122335	-	0.512423	-	-4.2	-	-2.1	-	Parada (2013)
CHY-10	Los Tilos Fm.	Rhy.	232	8.12	39.5	0.1243	-	0.512435	-	-4	-	-1.8	-	Parada (2013)
CHY-14	La Tabla Fm.	Tuff	282	11.08	57.3	0.11693	-	0.512324	-	-6.1	-	-3.3	-	Parada (2013)
CHY-15	La Tabla Fm.	Tuff	272	4.1	21.9	0.113209	-	0.512391	-	-4.8	-	-1.9	-	Parada (2013)
CHY-22	La Tabla Fm.	Rhy.	270	5.7	30.9	0.111547	-	0.512294	-	-6.7	-	-3.8	-	Parada (2013)
ACON103	C° Aconcagua	And.	8.9	-	-	-	-	0.512597	8.0E-4	-	-	-0.3	-	Reich et al. (2003)
8077	La Negra Fm.	-	187	8.17	34.7	-	-	0.51287	-	-	-	5.74	-	Rogers & Hawkesworth (1989)
8078	La Negra Fm.	-	187	8.28	35.6	-	-	0.51282	-	-	-	4.88	-	Rogers & Hawkesworth (1989)
8086	La Negra Fm.	-	187	6.51	27.5	-	-	0.51278	-	-	-	3.9	-	Rogers & Hawkesworth (1989)
8084	La Negra Fm.	-	187	7.03	29	-	-	0.51292	-	-	-	6.62	-	Rogers & Hawkesworth (1989)
8092	La Negra Fm.	-	187	6.01	26.5	-	-	0.51289	-	-	-	6.34	-	Rogers & Hawkesworth (1989)
8093	La Negra Fm.	-	187	8.17	34.6	-	-	0.51284	-	-	-	5.11	-	Rogers & Hawkesworth (1989)
8097	La Negra Fm.	-	187	7.29	30.3	-	-	0.51287	-	-	-	5.68	-	Rogers & Hawkesworth (1989)
8098	La Negra Fm.	-	187	9.45	39.5	-	-	0.51288	-	-	-	5.84	-	Rogers & Hawkesworth (1989)
81055	Indio Muerto Fm.	-	130	6.75	31.9	-	-	0.51251	-	-	-	-1.5	-	Rogers & Hawkesworth (1989)
81056	Indio Muerto Fm.	-	130	5.7	26.3	-	-	0.51261	-	-	-	0.51	-	Rogers & Hawkesworth (1989)
81130	Augusta Victoria Fm.	-	105	11.3	67.8	-	-	0.51276	-	-	-	3.55	-	Rogers & Hawkesworth (1989)

ESM – Table 9. (continued)

Sample	Unit	Petrography	Age (Ma)	Sm (ppm)	Nd (ppm)	$^{147}Sm/^{144}Nd$	± σ	$^{143}Nd/^{144}Nd$	± σ	εNd	I_{Nd}	$εNd_i$	T_{DM} (Ga)	Reference
81131	Augusta Victoria Fm.	-	105	6.48	39.1	-	-	0.51282	-	-	-	4.95	-	Rogers & Hawkesworth (1989)
81132	Augusta Victoria Fm.	-	105	8.05	46.2	-	-	0.51285	-	-	-	5.24	-	Rogers & Hawkesworth (1989)
81134	Augusta Victoria Fm.	-	105	4.9	21.2	-	-	0.51278	-	-	-	3.57	-	Rogers & Hawkesworth (1989)
81136	Augusta Victoria Fm.	-	105	6.72	28.5	-	-	0.5128	-	-	-	3.9	-	Rogers & Hawkesworth (1989)
81019	C° Negro Fm.	-	70	3.5	22	-	-	0.51272	-	-	-	2.44	-	Rogers & Hawkesworth (1989)
81020	C° Negro Fm.	-	70	4	19.6	-	-	0.51273	-	-	-	2.46	-	Rogers & Hawkesworth (1989)
PR-09-22	Qda. Vicuñita Beds	Bas. And.	150	-	-	-	-	0.5129	-	5.1	0.51274	6	-	Rossel et al. (2013)
PR-10-31	Qda. Vicuñita Beds	Bas. And.	150	-	-	-	-	0.51286	-	4.4	0.51272	5.4	-	Rossel et al. (2013)
PR-10-32	Qda. Vicuñita Beds	Bas. And.	150	-	-	-	-	0.5128	-	3.2	0.51265	4.1	-	Rossel et al. (2013)
PR-10-33	Qda. Vicuñita Beds	And.	150	-	-	-	-	0.51281	-	3.4	0.5127	5	-	Rossel et al. (2013)
PR-10-36B	Qda. Vicuñita Beds	Bas.	150	-	-	-	-	0.51289	-	5	0.51274	5.7	-	Rossel et al. (2013)
PR-09-28	Lagunillas Fm.	Bas.	150	-	-	-	-	0.51323	-	11.5	0.51281	7.1	-	Rossel et al. (2013)
PR-10-71	Lagunillas Fm.	Bas.	150	-	-	-	-	0.51267	-	0.6	0.51253	1.6	-	Rossel et al. (2013)
PR-10-72	Lagunillas Fm.	Bas.	150	-	-	-	-	0.51271	-	1.4	0.51259	2.8	-	Rossel et al. (2013)
PR-10-73	Lagunillas Fm.	Bas.	150	-	-	-	-	0.51268	-	0.9	0.51255	2.1	-	Rossel et al. (2013)
PR-10-80	Lagunillas Fm.	Bas.	150	-	-	-	-	0.51274	-	1.9	0.51261	3.3	-	Rossel et al. (2013)
PR-10-81	Lagunillas Fm.	Bas. And.	150	-	-	-	-	0.5127	-	1.1	0.51256	2.5	-	Rossel et al. (2013)
PR-10-94B	Lagunillas Fm.	Bas.	150	-	-	-	-	0.51274	-	2	0.51262	3.3	-	Rossel et al. (2013)
PR-10-120	Lagunillas Fm.	Bas. And.	150	-	-	-	-	0.51281	-	3.3	0.51267	4.6	-	Rossel et al. (2013)
PR-11-177	Lagunillas Fm.	Bas.	150	-	-	-	-	0.51289	-	4.9	0.51277	6.3	-	Rossel et al. (2013)
PR-11-178	Lagunillas Fm.	Dac.	150	-	-	-	-	0.51252	-	-2.4	0.51239	-1	-	Rossel et al. (2013)
PR-11-179	Lagunillas Fm.	Bas.	150	-	-	-	-	0.51266	-	0.5	0.51251	1.2	-	Rossel et al. (2013)
PR-11-188	Lagunillas Fm.	Bas.	150	-	-	-	-	0.51287	-	4.6	0.51268	4.5	-	Rossel et al. (2013)
PR-11-193	Lagunillas Fm.	Dacite	150	-	-	-	-	0.51256	-	-1.6	0.51239	-1	-	Rossel et al. (2013)
PR-11-202	Lagunillas Fm.	Bas.	150	-	-	-	-	0.51276	-	2.4	0.51262	3.5	-	Rossel et al. (2013)
PR-11-204	Lagunillas Fm.	Bas.	150	-	-	-	-	0.51279	-	3	0.51265	3.9	-	Rossel et al. (2013)
PR-09-04	Picudo Fm.	Rhy.	150	-	-	-	-	0.5127	-	1.2	0.51255	2.1	-	Rossel et al. (2013)
PR-09-05	Picudo Fm.	Bas. And.	150	-	-	-	-	0.51263	-	-0.1	0.51251	1.3	-	Rossel et al. (2013)
PR-09-06	Picudo Fm.	Bas. And.	150	-	-	-	-	0.5127	-	1.1	0.5126	3	-	Rossel et al. (2013)
PR-10-41	Picudo Fm.	Bas. And.	150	-	-	-	-	0.51257	-	-1.4	0.51245	0.2	-	Rossel et al. (2013)
PR-10-42B	Picudo Fm.	Dac.	150	-	-	-	-	0.51273	-	2.2	0.51262	3.3	-	Rossel et al. (2013)
PR-10-45	Picudo Fm.	Bas.	150	-	-	-	-	0.51272	-	1.7	0.51258	2.7	-	Rossel et al. (2013)
PR-11-164	Picudo Fm.	Bas. And.	150	-	-	-	-	0.51275	-	2.1	0.51262	3.5	-	Rossel et al. (2013)

ESM – Table 9. (continued)

Sample	Unit	Petrography	Age (Ma)	Sm (ppm)	Nd (ppm)	$^{147}Sm/^{144}Nd$	± σ	$^{143}Nd/^{144}Nd$	± σ	εNd	I_{Nd}	$εNd_i$	T_{DM} (Ga)	Reference
M-14	Algarrobal Fm.	Bas. And.	150	-	-	-	-	0.5127	-	1.3	0.51259	2.7	-	Rossel et al. (2013)
M-17	Algarrobal Fm.	And.	150	-	-	-	-	0.5126	-	-0.7	0.51248	0.6	-	Rossel et al. (2013)
M-22	Algarrobal Fm.	And.	150	-	-	-	-	0.51275	-	2.1	0.51261	3.2	-	Rossel et al. (2013)
M-25	Algarrobal Fm.	And.	150	-	-	-	-	0.51262	-	-0.3	0.51248	0.7	-	Rossel et al. (2013)
PR-11-132A	Agua Salada Volcanic Comp.	Bas. And.	150	-	-	-	-	0.5128	-	3.1	0.51266	4.2	-	Rossel et al. (2013)
PR-11-134C	Agua Salada Volcanic Comp.	Bas. And.	150	-	-	-	-	0.5128	-	3.2	0.51267	4.3	-	Rossel et al. (2013)
PR-11-139	Agua Salada Volcanic Comp.	Bas. And.	150	-	-	-	-	0.51286	-	4.3	0.51272	5.3	-	Rossel et al. (2013)
PR-11-153	Agua Salada Volcanic Comp.	Bas. And.	150	-	-	-	-	0.51274	-	2	0.51258	2.7	-	Rossel et al. (2013)
PR-11-154	Agua Salada Volcanic Comp.	Bas. And.	150	-	-	-	-	0.51285	-	4.1	0.51266	4.2	-	Rossel et al. (2013)
ST-62q	San Félix Fm.	Rhy.	213.7	-	-	0.148798	-	0.512616	4.0E-6	-0.43	0.51241	0.88	-	Salazar et al. (2013)
COP-18-02A	Punta del Cobre Fm., Dacite Member	Alb.	130	3.4	14.4	-	-	0.512696	1.4E-5	-	-	2	-	Tornos et al. (2020)
COP-18-02-B	Punta del Cobre Fm., Dacite Member	Alb.	130	2.1	9.3	-	-	0.512689	1.3E-5	-	-	2	-	Tornos et al. (2020)
<u>Mafic-ultramafic magmatism</u>														
cc-03-01	Concon Maf. Dike Swarms	-	160	3.44	14.43	-	-	0.512649	-	-	0.5125	1.29	1.097	Creixell (2007)
cc-03-32	Concon Maf. Dike Swarms	-	160	9.38	41.55	-	-	0.512678	-	-	0.51254	2.01	0.932	Creixell (2007)
cc-03-42	Cartagena Maf. Dike Swarms	-	160	3.64	13.65	-	-	0.51266	-	-	0.51249	1.15	1.418	Creixell (2007)
cc-03-27	El Tabo Maf. Dike Swarms	-	140	2.2	8.5	-	-	0.512525	-	-	0.51238	-1.5	1.673	Creixell (2007)
cc-03-38	El Tabo Maf. Dike Swarms	-	140	10.47	43.64	-	-	0.512511	-	-	0.51238	-1.56	1.416	Creixell (2007)
cc-03-24	El Tabo Maf. Dike Swarms	-	140	2.19	7.93	-	-	0.512698	-	-	0.51255	1.7	1.466	Creixell (2007)
cc-04-51	El Tabo Maf. Dike Swarms	-	140	4.93	17.66	-	-	0.512851	-	-	0.5127	4.65	1.015	Creixell (2007)
cc-03-62	El Tabo Maf. Dike Swarms	-	140	10.28	41.11	-	-	0.512661	-	-	0.5125	1.38	1.192	Creixell (2007)
cc-04-15	Elqui Maf. Dike Swarms	-	200	5.95	24.69	-	-	0.512719	-	-	0.51253	2.88	0.968	Creixell (2007)
cc-04-29	Elqui Maf. Dike Swarms	-	200	5.43	23.62	-	-	0.512665	-	-	0.51248	1.99	0.99	Creixell (2007)
cc-04-34	Elqui Maf. Dike Swarms	-	200	5.74	25.66	-	-	0.512832	-	-	0.51266	5.35	0.618	Creixell (2007)
cc-04-40	Elqui Maf. Dike Swarms	-	200	6.32	25.62	-	-	0.512835	-	-	0.51264	5.06	0.744	Creixell (2007)
CaB-246	S. Atacama Diorite	Gab.	101.7	1.74	6.77	0.155	-	0.512913	7.0E-6	-	0.51281	5.9	0.385	Girardi (2014)
CaB-211b	Gabbro	Gab.	134.5	2.93	10.42	0.17	-	0.512921	8.0E-6	-	0.51277	6	0.473	Girardi (2014)
C9G-386b	Caldera Gabbro	Gab.	181.5	5.95	23.86	0.151	-	0.512774	7.0E-6	-	0.5126	3.7	0.672	Girardi (2014)
CB3	-	Gab.	185	0.58	1.785	0.1951	-	0.512938	8.0E-6	-	-	5.89	-	Lucassen & Thirlwall (1998)
CB11	-	Gab.	185	0.99	2.305	0.2587	-	0.513019	6.0E-6	-	-	5.97	-	Lucassen & Thirlwall (1998)
CB33	-	Gab.	185	0.73	2.075	0.2117	-	0.512968	7.0E-06	-	-	6.09	-	Lucassen & Thirlwall (1998)
07-10	La Laguna Gabbro	Gab.	218.1	-	-	0.1323	-	0.512463	-	-3.41	0.51227	−1.62	-	Oliveros et al. (2020)
07-11	La Laguna Gabbro	Gab.	218.1	-	-	0.1327	-	0.512482	-	-3.04	0.51229	−1.26	-	Oliveros et al. (2020)
F2-25a	Sto. Domingo Comp.	Maf. Enc.	308	6.8	26.6	-	-	0.512451	-	-2	0.51214	-	1.5	Parada et al. (1999)

ESM – Table 9. (continued)

Sample	Unit	Petrography	Age (Ma)	Sm (ppm)	Nd (ppm)	$^{147}Sm/^{144}Nd$	± σ	$^{143}Nd/^{144}Nd$	± σ	εNd	I_{Nd}	$εNd_i$	T_{DM} (Ga)	Reference
F2-29	Sto. Domingo Comp.	Maf. Enc.	308	14.1	62.7	-	-	0.512337	-	-3.5	0.51206	-	1.38	Parada et al. (1999)
CBR-7	Limarí Comp.	Gab.	203	2.9	9.4	-	-	0.512808	-	3.6	0.51256	-	1.32	Parada et al. (1999)
D18A	Limarí Comp.	Gab.	203	1.1	3.5	-	-	0.512867	-	4.6	0.51261	-	1.18	Parada et al. (1999)
CBR-1E	Papudo-Quintero Comp.	Maf. Enc.	170	5.3	22	-	-	0.51268	-	1.9	0.51252	-	0.88	Parada et al. (1999)
F2-5	Papudo-Quintero Comp.	Maf. Enc.	164	5.2	22.1	-	-	0.512762	-	3.6	0.51261	-	0.67	Parada et al. (1999)
F2-6	Papudo-Quintero Comp.	Maf. Enc.	164	6.8	27.8	-	-	0.5127	-	2.2	0.51254	-	0.86	Parada et al. (1999)
<u>**I-type granitoids**</u>														
IC-17	Montosa-El Potro Bath., La Estancilla Unit	Ton.	286	3.28	15.7	-	-	0.51261	-	-	0.51238	2.09	-	del Rey et al. (2019)
IC-22	Montosa-El Potro Bath., Montosa Unit	Ton.	253	4.87	25.6	-	-	0.51239	-	-	0.5122	-2.13	-	del Rey et al. (2019)
IC-23	Montosa-El Potro Bath., Montosa Unit	Sgr	264	2.68	19.3	-	-	0.51237	-	-	0.51223	-1.36	-	del Rey et al. (2019)
IC-99	Montosa-El Potro Bath., Montosa Unit	Ton.	253	2.7	17.4	-	-	0.51244	-	-	0.51228	-0.51	-	del Rey et al. (2019)
IC-102	Montosa-El Potro Bath., Montosa Unit	Php. Rhy.	252	4.44	25	-	-	0.51281	-	-	0.51263	6.17	-	del Rey et al. (2019)
IC-106	Montosa-El Potro Bath., Montosa Unit	Grd.	244	4.99	30	-	-	0.51299	-	-	0.51283	10.04	-	del Rey et al. (2019)
RdM-09	Montosa-El Potro Bath., Montosa Unit	Sgr.	255	2.38	14.5	-	-	0.51234	-	-	0.51218	-2.62	-	del Rey et al. (2019)
IC-58	Montosa-El Potro Bath., El León Unit	Mgr.	257	5.36	26.6	-	-	0.51236	-	-	0.51216	-2.87	-	del Rey et al. (2019)
IC-94	Montosa-El Potro Bath., El León Unit	Sgr.	244	2.73	12.9	-	-	0.51239	-	-	0.51219	-2.6	-	del Rey et al. (2019)
IC-14	Montosa-El Potro Bath., Colorado Unit	Mgr.	250	6.22	31.8	-	-	0.5124	-	-	0.51221	-2.09	-	del Rey et al. (2019)
IC-93	Montosa-El Potro Bath., Colorado Unit	Sgr.	248	3.57	19.4	-	-	0.51245	-	-	0.51227	-0.92	-	del Rey et al. (2019)
IC-46	Montosa-El Potro Bath., Chollay Unit	Sgr.	248	4.31	27.2	-	-	0.51257	-	-	0.51233	0.29	-	del Rey et al. (2019)
IC-47	Montosa-El Potro Bath., Chollay Unit	Grt.	245	4.76	17.6	-	-	0.51246	-	-	0.51229	-0.73	-	del Rey et al. (2019)
IC-81	Montosa-El Potro Bath., Chollay Unit	Mgr.	242	7.96	47.4	-	-	0.5124	-	-	0.51225	-1.64	-	del Rey et al. (2019)
IC-91	Montosa-El Potro Bath., Chollay Unit	Sgr.	259	4.71	25.7	-	-	0.51186	-	-	0.51168	-12.17	-	del Rey et al. (2019)
IC-92	Montosa-El Potro Bath., Chollay Unit	Php. Lat.	216	4.89	25.9	-	-	0.51246	-	-	0.5123	-1.18	-	del Rey et al. (2019)
C9G-170	S. Pajas Blancas Granodiorite	Ton.	105.9	2.96	15.44	0.116	-	0.512873	6.0E-6	-	0.51279	5.7	0.296	Girardi (2014)
CaB-171a	S. Pajas Blancas Granodiorite	Ton.	106.8	3.52	19.91	0.107	-	0.51288	8.0E-6	-	0.51281	5.9	0.263	Girardi (2014)
C9G-074	La Borracha Pluton	Qtz-dio.	111	7.9	37.25	0.128	-	0.512889	7.0E-6	-	0.5128	5.9	0.309	Girardi (2014)
Tig890	Dike near to Moradito area	And. Dike	116.3	3.61	16.19	0.135	-	0.512883	6.0E-6	-	0.51278	5.7	0.344	Girardi (2014)
C9G-210	S. Atacama Diorite	Dio.	116.5	8.62	38.98	0.134	-	0.512889	6.0E-6	-	0.51279	5.8	0.328	Girardi (2014)
CaB-296	Felsic near to S. Chicharra	Grt.	127.3	3.99	19.67	0.123	-	0.512848	7.0E-6	-	0.51275	5.3	0.355	Girardi (2014)
C9G-128a	S. Chicharra Quartz-diorite	Dio.	128.5	4.7	19.25	0.148	-	0.512873	8.0E-6	-	0.51275	5.4	0.426	Girardi (2014)
C9G-140	S. Chicharra Quartz-diorite	Qtz-dio.	130.1	3.32	13.36	0.15	-	0.51281	7.0E-6	-	0.51268	4.1	0.585	Girardi (2014)
C9G-108c	Felsic near to S. Chicharra	Ton.	130.7	5.66	22.77	0.15	-	0.512876	7.0E-6	-	0.51275	5.4	0.437	Girardi (2014)
C9G-320	C° Moradito Pluton	Ton.	136.6	4.16	17.09	0.147	-	0.512918	1.0E-5	-	0.51279	6.3	0.329	Girardi (2014)
C9G-514b	Felsic near to Moradito area	Ton.	137	3.09	13.55	0.138	-	0.512853	7.0E-6	-	0.51273	5.2	0.413	Girardi (2014)
CaB-004b	Felsic near to Moradito area	Ton.	137.1	2.98	14.22	0.127	-	0.512804	7.0E-6	-	0.51269	4.5	0.445	Girardi (2014)
CaB-295	C° Morado Pluton	Dio.	137.5	4.23	18.27	0.14	-	0.512851	8.0E-6	-	0.51273	5.2	0.428	Girardi (2014)
C9G-388	S. El Roble Pluton	Ton.	164.4	5.84	26.9	0.131	-	0.512791	7.0E-6	-	0.51265	4.4	0.49	Girardi (2014)
CaB-292	C° Chascon Granodiorite	Grd.	195.5	4.4	19.82	0.134	-	0.512586	6.0E-6	-	0.51241	0.5	0.883	Girardi (2014)

ESM – Table 9. (continued)

Sample	Unit	Petrography	Age (Ma)	Sm (ppm)	Nd (ppm)	$^{147}Sm/^{144}Nd$	± σ	$^{143}Nd/^{144}Nd$	± σ	εNd	I_{Nd}	$εNd_i$	T_{DM} (Ga)	Reference
CaB-293	Pto. Viejo Monzogranite	Ton.	196.1	4.61	21	0.133	-	0.512555	6.0E-6	-	0.51239	0	0.924	Girardi (2014)
CaB-294	Permian Pluton	Grt.	256	5.56	23.33	0.134	-	0.512397	7.0E-6	-	0.51216	-3	1.408	Girardi (2014)
GUC-34q	Colorado Syenogranite	And. Dike	224	5.2	23	0.137	-	0.512772	1.5E-6	-	0.51257	4.33	-	González et al. (2018)
GUC-37Aq	Colorado Syenogranite	Mzd. Dike	224	4.17	18.7	0.135	-	0.512533	2.8E-6	-	0.51234	-0.29	-	González et al. (2018)
GUC-37Cq	Colorado Syenogranite	Dio. Dike	224	7.76	34.6	0.136	-	0.51256	1.7E-6	-	0.51236	0.22	-	González et al. (2018)
115	C° Argolla, S. of Taltal	-	140	10.3	44.6	0.14	-	0.512723	5.0E-6	-	0.5126	2.7	-	Lucassen et al. (2006)
181	C° Argolla, S. of Taltal	-	140	11.4	44.7	0.154	-	0.512905	5.0E-6	-	0.51276	6	-	Lucassen et al. (2006)
203	C° Argolla, S. of Taltal	-	140	10.2	44.7	0.138	-	0.512727	6.0E-6	-	0.5126	2.8	-	Lucassen et al. (2006)
231	C° Argolla, S. of Taltal	-	140	8.1	35.1	0.14	-	0.512767	5.0E-6	-	0.51264	3.5	-	Lucassen et al. (2006)
233	C° Argolla, S. of Taltal	-	140	8.86	35.8	0.15	-	0.512853	5.0E-6	-	0.51272	5	-	Lucassen et al. (2006)
234	C° Argolla, S. of Taltal	-	140	8.94	38.1	0.142	-	0.512725	5.0E-6	-	0.5126	2.7	-	Lucassen et al. (2006)
U-8	Deep section of the Coastal Bath.	-	140	3.41	14.1	0.146	-	0.512876	6.0E-6	-	0.51274	5.5	-	Lucassen et al. (2006)
U-24	Deep section of the Coastal Bath.	-	140	2.53	11.3	0.136	-	0.512858	6.0E-6	-	0.51273	5.4	-	Lucassen et al. (2006)
U-83	Deep section of the Coastal Bath.	-	140	2.51	11.5	0.132	-	0.51287	5.0E-6	-	0.51275	5.7	-	Lucassen et al. (2006)
U-85	Deep section of the Coastal Bath.	-	140	3.5	15.6	0.136	-	0.512854	-	-	0.51273	5.3	-	Lucassen et al. (2006)
MCP-1	Shallow section of the Coastal Bath.	-	160	7.11	30.1	0.143	-	0.512896	5.0E-6	-	0.51275	6.1	-	Lucassen et al. (2006)
MCP-11	Shallow section of the Coastal Bath.	-	160	5.94	23.9	0.15	-	0.512886	4.0E-06	-	0.51273	5.8	-	Lucassen et al. (2006)
QPA-2	Shallow section of the Coastal Bath.	-	160	3.87	17	0.138	-	0.512887	5.0E-6	-	0.51274	6.1	-	Lucassen et al. (2006)
QPA-4	Shallow section of the Coastal Bath.	-	160	6.15	26.2	0.142	-	0.512882	5.0E-6	-	0.51273	5.9	-	Lucassen et al. (2006)
QMA-1	Shallow section of the Coastal Bath.	-	160	5.43	24.9	0.132	-	0.512803	3.0E-6	-	0.51266	4.5	-	Lucassen et al. (2006)
QMA-2	Shallow section of the Coastal Bath.	-	160	5.95	27.1	0.133	-	0.512815	5.0E-6	-	0.51268	4.8	-	Lucassen et al. (2006)
QBA-1	Shallow section of the Coastal Bath.	-	160	5.91	25.9	0.138	-	0.512784	4.0E-6	-	0.51264	4	-	Lucassen et al. (2006)
QBA-5	Shallow section of the Coastal Bath.	-	160	4.33	22.8	0.115	-	0.512808	4.0E-6	-	0.51269	5	-	Lucassen et al. (2006)
QSR-1	Shallow section of the Coastal Bath.	-	160	3.71	17.2	0.13	-	0.51274	6.0E-6	-	0.5126	3.3	-	Lucassen et al. (2006)
QSR-8	Shallow section of the Coastal Bath.	-	160	1.88	6.31	0.18	-	0.512859	5.0E-6	-	0.51267	4.7	-	Lucassen et al. (2006)
QCA-5	Shallow section of the Coastal Bath.	-	160	6.28	30.5	0.125	-	0.512585	5.0E-6	-	0.51245	0.4	-	Lucassen et al. (2006)
QCA-6	Shallow section of the Coastal Bath.	-	160	6.53	32.5	0.121	-	0.512628	7.0E-6	-	0.5125	1.3	-	Lucassen et al. (2006)
QCA-7	Shallow section of the Coastal Bath.	-	160	4.7	18.3	0.155	-	0.512676	5.0E-6	-	0.51251	1.6	-	Lucassen et al. (2006)
QCA-9	Shallow section of the Coastal Bath.	-	160	3.64	17.3	0.128	-	0.512688	5.0E-6	-	0.51255	2.4	-	Lucassen et al. (2006)
MCP-5	Shallow section of the Coastal Bath.	-	160	2.53	13.2	0.116	-	0.512855	6.0E-6	-	0.51273	5.9	-	Lucassen et al. (2006)
PC97001	Copiapó Plutonic Comp.	Dio.	115	7.5	34.2	0.22	-	0.51287	1.0E-5	5.5	0.51277	-	-	Marschik et al. (2003b)
PC1498	Copiapó Plutonic Comp.	Dio.	115	6.3	27.7	0.23	-	0.512865	1.2E-5	5.3	0.51276	-	-	Marschik et al. (2003b)
PC97010	Copiapó Plutonic Comp.	Dio.	115	6.4	29.7	0.22	-	0.512843	9.0E-6	5	0.51275	-	-	Marschik et al. (2003b)
PC97006	Copiapó Plutonic Comp.	Dio.	115	8.1	36	0.23	-	0.512869	9.0E-6	5.4	0.51277	-	-	Marschik et al. (2003b)
PC97008	Copiapó Plutonic Comp.	Dio.	115	4.4	17	0.26	-	0.512881	1.2E-5	5.3	0.51276	-	-	Marschik et al. (2003b)
PC97009	Copiapó Plutonic Comp.	Ton.	110	3.4	13.6	0.25	-	0.512841	9.0E-6	4.6	0.51273	-	-	Marschik et al. (2003b)
PC97002	Copiapó Plutonic Comp.	Mzd.	111.5	7.1	32.6	0.22	-	0.512877	8.0E-6	5.6	0.51278	-	-	Marschik et al. (2003b)
PC97003	Copiapó Plutonic Comp.	Mzd.	111.5	6.8	31.1	0.22	-	0.512852	1.0E-5	5.1	0.51276	-	-	Marschik et al. (2003b)
PC97004	Copiapó Plutonic Comp.	Qtz. Mnz. Php.	115	6.1	31	0.2	-	-	-	-	-	-	-	Marschik et al. (2003b)
HC211	Guanta Plutonic Comp.	-	303	-	-	-	-	0.512276	9.0E-4	-	-	-3.7	-	Mpodozis & Kay (1992)
EV-GU	Guanta Plutonic Comp.	-	303	-	-	-	-	0.51233	7.0E-4	-	-	-2.9	-	Mpodozis & Kay (1992)

ESM – Table 9. (continued)

Sample	Unit	Petrography	Age (Ma)	Sm (ppm)	Nd (ppm)	$^{147}Sm/^{144}Nd$	± σ	$^{143}Nd/^{144}Nd$	± σ	εNd	I_{Nd}	$εNd_i$	T_{DM} (Ga)	Reference
GIS155	Los Carricitos Plutonic Comp.	Ton.	221	-	-	-	-	0.51223	6.0E-4	-7.9	0.51201	-6.6	-	Murillo et al. (2017)
GUF-04	Los Carricitos Plutonic Comp.	Grd.	221	-	-	-	-	0.51245	4.2E-4	-3.7	0.51222	-2.7	-	Murillo et al. (2017)
GUR-139	Piuquenes Monzogranites	Grt.	239.5	-	-	-	-	0.51231	2.9E-4	-6.4	0.51208	-4.8	-	Murillo et al. (2017)
GUR-164	Los Carricitos Plutonic Comp.	Grd.	221	-	-	-	-	0.51243	3.8E-5	-4.1	0.51226	-2.0	-	Murillo et al. (2017)
GUR-166	Los Carricitos Plutonic Comp.	Grt.	221	-	-	-	-	0.51235	1.7E-4	-5.6	0.51218	-3.5	-	Murillo et al. (2017)
GUR-170	Los Carricitos Plutonic Comp.	Ton.	221	-	-	-	-	0.51233	1.5E-4	-6.0	0.51215	-4.0	-	Murillo et al. (2017)
GUR-190	Los Carricitos Plutonic Comp.	Grt.	221	-	-	-	-	0.51250	5.3E-4	-2.7	0.51235	-0.2	-	Murillo et al. (2017)
CPV-1292	Algodones Granite	Qtz. Dio.	203	-	-	0.136	-	0.51276	-	2.3	0.5126	3.85	-	Oliveros et al. (2020)
CPV-1291A	Carrizal Bajo Comp.	Dio.	208	-	-	0.157	-	0.51222	-	-8.2	0.51201	−7.14	-	Oliveros et al. (2020)
CPV-1291B	Carrizal Bajo Comp.	Ton.	208	-	-	0.108	-	0.51249	-	-3.0	0.51234	−0.63	-	Oliveros et al. (2020)
CPV-1293	Carrizal Bajo Comp.	Grt.	206.2	-	-	0.148	-	0.51269	-	1.0	0.51249	2.28	-	Oliveros et al. (2020)
CPV-14 180A	Cifuncho Plutonic Comp.	Mgr.	284.8	-	-	0.134	-	0.51230	-	-6.7	0.51205	−4.39	-	Oliveros et al. (2020)
CPV-14-191	Cifuncho Plutonic Comp.	Mgr.	265	-	-	0.131	-	0.51229	-	-6.8	0.51207	−4.62	-	Oliveros et al. (2020)
RCM-61q	Colorado Syenogranite	Sgr.	229.6	-	-	0.131	-	0.51251	-	-2.4	0.51232	−0.51	-	Oliveros et al. (2020)
MCM-010q	El León Monzogranites	Mgr.	252.3	-	-	0.117	-	0.51231	-	-6.4	0.51212	−3.78	-	Oliveros et al. (2020)
O7–13	Guanta Plutonic Comp.	Grd.	290	-	-	0.104	-	0.51230	-	-6.7	0.5121	−3.25	-	Oliveros et al. (2020)
O7–15	Guanta Plutonic Comp.	Ton.	296	-	-	0.130	-	0.51231	-	-6.4	0.51206	−3.88	-	Oliveros et al. (2020)
MCM-205q	Guanta Plutonic Comp.	Grd.	291.3	-	-	0.127	-	0.51236	-	-5.4	0.51212	−2.76	-	Oliveros et al. (2020)
MCM-280q	Guanta Plutonic Comp.	Grd.	300.9	-	-	0.131	-	0.51236	-	-5.3	0.51211	−2.83	-	Oliveros et al. (2020)
RCM-015q	Guanta Plutonic Comp.	Sgr.	293.8	-	-	0.166	-	0.51234	-	-5.8	0.51203	−4.59	-	Oliveros et al. (2020)
CPV-12-01	La Vaca Granodiorite	Dia.	180	-	-	0.173803	-	0.512955	-	6.18	0.51275	6.71	-	Oliveros et al. (2020)
CPV-12-03	La Vaca Granodiorite	Grd.	198	-	-	0.124258	-	0.512672	-	0.66	0.51251	2.5	-	Oliveros et al. (2020)
CPV-14-181B	S. Esmeralda Plutonic Comp.	Mzd.	193.5	-	-	0.164938	-	0.512775	-	2.66	0.51257	3.45	-	Oliveros et al. (2020)
CPV-14-182B	S. Esmeralda Plutonic Comp.	Ton.	193.5	-	-	0.135504	-	0.512717	-	1.54	0.51255	3.05	-	Oliveros et al. (2020)
CHY-06	Elqui Comp. - Guanta Unite	Grd.	307	14.42	93	0.093761	-	0.512255	-	-7.5	-	-3.4	-	Parada (2013)
CBR-5	Limarí Comp.	Grt.	203	5.4	22.5	-	-	0.51254	-	-0.6	0.51235	-	1.14	Parada et al. (1999)
TEN-32	Limarí Comp.	Grt.	203	3.8	14.5	-	-	0.51255	-	-0.7	0.51234	-	1.35	Parada et al. (1999)
CBR-1A	Papudo-Quintero Comp.	Ton.	170	7.4	32.5	-	-	0.51268	-	2.2	0.51253	-	0.78	Parada et al. (1999)
CBV-69	Papudo-Quintero Comp.	Grt	164	1.6	11	-	-	0.51257	-	0.9	0.51248	-	0.62	Parada et al. (1999)
CBV-75	Papudo-Quintero Comp.	Grd.	164	4.8	21	-	-	0.51277	-	3.7	0.51262	-	0.63	Parada et al. (1999)
CBV-67	Papudo-Quintero Comp.	Ton.	164	6.7	27	-	-	0.51274	-	3	0.51258	-	0.79	Parada et al. (1999)
F2-9	Papudo-Quintero Comp.	Ton.	164	5	22.1	-	-	0.51270	-	2.4	0.51255	-	0.75	Parada et al. (1999)
CBV-73	Papudo-Quintero Comp.	Dio.	164	5.8	26	-	-	0.51274	-	3.3	0.51260	-	0.66	Parada et al. (1999)
060496-1	Illapel Comp.	Trond.	109	5	23	-	-	0.51281	-	4.3	0.51272	-	0.51	Parada et al. (1999)
060496-2	Illapel Comp.	Grd.	94	2.4	14	-	-	0.51281	-	4.5	0.51275	-	0.39	Parada et al. (1999)
060496-3	Illapel Comp.	Trond.	94	5	17	-	-	0.51288	-	5	0.51277	-	0.79	Parada et al. (1999)
060496-4	Illapel Comp.	Ton.	91	6.8	31	-	-	0.51282	-	4.3	0.51274	-	0.5	Parada et al. (1999)
060496-5	Illapel Comp.	Ton.	91	7.5	36	-	-	0.51287	-	5.4	0.51280	-	0.38	Parada et al. (1999)
CA99-1	Caleu Pluton	-	125	8.15	34.14	-	-	0.512893	1.5E-3	-	0.51279	5.7	-	Parada et al. (2002)
970118-3	Caleu Pluton	-	125	6.39	33	-	-	0.512854	1.0E-3	-	0.51276	5.1	-	Parada et al. (2002)

ESM – Table 9. (continued)

Sample	Unit	Petrography	Age (Ma)	Sm (ppm)	Nd (ppm)	$^{147}Sm/^{144}Nd$	± σ	$^{143}Nd/^{144}Nd$	± σ	εNd	I_{Nd}	$εNd_i$	T_{DM} (Ga)	Reference
CA99-6	Caleu Pluton	-	125	5.06	20.93	-	-	0.512905	1.5E-3	-	0.5128	5.9	-	Parada et al. (2002)
970121	Caleu Pluton	-	125	4.42	21	-	-	0.512916	1.4E-3	-	0.51283	6.5	-	Parada et al. (2002)
CA99-7	Caleu Pluton	-	125	7.48	33.71	-	-	0.512906	1.3E-3	-	0.51281	6.1	-	Parada et al. (2002)
970524-3	Caleu Pluton	-	125	4.46	20	-	-	0.512919	1.2E-3	-	0.51281	6.1	-	Parada et al. (2002)
CA99-4	Caleu Pluton	-	125	5.76	22.59	-	-	0.512916	1.4E-3	-	0.51281	5.9	-	Parada et al. (2002)
970616-1	Caleu Pluton	-	125	7.65	34	-	-	0.512913	6.0E-3	-	0.51281	6	-	Parada et al. (2002)
MB1	Coastal Bath.	Rhyol. Intrus.	155	4.236	16.511	0.1551	0.0008	0.51249	6.0E-6	-2	0.51234	-	-	Ramírez et al. (2008)
MB6	Coastal Bath.	-	142	1.211	3.352	0.2184	0.0011	0.51267	8.0E-6	0.1	0.51247	-	-	Ramírez et al. (2008)
MB3	Coastal Bath.	Grd. Php.	142	4.29	24.32	0.1067	0.0005	0.51272	8.0E-6	3.2	0.51263	-	-	Ramírez et al. (2008)
MB4	Coastal Bath.	Grd. Php.	142	4.351	23.199	0.1134	0.0006	0.51274	7.0E-6	3.5	0.51264	-	-	Ramírez et al. (2008)
MB-sp-7	Coastal Bath.	Diorite Php.	142	2	6.56	0.162	-	0.512646	-	0.77	0.5125	-	-	Ramírez et al. (2008)
MB-sp-46	Coastal Bath.	Diorite Php.	142	5.64	24.82	0.1208	-	0.512694	-	2.45	0.51258	-	-	Ramírez et al. (2008)
MB-sp-60	Coastal Bath.	Diorite Php.	142	5.49	23.73	0.123	-	0.512569	-	-0.03	0.51246	-	-	Ramírez et al. (2008)
F-51	Los Pelambres Porphyries	Ton.	9.9	-	-	-	-	0.512619	2.0E-3	-	-	-0.25	-	Reich et al. (2003)
LP-48	Los Pelambres Porphyries	Ton.	9.9	-	-	-	-	0.512635	1.6E-3	-	-	0.06	-	Reich et al. (2003)
LP-75	Los Pelambres Porphyries	Ton.	9.9	-	-	-	-	0.512626	2.0E-3	-	-	-0.11	-	Reich et al. (2003)
G-318	La Gloria Pluton	Grd.	9.8	-	-	-	-	0.512771	2.0E-3	-	-	2.7	-	Reich et al. (2003)
8059	Gatico Pluton	-	158	2.42	9.5	-	-	0.5129	-	-	-	5.93	-	Rogers & Hawkesworth (1989)
8062	Gatico Pluton	-	158	2.86	10.7	-	-	0.51294	-	-	-	6.55	-	Rogers & Hawkesworth (1989)
8073	Gatico Pluton	-	158	4.86	20.4	-	-	0.51292	-	-	-	6.53	-	Rogers & Hawkesworth (1989)
81075	Tocopilla Pluton	-	155	2.65	11.3	-	-	0.51279	-	-	-	3.9	-	Rogers & Hawkesworth (1989)
81076	Tocopilla Pluton	-	155	8.36	39.3	-	-	0.51276	-	-	-	3.71	-	Rogers & Hawkesworth (1989)
81078	Tocopilla Pluton	-	155	5.04	23.2	-	-	0.51283	-	-	-	5.03	-	Rogers & Hawkesworth (1989)
TOC4	Tocopilla Pluton	-	155	5.13	22.3	-	-	0.51285	-	-	-	5.27	-	Rogers & Hawkesworth (1989)
TOC5	Tocopilla Pluton	-	155	4.42	20	-	-	0.51277	-	-	-	3.77	-	Rogers & Hawkesworth (1989)
TOC6	Tocopilla Pluton	-	155	3.37	16.5	-	-	0.5128	-	-	-	4.55	-	Rogers & Hawkesworth (1989)
TOC7	Tocopilla Pluton	-	155	4.45	19.1	-	-	0.51289	-	-	-	5.89	-	Rogers & Hawkesworth (1989)
81094	C° Colpuito Pluton	-	155	4.2	18.4	-	-	0.51277	-	-	-	4.26	-	Rogers & Hawkesworth (1989)
81105	S. de la Cruz Pluton	-	156	3.67	16.7	-	-	0.51282	-	-	-	4.74	-	Rogers & Hawkesworth (1989)
81106	S. de la Cruz Pluton	-	156	3.17	14.7	-	-	0.5128	-	-	-	4.39	-	Rogers & Hawkesworth (1989)
81126	C° de Montecristo Pluton	-	102	5.1	26.3	-	-	0.51268	-	-	-	1.71	-	Rogers & Hawkesworth (1989)
81129	C° de Montecristo Pluton	-	102	5.08	26	-	-	0.5127	-	-	-	1.99	-	Rogers & Hawkesworth (1989)
81139	C° de Montecristo Pluton	-	102	6.19	30.2	-	-	0.51269	-	-	-	1.87	-	Rogers & Hawkesworth (1989)
81038	Cerritos Bayos Pluton	-	100	7.04	33.2	-	-	0.51271	-	-	-	2.26	-	Rogers & Hawkesworth (1989)
81048	Cerritos Bayos Pluton	-	100	4.09	17.6	-	-	0.51273	-	-	-	2.49	-	Rogers & Hawkesworth (1989)
81051	Cerritos Bayos Pluton	-	100	4.62	21.3	-	-	0.51275	-	-	-	2.94	-	Rogers & Hawkesworth (1989)
81089	Pampa Negra Pluton	-	79	6.08	26.2	-	-	0.51267	-	-	-	1.15	-	Rogers & Hawkesworth (1989)
81091	Pampa Negra Pluton	-	79	2.77	11.2	-	-	0.51262	-	-	-	0.15	-	Rogers & Hawkesworth (1989)
S-type granitoids														
H219	Cochiguás Comp.	-	301	-	-	-	-	0.51214	7.0E-4	-	-	-5.3	-	Mpodozis & Kay (1992)

ESM – Table 9. (continued)

Sample	Unit	Petrography	Age (Ma)	Sm (ppm)	Nd (ppm)	$^{147}Sm/^{144}Nd$	± σ	$^{143}Nd/^{144}Nd$	± σ	εNd	I_{Nd}	$εNd_i$	T_{DM} (Ga)	Reference
RCM-077q	Chacaicito Pluton	Sgr.	329	-	-	0.158	-	0.51234	-	-5.91	0.5120	−4.27	-	Oliveros et al. (2020)
MCM-129q	Chanchoquín Comp.	Qtz. Mzd.	297	-	-	0.161	-	0.51212	-	-10.18	0.5118	−8.87	-	Oliveros et al. (2020)
RCM-133q	Chanchoquín Comp.	Grd.	293.2	-	-	0.125	-	0.51234	-	-5.87	0.5121	−3.20	-	Oliveros et al. (2020)
SCL-02q	Chollay Comp.	Mgr.	245.5	-	-	0.117	-	0.51250	-	-2.74	0.5123	−0.25	-	Oliveros et al. (2020)
SCL-09q	Chollay Comp.	Grd.	245.5	-	-	0.115	-	0.51243	-	-4	0.5122	−1.44	-	Oliveros et al. (2020)
MCM-022q	Chollay Comp.	Sgr.	248.2	-	-	0.114	-	0.51235	-	-5.72	0.5122	−3.09	-	Oliveros et al. (2020)
MCM-265q	Chollay Comp.	Mgr.	239.7	-	-	0.113	-	0.51242	-	-4.35	0.5122	−1.80	-	Oliveros et al. (2020)
RCM-040q	Chollay Comp.	Ton.	234.9	-	-	0.209	-	0.51240	-	-4.72	0.5121	−5.10	-	Oliveros et al. (2020)
CPV-14-192	Pan de Azúcar Pluton	Grt.	276.6	-	-	0.164	-	0.51235	-	-5.54	0.5121	−4.42	-	Oliveros et al. (2020)
CPV-15-320	S. de Doña Inés Chica Comp.	Qtz. Mzd.	285.3	-	-	0.126	-	0.51230	-	-6.52	0.5121	−3.94	-	Oliveros et al. (2020)
O7–06	Montegrande Granite	Grt.	214.7	-	-	0.082	-	0.51220	-	-8.56	0.5121	−5.42	-	Oliveros et al. (2020)
O7–07	Montegrande Granite	Grt.	214.7	-	-	0.096	-	0.51251	-	-2.59	0.5124	0.16	-	Oliveros et al. (2020)
CHY-07	Elqui Comp. - Cochiguaz Unite	Mgr.	286	2.92	16.8	0.105	-	0.51217	-	-9.2	-	-5.9	-	Parada (2013)
CHY-16	La Tabla Fm.	And. Dike	264	5.6	28.4	0.119	-	0.51231	-	-6.4	-	-3.8	-	Parada (2013)
CHY-05	Elqui Comp. - Cochiguaz Unite	Mgr.	315	7.58	43.7	0.105	-	0.51235	-	-5.6	-	-1.9	-	Parada (2013)
F2-24	Santo Domingo Comp.	Grt.	308	6.5	35.7	-	-	0.51225	-	-4.2	0.5120	-	1.18	Parada et al. (1999)
F2-25	Santo Domingo Comp.	Ton.	308	3.5	23.6	-	-	0.51234	-	-1.7	0.5122	-	0.9	Parada et al. (1999)
F2-28	Santo Domingo Comp.	Ton.	308	6.1	29.6	-	-	0.51234	-	-3	0.5121	-	1.21	Parada et al. (1999)
CT-228q	Chollay Comp.	Grd.	249	-	-	-	-	0.51228	-	-	0.5121	-4.56	-	Salazar et al. (2013)
CT-167q	Chollay Comp.	Ton.	237.6	-	-	-	-	0.51242	-	-	0.5122	-2.74	-	Salazar et al. (2013)
CT-193q	Chollay Comp.	Gab. Dio.	242.1	-	-	-	-	0.512333	-	-	0.5121	-4.13	-	Salazar et al. (2013)
Granulites														
CB19 wr	-	Gran.	200	2.63	10.4	0.153	-	0.51291	6.0E-6	5.27	-	6.39	-	Lucassen & Thirlwall (1998)
CB42 wr	-	Gran.	200	2.86	11.8	0.147	-	0.51290	5.0E-6	5.01	-	6.28	-	Lucassen & Thirlwall (1998)
CB46 wr	-	Gran.	200	3.00	11.7	0.155	-	0.51293	5.0E-6	5.77	-	6.83	-	Lucassen & Thirlwall (1998)
CB51 wr	-	Gran.	200	2.43	9.04	0.163	-	0.51293	6.0E-6	5.62	-	6.49	-	Lucassen & Thirlwall (1998)
CB74 wr	-	Gran.	200	0.91	3.87	0.142	-	0.51293	6.0E-6	5.66	-	7.05	-	Lucassen & Thirlwall (1998)
CB76 wr	-	Gran.	200	1.57	5.20	0.182	-	0.51297	6.0E-6	6.44	-	6.81	-	Lucassen & Thirlwall (1998)
KU5 wr	-	Gran.	200	1.09	3.43	0.192	-	0.51298	6.0E-6	6.69	-	6.8	-	Lucassen & Thirlwall (1998)
IOA														
Ca-10	Carmen	Ap.	130.6	586	2645	0.134	6.70E-04	0.51289	8.00E-06	5.9	-	-	-	Palma et al. (2019)
Ca-8	Carmen	Ap.	130.6	392	1942	0.122	6.10E-04	0.51291	9.00E-06	6.5	-	-	-	Palma et al. (2019)

ESM – Table 9. (continued)

Sample	Unit	Petrography	Age (Ma)	Sm (ppm)	Nd (ppm)	$^{147}Sm/^{144}Nd$	± σ	$^{143}Nd/^{144}Nd$	± σ	εNd	I_{Nd}	$εNd_i$	T_{DM} (Ga)	Reference
Ca-2	Carmen	Ap.	130.6	429	2211	0.117	5.87E-04	0.51290	1.10E-05	6.4	-	-	-	Palma et al. (2019)
Ca-1	Carmen	Ap.	130.6	404	2100	0.116	5.82E-04	0.51289	1.00E-06	6.3	-	-	-	Palma et al. (2019)
Fre-20	Fresia	Ap.	130	86	360	0.145	7.24E-04	0.51226	2.56E-03	-0.3	-	-	-	Palma et al. (2019)
Fre-5	Fresia	Ap.	130	200	1019	0.119	5.94E-04	0.51278	2.56E-03	4.1	-	-	-	Palma et al. (2019)
Fre-19	Fresia	Ap.	130	101	400	0.153	7.67E-04	0.51264	E-62563	0.7	-	-	-	Palma et al. (2019)
Ma-3	Mariela	Ap.	130	34	214	0.095	4.75E-04	0.51283	2.56E-03	5.5	-	-	-	Palma et al. (2019)
Ma-11	Mariela	Ap.	130	35	224	0.093	4.67E-04	0.51285	2.56E-03	5.9	-	-	-	Palma et al. (2019)
Ma-11	Mariela	Ap.	130	36	241	0.090	4.50E-04	0.51284	2.56E-03	5.7	-	-	-	Palma et al. (2019)
Ma-0	Mariela	Ap.	130	27	193	0.086	4.28E-04	0.51285	2.56E-03	6	-	-	-	Palma et al. (2019)
ABU-1	Montecristo-Abundancia	Act.	130	4.82	32.25	-	-	0.51291	1.30E-05	-	-	7.1	-	Tornos et al. (2020)
ABU-2	Montecristo-Abundancia	Act.	130	2.32	11.56	-	-	0.51294	1.40E-05	-	-	7.2	-	Tornos et al. (2020)
ABU-7	Montecristo-Filon San Juan	Act.	130	31.12	210.07	-	-	0.51281	1.60E-05	-	-	5.1	-	Tornos et al. (2020)
ABU-8	Montecristo-Filon San Juan	Ap.	130	9.99	39.91	-	-	0.51294	1.00E-06	-	-	6.6	-	Tornos et al. (2020)
JUL-2	Mina Julia	Act.	130	1.81	8.55	-	-	0.51296	1.40E-05	-	-	7.5	-	Tornos et al. (2020)
TOC-1	Tocopilla	Ap.	130	24.11	140.15	-	-	0.51291	1.30E-05	-	-	6.8	-	Tornos et al. (2020)
TOC-5	Tocopilla	Act.	130	1.22	4.8	-	-	0.51295	2.60E-05	-	-	6.8	-	Tornos et al. (2020)
TOC-11	Tocopilla	Ap.	130	7.63	33.44	-	-	0.51292	1.50E-05	-	-	6.6	-	Tornos et al. (2020)
ROM-3	Romeral	Ap.	130	4.2	21.5	-	-	0.51278	3.00E-06	-	-	4.1	-	Tornos et al. (2020)
COL-1-AP	Los Colorados	Ap.	130	83.6	260.7	-	-	0.51290	2.00E-06	-	-	5.1	-	Tornos et al. (2020)
COL-2-AP	Los Colorados	Ap.	130	87.3	475.5	-	-	0.51282	1.50E-05	-	-	5	-	Tornos et al. (2020)
COL-3	Los Colorados	Ap.	130	32.9	145.6	-	-	0.51279	2.00E-06	-	-	3.9	-	Tornos et al. (2020)
COL-7-AP	Los Colorados	Ap.	130	83.6	260.7	-	-	0.51290	1.90E-05	-	-	5.1	-	Tornos et al. (2020)
COL-22	Los Colorados	Act.	130	2.85	10.54	-	-	0.51293	1.70E-05	-	-	6.3	-	Tornos et al. (2020)
COL-23	Los Colorados	Act.	130	0.65	1.37	-	-	0.51293	1.70E-05	-	-	4.3	-	Tornos et al. (2020)
PM-1	Bronce Sur	WR	130	13.5	104.9	-	-	0.51279	2.00E-06	-	-	4.9	-	Tornos et al. (2020)
PM-2	Bronce Sur	WR	130	8.2	45	-	-	0.51285	1.00E-06	-	-	5.7	-	Tornos et al. (2020)
CA-01	Carmen de Fierro	Ap.	130	53.8	248.1	-	-	0.51295	2.60E-05	-	-	7.2	-	Tornos et al. (2020)
CA-01-ANF	Carmen de Fierro	Act.	130	63.8	303.7	-	-	0.51293	1.20E-05	-	-	6.8	-	Tornos et al. (2020)
CA-03	Carmen de Fierro	Act.	130	58.6	255	-	-	0.51295	6.00E-06	-	-	7	-	Tornos et al. (2020)
CA-04	Carmen de Fierro	Ap.	130	417.3	2367	-	-	0.51289	4.00E-06	-	-	6.5	-	Tornos et al. (2020)
CA-05	Carmen de Fierro	Act.	130	2.5	11.2	-	-	0.51281	1.30E-05	-	-	4.4	-	Tornos et al. (2020)
CA-AP	Carmen de Fierro	Ap.	130	492.3	2475.4	-	-	0.51289	3.00E-06	-	-	6.2	-	Tornos et al. (2020)
CA-AP-1-18	Carmen de Fierro	Ap.	130	285.2	1470.6	-	-	0.51291	3.00E-06	-	-	6.7	-	Tornos et al. (2020)
CA-AP-1-2	Carmen de Fierro	Ap.	130	784	3504.7	-	-	0.51291	3.10E-05	-	-	6.3	-	Tornos et al. (2020)
CA-AP-3	Carmen de Fierro	Ap.	130	153.1	505.5	-	-	0.51292	4.00E-06	-	-	5.7	-	Tornos et al. (2020)
CAS-35-anf	Carmen de Fierro	Act.	130	2.8	10.8	-	-	0.51292	1.30E-05	-	-	6.1	-	Tornos et al. (2020)
CNN-3	C° Negro Norte	WR	130	1	3	-	-	0.51308	3.40E-05	-	-	8.6	-	Tornos et al. (2020)
CNN-6	C° Negro Norte	WR	130	0.6	2.2	-	-	0.51303	2.60E-05	-	-	8.2	-	Tornos et al. (2020)
MOL-1	Los Molles	Ap.	130	5.2	11.24	-	-	0.51308	1.30E-05	-	-	7.3	-	Tornos et al. (2020)
MOL-2	Los Molles	Ap.	130	7.81	20.1	-	-	0.51303	1.20E-05	-	-	7	-	Tornos et al. (2020)
MOL-3	Los Molles	Ap.	130	65.56	322	-	-	0.51282	1.30E-05	-	-	4.8	-	Tornos et al. (2020)

ESM – Table 9. (continued)

Sample	Unit	Petrography	Age (Ma)	Sm (ppm)	Nd (ppm)	$^{147}Sm/^{144}Nd$	± σ	$^{143}Nd/^{144}Nd$	± σ	εNd	I_{Nd}	$εNd_i$	T_{DM} (Ga)	Reference
CLF-1	California	Act.	130	41.14	145.54	-	-	0.51289	3.00E-06	-	-	5.3	-	Tornos et al. (2020)
CLF-1-1	California	Act.	130	-	-	-	-	0.51300	1.50E-05	-	-	-	-	Tornos et al. (2020)
CLF-2	California	Act.	130	44.8	202.6	-	-	0.51285	7.20E-05	-	-	5.1	-	Tornos et al. (2020)
PM-3	California	Ap.	130	33	137.2	-	-	0.51288	2.00E-06	-	-	5.5	-	Tornos et al. (2020)
MI-1	Maria Ignacia	Ap.	130	37.3	243.8	-	-	0.51287	1.00E-06	-	-	6.2	-	Tornos et al. (2020)
MI-2	Maria Ignacia	Ap.	130	28.8	182.3	-	-	0.51285	1.00E-06	-	-	5.9	-	Tornos et al. (2020)
PI-4	Maria Ignacia	Ap.	130	1.2	13.6	-	-	0.51278	1.00E-06	-	-	5.2	-	Tornos et al. (2020)

Abbreviations: *Alb – albitophyre; And – andesite; Ap – apatite; Act – actinolite; Bas – basalt; Bath. – batholith; C° – Cerro (Hill); Comp. – complex; Dac – dacite; Dia – diabase; Dio – diorite; Fm. – Formation; Gab – gabbro; Gran – granulite; Grd – granodiorite; Grt – granite; Lat – latite; Maf. Enc. – mafic enclave; Mgr – monzogranite; Mzd – monzodiorite; Php – porphyry; Qtz – quartz; Rhy – rhyolite; Sgr – syenogranite; Trach – trachyandesite; Trond – trondhjemite; WR – whole rock.*

Supplementary 9 - References

Bartsch, V., 2004. Magmengenese der obertriasssischen bis unterkretazischen Vulkanite in der Ku¨ stenkordillere von Nord-Chile zwischen 24° und 27°S. PhD. dissertation. Technical University of Berlin, Germany.

Creixell, C., 2007. Petrogénesis y emplazamiento de enjambre de diques máficos Mesozoicos de Chile Central: Implicancias tectónicas en el desarrollo del arco Jurásico-Cretácico temprano. PhD. thesis. University of Chile, Chile.

del Rey, Á., Deckart, K., Planavsky, N., Arriagada, C., Martínez, F., 2019. Tectonic evolution of the southwestern margin of Pangea and its global implications: Evidence from the mid Permian–Triassic magmatism along the Chilean-Argentine border. Gondwana Res. 76, 303–321. https://doi.org/10.1016/j.gr.2019.05.007

Girardi, J.D., 2014. Comparison of Mesozoic magmatic evolution and iron oxide (-copper-gold) ('IOCG') mineralization, Central Andes and western North America. PhD. thesis dissertation. The University of Arizona, USA.

González, J., Oliveros, V., Creixell, C., Velásquez, R., Vásquez, P., Lucassen, F., 2018. The Triassic magmatism and its relation with the Pre-Andean tectonic evolution: Geochemical and petrographic constrains from the High Andes of north Central Chile (29°30′ - 30°S). J. S. Am. Earth Sci. 87, 95–112. https://doi.org/10.1016/j.jsames.2017.12.009

Hasler, K., 2007. Petrogénesis del magmatismo bimodal y metamorfismo de muy bajo grado del Cretácico inferior de la Cordillera de la Costa, Chile Central. MSc. thesis. University of Chile, Chile.

Lucassen, F., Franz, G., 1994. Arc related Jurassic igneous and meta-igneous rocks in the Coastal Cordillera of northern Chile/Region Antofagasta. Lithos 32, 273–298. https://doi.org/10.1016/0024-4937(94)90044-2.

Lucassen, F., Thirlwall, M.F., 1998. Sm–Nd ages of mafic rocks from the Coastal Cordillera at 24 S, northern Chile. Geol. Rundsch. 86, 767–774. https://doi.org/10.1007/s005310050175

Lucassen, F., Kramer, W., Bartsch, V., Wilke, H.-G., Franz, G., Romer, R.L., Dulski, P., 2006. Nd, Pb, and Sr isotope composition of juvenile magmatism in the Mesozoic large magmatic province of northern Chile (18–27°S): indications for a uniform subarc mantle. Contrib. Mineral. Petrol. 152, 571–589. https://doi.org/10.1007/s00410-006-0119-y

Marschik, R., Fontignie, D., Chiaradia, M., Voldet, P., 2003b. Geochemical and Sr–Nd–Pb–O isotope composition of granitoids of the Early Cretaceous Copiapó plutonic complex (27° 30′ S), Chile. J. S. Am. Earth Sci. 16, 381–398. https://doi.org/10.1016/S0895-9811(03)00104-4

Morata, D., Aguirre, L., 2003. Extensional Lower Cretaceous volcanism in the Coastal Range (29°20′–30°S), Chile: geochemistry and petrogenesis. J. S. Am. Earth Sci. 16, 459–476. https://doi.org/10.1016/j.jsames.2003.06.001

Morata, D., Aguirre, L., Oyarzun, M., Vergara, M., 2000. Crustal contribution in the genesis of the bimodal Triassic volcanism from the Coastal Range, central Chile. Rev. Geol. Chile 27, 83–98. https://doi.org/10.4067/S0716-02082000000100006

Morata, D., Féraud, G., Aguirre, L., Arancibia, G., Belmar, M., Morales, S., Carrillo, J., 2008. Geochronology of the Lower Cretaceous volcanism from the Coastal Range (29° 20'-30° S), Chile. Rev. Geol. Chile. 35, 123–145. http://dx.doi.org/10.5027/andgeoV35n1-a06

Mpodozis, C., Kay, S.M., 1992. Late Paleozoic to Triassic evolution of the Gondwana margin: evidence from Chilean Frontal Cordilleran batholiths (28°S to 31°S). Geol. Soc. Am. Bull. 104, 999–1014. https://doi.org/10.1130/0016-7606(1992)104<0999:LPTTEO>2.3.CO;2

Murillo, I., Velásquez, R., Creixell, C., 2017. Geología de la Áreas Guanta - Los Cuartitos y Paso de Vacas Heladas, Regiones de Atacama y Coquimbo, escala 1:100.000. Servicio Nacional de Geología y Minería, Chile.

Oliveros, V., Vásquez, P., Creixell, C., Lucassen, F., Ducea, M.N., Ciocca, I., González, J., Espinoza, M., Salazar, E., Coloma, F., Kasemann, S.A., 2020. Lithospheric evolution of the Pre-and Early Andean convergent margin, Chile. Gondwana Res. 80, 202–227. https://doi.org/10.1016/j.gr.2019.11.002

Palma, G., Barra, F., Reich, M., Valencia, V., Simon, A.C., Vervoort, J. Leisen, M., Romero, R., 2019. Halogens, trace element concentrations, and Sr-Nd isotopes in apatite from iron oxide-apatite (IOA) deposits in the Chilean iron belt: Evidence for magmatic and hydrothermal stages of mineralization. Geochim. Cosmochim. Acta 246, 515–540. https://doi.org/10.1016/j.gca.2018.12.019

Parada, V.F.N., 2013. Geoquímica de las rocas ígneas del Carbonífero-Triásico de la Alta Cordillera, Región de Atacama, Chile. BSc. thesis. University of Chile, Chile.

Parada, M.A., Nyström, J.O., Levi, B., 1999. Multiple sources for the Coastal batholith of central Chile (31–34°S): Geochemical and Sr-Nd isotopic evidence and tectonic implications: Lithos 46, 505–521. https://doi.org/10.1016/s0024-4937(98)00080-2

Parada, M. A., Larrondo, P., Guiresse, C., Roperch, P., 2002. Magmatic gradients in the Cretaceous Caleu pluton (central Chile): injections of pulses from a stratified magma reservoir. Gondwana Res. 5, 307–324. https://doi.org/10.1016/S1342-937X(05)70725-5

Ramírez, L.E., Parada, M.A., Palacios, C., Wittenbrink, J., 2008. Magmatic evolution of the Mantos Blancos copper deposit, Coastal Range of northern Chile: insight from Sr–Nd isotope, geochemical data and silicate melt inclusions. Resour. Geol. 58, 124–142. https://doi.org/10.1111/j.1751-3928.2008.00049.x

Reich, M., Parada, M.A., Palacios, C., Dietrich, A., Schultz, F., Lehmann, B., 2003. Adakite-like signature of Late Miocene intrusions at the Los Pelambres giant porphyry copper deposit in the Andes of central Chile: metallogenic implications. Miner. Deposita 38, 876–885. https://doi.org/10.1007/s00126-003-0369-9

Rogers, G., Hawkesworth, C.J., 1989. A geochemical traverse across the North Chilean Andes: evidence for crust generation from the mantle wedge. Earth Planet. Sci. Lett. 91, 271–285. https://doi.org/10.1016/0012-821X(89)90003-4

Rossel, P., Oliveros, V., Ducea, M.N., Charrier, R., Scaillet, S., Retamal, L., Figueroa, O., 2013. The Early Andean subduction system as an analog to island arcs: Evidence from cross-arc geochemical variations in northern Chile. Lithos, 179, 211–230. https://doi.org/10.1016/j.lithos.2013.08.014

Salazar, E., Coloma, F., Creixell, C., 2013. Geología del Área El Tránsito-Lagunillas, escala 1:100.000. Servicio Nacional de Geología y Minería-Gobierno Regional de Atacama, Chile.

Tornos, F., Hanchar, J.M., Munizaga, R., Velasco, F., Galindo, C., 2020. The role of the subducting slab and melt crystallization in the formation of magnetite-(apatite) systems, Coastal Cordillera of Chile. Miner. Deposita. https://doi.org/10.1007/s00126-020-00959-9

ESM – Table 16. Compiled radiometric ages for the Central Andes of Chile between 22°S to 33°S and east of 71°W.

Age (Ma)	±σ	Unit	Method	Application	Reference
Neoproterozoic granitoids					
800	-	Caleta Turenne Gneiss	U-Pb	Zr	Godoy et al. (2003)
1000	-	Caleta Turenne Gneiss	U-Pb	Zr	Godoy et al. (2003)
Paleozoic granitoids					
290	4	Antigua Porphyry	U-Pb	Zr	Richards et al. (1999)
286.3	6.2	Burro Muerto Pluton	U-Pb	Zr	Maksaev et al. (2014)
263.5	3.4	Caballo Muerto Pluton	U-Pb	Zr	Maksaev et al. (2014)
291.2	2.7	Chapilca Pluton	U-Pb	Zr	Hervé et al. (2014)
247	3	Cochiguás Unit	U-Pb	Zr	Coloma et al. (2012)
289.7	1.8	Cochiguás Unit	U-Pb	Zr	Hervé et al. (2014)
296.3	2.9	Dacite Porphyry	U-Pb	Zr	Venegas et al. (2013)
264.6	7	Dike in La Tabla Fm.	U-Pb	Zr	Maksaev et al. (2014)
266.1	3.5	Diorite	U-Pb	Zr	Niemeyer (2013)
267.9	3.8	El Hielo Bath.	U-Pb	Zr	Maksaev et al. (2014)
256	2	Feldspar Porphyry	U-Pb	Zr	Niemeyer (2013)
254.2	2.3	Feldspar Porphyry	U-Pb	Zr	Niemeyer (2013)
328.1	2.8	Foliated Granite	U-Pb	Zr	Pineda & Calderón (2008)
288	5	Foliated Tonalite	U-Pb	Zr	Marinovic et al. (1995)
292	5	Foliated Tonalite	U-Pb	Zr	Marinovic et al. (1995)
293.7	2.4	Foliated Tonalite	U-Pb	Zr	Pineda & Calderón (2008)
294	3	Foliated Tonalite	U-Pb	Zr	Marinovic et al. (1995)
252.5	2.8	Granite	U-Pb	Zr	Vergara & Thomas (1984)
255.3	4	Granite	U-Pb	Zr	Salazar et al. (2013)
277	4	Granite	U-Pb	Zr	Marinovic et al. (1995)
279	2.4	Granite	U-Pb	Zr	Marinovic (2007)
268	5	Granodiorite	U-Pb	Zr	Damm et al. (1990)
285.7	0.6	Granodiorite	U-Pb	Zr	Pankhurst et al. (1996)
273	4	Granodiorite at Prospecto Jardín	U-Pb	Zr	Cornejo et al. (2006)
279	2.3	Granodiorite at Prospecto Jardín	U-Pb	Zr	Cornejo et al. (2006)
315.7	4.6	Guachicay Pluton	U-Pb	Zr	Maksaev et al. (2014)
265	5.6	Guanaco Sonso Volc.	U-Pb	Zr	Martin et al. (1999)
288.2	1.5	Guanta Unit	U-Pb	Zr	Hervé et al. (2014)
291.5	3.4	Guanta Unit	U-Pb	Zr	Coloma et al. (2012)
295.4	3.3	Guanta Unit	U-Pb	Zr	Coloma et al. (2012)
296.1	4.8	Guanta Unit	U-Pb	Zr	Coloma et al. (2012)
307.1	4.8	Guanta Unit	U-Pb	Zr	Maksaev et al. (2014)
311.9	6	Guanta Unit	U-Pb	Zr	Maksaev et al. (2014)
266.1	3.5	La Totora Pluton	U-Pb	Zr	Álvarez et al. (2013)
267.3	2.5	Monzodiorite	U-Pb	Zr	Niemeyer (2013)
283.6	2.8	Monzodiorite at Prospecto C° Lija	U-Pb	Zr	Cornejo et al. (2006)
296.8	3.2	Monzodiorite Porphyry	U-Pb	Zr	Hervé et al. (2012)
310.1	4.8	Monzogranite	U-Pb	Zr	Cortés (2000)
323.9	2.6	Monzogranite	U-Pb	Zr	Venegas et al. (2013)
296.4	4.4	Monzogranite Porphyry	U-Pb	Zr	Hervé et al. (2012)
290	2	Monzogranite Porphyry at La Escondida district	U-Pb	Zr	Urzúa (2009)
293	6	Monzogranite Porphyry at La Escondida district	U-Pb	Zr	Urzúa (2009)
197.9	2.5	Pan de Azúcar Pluton	Rb-Sr	WR	Berg & Baumann (1985)
230	8	Pan de Azúcar Pluton	U-Pb	Zr	Godoy & Lara (1998)
269.5	4	Pan de Azúcar Pluton	U-Pb	Zr	Maksaev et al. (2014)
276.6	3.6	Pan de Azúcar Pluton	U-Pb	Zr	Maksaev et al. (2014)
287	4.2	Pedernales Bath.	U-Pb	Zr	Maksaev et al. (2014)
280.6	4.2	Pedernales Bath.	U-Pb	Zr	Maksaev et al. (2014)
264.9	7	Pedernales Bath.	U-Pb	Zr	Maksaev et al. (2014)
256	4	Permian Pluton	U-Pb	Zr	Girardi (2014)
287.6	3.3	Quartz Monzodiorite Porphyrry	U-Pb	Zr	Hervé et al. (2012)
298.9	2.6	Quartz Porphyry at La Escondida district	U-Pb	Zr	Urzúa (2009)
258.9	5	Qda. Pintado Tonalite	U-Pb	Zr	Maksaev et al. (2014)
299.4	2.5	Rhyolite Porphyry	U-Pb	Zr	Venegas et al. (2013)
328.3	3.4	Rhyolite Porphyry	U-Pb	Zr	Venegas et al. (2013)
294.2	2.4	Rhyolite Porphyry at La Escondida district	U-Pb	Zr	Urzúa (2009)
285.3	6.4	S. Castillo Bath.	U-Pb	Zr	Maksaev et al. (2014)
291.8	14.3	Syenogranite	U-Pb	Zr	Berg et al. (1983)
295.6	2.6	Syenogranite	U-Pb	Zr	Venegas et al. (2013)
300.1	3.5	Tonalite	U-Pb	Zr	Hervé et al. (2012)
270.8	4	Tonalite	U-Pb	Zr	Salazar et al. (2013)

ESM – Table 10. (continued)

Age (Ma)	±σ	Unit	Method	Application	Reference
Mesozoic granitoids					
152	4	Agua del Sol Pluton	K-Ar	Bt	Lara & Godoy (1998)
150.6	0.3	Agua del Sol Pluton	U-Pb	Zr	Lara & Godoy (1998)
150.6	0.1	Agua del Sol Pluton	U-Pb	Zr	Lara & Godoy (1998)
121.8	0.1	Alice Granodiorite Porphyry	U-Pb	Zr	Fox (2000)
160	5	Añañucal Quartz-diorite	K-Ar	Ms	Zentilli (1974)
172	6	Añañucal Quartz-diorite	K-Ar	Ser	Farrar et al. (1970)
207	5	Añañucal Quartz-diorite	K-Ar	Bt	Godoy et al. (2003)
98	3	Andesite Porphyry	K-Ar	WR	Arévalo (2005a)
101	3	Andesitic Dike	K-Ar	WR	Lledó (1998)
109.9	4	Andesitic Dike	U-Pb	Zr	Seymour et al. (2020)
119	6.6	Andesitic Dike	U-Pb	Zr	Seymour et al. (2020)
119.7	0.9	Andesitic Dike	U-Pb	Zr	Seymour et al. (2020)
245.4	1.8	Andesitic Dike	U-Pb	Zr	Seymour et al. (2020)
198.9	3.2	Barquito Pluton	Rb-Sr	WR	Berg & Breitkreutz (1983)
204	4	Barquito Pluton	K-Ar	Bt	Godoy & Lara (1998)
199	7	Capitana Pluton	K-Ar	Hb	Godoy & Lara (1998)
202	5	Capitana Pluton	K-Ar	Hb	Godoy & Lara (1998)
215	0.7	Capitana Pluton	U-Pb	Zr	Godoy & Lara (1998)
134	3	Carmen (Cu) mine at C° Moradito Pluton	K-Ar	Ms	Arévalo (1995)
202	2.6	C° Castillo Pluton	Rb-Sr	WR	Berg & Baumann (1985)
188	4	C° Chascon Granodiorite	K-Ar	Bt	Godoy et al. (2003)
195.5	3.2	C° Chascón Granodiorite	U-Pb	Zr	Girardi (2014)
195.6	1	C° Concha Granodiorite	U-Pb	Zr	Seymour et al. (2020)
196.4	2.2	C° Concha Granodiorite	U-Pb	Zr	Seymour et al. (2020)
118.6	2.1	C° del Pingo Comp.	U-Pb	Zr	Seymour et al. (2020)
128.1	0.5	C° del Pingo Comp.	U-Pb	Zr	Seymour et al. (2020)
132.3	1.3	C° del Pingo Comp.	U-Pb	Zr	Seymour et al. (2020)
132.6	0.9	C° del Pingo Comp.	U-Pb	Zr	Seymour et al. (2020)
136.6	2.2	C° Moradito Pluton	U-Pb	Zr	Girardi (2014)
138.9	0.4	C° Moradito Pluton	Ar-Ar	Hb	Dallmeyer et al. (1996)
141	4	C° Moradito Pluton	K-Ar	Bt	Godoy et al. (2003)
146	4	C° Moradito Pluton	K-Ar	Bt	Godoy et al. (2003)
149	0.23	C° Moradito Pluton	U-Pb	Zr	Girardi (2014)
137	2.6	C° Morado Pluton	U-Pb	Zr	Girardi (2014)
137.1	2.3	C° Morado Pluton	U-Pb	Zr	Girardi (2014)
137.5	2.5	C° Morado Pluton	U-Pb	Zr	Girardi (2014)
137.6	0.5	C° Morado Pluton	Ar-Ar	Hb	Dallmeyer et al. (1996)
141	0.16	C° Morado Pluton	U-Pb	Zr	Girardi (2014)
121	4	C° Morado Pluton	K-Ar	WR	Benavides (2000)
124	4	C° Morado Pluton	K-Ar	Bt	Zentilli (1974)
125	3	C° Morado Pluton	K-Ar	Bt	Godoy et al. (2003)
126	4	C° Morado Pluton	K-Ar	Bt	Zentilli (1974)
132	3	C° Morado Pluton	K-Ar	Ms	Benavides (2000)
133	3	C° Morado Pluton	K-Ar	Ms	Benavides (2000)
136	3	C° Morado Pluton	K-Ar	Ser	Benavides (2000)
137	3	C° Morado Pluton	K-Ar	Bt	Arévalo (2005a)
137	3	C° Morado Pluton	K-Ar	Bt	Godoy et al. (2003)
138	3	C° Morado Pluton	K-Ar	Bt	Arévalo (2005a)
138.4	0.9	C° Morado Pluton	Ar-Ar	Hb	Dallmeyer et al. (1996)
139.6	0.6	C° Morado Pluton	Ar-Ar	Hb	Dallmeyer et al. (1996)
140	3	C° Morado Pluton	K-Ar	Ms	Benavides (2000)
129.2	0.5	C° Vetado Granite	Ar-Ar	WR	Dallmeyer et al. (1996)
217	12	C° Vetado Granite	U-Pb	Zr	Berg & Baumann (1985)
236	3	C° Vetado Granite	RbSr	WR	Godoy & Lara (1998)
237	4	C° Vetado Granite	U-Pb	Zr	Maksaev et al. (2014)
246.5	4	C° Vetado Granite	U-Pb	Zr	Maksaev et al. (2014)
140	3	Chañaral Melange	K-Ar	Bt	Godoy et al. (2003)
165	4	Chañaral Melange	K-Ar	Bt	Godoy et al. (2003)
164	5	Chañaral Melange	K-Ar	WR	Benavides (2000)
240.3	1.7	Chollay Unit	U-Pb	Zr	Coloma et al. (2012)
242	1.5	Chollay Unit	U-Pb	Zr	Martin et al. (1999)
242.5	1.5	Chollay Unit	U-Pb	Zr	Martin et al. (1999)
242.6	2.2	Chollay Unit	U-Pb	Zr	Hervé et al. (2014)
244	2.8	Chollay Unit	U-Pb	Zr	Maksaev et al. (2014)
116.3	0.4	Copiapó Bath. - Adamelite	U-Pb	Zr	Marschik & Söllner (2006)
115.2	1.8	Copiapó Bath. - Dacite dikes	U-Pb	Zr	del Real et al. (2018)
112.8	1.3	Copiapó Bath. - Dacite dikes	U-Pb	Zr	del Real et al. (2018)
129.6	1	Copiapó Bath. - La Brea member	U-Pb	Zr	Salazar (2018)
118	1	Copiapó Bath. - La Brea member	U-Pb	Zr	Marschik & Söllner (2006)
110.7	0.4	Copiapó Bath. - Los Lirios member	U-Pb	Zr	Marschik & Söllner (2006)

ESM – Table 10. (continued)

Age (Ma)	±σ	Unit	Method	Application	Reference
115.5	0.4	Copiapó Bath. - San Gregorio member	U-Pb	Zr	Marschik & Söllner (2006)
124.9	0.4	Dacite Dike	U-Pb	Zr	Pop et al. (2000)
121.9	2.4	Dacite Dike	U-Pb	Zr	Pop et al. (2000)
47.3	3.9	Dacite Dike	U-Pb	Zr	del Real et al. (2018)
205.9	0.5	Dacite Porphyry	U-Pb	Zr	Marinovic & García (1999)
206.1	1	Dacite Porphyry	U-Pb	Zr	Marinovic & García (1999)
117.1	0.9	Dacitic Dike	U-Pb	Zr	Seymour et al. (2020)
116.3	2.6	Dike	U-Pb	Zr	Girardi (2014)
116.4	1.9	Dike	U-Pb	Zr	Girardi (2014)
116.5	1.9	Dike	U-Pb	Zr	Girardi (2014)
117.1	1.8	Dike	U-Pb	Zr	Girardi (2014)
116.2	1.9	Diorite	U-Pb	Zr	Girardi (2014)
128.4	2	Diorite Porphyry	U-Pb	Zr	Girardi (2014)
80	3	Dioritic Dike	K-Ar	Amp	Lledó (1998)
67.2	1.1	Dioritic Stock	U-Pb	Zr	Girardi (2014)
67.5	0.5	Dioritic Stock	Ar-Ar	Bt	Arévalo (2005b)
68	2	Dioritic Stock	K-Ar	Bt	Arévalo (2005b)
69.2	1	Dioritic Stock	U-Pb	Zr	Girardi (2014)
83	6	Dioritic Stock	K-Ar	Amp	Arévalo (2005a)
86.5	0.8	Dioritic Stock	Ar-Ar	Amp	Arévalo (2005b)
249.7	3.4	El Colorado Unit	U-Pb	Zr	Martin et al. (1999)
215.8	1.2	El Leon Porphyry	U-Pb	Zr	Hervé et al. (2014)
129	0.9	El Romeral Diorite	U-Pb	Zr	Rojas et al. (2018b)
227	3	Feldspar Porphyry at La Escondida district	U-Pb	Zr	Urzúa (2009)
223	4	Feldspar Porphyry at La Escondida district	U-Pb	Zr	Urzúa (2009)
127.3	2.5	Felsic rock	U-Pb	Zr	Girardi (2014)
130.7	2.2	Felsic rock	U-Pb	Zr	Girardi (2014)
188.7	0.7	Flamenco Pluton	Ar-Ar	Hb	Dallmeyer et al. (1996)
189.9	2.9	Flamenco Pluton	U-Pb	Zr	Godoy & Lara (1998)
190.1	1.9	Flamenco Pluton	U-Pb	Zr	Godoy & Lara (1998)
191.1	0.4	Flamenco Pluton	U-Pb	Zr	Gelcich et al. (2003)
198.2	0.6	Flamenco Pluton	Ar-Ar	Hb	Dallmeyer et al. (1996)
202	4	Flamenco Pluton	U-Pb	Zr	Godoy & Lara (1998)
135.6	1.5	Granite	U-Pb	Zr	Seymour et al. (2020)
96.6	1.9	Granitoid	U-Pb	Zr	Girardi (2014)
135.2	1.3	Granodiorite	U-Pb	Zr	del Real et al. (2018)
153.3	1.3	Granodiorite	U-Pb	Zr	Seymour et al. (2020)
86	5	Hypablisal Dacitic Intrusives	K-Ar	Amp	Arévalo (2005a)
88.5	0.8	Hypablisal Dacitic Intrusives	Ar-Ar	Amp	Arévalo (2005b)
90.4	0.5	Hypablisal Dacitic Intrusives	U-Pb	Zr	Arévalo (2005b)
109	0.8	Illapel Bath.	U-Pb	Zr	del Real & Arriagada (2015)
103.8	1.8	Illapel Bath.	U-Pb	Zr	del Real & Arriagada (2015)
93.3	2.7	Illapel Bath.	U-Pb	Zr	del Real & Arriagada (2015)
89.6	1.1	Illapel Bath.	U-Pb	Zr	del Real & Arriagada (2015)
88.5	1.7	Illapel Bath.	U-Pb	Zr	Lopez et al. (2014)
88.1	1.1	Illapel Bath.	U-Pb	Zr	Lopez et al. (2014)
116.7	1.6	Jesus Maria Pluton	U-Pb	Zr	Girardi (2014)
121.9	2.4	La Batea Dacite	U-Pb	Zr	Pop et al. (2000)
106.3	0.7	La Borracha Pluton	Ar-Ar	Hb	Dallmeyer et al. (1996)
107.1	0.9	La Borracha Pluton	U-Pb	Zr	Seymour et al. (2020)
108	3	La Borracha Pluton	K-Ar	Bt	Arévalo (1995)
111	1.6	La Borracha Pluton	U-Pb	Zr	Girardi (2014)
112	3	La Borracha Pluton	K-Ar	Bt	Arévalo (1995)
112	3	La Borracha Pluton	K-Ar	Bt	Arévalo (1995)
114	3	La Borracha Pluton	K-Ar	Bt	Arévalo (2005a)
100.5	2	La Brea Pluton	U-Pb	Zr	Girardi (2014)
110.2	1.8	La Brea Pluton	U-Pb	Zr	Girardi (2014)
110.4	1.8	La Brea Pluton	U-Pb	Zr	Girardi (2014)
115	4	La Brea Pluton	K-Ar	Amp	Arévalo (2005a)
116.2	1.8	La Brea Pluton	U-Pb	Zr	Girardi (2014)
117	4	La Brea Pluton	K-Ar	Amp	Arévalo (2005a)
117.2	1.7	La Brea Pluton	U-Pb	Zr	Girardi (2014)
117.8	1.4	La Brea Pluton	U-Pb	Zr	Girardi (2014)
118.3	1.7	La Brea Pluton	U-Pb	Zr	Girardi (2014)
119	3	La Brea Pluton	K-Ar	Bt	Arévalo (2005a)
119	3	La Brea Pluton	K-Ar	Bt	Arévalo (2005a)
119	2	La Brea Pluton	K-Ar	Bt	Arévalo (1995)
119.4	1.3	La Brea Pluton	Ar-Ar	Amp	Arévalo (2005a)
119.5	1.3	La Brea Pluton	U-Pb	Zr	Girardi (2014)
120.9	2.2	La Brea Pluton	U-Pb	Zr	Girardi (2014)

ESM – Table 10. (continued)

Age (Ma)	±σ	Unit	Method	Application	Reference
121	3	La Brea Pluton	K-Ar	Bt	Arévalo (2005a)
123	4	La Brea Pluton	K-Ar	Amp	Arévalo (2005a)
229.6	5.2	La Coneja Pluton - Colorado unit	U-Pb	Zr	Maksaev et al. (2014)
241.7	3	La Pampa Pluton	U-Pb	Zr	Álvarez et al. (2013)
247.7	3.4	La Pampa Pluton	U-Pb	Zr	Álvarez et al. (2013)
85	3	Lamprophyres	K-Ar	WR	Lledó (1998)
89	3	Lamprophyres	K-Ar	WR	Lledó (1998)
90	3	Lamprophyres	K-Ar	WR	Lledó (1998)
91	3	Lamprophyres	K-Ar	WR	Lledó (1998)
85.2	4	Lamprophyric dikes	K-Ar	WR	Pop et al. (2000)
63.2	2.5	Lamprophyric dikes	K-Ar	WR	Pop et al. (2000)
126	10	Las Animas Pluton	K-Ar	Hb	Naranjo & Puig (1984)
129	4	Las Animas Pluton	K-Ar	Bt	Ulriksen (1979)
130.1	1.9	Las Animas Pluton	Rb-Sr	WR	Berg & Breitkreutz (1983)
131	4	Las Animas Pluton	K-Ar	Bt	Naranjo & Puig (1984)
148	7	Las Animas Pluton	K-Ar	Bt	Godoy & Lara (1998)
150.4	1.7	Las Animas Pluton	Rb-Sr	WR	Berg & Breitkreutz (1983)
153.4	0.6	Las Animas Pluton	Ar-Ar	WR	Dallmeyer et al. (1996)
157.6	2.6	Las Animas Pluton	Rb-Sr	WR	Berg & Breitkreutz (1983)
159.7	1.6	Las Animas Pluton	K-Ar	Bt	Gelcich (1998)
160	2	Las Animas Pluton	U-Pb	Zr	Berg & Breitkreutz (1983)
160	4	Las Animas Pluton	K-Ar	Bt	Godoy & Lara (1998)
160.6	0.2	Las Animas Pluton	U-Pb	Zr	Girardi (2014)
161	4	Las Animas Pluton	K-Ar	Bt	Godoy & Lara (1998)
161	0.2	Las Animas Pluton	U-Pb	Zr	Girardi (2014)
162	4	Las Animas Pluton	K-Ar	Bt	Godoy & Lara (1998)
164.1	3.8	Las Animas Pluton	Ar-Ar	Amp	Dallmeyer et al. (1996)
219.5	1.7	Las Breas Fm.	U-Pb	Zr	Hervé et al. (2014)
123	4	Las Tazas Pluton	K-Ar	Bt	Godoy & Lara (1998)
129.1	1	Las Tazas Pluton	Rb-Sr	WR	Berg & Breitkreutz (1983)
129.2	1.5	Las Tazas Pluton	Ar-Ar	Amp	Dallmeyer et al. (1996)
130	4	Las Tazas Pluton	K-Ar	Bt	Ulriksen (1979)
130	3	Las Tazas Pluton	K-Ar	Bt	Naranjo & Puig (1984)
130	1	Las Tazas Pluton	Rb-Sr	WR	Berg & Breitkreutz (1983)
130.7	1	Las Tazas Pluton	Rb-Sr	WR	Berg & Breitkreutz (1983)
132.1	1.9	Las Tazas Pluton	U-Pb	Zr	Seymour et al. (2020)
133	2	Las Tazas Pluton	Ar-Ar	Amp	Dallmeyer et al. (1996)
133.3	0.4	Las Tazas Pluton	Ar-Ar	Hb	Wilson et al. (2000)
134	0.19	Las Tazas Pluton	U-Pb	Zr	Girardi (2014)
139	0.17	Las Tazas Pluton	U-Pb	Zr	Girardi (2014)
78	5	Llano Tirado Diorite	K-Ar	Plg	Arévalo (1994)
109.7	1.7	Los Lirios Pluton	Ar-Ar	Amp	Arévalo et al. (2006)
109.9	0.4	Los Lirios Pluton	Ar-Ar	Bt	Arévalo (2005b)
110.8	2.4	Los Lirios Pluton	U-Pb	Zr	Girardi (2014)
111	3	Los Lirios Pluton	K-Ar	Bt	Arévalo (1994)
215.6	1.9	Los Tilos Pluton	U-Pb	Zr	Hervé et al. (2014)
225.9	1.8	Los Tilos Pluton	U-Pb	Zr	Hervé et al. (2014)
221.6	3.4	Los Tilos Seq.	U-Pb	Zr	Maksaev et al. (2014)
224	3.4	Los Tilos Seq.	U-Pb	Zr	Maksaev et al. (2014)
232.1	4.6	Los Tilos Seq.	U-Pb	Zr	Maksaev et al. (2014)
75.2	3.4	Microdiorite Sills	K-Ar	WR	Pop et al. (2000)
180	4	Morro Copiapó Granodiorite	K-Ar	Bt	Godoy et al. (2003)
186	3	Morro Copiapó Granodiorite	K-Ar	Bt	Farrar et al. (1970)
187	3	Morro Copiapó Granodiorite	K-Ar	Bt	Farrar et al. (1970)
188.8	1.2	Morro Copiapó Granodiorite	Ar-Ar	Hb	Dallmeyer et al. (1996)
189.6	0.9	Morro Copiapó Granodiorite	Ar-Ar	Hb	Dallmeyer et al. (1996)
208	2	Morro de Mejillones Pluton	U-Pb	Zr	Casquet et al. (2014)
115.9	1.9	Ojancos Viejos Pluton	U-Pb	Zr	Girardi (2014)
102	4	Pampa Austral Pluton	K-Ar	WR	Godoy & Lara (1998)
248	3	Peine Group	U-Pb	Zr	Breitkreuz & VanSchmus (1996)
110	4	Portezuelo Cucharas Pluton	K-Ar	Bt	Arévalo (2005a)
158	4	Puerto Viejo Monzogranite	K-Ar	Bt	Godoy et al. (2003)
158	4	Puerto Viejo Monzogranite	K-Ar	Ser	Benavides (2000)
161	4	Puerto Viejo Monzogranite	K-Ar	Ms	Benavides (2000)
192	1	Puerto Viejo Monzogranite	Ar-Ar	Hb	Dallmeyer et al. (1996)
192	2.7	Puerto Viejo Monzogranite	U-Pb	Zr	Girardi (2014)
192.3	0.8	Puerto Viejo Monzogranite	Ar-Ar	Hb	Dallmeyer et al. (1996)
193	5	Puerto Viejo Monzogranite	K-Ar	Bt	Godoy et al. (2003)
196.1	3.3	Puerto Viejo Monzogranite	U-Pb	Zr	Girardi (2014)
202	5	Puerto Viejo Monzogranite	K-Ar	Bt	Godoy et al. (2003)

ESM – Table 10. (continued)

Age (Ma)	±σ	Unit	Method	Application	Reference
203	5	Puerto Viejo Monzogranite	K-Ar	Bt	Godoy et al. (2003)
205	5	Puerto Viejo Monzogranite	K-Ar	Bt	Godoy et al. (2003)
102.2	2	Punta de Piedra Bath.	U-Pb	Zr	Rojas et al. (2018b)
99.4	3.9	Quartz-microdiorite at Cobriza mine	K-Ar	WR	Pop et al. (2000)
230	8	Qda. Castillo monzogranite	U-Pb	Zr	Berg & Baumann (1985)
79	3	Qda. Poblete (Fe) mine at C° Morado Pluton	K-Ar	Bt	Benevides (2000)
132	3	Qda. Poblete Comp.	K-Ar	Ms	Godoy et al. (2003)
187.5	1.4	Relincho Pluton	Ar-Ar	Hb	Dallmeyer et al. (1996)
189.6	0.6	Relincho Pluton	Ar-Ar	Hb	Dallmeyer et al. (1996)
190.2	0.6	Relincho Pluton	Ar-Ar	Hb	Dallmeyer et al. (1996)
191.5	0.7	Relincho Pluton	Ar-Ar	Hb	Dallmeyer et al. (1996)
193.5	5.6	Relincho Pluton	K-Ar	Bt	Godoy & Lara (1998)
193.6	0.6	Relincho Pluton	Ar-Ar	Hb	Dallmeyer et al. (1996)
132	3	Relincho-1 (Fe) mine at C° Morado Pluton	K-Ar	Ms	Benavides (2000)
130.3	1.7	Remiendos Tonalite	U-Pb	Zr	Seymour et al. (2020)
126.8	0.5	Remolino Plutonic Comp.	Ar-Ar	Hb	Dallmeyer et al. (1996)
138	3	Rosario-1 (Cu) mine at C° Moradito Pluton	K-Ar	Ms	Benavides (2000)
96.1	0.2	Ruta Cinco Bath.	U-Pb	Zr	Fox (2000)
92	1	Ruta Cinco Bath. - Cachiyuyito Tonalite	U-Pb	Zr	Escolme et al. (2020)
129.8	0.1	Ruta Cinco Bath. - Cachiyuyito Tonalite	U-Pb	Zr	Fox (2000)
111.5	0.4	San Gregorio Pluton	Ar-Ar	Bt	Arévalo et al. (2006)
114.9	1.7	San Gregorio Pluton	U-Pb	Zr	Girardi (2014)
116	3	San Gregorio Pluton	K-Ar	WR	Arévalo (1999)
116.7	1.6	San Gregorio Pluton	U-Pb	Zr	Girardi (2014)
131.4	0.3	S. Aspera Pluton	U-Pb	Zr	Girardi (2014)
131	3	S. Aspera Pluton	K-Ar	Bt	Godoy & Lara (1998)
131	5	S. Aspera Pluton	K-Ar	Bt	Godoy & Lara (1998)
131	5	S. Aspera Pluton	K-Ar	Bt	Godoy & Lara (1998)
130.6	0.3	S. Aspera Pluton	U-Pb	Zr	Gelcich et al. (2005)
128	3	S. Aspera Pluton	Ar-Ar	Bt	Godoy & Lara (1998)
126	2	S. Aspera Pluton	Rb-Sr	WR	Brook et al. (1986)
131.3	0.4	S. Aspera Pluton	U-Pb	Zr	Gelcich et al. (2005)
127.4	0.1	S. Aspera Pluton	U-Pb	Zr	Gelcich et al. (2005)
101.7	1.7	S. Atacama Diorite	U-Pb	Zr	Girardi (2014)
104	0.6	S. Atacama Diorite	Ar-Ar	Bt	Arévalo (2005b)
106.9	1.4	S. Atacama Diorite	Ar-Ar	Amp	Arévalo (2005b)
108	3	S. Atacama Diorite	K-Ar	Bt	Arévalo (2005b)
109	3	S. Atacama Diorite	K-Ar	Bt	Arévalo (1994)
111	3	S. Atacama Diorite	K-Ar	Bt	Arévalo (2005b)
115	3	S. Atacama Diorite	K-Ar	Bt	Godoy et al. (2003)
116.5	1.7	S. Atacama Diorite	U-Pb	Zr	Girardi (2014)
116.8	0.8	S. Atacama Diorite	Ar-Ar	Bt	Blanco et al. (2003)
220	19	S. Miranda Rhyolite	U-Pb	Zr	Basso (2004)
126.8	1	S. Dieciocho Pluton	U-Pb	Zr	Lara & Godoy (1998)
129.6	0.3	S. Dieciocho Pluton	U-Pb	Zr	Girardi (2014)
137	4	S. El Roble Pluton	K-Ar	Ser	Benavides (2000)
155	4	S. El Roble Pluton	K-Ar	Bt	Godoy et al. (2003)
162	4	S. El Roble Pluton	K-Ar	Bt	Godoy et al. (2003)
164.4	3.4	S. El Roble Pluton	U-Pb	Zr	Girardi (2014)
165	4	S. El Roble Pluton	K-Ar	Bt	Godoy et al. (2003)
233	12	S. Miranda Rhyolite	U-Pb	Zr	Basso (2004)
103	3	S. Pajas Blancas Granodiorite	K-Ar	Bt	Arévalo (1995)
105.9	2.6	S. Pajas Blancas Granodiorite	U-Pb	Zr	Girardi (2014)
106	3	S. Pajas Blancas Granodiorite	K-Ar	Bt	Arévalo (2005a)
106.8	2	S. Pajas Blancas Granodiorite	U-Pb	Zr	Girardi (2014)
108	3	S. Pajas Blancas Granodiorite	K-Ar	Bt	Arévalo (2005a)
130	5	S. Pastenes Pluton	K-Ar	Bt	Godoy & Lara (1998)
124.2	5.5	S. Santo Domingo Dioritic Stock	U-Pb	Zr	Girardi (2014)
108.8	2.8	Tonalite	U-Pb	Zr	Seymour et al. (2020)
104.1	2.9	Tonalite	U-Pb	Zr	Seymour et al. (2020)
188.6	0.8	Unnamed Jurassic Tonalite	U-Pb	Zr	Seymour et al. (2020)
137	5	Wanda-Lorena (Au) mine at C° Morado Pluton	K-Ar	Ser	Benavides (2000)
182.7	0.8	Yumbes Tonalite	U-Pb	Zr	Seymour et al. (2020)
118.9	0.9	Zapallo Granodiorite Porphyry	U-Pb	Zr	Fox (2000)
Cenozoic granitoids					
58.9	6.2	Andesitic Dike	K-Ar	Amp	Lledó (1998)
65	7	Andesitic Dike	K-Ar	Amp	Arévalo (2005b)
58.9	2.3	Cabeza de Vaca Pluton	K-Ar	Bt	Arévalo (1994)
63	2	Cabeza de Vaca Pluton	K-Ar	Bt	Rivera & Mpodozis (1994)
65	1.9	Cabeza de Vaca Pluton	U-Pb	Zr	Girardi (2014)

ESM – Table 10. (continued)

Age (Ma)	±σ	Unit	Method	Application	Reference
59.6	2.8	Cachiyuyo Pluton	K-Ar	WR	Arévalo (1995)
54.7	1.5	Lomas Bayas Caldera	K-Ar	Bt	Rivera (1992)
55.4	1.5	Lomas Bayas Caldera	K-Ar	Bt	Rivera (1992)
56.5	1.8	Lomas Bayas Caldera	K-Ar	Bt	Rivera (1992)
56.8	2.1	Lomas Bayas Caldera	K-Ar	Plg	Rivera (1992)
60	2	Lomas Bayas Porphyry	K-Ar	Bt	Rivera (1992)
61.2	2	Lomas Bayas Porphyry	K-Ar	Bt	Rivera (1992)
62	2	Lomas Bayas Caldera	K-Ar	Bt	Rivera (1992)
Paleozoic volcanic rocks					
255.9	6.2	Cas Fm.	U-Pb	Zr	Maksaev et al. (2014)
242.7	5.8	Cas Fm.	U-Pb	Zr	Maksaev et al. (2014)
300.8	4.6	C° Bayo Volcanic Beds	U-Pb	Zr	Salazar et al. (2009)
323.1	5.8	C° Bayo Volcanic Beds	U-Pb	Zr	Maksaev et al. (2014)
324.7	4	C° Bayo Volcanic Beds	U-Pb	Zr	Maksaev et al. (2014)
320	9	C° del Árbol Fm.	U-Pb	Zr	Maksaev et al. (2014)
259	3.4	La Tabla Fm.	U-Pb	Zr	Venegas et al. (2013)
262	2.8	La Tabla Fm.	U-Pb	Zr	Maksaev et al. (2014)
262.9	2	La Tabla Fm.	U-Pb	Zr	Cornejo et al. (2009)
270.4	4.6	La Tabla Fm.	U-Pb	Zr	Maksaev et al. (2014)
272.6	6.8	La Tabla Fm.	U-Pb	Zr	Maksaev et al. (2014)
273.9	6.6	La Tabla Fm.	U-Pb	Zr	Maksaev et al. (2014)
276.6	4	La Tabla Fm.	U-Pb	Zr	Maksaev et al. (2014)
282	2	La Tabla Fm.	U-Pb	Zr	Urzúa (2009)
282	11.4	La Tabla Fm.	U-Pb	Zr	Maksaev et al. (2014)
284	4	La Tabla Fm.	U-Pb	Zr	Urzúa (2009)
286	2	La Tabla Fm.	U-Pb	Zr	Urzúa (2009)
287	3	La Tabla Fm.	U-Pb	Zr	Urzúa (2009)
287.1	4.4	La Tabla Fm.	U-Pb	Zr	Jara et al. (2009)
288	2.4	La Tabla Fm.	U-Pb	Zr	Hervé et al. (2012)
288.8	2.4	La Tabla Fm.	U-Pb	Zr	Hervé et al. (2012)
293	4	La Tabla Fm.	U-Pb	Zr	Urzúa (2009)
294.4	4.6	La Tabla Fm.	U-Pb	Zr	Jara et al. (2009)
294.6	2.1	La Tabla Fm.	U-Pb	Zr	Venegas et al. (2013)
296.8	0.2	La Tabla Fm.	U-Pb	Zr	Cornejo et al. (2006)
298.2	5.5	La Tabla Fm.	U-Pb	Zr	Jara et al. (2009)
309.9	2.2	La Tabla Fm.	U-Pb	Zr	Venegas et al. (2013)
292.2	4.2	Paipote Valley Volc.	U-Pb	Zr	Maksaev et al. (2014)
296.6	4.2	Paipote Valley Volc.	U-Pb	Zr	Maksaev et al. (2014)
266.1	4.4	Pantanoso Fm.	U-Pb	Zr	Maksaev et al. (2014)
269.9	4	Pantanoso Fm.	U-Pb	Zr	Maksaev et al. (2014)
270.3	4.2	Pantanoso Fm.	U-Pb	Zr	Maksaev et al. (2014)
292	5	S. del Jardin Rhyolites	U-Pb	Zr	Marinovic (2007)
292	5	S. del Jardin Rhyolites	U-Pb	Zr	Marinovic (2007)
Mesozoic volcanic rocks					
128	0.9	Bandurrias Fm.	U-Pb	Zr	Escolme et al. (2020)
128.7	1.3	Bandurrias Fm.	U-Pb	Zr	Escolme et al. (2020)
126.1	0.1	Cerrillos Fm.	U-Pb	Zr	Creixell et al. (2020)
110.7	1.7	Cerrillos Fm.	U-Pb	Zr	Maksaev et al. (2009)
99.7	1.6	Cerrillos Fm.	U-Pb	Zr	Maksaev et al. (2009)
110.7	1.7	Cerrillos Fm.	U-Pb	Zr	Maksaev et al. (2009)
102.2	2	Cerrillos Fm.	U-Pb	Zr	Maksaev et al. (2009)
99.7	1.6	Cerrillos Fm.	U-Pb	Zr	Maksaev et al. (2009)
69.5	1	Cerrillos Fm.	U-Pb	Zr	Maksaev et al. (2009)
65.2	1.2	Cerrillos Fm.	U-Pb	Zr	Maksaev et al. (2009)
65.2	1	Cerrillos Fm.	U-Pb	Zr	Maksaev et al. (2009)
194	9.2	C° La Ballena Fm.	U-Pb	Zr	Marinovic (2007)
238.7	0.4	El Bordo Volcanic Beds	U-Pb	Zr	Basso & Marinovic (2003)
240.8	0.3	El Bordo Volcanic Beds	U-Pb	Zr	Basso & Marinovic (2003)
291.5	4	El Mono Volcanic Beds	U-Pb	Zr	Maksaev et al. (2014)
127.9	1.8	Falla Poblete Volcanics	U-Pb	Zr	Girardi (2014)
128	4	Falla Poblete Volcanics	K-Ar	Bt	Arévalo (2005a)
65	3	Hornitos Fm.	K-Ar	Plg	Arévalo (1994)
65.2	1	Hornitos Fm.	U-Pb	Zr	Maksaev et al. (2009)
65.6	0.2	Hornitos Fm.	U-Pb	Zr	Arévalo (2005b)
66	1.3	Hornitos Fm.	U-Pb	Zr	Maksaev et al. (2009)
66.1	0.5	Hornitos Fm.	U-Pb	Zr	Arévalo (2005b)
66.9	1	Hornitos Fm.	U-Pb	Zr	Maksaev et al. (2009)
156.3	1.4	La Negra Fm.	Ar-Ar	Plg	Oliveros et al. (2008)
193.6	0.6	La Negra Fm.	U-Pb	Zr	Girardi (2014)

ESM – Table 10. (continued)

Age (Ma)	±σ	Unit	Method	Application	Reference
167.1	1.8	La Negra Fm.	U-Pb	Zr	Rossel et al. (2013)
210.4	2.9	La Totora Fm.	U-Pb	Zr	Salazar et al. (2013)
216.2	1.6	La Totora Fm.	U-Pb	Zr	Salazar et al. (2013)
217.9	1.4	La Totora Fm.	U-Pb	Zr	Salazar et al. (2012)
221	2.6	La Totora Fm.	U-Pb	Zr	Maksaev et al. (2014)
249.7	3.8	La Totora Fm.	U-Pb	Zr	Maksaev et al. (2014)
154.3	3.8	Lagunillas Fm.	U-Pb	Zr	Maksaev et al. (2014)
148.9	2.1	Lagunillas Fm.	U-Pb	Zr	Rossel et al. (2013)
124.9	0.4	Nantoco Fm.	U-Pb	Zr	Girardi (2014)
119.1	2	Nantoco Fm.	U-Pb	Zr	Girardi (2014)
118.6	1	Pabellon Fm.	U-Pb	Zr	Creixell et al. (2020)
151.4	2.7	Picudo Fm.	U-Pb	Zr	Rossel et al. (2013)
121	1.9	Punta del Cobre Fm.	U-Pb	Zr	Girardi (2014)
121.8	2.6	Punta del Cobre Fm.	U-Pb	Zr	Girardi (2014)
122.4	1.7	Punta del Cobre Fm.	U-Pb	Zr	Girardi (2014)
131.3	1.4	Punta del Cobre Fm.	U-Pb	Zr	Pop et al. (2000)
136	1.9	Punta del Cobre Fm.	U-Pb	Zr	Girardi (2014)
136.8	3.7	Punta del Cobre Fm.	U-Pb	Zr	Girardi (2014)
137.1	2.9	Punta del Cobre Fm.	U-Pb	Zr	Girardi (2014)
137.3	2.6	Punta del Cobre Fm.	U-Pb	Zr	Girardi (2014)
132	1.3	Punta del Cobre Fm. - Dacite member	U-Pb	Zr	del Real et al. (2018)
136	-	Punta del Cobre Fm. - Dacite member	U-Pb	Zr	Pop et al. (2000)
135.3	1	Punta del Cobre Fm. - Lower Andesite member	U-Pb	Zr	del Real et al. (2018)
131.3	1.4	Punta del Cobre Fm. - Lower Andesite member	U-Pb	Zr	Pop et al. (2000)
132.4	2.9	Punta del Cobre Fm. - Upper Andesite member	U-Pb	Zr	del Real et al. (2018)
212.8	2	Qda. del Salitre Fm.	U-Pb	Zr	Venegas et al. (2013)
214.2	2	Qda. del Salitre Fm.	U-Pb	Zr	Venegas et al. (2013)
232.9	0.2	Qda. del Salitre Fm.	U-Pb	Zr	Cornejo et al. (2009)
222.8	2.1	San Felix Fm.	U-Pb	Zr	Padel et al. (2012)
212.4	2.6	San Felix Fm.	U-Pb	Zr	Salazar et al. (2013)
128.5	2.5	S. Chichara Quartz-diorite	U-Pb	Zr	Girardi (2014)
130.1	2.7	S. Chichara Quartz-diorite	U-Pb	Zr	Girardi (2014)
116.7	2	S. Chichara Quartz-diorite	Ar-Ar	Amp	Arévalo (2005a)
119	3	S. Chichara Quartz-diorite	K-Ar	Bt	Godoy et al. (2003)
122	3	S. Chichara Quartz-diorite	K-Ar	Bt	Arévalo (1995)
125	3	S. Chichara Quartz-diorite	K-Ar	Bt	Arévalo (2005a)
125	3	S. Chichara Quartz-diorite	K-Ar	Bt	Godoy et al. (2003)
126	4	S. Chichara Quartz-diorite	K-Ar	Bt	Arévalo (2005a)
128	3	S. Chichara Quartz-diorite	K-Ar	Bt	Arévalo (2005a)
128.9	1	S. Chichara Quartz-diorite	Ar-Ar	Amp	Arévalo (2005a)
Mafic-ultramafic magmatism					
181.5	2.7	Caldera Gabbro	U-Pb	Zr	Girardi (2014)
192	3	Caldera Gabbro	K-Ar	Bt	Farrar et al. (1970)
134.5	2	Gabbro	U-Pb	Zr	Girardi (2014)
255.2	1.8	La Laguna Gabbro	U-Pb	Zr	Hervé et al. (2014)
25.2	4.8	Mafic Dike	U-Pb	Zr	Girardi (2014)
125.1	7.7	Microgabbro at Santos Deposit	K-Ar	WR	Pop et al. (2000)
IOA deposits					
123	-	Fe-P deposits from IV Region	-	-	Jorquera et al. (2011)
129	-	Fe-P deposits from IV Region	-	-	Jorquera et al. (2011)
126	-	Fe-P deposits from IV Region	-	-	Jorquera et al. (2011)
99.3	1.3	San Vicente Viñitas	Ar-Ar	Act	Diaz et al. (2003)
98.3	1.8	Fel	Ar-Ar	Act	Diaz et al. (2003)
99	4	Al sur Bella Ester	Ar-Ar	Act	Diaz et al. (2003)
102.7	1.4	San Vicente Viñitas	Ar-Ar	Act	Diaz et al. (2003)
103	6	Bella Ester	Ar-Ar	Act	Diaz et al. (2003)
108	3	Al sur vetas C° Bodega	Ar-Ar	Act	Diaz et al. (2003)
112	3	Teresita	Ar-Ar	Act	Diaz et al. (2003)
121.3	2	Al Norte C° Negro Norte	Ar-Ar	Act	Diaz et al. (2003)
125.3	2	C° Iman	Ar-Ar	Act	Diaz et al. (2003)
120	8	Olvido	Ar-Ar	Act	Diaz et al. (2003)
128	2	s/n	Ar-Ar	Act	Diaz et al. (2003)
127	1.6	Apache	Ar-Ar	Act	Diaz et al. (2003)
127	1.6	Compadre Sur	Ar-Ar	Act	Diaz et al. (2003)
129	3	s/n	Ar-Ar	Act	Diaz et al. (2003)
120	7	Jerusalem	Ar-Ar	Act	Gelcich et al. (2005)
118.3	0.2	El Romeral	Ar-Ar	Bt	Rojas et al. (2018b)
128	-	El Romeral	Ar-Ar	Act	Rojas et al. (2018b)
125.3	2	Fortuna	Ar-Ar	Act	Díaz et al. (2003)

ESM – Table 10. (continued)

Age (Ma)	±σ	Unit	Method	Application	Reference
115.6	5.8	El Algarrobo	K-Ar	WR	Montecinos (1985)
110	3	El Romeral	K-Ar	Bt	Munizaga et al. (1985)
111	-	Los Colorados	K-Ar	Bt	Pichon (1981)
128	4	Boqueron Chañar	K-Ar	Bt	Zentilli (1974)
102	3	C° Iman	K-Ar	WR	Zentilli (1974)
116	6.2	Los Colorados	Re-Os	Mag	Barra et al. (2017)
118.5	4.9	El Romeral	Re-Os	Py	Barra et al. (2017)
129.8	3	Carmen	U-Pb	Zr	Gelcich et al. (2003)
131	1	Carmen	U-Pb	Ap	Gelcich et al. (2005)
116	-	C° Negro Norte	U-Pb	Ti	Raab (2002)
130.05	0.72	C° Negro Norte	U-Pb	Zr	Salazar (2018)
IOCG deposits					
112.6	1.3	Al suroeste de Amapola 1/5	Ar-Ar	Act	Diaz et al. (2003)
124.1	0.6	Alice	Re-Os	Mo	Escolme et al. (2020)
139	8.3	Atakama Kozan	Re-Os	Cpy	Ogata et al. (2019)
103.8	20.9	Barreal Seco	Re-Os	Cpy	Barra et al. (2017)
130	4	Buenaventura	K-Ar	Ser	Diaz et al. (2003)
111	1.4	Candelaria	Ar-Ar	Bt	Arévalo et al. (2006)
110.7	1.6	Candelaria	Ar-Ar	Bt	Arévalo et al. (2006)
109.1	4.6	Candelaria	Re-Os	Cpy	Barra et al. (2017)
124.2	1.6	Candelaria	Re-Os	Cpy	Barra et al. (2017)
116.51	0.26	Candelaria	Ar-Ar	Bt	Marschik & Fontboté (2001a)
115.14	0.18	Candelaria	Ar-Ar	Bt	Marschik & Fontboté (2001a)
118.4	1.5	Candelaria	Ar-Ar	Bt	Marschik & Fontboté (2001a)
116.6	1.2	Candelaria	Ar-Ar	Amp	Marschik & Fontboté (2001a)
116.6	1.2	Candelaria	Ar-Ar	Amp	Marschik & Fontboté (2001a)
115.2	0.6	Candelaria	Re-Os	Mo	Mathur et al. (2002)
114.2	0.6	Candelaria	Re-Os	Mo	Mathur et al. (2002)
110	9	Candelaria	Re-Os	Mag	Mathur et al. (2002)
110	9	Candelaria	Re-Os	Cpy	Mathur et al. (2002)
114.1	0.8	Candelaria	Ar-Ar	Bt	Ullrich & Clark (1999)
111.7	0.8	Candelaria	Ar-Ar	Amp	Ullrich & Clark (1999)
118	-	Casualidad	Ar-Ar	Act	Kovacic (2014)
100	-	Casualidad	U-Pb	Zr	Kovacic (2014)
100	-	Casualidad	Ar-Ar	Bt	Kovacic (2014)
94	-	Casualidad	Ar-Ar	Bt	Kovacic (2014)
94	-	Casualidad	Ar-Ar	Act	Kovacic (2014)
84	-	Casualidad	Ar-Ar	Act	Kovacic (2014)
99.8	0.6	Casualidad	Ar-Ar	Bt	Kovacic et al. (2012)
134	0.76	Chañarcillo Group	U-Pb	Zr	Ogata et al. (2019)
133	0.87	Chañarcillo Group	U-Pb	Zr	Ogata et al. (2019)
134.8	0.93	Chañarcillo Group	U-Pb	Zr	Ogata et al. (2019)
168.1	9.6	Diego de Almagro	Re-Os	Py	Barra et al. (2017)
127	0.6	Dominga	Re-Os	Mo	Veloso et al. (2017)
127	15	Dominga	U-Pb	Ap	Veloso et al. (2017)
88.4	1.2	El Espino	Ar-Ar	Act	Lopez et al. (2014)
109.1	1.5	En Torno de Bella Ester	Ar-Ar	Act	Diaz et al. (2003)
109	5	Fresia y Pique Pardo	Ar-Ar	Act	Diaz et al. (2003)
167	7	Guanillos	K-Ar	Act	Boric et al. (1990)
110	2	Josefina-Triunfo-Laura	Ar-Ar	Act	Diaz et al. (2003)
164	11	Julia	K-Ar	Act	Boric et al. (1990)
162	4	Las Animas	N/A	-	Gelcich et al. (1998)
111.8	2	Lautaro 2	Ar-Ar	Act	Diaz et al. (2003)
112.6	1.3	Mag-act vein from Punta del Cobre Fm.	Ar-Ar	Act	Díaz et al. (2003)
108	3	Mag-act-qtz-ap vein from Punta del Cobre Fm.	Ar-Ar	Act	Díaz et al. (2003)
148	2.2	Mantoverde	Re-Os	Py	Barra et al. (2017)
115	1.7	Mantoverde	Re-Os	Py	Barra et al. (2017)
131.9	1.5	Mantoverde	Re-Os	Py+Mag	Barra et al. (2017)
126.4	0.5	Mantoverde	U-Pb	Ti	Gelcich et al. (2003)
128.9	0.6	Mantoverde	U-Pb	Zr	Gelcich et al. (2005)
117	3	Mantoverde	K-Ar	Ser	Vila et al. (1996)
121	3	Mantoverde	K-Ar	Ser	Vila et al. (1996)
119	-	Mantoverde	Ar-Ar	Ser	Vila et al. (1996)
140	-	Minita-Despreciada	Ar-Ar	Act	Boric et al. (1990)
164	11	Montecristo	K-Ar	Act	Boric et al. (1990)
154	-	Naguayán-Desesperado	Ar-Ar	Act	Boric et al. (1990)
115	3	Panulcillo	K-Ar	Phl	Ardila (1993)
104	3	Porvenir	Ar-Ar	Act	Diaz et al. (2003)
130.1	0.6	Productora	Re-Os	Mo	Escolme et al. (2020)
91.4	0.2	Productora	Ar-Ar	Kfd	Fox (2000)

ESM – Table 10. (continued)

Age (Ma)	±σ	Unit	Method	Application	Reference
90.7	0.7	Productora	Ar-Ar	Kfd	Fox (2000)
128.9	0.6	Productora	Re-Os	Mo	Marquardt et al. (2015)
111.6	1.4	Punta del Cobre	Ar-Ar	Bt	Marschik et al. (1997)
109.7	1.6	Punta del Cobre	K-Ar	WR	Marschik et al. (1997)
114.9	1	Punta del Cobre	Ar-Ar	Bt	Marschik et al. (1997)
114.6	1.6	Punta del Cobre	Ar-Ar	Bt	Marschik et al. (1997)
116.8	2.7	Punta del Cobre	Rb-Sr	WR	Marschik et al. (1997)
96.1	1.9	Que Suerte y Via Norte	Ar-Ar	Act	Diaz et al. (2003)
111.6	1.4	Resguardo	Ar-Ar	Bt	Arévalo (1999)
114.9	1	Resguardo	Ar-Ar	Bt	Marschik et al. (1997)
139	5	Santo Domingo	K-Ar	Act	Boric et al. (1990)
129	4	Santo Domingo	K-Ar	Act	Boric et al. (1990)
124	-	Santo Domingo	U-Pb	Ti	Daroch et al. (2015)
114.9	1	Santos	Ar-Ar	Bt	Marschik et al. (1997)
141	21	Sol Naciente	Re-Os	Mag	Ogata et al. (2019)
155	13	Tocopilla	Rb-Sr	WR	Boric et al. (1990)
165	3	Tocopilla	K-Ar	Bt	Ruiz et al. (1965)
117.8	1.9	Todos los Santos	Ar-Ar	Act	Gelcich et al. (2005)
121.9	1.5	Trapiche	Ar-Ar	Act	Creixell et al. (2009)
119.8	1.6	Trapiche	Ar-Ar	Act	Creixell et al. (2009)
110	2.1	Tropezon	U-Pb	Zr	Tornos et al. (2010)
Manto-type Cu deposits					
86.6	4.9	Altamira	Re-Os	Cc	Barra et al. (2017)
99.5	17.6	Altamira	Re-Os	Cc	Barra et al. (2017)
168	5	Buena Esperanza	K-Ar	Plg	Boric et al. (1990)
100	4	Chacana Area	Ar-Ar	Kfd	Aguila et al. (2019)
103.6	0.2	Cobriza	Ar-Ar	Kfd	Aguila et al. (2019)
105.2	0.18	Cobriza	Ar-Ar	Kfd	Aguila et al. (2019)
103	2	El Soldado	K-Ar	Adl	Boric et al. (2002)
124	0.9	Franke	Re-Os	Cc	Barra et al. (2017)
178	2.3	Franke	Re-Os	Cc	Barra et al. (2017)
98.6	0.2	Granada	Ar-Ar	Kfd	Aguila et al. (2019)
102.22	0.18	La Cocinera	Ar-Ar	Kfd	Aguila et al. (2019)
102	5	Lo Aguirre	K-Ar	Ab	Maksaev & Zentilli (2002)
113	3	Lo Aguirre	Rb-Sr	WR	Munizaga et al. (1988)
97.77	0.19	Loma Verde	Ar-Ar	Kfd	Aguila et al. (2019)
141.1	0.5	Mantos Blanco	Ar-Ar	Amp	Oliveros (2005)
142.2	1	Mantos Blanco	Ar-Ar	Amp	Oliveros (2005)
142.7	2.1	Mantos Blanco	Ar-Ar	Hb	Oliveros (2005)
150	-	Mantos Blanco	Rb-Sr	WR	Tassinari et al. (1993)
142	2	Michilla	Ar-Ar	Plg	Boric et al. (1990)
103	5	Quitalcura	Ar-Ar	Kfd	Aguila et al. (2019)
107.69	0.16	Resguardo	Ar-Ar	Kfd	Aguila et al. (2019)
Zn-Pb Skarn deposits					
93.6	0.4	Maria Cristina	Ar-Ar	Amp	Lieben et al. (2000)
90.1	0.4	Maria Cristina	Ar-Ar	Kfd	Lieben et al. (2000)
Cu-Au and Mo occurrences					
153	4	Carrizal Alto	K-Ar	Ser	Diaz (2019)
218	1	Cu-Mo ore at Domeyko Cordillera	Re-Os	Mo	Cornejo et al. (2006)
Cu-Au porphyry deposits					
141.9	1.4	Antucoya	U-Pb	Zr	Maksaev et al. (2006)
132.4	4	Buey Muerto	K-Ar	Bt	Perelló et al. (2003)
111	1.9	Cachiyuyo	U-Pb	Zr	Creixell et al. (2015)
104	3	Carmen de Andacollo	K-Ar	WR	Reyes (1991)
103.9	0.5	Carmen de Andacollo	Re-Os	Mo	Richards et al. (2017)
103.6	0.5	Carmen de Andacollo	Re-Os	Mo	Richards et al. (2017)
129	-	Colliguay	K-Ar	WR	Maksaev et al. (2010)
87	-	Cortadera	U-Pb	Zr	Creixell et al. (2015)
106.1	3.5	Dos Amigos	U-Pb	Zr	Creixell et al. (2015)
104	3.5	Dos Amigos	U-Pb	Zr	Creixell et al. (2015)
106.1	3.5	Dos Amigos	U-Pb	Zr	Maksaev et al. (2010)
92.4	1.1	Elisa	U-Pb	Zr	Creixell et al. (2015)
109	5	Fresia y Pique Pardo Au mines	Ar-Ar	Act	Diaz et al. (2003)
87.4	1.2	Johana	U-Pb	Zr	Creixell et al. (2020)
87.4	1.2	Johana o Cortadera	U-Pb	Zr	Creixell et al. (2015)
112	2.1	La Union	U-Pb	Zr	Creixell et al. (2015)
88.4	1.2	La Verde	U-Pb	Zr	Creixell et al. (2015)

ESM – Table 10. (continued)

Age (Ma)	±σ	Unit	Method	Application	Reference
90.1	0.9	Las Campanas	U-Pb	Zr	Creixell et al. (2015)
110	2	Laura-Triunfo-Josefina Cu mine	Ar-Ar	Act	Diaz et al. (2003)
92	-	Llahuin	Ar-Ar	Bt	Maksaev et al. (2010)
106.6	0.5	Los Negritos	Re-Os	Mo	Montes (2016)
92.4	1.1	Mina Elisa	U-Pb	Zr	Creixell et al. (2020)
116.6	4	Pajonales	U-Pb	Zr	Creixell et al. (2015)
92.5	1.4	Porteña	U-Pb	Zr	Maksaev et al. (2006)
109.7	0.9	Punta Colorada	U-Pb	Zr	Creixell et al. (2015)
99.3	1.3	San Vicente-Viñitas	Ar-Ar	Act	Díaz et al. (2003)
102.7	1.4	San Vicente-Viñitas	Ar-Ar	Act	Díaz et al. (2003)
120	-	Totora	U-Pb	Zr	Creixell et al. (2015)
121	-	Totora	U-Pb	Zr	Creixell et al. (2015)
108.5	3.4	Tricolor	U-Pb	Zr	Creixell et al. (2015)

Abbreviations: *Ab – albite; Act – actinolite; Adl – adularia; Amp – amphibole; Ap – apatite; Bt – biotite; Cc – chalcocite; Cpy – chalcopyrite; Hb – hornblende; Kfd – potassic feldspar; Mag – magnetite; Mo – molybdenite; Ms – muscovite; Phl – phlogopite; Plg – plagioclase; Py – pyrite; Ser – sericite; Ti – titanite; WR – whole rock; Zr – zircon.*

Supplementary 10 – References

Aguila, B.I.A., 2019. Alteración y mineralización distrito minero Quitalcura, Región de Valparaíso, Chile implicancias en la génesis de depósitos estratoligados Cu-(Ag). PhD. dissertation. University of Concepción, Chile.

Álvarez, J., Mpodozis, C., Blanco-Quintero, I., García-Casco, A., Arriagada, C., Morata, D., 2013. U–Pb ages and metamorphic evolution of the La Pampa Gneisses: Implications for the evolution of the Chilenia Terrane and Permo-Triassic tectonics of north Central Chile. J. S. Am. Earth Sci. 47, 100–115. https://doi.org/10.1016/j.jsames.2013.07.001

Ardila, R., 1993. Génesis de los yacimientos de cobre tipo skarn en el distrito minero de San Antonio y el yacimiento Panulcillo, IV Región, Chile. PhD. thesis. University of Chile, Chile.

Arévalo, C., 1994. Mapa Geológico de la Hoja Los Loros, escala 1:100.0000. Servicio Nacional de Geología y Minería, Chile.

Arévalo, C., 1995. Mapa Geológico de la Hoja Copiapó, Región de Atacama, escala 1:100.000. Servicio Nacional de Geología y Minería, Chile.

Arévalo, C., 1999. The Coastal Cordillera/Precordillera boundary in the Tierra Amarilla Area (27°20'-27°40'S/70°05'-70°20'W), Northern Chile, and the Structural Setting of the Candelaria Cu-Au Ore Deposit. PhD. thesis. Kingston University, England.

Arévalo, C., 2005a. Carta Copiapó, Región de Atacama, escala 1: 100.000. Servicio Nacional de Geología y Minería, Chile.

Arévalo, C., 2005b. Carta Los Loros, Región de Atacama, escala 1:100.000. Servicio Nacional de Geología y Minería, Chile.

Arévalo, C., Grocott, J., Martin, W., Pringle, M., Taylor, G., 2006. Structural Setting of the Candelaria Fe Oxide Cu-Au Deposit, Chilean Andes (27° 30′ S). Econ. Geol. 101, 819–841. https://doi.org/10.2113/gsecongeo.101.4.819

Barra, F., Reich, M., Selby, D., Rojas, P., Simon, A., Salazar, E., Palma, G., 2017. Unraveling the origin of the Andean IOCG clan: A Re-Os isotope approach. Ore Geol. Rev. 81, 62–78. https://doi.org/10.1016/j.oregeorev.2016.10.016

Basso, M., 2004. Carta Baquedano, Región de Antofagasta, escala 1:100.000. Servicio Nacional de Geología y Minería, Chile.

Basso, M., Marinovic, N., 2003. Antecedentes geocronológicos de volcanismo Triásico en la zona de los Estratos El Bordo, Antofagasta, Chile. X Congreso Geológico Chileno, Antofagasta, Chile.

Benavides, J., 2000. Génesis de los depósitos vetiformes metalíferos, Hoja Caldera (27°00'-27°30'), III Región de Atacama, Chile. MSc. thesis. University of Chile, Chile.

Berg, K., Baumann, A., 1985. Plutonic and metasedimentary rocks from the Coastal Range of northern Chile: Rb- Sr and U-Pb systematic. Earth Planet. Sci. Lett. 75, 101–115. https://doi.org/10.1016/0012-821X(85)90093-7

Berg, K., Breitkreuz, C., 1983. Mesozoische Plutone in der nordchilenischen Küstenkordillere; Petrogenese, Geochronologie, Geochemie und Geodynamik mantelbetonter Magmatite. Geotekt. Forsch. 66, 1–107.

Berg, K., Breitkreuz, C., Damm, K.W., Pichowiak, S., Zeil, W., 1983. The North-Chilean Coast Range—an example for the development of an active continental margin. Geologische Rundschau 72, 715–731. https://doi.org/10.1007/BF01822090

Blanco, N., Godoy, E., Marquardt, C., 2003. Cartas Castilla y Totoral Bajo, Región de Atacama, escala 1:100.000. Servicio Nacional de Geología y Minería, Chile.

Boric, R., Díaz, F., Maksaev, V., 1990. Geología y yacimientos metalíferos de la Región de Antofagasta, escala 1:500.000. Servicio Nacional de Geología y Minería, Chile.

Boric, R., Holmgren, C., Wilson, N.S.F., Zentilli, M. 2002. The Geology of El Soldado Manto Type Cu (Ag) Deposit, Central Chile, in: Porter, T.M. (Ed.), Hydrothermal Iron Oxide Copper-Gold & Related Deposits: A Global Perspective, Second Edition. PGC Publishing, Adelaide, pp. 163–184.

Breitkreuz, C., Van Schmus, W.R., 1996. U-Pb geochronology and significance of Late Permian ignimbrites in Northern Chile. J. S. Am. Earth Sci. 9, 281–293. https://doi.org/10.1016/S0895-9811(96)00014-4

Brook, M., Pankhurst, R.J., Shephard, T.J., Spiro, B., 1986. Andchron: Andean geochronology and metalogenesis. Overseas Development Agency Open-File Report, 1–83.

Casquet, C., Hervé, F., Pankhurst, R.J., Baldo, E., Calderón, M., Fanning, C. M., Rapela, C.W., Dahlquist, J. (2014). The Mejillonia suspect terrane (Northern Chile): Late Triassic fast burial and metamorphism of sediments in a magmatic arc environment extending into the Early Jurassic. Gondwana Res. 25, 1272–1286. https://doi.org/10.1016/j.gr.2013.05.016

Coloma, F., Salazar, E., Creixell, C., 2012. Nuevos antecedentes acerca de la construcción de los plutones Pérmicos y Permo-Triásicos en el valle del río Tránsito, Región de Atacama, Chile. XIII Congreso Geológico Chileno, Antofagasta, 330–332.

Cornejo, P., Matthews, S., Marinovic, N., Pérez de Arce, C., Basso, M., Alfaro, J., Navarro, M., 2006. Alteración hidrotermal y mineralización recurrente de Cu y Cu-Mo durante el Pérmico y el Triásico en la Cordillera de Domeyko (Zona de Zaldívar-Salar de los Morros): antecedentes geocronológicos U-Pb, $^{40}Ar/^{39}Ar$ y Re-Os. XI Congreso Geológico Chileno, Antogasta, Chile, 219–222.

Cornejo, P., Mpodozis, C., Rivera, O., Matthews, S.J., 2009. Carta Exploradora, Región de Antofagasta y Atacama, escala 100.000. Servicio Nacional de Geología y Minería, Carta Geológica de Chile, Chile.

Cortés, J. 2000. Hoja Palestina, Región de Antofagasta, escala 1:100.000. Servicio Nacional de Geología y Minería, Chile.

Creixell, C., Arévalo, C., Fanning, M., 2009. Geochronology of the cretaceous magmatism from the Coastal Cordillera of north-central Chile (29º15’ to 29º30’ S): metallogenic implications. XII Congreso Geológico Chileno, Santiago, Chile.

Creixell, C., Fuentes, J., Bierma, H., Salazar, E., 2015. Tectónica regional y metalogénesis asociada al emplazamiento de la franja de pórfidos cupríferos cretácicos del norte de Chile (28°–30° S). XIV Congreso Geológico Chileno, La Serena, Chile.

Creixell, C., Fuentes, J., Bierma, H., Salazar, E., 2020. Tectonic setting of Cretaceous porphyry copper deposits of northern Chile (28°-30° S) and its relations with magmatic evolution and metallogeny. Andean Geol. 47, 469–507. https://doi.org/10.5027/andgeoV47n3-3035

Dallmeyer, R.D., Brown, M., Grocott, J., Taylor, G.K., Treloar, P.J., 1996. Mesozoic magmatic and tectonic events within the Andean Plate boundary zone, 26°-27° 30'S, North Chile: constraints from 40Ar/39Ar mineral ages. J. Geol. 104, 19–40. https://doi.org/10.1086/629799

Damm, W., Pichowiak, S., Harmon, R.S., Todt, W., Kelley, S., Omarini, R., Niemeyer, H., 1990. Pre-Mesozoic evolution of the Central Andes, the basement revisited, in: Kay, M.S., Rapela, C.W. (Eds.), Plutonism from Antarctica to Alaska, Special Papers 241. The Geological Society of America. Boulder, Colorado, pp. 101–126. https://doi.org/10.1130/SPE241-p101

Daroch, G.A., Anguita, N., Cortes, M., 2015. Geología y zonación hidrotermal del depósito Fe (-Cu-Au) Santo Domingo, Región de Atacama, Chile. XIV Congreso Geológico Chileno, La Serena, Chile.

del Real, I., Arriagada, C., 2015. Inversión tectónica positiva en el distrito El Espino: Relaciones entre deformación, magmatismo y mineralización IOCG, Provincia de Choapa, Chile. XIV Congreso Geológico Chileno, La Serena, Chile.

del Real, I., Thompson, J.F., Carriedo, J., 2018. Lithological and structural controls on the genesis of the Candelaria-Punta del Cobre Iron Oxide Copper Gold district, Northern Chile. Ore Geol. Rev. 102, 106–153. https://doi.org/10.1016/j.oregeorev.2018.08.034

Diaz, A. 2019. Deposits of Cobalt and Its Relationship with IOCG and IOA Types of the Metallogenic Province of the Cordillera de la Costa, Northern Chile. SEG 2019 Conference Proceedings, Santiago, Chile.

Diaz, A., Vivallo, W., Jorquera, R., Pizarro, N., 2003. Depósitos de Fe-Cu-Au y su relación con el magmatismo del Cretácico Inferior, III Región de Atacama, Chile. X Congreso Geológico Chileno, Concepción, Chile.

Escolme, A., Cooke, D.R., Hunt, J., Berry, R.F., Maas, R., Creaser, R.A., 2020. The Productora Cu-Au-Mo Deposit, Chile: A Mesozoic Magmatic-Hydrothermal Breccia Complex with Both Porphyry and Iron Oxide Cu-Au Affinities. Econ. Geol. 115, 534–580. https://doi.org/10.5382/econgeo.4718

Farrar, E., Clark, A., Haynes, J., Quirt, G., Conn, H., Zentilli, M., 1970. K-Ar evidence for the post-Paleozoic migration of granitic intrusion foci in the Andes of northern Chile. Earth Planet. Sci. Lett. 10, 60–66. https://doi.org/10.1016/0012-821X(70)90064-6

Fox, K.A., 2000. Fe-oxide (Cu-U-Au-REE) mineralisation and alteration at the Productora prospect. Ph.D. thesis. Colorado School of Mines, USA.

Gelcich, S.H., 1998. Metalogénesis de los cuadrángulos El Salado y Quebrada Guamanga, Cordillera de la Costa, III Región. MSc. thesis. University of Chile, Chile.

Gelcich, S.H., Espinoza, C., Vivallo, W., 1998. Yacimientos metaliferos de las Hojas Chañaral y Diego de Almagro, Región de Atacama, escala 1:100.000. Servicio Nacional de Geología y Minería, Chile.

Gelcich, S.H., Davis, D.W., Spooner, E.T.C., 2003. New U-Pb ages for host rocks, mineralization and alteration of iron oxide (Cu-Au) deposits in the coastal cordillera of northern Chile. IV South American Symposium on Isotope Geology, Salvador de Bahia, Brazil, 63–66.

Gelcich, S.H., Davis, D.W., Spooner, E.T.C., 2005. Testing the apatite-magnetite geochronometer: U-Pb and 40Ar/39Ar geochronology of plutonic rocks, massive magnetite-apatite tabular bodies, and IOCG mineralization in Northern Chile. Geochim. Cosmochim. Acta 69, 3367–3384. https://doi.org/10.1016/j.gca.2004.12.020

Girardi, J.D., 2014. Comparison of Mesozoic magmatic evolution and iron oxide (-copper-gold) ('IOCG') mineralization, Central Andes and western North America. PhD. thesis dissertation. The University of Arizona, USA.

Godoy, E., Lara, L., 1998. Hojas Chañaral y Diego de Almagro, Region de Atacama, escala 1:100.000. Servicio Nacional de Geología y Minería, Chile.

Godoy, E., Marquardt, C., Blanco, N., 2003. Carta Caldera, Region de Atacama, escala 1:100.000. Servicio Nacional de Geología y Minería, Chile.

Hervé, M., Sillitoe, R.H., Wong, C., Fernández, P., Crignola, F., Ipinza, M., Urzúa, F., 2012. Geologic Overview of the Escondida Porphyry Copper District, Northern Chile, in: Hedenquist, J.W., Harris, M., Camus, F. (Eds.), Geology and Genesis of Major Copper Deposits and Districts of the World: A Tribute to Richard H. Sillitoe. Society of Economic Geologists, Inc. Special Publications 16, Littleton, Colorado, pp. 55–78. https://doi.org/10.5382/SP.16.03

Hervé, F., Fanning, C.M., Calderón, M., Mpodozis, C., 2014. Early Permian to Late Triassic batholiths of the Chilean Frontal Cordillera (28–31 S): SHRIMP U–Pb zircon ages and Lu–Hf and O isotope systematics. Lithos 184, 436–446. https://doi.org/10.1016/j.lithos.2013.10.018

Jara, C., Rabbia, O., Valencia, V., 2009. Petrología y dataciones U-Pb del depósito tipo pórfido Cu Zaldívar, II Región de Antofagasta, Chile. XII Congreso Geológico Chileno, Santiago, Chile, 1–4.

Jorquera, R., Pizarro, N., Vogel, S., Díaz, A., Vivallo, W., 2011. Yacimientos Metalíferos del Área La Serena-La Higuera, Región de Coquimbo, escala 1:100.000. Servicio Nacional de Geología y Minería, Chile.

Kovacic, P. 2014. Geología y metalogénesis del Yacimoento IOCG Casualidad, Distrito Sierra Overa, Segunda Región de Antofagasta, Chile. MSc thesis. University of Antofagasta, Chile.

Kovacic, P., Barra, F., Tornos, F., Morata, D., Cerda, A., 2012. Nuevos antecedentes geológicos y geoquímicos del yacimiento tipo IOCG Casualidad, Distrito Sierra Overa, II Región de Antofagasta, Chile. XIII Congreso Geológico Chileno, Antofagasta, Chile, 43–45.

Lara, L., Godoy, E., 1998. Hoja Quebrada Salilrosa, Región de Atacama, escala 1:100.000. Servicio Nacional de Geología y Minería, Chile.

Lieben, F., Moritz, R., Fontboté, L., 2000. Mineralogy, Geochemistry, and Age Constraints on the Zn-Pb Skarn Deposit of Maria Cristina, Quebrada Galena, Northern Chile. Econ. Geol. 95, 1185–1196. https://doi.org/10.2113/gsecongeo.95.6.118

Lledó, H., 1998. Metalogénesis de los cuadrángulos Copiapó, Cerro Chamonate y Nantoco. MSc. thesis. University of Chile, Chile.

Lopez, G.P., Hitzman, M.W., Nelson, E.P., 2014. Alteration patterns and structural controls of the El Espino IOCG mining district, Chile. Miner. Deposita 49, 235–259. https://doi.org/10.1007/s00126-013-0485-0

Maksaev, V., Zentilli, M., 2002. Chilean strata bound Cu (Ag) Deposits. An overview, in: Porter, T.M. (Ed.), Hydrothermal Iron Oxide Copper-Gold & Related Deposits: A Global Perspective, Second Edition. PGC Publishing, Adelaide, pp. 163–184.

Maksaev, V., Munizaga, F., Valencia, V., Barra, F., McWilliams, M., Mathur, R., 2006. Geochronology of Cretaceous porphyry copper deposits of the Coastal Cordillera of northern Chile (latitudes 26°30' to 30°30'S). 38th Geological Society of America Abstracts, Philadelphia, USA, 347.

Maksaev, V., Munizaga, F., Valencia, V., Barra, F., 2009. LA-ICP-MS zircon U-Pb geochronology to constrain the age of post-Neocomian continental deposits of the Cerrillos Formation, Atacama Region, northern Chile: tectonic and metallogenic implications. Andean Geol. 36, 264–287.

Maksaev, V., Almonacid, T.A., Munizaga, F., Valencia, V., McWilliams, M., Barra, F., 2010. Geochronological and thermochronological constraints on porphyry copper mineralization in the Domeyko alteration zone, northern Chile. Andean Geol. 37 144–176.

Maksaev, V., Munizaga, V., Tassinari, C., 2014. Timing of the magmatism of the paleo-Pacific border of Gondwana: U-Pb geochronology of Late Paleozoic to Early Mesozoic igneous rocks of the north Chilean Andes between 20° and 31°S. Andean Geol. 41, 447–506. https://doi.org/10.5027/andgeoV41n3-a01

Marinovic, N., 2007. Carta Oficina Domeyko, Región de Antofagasta, escala 1:100.000. Servicio Nacional de Geología y Minería, Chile.

Marinovic, N., Smoje, I., Maksaev, V., Hervé, M., Mpodozis, C., 1995. Hoja Aguas Blancas, Región de Antofagasta, escala 1:250.000. Servicio Nacional de Geología y Minería, Chile.

Marinovic, N., García, M., 1999. Hoja Pampa Unión, Región de Antofagasta, escala 1:100.000. Servicio Nacional de Geología y Minería, Chile.

Marquardt, M., Cembrano, J., Bissig, T., Vázquez, C., 2015. Mid Cretaceous Cu-Au (Mo) mineralization in the Vallenar district: new Re-Os age constrains from Productora deposit, northern Chile. XIV Congreso Geológico Chileno, La Serena, Chile, 421–424.

Marschik, R., Fontboté, L., 2001a. The Candelaria-Punta del Cobre Iron Oxide Cu-Au(-Zn-Ag) Deposits, Chile. Econ. Geol. 96, 1799–1826. https://doi.org/10.2113/gsecongeo.96.8.1799

Marschik, R., Söllner, F., 2006. Early Cretaceous U–Pb zircon ages for the Copiapó plutonic complex and implications for the IOCG mineralization at Candelaria, Atacama Region, Chile. Miner. Deposita 41, 785–801. https://doi.org/10.1007/s00126-006-0099-x

Marschik, R., Singer, B.S., Munizaga, F., Tassinari, C., Moritz, R., Fontboté, L., 1997. Age of Cu(-Fe)-Au mineralization and thermal evolution of the Punta del Cobre district, Chile. Miner. Deposita 32, 531–546. https://doi.org/10.1007/s001260050120

Martin, M.W., Clavero, J., Mpodozis, C., 1999. Late Paleozoic to early Jurassic tectonic development of the high Andean principal Cordillera, El Indio region, Chile (29–30 S). J. S. Am. Earth Sci. 12, 33–49. https://doi.org/10.1016/S0895-9811(99)00003-6

Mathur, R., Marschik, R., Ruiz, J., Munizaga, F., Leveille, R.A., Martin, W., 2002. Age of mineralization of the Candelaria Fe oxide Cu-Au deposit and the origin of the Chilean iron belt, based on Re-Os isotopes." Econ. Geol. 97, 59–71. https://doi.org/10.2113/gsecongeo.97.1.59

Montecinos, P., 1985. Petrologie des roches intrusives associes au gisement de fer El Algarrobal, Chile. PhD. thesis. Universite de Paris-Sud, France.

Montes, M., 2016. The Evolution of the Los Negritos Porphyry Copper Deposit, Coquimbo, Chile: Geological, Geocrhonological, Mineralogical and Geochemical Evidence. MSc. thesis. Queens University, Canada.

Munizaga, F., Huete, C., Hervé, F., 1985. Geocronología K-Ar y razones iniciales 87Sr/86Sr de la Franja Pacífica de Desarrollos Hidrotermales. IV Congreso Geológico Chileno, Antofagasta.

Munizaga, F., Holmgren, C. Huete, C., Kawashita, K., 1998. Geocronologia de los yacimientos de cobre El Soldado y Lo Aguirre, Chile, Central. V Congreso Geologico Chileno, Santiago, Chile.

Naranjo, J.A., Puig, A., 1984. Hojas Taltal y Chañaral, regiones de Antofagasta y Atacama, escala 1:250.000. Servicio Nacional de Geología y Minería, Chile.

Niemeyer, H. 2013. Geología del área Cerro Lila- Peine, Región de Antofagasta, escala 1:100.000. Servicio Nacional de Geología y Minería, Chile.

Ogata, T., Ichii, Y., Erdenebayar, J., Nozaki, T., Takaya, Y., 2019. U-Pb Zircon and Tentatively Determined Re-Os Isotope Geochronology for the Atacama Kozan Mine and Sol Nasciente Mine, Region III, Chile. SEG 2019 Conference Proceedings, Santiago, Chile.

Oliveros, V., 2005. Les formations magmatiques jurassiques et mineralisation du nord Chili, origine, mise en place, alteration, metamorphisme: etude geochronologique et geochemie. PhD. thesis. Universite de Nice-Sophia Antipolis, France.

Oliveros, V., Féraud, G., Aguirre, L., Ramírez, L., Fornari, M., Palacios, C., Parada, M., 2007. Detailed 40Ar/39Ar dating of geologic events associated with the Mantos Blancos copper deposit, northern Chile. Miner. Deposita 43, 281–293. https://doi.org/10.1007/s00126-007

Padel, M., Salazar, E., Coloma, F., 2012. Arquitectura y evolución tectonoestratigráfica del Depocentro de San Félix, Triásico medio a superior: Resultados preliminares. XIII Congreso Geológico Chileno, Antofagasta, Chile, 715–717.

Pankhurst, R., Millar, I., Herve, F., 1996. A Permo-Carboniferous U-Pb age for part of the Guanta Unit of the Elqui-Limari Batholith at Rio del Transito, Northern Chile. Rev. Geol. Chile 23, 35-42. http://dx.doi.org/10.5027/andgeoV23n1-a03

Perelló, J., Martini, R., Arcos, R., Muhr, R., 2003. Buey Muerto: porphyry copper mineralization in the Early Cretaceous arc of northern Chile. X Congreso Geológico Chileno, Concepción, Chile.

Pichon, R., 1981. Contribution a l'etude de la ceiunture de fer du Chili, les gisements de Bandurrias (Province d'Atacama) et Los Colorados Norte (Province de Huasco). PhD. thesis. Universite de Paris, France.

Pineda, G., Calderón, M., 2008. Geología del área Monte Patria-El Maqui, Región de Coquimbo, escala 1:100.000. Servicio Nacional de Geología y Minería, Chile.

Pop, N., Heaman, L., Edelstein, O., Isache, C., Zentilli, M., Pecskay, Z., Valdman, S., Rusu, C., 2000. Geocronología de las rocas ígneas y los productos de alteración hidrotermal relacionados con la mineralización de Cu–Fe (Au) del sector Adriana – Carola–Cobriza (parte este del distrito Punta del Cobre – Candelaria), en base a dataciones UPb (en circon). IX Congreso Geológico Chileno, Puerto Varas, Chile.

Raab, A., 2002. Geology of the Cerro Negro Norte Fe-oxide (Cu-Au) district, Coastal Cordillera, northern Chile. MSc. thesis. Oregon State University, USA.

Reyes, M., 1991. The Andacollo strata-bound gold deposit, Chile, and its position in a porphyry copper-gold system. Econ. Geol. 86, 1301–1316. https://doi.org/10.2113/gsecongeo.86.6.1301

Richards, J.P., Noble, S.R., Pringle, M.S., 1999. A revised late Eocene age for porphyry Cu magmatism in the Escondida area, northern Chile. Econ. Geol. 94, 1231–1247. https://doi.org/10.2113/gsecongeo.94.8.1231

Richards, J.P., López, G.P., Zhu, J.J., Creaser, R.A., Locock, A.J., Mumin, A.H., 2017. Contrasting tectonic settings and sulfur contents of magmas associated with Cretaceous porphyry Cu±Mo±Au and intrusion-related iron oxide Cu-Au deposits in northern Chile. Econ. Geol. 112, 295–318. https://doi.org/10.2113/econgeo.112.2.295

Rivera, O., 1992. El complejo volcánico plutónico del Paleoceno-Eoceno del cerro Durazno Alto: Las Calderas, el Durazno Alto y Lomas Bayas, Región de Atacama, Chile. PhD. thesis. University of Chile, Chile.

Rivera, O., Mpodozis, C., 1994. La Megacaldera Carrizalillo y sus calderas anidadas: volcanismo sinextensional cretácico superior-terciario inferior en la Precordillera de Copiapó. VII Congreso Geológico Chileno, Concepción, Chile, 149–153.

Rojas, P., Barra, F., Reich, M., Deditius, A., Simon, A., Uribe, F., Romero, R., Rojo, M. 2018b. A genetic link between magnetite mineralization and diorite intrusion at the El Romeral iron oxide-apatite deposit, northern Chile. Miner. Deposita 53, 947–966. https://doi.org/10.1007/s00126-017-0777-x

Rossel, P., Oliveros, V., Ducea, M.N., Charrier, R., Scaillet, S., Retamal, L., Figueroa, O., 2013. The Early Andean subduction system as an analog to island arcs: Evidence from across-arc geochemical variations in northern Chile. Lithos 179, 211–230. https://doi.org/10.1016/j.lithos.2013.08.014

Ruiz, F.C., Aguirre, L., Corvalacn, J., Klohn, C., Klohn, E., Levi, B., 1965. Geología y Yacimientos Metalíferos de Chile, 18 ed. Instituto de Investigaciones Geológicas de Chile. Santiago.

Salazar, A.E A., 2018. Geoquímica de elementos traza en magnetita del depósito de hierro-apatito Cerro Negro Norte, Chile. MSc. thesis. University of Chile, Chile.

Salazar, E., Arriagada, C., Mpodozis, C., Martínez, F., Peña, M., Álvarez, J., 2009. Análisis estructural del Oroclino de Vallenar: primeros resultados. XII Congreso Geológico Chileno, Santiago, Chile, 1–4.

Salazar, E., Mpodozis, C., Arriagada, C., Coloma, F., 2012. Evolución tectonoestratigráfica post-paleozoica de la Cordillera de Vallenar. XIII Congreso Geológico Chileno, Antofagasta, 265–267.

Salazar, E., Coloma, F., Creixell, C., 2013. Geología del área El Tránsito-Lagunillas, Región de Atacama, escala 1:100.000. Servicio Nacional de Geología y Minería, Chile.

Seymour, N.M., Singleton, J.S., Mavor, S.P., Gomila, R., Stockli, D.F., Heuser, G., Arancibia, G., 2020. The relationship between magmatism and deformation along the intra-arc strike-slip Atacama fault system, northern Chile. Tectonics 39, e2019TC005702. https://doi.org/10.1029/2019TC005702

Tassinari, C.C.G., Munizaga, F., Ramírez, R., 1993. Edad y geoquímica isotópica Rb–Sr del yacimiento de cobre Mantos Blancos: relación temporal con el magmatismo jurásico. Rev. Geol. Chile 20, 193–205. https://doi.org/10.5027/andgeoV20n2-a04

Tornos, F., Velasco, F., Barra, F., Morata, D., 2010. The Tropezón Cu–Mo–(Au) deposit, Northern Chile: the missing link between IOCG and porphyry copper systems?. Minera. Deposita 45, 313–321. https://doi.org/10.1007/s00126-010-0277-8

Ullrich, T.D., Clark, A.H., 1999. The Candelaria copper-gold deposit, Región III, Chile: Paragenesis, geochronology and fluid composition, in: Stanley, C.J. et al. (Eds.), Mineral deposits: Processes to processing. Rotterdam, Balkema, pp. 201–204.

Ulriksen, C., 1979. Regional geology, geochronology and metallogeny of the Coastal Cordillera of Chile between 25°30' y 26°00'S. MSc. thesis. Dallhousie University, Canada.

Urzúa, F., 2009. Geology, geochronology and structural evolution of La Escondida copper district, northern Chile. PhD. thesis. University of Tasmania, Australia.

Veloso, E., Cembrano, J., Arancibia, G., Heuser, G., Neira, S., Siña, A., Garrido, I., Vermeesch, P., Selby, D., 2017. Tectono-metallogenetic evolution of the Fe–Cu deposit of Dominga, northern Chile. Miner. Deposita 52, 595–620. https://doi.org/10.1007/s00126-016-0682-8

Venegas, C., Cervetto, M., Astudillo, N., Espinoza, F., 2013. Carta Sierra Vaquillas Altas, Regiones de Antofagasta y Atacama, escala 1:100.000. Servicio Nacional de Geología y Minería, Chile.

Vergara, H., Thomas, A., 1984. Hoja Collacagua, Región de Tarapacá, escala 1:250.000. Servicio Nacional de Geología y Minería, Chile.

Vila, T., Lindsay, N., Zamora, R., 1996. Geology of the Mantoverde copper deposit, northern Chile: a specularite-rich hydrothermal tectonic breccia related to the Atacama fault zone. Geol. Soc. Spec. Publ. 5, 157–170. https://doi.org/10.5382/SP.05.11

Wilson, J., Dallmeyer, D., Grocott, J., 2000. New 40Ar/39Ar dates from the Las Tazas complex, northern Chile: Tectonic significance. J. S. Am. Earth Sci. 13, 115–122. https://doi.org/10.1016/S0895-9811(00)00008-0

Zentilli, M., 1974. Geological Evolution and Metallogenetic Relationships in the Andes of Northern Chile between 26 and 29° south. PhD. thesis dissertation. Queens University, Canada.

ESM – Table 17. Compiled Sr–Nd isotopic data for the Central Andes of Chile between 22°S to 33°S and east of 71°W.

Sample	Unit	Petrography	Age (Ma)	$^{87}Rb/^{86}Sr$	$^{87}Sr/^{86}Sr$	I_{Sr}	$^{147}Sm/^{144}Nd$	$^{143}Nd/^{144}Nd$	εNd	I_{Nd}	$εNd_i$	Reference
Volcanic rocks												
MARQ-76	Arqueros Fm.	Bas. And.	117	-	0.70515	0.70356	-	0.512831	-	0.51273	4.7	Morata & Aguirre (2003)
ARQ99-7	Arqueros Fm.	Bas.	117	-	0.70415	0.70372	-	0.512847	-	0.51273	4.7	Morata & Aguirre (2003)
ARQ99-4	Arqueros Fm.	Bas. And.	115	-	0.70446	0.70344	-	0.512744	-	0.51265	3.1	Morata & Aguirre (2003)
ARQ00-13	Arqueros Fm.	Bas. And.	115	-	0.70445	0.70343	-	0.512745	-	0.51266	3.3	Morata & Aguirre (2003)
ARQ00-9	Qda. Marquesa Fm.	Bas. And.	110	-	0.70501	0.70397	-	0.512805	-	0.51272	4.3	Morata & Aguirre (2003)
ARQ00-19	Intrusive Andesites	Bas. And.	100	-	0.70410	0.70336	-	0.512865	-	0.51278	5.3	Morata & Aguirre (2003)
TC00-13	Arqueros Fm. (?)	Bas. And.	115	-	0.70418	0.70361	-	0.512732	-	0.51264	2.9	Morata & Aguirre (2003)
TC99-2	Intrusive Andesites (?)	And.	100	-	0.70423	0.70336	-	0.512873	-	0.51278	5.3	Morata & Aguirre (2003)
164	Qda. La Negra	-	186	0.174	0.70344	0.70298	0.158	0.512946	-	0.51275	6.9	Lucassen et al. (2006)
9	C° del Difunto	-	160	1.376	0.70820	0.70507	0.153	0.512857	-	0.51270	5.2	Lucassen et al. (2006)
97–5	Sierra Fraga	-	160	0.486	0.70458	0.70347	0.160	0.512953	-	0.51279	7.1	Lucassen et al. (2006)
97–213	C° Yumbes	-	211	0.581	0.70871	0.70696	0.139	0.512412	-	0.51222	–2.9	Lucassen et al. (2006)
97–218	C° Yumbes	-	211	3.61	0.71854	0.70771	0.122	0.512390	-	0.51222	–2.8	Lucassen et al. (2006)
K 116	Qda. Cachina	-	211	4.773	0.71885	0.70453	0.116	0.512597	-	0.51244	1.4	Lucassen et al. (2006)
K 118	Qda. Cachina	-	211	2.477	0.71104	0.70360	0.135	0.512721	-	0.51253	3.3	Lucassen et al. (2006)
K 51	Sierra de Candeleros	Bas.	163	0.174	0.70502	0.70462	0.154	0.512847	4.1	0.51268	5	Bartsch (2004)
96–310	C° Blanco, C° Plomo, S. of Taltal	Bas. Trach.	170	0.667	0.70626	0.70464	0.160	0.512997	7	0.51282	7.8	Bartsch (2004)
97-239	C° Blanco, C° Plomo, S. of Taltal	Bas.	154	0.49989	0.70567	0.70457	0.154	0.512911	5.3	0.51276	6.16	Bartsch (2004)
96–21	C° del Difunto	Bas.	194	0.288	0.70509	0.70430	0.178	0.512800	3.2	0.51257	3.6	Bartsch (2004)
95–21	C° del Difunto	Bas.	154	0.844	0.70572	0.70387	0.147	0.512777	2.7	0.51263	3.7	Bartsch (2004)
95–45	C° del Difunto	Bas. Trach.	154	1.065	0.70830	0.70597	0.163	0.512856	4.3	0.51269	4.9	Bartsch (2004)
95–70a	C° del Difunto	Bas.	154	0.549	0.70497	0.70377	0.157	0.512800	3.2	0.51264	3.9	Bartsch (2004)
96-68	C° del Difunto	Trach.	154	23.902	0.75810	0,70577	0.152	0.512757	2.3	0.51260	3.2	Bartsch (2004)
96–192	C° del Difunto	Bas. Trach.	140	0.223	0.70415	0.70370	0.154	0.512885	4.8	0.51274	5.6	Bartsch (2004)
95-58	C° del Difunto	Trach	154	10.1074	0.72493	0.70281	0.151	0.512823	3.6	0.51267	4.51	Bartsch (2004)
96-164a	C° del Difunto	And.	140	0.327	0.70407	0.70341	0.148	0.512769	2.6	0.51263	3.4	Bartsch (2004)
96-196	C° del Difunto	And.	140	0.32729	0.70407	0.70341	0.148	0.512769	2.6	0.51263	3.43	Bartsch (2004)
K 32	Qda. La Tranquita	Bas.	165	0.147	0.70409	0.70375	0.154	0.512850	4.1	0.51269	5	Bartsch (2004)
K 37	Qda. La Tranquita	Bas. Trach.	161	0.32326	0.70578	0.70504	0.148	0.512870	4.5	0.51271	5.52	Bartsch (2004)
96–77a	Qda. Cachina	Dac.	211	0.381	0.70585	0.70471	0.125	0.512631	-0.1	0.51246	1.8	Bartsch (2004)
K 27	Sierra Minillas	Trach.	170	5.0712	0.71858	0.70632	0.136	0.512710	1.4	0.51256	2.73	Bartsch (2004)
PR-09-22	Qda. Vicuñita Beds	Bas. And.	150	-	0.70500	0.70460	-	0.512900	5.1	0.51274	6	Rossel et al. (2013)
PR-10-31	Qda. Vicuñita Beds	Bas. And.	150	-	0.70450	0.70420	-	0.512860	4.4	0.51272	5.4	Rossel et al. (2013)
PR-10-32	Qda. Vicuñita Beds	Bas. And	150	-	0.70490	0.70470	-	0.512800	3.2	0.51265	4.1	Rossel et al. (2013)
PR-10-33	Qda. Vicuñita Beds	And.	150	-	0.70550	0.70440	-	0.512810	3.4	0.51270	5	Rossel et al. (2013)
PR-10-36B	Qda. Vicuñita Beds	Bas.	150	-	0.70500	0.70440	-	0.512890	5	0.51274	5.7	Rossel et al. (2013)
PR-09-28	Lagunillas Fm.	Bas.	150	-	0.70410	0.70390	-	0.513230	11.5	0.51281	7.1	Rossel et al. (2013)
PR-10-71	Lagunillas Fm.	Bas.	150	-	0.70500	0.70480	-	0.512670	0.6	0.51253	1.6	Rossel et al. (2013)

ESM – Table 11. (continued)

Sample	Unit	Petrography	Age (Ma)	$^{87}Rb/^{86}Sr$	$^{87}Sr/^{86}Sr$	I_{Sr}	$^{147}Sm/^{144}Nd$	$^{143}Nd/^{144}Nd$	εNd	I_{Nd}	$εNd_i$	Reference
PR-10-72	Lagunillas Fm.	Bas.	150	-	0.70420	0.70400	-	0.512710	1.4	0.51259	2.8	Rossel et al. (2013)
PR-10-73	Lagunillas Fm.	Bas.	150	-	0.70490	0.70470	-	0.512680	0.9	0.51255	2.1	Rossel et al. (2013)
PR-10-80	Lagunillas Fm.	Bas.	150	-	0.70430	0.70410	-	0.512740	1.9	0.51261	3.3	Rossel et al. (2013)
PR-10-81	Lagunillas Fm.	Bas. And.	150	-	0.70480	0.70450	-	0.512700	1.1	0.51256	2.5	Rossel et al. (2013)
PR-10-94B	Lagunillas Fm.	Bas.	150	-	0.70500	0.70500	-	0.512740	2	0.51262	3.3	Rossel et al. (2013)
PR-10-120	Lagunillas Fm.	Bas. And.	150	-	0.70360	0.70350	-	0.512810	3.3	0.51267	4.6	Rossel et al. (2013)
PR-11-177	Lagunillas Fm.	Bas.	150	-	0.70590	0.70580	-	0.512890	4.9	0.51277	6.3	Rossel et al. (2013)
PR-11-178	Lagunillas Fm.	Dac.	150	-	0.71250	0.70060	-	0.512520	-2.4	0.51239	-1	Rossel et al. (2013)
PR-11-179	Lagunillas Fm.	Bas.	150	-	0.70530	0.70530	-	0.512660	0.5	0.51251	1.2	Rossel et al. (2013)
PR-11-188	Lagunillas Fm.	Bas.	150	-	0.70560	0.70540	-	0.512870	4.6	0.51268	4.5	Rossel et al. (2013)
PR-11-193	Lagunillas Fm.	Dac.	150	-	0.71990	0.70520	-	0.512560	-1.6	0.51239	-1	Rossel et al. (2013)
PR-11-202	Lagunillas Fm.	Bas.	150	-	0.70440	0.70430	-	0.512760	2.4	0.51262	3.5	Rossel et al. (2013)
PR-11-204	Lagunillas Fm.	Bas.	150	-	0.70460	0.70440	-	0.512790	3	0.51265	3.9	Rossel et al. (2013)
PR-09-04	Picudo Fm.	Rhy.	150	-	0.70900	0.70470	-	0.512700	1.2	0.51255	2.1	Rossel et al. (2013)
PR-09-05	Picudo Fm.	Bas. And.	150	-	0.70520	0.70450	-	0.512630	-0.1	0.51251	1.3	Rossel et al. (2013)
PR-09-06	Picudo Fm.	Bas. And	150	-	0.70420	0.70410	-	0.512700	1.1	0.51260	3	Rossel et al. (2013)
PR-10-41	Picudo Fm.	Bas. And.	150	-	0.70470	0.70420	-	0.512570	-1.4	0.51245	0.2	Rossel et al. (2013)
PR-10-42B	Picudo Fm.	Dac.	150	-	0.70570	0.70290	-	0.512730	2.2	0.51262	3.3	Rossel et al. (2013)
PR-10-45	Picudo Fm.	Bas.	150	-	0.70440	0.70420	-	0.512720	1.7	0.51258	2.7	Rossel et al. (2013)
PR-11-164	Picudo Fm.	Bas. And.	150	-	0.70440	0.70420	-	0.512750	2.1	0.51262	3.5	Rossel et al. (2013)
PR-11-168	Picudo Fm.	And.	150	-	0.70420	0.70410	-	0.512720	1.7	0.51264	3.8	Rossel et al. (2013)
M-14	Algarrobal Fm.	Bas. And.	150	-	0.70480	0.70450	-	0.512700	1.3	0.51259	2.7	Rossel et al. (2013)
M-17	Algarrobal Fm.	And.	150	-	0.70520	0.70430	-	0.512600	-0.7	0.51248	0.6	Rossel et al. (2013)
M-22	Algarrobal Fm.	And.	150	-	0.70610	0.70400	-	0.512750	2.1	0.51261	3.2	Rossel et al. (2013)
M-25	Algarrobal Fm.	And.	150	-	0.70550	0.70420	-	0.512620	-0.3	0.51248	0.7	Rossel et al. (2013)
PR-11-132A	Agua Salada Volcanic Complex	Bas. And.	150	-	0.70480	0.70350	-	0.512800	3.1	0.51266	4.2	Rossel et al. (2013)
PR-11-134C	Agua Salada Volcanic Complex	Bas. And.	150	-	0.70520	0.70370	-	0.512800	3.2	0.51267	4.3	Rossel et al. (2013)
PR-11-139	Agua Salada Volcanic Complex	Bas. And.	150	-	0.70370	0.70310	-	0.512860	4.3	0.51272	5.3	Rossel et al. (2013)
PR-11-153	Agua Salada Volcanic Complex	Bas. And.	150	-	0.70430	0.70400	-	0.512740	2	0.51258	2.7	Rossel et al. (2013)
PR-11-154	Agua Salada Volcanic Complex	Bas. And.	150	-	0.70500	0.70440	-	0.512850	4.1	0.51266	4.2	Rossel et al. (2013)
CPV-14-194	Agua Chica Fm.	Dac.	200.4	0.402	0.70666	0.70552	0.135	0.512647	0.17	0.51247	1.75	Oliveros et al. (2020)
CPV-14-198	Agua Chica Fm.	And.	200.4	0.79748	0.70746	0.70519	0.134	0.512557	-1.58	0.51238	0.03	Oliveros et al. (2020)
CPV-12-26B	Algarrobal Fm.	And.	152.7	0.25273	0.70543	0.70488	0.160	0.512616	-0.43	0.51246	0.29	Oliveros et al. (2020)
CPV-12-28x	Algarrobal Fm.	Bas. And.	152.7	0.35134	0.70602	0.70526	0.153	0.512803	3.22	0.51265	4.07	Oliveros et al. (2020)
CPV-12-30x	Algarrobal Fm.	And.	152.7	1.05902	0.70658	0.70429	0.134	0.512637	-0.02	0.51250	1.2	Oliveros et al. (2020)
CPV-12-90	Canto del Agua Fm.	Tuff	212.75	17.2546	0.75303	0.70082	0.150	0.512454	-3.59	0.51225	−2.32	Oliveros et al. (2020)
CPV-14-263	C° Rincones Beds	Dac.	328.3	0.92317	0.71277	0.70892	0.117	0.512332	-5.97	0.51211	−2.97	Oliveros et al. (2020)
CPV-14-184	Cifuncho Fm.	And.	212	0.40796	0.70620	0.70497	0.133	0.512693	1.07	0.51251	2.79	Oliveros et al. (2020)
CPV-14-187	Cifuncho Fm.	And.	210.1	0.48067	0.70605	0.70461	0.130	0.512675	0.72	0.51250	2.5	Oliveros et al. (2020)

ESM – Table 11. (continued)

Sample	Unit	Petrography	Age (Ma)	$^{87}Rb/^{86}Sr$	$^{87}Sr/^{86}Sr$	I_{Sr}	$^{147}Sm/^{144}Nd$	$^{143}Nd/^{144}Nd$	εNd	I_{Nd}	$εNd_i$	Reference
CPV-14-190	Cifuncho Fm.	Dac.	212	0.43756	0.70593	0.70461	0.141	0.512683	0.87	0.51249	2.39	Oliveros et al. (2020)
SCL-28q	Guanaco Sonso Fm.	Rhy.	249.1	11.4331	0.74443	0.70394	0.138	0.512444	-3.78	0.51222	−1.91	Oliveros et al. (2020)
RCM-150q	Guanaco Sonso Fm.	Rhy.	252.4	15.8266	0.72508	0.66825	0.108	0.512410	-4.44	0.51223	−1.59	Oliveros et al. (2020)
SCL-96	Guanaco Sonso Fm.	Dac.	248.8	0.38313	0.70955	0.70819	0.144	0.512637	-0.02	0.51240	1.66	Oliveros et al. (2020)
CPV-14-176	La Tabla Fm.	Rhy.	295.1	3.39141	0.71653	0.70229	0.119	0.512341	-5.79	0.51211	−2.85	Oliveros et al. (2020)
CPV-14-249	La Tabla Fm.	Rhy.	307	49.0189	0.87692	0.67324	0.132	0.512322	-6.16	0.51207	−3.76	Oliveros et al. (2020)
CPV-12-23	La Totora Fm.	And.	221	0.19208	0.70528	0.70469	0.132	0.512630	-0.16	0.51244	1.63	Oliveros et al. (2020)
CPV-12-24	La Totora Fm.	And.	221	0.02301	0.70623	0.70616	0.161	0.512789	2.95	0.51256	3.94	Oliveros et al. (2020)
CPV-12-60	La Totora Fm.	Bas.	221	0.05814	0.70525	0.70507	0.123	0.512605	-0.64	0.51243	1.39	Oliveros et al. (2020)
SCL-26q	La Totora Fm.	Rhy.	217.9	7.41884	0.72056	0.69757	0.107	0.512568	-1.36	0.51242	1.13	Oliveros et al. (2020)
CPV-12-105	Llano de Chocolate Beds	Rhy.	318.8	3.57748	0.71736	0.70112	0.133	0.512329	-6.03	0.51205	−3.42	Oliveros et al. (2020)
CPV-12-12	Llano de Chocolate Beds	Dac.	303.8	2.10052	0.71174	0.70266	0.122	0.512325	-6.11	0.51208	−3.22	Oliveros et al. (2020)
CPV-12-127	Llano de Chocolate Beds	Rhy.	291.4	7.10419	0.72883	0.69811	0.157	0.512782	2.81	0.51248	4.31	Oliveros et al. (2020)
RCM-78q	Pastos Blancos Fm.	And.	231.7	0.16632	0.70604	0.70550	0.129	0.512438	-3.9	0.51225	−1.95	Oliveros et al. (2020)
CPV-14-245	Qda. del Salitre Fm.	Bas. And.	212	0.02771	0.70523	0.70514	0.163	0.512677	0.76	0.51245	1.68	Oliveros et al. (2020)
CPV-14-247	Qda. del Salitre Fm.	Tuff	212	0.11573	0.70771	0.70736	0.137	0.512512	-2.46	0.51232	−0.84	Oliveros et al. (2020)
CPV-14-253	Qda. del Salitre Fm.	Bas.	212	0.05066	0.70746	0.70731	0.164	0.512676	0.74	0.51245	1.64	Oliveros et al. (2020)
CPV-14-256	Qda. del Salitre Fm.	Bas. And.	233	0.11328	0.70612	0.70575	0.157	0.512739	1.97	0.51250	3.17	Oliveros et al. (2020)
CPV-15-303	Qda. del Salitre Fm.	Bas. And.	232.9	0.4703	0.70707	0.70565	0.153	0.512704	1.29	0.51249	2.46	Oliveros et al. (2020)
CPV-15-310	Qda. del Salitre Fm.	Rhy.	232.9	19.1354	0.78339	0.72570	0.143	0.512672	0.66	0.51247	2.11	Oliveros et al. (2020)
CPV-15-311	Qda. del Salitre Fm.	Bas.	232.9	0.14266	0.70626	0.70579	0.159	0.512814	3.43	0.51257	4.56	Oliveros et al. (2020)
CPV-15-312	Qda. del Salitre Fm.	And.	232.9	3.19012	0.71131	0.70074	0.126	0.512519	-2.32	0.51233	−0.22	Oliveros et al. (2020)
CPV-15-314	Qda. del Salitre Fm.	Rhy.	232.9	4.62666	0.72458	0.70925	0.133	0.512614	-0.47	0.51241	1.42	Oliveros et al. (2020)
CPV-15-319	Qda. del Salitre Fm.	Dac.	232.9	1.44286	0.70975	0.70540	0.135	0.512638	0	0.51245	1.68	Oliveros et al. (2020)
CPV-15-322	Qda. del Salitre Fm.	And.	232.9	0.16947	0.70809	0.70755	0.167	0.512930	5.7	0.51269	6.54	Oliveros et al. (2020)
CPV-12-38	San Félix Fm.	Tuff	252	24.3422	0.77277	0.68811	0.117	0.512308	-6.44	0.51212	−3.94	Oliveros et al. (2020)
CPV-12-49b	San Félix Fm.	Tuff	252	2.56498	0.71391	0.70499	0.124	0.512363	-5.36	0.51216	−3.11	Oliveros et al. (2020)
COP-18-02A	Punta del Cobre Fm., Dacite Member	Alb.	130	-	0.71025	0.70432	-	0.512696	-	-	2	Tornos et al. (2020)
COP-18-02-B	Punta del Cobre Fm., Dacite Member	Alb.	130	-	0.71203	0.70422	-	0.512689	-	-	2	Tornos et al. (2020)
ACON103	C° Aconcagua andesites	And.	8.9	-	0.70455	0.70446	-	0.512597	-	-	-0.3	Reich et al. (2003)
CaB-079	Falla Poblete volcanics	And.	127.9	0.369	0.70387	0.70320	0.143	0.512918	-	0.51280	6.3	Girardi (2014)
Veta Negra	Veta Negra Fm.	-	120	-	-	0.70407	-	-	-	0.51273	4.85	Hesler (2007)
Veta Negra	Veta Negra Fm.	-	120	-	-	0.70392	-	-	-	0.51262	2.6	Hesler (2007)
Yerbas Buenas	Upper member Lo Prado Fm.	-	120	-	-	0.70429	-	-	-	0.51264	3	Hesler (2007)
Yerbas Buenas	Upper member Lo Prado Fm.	-	120	-	-	0.70395	-	-	-	0.51254	2.8	Hesler (2007)
Abuelitas	Upper member Lo Prado Fm.	-	120	-	-	0.70429	-	-	-	0.51266	3.45	Hesler (2007)
Abuelitas	Upper member Lo Prado Fm.	-	120	-	-	0.70395	-	-	-	0.51259	2.08	Hesler (2007)
Poca Pena	Upper member Lo Prado Fm.	-	130	-	-	0.70624	-	-	-	0.51264	3.36	Hesler (2007)

ESM – Table 11. (continued)

Sample	Unit	Petrography	Age (Ma)	$^{87}Rb/^{86}Sr$	$^{87}Sr/^{86}Sr$	I_{Sr}	$^{147}Sm/^{144}Nd$	$^{143}Nd/^{144}Nd$	εNd	I_{Nd}	$εNd_i$	Reference
Poca Pena	Upper member Lo Prado Fm.	-	130	-	-	0.70205	-	-	-	0.51255	1.5	Hesler (2007)
CaB-287b	Andesite near to Las Animas area	And.	131	0.249	0.70407	0.70360	0.148	0.512908	-	0.51278	6.1	Girardi (2014)
TC99-5a	Arqueros Fm.	Bas. And.	111.3	0.452	0.70437	-	0.135	0.512750	-	-	-	Morata et al. (2008)
CHY-01	Los Tilos Fm.	Rhy.	224	4.82993	0.72099	0.70560	0.123	0.512422	-4.2	-	-2.1	Parada (2013)
CHY-02	Los Tilos Fm.	Tuff	221	2.19017	0.71298	0.70608	0.122	0.512423	-4.2	-	-2.1	Parada (2013)
CHY-10	Los Tilos Fm.	Rhy	232	3.81854	0.71848	0.70588	0.124	0.512435	-4	-	-1.8	Parada (2013)
CHY-14	La Tabla Fm.	Tuff	282	1.68573	0.71337	0.70660	0.117	0.512324	-6.1	-	-3.3	Parada (2013)
CHY-15	La Tabla Fm.	Tuff	272	0.7756	0.70991	0.70690	0.113	0.512391	-4.8	-	-1.9	Parada (2013)
CHY-22	Dike cut La Tabla Formaiton	Rhy.	270	2.33542	0.71625	0.70727	0.112	0.512294	-6.7	-	-3.8	Parada (2013)
GUC-05q	Pastos Blancos Fm.	Rhy.	224	1.063	0.71062	0.70723	0.108	0.512494	-	0.51232	-0.5	González et al. (2018)
GUC-32q	Pastos Blancos Fm.	And.	224	0.185	0.70566	0.70507	0.134	0.512623	-	0.51253	1.5	González et al. (2018)
GUC-33q	Pastos Blancos Fm.	Dac.	224	3.85	0.71686	0.70460	0.123	0.512462	-	0.51228	-1.34	González et al. (2018)
GUC-38Bq	Pastos Blancos Fm.	-	224	0.019	0.70562	0.70556	0.164	0.512554	-	0.51231	-0.72	González et al. (2018)
GUC-41q	Pastos Blancos Fm.	Rhy.	224	3.446	0.71218	0.70121	0.129	0.512586	-	0.51240	0.91	González et al. (2018)
GUC-45q	Pastos Blancos Fm.	Rhy.	224	2.112	0.71206	0.70533	0.117	0.512565	-	0.51239	0.87	González et al. (2018)
GUC-46q	Pastos Blancos Fm.	Rhy.	224	1.533	0.71000	0.70511	0.124	0.512468	-	0.51229	-1.24	González et al. (2018)
GUC-47q	Pastos Blancos Fm.	Dac.	224	2.921	0.71700	0.70769	0.121	0.512497	-	0.51232	-0.58	González et al. (2018)
AS1	Caleta Agua Salada	-	160	0.16536	0.70430	0.70392	0.179	0.512945	-	0.51276	6.36	Lucassen & Franz (1994)
AS5	Caleta Agua Salada	-	160	0.0262	0.70379	0.70373	0.104	0.512874	-	0.51277	6.5	Lucassen & Franz (1994)
AS9	Caleta Agua Salada	-	160	0.09297	0.70409	0.70388	0.137	0.512892	-	0.51275	6.18	Lucassen & Franz (1994)
AS10	Caleta Agua Salada	-	160	0.04117	0.70337	0.70327	0.158	0.512937	-	0.51277	6.63	Lucassen & Franz (1994)
AS72	Caleta Agua Salada	-	160	0.01679	0.70393	0.70389	0.153	0.512921	-	0.51276	6.42	Lucassen & Franz (1994)
ST-62q	San Félix Fm.	Rhy.	213.7	0.29859	0.70510	0.70419	0.149	0.512616	-0.43	0.51241	0.88	Salazar et al. (2013)
GIS-115	Pastos Blancos Fm.	And.	236	-	0.70578	0.70556	-	0.512479	-3.10	0.51227	-1.5002	Murillo et al. (2017)
GUM-31	Las Breas Fm.	Bas. And.	219.5	-	0.70604	0.63807	-	0.512752	2.22	0.51258	4.35891	Murillo et al. (2017)
111	Pichidangui Fm.	Bas.	220	-	0.70695	0.70597	-	0.512787	3.72	0.51255	-	Morata et al. (2000)
124	Pichidangui Fm.	Bas.	220	-	0.70598	0.70396	-	0.512859	4.95	0.51261	-	Morata et al. (2000)
114	Pichidangui Fm.	Bas.	220	-	0.70571	0.70455	-	0.512761	3.12	0.51252	-	Morata et al. (2000)
118	Pichidangui Fm.	Bas.	220	-	0.70623	0.70526	-	0.512780	3.7	0.51254	-	Morata et al. (2000)
113	Pichidangui Fm.	Rhy.	220	-	0.71476	0.70514	-	0.512670	2.5	0.51248	-	Morata et al. (2000)
142	Pichidangui Fm.	Rhy.	220	-	0.71472	0.70946	-	0.512719	3.34	0.51253	-	Morata et al. (2000)
120	Pichidangui Fm.	Rhy.	220	-	0.70751	0.70749	-	0.512640	1.61	0.51244	-	Morata et al. (2000)
110	Pichidangui Fm.	Rhy.	220	-	0.71843	0.71161	-	0.512304	-4.81	0.51211	-	Morata et al. (2000)
8077	La Negra Fm.	-	187	-	0.70644	-	-	0.512870	-	-	5.74	Rogers & Hawkesworth (1989)
8078	La Negra Fm.	-	187	-	0.70654	-	-	0.512820	-	-	4.88	Rogers & Hawkesworth (1989)

ESM – Table 11. (continued)

Sample	Unit	Petrography	Age (Ma)	$^{87}Rb/^{86}Sr$	$^{87}Sr/^{86}Sr$	I_{Sr}	$^{147}Sm/^{144}Nd$	$^{143}Nd/^{144}Nd$	εNd	I_{Nd}	$εNd_i$	Reference
8092	La Negra Fm.	-	187	-	0.70962	-	-	0.512890	-	-	6.34	Rogers & Hawkesworth (1989)
8093	La Negra Fm.	-	187	-	0.70785	-	-	0.512840	-	-	5.11	Rogers & Hawkesworth (1989)
8097	La Negra Fm.	-	187	-	0.70601	-	-	0.512870	-	-	5.68	Rogers & Hawkesworth (1989)
8098	La Negra Fm.	-	187	-	0.70559	-	-	0.512880	-	-	5.84	Rogers & Hawkesworth (1989)
81055	Indio Muerto Fm.	-	130	-	0.70617	-	-	0.512510	-	-	-1.5	Rogers & Hawkesworth (1989)
81056	Indio Muerto Fm.	-	130	-	0.70535	-	-	0.512610	-	-	0.51	Rogers & Hawkesworth (1989)
81130	Augusta Victoria Fm.	-	105	-	0.70489	-	-	0.512760	-	-	3.55	Rogers & Hawkesworth (1989)
81131	Augusta Victoria Fm.	-	105	-	0.70741	-	-	0.512820	-	-	4.95	Rogers & Hawkesworth (1989)
81132	Augusta Victoria Fm.	-	105	-	0.70514	-	-	0.512850	-	-	5.24	Rogers & Hawkesworth (1989)
81134	Augusta Victoria Fm.	-	105	-	0.70433	-	-	0.512780	-	-	3.57	Rogers & Hawkesworth (1989)
81136	Augusta Victoria Fm.	-	105	-	0.70451	-	-	0.512800	-	-	3.9	Rogers & Hawkesworth (1989)
81019	C° Negro Fm.	-	70	-	0.70586	-	-	0.512720	-	-	2.44	Rogers & Hawkesworth (1989)
81020	C° Negro Fm.	-	70	-	0.70514	-	-	0.512730	-	-	2.46	Rogers & Hawkesworth (1989)
IOA												
ABU-1	Montecristo-Abundancia	Act	130	-	0.70464	0.70457	-	0.512913	-	-	7.1	Tornos et al. (2020)
ABU-2	Montecristo-Abundancia	Act	130	-	0.70424	0.70422	-	0.512941	-	-	7.2	Tornos et al. (2020)
ABU-7	Montecristo-Filon San Juan	Act	130	-	0.70629	0.70629	-	0.512807	-	-	5.1	Tornos et al. (2020)
ABU-8	Montecristo-Filon San Juan	Ap	130	-	0.70448	0.70446	-	0.512935	-	-	6.6	Tornos et al. (2020)
JUL-2	Mina Julia	Act	130	-	0.71106	0.70970	-	0.512964	-	-	7.5	Tornos et al. (2020)
TOC-1	Tocopilla	Ap	130	-	0.70567	0.70566	-	0.512910	-	-	6.8	Tornos et al. (2020)
TOC-5	Tocopilla	Act	130	-	0.70585	0.70681	-	0.512948	-	-	6.8	Tornos et al. (2020)
TOC-11	Tocopilla	Ap	130	-	0.70456	0.70451	-	0.512924	-	-	6.6	Tornos et al. (2020)
ROM-3	Romeral	Ap	130	-	0.70501	0.70429	-	0.512781	-	-	4.1	Tornos et al. (2020)
COL-1-AP	Los Colorados	Ap	130	-	0.70425	0.70424	-	0.512896	-	-	5.1	Tornos et al. (2020)
COL-3	Los Colorados	Ap	130	-	0.70590	0.70590	-	0.512785	-	-	3.9	Tornos et al. (2020)
COL-7-AP	Los Colorados	Ap	130	-	0.70425	0.70424	-	0.512896	-	-	5.1	Tornos et al. (2020)
COL-22	Los Colorados	Act	130	-	0.70522	0.70508	-	0.512932	-	-	6.3	Tornos et al. (2020)
COL-23	Los Colorados	Act	130	-	0.70622	0.70577	-	0.512932	-	-	4.3	Tornos et al. (2020)
PM-1	Bronce Sur	WR	130	-	0.70430	0.70430	-	0.512788	-	-	4.9	Tornos et al. (2020)
PM-2	Bronce Sur	WR	130	-	0.70548	0.70547	-	0.512854	-	-	5.7	Tornos et al. (2020)
CA-01	Carmen de Fierro	Ap	130	-	0.70779	0.70485	-	0.512950	-	-	7.2	Tornos et al. (2020)
CA-01-ANF	Carmen de Fierro	Act	130	-	0.70416	0.70409	-	0.512928	-	-	6.8	Tornos et al. (2020)
CA-03	Carmen de Fierro	Act	130	-	0.70447	0.70418	-	0.512947	-	-	7	Tornos et al. (2020)
CA-04	Carmen de Fierro	Ap	130	-	0.70381	0.70381	-	0.512894	-	-	6.5	Tornos et al. (2020)
CA-05	Carmen de Fierro	Act	130	-	0.70582	0.70478	-	0.512810	-	-	4.4	Tornos et al. (2020)
CA-AP	Carmen de Fierro	Ap	130	-	0.70373	0.70332	-	0.512889	-	-	6.2	Tornos et al. (2020)
CA-AP-1-18	Carmen de Fierro	Ap	130	-	0.70369	0.70339	-	0.512912	-	-	6.7	Tornos et al. (2020)
CA-AP-1-2	Carmen de Fierro	Ap	130	-	0.70367	0.70367	-	0.512906	-	-	6.3	Tornos et al. (2020)
CA-AP-3	Carmen de Fierro	Ap	130	-	0.70675	0.70435	-	0.512919	-	-	5.7	Tornos et al. (2020)
CAS-35-anf	Carmen de Fierro	Act	130	-	0.70490	0.70429	-	0.512917	-	-	6.1	Tornos et al. (2020)

ESM – Table 11. (continued)

Sample	Unit	Petrography	Age (Ma)	$^{87}Rb/^{86}Sr$	$^{87}Sr/^{86}Sr$	I_{Sr}	$^{147}Sm/^{144}Nd$	$^{143}Nd/^{144}Nd$	εNd	I_{Nd}	$εNd_i$	Reference
CNN-3	C° Negro Norte	WR	130	-	0.70658	0.70412	-	0.513084	-	-	8.6	Tornos et al. (2020)
CNN-6	C° Negro Norte	WR	130	-	0.70508	0.70372	-	0.513030	-	-	8.2	Tornos et al. (2020)
MOL-1	Los Molles	Ap	130	-	0.70503	0.70497	-	0.513082	-	-	7.3	Tornos et al. (2020)
MOL-2	Los Molles	Ap	130	-	0.70468	0.70465	-	0.513027	-	-	7	Tornos et al. (2020)
MOL-3	Los Molles	Ap	130	-	0.70430	0.70430	-	0.512822	-	-	4.8	Tornos et al. (2020)
CLF-1	California	Act	130	-	0.70429	0.70428	-	0.512886	-	-	5.3	Tornos et al. (2020)
CLF-1-1	California	Act	130	-	0.70574	0.70520	-	0.513004	-	-	-	Tornos et al. (2020)
CLF-2	California	Act	130	-	0.70987	0.70647	-	0.512847	-	-	5.1	Tornos et al. (2020)
PM-3	California	Ap	130	-	0.70516	0.70514	-	0.512878	-	-	5.5	Tornos et al. (2020)
MI-1	Maria Ignacia	Ap	130	-	0.70467	0.70466	-	0.512868	-	-	6.2	Tornos et al. (2020)
MI-2	Maria Ignacia	Ap	130	-	0.70409	0.70409	-	0.512853	-	-	5.9	Tornos et al. (2020)
PI-4	Maria Ignacia	Ap	130	-	0.70483	0.70435	-	0.512781	-	-	5.2	Tornos et al. (2020)
Ca-10	Carmen	Ap	130.6	-	0.70463	-	0.134	0.512888	5.9	-	-	Palma et al. (2019)
Ca-8	Carmen	Ap	130.6	-	0.70474	-	0.122	0.512906	6.5	-	-	Palma et al. (2019)
Ca-2	Carmen	Ap	130.6	-	0.70382	-	0.117	0.512900	6.4	-	-	Palma et al. (2019)
Ca-1	Carmen	Ap	130.6	-	0.70417	-	0.116	0.512893	6.3	-	-	Palma et al. (2019)
Fre-20	Fresia	Ap	130	-	0.70490	-	0.145	0.512258	-0.3	-	-	Palma et al. (2019)
Fre-5	Fresia	Ap	130	-	0.70464	-	0.119	0.512780	4.1	-	-	Palma et al. (2019)
Fre-19	Fresia	Ap	130	-	0.70411	-	0.153	0.512635	0.7	-	-	Palma et al. (2019)
Ma-3	Mariela	Ap	130	-	0.70407	-	0.095	0.512833	5.5	-	-	Palma et al. (2019)
Ma-11	Mariela	Ap	130	-	0.70398	-	0.093	0.512849	5.9	-	-	Palma et al. (2019)
Ma-11	Mariela	Ap	130	-	0.70393	-	0.090	0.512842	5.7	-	-	Palma et al. (2019)
Ma-0	Mariela	Ap	130	-	0.70390	-	0.086	0.512850	6	-	-	Palma et al. (2019)
I-type granitoids												
U-8	Deep section of the Coastal Batholith, C° Cristales	-	140	0.181	0.70377	0.70341	0.146	0.512876	-	0.51274	5.5	Lucassen et al. (2006)
U-24	Deep section of the Coastal Batholith, C° Cristales	-	140	0.156	0.70361	0.70330	0.136	0.512858	-	0.51273	5.4	Lucassen et al. (2006)
U-83	Deep section of the Coastal Batholith, C° Cristales	-	140	0.217	0.70373	0.70330	0.132	0.512870	-	0.51275	5.7	Lucassen et al. (2006)
U-85	Deep section of the Coastal Batholith, C° Cristales	-	140	0.268	0.70386	0.70332	0.136	0.512854	-	0.51273	5.3	Lucassen et al. (2006)
MCP-1	Shallow section of the Coastal batholith	-	160	0.671	0.70510	0.70357	0.143	0.512896	-	0.51275	6.1	Lucassen et al. (2006)
MCP-11	Shallow section of the Coastal batholith	-	160	0.585	0.70514	0.70381	0.150	0.512886	-	0.51273	5.8	Lucassen et al. (2006)
QPA-2	Shallow section of the Coastal batholith	-	160	0.032	0.70399	0.70391	0.138	0.512887	-	0.51274	6.1	Lucassen et al. (2006)
QPA-4	Shallow section of the Coastal batholith	-	160	0.445	0.70442	0.70341	0.142	0.512882	-	0.51273	5.9	Lucassen et al. (2006)
QMA-1	Shallow section of the Coastal batholith	-	160	0.955	0.70553	0.70336	0.132	0.512803	-	0.51266	4.5	Lucassen et al. (2006)
QMA-2	Shallow section of the Coastal batholith	-	160	2.159	0.70803	0.70312	0.133	0.512815	-	0.51268	4.8	Lucassen et al. (2006)
QBA-1	Shallow section of the Coastal batholith	-	160	1.803	0.70761	0.70351	0.138	0.512784	-	0.51264	4	Lucassen et al. (2006)
QBA-5	Shallow section of the Coastal batholith	-	160	1.232	0.70669	0.70389	0.115	0.512808	-	0.51269	5	Lucassen et al. (2006)
QSR-1	Shallow section of the Coastal batholith	-	160	0.362	0.70440	0.70357	0.130	0.512740	-	0.51260	3.3	Lucassen et al. (2006)
QSR-8	Shallow section of the Coastal batholith	-	160	0.078	0.70407	0.70389	0.180	0.512859	-	0.51267	4.7	Lucassen et al. (2006)

ESM – Table 11. (continued)

Sample	Unit	Petrography	Age (Ma)	$^{87}Rb/^{86}Sr$	$^{87}Sr/^{86}Sr$	I_{Sr}	$^{147}Sm/^{144}Nd$	$^{143}Nd/^{144}Nd$	εNd	I_{Nd}	$εNd_i$	Reference
QCA-5	Shallow section of the Coastal batholith	-	160	0.447	0.70726	0.70624	0.125	0.512585	-	0.51245	0.4	Lucassen et al. (2006)
QCA-6	Shallow section of the Coastal batholith	-	160	0.307	0.70619	0.70549	0.121	0.512628	-	0.51250	1.3	Lucassen et al. (2006)
QCA-7	Shallow section of the Coastal batholith	-	160	1.682	0.70860	0.70478	0.155	0.512676	-	0.51251	1.6	Lucassen et al. (2006)
QCA-9	Shallow section of the Coastal batholith	-	160	0.417	0.70445	0.70350	0.128	0.512688	-	0.51255	2.4	Lucassen et al. (2006)
QCA-1	Shallow section of the Coastal batholith	-	160	7.596	0.73052	0.71324	0.121	0.512127	-	0.51200	–8.4	Lucassen et al. (2006)
QCA-2	Shallow section of the Coastal batholith	-	160	7.662	0.73041	0.71299	0.118	0.512119	-	0.51200	–8.5	Lucassen et al. (2006)
QCA-3	Shallow section of the Coastal batholith	-	160	2.24	0.71560	0.71050	0.138	0.512143	-	0.51200	–8.5	Lucassen et al. (2006)
MCP-5	Shallow section of the Coastal batholith	-	160	0.118	0.70468	0.70441	0.116	0.512855	-	0.51273	5.9	Lucassen et al. (2006)
CPV-12-92	Algodones Granite	Dio.	203	0.18464	0.70525	0.70472	0.136	0.512756	2.3	0.51258	3.85	Oliveros et al. (2020)
CPV-12-91A	Carrizal Bajo Complex	Dio.	208	0.46311	0.70760	0.70624	0.157	0.512218	-8.19	0.51201	−7.14	Oliveros et al. (2020)
CPV-12-91B	Carrizal Bajo Complex	Ton.	208	0.94181	0.71009	0.70732	0.108	0.512485	-2.98	0.51234	−0.63	Oliveros et al. (2020)
CPV-12-93	Carrizal Bajo Complex	Grt.	206.2	11.5852	0.74068	0.70657	0.148	0.512689	0.99	0.51249	2.28	Oliveros et al. (2020)
CPV-14-180A	Cifuncho Plutonic Complex	Mgr.	284.8	1.87605	0.71368	0.70612	0.134	0.512297	-6.66	0.51205	−4.39	Oliveros et al. (2020)
CPV-14-191	Cifuncho Plutonic Complex	Mgr.	265	3.94336	0.72499	0.71054	0.131	0.512291	-6.77	0.51207	−4.62	Oliveros et al. (2020)
RCM-61q	Colorado Syenogranite	Sgr.	229.6	6.85207	0.72031	0.69838	0.131	0.512514	-2.41	0.51232	−0.51	Oliveros et al. (2020)
GUC-34q	Colorado Syenogranite	Dike	224	0.504	0.70658	0.70498	0.137	0.512772	-	0.51257	4.33	González et al. (2018)
GUC-37Aq	Colorado Syenogranite	Dike	224	2.873	0.71567	0.70651	0.135	0.512533	-	0.51234	-0.29	González et al. (2018)
GUC-37Cq	Colorado Syenogranite	Dike	224	2.57	0.71196	0.70377	0.136	0.512560	-	0.51236	0.22	González et al. (2018)
MCM-010q	El León Monzogranites	Mgr.	252.3	1.28032	0.71222	0.70762	0.117	0.512312	-6.36	0.51212	−3.78	Oliveros et al. (2020)
O7–13	Guanta Plutonic Complex	Grd.	290	0.3389	0.70795	0.70655	0.104	0.512296	-6.67	0.51210	−3.25	Oliveros et al. (2020)
O7–15	Guanta Plutonic Complex	Ton.	296	0.98023	0.70961	0.70549	0.130	0.512310	-6.4	0.51206	−3.88	Oliveros et al. (2020)
MCM-205q	Guanta Plutonic Complex	Grd.	291.3	0.65796	0.70939	0.70667	0.127	0.512363	-5.36	0.51212	−2.76	Oliveros et al. (2020)
MCM-280q	Guanta Plutonic Complex	Grd.	300.9	0.44361	0.70784	0.70594	0.131	0.512364	-5.34	0.51211	−2.83	Oliveros et al. (2020)
RCM-015q	Guanta Plutonic Complex	Sgr.	293.8	269.901	0.75687	-	0.166	0.512343	-5.75	0.51203	−4.59	Oliveros et al. (2020)
HC211	Guanta Plutonic Complex	-	303	-	0.71355	0.70627	-	0.512276	-	-	-3.7	Mpodozis & Kay (1992)
EV-GU	Guanta Plutonic Complex	-	303	-	0.70993	0.70578	-	0.512330	-	-	-2.9	Mpodozis & Kay (1992)
CPV-12-03	La Vaca Granodiorite	Grd.	198	0.71217	0.70576	0.70375	0.124	0.512672	0.66	0.51251	2.5	Oliveros et al. (2020)
CPV-14-182B	Sierra Esmeralda Plutonic Complex	Ton.	193.5	0.66201	0.70645	0.70462	0.136	0.512717	1.54	0.51255	3.05	Oliveros et al. (2020)
IC-17	La Estancilla Unit	Ton.	286	-	0.70865	0.70528	-	0.512612	-	0.51238	2.09	del Rey et al. (2019)
IC-22	Montosa Unit	Ton.	253	-	0.71067	0.70399	-	0.512393	-	0.51220	-2.13	del Rey et al. (2019)
IC-99	Montosa Unit	Ton.	253	-	0.70657	0.70460	-	0.512440	-	0.51228	-0.51	del Rey et al. (2019)
RdM-09	Montosa Unit	Sgr.	255	-	0.72750	0.70794	-	0.512340	-	0.51218	-2.62	del Rey et al. (2019)
IC-58	El León Unit	Mgr.	257	-	0.71683	0.70790	-	0.512364	-	0.51216	-2.87	del Rey et al. (2019)
IC-94	El León Unit	Sgr.	244	-	0.72891	0.70810	-	0.512394	-	0.51219	-2.6	del Rey et al. (2019)
IC-14	Colorado Unit	Mgr.	250	-	0.70936	0.70569	-	0.512403	-	0.51221	-2.09	del Rey et al. (2019)
IC-93	Colorado Unit	Sgr.	248	-	0.71733	0.70614	-	0.512451	-	0.51227	-0.92	del Rey et al. (2019)
IC-81	Chollay Unit	Mgr.	242	-	0.71892	0.70592	-	0.512404	-	0.51225	-1.64	del Rey et al. (2019)
IC-91	Chollay Unit	Sgr.	259	-	0.71111	0.70509	-	0.511858	-	0.51168	-12.17	del Rey et al. (2019)
PC97001	Copiapó Plutonic Complex	Dio.	115	0.099	0.70354	0.70307	0.220	0.512870	5.5	0.51277	-	Marschik et al. (2003b)
PC1498	Copiapó Plutonic Complex	Dio.	115	0.177	0.70407	0.70323	0.230	0.512865	5.3	0.51276	-	Marschik et al. (2003b)

ESM – Table 11. (continued)

Sample	Unit	Petrography	Age (Ma)	$^{87}Rb/^{86}Sr$	$^{87}Sr/^{86}Sr$	I_{Sr}	$^{147}Sm/^{144}Nd$	$^{143}Nd/^{144}Nd$	εNd	I_{Nd}	$εNd_i$	Reference
PC97010	Copiapó Plutonic Complex	Dio.	115	0.274	0.70446	0.70316	0.220	0.512843	5	0.51275	-	Marschik et al. (2003b)
PC97006	Copiapó Plutonic Complex	Dio.	115	0.091	0.70364	0.70321	0.230	0.512869	5.4	0.51277	-	Marschik et al. (2003b)
PC97008	Copiapó Plutonic Complex	Dio.	115	0.045	0.70343	0.70322	0.260	0.512881	5.3	0.51276	-	Marschik et al. (2003b)
PC97009	Copiapó Plutonic Complex	Ton.	110	0.079	0.70356	0.70320	0.250	0.512841	4.6	0.51273	-	Marschik et al. (2003b)
PC97002	Copiapó Plutonic Complex	Mdi.	111.5	0.383	0.70495	0.70319	0.220	0.512877	5.6	0.51278	-	Marschik et al. (2003b)
PC97003	Copiapó Plutonic Complex	Mdi.	111.5	0.22	0.70408	0.70307	0.220	0.512852	5.1	0.51276	-	Marschik et al. (2003b)
MB3	Coastal Range intrusive rocks	Grd.	142	0.6	0.70510	0.70390	0.107	0.512720	3.2	0.51263	-	Ramírez et al. (2008)
MB4	Coastal Range intrusive rocks	Grd.	142	0.605	0.70480	0.70360	0.113	0.512740	3.5	0.51264	-	Ramírez et al. (2008)
MB-sp-7	Coastal Range intrusive rocks	Dio.	142	4.94	0.71452	0.74549	0.162	0.512646	0.77	0.51250	-	Ramírez et al. (2008)
MB-sp-46	Coastal Range intrusive rocks	Dio.	142	4.04	0.71374	0.70559	0.121	0.512694	2.45	0.51258	-	Ramírez et al. (2008)
MB-sp-60	Coastal Range intrusive rocks	Dio.	142	2.42	0.71061	0.70573	0.123	0.512569	-0.03	0.51246	-	Ramírez et al. (2008)
F-51	Los Pelambres porphyries	Ton.	9.9	-	0.70456	0.70439	-	0.512619	-	-	-0.25	Reich et al. (2003)
LP-48	Los Pelambres porphyries	Ton.	9.9	-	0.70471	0.70465	-	0.512635	-	-	0.06	Reich et al. (2003)
LP-75	Los Pelambres porphyries	Ton.	9.9	-	0.70468	0.70461	-	0.512626	-	-	-0.11	Reich et al. (2003)
G-318	La Gloria pluton	Grd.	9.8	-	0.70408	0.70401	-	0.512771	-	-	2.7	Reich et al. (2003)
C9G-170	Sierra Pajas Blancas granodiorite	Ton.	105.9	0.336	0.70387	0.70337	0.116	0.512873	-	0.51279	5.7	Girardi (2014)
CaB-171a	Sierra Pajas Blancas granodiorite	Ton.	106.8	0.289	0.70370	0.70326	0.107	0.512880	-	0.51281	5.9	Girardi (2014)
C9G-074	La Borracha pluton	Dio.	111	1.421	0.70552	0.70327	0.128	0.512889	-	0.51280	5.9	Girardi (2014)
C9G-210	Sierra Atacama diorite	Dio.	116.5	0.575	0.70410	0.70315	0.134	0.512889	-	0.51279	5.8	Girardi (2014)
CaB-296	Felsic near to Sierra Chicharra	Grt.	127.3	5.576	0.71347	0.70339	0.123	0.512848	-	0.51275	5.3	Girardi (2014)
C9G-128a	Sierra Chicharra quartz-diorite	Dio.	128.5	0.616	0.70461	0.70348	0.148	0.512873	-	0.51275	5.4	Girardi (2014)
C9G-140	Sierra Chicharra quartz-diorite	Dio.	130.1	0.192	0.70408	0.70372	0.150	0.512810	-	0.51268	4.1	Girardi (2014)
C9G-108c	Felsic near to Sierra Chicharra	Ton.	130.7	0.553	0.70441	0.70338	0.150	0.512876	-	0.51275	5.4	Girardi (2014)
C9G-320	C° Moradito pluton	Ton.	136.6	0.351	0.70409	0.70341	0.147	0.512918	-	0.51279	6.3	Girardi (2014)
C9G-514b	Felsic near to Moradito area	Ton.	137	0.342	0.70414	0.70347	0.138	0.512853	-	0.51273	5.2	Girardi (2014)
CaB-004b	Felsic near to Moradito area	Ton.	137.1	0.55	0.70453	0.70345	0.127	0.512804	-	0.51269	4.5	Girardi (2014)
CaB-295	C° Morado pluton	Dio.	137.5	0.457	0.70431	0.70341	0.140	0.512851	-	0.51273	5.2	Girardi (2014)
C9G-388	Sierra El Roble pluton	Ton.	164.4	2.915	0.70998	0.70317	0.131	0.512791	-	0.51265	4.4	Girardi (2014)
CaB-292	C° Chascon granodiorite	Grd.	195.5	0.884	0.70629	0.70383	0.134	0.512586	-	0.51241	0.5	Girardi (2014)
CaB-293	Puerto Viejo monzogranite	Ton.	196.1	1.638	0.70904	0.70447	0.133	0.512555	-	0.51239	0	Girardi (2014)
CaB-294	Permian pluton	Grt.	256	3.076	0.71965	0.70845	0.134	0.512397	-	0.51216	-3	Girardi (2014)
CBR-5	Limarí Complex	Grt.	203	-	0.75137	0.71540	-	0.512541	-0.6	0.51235	-	Parada et al. (1999)
TEN-32	Limarí Complex	Grt.	203	-	0.78059	0.71210	-	0.512549	-0.7	0.51234	-	Parada et al. (1999)
CBR-1A	Papudo-Quintero Complex	Ton.	170	-	0.70621	0.70470	-	0.512683	2.2	0.51253	-	Parada et al. (1999)
CBV-69	Papudo-Quintero Complex	Grt.	164	-	0.70750	0.70440	-	0.512570	0.9	0.51248	-	Parada et al. (1999)
CBV-75	Papudo-Quintero Complex	Grt.	164	-	0.70693	0.70340	-	0.512767	3.7	0.51262	-	Parada et al. (1999)
CBV-67	Papudo-Quintero Complex	Ton.	164	-	0.70594	0.70400	-	0.512742	3	0.51258	-	Parada et al. (1999)
F2-9	Papudo-Quintero Complex	Ton.	164	-	0.70556	0.70380	-	0.512697	2.4	0.51255	-	Parada et al. (1999)
CBV-73	Papudo-Quintero Complex	Dio.	164	-	0.70384	0.70340	-	0.512740	3.3	0.51260	-	Parada et al. (1999)

ESM – Table 11. (continued)

Sample	Unit	Petrography	Age (Ma)	$^{87}Rb/^{86}Sr$	$^{87}Sr/^{86}Sr$	I_{Sr}	$^{147}Sm/^{144}Nd$	$^{143}Nd/^{144}Nd$	εNd	I_{Nd}	$εNd_i$	Reference
060496-1	Illapel Complex	Trond.	109	-	0.70415	0.70370	-	0.512810	4.3	0.51272	-	Parada et al. (1999)
060496-2	Illapel Complex	Grd.	94	-	0.70480	0.70340	-	0.512809	4.5	0.51275	-	Parada et al. (1999)
060496-3	Illapel Complex	Trond.	94	-	0.70355	0.70350	-	0.512882	5	0.51277	-	Parada et al. (1999)
060496-4	Illapel Complex	Ton.	91	-	0.70409	0.70340	-	0.512821	4.3	0.51274	-	Parada et al. (1999)
060496-5	Illapel Complex	Ton.	91	-	0.70495	0.70390	-	0.512873	5.4	0.51280	-	Parada et al. (1999)
CHY-06	Elqui Complex - Guanta Unite	Grd.	307	0.52428	0.70795	0.70566	0.094	0.512255	-7.5	-	-3.4	Parada (2013)
CA99-1	Caleu Pluton	-	125	-	0.70341	0.70323	-	0.512893	-	0.51279	5.7	Parada et al. (2002)
970118-3	Caleu Pluton	-	125	-	0.70415	0.70325	-	0.512854	-	0.51276	5.1	Parada et al. (2002)
CA99-6	Caleu Pluton	-	125	-	0.70438	0.70330	-	0.512905	-	0.51280	5.9	Parada et al. (2002)
970121	Caleu Pluton	-	125	-	0.70446	0.70331	-	0.512916	-	0.51283	6.5	Parada et al. (2002)
CA99-7	Caleu Pluton	-	125	-	0.70452	0.70322	-	0.512906	-	0.51281	6.1	Parada et al. (2002)
970524-3	Caleu Pluton	-	125	-	0.70442	0.70333	-	0.512919	-	0.51281	6.1	Parada et al. (2002)
CA99-4	Caleu Pluton	-	125	-	0.70703	0.70330	-	0.512916	-	0.51281	5.9	Parada et al. (2002)
970616-1	Caleu Pluton	-	125	-	0.70688	0.70336	-	0.512913	-	0.51281	6	Parada et al. (2002)
GIS155	Los Carricitos Plutonic Complex	Ton.	221	-	0.71253	0.70944	-	0.512232	-7.9263	0.51201	-6.5994	Murillo et al. (2017)
GUF-04	Los Carricitos Plutonic Complex	Grd.	221	-	0.72054	0.70585	-	0.512448	-3.7157	0.51222	-2.7002	Murillo et al. (2017)
GUR-139	Piuquenes Monzogranites	Grt.	239.5	-	0.71822	0.70783	-	0.512310	-6.4043	0.51208	-4.8303	Murillo et al. (2017)
GUR-164	Los Carricitos Plutonic Complex	Grd.	221	-	0.71128	0.70605	-	0.512427	-4.1247	0.51226	-2.0381	Murillo et al. (2017)
GUR-166	Los Carricitos Plutonic Complex	Grt.	221	-	0.70748	0.70590	-	0.512350	-5.6137	0.51218	-3.479	Murillo et al. (2017)
GUR-170	Los Carricitos Plutonic Complex	Ton.	221	-	0.70726	0.70606	-	0.512329	-6.0185	0.51215	-3.9921	Murillo et al. (2017)
GUR-190	Los Carricitos Plutonic Complex	Grt.	221	-	0.72798	0.70614	-	0.512499	-2.7033	0.51235	-0.1979	Murillo et al. (2017)
S-type granitoids												
RCM-077q	Chacaicito Pluton	Sgr.	329	226.125	0.74926	-0.30963	0.158	0.512335	-5.91	0.51200	−4.27	Oliveros et al. (2020)
MCM-129q	Chanchoquín Plutonic Complex	Mzd.	297	0.85709	0.71383	0.71028	0.161	0.512116	-10.18	0.51181	−8.87	Oliveros et al. (2020)
RCM-133q	Chanchoquín Plutonic Complex	Grd.	293.2	8.39507	0.71069	0.67566	0.125	0.512337	-5.87	0.51210	−3.20	Oliveros et al. (2020)
SCL-02q	Chollay Plutonic Complex	Mgr.	245.5	9.52612	0.72895	0.69568	0.117	0.512498	-2.74	0.51231	−0.25	Oliveros et al. (2020)
SCL-09q	Chollay Plutonic Complex	Grd.	245.5	1.28993	0.70908	0.70458	0.115	0.512433	-4	0.51225	−1.44	Oliveros et al. (2020)
MCM-022q	Chollay Plutonic Complex	Sgr.	248.2	3.31275	0.71641	0.70471	0.114	0.512345	-5.72	0.51216	−3.09	Oliveros et al. (2020)
MCM-265q	Chollay Plutonic Complex	Mgr.	239.7	0.03581	0.71079	0.71067	0.113	0.512415	-4.35	0.51224	−1.80	Oliveros et al. (2020)
RCM-040q	Chollay Plutonic Complex	Ton.	234.9	271.909	0.75763	-0.15086	0.209	0.512396	-4.72	0.51207	−5.10	Oliveros et al. (2020)
O7–06	Montegrande Granite	Grt.	214.7	2.56141	0.71741	0.70961	0.082	0.512199	-8.56	0.51209	−5.42	Oliveros et al. (2020)
O7–07	Montegrande Granite	Grt.	214.7	12.3136	0.73941	0.70194	0.096	0.512505	-2.59	0.51237	0.16	Oliveros et al. (2020)
CPV-14-192	Pan de Azúcar Pluton	Grt.	276.6	13.3446	0.76429	0.71283	0.164	0.512354	-5.54	0.51206	−4.42	Oliveros et al. (2020)
CPV-15-320	Sierra de Doña Inés Chica	Mzd.	285.3	0.90569	0.71325	0.70958	0.126	0.512304	-6.52	0.51207	−3.94	Oliveros et al. (2020)
CHY-07	Elqui Complex - Cochiguaz Unite	Mgr.	286	1.08021	0.71284	0.70844	0.105	0.512166	-9.2	-	-5.9	Parada (2013)
CHY-05	Elqui Complex - Cochiguaz Unite	Mgr.	315	2.58529	0.71732	0.70570	0.105	0.512350	-5.6	-	-1.9	Parada (2013)
H219	Cochiguás Plutonic Complex	-	301	-	0.71133	0.70650	-	0.512144	-	-	-5.3	Mpodozis & Kay (1992)
Mafic-ultramafic magmatism												
O7–10	La Laguna Gabbro	Gab.	218.1	0.31153	0.70691	0.70594	0.132	0.512463	-3.41	0.51227	−1.62	Oliveros et al. (2020)

ESM – Table 11. (continued)

Sample	Unit	Petrography	Age (Ma)	$^{87}Rb/^{86}Sr$	$^{87}Sr/^{86}Sr$	I_{Sr}	$^{147}Sm/^{144}Nd$	$^{143}Nd/^{144}Nd$	εNd	I_{Nd}	$εNd_i$	Reference
O7–11	La Laguna Gabbro	Gab.	218.1	0.35731	0.70678	0.70568	0.133	0.512482	-3.04	0.51229	−1.26	Oliveros et al. (2020)
CaB-246	Sierra Atacama diorite	Gab.	101.7	0.013	0.70340	0.70338	0.155	0.512913	-	0.51281	5.9	Girardi (2014)
CaB-211b	Gabbro	Gab.	134.5	0.07	0.70361	0.70348	0.170	0.512921	-	0.51277	6	Girardi (2014)
C9G-386b	Caldera Gabbro	Gab.	181.5	0.433	0.70481	0.70369	0.151	0.512774	-	0.51260	3.7	Girardi (2014)
F2-25A	Santo Domingo Complex	Maf. Enclave	308	-	0.70723	0.70570	-	0.512451	-2	0.51214	-	Parada et al. (1999)
F2-29	Santo Domingo Complex	Maf. Enclave	308	-	0.70749	0.70570	-	0.512337	-3.5	0.51206	-	Parada et al. (1999)
CBR-7	Limarí Complex	Gab.	203	-	0.70477	0.70350	-	0.512808	3.6	0.51256	-	Parada et al. (1999)
D-18A	Limarí Complex	Gab.	203	-	0.70361	0.70330	-	0.512867	4.6	0.51261	-	Parada et al. (1999)
CBR-1E	Papudo-Quintero Complex	Maf. Enclave	170	-	0.70430	0.70380	-	0.512680	1.9	0.51252	-	Parada et al. (1999)
F2-5	Papudo-Quintero Complex	Maf. Enclave	164	-	0.70385	0.70350	-	0.512762	3.6	0.51261	-	Parada et al. (1999)
F2-6	Papudo-Quintero Complex	Maf. Enclave	164	-	0.70575	0.70340	-	0.512700	2.2	0.51254	-	Parada et al. (1999)
CT-193q	Chollay Plutonic Complex	Gab.-Dio.	242.1	-	0.70914	0.70698	-	0.512333	-	0.51212	-4.13	Salazar et al. (2013)
cc-03-01	Concon mafic dike swarms	-	160	-	0.70387	0.70361	-	0.512649	-	0.51250	1.29	Creixell (2007)
cc-03-32	Concon mafic dike swarms	-	160	-	0.70496	0.70348	-	0.512678	-	0.51254	2.01	Creixell (2007)
cc-03-42	Cartagena mafic dike swarms	-	160	-	0.70667	0.70461	-	0.512660	-	0.51249	1.15	Creixell (2007)
cc-03-27	El Tabo mafic dike swarms	-	140	-	0.70721	0.70594	-	0.512525	-	0.51238	-1.5	Creixell (2007)
cc-03-38	El Tabo mafic dike swarms	-	140	-	0.70488	0.70353	-	0.512511	-	0.51238	-1.56	Creixell (2007)
cc-03-24	El Tabo mafic dike swarms	-	140	-	0.70649	0.70528	-	0.512698	-	0.51255	1.7	Creixell (2007)
cc-04-51	El Tabo mafic dike swarms	-	140	-	0.70565	0.70482	-	0.512851	-	0.51270	4.65	Creixell (2007)
cc-03-62	El Tabo mafic dike swarms	-	140	-	0.70519	0.70439	-	0.512661	-	0.51250	1.38	Creixell (2007)
cc-04-15	Elqui mafic dike swarms	-	200	-	0.70596	0.70506	-	0.512719	-	0.51253	2.88	Creixell (2007)
cc-04-29	Elqui mafic dike swarms	-	200	-	0.70456	0.70438	-	0.512665	-	0.51248	1.99	Creixell (2007)
cc-04-34	Elqui mafic dike swarms	-	200	-	0.70497	0.70413	-	0.512832	-	0.51266	5.35	Creixell (2007)
cc-04-40	Elqui mafic dike swarms	-	200	-	0.70495	0.70413	-	0.512835	-	0.51264	5.06	Creixell (2007)
CT-228q	Chollay Plutonic Complex	Grd.	249	-	0.71335	0.70836	-	0.512279	-	0.51208	-4.56	Salazar et al. (2013)
CT-167q	Chollay Plutonic Complex	Ton.	237.6	-	0.70648	0.70582	-	0.512419	-	0.51219	-2.74	Salazar et al. (2013)
F2-24	Santo Domingo Complex	Grt.	308	-	0.72784	0.70980	-	0.512249	-4.2	0.51203	-	Parada et al. (1999)
F2-25	Santo Domingo Complex	Ton.	308	-	0.70688	0.70600	-	0.512336	-1.7	0.51216	-	Parada et al. (1999)
F2-28	Santo Domingo Complex	Ton.	308	-	0.70898	0.70660	-	0.512339	-3	0.51209	-	Parada et al. (1999)
Additionally analyses												
PdC-A	Lower Andesite - Pta. Cobre Fm.	And	135	2.5695	0.71205	0.70712	-	0.512712	1.45	0.51271	4.83	This work
COP10	Lower Andesite - Pta. Cobre Fm.	And	135	0.0617	0.70415	0.70403	0.138	0.512939	5.86	0.51281	6.88	This work
COP16	Volcanic sedimentary - Pta. Cobre Fm.	Breccia	132	0.9968	0.70495	0.70308	0.147	0.512925	5.59	0.51279	6.42	This work
COP15	Dacite - Pta. Cobre Fm.	Dacite	132	6.1422	-	-	0.112	0.512791	2.98	0.51269	4.41	This work
COP1	Upper Andesite - Pta. Cobre Fm.	Metandesite	132	0.2792	0.7099	0.70937	0.135	0.512987	6.81	0.51287	7.84	This work
COP08	Upper Andesite - Pta. Cobre Fm.	Metandesite	132	10.789	0.70314	0.68289	-					This work
COP18b	Upper Andesite	Metandesite	132	0.1455	0.70535	0.70507	0.138	0.512859	4.30	0.51274	5.30	This work
COP18a	Upper Andesite	Metandesite	132	1.7082	0.70442	0.70121	-	0.512811	3.38	0.51281	6.69	This work

Sample	Unit	Petrography	Age (Ma)	$^{87}Rb/^{86}Sr$	$^{87}Sr/^{86}Sr$	I_{Sr}	$^{147}Sm/^{144}Nd$	$^{143}Nd/^{144}Nd$	εNd	I_{Nd}	$εNd_i$	Reference
COP20	Upper Andesite	Metandesite	132	0.1004	0.70483	0.704642	0.199	0.513068	8.39	0.51289	8.34	This work
COP11	La Brea Phase - Copiapó Batholith	-	118	0.3334	0.70419	0.703631	0.124	0.512913	5.37	0.51281	6.45	This work
COP13	Los Lirios Phase - Copiapó Batholith	-	110	5.2610	0.71288	0.704656	0.119	0.512946	6.00	0.51286	7.09	This work

Abbreviations: *Alb – albitophyre; And – andesite; Ap – apatite; Act – actinolite; Bas – basalt; Bath. – batholith; C° – Cerro (Hill); Comp. – complex; Dac – dacite; Dia – diabase; Dio – diorite; Fm. – Formation; Gab – gabbro; Gran – granulite; Grd – granodiorite; Grt – granite; Lat – latite; Maf. Enc. – mafic enclave; Mgr – monzogranite; Mzd – monzodiorite; Php – porphyry; Qtz – quartz; Rhy – rhyolite; Sgr – syenogranite; Trach – trachyandesite; Trond – trondhjemite; WR – whole rock.*

Supplementary 11 - References

Bartsch, V., 2004. Magmengenese der obertriasssischen bis unterkretazischen Vulkanite in der Ku¨ stenkordillere von Nord-Chile zwischen 24° und 27°S. PhD. dissertation. Technical University of Berlin, Germany.

del Rey, Á., Deckart, K., Planavsky, N., Arriagada, C., Martínez, F., 2019. Tectonic evolution of the southwestern margin of Pangea and its global implications: Evidence from the mid Permian–Triassic magmatism along the Chilean-Argentine border. Gondwana Res. 76, 303–321. https://doi.org/10.1016/j.gr.2019.05.007

Creixell, C., 2007. Petrogénesis y emplazamiento de enjambre de diques máficos Mesozoicos de Chile Central: Implicancias tectónicas en el desarrollo del arco Jurásico-Cretácico temprano. PhD. thesis. University of Chile, Chile.

Girardi, J.D., 2014. Comparison of Mesozoic magmatic evolution and iron oxide (-copper-gold) ('IOCG') mineralization, Central Andes and western North America. PhD. thesis dissertation. The University of Arizona, USA.

Lucassen, F., Kramer, W., Bartsch, V., Wilke, H.-G., Franz, G., Romer, R.L., Dulski, P., 2006. Nd, Pb, and Sr isotope composition of juvenile magmatism in the Mesozoic large magmatic province of northern Chile (18–27°S): indications for a uniform subarc mantle. Contrib. Mineral. Petrol. 152, 571–589. https://doi.org/10.1007/s00410-006-0119-y

Marschik, R., Fontignie, D., Chiaradia, M., Voldet, P., 2003b. Geochemical and Sr–Nd–Pb–O isotope composition of granitoids of the Early Cretaceous Copiapó plutonic complex (27° 30′ S), Chile. J. S. Am. Earth Sci. 16, 381–398. https://doi.org/10.1016/S0895-9811(03)00104-4

Morata, D., Aguirre, L., 2003. Extensional Lower Cretaceous volcanism in the Coastal Range (29°20′–30°S), Chile: geochemistry and petrogenesis. J. S. Am. Earth Sci. 16, 459–476. https://doi.org/10.1016/j.jsames.2003.06.001

Ramírez, L.E., Parada, M.A., Palacios, C., Wittenbrink, J., 2008. Magmatic evolution of the Mantos Blancos copper deposit, Coastal Range of northern Chile: insight from Sr–Nd isotope, geochemical data and silicate melt inclusions. Resour. Geol. 58, 124–142. https://doi.org/10.1111/j.1751-3928.2008.00049.x

Reich, M., Parada, M.A., Palacios, C., Dietrich, A., Schultz, F., Lehmann, B., 2003. Adakite-like signature of Late Miocene intrusions at the Los Pelambres giant porphyry copper deposit in the Andes of central Chile: metallogenic implications. Miner. Deposita 38, 876–885. https://doi.org/10.1007/s00126-003-0369-9

Rossel, P., Oliveros, V., Ducea, M.N., Charrier, R., Scaillet, S., Retamal, L., Figueroa, O., 2013. The Early Andean subduction system as an analog to island arcs: Evidence from cross-arc geochemical variations in northern Chile. Lithos, 179, 211–230. https://doi.org/10.1016/j.lithos.2013.08.014

Oliveros, V., Vásquez, P., Creixell, C., Lucassen, F., Ducea, M.N., Ciocca, I., González, J., Espinoza, M., Salazar, E., Coloma, F., Kasemann, S.A., 2020. Lithospheric evolution of the Pre-and Early Andean convergent margin, Chile. Gondwana Res. 80, 202–227. https://doi.org/10.1016/j.gr.2019.11.002

Palma, G., Barra, F., Reich, M., Valencia, V., Simon, A.C., Vervoort, J. Leisen, M., Romero, R., 2019. Halogens, trace element concentrations, and Sr-Nd isotopes in apatite from iron oxide-apatite (IOA) deposits in the Chilean iron belt: Evidence for magmatic and hydrothermal stages of mineralization. Geochim. Cosmochim. Acta 246, 515–540. https://doi.org/10.1016/j.gca.2018.12.019

CHAPTER 4 – CONCLUSIONS AND RECOMMENDATIONS

This study provided new clues on the source of metals from IOCG systems by combining Sr-Nd isotopes and trace elements applied on Cu-Au and Fe minerals together with an extensive data compilation from literature. Based on this view, we can conclude that:

- Heterogeneity in the source of metals from the Carajás Mineral Province can be interpreted from the $^{87}Sr/^{86}Sr_i$ against εNd(t) plot.
- Prolongated crustal residence times on magnetite and chalcopyrite concentrates ($T_{DM\text{-}IOCG}$ = 3.35–2.74 Ga) and the $\varepsilon Nd_{(t)}$ data (εNd_{IOCG} = –3.30 to +2.19) suggest that initial mineralizing fluids and metals for Neoarchean IOCG (Salobo, Sequeirinho, and Alemão), were probably derived from reworked ancient crust through the leaching of Mesoarchean basement rocks. However, the assimilation and/or contribution from Neoarchean juvenile mantellic components were also involved in their genesis.
- The generation of specialized magmas throughout the province could have exerted the primary heat source for regional circulation of previously formed mineralizing fluids, rather than the source of metals.
- The metal source for magnetite and chalcopyrite in the Orosirian Cu-Au systems ($T_{DM\ Cu\text{-}Au}$ = 3.22–2.71 Ga; $\varepsilon Nd_{Cu\text{-}Au}$ = –11.68 to –9.22) involves derivation from Archean igneous crustal sources.
- Cretaceous IOCG deposits from the Candelaria-Punta del Cobre district derived metals from primitive sources compositionally similar to the arc-volcanic rocks, probably by heterogeneities in the mantle source, rather than a single specialized source.
- Trace element and REE data suggest more mafic compositions in Carajás IOCG and Cu-Au deposits rather than Andean IOCG deposits.
- Long periods of incubations for metals is a requirement for Cu-Au precipitation during tectonic shifts.

REFERENCES

These references were used to elaborate the Chapter I and II from this work.

Amilibia, A., 2009. Compressional deformation along the Chañarcillo basin west margin: North Chilean Late Jurassic-Early Cretaceous back-arc basin: Trabajos Geológicos. Univ. Oviedo 29, 78–83.

Anthony, J. W., Bideaux, R. A., Bladh, K. W., Nichols M. C., 1990. Handbook of Mineralogy, Mineral Data Publishing, Tucson Arizona, USA, 4.

Araújo, O. J. B., Maia, R. G. N., Jorge-João, X. S., Costa, J. B. S., 1988. A megaestruturação Arqueana da Folha Serra dos Carajás. In: 7th Congresso Latino Americano de Geologia. Belém, SBG, 324–338.

Arévalo, C., 1999. The Coastal Cordillera/Precordillera Boundary in the Tierra Amarilla area (27° 20′ 27 40′S/70° 05′–70 20′W), northern Chile, and the structural setting of the Candelaria Cu-Au ore deposit: Unpublished. PhD. thesis. University of Queens, Kingston, Canada.

Arévalo, C. 2005a. Carta Los Loros, Región de Atacama. Servicio Nacional de Geología y Minería. Carta Geológica de Chile. Serie Geología Básica, 92, 53, 1. Mapa escala 1:100.000.

Arévalo, C. 2005b. Carta Copiapó, Región de Atacama. Servicio Nacional de Geología y Minería. Carta Geológica de Chile, Serie Geología Básica, 92, 53, 1. Mapa escala 1:100.000.

Arévalo, C., Grocott, J., Martin, W., Pringle, M., Taylor, G., 2006. Structural setting of the Candelaria Fe-oxide Cu-Au deposit, Chilean Andes (27° 30′ S). Econ. Geol. 101, 819–841.

Austin, J., Björk, A., Patterson, B., 2019. Structural controls of the Ernest Henry IOCG deposit: Insights from integrated structural, geophysical and mineralogical analyses. ASEG Extended Abstracts, 1, 1–5.

Avelar, V. G., Lafon, J. M., Correia Jr, F. C., Macambira, E. M. B., 1999. O Magmatismo arqueano da região de Tucumã-Província Mineral de Carajás: novos resultados geocronológicos. Revista Brasileira de Geociências, 29, 453–460.

Baba, A. A., Ayinla, K. I., Adekola, F. A., Ghosh, M. K., Ayanda, O. S., Bale, R. B., Sheik, A. R., Pradhan, S. R., 2012. A review on novel techniques for chalcopyrite ore processing. International Journal of Mining Engineering and Mineral Processing, 1, 1-16.

Balaram, V., 2019. Rare earth elements: A review of applications, occurrence, exploration, analysis, recycling, and environmental impact. Geoscience Frontiers.

Barbosa, J. P. O., 2004. Geologia estrutural, geoquímica, petrografia e geocronologia de granitóides da região de Igarapé Gelado, Norte da Província Mineral de Carajás. University of Pará, Brazil.

Barreira, C. F., Soares, A. D. V., Ronzê, P. C., 1999 Descoberta do depósito Cu–Au Alemão—Província Mineral de Carajás (PA). In: SBG, 6° Simpósio de Geologia da Amazônia, Manaus, Bol Res Expandidos, 6, 136–139

Barros, C. E. D. M., Macambira, M. J. B., Barbey, P., Scheller, T., 2004. Dados isotópicos Pb-Pb em zircão (evaporação) e Sm-Nd do Complexo Granítico Estrela, província Mineral de carajás, Brasil: implicações petrológicas e tectônicas. Revista Brasileira de Geociências, 34, 531–538.

Barton, M.D., 2014. Iron oxide (–Cu–Au–REE–P– Ag–U–Co) systems. In: Holland, H.D., Turekian, K.K. (Eds.), Treatise on Geochemistry, second ed. Elsevier, Oxford, 515–541.

Barton, M. D., Jensen, E. P., Ducea, M., 2005. Fluid Sources for IOCG (Candelaria, Punta del Cobre) and Porphyry Cu-Style Mineralization, Copiapó batholith, Chile, Geologic and Sr Isotopic Constraints. Salt Lake City Annual Meeting.

Barton, M. D., Johnson, D. A., 1996. Evaporitic-Source Model for Igneous-Related Fe Oxide (REE-CuAu-U) Mineralization: Geology (Boulder), 24, 259–262.

Barton, M. D., Johnson, D. A., 2000. Alternative brine sources for Fe-Oxide(-Cu-Au) systems: Implications for hydrothermal alteration and metals. In: Porter, T.M. (Ed.), Hydrothermal Iron Oxide Copper-Gold & Related Deposits: A Global Perspective, Australian Mineral Foundation, 1, 43–60.

Becker, M., De Villiers, J., Bradshaw, D., 2010. The mineralogy and crystallography of pyrrhotite from selected nickel and PGE ore deposits. Economic Geology, 105, 1025-1037.

Belzile, N., Chen, Y.-W., Cai, M.-F., Li, Y., 2004. A review of pyrrhotite oxidation: Journal of Geochemical Exploration, 84, 65–76

Benavides, J., Kyser, T. K., Clark, A. H., Oates, C. J., Zamora, R., Tarnovschi, R., Castillo, B., 2007. The Mantoverde iron oxide-copper-gold district, III Región, Chile: the role of regionally derived, non-magmatic fluids in chalcopyrite mineralization. Economic Geology, 102, 415–440.

Beni, Z. H. M., Panahpour, E., 2015. Geochemistry of rare earth elements of magnetite and apatite in choghartiron depositand comparison with kirunairon depositand study the origin of choghart deposit (Bafq, Central Iran).

Biagioni, C., Pasero, M., 2014. The systematics of the spinel-typeminerals: An overview. Am Mineral , 99, 1254–1264.

Bilenker, L. D., Weis, D., Scoates, J. S., Perry, E., 2018. The application of Stable Fe isotopes to magmatic sulfide systems: constraints on the Fe isotope composition of magmatic pyrrhotite. Economic Geology, 113, 1181–1192.

Bonyadi, Z., Davidson, G. J., Mehrabi, B., Meffre, S., Ghazban, F., 2011. Significance of apatite REE depletion and monazite inclusions in the brecciated Se–Chahun iron oxide–apatite deposit, Bafq district, Iran: Insights from paragenesis and geochemistry. Chemical Geology, 281, 253–269

Cao, J., Wu, Q., Yang, X., Kong, H., Li, H., Xi, X., Huang, Q., Liu, B., 2018. Geochronology and Genesis of the Xitian W-Sn Polymetallic Deposit in Eastern Hunan Province, South China: Evidence from Zircon U-Pb and Muscovite Ar-Ar Dating, Petrochemistry, and Wolframite Sr-Nd-Pb Isotopes. Minerals, 8, 111.

Carr, G.R., Dean, J.A., Suppel, D.W., Heithersay, P.S., 1995. Precise lead isotope fingerprinting of hydrothermal activity associated with Ordovician to Carboniferous metallogenic events in the Lachlan fold belt of New South Wales. Economic Geology, 90, 1477–1505.

Carvalho, E. R., 2009. Caracterização geológica e gênese das mineralizações de óxido de Fe-Cu-Au e metais associados na Província Mineral de Carajás: estudo de caso do depósito de Sossego. D dissertation, Campinas, Brazil, Universidade Estadual de Campinas.

Castillo, B., Zamora, R., 2003. Iron Oxide Copper (Gold) Mineralization in the Mantoverde District, Atacama Region, Northern Chile. In: 10° Congreso Geológico Chileno, 2003, Universidad de Concepción, Chile.

Cave, B., Lilly, R., Glorie, S., Gillespie, J., 2018. Geology, Apatite Geochronology, and Geochemistry of the Ernest Henry Inter-lens: Implications for a Re-Examined Deposit Model. Minerals, 8, 405.

Chapman, N. D., Ferguson, M., Meffre, S. J., Stepanov, A., Maas, R., Ehrig, K. J., 2019. Pb-isotopic constraints on the source of A-type Suites: Insights from the Hiltaba Suite-Gawler Range Volcanics Magmatic Event, Gawler Craton, South Australia. Lithos, 346, 105156.

Champion, D. C., 2013. Neodymium depleted mantle model age map of Australia: explanatory notes and user guide. Geoscience Australia.

Champion, D. C., Huston, D. L., 2016. Radiogenic isotopes, ore deposits and metallogenic terranes: Novel approaches based on regional isotopic maps and the mineral systems concept. Ore Geology Reviews, 76, 229–256.

Charrier, R., Pinto, L., Rodríguez, M. P., 2007. Tectonostratigraphic evolution of the Andean Orogen in Chile. In: Moreno, T., Gibbons, W. (Eds), The geology of Chile. Geological Society of London, 21–114.

Chappell, B. W., White, A., 1974. Two contrasting granite types: Pacific Geology, 8, 173–174.

Chen, H., 2013. External sulphur in IOCG mineralization: Implications on definition and classification of the IOCG clan. Ore Geology Reviews, 51, 74-78

Chen, H., Cooke, D. R., Baker, M. J., 2013. Mesozoic iron oxide copper-gold mineralization in the central Andes and the Gondwana Supercontinent breakup. Economic Geology, 108, 37-44.

Cherry, A. R., Ehrig, K., Kamenetsky, V. S. McPhie, J., Crowley, J. L., Kamenetsky, M. B., 2018. Precise geochronological constraints on the origin, setting and incorporation of ca. 1.59 Ga surficial facies into the Olympic Dam Breccia Complex, South Australia. Precambrian Research, 315, 162–178.

Childress, T., 2019. Fingerprinting Source Fluids of Iron Oxide-Copper-Gold and Iron Oxide-Apatite Deposits Using Traditional and Non-Traditional Stable Isotope Geochemistry. PhD. Thesis, University of Michigan, USA

Chorlton, L. B., 2007. Generalized geology of the world: bedrock domains and major faults in GIS format: a small-scale world geology map with an extended geological attribute database, Geological Survey of Canada, Open File 5529.

Ciobanu, C. L., Cook, N. J., Ehrig, K., 2017. Ore minerals down to the nanoscale: Cu-(Fe)-sulphides from the iron oxide copper gold deposit at Olympic Dam, South Australia. Ore Geol Rev, 81, 1218–1235.

Cohen, K. M., Harper, D. A. T., Gibbard, P. L., 2019. ICS International Chronostratigraphic Chart 2019/05. International Commission on Stratigraphy.

Cook, N. J., Ciobanu, C. L., Danyushevsky, L. V., Gilbert, S., 2011. Minor and trace elements in bornite and associated Cu–(Fe)-sulfides: A LA-ICP-MS study Bornite mineral chemistry. Geochimica et Cosmochimica Acta, 75, 6473-6496.

Cordani, U., 1981. Comentários sobre as determinações geocronológicas da região da Serra dos Carajás. Report,Universidade de São Paulo-Docegeo.

Cornejo, P., Mpodozis, C., Kay, S., Tomlinson, A., Ramirez, C., 1993. Upper Cretaceous-Lower Eocene potasic volcanism in an extensional regime in the precordillera of Copiapó, Chile. In: Second IASG, Oxford, 347-350.

Cornell R. M., Schwertmann U., 2003. The Iron Oxides: Structure, Properties, Reactions, Occurrences and Uses. WileyVCH Verlag GmbH & Co. KGaA, Weinheim, p. 664.

Corriveau, L., Bonnet, A. L., 2004. Diagnostic geological tools to recognize metamorphosed VHMS, sedex and iron oxide– Cu–Au hydrothermal systems in the Frontier high-grade meta morphic terrains of the Grenville Province. In: Geological Society of America, Abstracts with Programs, 35, 51.

Corvalán, D., 1973. Estratigrafía del Neocomiano Marino de la Región al sur de Copiapó, Provincia de Atacama. Revista Geológica de Chile, 13-36.

Costa, U. A. P., Paula, R. R., Silva, D. P. B., Barbosa, J. P. O., Silva, C. M. G., Tavares, F. M., Oliveira, J. K. M., Justo A. P. 2015. Programa Geologia do Brasil-PGB. Mapa de integração geológico-geofisica da ARIM Carajás. Estado do Pará, Belem. CPRM. Escala 1:250.000.

Courtney-Davies, L., Ciobanu, C. L., Verdugo-Ihl, M. R., Dmitrijeva, M., Cook, N. J., Ehrig, K., & Wade, B. P., 2019a. Hematite geochemistry and geochronology resolve genetic and temporal links among iron-oxide copper gold systems, Olympic Dam district, South Australia. Precambrian Research, 335, 105480.

Courtney-Davies, L., Tapster, S. R., Ciobanu, C. L., Cook, N. J., Verdugo-Ihl, M. R., Ehrig, K. J., Kennedy, A. K., Gilbert, S. E., Condon, D. J., Wade, B. P., 2019b. A multi-technique evaluation of hydrothermal hematite UPb isotope systematics: Implications for ore deposit geochronology. Chemical Geology, 513, 54-72.

Couture, J.F., Cole, G., Zhang, B., Nilsson, J., Dance, A., Scott, C., Vidal, M.I., 2017. Technical Report for the Candelaria Copper Mining Complex, Atacama Province, Region III, Chile: 43-101 Report. Prepared for Lundin Mining Corporation.

Couture, J., Cole, G., Nilsson, J., Zhang, B., Dance, A., Scott, C. C., Vidal, M. I., Kautzman, S., 2018. Technical Report for the Candelaria Copper Mining Complex, Atacama Province, Region III, Chile. 1-176 Report. Prepared for Lundin Mining Corporation

Dall'Agnol, R., Teixeira, N. P., Rämö, O. T., Moura, C. A. V., Macambira, M. J. B., Oliveira, D. C., 2005. Petrogenesis of the Paleoproterozoic rapakivi A-type granites of the Archean Carajás metallogenic province, Brazil. Lithos, 80, 101–129.

Daly, S. J., Fanning, C. M., Fairclough, M. C., 1998. Tectonic evolution and exploration potential of the Gawler Craton, South Australia. J Aust Geol Geophys, 17, 145–168.

Dare, S. A., Barnes, S. J., Beaudoin, G., Méric, J., Boutroy, E., Potvin-Doucet, C., 2014. Trace elements in magnetite as petrogenetic indicators. Mineralium Deposita, 49, 785-796.

Dardenne, M.A., Ferreira Filho, C.F., Meirelles, M.R., 1988. The role of shoshonitic and calc- alkaline suites in the tectonic evolution of the Carajás District, Brazil. Journal of South American Earth Sciences, 1, 363–372.

Debruyne, D., Hulsbosch, N., Muchez, P., 2016. Unraveling rare earth element signatures in hydrothermal carbonate minerals using a source-sink system. Ore Geology Reviews, 72, 232–252.

Dekov, V. M., Garbe-Schönberg, D., Kamenov, G. D., Guéguen, B., Bayon, G., Bindi, L., Asael, D., Fouquet, Y., 2018. Redox changes in a seafloor hydrothermal system recorded in hematite chalcopyrite chimneys. Chemical Geology, 483, 351–371.

del Real, I., Thompson, J. F., Carriedo, J., 2018. Lithological and structural controls on the genesis of the Candelaria-Punta del Cobre Iron Oxide Copper Gold district, Northern Chile. Ore Geology Reviews, 102, 106-153.

del Real, I., Thompson, J., 2019. Geology and Evolution of the Candelaria-Punta del Cobre IOCG District. In: South American Metallogeny: Sierra to Craton, Society of Economic Geologist, Santiago, Chile.

Delinardo, M. A. S., 2014. Metatexitos e diatexitos do Complexo Xingu na região de Canaã dos Carajás: implicações para a evolução mesoarqueana do Domínio Carajás. M. Sc. Dissertation, Universidade Estadual de Campinas.

Deng, X. H., Chen, Y. J., Bagas, L., Zhou, H. Y., Yao, J. M., Zheng, Z., Wang, P., 2015. Isotope (S–Sr–Nd–Pb) constraints on the genesis of the ca. 850 Ma Tumen Mo–F deposit in the Qinling Orogen, China. Precambrian Research, 266, 108-118.

Deng, X. H., Chen, Y. J., Santosh, M., Yao, J. M., Sun, Y. L., 2016. Re–Os and Sr–Nd–Pb isotope constraints on source of fluids in the Zhifang Mo deposit, Qinling Orogen, China. Gondwana Research, 30, 132-143.

DePaolo, D.J. 1981. A neodymium and strontium isotopic study of the Mesozoic calc-alkaline granitic batholiths of the Sierra Nevada and Peninsular Ranges, California. J. Geophysical Research, 86.

DePaolo, D. J., 1988. Age dependence of the composition of continental crust: evidence from Nd isotopic variations in granitic rocks. Earth and Planetary Science Letters, 90, 263-271.

DePaolo, D. J., Wasserburg, G. J., 1976. Inferences about magma sources and mantle structure from variations of $^{143}Nd/^{144}Nd$. Geophysical Research Letters, 3, 743-746.

Dias, G. S., Macambira, M. J. B., Dall'Agnol, R., Soares, A. D. V., Barros, C. E. M., 1996. Datações de zircões de sill de metagabro: comprovação de idade arqueana da Formação Águas Claras, Carajás, Pará. In: Simpósio de Geologia da Amazônia, 5, Sociedade Brasileira de Geologia, Belém, 376–378.

Dmitrijeva, M., Ehrig, K. J., Ciobanu, C. L., Cook, N. J., Verdugo-Ihl, M. R., Metcalfe, A. V., 2019. Defining IOCG signatures through compositional data analysis: A case study of lithogeochemical zoning from the Olympic Dam deposit, South Australia. Ore Geology Reviews, 105, 86-101.

DOCEGEO., 1988. Revisão litoestratigráfica da Província Mineral de Carajás—Litoestratigrafia e principais depósitos minerais. In: 35th Congresso Brasileiro de Geologia, Belém, 11–56 (Proceedings).

Dupuis, C., Beaudoin, G., 2011. Discriminant diagrams for iron oxide trace element fingerprinting of mineral deposit types. Miner Depos, 46, 319–335.

Domingos, F., 2009. The structural setting of the Canaã dos Carajás region and Sossego-Sequeirinho deposits, Carajás, Brazil. Doctoral dissertation, Durham University, England.

Ehrig, K., McPhie, J., Kamenetsky, V., 2012. Geology and mineralogical zonation of the Olympic Dam iron oxide Cu-U-Au-Ag deposit, South Australia. In: Hedenquist, J. W., Harris, M., Camus, F. (Eds), Geology and genesis of major copper deposits and districts of the world: a tribute to Richard H. Sillitoe. Soc of Econ Geol Spec Pub, 16, 237–267.

Einaudi, M. T., 1997. Mapping altered and mineralized rocks: An introduction to the Anaconda method.

Elizarova, I. R., Bayanova, T. B., 2012. Mass-spectrometric REE analysis in sulphide minerals. Journal of Biology and Earth Sciences, 2, E45-E49.

Fabre, S., Nédélec, A., Poitrasson, F., Strauss, H., Thomazo, C., Nogueira, A., 2011. Iron and sulphur isotopes from the Carajás mining province (Pará, Brazil): implications for the oxidation of the ocean and the atmosphere across the Archaean–Proterozoic transition. Chemical Geology, 289, 124-139.

Fanning, C. M., Reid, A. J., Teale, G. S., 2007. A geochronological framework for the Gawler Craton, South Australia. South Australia Geological Survey Bulletin, 55.

Faure, G., 1986. Principles of Isotope Geology. J. Wiley & Sons, Chichester, 1-589.

Faure, G., Powell, J.L., 1972. Strontium Isotope Geology. Springer-Verlag, Heidelberg. 188.

Ferguson, M. R. M., Ehrig, K., Meffre, S., Cherry, A. R., 2019. Associations between zircon and Fe–Ti oxides in Hiltaba event magmatic rocks, South Australia: atomic- or pluton-scale processes?. Australian Journal of Earth Sciences, 1–20.

Ferris, G. M., Schwarz, M. P., Heithersay, P., 2002. The Geological Framework, Distribution and Controls of Fe-Oxide Cu-Au Mineralisation in the Gawler Craton, South Australia. Part I–Geological and Tectonic Framework. In: Porter, T. M. (Ed), Hydrothermal iron oxide copper-gold and related deposits: A global perspective, 2, 9-31.

Fisher, L. A., Kendrick, M. A., 2008. Metamorphic fluid origins in the Osborne Fe oxide-Cu-Au deposit, Australia: evidence from noble gases and halogens. Mineral Deposits, 43, 483–497.

Flint, R. B., Blissett, A. H., Conor, C. H. H., Cowley, W. M., Cross, K. C., Creaser, R. A., Daly, S. J., Krieg, G. W., Major, R. B., Teale, G. S., Parker, A. J., 1993. Mesoproterozoic. In: Drexel, J. F., Preiss, W. V., Parker, A. J. (Eds), The geology of South Australia, Volume 1, The Precambrian, Bulletin 54. Geological Survey of South Australia, Adelaide,106–169

Fontboté, L., 2018. Ore Deposits of the Central Andes. Elements, 14, 257-261.

Foster, A. R., Williams, P. J., Ryan, C. G., 2007. Distribution of gold in hypogene ore at the Ernest Henry iron oxide copper-gold deposit, Cloncurry district, NW Queensland. Exploration and Mining Geology, 16, 125-143.

Fraser, G., McAvaney, S., Neumann, N., Szpunar, M., Reid, A., 2010. Discovery of early Mesoarchean crust in the eastern Gawler Craton, South Australia. Precambrian Research, 179, 1-21.

Frierdich, A. J., Nebel, O., Beard, B. L., Johnson, C. M., 2018. Iron Isotope Exchange and Fractionation between Hematite (α-Fe2O3) and Aqueous Fe(II): A Combined Three-Isotope and Reversal-Approach to Equilibrium Study. Geochimica et Cosmochimica Acta.

Galarza, M. A., Macambira, M. J. B., 2002. Geocronologia e Evolução Crustal da Área do Depósito de Cu-Au Gameleira, Província Mineral de Carajás (Pará), Brasil. Geologia USP Série Científica, 2, 143–159.

Galarza, M.A., Macambira, M.J.B., Villas, R.N., 2008. Dating and isotopic characteristics (Pb and S) of the Fe oxide–Cu–Au–U–REE Igarapé Bahia ore deposit, Carajás mineral province, Pará state, Brazil. J S Am Earth Sci, 25, 377–397.

Garcia, V. B. P., 2018. A raiz do Sistema IOCG de Carajás: alterações hidrotermais e mineralização niquelífera neoarqueana no depósito GT-34. M. Sc. Dissertation, University of Brasilia, Brazil.

Gauthier, M., Chartrand, F., Cayer, A., David, J., 2004. The Kwyjibo Cu-REE-U-Au-Mo-F Property, Quebec: A Mesoproterozoic Polymetallic Iron Oxide Deposit in the Northeastern Grenville Province. Economic Geology, 99, 1177–1196.

Gelcich, S. H., Davis, D. W., Spooner, E. T. C., 2003. New U-Pb ages for host rocks, mineralization and alteration of iron oxide (Cu-Au) deposits in the Coastal Cordillera of northern Chile. In: South American Symposium on Isotope Geology, 4, 63-66.

Gelcich, S., Davis, D. W., Spooner, E. T. C., 2005. Testing the apatite-magnetite geochronometer: U-Pb and 40Ar/39Ar geochronology of plutonic rocks, massive magnetite-apatite tabular bodies, and IOCG mineralization in Northern Chile. Geochim Cosmochim Acta 69, 3367–3384.

George, L. L., Cook, N. J., Crowe, B. B., Ciobanu, C. L. 2018. Trace elements in hydrothermal chalcopyrite. Mineralogical Magazine, 82, 59-88.

Gibbs, A. K., Wirth, K. R., Hirata, W. K., Olszewski, W. J., 1986. Age and composition of the grão pará group volcanics, Serra dos Carajás. Revista Brasileira de Geociências, 16, 201–211.

Gioia, S. M. C. L., 2004. Caracterizaçao da assinatura isotópica de Pb atual na atmosfera e no sistema lacustre do Distrito Federal e pré-antropogênica em Lagoa Feia-GO (Doctoral dissertation, PhD. Dissertation, University of Brasilia, Brazil.

Gioia, S. M. C. L., Pimentel, M. M., 2000. The Sm- Nd isotopic method in the geochronology laboratory of the University of Brasília. Anais da Academia Brasileira de Ciências, 72, 219- 245.

Giovanardi, T., Girardi, V. A., Teixeira, W., Mazzucchelli, M., 2019. Mafic dyke swarms at 1882, 535 and 200 Ma in the Carajás region, Amazonian Craton: SrNd isotopy, trace element geochemistry and inferences on their origin and geological settings. Journal of South American Earth Sciences, 92, 197-208.

Goldsmith, S. D., 2014. The Samphire Project: A distal IOCG and evidence for Mesoarchean crust in the Gawler Craton. PhD. Dissertation, University of Adelaide, Australia.

Gordon, S. C., McDonald, A. M., 2015. A Study of the Composition, Distribution, and Genesis of Pyrrhotite In the Copper Cliff Offset, Sudbury, Ontario, Canada. The Canadian Mineralogist, 53, 859–878.

Govindaraju, G., 1994. Compilation ofworking values and sample description for 383 geostandards. Geostand. Newslett. 18, 1–158

Groves, D. I., Bierlein, F. P., Meinert, L. D., Hitzman, M. W., 2010. Iron oxide copper-gold (IOCG) deposits through Earth history: Implications for origin, lithospheric setting, and distinction from other epigenetic iron oxide deposits. Economic Geology, 105, 641–654.

Grocott, J., Taylor, G. K., 2002. Magmatic arc fault systems, deformation partitioning and emplacement of granitic complexes in the Coastal Cordillera, north Chilean Andes (25 30′ S to 27 00′ S). Journal of the Geological Society, 159, 425-443.

Gulson, B.L., 1986. Lead isotopes in mineral exploration. Elsevier, Amsterdam, 245.

Gupta, A., Yan, D. S., 2016. Mineral processing design and operations: an introduction. Elsevier.

Haldar, S. K., & Haldar, S. K. (2017). Platinum-Nicel-Chromium Deposits.

Hand, M., Reid, A., Jagodzinski, L., 2007. Tectonic framework and evolution of the Gawler Craton, Southern Australia. Economic Geology, 102, 1377-1395.

Hart, S.R., 1984, A large-scale isotope anomaly in the southern hemisphere mantle: Nature 309, 753–757.

Hart, S. R., Gaetani, G. A., 2006. Mantle Pb paradoxes: the sulfide solution. Contributions to Mineralogy and Petrology, 152, 295-308.

Hautmann, S., Witham, F., Christopher, T., Cole, P., Linde, A. T., Sacks, S., Sparks, S. J., 2014. Strain field analysis on Montserrat (W.I.) as tool for assessing permeable flow paths in the magmatic system of Soufriere Hills Volcano. Geochemistry Geophysics Geosystems, 15, 676–690

Hawley, J. E., Nichol, I., 1961. Trace elements in pyrite, pyrrhotite and chalcopyrite of different ores. Economic Geology, 56, 467–487.

Hersum, T., Hilpert, M., Marsh, B., 2005. Permeability and melt flow in simulated and natural partially molten basaltic magmas. Earth and Planetary Science Letters, 237, 798–814.

Hezarkhani, A., Williams-Jones, A. E., Gammons, C. H., 1999. Factors controlling copper solubility and chalcopyrite deposition in the Sungun porphyry copper deposit, Iran. Mineralium deposita, 34, 770-783.

Hickson, C.J., Juras, S.J., 1986. Sample contamination by grinding. Can. Mineral. 24, 585–589.

Hitzman, M.W., Oreskes, N., Einaudi, M.T., 1992. Geological characteristics and tectonic setting of Proterozoic iron oxide (Cu-U-Au-REE) deposits. Precambrian Research, 58, 241–287.

Hoatson, D. M., Sun, S. -S., Duggan, M. B., Davies, M. B., Daly, S. J., Purvis, A. C., 2005. Late Archean Lake Harris Komatiite, central Gawler Craton, South Australia: geologic setting and geochemistry: Economic Geology, 100, 349–374.

Hofmann, A. W., 1997. Mantle geochemistry: the message from oceanic volcanism. Nature 385, 219-229.

Huang, X.-W., Zhou, M.-F., Qiu, Y.-Z., Qi, L., 2015. In-situ LA-ICP-MS trace elemental analyses of magnetite: The Bayan Obo Fe-REE-Nb deposit, North China. Ore Geology Reviews, 65, 884–899.

Huang, Q., Kamenetsky, V. S., McPhie, J., Ehrig, K., Meffre, S., Maas, R., Thompson, J., Kamenetsky, M., Chambefort, I., Apukhtina, O., Hu, Y., 2015. Neoproterozoic (ca. 820–830 Ma) mafic dykes at Olympic Dam, South Australia: Links with the Gairdner Large Igneous Province. Precambrian Research, 271, 160–172.

Huang, X.-W., Boutroy, É., Makvandi, S., Beaudoin, G., Corriveau, L., De Toni, A. F., 2018. Trace element composition of iron oxides from IOCG and IOA deposits: relationship to hydrothermal alteration and deposit subtypes. Mineralium Deposita.

Huang, X. W., Beaudoin, G., 2019. Textures and Chemical Compositions of Magnetite from Iron Oxide Copper-Gold (IOCG) and Kiruna-Type Iron Oxide-Apatite (IOA) Deposits and Their Implications for Ore Genesis and Magnetite Classification Schemes. Economic Geology, 114, 953-979.

Huang, X. W., Boutroy, É., Makvandi, S., Beaudoin, G., Corriveau, L., De Toni, A. F. 2019. Trace element composition of iron oxides from IOCG and IOA deposits: relationship to hydrothermal alteration and deposit subtypes. Mineralium Deposita, 54, 525-552.

Huhn, S. R. B., Macambira, M. J. B, Dall'agnol, R, 1999a. Geologia e geocronologia Pb/Pb do granito alcalino arqueano planalto, região da serra do rabo – Carajás – PA. In: 6th Simpósio de Geologia da Amazônia, Manaus. (Proceedings).

Huhn, S. R. B., Souza, C. D. J., Albuquerque, M. D., Leal, E. D., Brustolin, V., 1999b. Descoberta do depósito Cu (Au) Cristalino: geologia e mineralização associada- região da serra do rabo–Carajás–PA. In: 6th Simpósio de Geologia da Amazônia, Manaus, 140-143.

Hunger, R. B., Xavier, R. P., Moreto, C. P. N., Gao, J. F., 2018. Hydrothermal Alteration, Fluid Evolution, and Re-Os Geochronology of the Grota Funda Iron Oxide Copper-Gold Deposit, Carajás Province (Pará State), Brazil. Economic Geology, 113, 1769-1794.

Huston, D. L., Mernagh, T. P., Hagemann, S. G., Doublier, M. P., Fiorentini, M., Champion, D. C., Jaques, A. L., Cayley, K. C. R., Skirrow, R., Bastrakov, E., 2016. Tectono-metallogenic systems—the place of mineral systems within tectonic evolution, with an emphasis on Australian examples. Ore Geology Reviews, 76, 168–210.

Jacobsen, S. B., Wasserburg, G. J., 1980. Sm-Nd evolution of chondrites. Earth Planet. Sci. Lett. 50, 139-155.

Jaffey, A. H., Flynn, K. F., Glendenin, L. E., Bentley, W. C., Essling, A. M., 1971. Precision measurement of half-lives and specifi c activities of ^{235}U and ^{238}U. Physical Review, C4, 1889–1906

Johansson, C., Barra, F., Reich, M., Deditius, A., Simon, A., Rojas, P., 2018. Trace Elements in Cu-Fe Sulfides from the Mantoverde IOCG Deposit, Northern Chile. In: Metals, Minery, and Society, Society of Economic Geologist, Keystone, CO, USA.

Jonsson, E., Valentin, R. T., Högdahl, K., Harri, C., Weis, F., Nilsson, K. P., Skelton, A., 2013. Magmatic origin of giant 'Kiruna-type' apatite-iron-oxide ores in central Sweden. Scientific Reports, 3.

Jurgan, H., 1977. ZurGliederong der Unterkreide-Serien in der Provinz Atacama, Chile. Geologische Rundschau, 66, 404-434

Kanazawa, Y. A., Koto, K. I., Morimoto, N. O., 1978. Bornite (Cu_5FeS_4); stability and crystal structure of the intermediate form. The Canadian Mineralogist, 16, 397-404.

Kaur, P., Chaudhri, N., Okrusch, M., Koepke, J., 2006. Palaeoproterozoic A-type felsic magmatism in the Khetri Copper Belt, Rajasthan, northwestern India: petrologic and tectonic implications. Mineral. Petrol. 87, 81–122.

Kimball, B. E., 2013. Chalcopyrite-bearer of a precious, non-precious metal. Geology Today, 29, 30–35.

Kiseeva, E. S., Fonseca, R. O., Smythe, D. J., 2017. Chalcophile elements and sulfides in the upper mantle. Elements, 13, 111-116.

Kistler, R. W., McKee, E. H., 1985. A reconnaissance Rb–Sr, Sm– Nd, U–Pb, and K– Ar study of some host rocks and ore minerals in the West Shasta Cu– Zn District, California. Economic Geology, 80, 2128–2135.

Knight, J., Joy, S., Lowe, J., Cameron, J., Merrillees, J., Nag, S., Shah, N., Dua, G., Jhala, K., 2002. The Khetri copper belt, Rajasthan: iron-oxide copper-gold terrane in the Proterozoic of NW India. In: Porter, T. M. (Ed.), Hydrothermal Iron Oxide Copper-Gold & Related Deposits: A Global Perspective. vol. 2. PGC Publishing, Adelaide, 321–341.

Knipping, J. L., Bilenker, L. D., Simon, A. C., Reich, M., Barra, F., Deditius, A. P., Lundstrom, C., Bindeman, I., Munizaga, R., 2015a. Giant Kiruna-type deposits form by efficient flotation of magmatic magnetite suspensions. Geology, 43, 491–594.

Knipping, J. L., Bilenker, L. D., Simon, A. C., Reich, M., Barra, F., Deditius, A. P., Wälle, M., Heinrich, C. A., Holtz, F., Munizaga, R., 2015b. Trace elements in magnetite from massive iron oxide-apatite deposits indicate a combined formation by igneous and magmatic hydrothermal processes. Geochimica et Cosmochimica Acta, 171, 15–38.

Koŝler, J., 1998. Neodymium in igneous rocks. In: Geochemistry. Encyclopedia of Earth Science. Springer, Dordrecht.

Lancaster-Oliveira, J., Fanton, J., Almeida, A. J., Leveille, R. A., Vieira, S., 2000. Discovery and geology of the Sossego copper–gold deposit, Carajás District, Pará State, Brazil. In: IUGS, Intern Geol Congr, 31.

Landtwing, M., Pettke, T., Halter, W., Heinrich, C., Redmond, P., Einaudi, M., Kunze, K., 2005. Copper deposition during quartz dissolution by cooling magmatic–hydrothermal fluids: The Bingham porphyry. Earth and Planetary Science Letters, 235, 229–243.

Lazcano, C. A., Corvalán, S. M. M., 2006. Proyecto Candelaria Norte años 2004-2005. Internal technical report, 40.

Li, Y., Kawashima, N., Li, J., Chandra, A. P., Gerson, A. R., 2013. A review of the structure, and fundamental mechanisms and kinetics of the leaching of chalcopyrite. Advances in Colloid and Interface Science, 197, 1–32.

Li, J.-X., Qin, K.-Z., Li, G.-M., Xiao, B., Zhao, J.-X., Chen, L., 2014. Petrogenesis of Cretaceous igneous rocks from the Duolong porphyry Cu-Au deposit, central Tibet: evidence from zircon U-Pb geochronology, petrochemistry and Sr-Nd-Pb-Hf isotope characteristics. Geological Journal, 51, 285–307.

Li, S., Yang, X., Sun, W., 2015. The Lamandau IOCG deposit, southwestern Kalimantan Island, Indonesia: Evidence for its formation from geochronology, mineralogy, and petrogenesis of igneous host rocks. Ore Geology Reviews, 68, 43–58.

Li, F., Gong, A., Qiu, L., Zhang, W., Li, J., Liu, Y., Liu, Y, Yuan, H., 2017. Simultaneous determination of trace rare-earth elements in simulated water samples using ICP-OES with TODGA extraction/back-extraction. PloS one, 12.

Liles, D. C., Villiers, J. P., 2012. Redetermination of the structure of 5C pyrrhotite at low temperature and at room temperature. American Mineralogist, 97, 257-261.

Liu, J., Liang, C., Zhang, H., Tian, Z., Zhang, S., 2012. General Strategy for Doping Impurities (Ge, Si, Mn, Sn, Ti) in Hematite Nanocrystals. J. Phys. Chem. C, 116, 4986−4992.

Liu, X. Y., Wang, K. X., Chen, J. S., 2016. Template-directed metal oxides for electrochemical energy storage. Energy Storage Materials, 3, 1-17.

Lindenmayer, Z.G., Fleck, A., Gomes, C.H., Santos, A.B.S., Caron, R., Paula, F. de C., Laux, J.H., Pimentel, M.M., Sardinha, A.S., 2005. Caracterização geológica do Alvo Estrela (Cu-Au), Serra dos Carajás, Pará. In: Marini, O.J., Ramos, B.W., Queiroz, E.T., (Eds.). Caracterização de Depósitos Minerais de Distritos Mineiros da Amazônia. Brasília. DNPM-CT-Mineral-FINEP-ADIMB, pp. 137–205.

Lobato, L.M., Rosière, C.A., Silva, R.C.F., Zucchetti, M., Baars, F.J., Seoane, J.C.S., Rios, F.J., Pimentel, M., Mendes, G.E., Monteiro, A.M., 2005. A mineralização hidrotermal de ferro da Província Mineral de Carajás - controle estrutural e contexto na evolução metalogenética da Província. In: Marini J.O., Queiróz, E.T., Ramos, W.B. (Eds.), Caracterização de distritos mineiros da Amazônia. DNPM-CT-Mineral- ADIMB, 25–92 (in Portuguese).

Lorand, J. P., Pont, S., Chevrier, V., Luguet, A., Zanda, B., Hewins, R., 2018. Petrogenesis of martian sulfides in the Chassigny meteorite. American Mineralogist, 103, 872-885.

Lugmair, G.W., and Marti, K., 1978. Lunar initial ^{143}Nd/^{144}Nd: Differential evolution of the lunar crust and mantle: Earth and Planetary Science Letters, 39, 349-357.

Macambira, J.B., 2003. O ambiente deposicional da Formação Carajás e uma proposta de modelo evolutivo para a Bacia Grão Pará. Unpublish, Ph.D. Thesis, Universidade Estadual de Campinas (in Portuguese).

Macambira, E. M. B., Ricci, P. S. F., Anjos, G. C., 2014. Programa Geologia do Brasil - PGB Repartimento - SB.22-X-A Estado do Pará - Carta Geológica Belém: CPRM, Escala 1:250.000.

Machado, N., Lindenmayer, D. H., Krogh, T. E., Lindenmayer, Z.G., 1991. U-Pb geochronology of Archean magmatism and basement reactivation in the Carajás area, Amazon Shield, Brazil. Precambrian Research, 49, 329–354.

Maksaev, V., Munizaga, F., Valencia, V., Barra, F., 2009. LA-ICP-MS zircon U-Pb geochronology to constrain the age of post-Neocomian continental deposits of the Cerrillos Formation, Atacama Region, northern Chile. Andean Geol. 36, 264–287.

Mantoverde Ltda., 2019. Poster information. In: South American Metallogeny: Sierra to Craton, Society of Economic Geologist, Santiago, Chile.

Mark, G., Oliver, N., Williams, H., 2006. Mineralogical and chemical evolution of the Ernest Henry Fe oxide–Cu–Au ore system, Cloncurry district, northwest Queensland, Australia. Mineralium Deposita, 40, 769-801.

Marschik, R., Fontboté, L., 2001a. The Candelaria- Punta del Cobre iron oxide Cu-Au (-Zn-Ag) deposits, Chile. Economic Geology, 96, 1799–1826.

Marschik, R., Fontboté, L., 2001b. The Punta del Cobre Formation, Punta del Cobre–Candelaria area, northern Chile. Journal of South American Earth Sciences, 14, 401-433.

Marschik, R., Fontignie, D., Chiaradia, M., Voldet, P. 2003a. Geochemical and Sr–Nd–Pb–O isotope composition of granitoids of the Early Cretaceous Copiapó plutonic complex (27° 30′ S), Chile. Journal of South American Earth Sciences, 16, 381-398.

Marschik, R., Chiaradia, M., Fontboté, L., 2003b. Implications of Pb isotope signatures of rocks and iron oxide Cu-Au ores in the Candelaria-Punta del Cobre district, Chile. Mineralium Deposita, 38, 900-912.

Marschik, R., Spangenberg, J. E., Leveille, R. A., and de Almeida, A.J., 2003, The Sossego iron oxide-Cu-Au deposit, Carajás, Brazil. In: Eliopoulos, D. et al. (Ed), Mineral Exploration and Sustainable Development, 1, Rotterdam, Millpress, 331–334.

Marschik, R., Mathur, R., Ruiz, J., Leveille, R., Almeida, A. J., 2005. Late Archean Cu-Au-Mo mineralization at Gameleira and Serra Verde, Carajás mineral province, Brazil: Constraints from Re-Os molybdenite ages: Mineralium Deposita, 39, 983–991.

Marschik, R., Söllner, F., 2006. Early cretaceous U-Pb zircon ages for the Copiapó plutonic complex and implications for the IOCG mineralization at Candelaria, Atacama Region, Chile. Miner. Deposita 41, 785–801.

Marschik, R., Kendrick, M. A., 2015. Noble gas and halogen constraints on fluid sources in iron oxide-copper-gold mineralization: Mantoverde and La Candelaria, Northern Chile. Mineralium Deposita, 50, 357-371.

Mathur, R., Marschik, R., Ruiz, J., Munizaga, F., Leveille, R., 2002. Age of mineralization of the Candelaria Fe-oxide Cu-Au deposit and the origin of the Chilean iron belt, based on Re-Os isotopes. Econ. Geol. 97, 59–71.

Martínez, F., Arriagada, C., Peña, M., del Real, I., Deckart, K., 2013. The structure of the Chañarcillo Basin: an example of tectonic inversion in the Atacama region, northern Chile. J. S. Am. Earth Sci. 42, 1–16.

Martínez, F., Arriagada, C., Peña, M., Deckart, K., Charrier, R., 2016. Tectonic styles and crustal shortening of the Central Andes "Pampean" flat-slab segment in northern Chile (27–29 S). Tectonophysics, 667, 144-162.

Martinelli, A., Lepore, G. O., Bernardini, F., Giaccherini, A., Di Benedetto, F., 2018. The puzzling structure of Cu_5FeS_4 (bornite) at low temperature. Acta Crystallographica Section B: Structural Science, Crystal Engineering and Materials, 74.

Martins, P. L. G., Toledo, C. L. B., Silva, A. M., Chemale Jr, F., Santos, J. O. S., Assis, L. M., 2017. Neoarchean magmatism in the southeastern Amazonian Craton, Brazil: Petrography, geochemistry and tectonic significance of basalts from the Carajás Basin. Precambrian Research, 302, 340–357.

McAvaney, S., 2012. The Cooyerdoo Granite: Paleo-and Mesoarchean basement of the Gawler Craton. Age (Ma), 90, 80.

McPhie, J., Orth, K., Kamenetsky, V., Kamenetsky, M., Ehrig, K., 2016. Characteristics, origin and significance of Mesoproterozoic bedded clastic facies at the Olympic Dam Cu–U–Au–Ag deposit, South Australia. Precambrian Research, 276, 85-100.

Meirelles, M.R., Dardenne, M.A., 1991. Vulcanismo basáltico de afinidade shoshonítica e ambiente de arco arqueano, Grupo Grão-Pará, Serra dos Carajás, Pará. Revista Brasileira de Geociências, 21, 41–50 (in Portuguese).

Melfi, A. J., Misi, A., de Almeida Campos, D., Cordani, U. G., 2016. Recursos minerais no Brasil. Problemas e desafios. Academia Brasileira de Ciências, Rio de Janeiro, 417.

Melo, G. H. C., 2018. Temporal evolution and sources of fluids of the Salobo and Igarapé Bahia IOCG deposits, Carajás Province: Evolução temporal e fonte de fluidos dos depósitos IOCG Salobo e Igarapé Bahia, Província Carajás. PhD. Thesis, Universidade Estadual de Campinas, Brazil.

Melo, G.H.C., Monteiro, L.V.S., Xavier, R.P., Moreto, C.P.N., Santiago, É.S.B., Dufrane, S.A., Aires, B., Santos, A.F.F., 2017. Temporal evolution of the giant Salobo IOCG deposit, Carajás Province (Brazil): constraints from paragenesis of hydrothermal alteration and U-Pb geochronology. Miner. Deposita 52, 733–746.

Melo, G. H. C., Monteiro, L. V. S., Xavier, R. P., Moreto, C. P. N., Arquaz, R. M., Silva, M. A. D., 2019a. Evolution of the Igarapé Bahia Cu-Au deposit, Carajás Province (Brazil): early syngenetic chalcopyrite overprinted by IOCG mineralization. Ore Geology Reviews, 102993.

Melo, G. H., Monteiro, L. V., Xavier, R. P., Moreto, C. P., Santiago, E. 2019b. Tracing Fluid Sources for the Salobo and Igarapé Bahia Deposits: Implications for the Genesis of the Iron Oxide Copper-Gold Deposits in the Carajás Province, Brazil. Economic Geology, 114, 697-718.

Melo, G. H. C., Xavier, R. P., Toledo, P. I. F., 2019c. IOCG Systems of the Carajás Province, Amazon Craton, Northern Brazil. Guidebook SEG Conference Field Trip September 29–October 4, 2019.

Mellito, K. M., 1998. Aplicações dos sistemas Rb- Sr, Pb-Pb e Sm-Nd no depósito polimetálico do Salobo 3A, Província Mineral de Carajás, Pará. Doctoral dissertation, Universidade de São Paulo, Brazil.

Misra, K. C., 2012. Introduction to geochemistry: principles and applications. John Wiley & Sons.

Monteiro, L. V. S., Xavier, R. P., Hitzman, M. W., Juliani, C., de Souza Filho, C. R., Carvalho, E. R., 2008a. Mineral chemistry of ore and hydrothermal alteration at the Sossego iron oxide–copper–gold deposit, Carajás Mineral Province, Brazil. Ore Geology Reviews, 34, 317–336.

Monteiro, L. V., Xavier, R. P., de Carvalho, E. R., Hitzman, M. W., Johnson, C. A., de Souza Filho, C. R., Torresi, I., 2008b. Spatial and temporal zoning of hydrothermal alteration and mineralization in the Sossego iron oxide–copper–gold deposit, Carajás Mineral Province, Brazil: paragenesis and stable isotope constraints. Mineralium Deposita, 43, 129-159.

Monteiro, L. V. S., Xavier, R. P., Souza Filho, C. R. D., Moreto, C. P. N., 2014. Metalogênese da província Carajás. Metalogênese das províncias tectônicas brasileiras, 43–84.

Moreto, C. P. N., Monteiro, L. V. S., Xavier, R. P., Creaser, R. A., DuFrane, A. S., Tassinari, C. C. G., Sato, K., Kemp, A. I. S., Amaral, W. S., 2015a. Neoarchean and Paleoproterozoic iron oxide-copper-gold events at the Sossego Deposit, Carajás Province, Brazil: Re-Os and U-Pb geochronological evidence. Econ Geol, 110, 809–835.

Moreto, C. P., Monteiro, L. V., Xavier, R. P., Creaser, R. A., DuFrane, S. A., Melo, G. H., Silva, M. A. D., Tassinari, C. C. G., Sato, K., 2015b. Timing of multiple hydrothermal events in the iron oxide–copper–gold deposits of the Southern Copper Belt, Carajás Province, Brazil. Mineralium Deposita, 50, 517-546.

Morimoto, N., 1964. Structure of two polymorphic forms of Cu5FeS4. Acta Crystallographica, 17(4), 351-360.

Morrissey, L. J., Barovich, K. M., Hand, M., Howard, K. E., Payne, J. L., 2019. Magmatism and metamorphism at ca. 1.45 Ga in the northern Gawler Craton: The Australian record of rifting within Nuna (Columbia). Geoscience Frontiers, 10, 175-194.

Mougeot, R., Respaut, J. P., Briqueu, L., Ledru, P., Milesi, J. P., Macambira, M. J. B., Huhn, S. B., 1996a. Geochronological constrains for the age of the Águas Claras Formation (Carajás Province, Pará, Brazil). In: Congresso Brasileiro de Geologia, 39, Salvador, Anais, 6, 579–581.

Mourgues, F.A., 2004. Advances in ammonite biostratigraphy of the marine Atacama basin (Lower Cretaceous), northern Chile, and its relationship with the Neuquén basin, Argentina. J S Am Earth Sci, 17, 3–10.

Mourgues, F. A., Bulot, L. G., Frau, C., 2015. The Valanginian Olcostephaninae Haug, 1910 (Ammonoidea) from the Andean Lower Cretaceous Chañarcillo Basin, Northern Chile. Andean Geology, 42, 213-236

Mougeot, R., Respaut, J. P., Briqueu, L., Ledru, P., Milesi, J. P., Lerouge, C., Marcoux, E., Huhn, S. B., Macambira, M. J. B., 1996b. Isotope geochemistry constrains for Cu, Au mineralizations and evolution of the Carajás Province (Pará, Brazil). In: Congresso Brasileiro de Geologia, 39, Salvador, Anais.

Mpodozis, C., Ramos, V., 1990. The Andes of Chile and Argentina. In: Ericksen, G.E., Cañas-Pinochet, M.T., Reinemund, J.A. (Eds), Geology of the Andes and its relation to hydrocarbon and mineral resources. Houston, Texas, Circum-Pacific Council for Energy and Mineral Resources, Earth. Sciences Series, v. 11, p. 59–91.

Mukherjee, R., Venkatesh, A. S., Fareeduddin., 2017. Chemistry of magnetite-apatite from albitite and carbonate-hosted Bhukia Gold Deposit, Rajasthan, western India – An IOCG-IOA analogue from Paleoproterozoic Aravalli Supergroup: Evidence from petrographic, LA-ICP-MS and EPMA studies. Ore Geology Reviews, 91, 509–529.

Müller, D., Groves, D. I.,2019. Direct Associations Between Potassic Igneous Rocks and Copper–Gold Deposits on Craton Margins. In Potassic Igneous Rocks and Associated Gold-Copper Mineralization, Springer, Cham, 255-277.

Nadoll, P., Angerer, T., Mauk, J. L., French, D., Walshe J., 2014. The chemistry of hydrothermal magnetite: a review. Ore Geol Rev, 16, 1–32.

Nebel, O., Scherer, E. E., Mezger, K., 2011. Evaluation of the ^{87}Rb decay-constant by age comparison against the U–Pb system. Earth and Planetary Sci. Letters, 301, 1-8.

Negrão, M. M., 2008. Caracterização geológica e metalogenética da ocorrência de Cu-Au (Mo-Co), do Grupo Rio Novo, no contato S-SE com o Granito Cigano, Província Mineral de Carajás. M. Sc. Dissertation, University of Brasilia, Brazil.

Neves, M.P., 2006. Estudos isotópicos (Pb-Pb, Sm-Nd, C e O) do depósito Cu-Au do Sossego, Província Mineral de Carajás: Unpublished M.Sc. Thesis, Universidade Federal do Pará, Brazil.

Ni, Z. Y., Chen, Y. J., Li, N., Zhang, H., 2012. Pb–Sr–Nd isotope constraints on the fluid source of the Dahu Au–Mo deposit in Qinling Orogen, central China, and implication for Triassic tectonic setting. Ore Geology Reviews, 46, 60-67.

Nogueira, A. C. R., Truckenbrodt, W., Costa, J. B. S., Pinheiro, R. V. L., 1994. Analise faciologica e estructural da formação Aguas Claras, Pre-cambriano da Serra dos Carajás. In: IV Simpósio de Geologia da Amazônia. Belém, SBG, 363.

Norman, D. I., Landis, G. P., 1983. Source of ineralizing components in hydrothermal ore fluids as evidenced by ^{87}Sr/^{86}Sr and stable isotope data from the Pasto Bueno Deposit, Peru. Economic Geology, 78, 451–465.

Nyström, J. O., Henríquez, F., 1994. Magmatic features of iron ores of the Kiruna-type in Chile and Sweden: Ore textures and magnetite geochemistry. Economic Geology, 89, 820–839.

Nyström, J. O., Billström, K., Henríquez, F., Fallick, A. E., Naslund, H. R., 2008. Oxygen isotope composition of magnetite in iron ores of the Kiruna type in Chile and Sweden. Geologiska Föreningen, 130,177–188.

O'Brien, S., 2016. Structural and Mineralogical Controls on the Formation of the 'Inter-lens' at the Ernest Henry Deposit, Queensland. BSc honours thesis, Adelaide University.

Oliveira, R. G., 2018. Insights on the framework of the Carajás Province, Amazonian Craton, Brazil, and on the three-dimensional shape of the Carajás Basin, based on gravity data. Journal of the Geological Survey of Brazil, 1, 101–112.

Oliveira, V. E. S., Oliveira, D. C., Marangoanha, B., Lamarão, C. N., 2018. Geology mineralogy and petrological affinities of the Neoarchean granitoids from the central portion of the Canaã dos Carajás domain, Amazonian craton, Brazil. J S Am Earth Sci, 85, 135–159.

Olszewski, W. J., Wirth, K. R., Gibbs, A. K., Gaudette, H. E., 1989. The age, origin, and tectonics of the Grão Pará Group and associated rocks, Serra dos Carajás, Brazil: Archean continental volcanism and rifting. Precambrian Research, 42, 229–254.

Oreskes, N., Einaudi, M. T., 1990. Origin of rare-earth element-enriched hematite breccias at the Olympic-Dam Cu-U-Au-Ag Deposit, Roxby Downs, South Australia. Econ Geol, 85, 1–28.

Oyarzun, R., Rodriguez, M., Pincheira, M., Doblas, M., Helle, S., 1999. The Candelaria (Cu- Fe-Au) and Punta del Cobre (Cu-Fe) deposits (Copiapó, Chile): a case for extension-related granitoid emplacement and mineralization processes?. Mineralium Deposita, 34, 799–801.

Page, R. W., Sun, S., 1998. Aspects of geochronology and crustal evolution in the Eastern Fold Belt, Mt Isa Inlier. Aust J Earth Sci, 45, 343–361.

Peng, B., Frei, R., Tu, X., 2006. Nd–Sr–Pb isotopic geochemistry of scheelite from the Woxi W–Sb– Au Deposit, Western Hunan: implications for sources and evolution of ore-forming fluids. Acta Geol. Sin., 80, 561–570 (in Chinese with English Abstract).

Pérez-Flores, P., Sánchez, M. 2018a.Structural controls on mineralization in Candelaria Norte mine. Unpublished internal poster.

Pérez-Flores, P., Sánchez, M. 2018b.Structural controls on mineralization in Alcaparrosa mine. Unpublished internal poster.

Pérez-Flores, P., Sánchez, M. 2019c. Structural controls on mineralization in Santos mine. Unpusblished internal poster.

Pidgeon, R. T., Macambira, M. J. B., Lafon, J. M., 2000. Th–U–Pb isotopic systems and internal structures of complex zircons from an enderbite from the Pium Complex, Carajás Province, Brazil: evidence for the ages of granulite facies metamorphism and the protolith of the enderbite. Chemical Geology, 166, 159– 171.

Piccinin, S., 2019. The band structure and optical absorption of hematite (α-Fe2O3): a first-principles GW-BSE study. Physical Chemistry Chemical Physics.

Pimentel, M. M., Lindenmayer, Z. G., Laux, J. H., Armstrong, R., Araújo, J. C., 2003. Geochronology and Nd geochemistry of the Gameleira Cu-Au deposit, Serra dos Carajás, Brazil: 1.8–1.7 Ga hydrothermal alteration and mineralization: Journal of South American Earth Sciences, 15, 803–813.

Pinheiro, R. V. L., Kadekaru, K., Soares, A. V., Freitas, C., Ferreira, S. N., Matos, F. M. V., 2013. Carajás, Brazil – A short tectonic review. In: 13th Simpósio de Geologia da Amazônia, Belém.

Pollard, P. J., 2006. An intrusion-related origin for Cu-Au mineralization in iron oxide copper-gold (IOCG) provinces. Mineral. Deposita, 41, 179–187.

Pollard, P. J., Taylor, R. G., Peters, L., Matos, F., Freitas, C., Saboia, L., Hunh, S., 2018. ^{40}Ar-^{39}Ar dating of Archean iron oxide Cu-Au and Paleoproterozoic granite-related Cu-Au deposits in the Carajás Mineral Province, Brazil: implications for genetic models. Miner Depos 1–18.

Pop, N., Heaman, L., Edelstein, O., Isache, C., Zentilli, M., Pecskay, Z., Valdman, S., Rusu, C., 2000. Geocronologia de las rocas igneas y los productos de alteracion hidrotermal relacionados con la mineralization de Cu–Fe (Au) del sector Adriana–Carola–Cobriza (parte este del distrito Punta del Cobre – Candelaria), en base a dataciones Upb (en circon). In: IX Congreso Geologico Chileno, Puerto Varas, Chile Extended Abstract.

Rand, D. A. J., 1977. Oxygen reduction of sulphide minerals: Part III: Comparison of activities of various copper, iron, lead and nickel mineral electrodes. Journal of Electroanalytical Chemistry, 83, 19–32.

Reeve, J. S., Cross, K. C., Smith, R. N., Oreskes, N., 1990. Olympic Dam copper–uranium–gold–silver deposit. In F. E. Hughes (Ed), Geology of the mineral deposits of Australia and Papua New Guinea, Australasian Institute of Mining and Metallurgy, 14, 1009– 1035.

Reich, M., Simon, A.C., Deditius, A., Barra, F., Chryssoulis, S., Lagas, G., Tardani, D., Knipping, J., Bilenker, L., Sanchez-Alfaro, P., Roberts, M.P., Munizaga, R., 2016. Trace element signature of pyrite from the Los Colorados iron oxide-apatite (IOA) deposit, Chile: A missing link between Andean IOA and iron oxide copper-gold systems?: Economic Geology, 111, 743–761.

Reid, A., Hand, M., Jagodzinski, E., Kelsey, D., Pearson, N.J., 2008. Paleoproterozoic orogenesis in the southeastern Gawler craton, South Australia. Australian Journal of Earth Sciences, 55, 449–471.

Reid, A. J., Fricke, C., Cowley, W. M. 2009. Extent of the low-grade Archaean Devils Playground Volcanics in the north-eastern Gawler Craton: Evidence from recent PACE drilling. MESA J. 54, 9–19.

Reid, A. J., Jourdan, F., Jagodzinski, E. A., 2017. Mesoproterozoic fluid events affecting Archean crust in the northern Olympic Cu–Au Province, Gawler Craton: insights from 40Ar/39Ar thermochronology. Australian Journal of Earth Sciences, 64, 103-119.

Reid, A., 2019. The Olympic Cu-Au Province, Gawler Craton: a review of the lithospheric architecture, geodynamic setting, alteration systems, cover successions and prospectivity. Minerals, 9, 371.

Réquia, K., Stein, H., Fontboté, L., Chiaradia, M., 2003, Re-Os and Pb-Pb geochronology of the Archean Salobo iron oxide copper-gold deposit, Carajás Mineral Province, northern Brazil: Mineralium Deposita, 38, 727–738.

Reynolds, L. J., 2000. Geology of the olympic dam Cu-U-Au-Ag-REE deposit. In: Porter, T. M. (Ed). Hydrothermal iron oxide copper-gold and related deposits: A global perspective, 1, 93-104.

Richards, J. P., López, G. P., Zhu, J. J., Creaser, R. A., Locock, A. J., Mumin, A. H., 2017. Contrasting tectonic settings and sulfur contents of magmas associated with cretaceous porphyry Cu±Mo±Au and intrusion-related iron oxide Cu-Au deposits in Northern Chile. Economic Geology, 112, 295–318.

Richards, J. P., Mumin, A. H., 2013. Lithospheric fertilization and mineralization by arc magmas: Genetic links and secular differences between porphyry copper±molybdenum±gold and magmatic hydrothermal iron oxide copper-gold deposits. Society of Economic Geologists Special Publication, 17, 277–299.

Rieger, A. A., Marschik, R., Díaz, M., Hölzl, S., Chiaradia, M., Akker, B., Spangenberg, J. E., 2010. The hypogene IOCG mineralization in the Mantoverde district, northern Chile. Economic Geology, 105, 1271–1299.

Rieger, A. A., Marschik, R., Díaz, M., 2012. The evolution of the hydrothermal IOCG system in the Mantoverde district, northern Chile: new evidence from microthermometry and stable isotope geochemistry. Mineral Deposits, 47, 359–369.

Ronzê, P. C., Soares, A. D., Santos, M. D., Barreira, C. F., 2000. Alemão copper-gold (U-REE) deposit, Carajás, Brazil. Hydrothermal iron oxide copper-gold & related deposits: a global perspective. Australian Mineral Foundation, Adelaide, 191-202.

Rossel, P., Oliveros, V., Ducea, M. N., Charrier, R., Scaillet, S., Retamal, L., Figueroa, O., 2013. The Early Andean subduction system as an analog to island arcs: Evidence from across-arc geochemical variations in northern Chile. Lithos, 179, 211-230.

Rudnick, R. L., Gao, S., 2003. Composition of the continental crust. In: Rudnick, R. L. (Ed), The crust, 3, 1–64.

Sabet-Mobarhan-Talab, A., Alinia, F., Ghannadpour, S.-S., Hezarkhani, A., 2015. Geology, geochemistry, and some genetic discussion of the Chador-Malu iron oxide-apatite deposit, Bafq District, Central Iran. Arabian Journal of Geosciences, 8, 8399–8418.

Sánchez, M., 2018. Marco Estructural para la Exploración del Depósitos tipo IOCG del Distrito Candelaria -Punta del Cobre Tierra Amarilla, Chile. Unpublished Internal report, 1-138.

Sanhueza, A., Robles, W., 1999. Estudio Estructural del Distrito Mantoverde: Informe Final. Internal Report. Anglo American – Chile, Santiago.

Santos, M.G .S., 2002. Estudo dos isótopos de Pb e Nd do depósito de Cu- Au (U-ETR) Alemão, Província Mineral de Carajás (PA). M. Sc. Thesis, Federal University of Pará, Brazil.

Santos, J. O. S., 2003. Geotectônica do Escudo das Guianas e Brasil-Central. In: Bizzi, L. A., Schobbenhaus, C., Vidotti, R. M., Gonçalves, J. H., (Eds), Geologia, Tectônica e Recursos Minerais do Brasil. CPRM – Serviço Geológico do Brasil, Brasília, pp 169–226.

Sardinha, A. S., Dall'Agnol, R., Gomes, A. C. B., Macambira, M. J. B., Galarza, M. A., 2004. Geocronologia Pb–Pb e U–Pb em zircão de granitóides arqueanos da região de Canaã dos Carajás, Província Mineral de Carajás. Congresso Brasileiro de Geologia, 42. CDrom (in Portuguese).

Sardinha, A. S., Barros, C. E. M., Krymsky, M., 2006. Geology, geochemistry and U–Pb geochronology of the Archean (2.74 Ga) Serra do Rabo granite stocks, Carajás Metalogenetic Province, northern Brazil. J S Am Earth Sci, 20, 327–339.

Scheuber, E., Andriessen, P. A. M., 1990, The kinematic and geodynamic significance of the Atacama fault zone, northern Chile: Journal of Structural Geology, 12, 243–257.

Schuessler, J. A., Schoenberg, R., Behrens, H., Von Blanckenburg, F., 2007. The experimental calibration of the iron isotope fractionation factor between pyrrhotite and peralkaline rhyolitic melt. Geochimica et Cosmochimica Acta, 71, 417–433.

Segerstrom, K., 1960. Cuadrángulo Quebrada Paipote, Provincia de Atacama. Instituto de Investigaciones Geológicas.

Segerstrom, K., Parker, R.L., 1959. Cuadrángulo Cerrillos, Provincia de Atacama. Instituto de Investigaciones Geológicas, Chile.

Segerstrom, K., Ruiz, C., 1962. Geología del Cuadrángulo Copiapó, Provincia de Atacama. Instituto de Investigaciones Geológicas, Chile.

Sillitoe, R. M., Burrows, D. R., 2002. New field evidence bearing on the origin of the El Laco magnetite deposit, northern Chile. Economic Geology, 97, 1101–1109.

Sillitoe, R. H., 2003. Iron oxide-copper-gold deposits: an Andean view. Mineralium Deposita, 38, 787-812. Simonetti, A., Bell, K., 1995. Nd, Pb, and Sr isotope systematics of fluorite at the Amba Dongar carbonatite complex, India: evidence for hydrothermal and crustal fluid mixing. Economic Geology, 90, 2018–2027.

Silva, M. G., Teixeira, J. B. G., Pimentel, M. M., Vasconcelos, P. M., Arielo, A., Rocha, W. J. S. F., 2005. Geologia e mineralizações de Fe-Cu-Au do Alvo GT46 (Igarapé Cinzento, Carajás. In: Marini, O. J., Queiroz, E. T., Ramos, B. W. (Eds), Caracterização de Depósitos Minerais em Distritos Mineiros da Amazônia, 1st ed.: ADIMB/DNPM, 94–151.

Silva, A. R. C., Villas, R. N. N., Lafon, J. M., Craveiro, G. S., 2012. Idade da alteração e mineralização do depósito de Cu-Au Visconde, Província Mineral de Carajás (Pará), Brasil: Congresso Brasileiro de Geologia, 46th, Brazil, September 30-October 6, 2012, Proceedings, 1–2.

Silva, L. R., Oliveira, D. C., dos Santos, M. N. S., 2018. Diversity, origin and tectonic significance of the Mesoarchean granitoids of Ourilândia do Norte, Carajás Province (Brazil). J S Am Earth Sci, 82, 33–61.

Silva, F. R. C., Lobato, L. M., Zucchetti, M., Hagemann, S., Venemann, T., 2020. Geotectonic signature and hydrothermal alteration of metabasalts under- and overlying the giant Serra Norte iron deposits, Carajás Mineral Province. Ore Geology Reviews, 103407.

Simon, A. C., Knipping, J., Reich, M., Barra, F., Deditius, A. P., Bilenker, L., Childress, T., 2018. Kiruna-type iron oxide-apatite (IOA) and iron oxide copper-gold (IOCG) deposits form by a combination of igneous and magmatic-hydrothermal processes: evidence from the Chilean Iron Belt.

Simonetti, A., Bell, K., 1995. Nd, Pb, and Sr isotope systematics of fluorite at the Amba Dongar carbonatite complex, India: evidence for hydrothermal and crustal fluid mixing. Economic Geology, 90, 2018–2027.

Skirrow, R. G. 2010. Hematite-group. IOCG+ U ore systems: Tectonic settings, hydrothermal characteristics, and Cu-Au and U mineralizing processes: Geological Association of Canada Short Course Notes, 20, 39–59.

Skirrow, R. G., 2016. Lithospheric and tectonic settings of IOCG systems in Australia. In: 35th International Geological Congress, Cape Town, South Africa, 905.

Skirrow, R. G., Bastrakov, E. N, Baroncii, K., Fraser, G. L., Creaser, R. A., Fanning, C. M., Raymond, O. L., Davidson, G. J., 2007. Timing of iron oxide Cu-Au-(U) hydrothermal activity and Nd isotope constraints on metal sources in the Gawler craton, south Australia. Econ Geol, 102, 1441-1470.

Skirrow, R. G., van der Wielen, S. E., Champion, D. C., Czarnota, K., Thiel, S., 2018. Lithospheric architecture and mantle metasomatism linked to iron oxide Cu-Au ore formation: Multidisciplinary evidence from the Olympic Dam Region, South Australia. Geochemistry, Geophysics, Geosystems, 19, 2673–2705.

Skirrow, R. G., Murr, J., Schofield, A., Huston, D. L., van der Wielen, S., Czarnota, K., Coghlan, R., Highet, L. M., Connolly, D., Doublier, M., Duan, J., 2019. Mapping iron oxide Cu-Au (IOCG) mineral potential in Australia using a knowledge-driven mineral systems-based approach. Ore Geology Reviews, 1–42.

Soares, A. D. V., Macambira, M. J. B., Santos, M. G. S., Vieira, E. A. P., Massoti, F. S., Souza, C. I. J., Padilha, J. L., Magni, M. C. V., 2001. Depósito Cu-(Au) Cristalino, Serra dos Carajás, PA: Idade da mineralização com base em análises Pb-Pb em sulfetos (dados preliminares): Simpósio de Geologia da Amazônia, 7th, Brazil, November 4–9, 2001, Proceedings, 108–111.

Souza, S. Z., Dall'Agnol, R., Althoff, F. J., Leite, A. A. S., Barros, C. E. M., 1996. Carajás mineral province: geological, geochronological and tectonic constrasts on the Archean evolution of the Rio Maria granite-greenstone Terrain and the Carajás block. In: Symposium on Archean Terranes of South America Platform, Extended abstracts. Brasília, SBG, 31-32.

De Souza, S. R. C., Botelho, N. F., Dantas, E. L., Cuadros Jiménez, F. A., Reis, M. A., Viana, C. S. 2020. Geochemistry and isotopic geology of the Lagoa Seca gold deposit in the Andorinhas greenstone-belt, Carajás Province, Brazil. Journal of South American Earth Sciences, 102523.

Storey, C. D., Smith, M. P., 2017. Metal source and tectonic setting of iron oxide-copper-gold (IOCG) deposits: Evidence from an in-situ Nd isotope study of titanite from Norrbotten, Sweden. Ore Geology Reviews, 81, 1287–1302.

Stracke, A., 2012. Earth's heterogeneous mantle: A product of convection-driven interaction between crust and mantle. Chemical Geology 330-331, 274-299.

Sullivan, E., 2016. Geological Characteristics of the Ernie Junior Iron-Oxide-Copper- Gold Ore Body, Mt Isa Inlier, North West Queensland. BSc honours thesis, Adelaide University.

Sun, S. S., McDonough, W. F., 1989. Chemical and isotopic systematics of oceanic basalts: implications for mantle composition and processes. Geol. Soc. Lond. Spec. Publ. 42, 313–345.

Sun, K., Chen, B., Deng, J., Ma, X., 2018. Source of copper in the giant Shimensi W-Cu-Mo polymetallic deposit, South China: Constraints from chalcopyrite geochemistry and oxygen fugacity of ore-related granites. Ore Geology Reviews.

Swain, G.M., Hand, M., Teasdale, J., Rutherford, L., Clark, C., 2005. Age constraints on terrane-scale shear zones in the Gawler Craton, southern Australia. Precambrian Res. 139, 164–180.

Szpunar, M., Hand, M., Barovich, K., Belousova, E., Jagodzinski, E.A., 2011. Isotopic and geochemical constraints on the Paleoproterozoic Hutchison Group, southern Australia: Implications for Paleoproterozoic continental reconstructions. Precambrian Res, 187, 99–126.

Tallarico, F. H. B., 2003. O cinturão cupro-aurífero de Carajás, Brasil. Unpublished PhD. Dissertation, Universidade Estadual de Campinas.

Tallarico, F. H. B., McNaughton, N. J., Groves, D. I., Fletcher, I. R., Figueiredo, B. R., Carvalho, J. B., Rego, J. I., Nunes, A. R., 2004. Geological and SHRIMP II U-Pb constraints on the age and origin of the Breves Cu-Au-(W-Bi-Sn) deposit, Carajás, Brazil. Miner Depos, 39, 68-86.

Tallarico, F. H. B., Figueiredo, B. R., Groves, D. I., Kositcin, N., McNaughton, N. J., Fletcher, I. R., Rego, J. L., 2005. Geology and SHRIMP U-Pb geochronology of the Igarapé Bahia deposit, Carajás copper-gold belt, Brazil: An Archean (2.57 Ga) example of iron-oxide Cu-Au-(U-REE) mineralization. Economic Geology, 100, 7-28.

Tallarico, F. H. B., de Oliveira, C. G., Figueiredo, B. R., 2017. The Igarapé Bahia Cu-Au mineralization, Carajás Province. Revista Brasileira de Geociências, 30, 230-233.

Tappert, M., Rivard, B., Giles, D., Tappert, R., Mauger, A., 2011. Automated drill core logging using visible and near-infrared reflectance spectroscopy: a case study from the Olympic Dam IOCG deposit, South Australia. Economic Geology, 106, 289-296.

Tassinari, C. C. G., Mellito, K. M., Babinski, M., 2003. Age and origin of the Cu (Au-Mo-Ag) Salobo 3A ore deposit, Carajás Mineral Province, Amazonian Craton, northern Brazil. 26, 1.

Tatsumoto, M., Knight, R. J., Allègre, C. J., 1973. Time differences in the formation of meteorites as determined from the ratio of lead-207 to lead-206. Science, 180, 1279–1283.

Tavares, F.M., 2015. Evolução geotectônica do nordeste da Província Carajás. Unpublish, Ph.D. Thesis, Universidade Federal do Rio de Janeiro (in Portuguese).

Tavares, F. M., Trouw, R. A. J., da Silva, C. M. G., Justo, A. P., Oliveira, J. K. M., 2018. The multistage tectonic evolution of the northeastern Carajás Province, Amazonian Craton, Brazil: Revealing complex structural patterns. Journal of South American Earth Sciences, 88, 238–252.

Taylor, S.R., McLennan, S.M., 1985. The Continental Crust: Its Composition and Evolution. Cambridge, MA, Blackwell Scientific, 312.

Taylor, G., Grocott, J., Daswood, B., Gipson, M., Arévalo, C., 2007. Implications for crustal rotation and tectonic evolution in the Central Andes fore-arc: new paleomagnetic results from the Copiapó region of northern Chile, 26° to 28°S. Journal of Geophysical Research.

Teixeira, J.B.G., 1994. Geochemistry, Petrology, and Tectonic Setting of Archean Basaltic and Dioritic Rocks from the N4 Iron Deposit, Serra dos Carajás, Pará, Brazil. Thesis (Doctor of Philosophy). Department of Geosciences, Penn State University.

Teixeira, J.B.G., Eggler, D.H., 1994. Petrology, geochemistry, and tectonic setting of Archaean basaltic and dioritic rocks from the N4 iron deposit, Serra dos Carajás, Pará, Brazil. Acta Geologica Leopoldensia, 17, 71–114.

Teixeira, N. A., Ganade, C. E., Matos, F. M. V., Campos, L. D., Carvalho, M. T. N., 2015. Alkaline Porphyry Copper Deposits and IOCG–What is the link?. In: Simposio de Geologia da Amazonia, 14, SBG/NO (CD-ROM).

Tessalina, S. G., Herrington, R. J., Taylor, R. N., Sundblad, K., Maslennikov, V. V., Orgeval, J. J., 2016. Lead isotopic systematics of massive sulphide deposits in the Urals: Applications for geodynamic setting and metal sources. Ore Geology Reviews, 72, 22–36.

Toledo, F. P. I., Moreto, C. P. N., Xavier, R. P., Gao, J., de Melo, G. H. C., 2019. Multistage Evolution of the Neoarchean (ca. 2.7 Ga) Igarapé Cinzento (GT-46) Iron Oxide Copper-Gold Deposit, Cinzento Shear Zone, Carajás Province, Brazil. Economic Geology, 114, 1–34.

Torresi, I., Bortholoto, D. F. A., Xavier, R. P., Monteiro, L. V. S., 2012. Hydrothermal alteration, fluid inclusions and stable isotope systematics of the Alvo 118 iron oxide–copper–gold deposit, Carajás Mineral Province (Brazil): implications for ore genesis. Miner Deposita, 47, 299–323.

Trendall, A. F., Basei, M. A. S., De Laeter, J. R., Nelson, D. R., 1988. SHRIMP U-Pb constraints on the age of the Carajás formation, Grão Pará Group, Amazon Craton. J S Am Earth Sci, 11, 265–277.

Tosdal, R. M., Wooden, J. L., Bouse, R. M., 1999. Pb isotopes, ore deposits, and metallogenic terranes. In: Lambert, D. D., Brown, P.E. (Eds.,), Application of radiogenic isotopes to ore deposit research and exploration. Society of Economic Geologists, Littleton, 12, 1–28

Twyerould, S. C., 1997. The Geology and Genesis of the Ernest Henry Fe-Cu-Au Deposit,NWQueensland, Australia. Unpublished Ph.D. Thesis. University of Oregon, Australia.

Valadão, L. V., 2019. Mineralogia e relação textural e microestrutural do minério tipo IOCG da mina do Salobo, Província Mineral de Carajás: revisão da sequência paragenética. M. Sc. Dissertation, University of Brasilia, Brazil.

VALE, 2012. Viabilização da Mina de Cobre do Salobo, do Estratégico ao Tático. Technical Report. SIMEXMIN.

Valenta, R., 2018. NW Queensland Mineral Province Deposit Atlas Prototype Report – the Mount Isa and Ernest Henry Deposits. DNRME-GSQ Commissioned study and report.

Vasquez M.L., Rosa-Costa, L.T., 2008. Geologia e Recursos Mineraisdo Estado do Pará: Sistema de Informações Geográficas – SIG: texto explicativo dos mapas Geológico e Tectônico e de Recursos Minerais do Estado do Pará. Escala 1:1.000.000. CPRM-Serviço Geológico do Brasil, Superintendência Regional de Belém.

Verdugo-Ihl, M. R., Ciobanu, C. L., Cook, N. J., Ehrig, K., Courtney-Davies, L., Gilbert, S., 2017. Textures and U-W-Sn-Mo signatures in hematite from the Cu-U-Au-Ag orebody at Olympic Dam, South Australia: Defining the archetype for IOCG deposits. Ore Geology Reviews, 91, 173–195.

Verdugo-Ihl, M. R., Ciobanu, C. L., Cook, N. J., Ehrig, K. J., Courtney-Davies, L., 2019. Defining early stages of IOCG systems: evidence from iron oxides in the outer shell of the Olympic Dam deposit, South Australia. Mineralium Deposita.

Vila, T., 1996. Geology of the Manto Verde copper deposit, northern Chile: a specularite rich, hydrothermal-tectonic breccia related to the Atacama fault zone. Econ. Geol. Spec. Publ. 5, 157–169.

Volk, M., Feinberg, J. M., McCalla, E., Leighton, C., Voigt, B., 2018. Physical Properties of Phase Pure 4C Pyrrhotite (Fe7S8) during its Low Temperature Besnus Transition. In AGU Fall Meeting Abstracts.

Waight, T., 2013. Rb–Sr Geochronology (Igneous Rocks). Encyclopedia of Scientific Dating Methods, 1–8.

Wasserburg, G. J., Jacobsen, S. B., DePaolo, D. J, McCulloch, M. T., Wen, T., 1981: Precise determination of Sm/Nd ratios, Sm and Nd isotopic abundances in standard solutions Geochim. Cosmochim. Acta 45, 2311–2324.

White, W. M., 2005. Geochemistry. On-line textbook, Cornell University, New York. 700 pp.

Williams, P. J., Barton, M. D., Johnson, D. A., Fontboté, L., De Haller, A., Mark, G., Oliver, N. H. S., Marschik, R., 2005. Iron oxide copper-gold deposits: Geology, space-time distribution, and possible modes of origin. Economic Geology, 371–405.

Wingate, M. T. D., Campbell, I. H., Compston, W., Gibson, G. M., 1998. Ion microprobe U–Pb ages for Neoproterozoic basaltic magmatism in south-central Australia and implications for the breakup of Rodinia. Precambrian Research, 87, 135–159.

Wirth, K.R., Gibbs, A.K., Olszewski, W.J., 1986. U-Pb ages of zircons from the Grão Pará Group and Serra dos Carajás Granite, Pará, Brazil. Rev. Brasil. Geociê. 16, 195–200

Wu, G., Li, X., Xu, L., Wang, G., Liu, J., Zhang, T. Quan, Z., Wu, H., Li, T., Zeng, Q., Chen, Y., 2017. Age, geochemistry, and Sr–Nd–Hf–Pb isotopes of the Caosiyao porphyry Mo deposit in Inner Mongolia, China. Ore Geology Reviews, 81, 706–727.

Wu, C., Chen, H., Hong, W., Li, D., Liang, P., Fang, J., Zhang, L., Lai, C., 2019. Magnetite chemistry and implications for the magmatic-hydrothermal ore-forming process: An example from the Devonian Yuleken porphyry Cu system, NW China. Chemical Geology, 522, 1-15.

Xavier, R.P., Moreto, C.P.N., de Melo, G.H.C., Toledo, P., Hunger, R., Deminardo, M., Faustinoni, J., Lopes, Ananda., 2017. Geology and metallogeny of Neoarchean and Paleoproterozoic copper systems of the Carajás Domain, Amazonian Craton, Brazil.In: Proceedings of the 14th Biennial SGA Meeting of the Society for Geology Applied to Mineral Deposits, Quebec, Canada, 3, 899–902.

Xu, B., Jiang, S.-Y., Luo, L., Zhao, K.-D., Ma, L., 2016. Origin of the granites and related Sn and Pb-Zn polymetallic ore deposits in the Pengshan district, Jiangxi Province, South China: constraints from geochronology, geochemistry, mineral chemistry, and Sr-Nd-Hf-Pb-S isotopes. Mineralium Deposita, 52, 337–360.

Yan, Q.-H., Li, S.-S., Qiu, Z.-W., Wang, H., Wei, X.-P., Pei-Li, Dong, R., Zhang, X.-Y., 2017. Geochronology, geochemistry and Sr–Nd–Hf–S–Pb isotopes of the Early Cretaceous Taoxihu Sn deposit and related granitoids, SE China. Ore Geology Reviews, 89, 350–368.

Yang, J., Zhou, X., 2001. Rb–Sr, Sm–Nd, and Pb isotope systematics of pyrite: implications for the age and genesis of lode gold deposits. Geology, 29, 711–714.

Young, L.E., 1995. Empirical applications of common lead- isotope ratios to explorations: Society of Economic Geologists Newsletter, 22, 1–12.

Yuwang, W., Jingbin, W., Lijuan, W., Yong, W., Caineng, T., 2010. REE Characteristics of the Kalatongke Cu-Ni Deposit, Xinjiang, China. Acta Geologica Sinica - English Edition, 78, 396–403.

Zamora, R., Castillo, B., 2001. Mineralización de Fe–Cu–Au en el distrito Mantoverde, Cordillera de la Costa, III Región de Atacama, Chile. 2nd Congreso Internacional de Prospectores y Exploradores (ProExplo 2001) Lima, Perú, Abstracts (CD-ROM).

Zarei, A., Shafaroudi, A. M., Karimpour, M. H., 2016. Geochemistry and Genesis of Iron-apatite Ore in the Khanlogh Deposit, Eastern Cenozoic Quchan-Sabzevar Magmatic Arc, NE Iran. Acta Geologica Sinica - English Edition, 90, 121–137.

Zartman, R. E., Doe, B. R., 1981. Plumbotectonics-the model. Tectonophysics, 75, 135–162.

Zentilli, M., 1974. Geological evolution and metallogenese relationships in the Andean of northern Chile between 26° and 29° south. PhD. Thesis, Queen’s University, Kingston, Canadá.

Zhang, Z., Zuo, R., 2014. Sr–Nd–Pb isotope systematics of magnetite: implications for the genesis of Makeng Fe deposit, southern China. Ore Geology Reviews, 57, 53–60.

Zhao, J., Brugger, J., Chen, G., Ngothai, Y., Pring, A., 2014. Experimental study of the formation of chalcopyrite and bornite via the sulfidation of hematite: Mineral replacements with a large volume increase. American Mineralogist, 99, 343-354.

Zhu, B.Q., 1998, The theory and application of the isotopic systematic in geoscience concurrent discussion of the continental crust and mantle evolvement in China. Beijing, Science Publishing House, 1–330. (in Chinese with English abstract)

Zindler, A., Hart, S., 1986. Chemical geodynamics. Annual review of earth and planetary sciences, 14, 493-571.

Zuchetti, M., 2007. Rochas máficas do Supergrupo Grão Pará e sua relação com a mineralização de ferro dos depósitos N4 e N5, Carajás, PA. Unpublish. Ph.D. Thesis, Universidade Federal de Minas Gerais, Brazil (in Portuguese).